

FLUIDS ENGINEERING DIVISION

Editor
J. KATZ (2009)
Assistant to the Editor
L. MURPHY (2009)
Associate Editors
M. J. ANDREWS (2009)
S. BALACHANDAR (2008)
A. BESKOK (2008)
S. L. CECCIO (2009)
D. DRIKAKIS (2008)
P. A. DURBIN (2008)
I. EAMES (2010)
A. GOTO (2007)
C. HAH (2009)
T. J. HEINDEL (2007)
H. JOHARI (2009)
J. KOMPENHANS (2009)
Y. T. LEE (2007)
J. A. LIBURDY (2007)
P. LIGRANI (2008)
R. MITTAL (2009)
T. J. O'HERN (2008)
U. PIOMELLI (2007)
S. ROY (2007)
D. SIGINER (2008)
S. P. VANKA (2007)
Y. ZHOU (2008)

PUBLICATIONS COMMITTEE
Chair, **B. RAVANI**

OFFICERS OF THE ASME
President, **T. E. SHOUP**
Executive Director, **V. R. CARTER**
Treasurer, **T. D. PESTORIUS**

PUBLISHING STAFF
Managing Director, Publishing
P. DI VIETRO
Manager, Journals
C. MCATEER
Production Assistant
M. ANDINO

TECHNICAL PAPERS

- 669 **Effect of Hydrofoil Shapes on Partial and Transitional Cavity Oscillations**
Akira Fujii, Damien T. Kawakami, Yoshinobu Tsujimoto, and Roger EA Arndt
- 674 **Influence of Boundary Layer Behavior on Aerodynamic Coefficients of a Swept-Back Wing**
S. C. Yen and C. M. Hsu
- 682 **Numerical Study of the Injection Process in a Transonic Wind Tunnel—Part I: The Design Point**
João B. P. Falcão Filho and Marcos A. Ortega
- 695 **Initial Stage of Natural Convection Over a Hot Aerosol Sphere**
Elaad Mograbi and Ezra Bar-Ziv
- 702 **Gas–Solid Particle Flow in Horizontal Channels: Decomposition of the Particle-Phase Flow and Interparticle Collision Effects**
Alexander Kartushinsky and Efstathios E. Michaelides
- 713 **Numerical Investigation of Liquid-Liquid Coaxial Flows**
Bhadraiah Vempati, Mahesh V. Panchagnula, Alparslan Öztekin, and Sudhakar Neti
- 720 **A Numerical Tool for the Design/Analysis of Dual-Cavitating Propellers**
Y. L. Young and Y. T. Shen
- 731 **Multifrequency Instability of Cavitating Inducers**
Christopher E. Brennen
- 737 **Experimental Investigation of the Fluid Motion in a Cylinder Driven by a Flat-Plate Impeller**
Douglas Bohl
- 747 **Effect of Turbulence Intensity and Periodic Unsteady Wake Flow Condition on Boundary Layer Development, Separation, and Reattachment Along the Suction Surface of a Low-Pressure Turbine Blade**
B. Öztürk and M. T. Schobeiri
- 764 **The Application of an Aerodynamic Shroud for Axial Ventilation Fans**
D. R. Neal and J. F. Foss
- 773 **Observation of Centrifugal Compressor Stall and Surge in Phase Portraits of Pressure Time Traces at Impeller and Diffuser Wall**
Chunwei Gu, Kazuo Yamaguchi, Toshio Nagashima, and Hirotaka Higashimori
- 780 **Modeling of Effect of Inflow Turbulence Data on Large Eddy Simulation of Circular Cylinder Flows**
M. Tutar, I. Celik, and I. Yavuz
- 791 **Development of a New Simulation Technique Based on the Modal Approximation for Fluid Transients in Complex Pipeline Systems With Time-Variant Nonlinear Boundary Conditions**
E. Kojima, T. Yamazaki, and M. Shinada
- 799 **Experimental Leak-Rate Measurement Through a Static Metal Seal**
Christophe Marie and Didier Lasseux

(Contents continued on inside back cover)

This journal is printed on acid-free paper, which exceeds the ANSI Z39.48-1992 specification for permanence of paper and library materials. ©™
♻️ 85% recycled content, including 10% post-consumer fibers.

Transactions of the ASME, Journal of Fluids Engineering (ISSN 0098-2202) is published monthly by The American Society of Mechanical Engineers, Three Park Avenue, New York, NY 10016. Periodicals postage paid at New York, NY and additional mailing offices.

POSTMASTER: Send address changes to Transactions of the ASME, Journal of Fluids Engineering, c/o THE AMERICAN SOCIETY OF MECHANICAL ENGINEERS, 22 Law Drive, Box 2300, Fairfield, NJ 07007-2300.

CHANGES OF ADDRESS must be received at Society headquarters seven weeks before they are to be effective.

Please send old label and new address.

STATEMENT from By-Laws. The Society shall not be responsible for statements or opinions advanced in papers or printed in its publications (B7.1, Par. 3).

COPYRIGHT © 2007 by the American Society of Mechanical Engineers. Authorization to photocopy material for internal or personal use under those circumstances not falling within the fair use provisions of the Copyright Act, contact the Copyright Clearance Center (CCC), 222 Rosewood Drive, Danvers, MA 01923, tel: 978-750-8400, www.copyright.com. Request for special permission or bulk copying should be addressed to Reprints/Permission Department, Canadian Goods & Services Tax Registration #126148048.

TECHNICAL BRIEF

- 806 Cosserrat Modeling of Turbulent Plane-Couette and Pressure-Driven Channel Flows
Amin Moosaie and Gholamali Atefi

ANNOUNCEMENT

- 811 Interested in Cavitation Erosion?

The ASME Journal of Fluids Engineering is abstracted and indexed in the following:

Applied Science & Technology Index, Chemical Abstracts, Chemical Engineering and Biotechnology Abstracts (Electronic equivalent of Process and Chemical Engineering), Civil Engineering Abstracts, Computer & Information Systems Abstracts, Corrosion Abstracts, Current Contents, Ei EncompassLit, Electronics & Communications Abstracts, Engineered Materials Abstracts, Engineering Index, Environmental Engineering Abstracts, Environmental Science and Pollution Management, Excerpta Medica, Fluidex, Index to Scientific Reviews, INSPEC, International Building Services Abstracts, Mechanical & Transportation Engineering Abstracts, Mechanical Engineering Abstracts, METADEX (The electronic equivalent of Metals Abstracts and Alloys Index), Petroleum Abstracts, Process and Chemical Engineering, Referativnyi Zhurnal, Science Citation Index, SciSearch (The electronic equivalent of Science Citation Index), Shock and Vibration Digest, Solid State and Superconductivity Abstracts, Theoretical Chemical Engineering

Akira Fujii

FLUENT Asia Pacific Co., Ltd.,
Nittochi Nishishinnjyuku Bldg. 18F, 6-10-1,
Nishishinnjyuku, Shinjyuku-ku,
Tokyo, 160-0023, Japan
e-mail: fujii@fluent.co.jp

Damien T. Kawakami

St. Anthony Falls Laboratory,
University of Minnesota,
Mississippi River at 3rd Ave.,
Minneapolis, MN 55414
e-mail: kawa0036@umn.edu

Yoshinobu Tsujimoto

Engineering Science,
Osaka University,
1-3 Machikaneyama, Toyonaka,
Osaka, 560-8531, Japan
e-mail: tsujimoto@me.es.osaka-u.ac.jp

Roger EA Arndt

St. Anthony Falls Laboratory,
University of Minnesota,
Mississippi River at 3rd Ave.,
Minneapolis, MN 55414
e-mail: arndt001@umn.edu

Effect of Hydrofoil Shapes on Partial and Transitional Cavity Oscillations

The effects of foil geometry on partial and transitional cavity oscillations were examined by experiments. The transitional cavity oscillation can be observed in the upstream pressure fluctuation for all foils and the amplitude of oscillation becomes larger when the maximum cavity length becomes larger than about 75% of the chord length. The Strouhal number based on the chord length correlated with the value of a parameter $\sigma/2\alpha$ and increased from 0.07 to 0.17 with the increase of $\sigma/2\alpha$ from 2.0 to 6.0 for all foils. For thicker foils, the partial cavity oscillation could not be detected in the upstream pressure fluctuation. However, semi-periodical cavity shedding corresponding to the partial cavity oscillation could be visually observed for all foils and the Strouhal number based on the mean cavity length was about 0.15–0.35 for all foils. Thus, the effect of foil geometry appears only in the strength of partial cavity oscillation. [DOI: 10.1115/1.2734183]

Keywords: cavitation, hydrofoil, oscillation, partial cavity, transitional cavity

1 Introduction

The effect of foil geometry on transitional and partial cavity oscillations was examined from the tests on seven foils with different thickness and nose radius. The transitional cavity oscillation typically occurs for the transition between partial and supercavitation, whereas a partial cavity oscillation is accompanied by cloud cavity shedding and is often simply called cloud cavitation. The observation of the oscillations was made by upstream pressure fluctuation measurements and by visual observations using high-speed video. The transitional cavity oscillation could be observed for all foils with nearly the same frequency. The partial cavity oscillation could be identified from the inlet pressure fluctuations only for thinner foils, but semi-periodical cavity shedding could be observed for all foils. Observation of the flow around thinner foils shows that the noncavitating flow is separated at the test incidence angle $\alpha=8$ deg and bubbly cavitation is observed, whereas for thicker foils the noncavitating flow is attached and a clear sheet cavity was observed. Irrespective of these differences, the Strouhal number was nearly the same for all foils, both for transitional and partial cavity oscillations. Discussions on the cause of those cavitation instabilities are made based on the experimental results.

2 Experimental Apparatus and Procedure

2.1 Experimental Apparatus. The experimental apparatus is shown in Fig. 1. This is a closed-loop tunnel at Osaka University, and the base pressure and, hence, cavitation number are adjusted by using a vacuum pump connected to the top of the pressure control tank. Tap water is used as the working fluid, which is degassed by leaving it at least one night under depressurized condition after circulating it for a certain amount of time. Typical air

content before the test was 3.3 mg/L or 3.5 ppm. The flow rate is measured by an electromagnetic flowmeter placed downstream of a circulating pump. A three-bladed inducer is used as the circulating pump at a flow coefficient $\phi=0.1$. At this flow coefficient, cavitation instabilities are observed only for $\sigma=0.03$. Since the minimum cavitation number in the present experiments is $\sigma=0.07$, any cavitation instability caused by the inducer is avoided. The resonant frequency of the hydraulic system was not measured, but it was confirmed in [1] that the frequency of the transitional cavity oscillation did not depend on the length of the upstream pipe L (L is fixed at 373 mm in the present study), while the frequency of the partial cavity oscillation approximately scaled with $1/\sqrt{L}$ (Franc and Michel [2], for this correlation).

2.2 Test Foils. The seven foils used in the present study are shown in Fig. 2. The foil shape shown in Fig. 2(a) “NACA0015” is the original NACA0015 geometry. “NACA0010 1/2” and “NACA0006,” shown in Figs. 2(b) and 2(c), are of a 70% and 40% thickness of the NACA0015 foil shape, respectively. The foils shown in Figs. 2(d)–2(f) are flat-plate foils with different leading-edge radii. The foil shown in Fig. 2(g) is the CAV2003 foil proposed by Franc and Schnerr [3] for the workshop on numerical comparison of cavitation codes. The chord length is $C=70$ mm for all foils, and the span is also 70 mm. The angle of attack α for flat-plate foils are defined as shown in Fig. 3.

2.3 Experimental Procedure. The height and width of the test section are 70 mm and 100 mm, respectively, as shown in Fig. 1(b). With this ratio of chord length to channel width 70/100, a linear closed-cavity model predicts a minimum at $\sigma/2\alpha=6.1$ and $l/C=0.73$ in a $\sigma/2\alpha-l/C$ plot, while those values for an isolated hydrofoil are $\sigma/2\alpha=5.2$ and $l/C=0.75$. Therefore, the blockage effect is expected to be small. The foils are placed in the test section without clearance on both sides. The leading edge of the test foil is placed 373 mm downstream of the water tunnel nozzle that has a contraction ratio of 4.65. The walls around the test section are made of transparent acrylic resin so that observa-

Contributed by the Fluids Engineering Division of ASME for publication in the JOURNAL OF FLUIDS ENGINEERING. Manuscript received July 12, 2005; final manuscript received January 9, 2007. Review conducted by Georges L. Chahine.

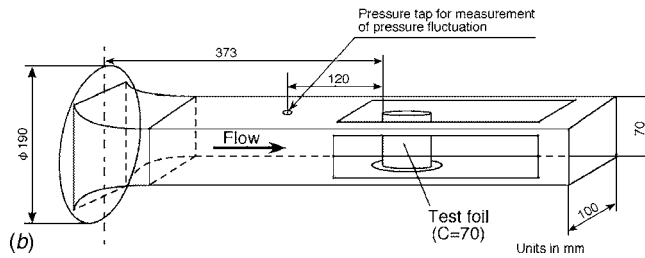
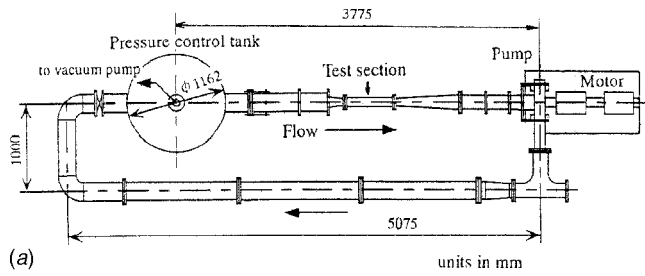


Fig. 1 Test apparatus and test section: (a) test apparatus and (b) test section

tions can be made with a high-speed video camera (4500 fps). The speed of the incoming flow is $U=5$ m/s for all tests, and the cavitation number is controlled by changing the base pressure in the tank. The pressure fluctuations at 120 mm upstream of the leading edge of the foil are measured by a flush-mounted pressure transducer (KYOWA PGM-2KC, strain-gage type) as shown in Fig. 1.

Cavitation number is defined as $\sigma=(p_1-p_v)/(\rho U^2/2)$, where p_1 is the inlet pressure measured at 120 mm upstream of the leading edge of test foil, p_v is the vapor pressure, and ρ is the density of water.

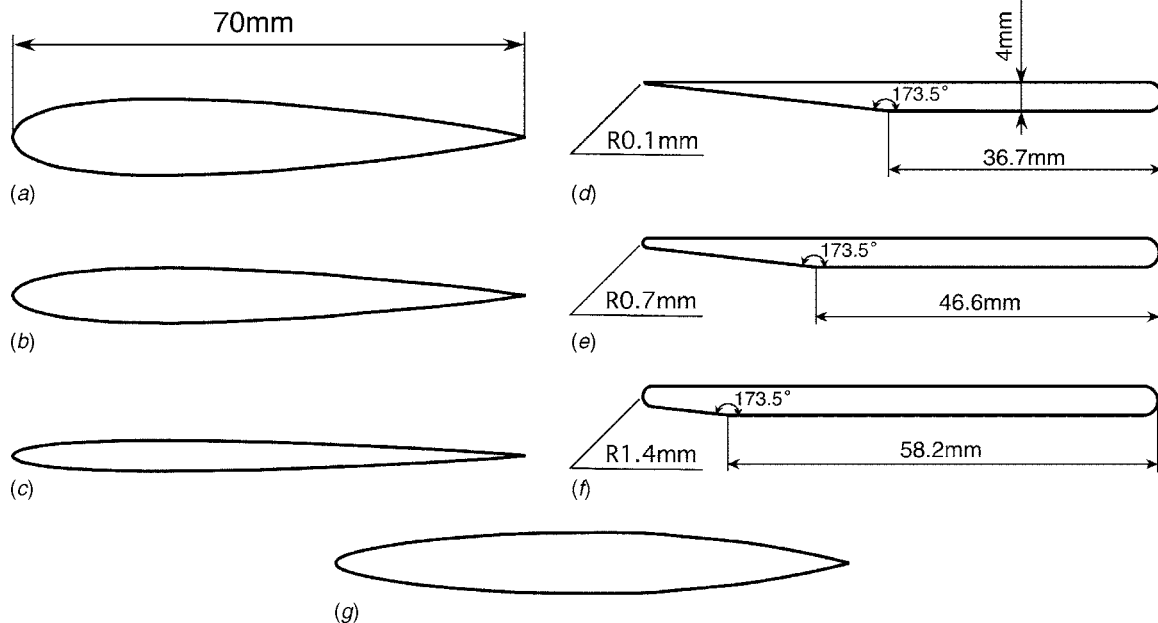


Fig. 2 Foil shapes: (a) NACA0015, (b) NACA0010 1/2, (c) NACA0006, (d) flat plate R0.1, (e) flat plate R0.7, (f) flat plate R1.4, and (g) CAV2003

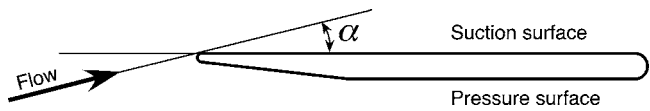


Fig. 3 Angle of attack for flat plate

3 Experimental Results

3.1 Upstream Pressure Fluctuation. In Fig. 4, the spectra of upstream pressure fluctuations for NACA-type foils are shown. The spectra for NACA0010 1/2 were quite similar to those of NACA0015 and omitted here to save space. The angle of attack for these tests is $\alpha=8$ deg. Obvious peaks are observed at about $f=10$ Hz with higher harmonic components in the range of cavitation number $0.8 < \sigma < 1.4$ for all NACA-type foils. This is the transitional cavity oscillation, as will be discussed later. For NACA0006 foil, higher-frequency components corresponding to the partial cavity oscillation can be observed at higher cavitation numbers. The frequency of this component is increasing rapidly with an increase of the cavitation number. Similar results are seen in Kjeldsen et al. [4] and Sato et al. [1]. This component was not observed for NACA0015 and NACA0010 1/2 foils.

The spectra of upstream pressure fluctuations for flat-plate foils are shown in Fig. 5. The spectra for flat plate R0.7 are quite similar to the examples shown and omitted here to save space. In these spectra, obvious peaks of transitional cavity oscillation are found at about $f=10$ Hz. The component corresponding to the partial cavity oscillation is clearer than for NACA0006 foil and can be observed for all flat-plate foils.

The spectra of upstream pressure fluctuation for the CAV2003 foil are shown in Fig. 6. The spectra are not so different from that of the NACA0015 foil. However, the range of cavitation number where pressure oscillations occur is significantly lower, as predicted by Qin's simulations [5]. The results with $\alpha=5$ deg are also shown in Fig. 6(b). In this case, the frequency of the component observed in the spectra is not very different from the case of

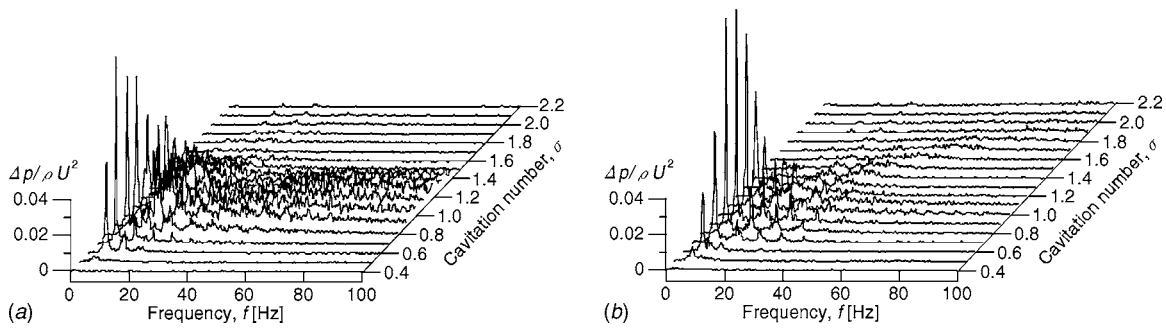


Fig. 4 Spectra of upstream pressure fluctuations for NACA foils, $\alpha=8$ deg (uncertainty in $f: \pm 0.25$ Hz, in $\Delta p/\rho U^2: \pm 0.0005$ in $\alpha: \pm 0.25$ deg): (a) NACA0015 and (b) NACA0006

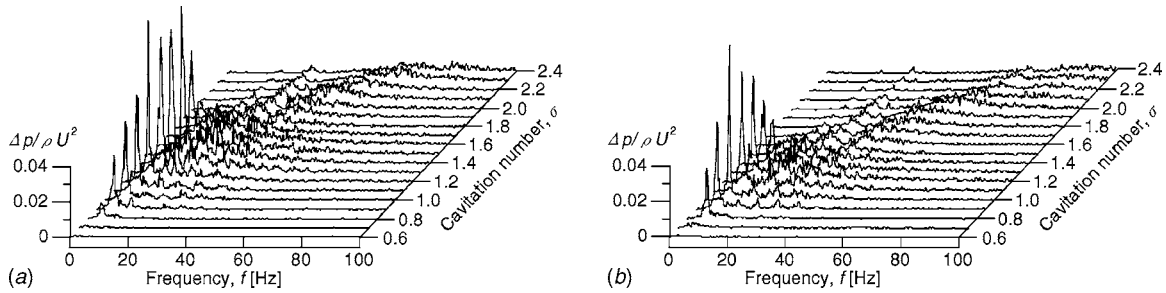


Fig. 5 Spectra of upstream pressure fluctuations for flat plate foils, $\alpha=8$ deg (uncertainty in $f: \pm 0.25$ Hz, in $\Delta p/\rho U^2: \pm 0.0005$ in $\alpha: \pm 0.25$ deg) (a) flat plate R0.1 and (b) flat plate R1.4

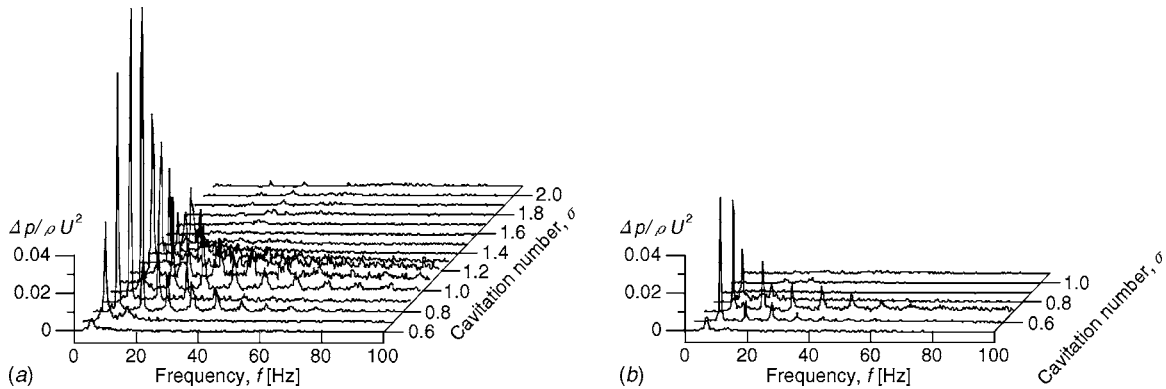


Fig. 6 Spectra of upstream pressure fluctuations for the CAV2003 foil (uncertainty in $f: \pm 0.25$ Hz, in $\Delta p/\rho U^2: \pm 0.0005$ in $\alpha: \pm 0.25$ deg): (a) $\alpha=8$ deg and (b) $\alpha=5$ deg

$\alpha=8$ deg, although the range of cavitation number is different and the amplitude is smaller.

The Strouhal number ($S_{tb}=fC/U$) determined from the pressure fluctuation is plotted against $\sigma/2\alpha$ (α expressed in radians) in Fig. 7 for transitional cavity oscillations. The Strouhal number increases with an increase of $\sigma/2\alpha$. Although some difference among the foils can be seen at a constant value of $\sigma/2\alpha$, the general tendency and the range of S_{tb} are nearly the same for all foils. The occurrence region in $\sigma/2\alpha$ and the values of S_{tb} is not so different between two angles of attack (5 deg and 8 deg). This shows that $\sigma/2\alpha$ is a good parameter for correlating cavitation instabilities.

3.2 Visual Observation by High-Speed Video. By using high-speed video, visual observation of cavity oscillation was made. Figure 8 shows the maximum, minimum, and mean cavity lengths plotted against $\sigma/2\alpha$. The maximum and minimum cavity lengths are evaluated by averaging over ten cycles of oscillation, and the mean cavity length is evaluated as their arithmetic mean.

For $\sigma/2\alpha > 5.5$, the maximum cavity lengths of flat-plate foils are longer than CAV2003 and NACA foils for which the amplitude of oscillation is smaller. The difference becomes smaller for $\sigma/2\alpha < 5.0$, where the transitional cavity oscillation occurs for all foils. It is interesting to note here, that the amplitude of oscillation becomes larger when the maximum, not the mean, cavity length exceeds $\sim 75\%$ of the chord length.

The main results of visual observation are summarized as follows:

1. The frequencies of the transitional cavity oscillations were the same as those determined from the spectrum of upstream pressure fluctuations.
2. Although no distinct peak corresponding to the partial cavity oscillation was found in the inlet pressure spectra for NACA 0015, 0010 1/2, and Cav2003 foils, nearly periodical cavity shedding corresponding to the partial cavity oscillation could be observed for all foils. The frequency determined from the visual observation approximately agrees with the

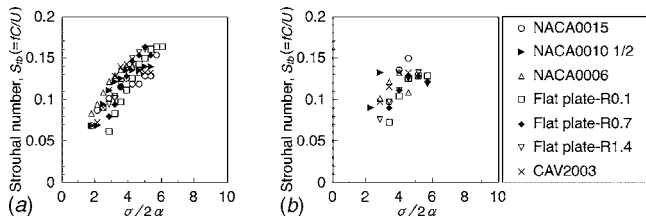


Fig. 7 Strouhal number ($S_{ib}=fC/U$) of transitional cavity oscillations obtained from upstream pressure fluctuations (uncertainty in $\sigma/2\alpha:\pm 0.15$, in $S_{ib}:\pm 0.004$): (a) $\alpha=8$ deg and (b) $\alpha=5$ deg

peak frequency shown in Figs. 4(b) and 5, for NACA 0006 and flat-plate foils.

Figure 9 shows the Strouhal numbers $S_{ib}=fC/U$ based on the chord length C and $S_{ic}=fl/U$ based on the mean cavity length l plotted against the mean cavity length l/C . The frequency was determined from the time elapsed during ten cycles of cavity shedding. The data with the Strouhal numbers S_{ib} and S_{ic} around 0.1 show transitional cavity oscillation, and those with higher values show the partial cavity oscillation. The value of S_{ic} is nearly constant for transitional cavity oscillation, but it increases as the cavity length is decreased for partial cavity oscillations. For partial cavitation, the effect of cavity length is smaller for S_{ic} . The effect of foil geometry is larger for partial cavity oscillations. However, the effect of foil geometry is smaller than the effects of cavity length and of cavity oscillation types.

4 Discussions and Conclusions

The flow under noncavitating conditions was examined by using tufts. At $\alpha=8$ deg, it was confirmed that the flow is separated on the NACA0006, flat plates-R0.1, and R1.4 foils, but no separation was observed on the NACA0015 and CAV2003 foils. Corresponding to this, we could find a clear sheet cavitation near the leading edge for NACA0015 and CAV2003 foils, but only bubbly cavitation for the NACA0006 and flat plate-R0.1 foils.

Irrespective of the differences of the flow and the cavity appearance, the results in Fig. 9 show that both partial and transitional cavity oscillations are not largely affected by the foil shape. This suggests that the flow details are not important for cavity oscillations. The spectrum of upstream pressure fluctuation shown in Figs. 4–6 suggest that the transitional cavity oscillation is not largely affected by the foil shape. However, the component corresponding to partial cavity oscillation can be found only for thinner

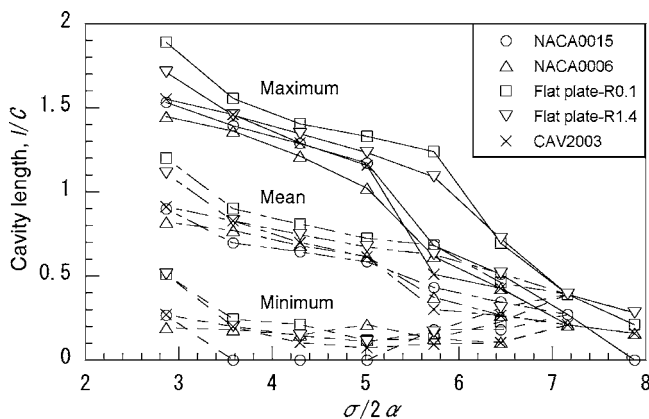


Fig. 8 Maximum, minimum, and mean cavity lengths obtained from high-speed video for $\alpha=8$ deg (uncertainty in $\sigma/2\alpha:\pm 0.15$, in $l/C:\pm 0.05$)

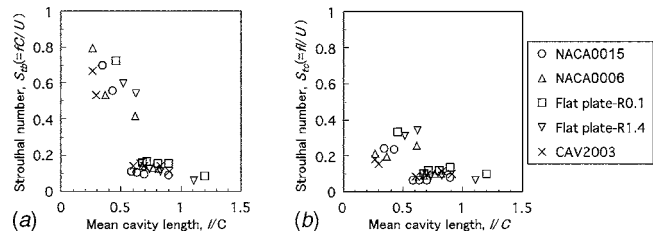


Fig. 9 Strouhal numbers obtained by high-speed video for $\alpha=8$ degrees (uncertainty in $S_{ib}:\pm 0.015$, in $S_{ic}:\pm 0.03$, in $\sigma/2\alpha:\pm 0.15$ and in $l/C:\pm 0.05$): (a) Strouhal number S_{ib} based on chord length C and (b) Strouhal number S_{ic} based on mean cavity length l

foils. This shows that the strength of partial cavity oscillation is affected by the foil shape. Although not very clear, reentrant jets are observed both for transitional and partial cavity oscillations. It is generally accepted that the partial cavity oscillation is caused by the reentrant jet [6] and affected by the pressure gradient near the cavity trailing edge [7]. This may be the reason why the strength of partial cavity oscillation was affected by the foil thickness. However, it was confirmed in [1] that the transitional cavity oscillation could not be suppressed by stopping the reentrant jet. This means that the reentrant jet is not important for transitional cavity oscillations.

Time marching calculations using linear closed-cavity model [8] show that the transitional cavity oscillation is caused by the negative cavitation compliance in the transitional region between partial cavitation and supercavitation: with negative cavitation compliance, the cavity volume increases if the ambient pressure is increased and the cavity volume increase causes a further increase of ambient pressure due to the inertia of the ambient fluid. This negative cavitation compliance is typical for transitional region and expected to occur irrespective of the foil shape, as far as the linear approximation is applicable. This might be the reason for the lack of sensitivity of the transitional cavity oscillation with the foil shape. This closed-cavity model predicts damping oscillations corresponding to the partial cavity oscillation. In real flows, it is considered that this damping mode is “excited” by the existence of the reentrant jets not considered in the model. This might be the reason why the frequency of the partial cavity oscillation is not largely affected by the foil shape and detailed flow structure.

Acknowledgment

This study was supported by the Grand-in-Aid for Science Research of the Ministry of Education, Science, Sports, and Culture. Kawakami was supported by a U.S. National Science Foundation grant.

Nomenclature

- C = chord length
- f = frequency
- l = mean cavity length
- L = upstream tunnel length
- p_1 and p_v = inlet pressure and vapor pressure
- $S_{ib}=fC/U$ = Strouhal number based on chord length
- $S_{ic}=fl/U$ = Strouhal number based on mean cavity length
- U = freestream velocity
- α = angle of attack
- $\sigma=(p_1-p_v)/(\rho U^2/2)$ = cavitation number

References

- [1] Sato, K., Tanada, M., Monden, S., and Tsujimoto, Y., 2002, “Observation of Oscillating Cavitation on a Flat Plate Hydrofoil,” *JSME Int. J., Ser. B*, **45**(3), pp. 646–654.

- [2] Franc, J.-P., and Michel, J.-M., 2004, *Fundamentals of Cavitation*, Kluwer, Dordrecht.
- [3] Franc, J.-P., and Schnerr, G. H., 2003, Workshop on Physical Models and CFD Tools for Computation of Cavitating Flows, 5th International Symposium on Cavitation, Osaka, <http://flow.me.es.osaka-u.ac.jp/cav2003/>
- [4] Kjeldsen, M., Arndt, R. E. A., and Efferz, M., 2000, "Spectral Characteristics of Sheet/Cloud Cavitation," *ASME J. Fluids Eng.*, **122**, pp. 481–487.
- [5] Qin, Q., 2004, "Numerical Modeling of Natural and Ventilated Cavitating Flows," Ph.D. dissertation, University of Minnesota.
- [6] Kawanami, K., Kato, H., Yamaguchi, H., Tanimura, M., and Tagaya, Y., 1997, "Mechanism and Control of Cloud Cavitation," *ASME J. Fluids Eng.*, **119**, pp. 788–794.
- [7] Callenaere, M., Franc, J.-P., Michel, J.-M., and Riondet, M., 2001, "The Cavitation Instability Induced by the Development of a Reentrant Jet," *J. Fluid Mech.*, **444**, pp. 223–256.
- [8] Watanabe, S., Tsujimoto, Y., and Furukawa, A., 2001, "Theoretical Analysis of Transitional and Partial Cavity Instabilities," *ASME J. Fluids Eng.*, **123**(3), pp. 692–697.

Influence of Boundary Layer Behavior on Aerodynamic Coefficients of a Swept-Back Wing

S. C. Yen¹

Assistant Professor
Department of Mechanical and Mechatronic Engineering,
National Taiwan Ocean University,
No. 2, Pei-Ning Road,
Keelung, Taiwan 202, Republic of China
e-mail: scyen@mail.ntou.edu.tw

C. M. Hsu

Department of Mechanical Engineering,
National Taiwan University of Science and Technology,
Taipei, Taiwan 106, Republic of China

The effects of the Reynolds number and angle of attack on the boundary layer and the aerodynamic performance of a finite swept-back wing are studied experimentally. The cross-sectional profile of the wing is NACA 0012 (aspect ratio=10), and the sweep-back angle is 15 deg. The Reynolds number is set in the range of 30,000–130,000. The boundary layer field is visualized with surface oil-flow techniques. Six characteristic flow regimes—laminar separation, separation bubble, leading-edge bubble, bubble burst, turbulent separation, and bluff-body wake—are categorized and studied by considering the Reynolds numbers and angles of attack. The characteristic behaviors of boundary layer significantly affect the lift, drag, and moment coefficients. The bubble length shortens significantly in the separation bubble and leading-edge bubble regimes as the angle of attack rises. The aerodynamic performances demonstrate that the swept-back wing model has no hysteresis. [DOI: 10.1115/1.2734212]

Keywords: swept-back wing, surface oil-flow, aerodynamic performances

1 Introduction

The geometrical theory of the swept-back wing indicates that the flow speed perpendicular to the leading edge is less than the flight speed; thus, the critical Mach number increases. This mechanism can be utilized to avoid or postpone the appearance of shock waves. Hence, a swept-back wing can increase the maximum air speed and Mach number, and reduce the drag and unfavorable effects when flying subsonically. However, the pitch up induced from the tip stall is a significant issue in flight safety [1], particularly, in the case of low air speed, such as takeoff and landing. The properties of the swept-back wing remain a field worthy of study, since they link to many significant steady/unsteady aerodynamic problems. For instance, on the suction surface, the characteristics of surface flow influence the laminar separation, transition, turbulent reattachment, and bubble bursting [2–6], due to its significant effect on aerodynamic performance [7–9].

Black [10] elucidated the general behavior of the wing surface flow on swept-back wings, in which the formation of short and long laminar separation bubbles on thin swept-back wings was studied. His tests demonstrated that the flow separates on the leading edge and then reattaches behind a short separation bubble over the inboard sections. However, in the outboard section, the flow only reattaches near the trailing edge, thus generating a long separation bubble and, otherwise, fails to attach. The separated flow in the tip stall takes the form of a tip vortex with the origin located at the junction of the two bubbles on the leading edge. The research on the thin oil flow can be traced back to the Squire's theoretical work [11]. Squire deduced two points in his paper. First, the oil flow is in the direction of the surface flow skin friction, except near the separation. This finding is independent of oil viscosity. Second, the effect of the oil flow on the surface flow motion is very small. Poll [12] adopted the surface oil-flow visualization technique to study the RAE 101 airfoil at $Re_c = 1.1 \times 10^6 - 2.7$

$\times 10^6$ and observed no spiral vortex flow at sweep angles of 0 deg and 15 deg. When the sweep angles were larger than 15 deg, the oil flows indicated that spiral vortices can be formed from one of three different mechanisms. First, a full-span vortex can be formed by rolling up the shear layer, leaving the airfoil surface at the primary separation line. Second, a part-span vortex can be formed when the shear layer from the primary separation reattaches to form a short bubble on the inboard portion of the wing. Third, a part-span vortex can be formed when the boundary layer flow downstream of a short separation bubble leaves the surface close to the bubble along a line of secondary separation.

The bubble generally extends a large portion of the chord length, then significantly changed the pressure distribution. The aerodynamic performance is thus manifestly altered. Mueller et al. [13] and Mueller [14] experimentally examined the hysteresis loop in aerodynamic performance with Lissaman 7769, Miley M06-13-128, and NACA 63₃-018 airfoils at low Reynolds numbers. Liu et al. [15] investigated the swept wing with a 30 deg swept-back angle and found that the lift increase results from the impact of the strake vortex, not only on the inner panel but also on the outer panel. Additionally, the additional strike to the wing at low speeds leads to a nonlinear pitching moment variation at low and high angles of attack. The lift increment falls with a rise in Mach number at transonic speeds. The rise of the lift-drag ratio is a result of the lift increase at low speeds and drag decrease at supersonic speeds. Huang et al. [16] explored the NACA 0012 airfoil aerodynamic performance resulting from the change of surface flow mode at various Reynolds numbers. The variations of surface flow due to the effect of the Reynolds number and the freestream turbulence inevitably change the aerodynamic performance. The laminar separation regime demonstrates the steepest lift coefficient curve. The increase rate of lift coefficient falls when the separation bubble is formed and stalling occurs in the turbulent separation regime. The drag coefficient, which decreases slightly in the laminar separation regime, remains almost constant in the separation bubble regime and increases in the transition regime.

The current work is motivated by the need to improve the low Reynolds number performance of guide vanes in the swirling gen-

¹Corresponding author.

Contributed by the Fluids Engineering Division of ASME for publication in the JOURNAL OF FLUIDS ENGINEERING. Manuscript received February 10, 2006; final manuscript received December 18, 2006. Review conducted by Joseph Katz.

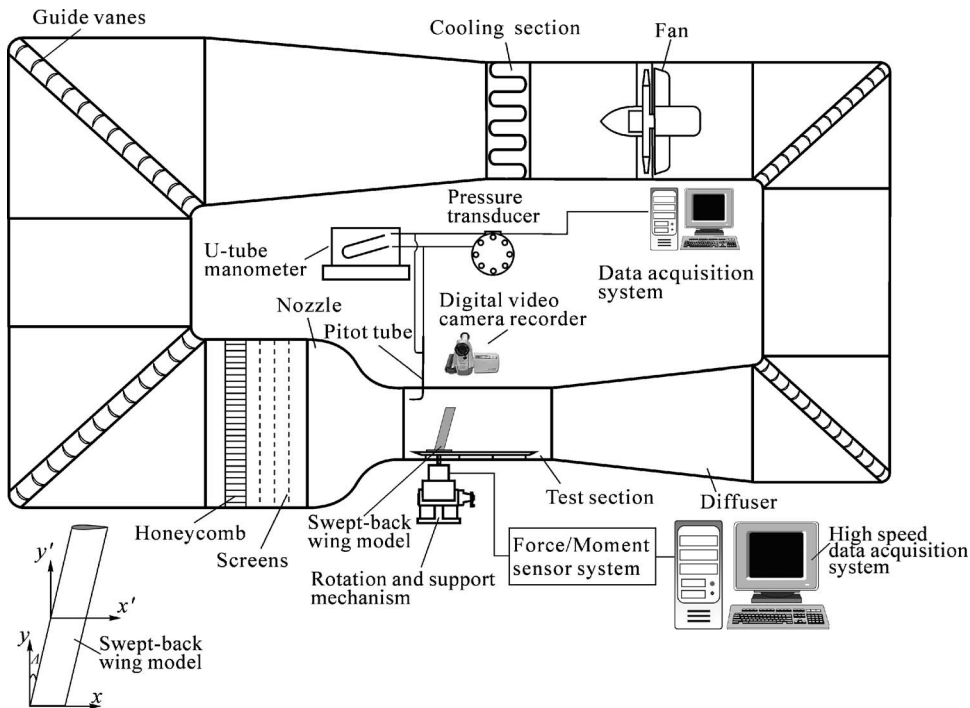


Fig. 1 Experimental setup

erator of a burner. The results of this work can also be applied to the design of rotary blades of fans, wind-power generators, fluid mixers, micro-UAVs, etc. Experimental results in this study indicate the characteristic behavior of boundary layer modes and their influence on the aerodynamic performances of swept-back wings. The objectives of this work are as follows: (i) to study the properties of the boundary layer modes with surface oil flow, (ii) to measure the aerodynamic coefficients with the six-component balance, (iii) to understand how the upper boundary layer features influence the aerodynamic coefficients, and (iv) to study the aerodynamic performance as a function of the angle of attack and the Reynolds number.

2 Experimental Arrangements

The experiments were performed in a closed-return wind tunnel, as depicted in Fig. 1. This wind tunnel consisted of a test section of $60\text{ cm} \times 60\text{ cm} \times 120\text{ cm}$, a polished aluminum alloy plate as the floor, and three highly transparent acrylic panels to be the ceiling and sidewalls for photography and visualization. The available operating velocity was in the range of $0.56\text{--}60\text{ m/s}$. In this velocity range, the maximum turbulence intensity was below 0.2% and the nonuniformity of the average velocity profile across the cross section was $<0.5\%$. The velocity of the approaching flow during the experiments was monitored by a Pitot-static tube. The thicknesses of the boundary layer [17] were about 4.0 mm and 1.7 mm , respectively, at freestream speeds of 5.0 m/s and 30.0 m/s . An aluminum plate with sharp leading and trailing edges was placed 50 mm over the floor of the test section to control the boundary layer thickness.

The airfoil model was made of stainless steel. The profile of the cross section was NACA 0012 [18], and the sweep-back angle was 15 deg . The chord length was 6 cm , and the span was 30 cm , yielding a full span wing aspect ratio of 10. The airfoil model was mounted on a support and protruded perpendicularly through the aluminum floor and the boundary layer thickness control plates.

The surface thin oil-flow technique, as described theoretically by Squire [11], was adopted to detect the variation of flow modes. Mineral oil mixed with blue dye powder was brush coated on the suction surface of the wing model. The dark traces on the wing

surface revealed where the massive dyed oil accumulated. The flow direction on the suction surface was observed in situ from the skin friction lines of the oil flow. The separation and reattachment positions of the boundary layer on the suction surface were obtained from the recorded video images of surface oil-flow patterns.

The aerodynamic performances were taken by a JR³ Universal Force-Moment System. The assembly of the wing model and balance was mounted on a rotary support. The resolution of rotary support is 0.012 deg . A monolithic six-degree-of-freedom force sensor was included in the JR³ balance. The output electronic signals of the sensor were sampled by a PC-based high-speed data acquisition system.

The measurement accuracy of the freestream velocity was affected primarily by the alignment of the Pitot tube and the calibration of the pressure transducer. The uncertainty of the freestream velocity was estimated as 3% by using a synchronized micropressure calibration system with a carefully aligned Pitot tube. The accuracy of the angle of attack was controlled within 0.5% . The uncertainty in the separation location was estimated to be $<4\%$. The uncertainty in the reattachment location was $<6\%$. The accuracy of the force-moment measurement was determined with the mounting and calibration method. The accuracies of lift, drag, and pitching moment measurements were estimated by using the calibration matrix and found to be about $\pm 1.5\%$, $\pm 2\%$, and $\pm 2.5\%$, respectively. Then, the overall accuracy of the lift coefficient, drag coefficient, and pitching moment coefficient were derived to be about $\pm 2.5\%$, $\pm 3\%$, and $\pm 3.5\%$, respectively.

3 Results and Discussion

3.1 Flow Over the Wing Surface. The surface oil-flow technique, or the skin-friction patterns, were applied to the regimes with a chord Reynolds number (Re_c) larger than $30,000$ [19].

3.1.1 Type of Surface Oil-Flow Patterns and Characteristic Flow Regimes. Figure 2 shows the surface oil-flow patterns on the suction surface of the NACA 0012 swept-back wing model at $Re_c = 4.55 \times 10^4$. Figure 3 displays the corresponding hand sketches. The bold lines delineate the separation or reattaching

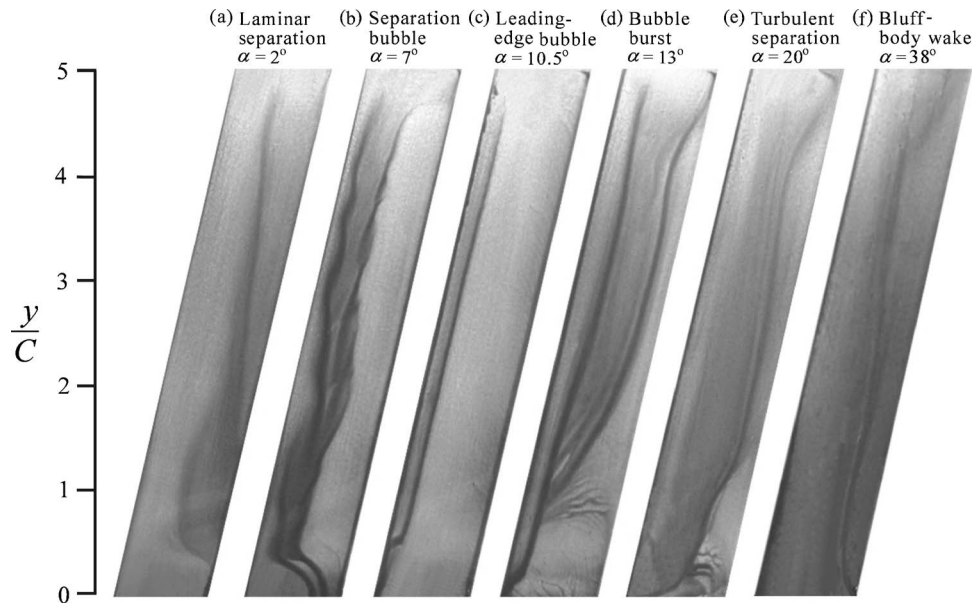


Fig. 2 Typical surface oil-flow patterns on the suction surface of a swept-back wing at $Re_c = 4.55 \times 10^4$

lines, whereas the thin lines with arrowheads indicate the paths and directions of oil flow on the suction surface. The hand sketches at the bottom of Fig. 3 delineate the side view of the imaginary boundary layer patterns in the two-dimensional region.

At $\alpha = 2$ deg, as revealed in Figs. 2(a) and 3(a), the bold line indicates approximately where the boundary layer separates. A large portion of the boundary layer is two-dimensional except near the wall and tip. The oil flow moves in the main stream direction within the attached flow area. With rising angle of attack, the direction of oil flow reversed in the separated area and the location of separation moved toward the upstream direction. No reattachment was observed in this regime. The wall and tip effect can

also be observed in Figs. 2 and 3. This boundary layer pattern exists at low Reynolds numbers and low angles of attack. It is identified as the mode of *laminar separation*.

Figures 2(b) and 3(b) show three dark lines at $\alpha = 7$ deg. The first (leftmost) line denotes where the boundary layer separates, the second line represents where the separated flows reattach together, and the third line represents where the turbulent boundary layer is separated near the trailing edge. The direction of the oil flow in the two-dimensional region demonstrates the existence of a separation bubble between the first and second lines, as depicted in the bottom part of Fig. 3(b). This bubble moves toward the upstream area and shrinks with the rise in angle of attack. This

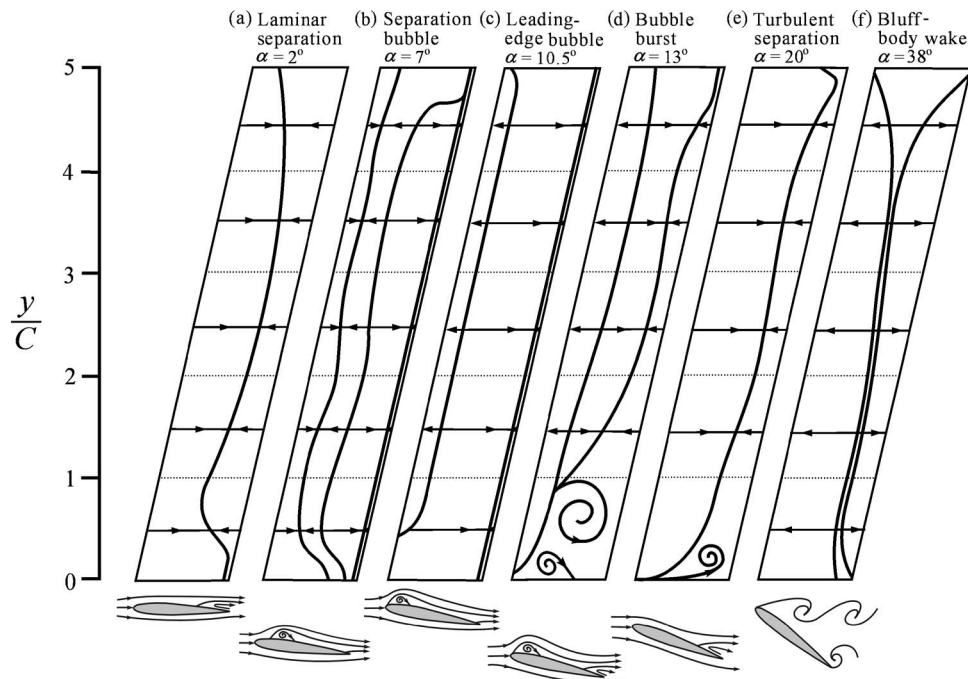


Fig. 3 Hand sketches of typical boundary layer patterns corresponding to Fig. 2

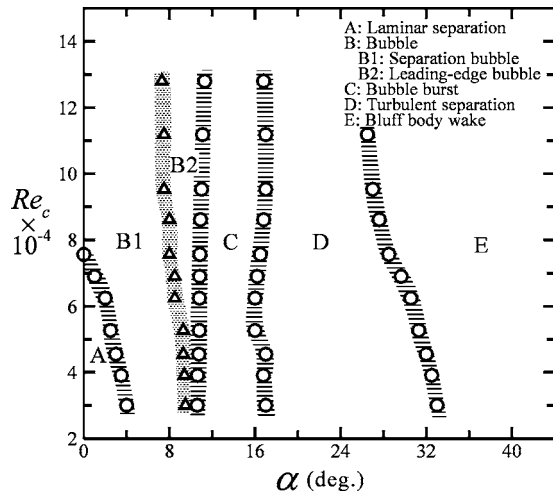


Fig. 4 Characteristic flow mode regimes

boundary layer pattern is identified as the of *separation bubble* mode.

At $\alpha=10.5$ deg, as shown in Figs. 2(c) and 3(c), the separation bubble becomes very small, so both the separation and reattachment lines are located very close to the leading edge. A short leading-edge separation bubble is then formed. In this regime, a turbulent separation also results from the accumulation of oil adjacent to the trailing edge. This boundary layer pattern is denoted as the *leading-edge bubble* mode.

At $\alpha=13$ deg, as indicated in Figs. 2(d) and 3(d), the separation bubbles near the leading edge burst and the reattachment lines move downstream. Simultaneously, the reattached turbulent boundary layer separates downstream. This boundary layer pattern is identified as the *bubble burst* mode. In the lower part of Figs. 2(d) and 3(d), the separation bubble becomes larger as the angle of attack increased and then causes two surface vortexes appearing near the juncture area.

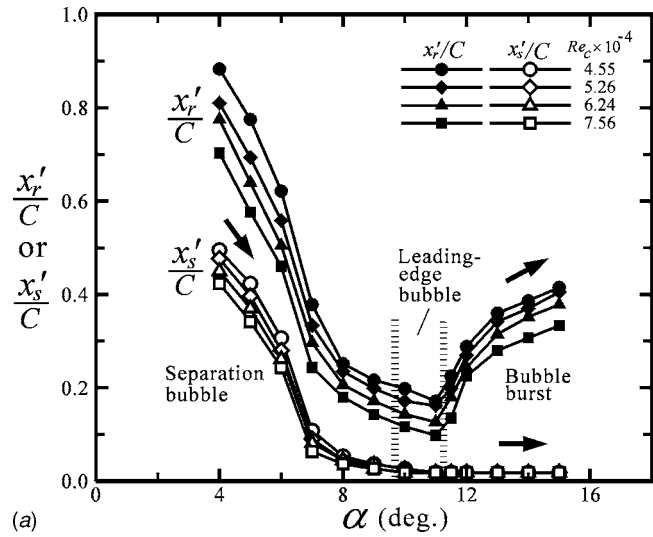
In Figs. 2(e) and 3(e), when $\alpha=20$ deg, the phenomenon represented as *turbulent separation* occurs near the trailing edge. The bold line in Figs. 2(e) and 3(e) demarcates the position of turbulent separation. Additionally, the surface vortex appears near the juncture area and the turbulent separation lags due to the tip effect.

The oil flow moves slowly at $\alpha=38$ deg, as revealed in Figs. 2(f) and 3(f). The two-dimensional hand sketches, shown in Fig. 3(f), demonstrate the airflow moves upstream and hits the wing surface. Therefore, the surface oil flow moves toward the leading and trailing edges, respectively. This flow pattern is called *bluff-body wake*.

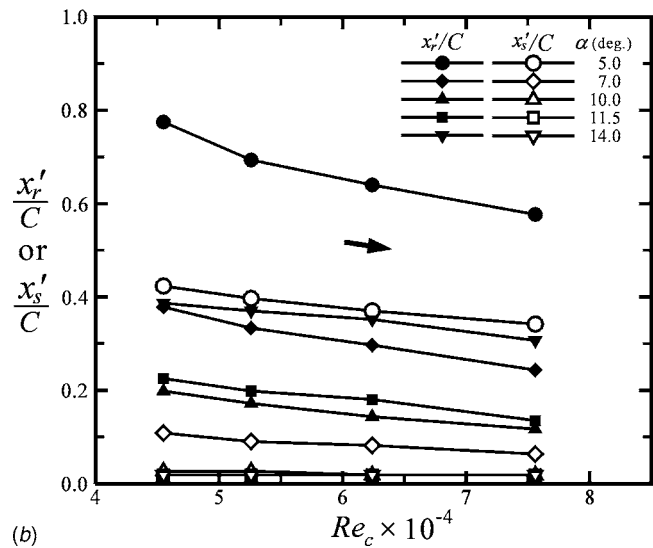
Parameters, the angle of attack α , and Reynolds number Re_c , were correlated and plotted in Fig. 4. Six flow regimes, namely, laminar separation (type A), separation bubble (type B1), leading-edge bubble (type B2), bubble burst (type C), turbulent separation (type D), and bluff-body wake (type E), are categorized according to their particle tracking flow patterns.

3.1.2 Separation and Reattachment Characteristics. Application of surface oil-flow visualization to investigate the flow behaviors on the suction surface of the swept-back wings reveals that the locations of the boundary layer separation, and the reattachment in the chord direction are influenced by the angle of attack and Reynolds number. Figure 5 shows the curves of x'_s/C and x'_r/C as the functions of α and Re_c , respectively, when $y/C=2.5$ in the separation bubble (region B1), the leading-edge bubble (region B2), and the bubble-burst (region C) regimes.

Figure 5(a) indicates that the separation point moves toward the leading edge when the angle of attack rises in the separation



(a)

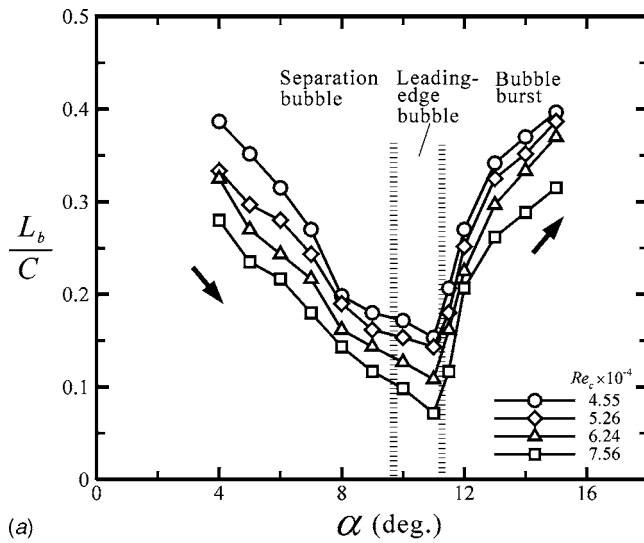


(b)

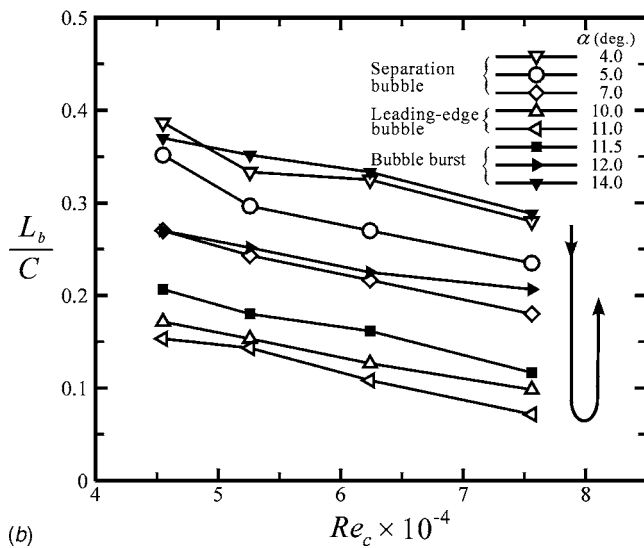
Fig. 5 Variation of chordwise location of separation and reattachment with (a) angle of attack and (b) chord Reynolds number

bubble regime. Figure 5(a) also reveals that the separation point is almost fixed at the leading edge in both the leading-edge bubble and bubble-burst regimes. With rising the angle of attack, Fig. 5(a) shows that the reattachment positions move toward the leading edge in the separation bubble and leading-edge bubble regimes, but rebound back toward the trailing edge in the bubble-burst regime. In Fig. 5(b), these curves exhibit the same trend that the separation points and reattachment points move toward the leading edge as Re_c becomes larger. In Fig. 6(a), the separation and reattachment causes the formation of separation bubbles between the separation points and reattachment points. In Fig. 6(a), where $Re_c=4.55 \times 10^4$, with the angles of attack adjusting from $\alpha=4$ deg–10.75 deg, the bubble-length/chord-length ratio is decreased from 38% to 17%. Rising the angle of attack further from 10.75 deg to 16 deg, it increases from 17% to 40%. Conversely, Fig. 6(b) demonstrates that the bubble-length/chord-length ratio decreases with the increase of Re_c .

3.2 Aerodynamic Performance. The aerodynamic performance of a wing is strongly affected by the behavior of the boundary layer on the suction surface and by the three-dimensional ef-



(a)



(b)

Fig. 6 Variation of chordwise location of bubble length with (a) angle of attack and (b) chord Reynolds number

fects of wall and tip.

3.2.1 Aerodynamic Coefficients. This study utilized a swept-back wing model with sweep-back angle $\Lambda=15$ deg to test the hysteresis phenomenon found by Mueller et al. [13] and Mueller [14]. Figure 7 shows the aerodynamic performance by plotting the lift coefficient C_L , drag coefficient C_D , and moment coefficient C_M as the functions of angle of attack subject to a chord Reynolds number of 4.55×10^4 .

Figure 7(a) indicates that the lift coefficient C_L rises monotonically with increasing angle of attack when the boundary layer on the suction surface is in the regimes of laminar separation, separation bubble, and leading-edge bubble. In the separation bubble regime, the value of the lift coefficient increases almost linearly with angle of attack. The increase rate, $\Delta C_L/\Delta\alpha$, is $\sim 1.21 \pi/\text{rad}$. The maximum value of C_L is ~ 0.85 at the leading-edge bubble regime. The lift starts to fall when the boundary layer is in the bubble-burst regime. In the bubble-burst regime, the reattached turbulent boundary layer separates again to form the second separation. The second separation line moves toward the leading edge with increasing angle of attack, and is depicted in Fig. 3(d). The wing stalls with the forward motion of the second separation line. The minimum C_L value is ~ 0.68 . The lift rises again as the angle

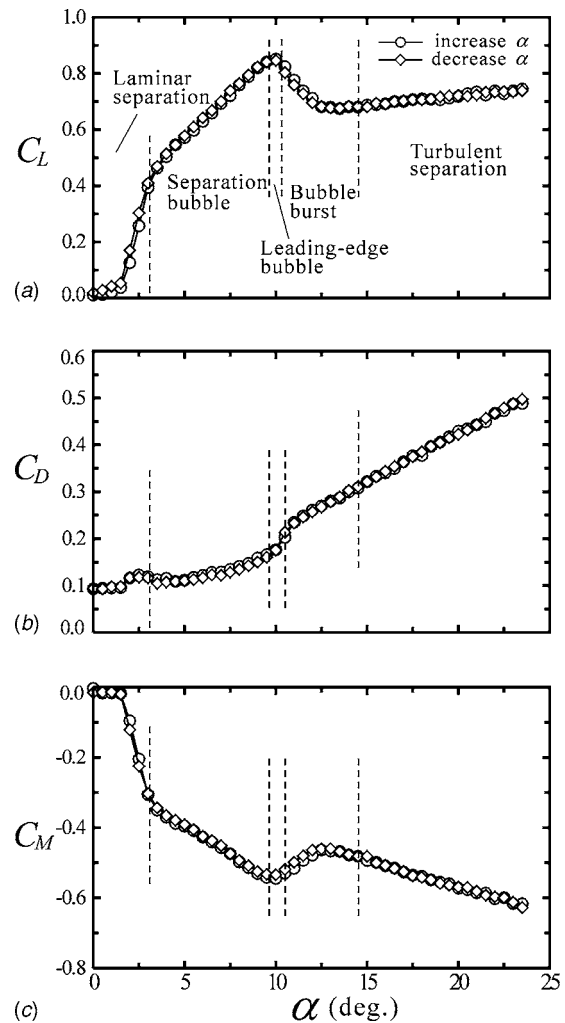


Fig. 7 Aerodynamic performances of swept-back wing: (a) lift coefficient, (b) drag coefficient, and (c) moment coefficient, respectively; $Re_c=4.55 \times 10^4$ for all cases

of attack is further increased into the turbulent-separation regime. This lift rise phenomenon is induced from the reaction of the scavenging effect on the suction surface and impact pressure on the pressure surface [20].

Figure 7(b) illustrates the value of the drag coefficient C_D in the laminar separation regime. Although the reverse flow on the suction surface contributes to the shear stress in the separation region, this rise in C_D is not significant. The value of C_D is ~ 0.1 in this regime. In the separation bubble regime, the bubble moves toward the leading edge and reduces its size with rising angle of attack. The reduction in shear stress lowers the shear drag and increase the form drag. Consequently, the drag coefficient does not vary significantly in the separation bubble regime. In the leading-edge bubble regime, the increase in skin friction and decrease in bubble size raise the drag coefficient. In the bubble-burst regime, the reattached turbulent boundary layer generates a large skin friction on the suction surface. The drag coefficient increases almost linearly with the rising angle of attack in the regime of turbulent separation, due to the significant increase in the form drag.

Figure 7(c) depicts the distribution of the quarter-chord moment coefficient C_M . In the region between the separation bubble and leading-edge bubble, owing to the movement toward the leading edge, the pressure center, which is the resultant force position of the lift and drag forces, moves toward the leading edge. This movement induces a counterclockwise moment to the aerody-

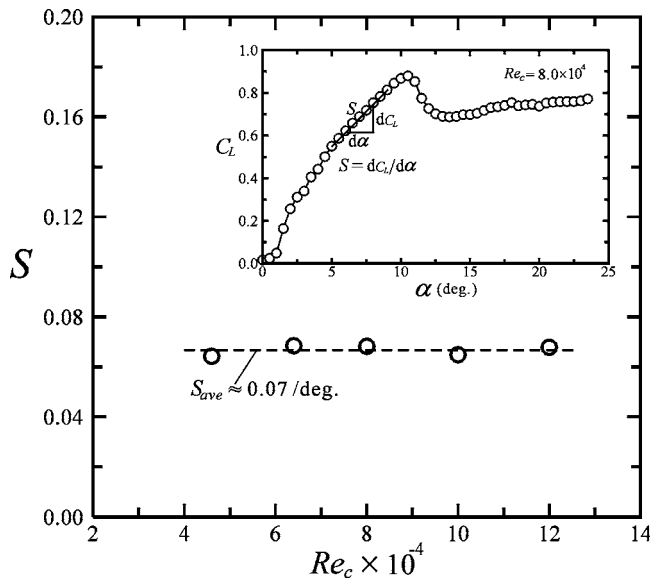


Fig. 8 Slope of the lift coefficient and the angle of attack versus the chord Reynolds numbers

namic center and derives a negative correlation between C_M and α . In the bubble-burst regime, due to the appearance of a stall, the decreased lift changes C_M profile. In the turbulent separation regime, the high angle of attack causes the increase in form drag and then lowers the moment coefficient. Figure 7 shows no hysteresis phenomenon for the finite swept-back wing modeled NACA 0012 because the increment of freestream turbulent strength can diminish the hysteresis phenomenon [21].

Hoerner and Borst have discussed the theoretical relationship among the lift coefficient, the angle of attack, and the swept-back angle in swept-back wing model [20]. They derived the following equation:

$$\frac{dC_L}{d\alpha} = \frac{\cos(\Lambda)}{10 + \left(\frac{20}{A}\right)} \quad (1)$$

where A denotes the aspect ratio. Substituting the experimental conditions, $A=10$ and $\Lambda=15$ deg, into Eq. (1), the theoretical result is $dC_L/d\alpha=0.08/\text{deg}$. Figure 8 shows the experimental change rate with various Reynolds numbers. The average result is found to be $0.07/\text{deg}$.

3.2.2 Lift-Drag Ratio. Figure 9(a) shows the value of C_L/C_D changing with angle of attack for $Re_c=4.55 \times 10^4$. In the laminar separation regime, the C_L/C_D ratio rises from 0 to 3.2 as the angle of attack increases. The value of C_L/C_D peaks at around 5.4 near the central area of the separation bubble regime. The existence of a bubble on the suction surface apparently retards the rate of increase of C_L/C_D . In the regime of the leading-edge bubble, C_L/C_D drops from 4.9 to 4.1 within only a 2 deg increase in angle of attack due to the abrupt loss of lift. The value of C_L/C_D then falls gradually with the rise in angle of attack in the bubble-burst and turbulent separation regimes, since C_L increases slightly and C_D increases rapidly in these regimes. Figure 9(b) illustrates the curve of drag coefficient with respect to the square of lift coefficient at a chord Reynolds number of 4.55×10^4 . The drag coefficient does not change significantly with the increase of the squared lift coefficient in the laminar separation and separation bubble regimes, but increases gradually with rising squared lift coefficient in the leading-edge bubble regime. The drag coefficient rises, while the squared lift coefficient falls, when the boundary layer proceeds to the bubble-burst regime. At high angles of at-

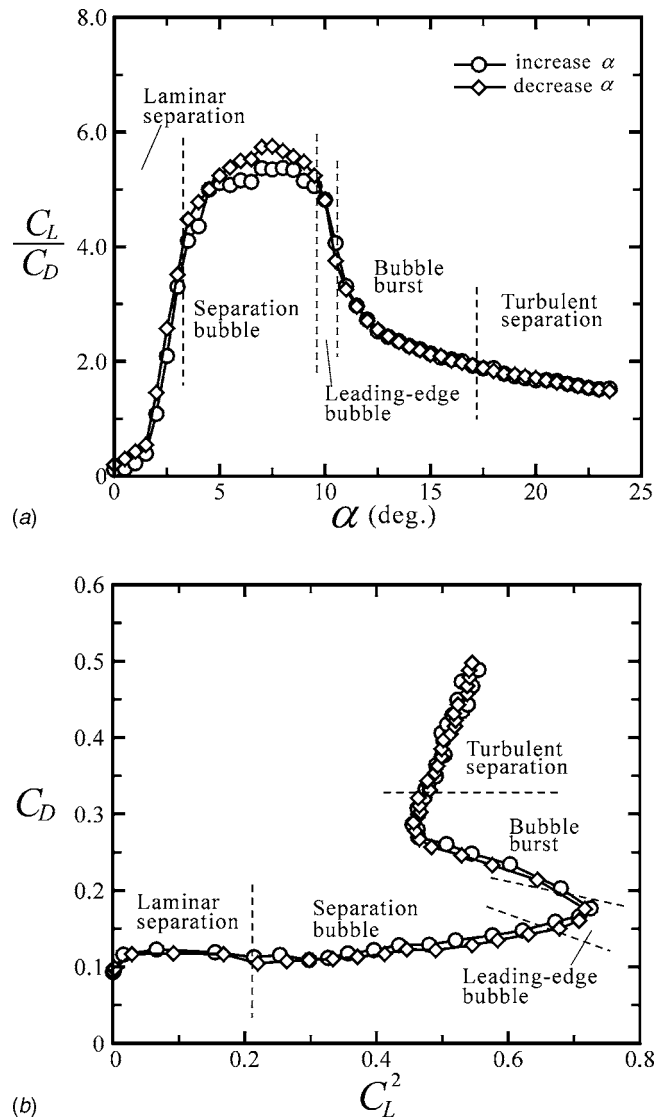


Fig. 9 (a) Lift-to-drag ratio versus the angle of attack and (b) drag coefficient versus squared lift coefficient; $Re_c=4.55 \times 10^4$

tack, that is, in the turbulent separation regime, the drag coefficient changes largely with only a small variation in the squared lift coefficient.

The maximum value of lift-drag ratio $(C_L/C_D)_{\max}$ and the lift-drag ratio at stalling point $C_{L\max}/C_{D\text{stall}}$ increases with the Reynolds number, as indicated in Fig. 10. Both of these two curves rise gradually with the Reynolds number. These results agree with the work of Lissaman [2].

3.2.3 Angle of Attack at Stall. The stall occurs at the transition from the *leading-edge bubble* to the *bubble-burst* regime. The curves of stall angle, maximum lift coefficient, drag coefficient at stalling point, and moment coefficient at the stalling point versus the chord Reynolds number are plotted in Fig. 11. In Fig. 11(a), the stalling angle rises from 10.624 deg to 11.252 deg and Re_c increases from 4.55×10^4 to 1.2×10^5 . Figure 11(b) indicates that the maximum lift coefficient increases with the increasing Reynolds number. However, the drag coefficient and the moment coefficient at stalling point fall with the increasing Reynolds number, as shown in Figures 11(c) and 11(d).

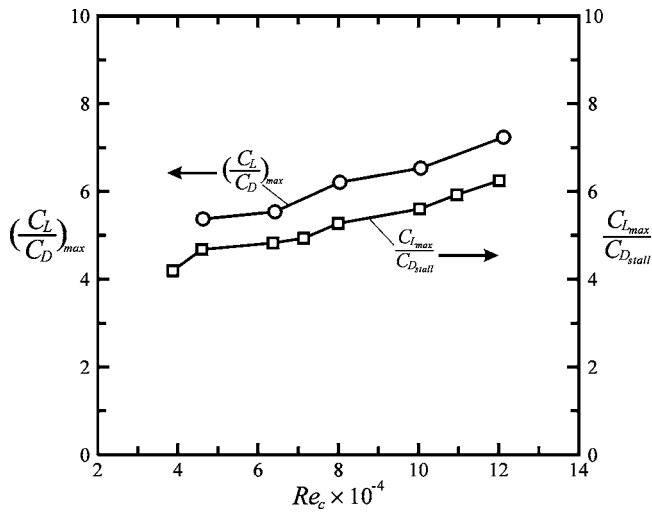


Fig. 10 Distributions of the maximum lift-to-drag ratio (circle) and lift-to-drag ratio at stalling point (square) as functions of chord Reynolds number, respectively

4 Concluding Remarks

The characteristics of the boundary layer patterns and the aerodynamic performances of a finite swept-back airfoil are studied experimentally. The following conclusions are drawn from the results and discussion:

1. The surface oil-flow patterns can be classified into six characteristic flow regimes according to the Reynolds numbers and angles of attack. These six flow patterns are called laminar separation, separation bubble, leading-edge bubble, bubble burst, turbulent separation, and bluff-body wake.
2. The bubble length is influenced by the change of angle of attack and chord Reynolds number. It falls significantly as the angle of attack rises in the separation bubble and leading-edge bubble regimes. The Reynolds number decreases with increasing Reynolds numbers in the separation bubble, leading-edge bubble, and bubble-burst regimes.
3. The lift coefficient C_L rises monotonically with increasing angle of attack in the regimes of laminar separation, separation bubble, and leading-edge bubble. In the separation bubble regime, C_L increases almost linearly with the angle of attack. The increase rate, $\Delta C_L/\Delta\alpha$, is $\sim 1.21 \pi/\text{rad}$. The

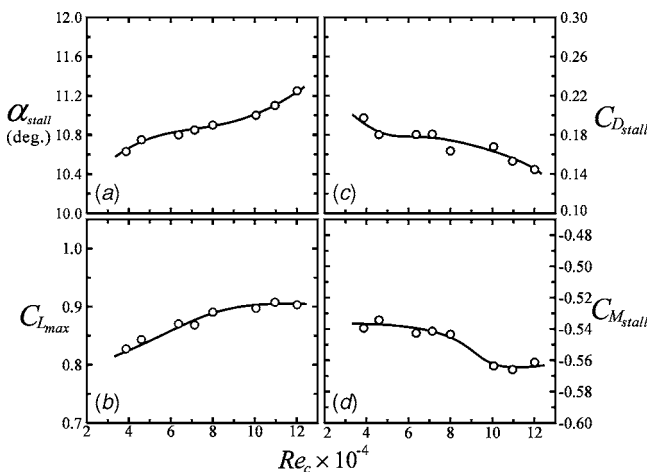


Fig. 11 Effect of Reynolds number on (a) stall angle of attack, (b) maximum lift coefficient, (c) stall drag coefficient, and (d) stall moment coefficient

maximum value of C_L is ~ 0.85 at the leading-edge bubble regime. The lift falls when the boundary layer is in the bubble-burst regime. In this regime, the reattached turbulent boundary layer separates again to form the second separation. The second separation line moves toward the leading edge with increasing angle of attack. The minimum C_L value is ~ 0.68 . The lift rises again as the angle of attack is further increased to the turbulent separation regime.

4. In the laminar separation regime, C_D does not vary significantly. In the separation bubble regime, the bubble moves toward the leading edge and reduces its size with rising angle of attack, and the drag coefficient does not change significantly. In the leading-edge bubble regime, the increase of skin friction and decrease of bubble size raise the drag coefficient. In the bubble-burst regime, the reattached turbulent boundary layer generates a large skin friction on the suction surface. The drag coefficient increases almost linearly with the rise in angle of attack in the regime of turbulent separation.
5. In the region between the separation bubble and leading-edge bubble, the pressure center moves toward the leading edge and derives a negative correlation between C_M and α . In the bubble-burst regime, due to the appearance of a stall, the decreased lift changes C_M profile. In the turbulent separation regime, the rising angle of attack lowers the moment coefficient.
6. The experimental data indicate no hysteresis phenomenon in the swept-back wing model. Additionally, the change rate of the lift coefficient with respect to the change of angle of attack is almost a constant 0.07, which is close to the theoretical value of 0.08.

Nomenclature

- b = span of airfoil, 30 cm
- C = chord length of wing, 6 cm
- C_L = lift coefficient ($=L/qbC$)
- C_D = drag coefficient ($=D/qbC$)
- C_M = moment coefficient of pitching at quarter chord ($=M/qbC$)
- D = drag force, measured by balance in freestream direction
- L = lift force, measured by balance in cross freestream direction
- L_b = chordwise length of separation bubble
- M = pitching moment about quarter chord location
- q = dynamic pressure of freestream ($=(1/2)\rho u^2$)
- Re_c = Reynolds number based on chord length of wing ($=uC/\nu$)
- u = x component of local instantaneous velocity
- x = streamwise coordinate, originated from leading edge of wing on root plane
- x'_r = streamwise location of reattachment point of boundary layer on suction surface of wing
- x'_s = streamwise location of separation point of boundary layer on suction surface of wing
- y = spanwise coordinate, originated from leading edge of wing model on root plane
- α = angle of attack
- Λ = sweep-back angle
- ρ = density of air stream
- ν = kinetic viscosity of air stream

Acknowledgment

This research was supported by the National Science Council of the Republic of China, under Grant No. NSC 94-2212-E-019-006.

References

- [1] Clancy, L. J., 1975, *Aerodynamics*, Wiley, New York, pp. 72–73.
- [2] Lissaman, P. B. S., 1983, “Low Reynolds Number Airfoils,” *Annu. Rev. Fluid Mech.*, **15**, pp. 223–239.
- [3] Crabtree, L. F., 1957, “Effects of Leading-Edge Separation on Thin Wings in Two-Dimensional Incompressible Flow,” *J. Aeronaut. Sci.*, **24**(8), pp. 597–604.
- [4] Ward, J. R., 1963, “The Behavior and Effects of Laminar Separation Bubbles on Airfoils in Incompressible Flow,” *J. R. Aeronaut. Soc.*, **67**(12), pp. 783–790.
- [5] Arena, A. V., and Mueller, T. J., 1980, “Laminar Separation, Transition, and Turbulent Reattachment Near the Leading Edge of Airfoils,” *AIAA J.*, **18**(7), pp. 747–753.
- [6] Katz, J., 1999, “Wing/Vortex Interactions and Wing Rock,” *Prog. Aerosp. Sci.*, **35**(7), pp. 727–750.
- [7] Mueller, T. J., and Batill, S. M., 1982, “Experimental Studies of Separation on a Two-Dimensional Airfoil at Low Reynolds Numbers,” *AIAA J.*, **20**(4), pp. 457–463.
- [8] Pohlen, L. J., and Mueller, T. J., 1984, “Boundary Layer Characteristics of the Miley Airfoil at Low Reynolds Numbers,” *J. Aircr.*, **21**(9), pp. 658–664.
- [9] Hsiao, F.-B., Liu, C.-F., and Tang, Z., 1989, “Aerodynamic Performance and Flow Structure Studies of a Low Reynolds Number Airfoil,” *AIAA J.*, **27**(2), pp. 129–137.
- [10] Black, J., 1956, “Flow Studies of the Leading Edge Stall on a Swept-Back Wing at High Incidence,” *J. R. Aeronaut. Soc.*, **60**(1), pp. 51–60.
- [11] Squire, L. C., 1961, “The Motion of a Thin Oil Sheet Under the Steady Boundary Layer on a Body,” *J. Fluid Mech.*, **11**(1), pp. 161–179.
- [12] Poll, D. I. A., 1986, “Spiral Vortex Flow Over a Swept-Back Wing,” *Aeronaut. J.*, **90**(895), pp. 185–199.
- [13] Mueller, T. J., Pohlen, L. J., Conigliaro, P. E., and Jansen, B. J., 1983, “The Influence of Free-Stream Disturbance on Low Reynolds Number Airfoil Experiments,” *Exp. Fluids*, **1**(1), pp. 3–14.
- [14] Mueller, T. J., 1985, “The Influence of Laminar Separation and Transition on the Low Reynolds Number Airfoil Hysteresis,” *J. Aircr.*, **22**(9), pp. 763–770.
- [15] Liu, M. J., Lü, Z. Y., Qiu, C. H., Su, W. H., Gao, X. K., Deng, X. Y., and Xiong, S. W., 1980, “Flow Patterns and Aerodynamics Characteristic of a Wing-Strake Configuration,” *J. Aircr.*, **17**(5), pp. 332–338.
- [16] Huang, R. F., Shy, W. W., Lin, S. W., and Hsiao, F.-B., 1996, “Influence of Surface Flow on Aerodynamic Loads of a Cantilever Wing,” *AIAA J.*, **34**(3), pp. 527–532.
- [17] Shames, I. H., 1992, *Mechanics of Fluid*, 3rd ed., McGraw-Hill, New York, p. 632.
- [18] Abbott, I. H., and Von Doenhoff, A. E., 1959, *Theory of Wing Section*, Dover, New York, pp. 113–115.
- [19] Merzkirch, W., 1974, *Flow Visualization*, Academic Press, New York, pp. 53–56.
- [20] Hoerner, S. F., and Borst, H. V., 1975, *Fluid Dynamic Lift*, published by Liselotte A. Hoerner, Brick Town, NJ, pp. 4.22–4.23 and 15.6–15.8.
- [21] Schewe, G., 2001, “Reynolds-Number Effects in Flow Around More-or-Less Bluff Bodies,” *J. Wind. Eng. Ind. Aerodyn.*, **89**(14), pp. 1267–1289.

Numerical Study of the Injection Process in a Transonic Wind Tunnel—Part I: The Design Point

João B. P. Falcão Filho

CTA—Aeronautics and Space Institute,
São José dos Campos,
SP 12228-900, Brazil
e-mail: jb.falcao@ig.com.br

Marcos A. Ortega

ITA—Technological Institute of Aeronautics,
São José dos Campos,
SP 12228-900, Brazil
e-mail: ortega@ita.br

Injectors are to be installed in a transonic wind tunnel with the ultimate objective of expanding the Reynolds number envelope. The aim of this research effort is to numerically simulate the steady mixing process involving the supersonic jets and the tunnel subsonic main stream. A three-dimensional, Reynolds-averaged Navier–Stokes numerical code was developed following the main lines of the finite-difference diagonal algorithm, and turbulence effects are accounted for through the use of the Spalart and Allmaras one-equation scheme. This paper focuses on the “design point” of the tunnel, which establishes (among other specifications) that the static pressures of both streams at the entrance of the injection chamber are equal. Three points are worth noting. The first is related to the numerical strategy that was introduced in order to mimic the real physical process in the entire circuit of the tunnel. The second corresponds to the solution per se of the three-dimensional mixing between several supersonic streams and the subsonic main flow. The third is the calculation of the “engineering” parameters, that is, the injection loss factor, gain, and efficiency. Many interesting physical aspects are discussed, and among them, the formation of three-dimensional shocks’ and expansions’ “domes” [DOI: 10.1115/1.2734236]

Keywords: numerical simulation, injection process, transonic wind tunnel, turbulent mixing layer

1 Introduction

Among the many ideas, processes, and capabilities that were introduced and aggregated to a wind tunnel circuit along the developmental history of this equipment, one of the smartest and most practical is the “injection.” The idea is in a way very simple, and corresponds, in general, to the convenient introduction of a high-speed gas jet inside the tunnel with the objective of “feeding” momentum to the main stream. Inclusively, some installations rely on injection as the only source of energy, and, as an example, some Russian facilities make use of the process [1]. Experiments by Muhlstein et al. [2] in a 6 in. transonic facility had the objective of assessing some very important aspects of the flow, e.g., energy level and flow quality, and how injection eventually affects them. If the main source of energy is injection, the operation is certainly intermittent. However, in many instances, it can be used as an auxiliary power source, as for example, in the well succeeded Calspan 8 ft transonic facility [3,4]. Originally, this tunnel operated continuously, but it was thereafter retrofitted to also run intermittently with the help of four injectors. The injected mass corresponds to 4% of the main stream flow rate and the Reynolds number range was duplicated. But, generally speaking, although the technique has been normally used, there are still serious concerns related to optimization of the running conditions, especially when injection is used in conjunction with the compressor [5,6]. The technique is being incorporated into the design of a new transonic facility in Brazil. The injectors would be installed at the entrance of the transition chamber (the element of the tunnel circuit that provides for the smooth passage between a rectangular and a circular cross section). Because of its novelty, both in position and geometrical form, a pilot wind tunnel is also being designed for the previous testing of this layout. The envelope of the

pilot transonic tunnel (PTT) is shown in Fig. 1. A theoretical study of the transients in the tunnel, including also the effects of injection, was developed some years ago by the present authors [7,8], and corroborated the idea in its general terms.

The objective of the present research effort is to investigate the mixing process between the supersonic jets coming out from the injectors and the tunnel subsonic main stream. This investigation will shed light on this new application of the injection process, and will certainly help in the next steps of detailed design, construction, calibration, and operation of both facilities, pilot and industrial. The details of the problem are discussed in Sec. 2. Because, at this stage, we are mostly interested in the engineering aspects of the problem, the focus of the analysis is on the steady-state solution. The study is done on a numerical basis, and, to this end, a new Reynolds-averaged Navier–Stokes (RANS) code was developed. The basics of the code follow the diagonal algorithm of Pulliam and Chaussee [9], and turbulence effects are accounted for through the use of the Spalart and Allmaras [10] one-equation model. To keep the numerical scheme stable nonlinear spectral artificial dissipation terms are included. For every tunnel there is always an “optimized” running condition that is usually known as the “design condition,” or “design point” as many experimentalists like to call it. In relation to the injection process, this condition corresponds to both currents having the same static pressure when they first meet at the entrance of the mixing chamber. This paper focuses the study on the design point. Some off-design cases are also being investigated and the results will be published in another paper.

In the next section the problem is formulated and the main simplifying assumptions are introduced. Following, details of the numerical scheme and validation cases are briefly discussed. Finally, results of the three-dimensional calculation are presented and discussed. Besides the main physical aspects, some engineering data— injection loss factor, gain, and efficiency—are also calculated and commented on. It is important to note that the calculations and results to be reported herein correspond to the geometry and conditions of the pilot tunnel circuit.

Contributed by the Fluids Engineering Division of ASME for publication in the JOURNAL OF FLUIDS ENGINEERING. Manuscript received June 19, 2006; final manuscript received December 5, 2006. Review conducted by Dimitris Drikakis.

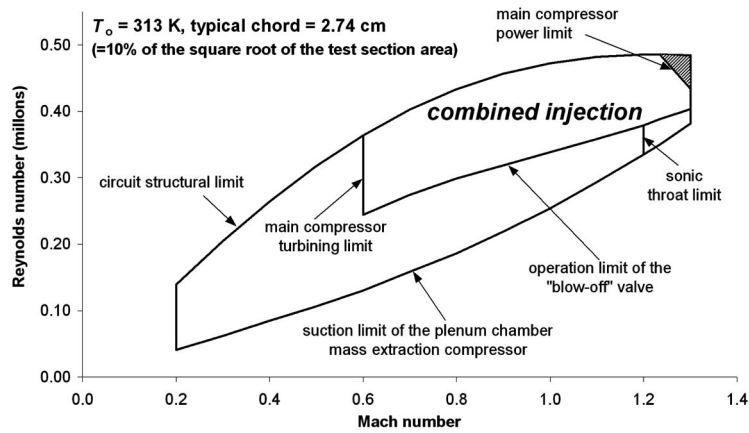


Fig. 1 PTT operational envelope; test section conditions

2 Basic Formulation

2.1 Statement of the Problem. The test section of the PTT has a width of 0.30 m and a height of 0.25 m. The circuit is closed and pressurized from 0.5 bar to 1.2 bar, the range of testing Mach number is 0.2–1.3, and the standard operation is to be continuous and driven by a two-stage, 830 kW main compressor, frequency controlled. There will be a complete controlling system to maintain the desired test section Mach number, stagnation pressure, and temperature. The entire facility is being designed taking as reference the “design point” condition. In this situation, and at the test section, the Mach number is 1, and stagnation pressure and temperature are 110 kPa and 313 K, respectively. At the entrance of the injection chamber the design point corresponds to a tunnel main stream Mach number equal to 0.51, and “asks” the same

static pressure, both for the main and the supersonic streams [8,11]. Figure 1 shows the operational envelope considering the PTT test section conditions. Observe the region labeled “combined injection”—here the running can be continuous by working with the compressor alone, or on an intermittent basis by coupling the compressor, not at full power, with the injection system. A remote region can be reached only on an intermittent basis by using the main compressor at full power combined with the injector system—observe the dashed region beyond the main compressor power limit curve.

The injection system is composed of high-pressure reservoirs that supply air to ten fixed-geometry convergent–divergent nozzles, through a pressure regulator valve that maintains an exit Mach number of 1.9 during about 45 s (at the design condition).

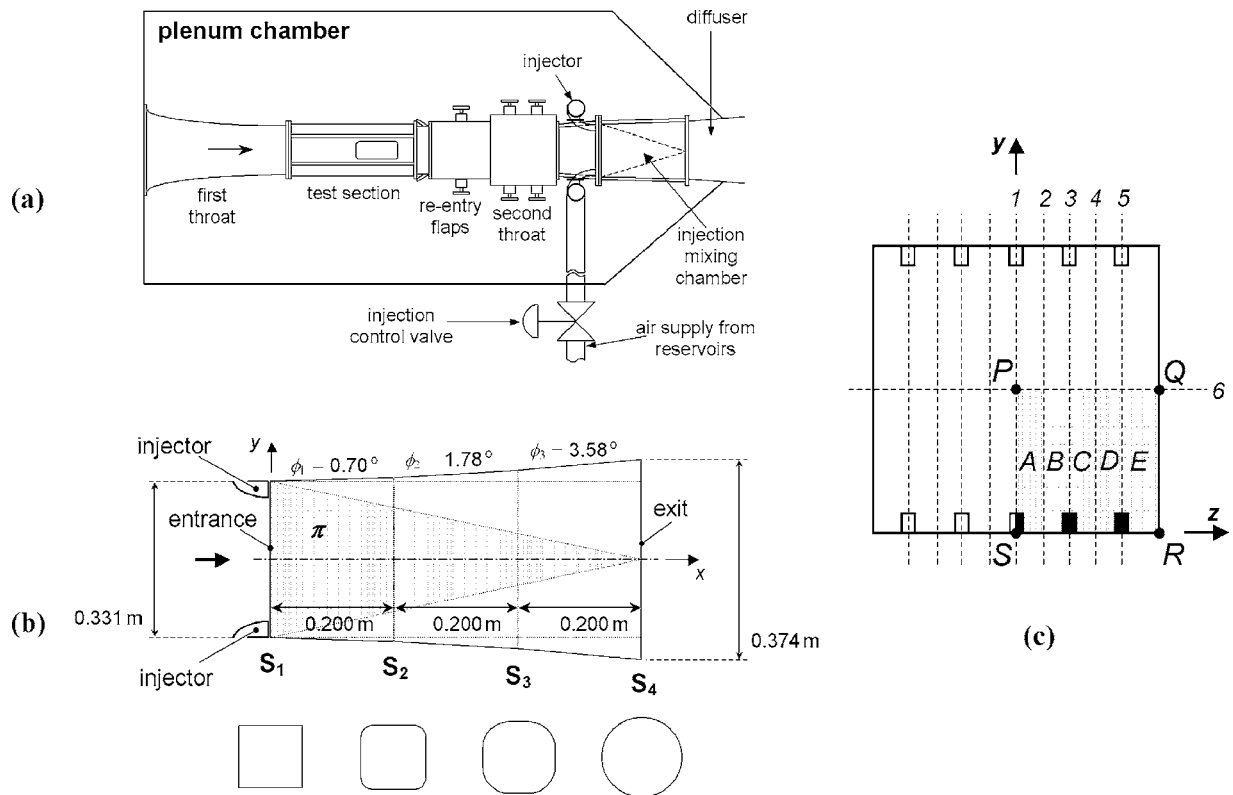


Fig. 2 Tunnel plenum chamber showing the injectors section and feeding system: (a) transition/injection chamber; (b) lateral view; and (c) inlet section

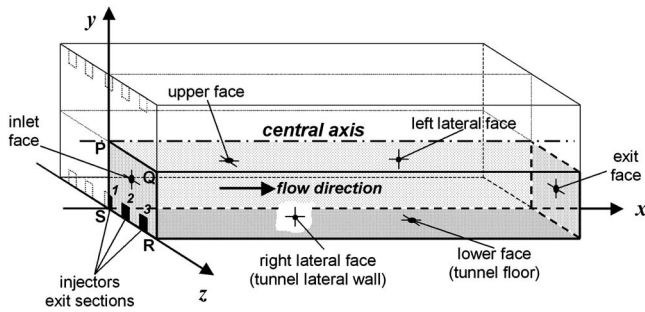


Fig. 3 Three-dimensional sketch of the simplified geometrical form of the mixing chamber. The domain of calculation is illustrated as the shadowed quarter volume. Also shown is the basic Cartesian reference system.

Figure 2(a) sketches the details of the injectors' installation into the tunnel main circuit. The supersonic jets are discharged at the entrance of the transition chamber, which is the longitudinal section of the circuit that provides for the passing from a square to a circular cross section. In Fig. 2(b) some details of the transition chamber are given—the exit section corresponds to the entrance of the first diffuser—and in Fig. 2(c) the transition chamber entrance cross section is shown, with the positioning of the injectors: five at the floor and five at the ceiling. The height and width of the nozzles at their exit section are 0.0226 m and 0.0157 m, respectively.

The domain of calculation corresponds to the volume embraced by the transition section (in Fig. 2(b), it is represented by the volume between planes S_1 and S_4), and its longitudinal length in the PTT is 60 cm. Let us imagine that the main compressor is running, and therefore there is already a steady main stream in the tunnel. Our goal is to calculate the flow that is established in the transition chamber after the nozzles feeding is opened. At the beginning and at the end of the injection operation there are quick transitions, but the reservoirs are able to sustain 45 s of injection operation (at the design condition, see Fig. 12). We shall focus on the steady state of the injection operation.

2.2 Simplifying Assumptions. In this section we shall discuss the main simplifying assumptions that were introduced in order to model the above physical situation. First of all, a simplified geometry was adopted. The main conceptual point in the transition element is to keep the cross-sectional area constant, in spite of the geometrical form variation along the axis of the tunnel. Hence, the cross-sectional form was then admitted as being square and equal in shape and area to the entrance section. The simplified geometry is shown in Fig. 3.

A second point refers to the treatment of the flow about, and inside, the injectors. Observe Fig. 2(b). The flow that reaches the nozzles, coming from the main stream and at this position mostly dominated by the tunnel wall boundary layer, has a very complicated three-dimensional topology around the pieces. Besides, and because the injectors protrude from the tunnel wall, (most probably) a horseshoe vortex will be formed in front of each of the nozzles. We did not tackle this topology, but rather, admitted the wall of the nozzles as flat plates, and calculated the outside boundary layers along them, considering as the starting point the conditions of the flow at the tunnel main stream. For the inner boundary layers, the reference was taken as the average between the states of the gas inside the nozzle's stagnation chamber and at the exit section. But, what exactly is the argument here? Well, one has to be concerned with the fate of the flow around and inside the nozzles, because this flow is going, ultimately, to compose part of the boundary conditions at the domain of calculation entrance plane (see Fig. 3).

We understand that the real geometric form of the transition chamber is an important issue for this problem, as well as the

exact flow about and inside the injectors. But, we also understand that a problem of such magnitude has to accommodate some simplifications at the first approach, otherwise the challenge turns out to be "almost impossible." This is the standard way of treating difficult research problems. After having coped with all the basic issues, it is our plan to extend the study further and possibly eliminate some of these assumptions.

At last, observe now Fig. 2(c). It represents the inlet section of the mixing region. There are two symmetry planes: one horizontal and one vertical (Planes 6 and 1). We have therefore considered as the computational domain one quarter of the whole mixing region. See also Fig. 3. However, a fine grid representation of this smaller volume, considering the resolution that has to be provided at all the viscous gradient regions, would still result in about 8×10^6 node points, a situation completely out of reach of the computational power available to the authors. Therefore, we proceeded as follows. We ran the code for the one-quarter region but considering a coarse grid (about 1×10^6 points). Then we transferred the resulting solution to each of the individual subregions, A, B, C, D, and E, obtained by dividing the original domain through planes 2, 3, 4, and 5 (Fig. 2(c)). We then reran the code for all of these sub-cells but considering a finer grid for each of them (about 1.5×10^6 points for each subregion).

2.3 The Engineering Parameters. Once the solution of the problem is obtained in converged form, one has the basic data for the evaluation of some "integral" parameters that are characteristic of the process. The injection "engineering" parameters are: (i) the loss factor; (ii) the injection gain; and (iii) the injection efficiency. In this subsection we shall derive the proper expressions for the calculation of these factors.

2.3.1 The Loss Factor. As the injection process is considered adiabatic, the loss in the injector chamber is directly related to the stagnation pressure drop, $\Delta \bar{p}_0$, that is, we can define the total pressure loss factor, K , by

$$K = \Delta \bar{p}_0 / q = (\bar{p}_{0,i} - \bar{p}_{0,e}) / q \quad (1)$$

where \bar{p}_0 is the cross-sectional mean stagnation pressure. Therefore, for obtaining K , one needs to calculate the mean stagnation pressure variation between the entrance and exit sections of the mixing chamber. We, now, will describe how this calculation is performed. The relation between the mean stagnation pressures can be obtained once the values of mean entropy at the inlet and exit planes are known

$$\frac{\bar{p}_{0,i}}{\bar{p}_{0,e}} = e^{-(\bar{s}_i - \bar{s}_e) / R} \quad (2)$$

The mean value of the entropy, \bar{s} , at a determined cross section can be evaluated by referring to Fig. 4. The area of the section is already divided by the grid nodes in cells. Because we already know the entropy values at the nodes, the following definition of the entropy at cell n is adopted

$$s_n = \frac{1}{4}(s_1 + s_2 + s_3 + s_4) \quad (3)$$

For the calculation of entropy values, one needs a reference state. This state can be anyone of convenience, but once defined, the reference must be kept the same for all entropy calculations, even for the case of different sections. Now the mean value of entropy for the section can be established as

$$\bar{s} = \frac{\sum_{n=1}^{nt} \dot{m}_n s_n}{\sum_{n=1}^{nt} \dot{m}_n} \quad (4)$$

What we need now is to devise an approach for the evaluation of $\bar{p}_{0,i}$ or $\bar{p}_{0,e}$. As already mentioned these symbols represent mean

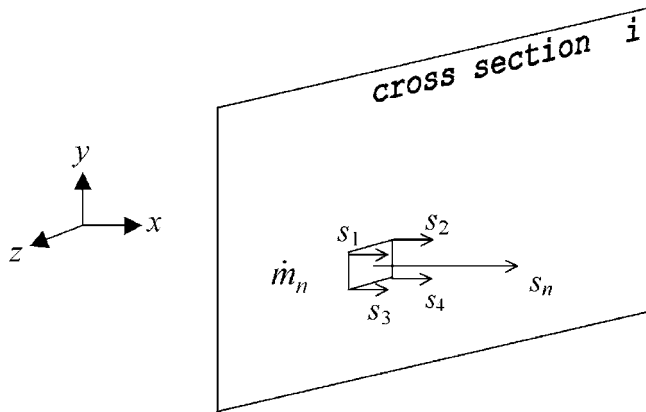


Fig. 4 Calculation cell at a cross section of the injection chamber

values of the stagnation pressures at a certain cross section. But one has to be careful with this concept. For example, whatever the evaluation strategy, it is more difficult to “visualize” a “mean stagnation pressure” at the injection chamber entrance plane because of the great differences in properties between the two streams (including the mass flow). This is not so for the exit section, where the mixing process is almost done, and the idea of a mean stagnation pressure is therefore more natural. We have then proceeded as follows. Let us suppose that $\bar{p}_{0,e}$, $\bar{T}_{0,e}$, and \bar{s}_e are the mean values of stagnation pressure, stagnation temperature, and entropy, respectively, at the exit section. For a generic cell n (at the same exit section), we can write that

$$\Delta s_n = s_n - \bar{s}_e = -R \ln\left(\frac{p_{0,n}}{\bar{p}_{0,e}}\right) + c_p \ln\left(\frac{T_{0,n}}{\bar{T}_{0,e}}\right) \quad (5)$$

If we multiply this equation by \dot{m}_n , and sum up for all cells, the first member will be equal to zero in accordance with Eq. (4), and observing that \bar{s}_e is the mean value. There results then the following expression for the evaluation of $\bar{p}_{0,e}$

$$\bar{p}_{0,e} = \exp\left\{ \frac{\sum_{n=1}^{nt} \left[\dot{m}_n \ln p_{0,n} - \frac{\gamma}{\gamma-1} \dot{m}_n \ln\left(\frac{T_{0,n}}{\bar{T}_{0,e}}\right) \right]}{\sum_{n=1}^{nt} \dot{m}_n} \right\} \quad (6)$$

The mean stagnation temperature, $\bar{T}_{0,e}$, is a consequence of the calculation of $\bar{h}_{0,e}$, the mean stagnation enthalpy, by an expression similar to Eq. (4). Because the gas is supposed to be calorically perfect, one has immediately

$$\bar{T}_{0,e} = \frac{\bar{h}_{0,e}}{c_p} \quad (7)$$

Now, $\bar{p}_{0,i}$ can be evaluated by Eq. (2), and the total loss factor K follows immediately from Eq. (1).

2.3.2 The Injection Gain. Another important parameter that is used to quantify the injection process is its gain, normally indicated by the symbol λ . There are different ways to define the gain depending on the specific engineering application. For this kind of problem, the best definition is [12]

$$\lambda = \frac{\bar{p}_{0,e} - \Delta \bar{p}_0}{\bar{p}_{0,2}} \quad (8)$$

where $\Delta \bar{p}_0$ is the variation of mean stagnation pressure in the mixing process; and $\bar{p}_{0,2}$ is the main flow mean stagnation pressure at the entrance plane, before the injection operation is started.

2.3.3 The Injection Efficiency. The efficiency is expressed in terms of the entropy variation between the inlet and exit sections. With this definition, all the irreversibilities are accounted for. Following Nogueira et al. [13], one writes

$$\eta = - \left(\frac{\bar{s}_{i2} - \bar{s}_e}{\bar{s}_{i1} - \bar{s}_e} \right) \cdot \left(\frac{\dot{m}_{i2}}{\dot{m}_{i1}} \right) \quad (9)$$

where subscripts “i1” and “i2” refer to the two separate inlet streams.

3 Computational Model

3.1 The Code. The mathematical model is represented by the Reynolds-averaged Navier–Stokes equations, written in generalized coordinates and conservation-law form. By “Navier–Stokes equations” we recognize the collection of the continuity, momentum, energy, and any constitutive equation necessary to represent the medium. The medium is air considered as an isotropic and Newtonian fluid, and as a thermally and calorically perfect gas. The numerical algorithm follows closely the main lines of the finite-difference, diagonal scheme due to Pulliam and Chaussee [9], complemented by a nonlinear, spectral-radius-based artificial dissipation strategy due to Pulliam [14]. A one-equation turbulence model as suggested by Spalart and Allmaras [10] is also aggregated to the system of equations.

3.2 Boundary Conditions. First, we focus on the problem of the larger domain. This volume, whose entrance face is the rectangle $PQRS$ (see Figs. 2(c) and 3), has six faces. Boundary conditions for the upper and left faces are established considering symmetry relative to Planes 6 and 1, respectively. The lower and right faces are solid walls, and the nonslip condition is to be enforced. We have also considered solid walls as adiabatic surfaces. At the exit plane extrapolation was done by means of a simplified convection equation. But, by far, the most difficult situation we have faced was the establishment of the boundary conditions at the entrance plane (rectangle $PQRS$). The difficulty comes from the various viscous regions that are present and that correspond to boundary layers that reach (and cross) the entrance plane. These layers are formed along the tunnel bottom, ceiling, and lateral walls, and along the external and internal surfaces of the injectors. But, even more difficult was the tackling of the viscous corners formed at each interaction of two of those boundary layers. Outside the viscous regions, there exist two “potential” cores: the supersonic, inside the nozzle, and here all conditions are fixed, and the subsonic, outside the nozzle, where we have relied on the one-dimensional longitudinal form of the nonviscous gas-dynamic characteristic equations.

Second, there were the cases of the smaller domains, i.e., subregions, or cells, A , B , C , D , and E . For all of them, the upper, lower, inlet, and exit faces require exactly the same corresponding conditions discussed above. The differences are related to the lateral surfaces. The boundary condition at the left face of cell A can be established considering symmetry relative to Plane 1. The conditions at the right face of cell A are fixed from the solution at the larger domain. The right face of cell E is a solid wall, therefore, the nonslip condition applies. For the left face of cell E the conditions are fixed and are obtained from the solution at the larger domain. Internal cells like B , C , and D , all have lateral faces whose boundary conditions are also fixed by the solution at the larger domain. Here, an important observation is due. Because the smaller domains have grids that are finer when compared to the corresponding regions of the larger volume, when passing values we have relied on a bilinear interpolation procedure [15].

3.3 Grids. A typical mesh needs to have several refinements to properly calculate regions of large viscous gradients. Close to solid walls and at the mixing interfaces, nodes’ clustering was a necessity. Figure 5 shows the grid topology at the inlet plane of subregion E , the one subregion that has as the right frontier the

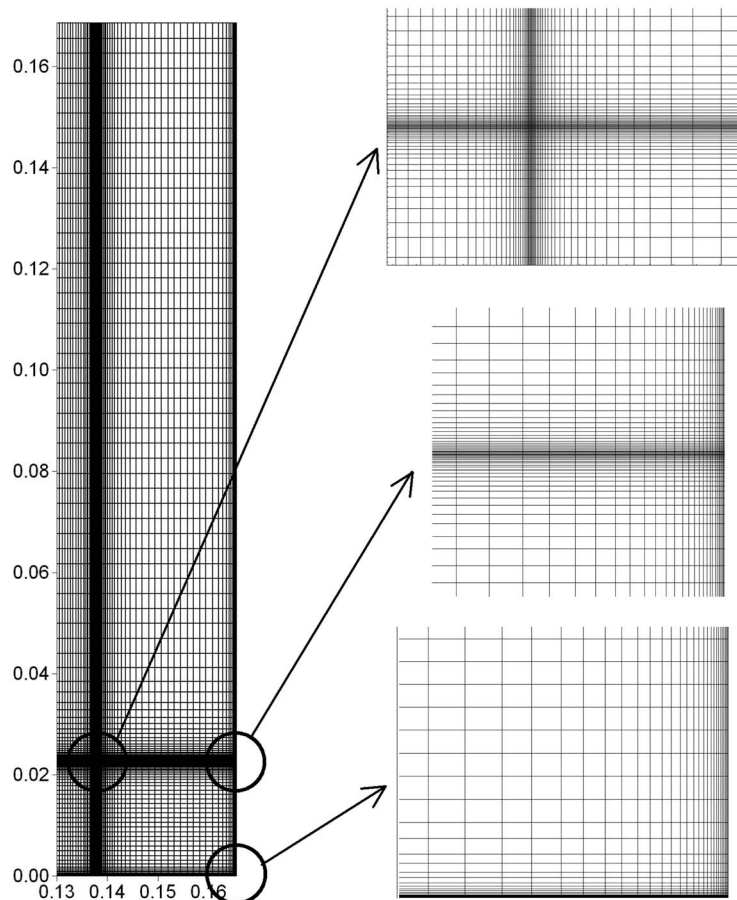


Fig. 5 Nodes distributions at the inlet face of subgrid *E*

right lateral wall of the tunnel. The inner subgrids have topologies similar to grid *E*, but without refinements at the right lateral faces, evidently. But, almost always, clustering brings with it code stiffness. In order to relieve this effect and achieve higher CFL number values, a radial “diffusion” of nodes along the vertical and lateral directions was adopted at the streams mixing regions. In other words, the “radial” positioning of the nodes followed the radial enlargement of the mixing jet as it grew along the tunnel.

3.4 Interim Comment. In the above, we presented a quick and very general overview of the many challenges that appeared in the development of this work. But, there is a whole myriad of details which are very important, and there is no room to describe them here. This same argument applies to the validation cases; we will only touch this matter in the next section. Anyway, details of the code development and other numerical information are not the focus of this paper, and all these subjects are being published elsewhere (see Ref. [16], to where the interested reader is referred).

4 Results and Discussion

4.1 Validation Cases. Before attempting to calculate the flow at the injectors’ mixing chamber, the new code was extensively validated. Several well-established physical situations of increasing complexity were simulated. These were: (i) Laminar and turbulent subsonic and supersonic flows along a two-dimensional flat plate (2D); (ii) nonviscous, laminar, and turbulent flows in a transonic convergent–divergent nozzle (2D); (iii) interaction of a shock wave and a laminar boundary layer (2D, 3D); (iv) interaction of a shock wave and a turbulent boundary layer (2D, 3D); (v) turbulent mixing of two parallel jets, one supersonic and the other

subsonic (2D, 3D); and (vi) turbulent mixing of two parallel supersonic jets (2D, 3D). 2D and 3D mean, respectively, two-dimensional and three-dimensional simulations. For the sake of conciseness we shall briefly discuss only cases (iv) and (vi). These test cases were run using the two-dimensional and the three-dimensional version of the new code. The results to be presented in the sequel come all from the three-dimensional simulations. The reader should observe that much attention was dedicated to the validation of the code for the turbulent jets mixing cases. This had to be so, because the nature of the problem to be tackled, namely the injection mixing process, is connected to the physics of the mixing jets.

With the objective of working with a smaller and, consequently, finer mesh, we followed Wilcox [17] and adopted the calculation domain represented in Fig. 6, for the simulation of the interaction of a shock wave and a turbulent boundary layer, where δ represents the boundary layer thickness just before the recirculation region. But before focusing on this grid, the flow starting at the leading edge of the plate had to be calculated with the basic aim of obtaining the boundary layer profile at the entrance of the smaller mesh.

Figure 7 is the resulting pressure field over which we have “marked” the limits of the recirculation region. The structure of the system of shock waves is quite apparent and the separation and reattachment waves are well represented. This case corresponds to $Re_\delta = 2.5 \times 10^5$, $M_\infty = 2.96$, and $\theta = 12.75$ deg, where Re_δ is the Reynolds number based on the boundary layer thickness at the entrance of the domain. The length of the separation bubble calculated by this method is equal to 3.54δ , a value that compares well with the result of Wilcox [17] for the same case, 3.87δ . Another pertinent comparison is made in Fig. 8, where experi-

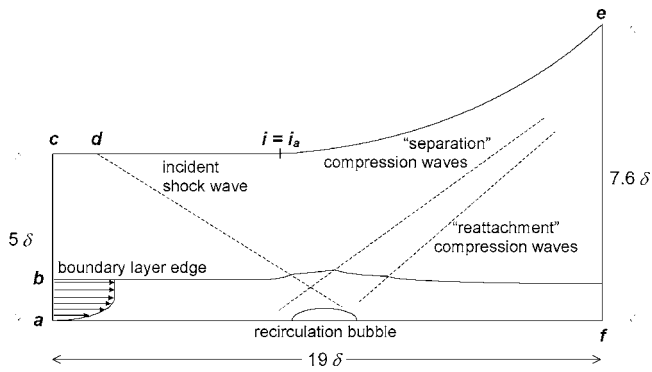


Fig. 6 Domain of calculation for the shock-wave/boundary-layer interaction

mental and numerical surface pressure distributions are plotted. As can be seen our prediction follows closely both the two different numerical results of Wilcox [17] ($Re_\delta = 2.5 \times 10^5$ and 1.0×10^6 , for 1 and 2, respectively) and the experiments of Reda and Murphy (without and with sidewalls treatment, for 1 and 2, respectively) [18,19]. The present simulation corresponds to $Re_\delta = 2.5 \times 10^5$.

The second validation test corresponds to the turbulent mixing of two high-speed streams. This research topic has received much attention, especially in recent years. Ota and Goldberg [20] have treated numerically the case of the layer between two supersonic streams, with a finite volume technique and the κ - ϵ turbulent model, for a mixing condition very similar to the one depicted in Fig. 9. Freund et al. [21] investigated the evolution of a supersonic jet and its acoustic field by means of direct simulation. A hybrid

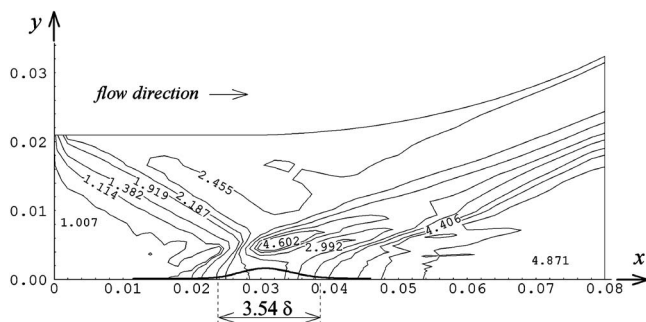


Fig. 7 Static pressure field for the shock-wave/turbulent boundary-layer problem. Values are made dimensionless by the inlet pressure. Coordinates are given in meters.

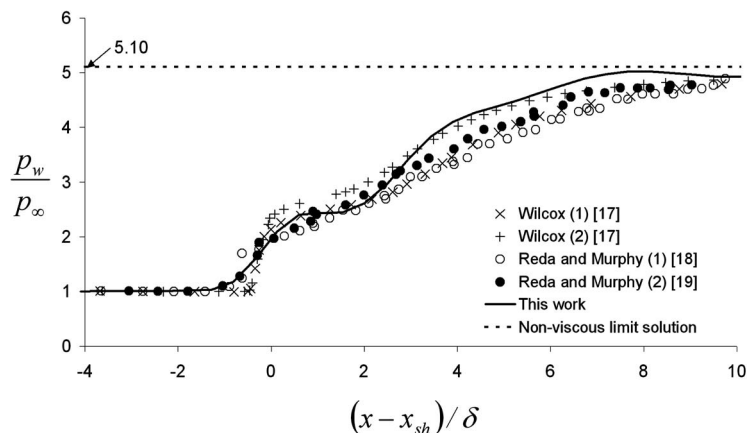


Fig. 8 Pressure distribution on the flat plate wall

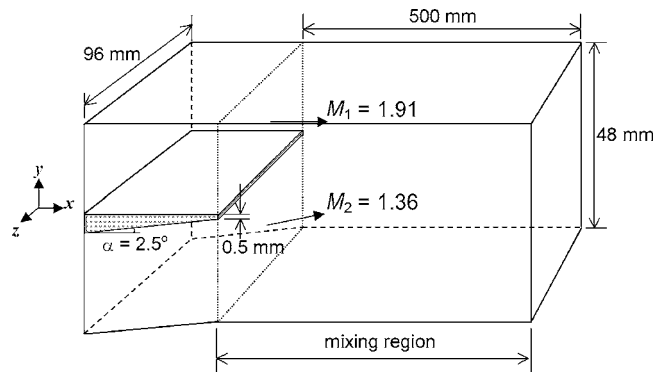


Fig. 9 Sketch of the experimental setup of Goebel and Dutton [23]

approach, RANS and LES, is applied by Georgiadis et al. [22], in the prediction of the interaction between two supersonic streams. This simulation corresponds to Case 2 of Goebel and Dutton [23], the details of which will be discussed below. Chinzei et al. [24] obtained, based on their experimental measurements, a correlation between the growth rate of the mixing layer and the streams velocity ratio. Samimy and Addy [25] presented results relative to a supersonic/supersonic mixing, and discussed the influence of the splitter plate (that separates the two jets) in the resulting flow. The turbulent structure of the layer in a supersonic/subsonic mixing is studied by Clemens and Mungal [26] in three different experiences. The relative Mach number, M_r , was made to vary and the effects of the compressibility in the mixing process were duly investigated. The authors found that a higher relative Mach number induces a three-dimensional character in the mixing layer. But, by far, the best collection of data for comparison purposes is that of Goebel and Dutton [23], who examined the total of seven cases. The authors investigated the turbulent mixing of two high-speed streams in the range of relative Mach numbers from 0.40 to 1.97, which covers a region of significant compressibility effects. Several important aspects were investigated and discussed: the similarity region, the growth rate, and some turbulent correlations, among other studies, for a number of combinations of supersonic and subsonic streams. The tunnel, a sketch of which is shown in Fig. 9, was duly prepared for the two-dimensional mixing of the streams. The reader should observe that, initially, the currents are not parallel but instead have a relative angularity of 2.5 deg. There is also a splitter plate separating the oncoming flows, whose trailing edge is 0.5 mm thick at the entrance of the mixing region. We shall present here the numerical simulation of Goebel and Dutton's Case 2. This physical case corresponds to the mixing of two

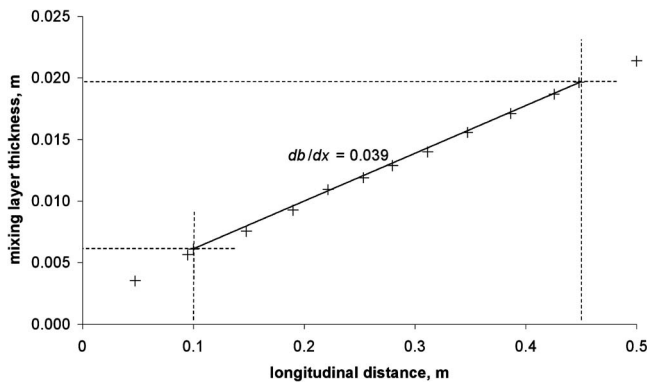


Fig. 10 Mixing layer thickness variation and db/dx in the growth region

supersonic flows with Mach numbers 1.96 and 1.36 ($M_t=0.91$). When entering the mixing chamber the conditions are set such that the two jets have practically the same static pressure. Because the flows are supersonic, the boundary conditions at the entrance of the computational domain are all fixed. The floor and the ceiling of the tunnel are simulated as solid walls, and at the exit section extrapolation was applied by means of a simplified convection equation. One of the most important parameters in the study of a mixing layer is its thickness, b . At the start of the mixing process there is a transition region, after which the mixing layer velocity profiles develop into a similar pattern. This pattern is lost when the layer starts to feel the presence of the walls. The growth of the layer at the similar stretch, characterized by the rate db/dx , is a basic parameter of the mixing process. Figure 10 shows the result of the numerical calculation, and the reader should note that the length of the similar stretch—between 0.10 and 0.45—was taken as equal to the experimental observation. The value of db/dx , obtained by linear regression, is equal to 0.039, while the experimental value is 0.038, a difference of about 2%.

To further illustrate the case in Fig. 11 we show the cross-sectional velocity profile in the middle of the growth region, plotted together with experimental values [23] and with another numerical simulation based on a hybrid approach, RANS and LES [22]. The reader can observe that the comparison of the present solution with the experimental data is very good.

As already stated, the validation results that were presented above come all from the three-dimensional version of the code, which confirms the overall accuracy of the numerical code. Nevertheless, we would like to comment on the 3D grid. In the

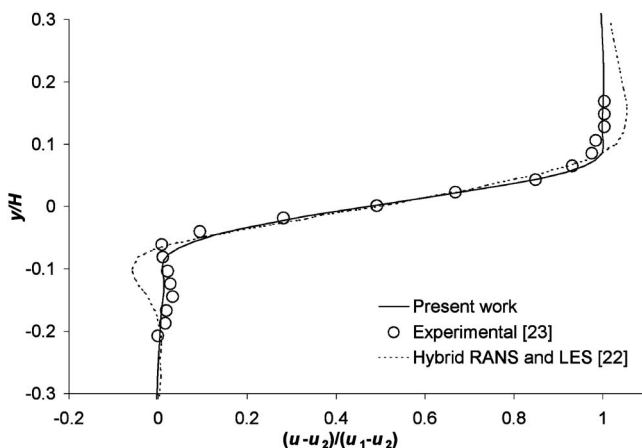


Fig. 11 Normalized mean streamwise velocity at the mixing region. Longitudinal position, $x=0.10$ m.

streamwise and vertical directions the grid was kept exactly equal to the two-dimensional case. To construct the 3D grid we introduced a certain length along the spanwise direction z , and established symmetrical boundary conditions at both lateral faces. With the objective of checking the possible influences of the spanwise length and discretization upon final values, we have investigated them with three different lengths, and for each length with three different resolutions. For example, in the case of the jets mixing, the lengths were defined as 0.05 m, 0.10 m, and 0.20 m, while 21, 41, and 81, were the adopted spanwise number of nodes (the number of points in the streamwise and vertical directions were, respectively, 81 and 105). Considering the level of precision of the algorithm, no significant differences were detected between different configurations.

For completeness, a verification of the code was also done. A grid refinement study was performed together with the determination of the order of the numerical method [27]. The physical case of reference was the two-dimensional turbulent boundary layer along a flat plate, which was calculated with grids 481×481 , 241×241 , 121×121 , 61×61 , and 31×31 . Solutions for the two finer grids were basically coincident, and therefore they served as reference for the calculation of the errors on the other grids. The mean value obtained for the order of the method was 2.25, very close to the theoretical value (that is equal to 2).

4.2 The Injection Process. When the control valve of the compressed air is opened (Fig. 2(a)), the supersonic streams start transferring momentum to the tunnel primary flow at the injection chamber. This induces an acceleration of the main stream until a final equilibrium condition is established, and this final condition is a function of the actual situation of the complete tunnel circuit. In other words, every element of the circuit has an influence on this final equilibrium state. A study of this dynamic process was undertaken some years ago by the authors of this work [7,8]. In this study a simplified mathematical model, based on the concept of “lumped parameters” [28], was used, with the basic aim of simulating the aerodynamic responses to various inputs to the tunnel stream, and among them, the injection of a supersonic stream. The analysis also included the many control devices that exist in a typical transonic circuit. The results of this simulation revealed that injection causes a new distribution of parameters along the circuit. In particular, there is a shift in the main compressor point of operation, with consequent variations in its performance and compression rate. Besides, other modifications appear and the tunnel circuit finally adapts to the new conditions imposed by the injection process. At the test section, a new upper level of stagnation pressure and Mach number, and a slight decrease in stagnation temperature, are finally established. Figure 12 illustrates the resulting stagnation pressure variation at the test section for the design point [7,8]—the reservoirs are able to sustain about 30 s of steady flow at the test section. Locally, at the injection chamber, there also happens to be a raise in stagnation pressure and Mach number.

For a running of the PTT at the design point the flow at the entrance of the mixing section is always subsonic, and the value of the Mach number is 0.51 [11]. But, what mostly characterizes the design condition (in terms of the injection process) is the equality of the static pressures between the main stream and the supersonic jets, exactly at the entrance of the injection chamber (for more details, see Sec. 2.1). This, in principle, is the optimum operation condition, because it will avoid the appearance of strong compression and/or expansion waves and, consequently, losses will be minimized. Due to the strong acceleration provided by the supersonic jet, the injection process will induce an increase in the Mach number of the subsonic stream, and this effect will be transmitted upstream to the entrance of the mixing chamber and also further up to the test section. Because the inlet static pressure is maintained, an increase in the Mach number will correspond to an increase in the stagnation pressure. The Mach number and the stagnation pressure simply do not rise even further, because of the

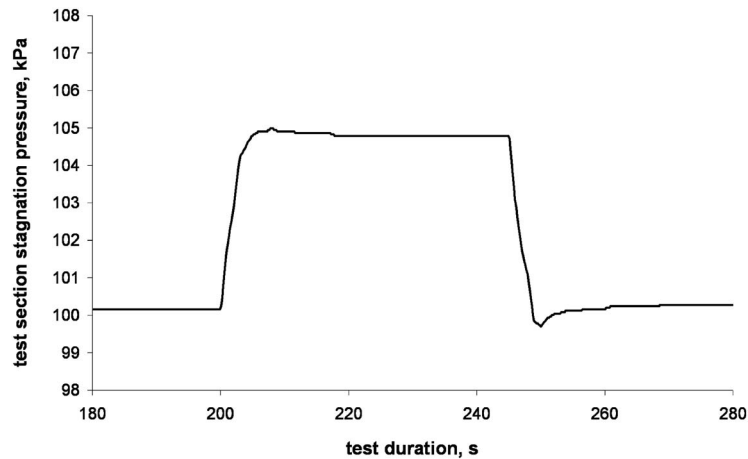


Fig. 12 Test section stagnation pressure variation as a result of the injection process. The injectors' stagnation pressure is set to the design condition (547 kPa).

counterbalancing effect of the pressure losses along the circuit. By the way, the ultimate rise of the stagnation pressure is the result of the net balance between “new energy” introduced by the supersonic stream and the losses along the tunnel circuit.

The point now is the following. This rising of the stagnation pressure at the entrance of the injection chamber has, in some way, to be “informed” to the numerical code; otherwise the simulation will not mimic properly the real physics of the process. How to achieve this goal? The following procedure was adopted. After calculation is started, one allows for the rise of the stagnation pressure at the mixing chamber entrance plane, until the plateau value given in Fig. 12 is reached. Let us note that the stagnation pressure rises due to the rise of the Mach number and the constancy of the static pressure at the entrance plane. After that point is reached, there is a shift of boundary conditions at the inlet section: from this moment on, the stagnation pressure is kept constant and the static pressure is left to change. The code is then run until final convergence. The practical mechanism that permits the augmentation of the stagnation pressure value is the “extrapolation from inside.” The tunnel stream is subsonic at the entrance of the mixing section, therefore information is transported upward because one of the longitudinal characteristic velocities, $(u-a)$, is negative. Therefore, extrapolation of values of u from plane $i=2$ to 1 (the entrance plane) is done using the corresponding characteristic equation. This procedure is performed at the “potential” core of the main subsonic stream. The point of concern now is the fate of the static pressure at the subsonic entrance. It should not “drift away” because this would mean that the design condition is no longer being satisfied. But, as we pointed out before, the ending point of this maneuver—the plateau value of the stagnation pressure in Fig. 12—is an equilibrium condition, and, most probably, the static pressure will not vary significantly. We show that this is so in Fig. 14.

4.3 The Physics of the Injection Process. We pass now to the discussion of the physical results. Before that, let us observe Fig. 13. Lines 1, 3, and 5 are the traces of vertical planes on the entrance plane. Lines 1, 3, and 5 contain the geometrical centers of the exit sections of Injectors 1, 2, and 3, respectively. Lines 6 and 7 are the traces of horizontal planes on the entrance plane. Line 6 contains the geometrical centers of Injectors 1, 2, and 3. The distance of Line 7 to the floor of the tunnel is $y=0.1$ m. Plotted on Fig. 14 are distributions of static pressure along these lines. The distributions correspond to the final converged solution. As the reader can observe, the static pressures of the main stream and the supersonic jet, at the entrance plane, are basically the same at the end of the converging process, which is a guarantee

that the design condition “was not lost” during the maneuvering strategy proposed above. The results to be presented, therefore, correspond all to the tunnel operating at the design condition.

Figure 15 shows the dimensionless static pressure fields on the vertical plane containing Line 1 (Fig. 13) and on the horizontal plane containing Line 6 (Fig. 13), respectively. In this last instance only the vicinity of Injector 1 is shown. The pressure fields are basically homogeneous but, nevertheless, a very small difference between the subsonic and supersonic values at the entrance to the injection chamber (in the vicinity of the injectors—see Fig. 14) is sufficient to give rise to compression and expansion regions, in spite of the fact that the strength of these disturbances are very mild in this situation. At the moment of writing this paper we are running some off-design cases and, in this instance, the strength of these waves is really very high. But, by far, the most interesting physical effect to be learned from these figures is the appearance of alternating expansion and compression regions. These have, in this three-dimensional situation, the form of domes, whose main dimensions are on the same order of magnitude as those of the injectors. But a quick physical reasoning

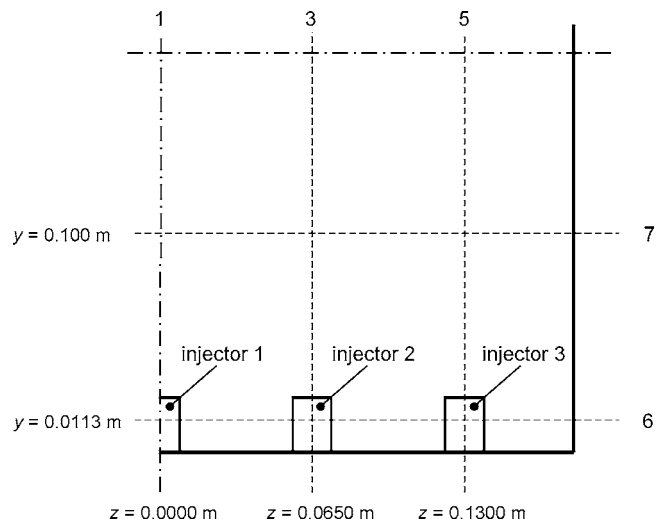


Fig. 13 Special lines definition at the entrance plane of the mixing chamber. Static pressure plots along these lines will illustrate the condition at the design point.

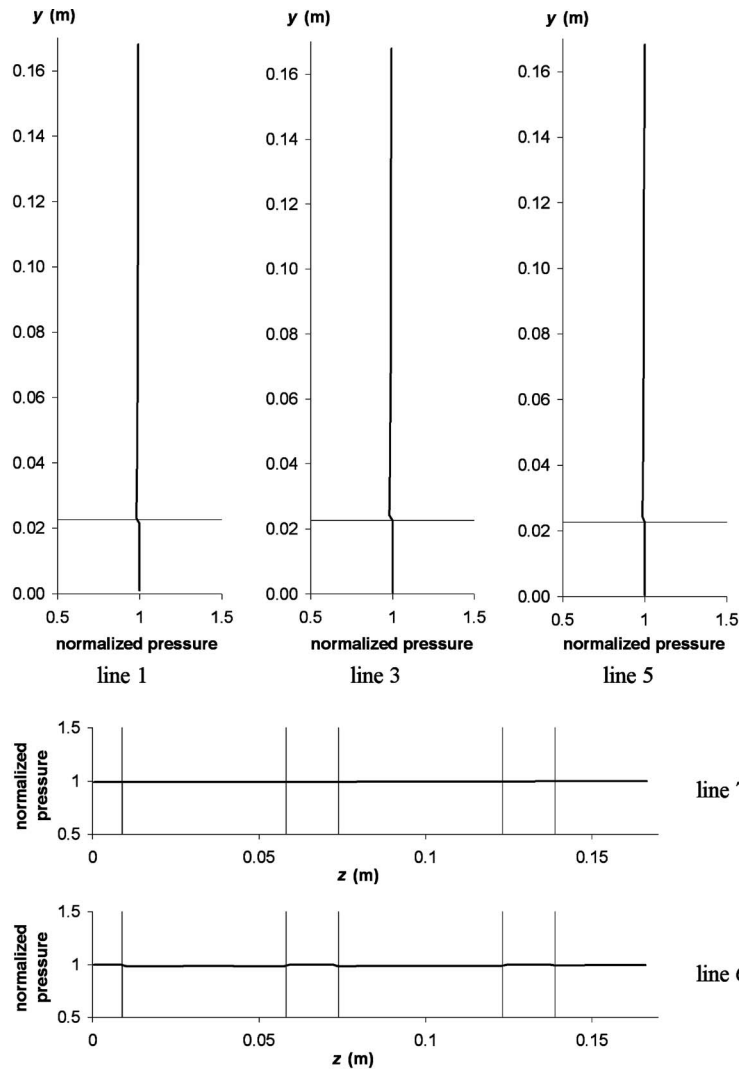


Fig. 14 Static pressure distributions along Lines 1, 3, 5, 6, and 7. Values are made dimensionless by the static pressure of the main stream at the entrance plane. Thin lines mark injectors' walls positions.

would confirm this result: the supersonic jets coming out of the nozzles have to develop between the floor of the tunnel and a kind of "conical subsonic envelope" that limits them.

Figure 16(b) is a general view (from above) of the Mach num-

ber field on the horizontal plane that contains Line 6. One can observe the influence of the supersonic streams in the overall acceleration at the end of the chamber. But as one moves away from the high-speed stream the acceleration falls accordingly. This can

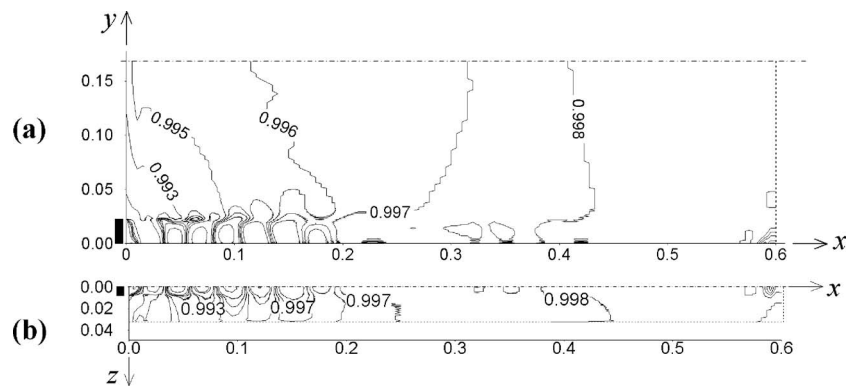


Fig. 15 Static pressure fields in regions close to Injector 1: (a) vertical plane; and (b) horizontal plane. The solid black rectangles at the left of the plots mark the position of the injector. Coordinates are given in meters.

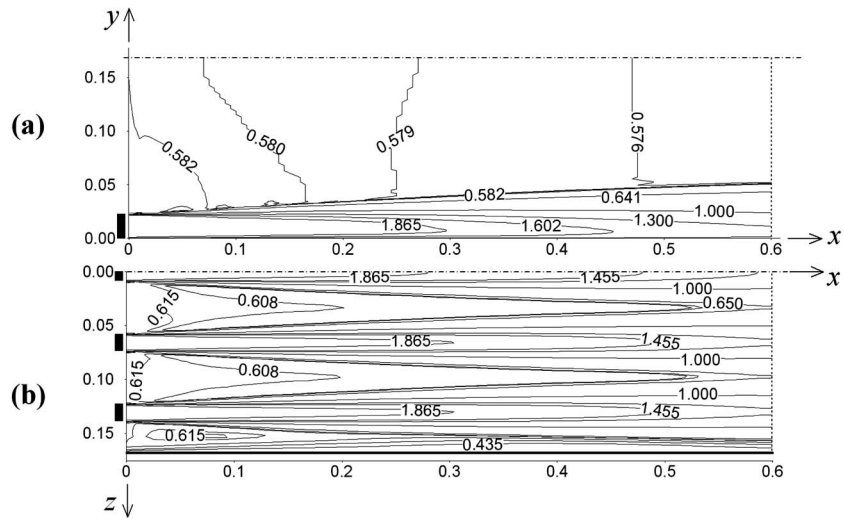


Fig. 16 Mach number fields: (a) on a vertical plane containing Line 3 (Fig. 13); (b) on a horizontal plane containing the geometrical centers of the injectors. The thick solid line at the bottom indicates the tunnel lateral wall. Coordinates are given in meters.

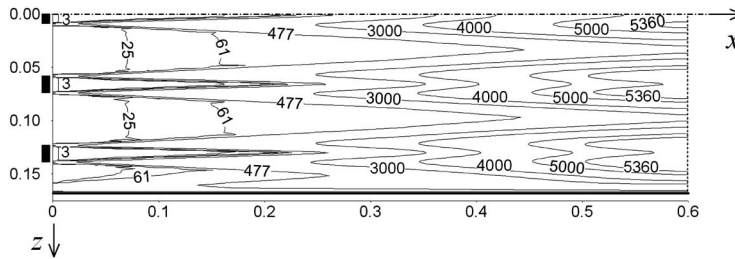


Fig. 17 Isolines of turbulent viscosity on a horizontal plane containing Line 6 (Fig. 13). Coordinates in meters.

be checked by observing Fig. 16(a), where the Mach lines are shown for a vertical plane passing by the center of Injector 2. The topology of the mixing layers can also be appreciated by inspect-

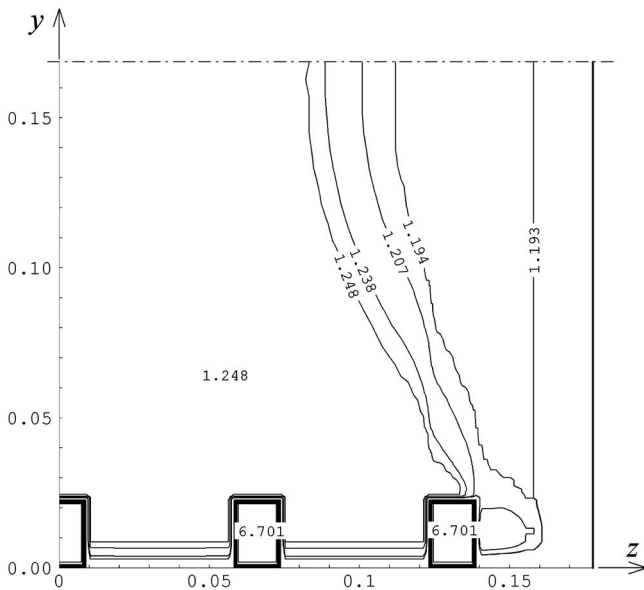


Fig. 18 Isolines of stagnation pressure at the entrance plane. Coordinates in meters.

ing Fig. 17, where isolines of turbulent viscosity are shown. Values in Fig. 17 are made dimensionless by the molecular viscosity at the exit section of the nozzles. The production is so high in the mixing layers that the level of turbulence at the exit of the chamber is about 3000 times that at the inlet of the supersonic stream. In spite of that, there is no complete mixing at the exit of the chamber, what means that the process will finally end inside the first diffuser. Another very interesting aspect can be observed in Fig. 18, where the map of dimensionless stagnation pressure at the entrance plane is shown. At the start of the calculation process, the main (subsonic) stream stagnation pressure at this plane was equal to 1.193—a value made dimensionless by the static pressure at the exit of the injectors. Observing the field one can see that the overall stagnation pressure was raised to 1.249 as a result of injection. But close to the right lateral plane, which happens to be the lateral wall of the tunnel (see Fig. 3), there appeared to be a difficulty in this process. But the explanation here is simple, because the wall with its boundary layer constitute what can be recognized as an important “loss region,” and therefore it represents a difficulty for raising the stagnation pressure.

Important views of the mixing layers are shown in Figs. 19 and 20. Figure 19 corresponds to the first stations, while Fig. 20 illustrates the last sections of the injection chamber. In Fig. 19 one can see the beginning and the evolution of the mixing process, and recognize clearly the presence of the “potential” cores. Here, one can observe the radial diffusion of nodes as mentioned earlier in Sec. 3.3, an expedient that was used in order to relieve grid stiffness. In Fig. 20 the reader can confirm the fact that the streams are not completely mixed when the end of the chamber is reached. The evolution of the mixing layers along all the longitudinal

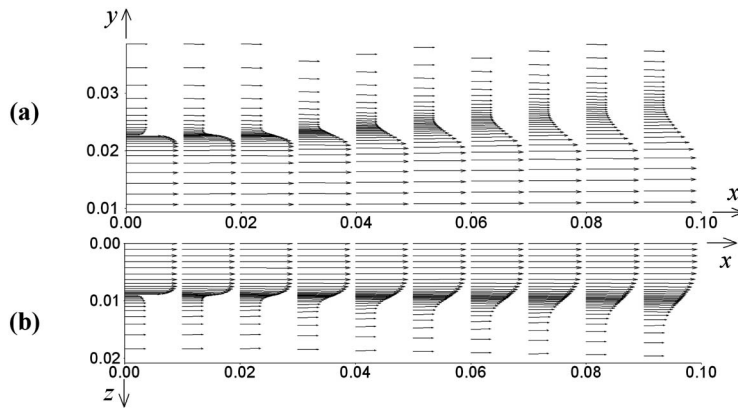


Fig. 19 Streamwise velocity profiles on vertical (a) and horizontal (b) planes containing the geometrical center of the injector 1. Coordinates in meters.

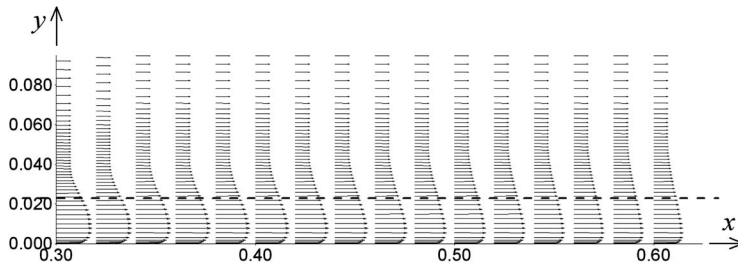


Fig. 20 Streamwise velocity profiles on a vertical plane containing the geometrical center of injector 1. Representation at the exit of the injection chamber. The dashed line represents the injector height. Coordinates in meters.

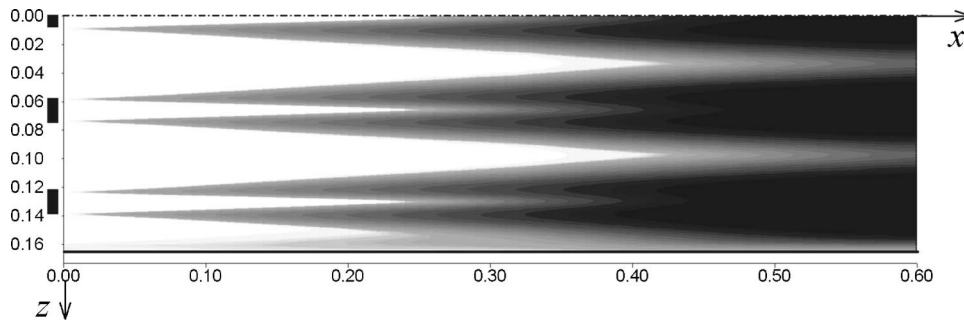


Fig. 21 Turbulent viscosity field on a horizontal plane passing by the geometrical center of the injectors' exit sections. Coordinates in meters.

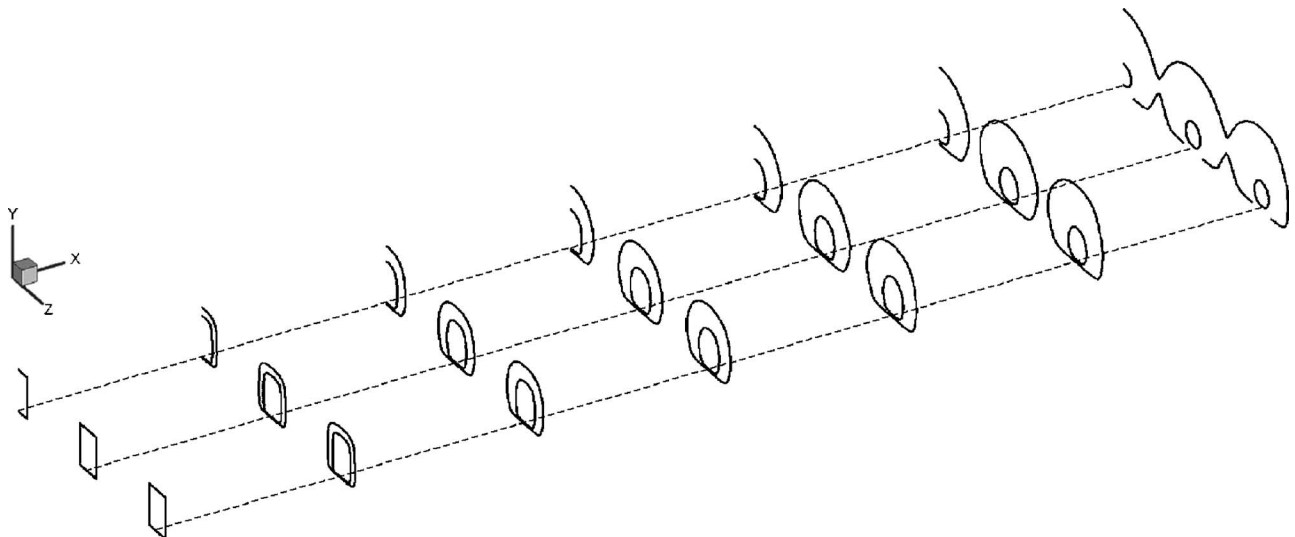


Fig. 22 Three-dimensional view of the jets development along the length of the mixing chamber

Table 1 Initial parameters at the entrance plane

	Supersonic	Subsonic
Mach number	1.90	0.51
Stagnation temperature (K)	300	313
Stagnation pressure (kPa)	547.2	97.5
Velocity (m/s)	503	176
Molecular dynamic viscosity (N s/m ²) ^a	1.15×10^{-5}	1.79×10^{-5}
Reynolds number ^b	1.61×10^6	0.212×10^6
Free stream specific entropy (J/(kg K)) ^c	150	688
Stagnation pressure ratio (supersonic to subsonic)		5.62
Area ratio (subsonic to supersonic)		30.0
Mass flow ratio (subsonic to supersonic)		6.15

^aCalculated using Sutherland formula based on the static temperature.

^bRelated to injector height, 0.0226 m.

^cReference conditions for entropy evaluation, pressure and temperature, 81.67 kPa and 150 K, respectively.

length of the chamber can be appreciated in Fig. 21, which is a flooded version of Fig. 17. Figure 22 is a three-dimensional perspective of the mixing layers represented by the radial limits of the potential cores. Here one can appreciate the very important fact that the supersonic jets exit the nozzles rectangularly, and ultimately evolve to an almost circular cross-section form (see also Ref. [29]). The flattening at the bottom of the jets is an influence of the tunnel floor.

An important aspect that should be stressed in our findings is the fact that the mixing process was not complete up to the end of the mixing chamber, which is attested to especially by Figs. 16 and 20. This might have an impact on the functioning of the first diffuser, because part of the flow at its inlet would be supersonic. Two extra lines of work present themselves now in this research project. The first is to investigate the flow at the entering region of the diffuser considering the mixed supersonic/subsonic inlet conditions. The second is an effort in the direction of eliminating some of the simplifying assumptions in order to assess whether they have any influence on the retarding of the mixing process. We are very confident in the accuracy of the code developed, and believe at this point that the length of the mixing chamber is too short. One should not forget that, as we have stressed above, the injection system was adapted to an already existent (the basic conceptual design of the tunnel was already frozen) transition chamber. But with the available numerical tool we now have on hand, it is not a difficult task to predict what the minimum chamber length for a complete mixing should be.

4.4 Performance of the Mixing Process. We now present the engineering parameters' numerical values for the injection operating at the design condition. Tables 1 and 2 summarize the main data for both flows at the start and end of the numerical simulation. The calculated value of K turned out to be 0.40. This is a high figure, especially when compared to 0.26, the value of the loss factor at the test section [11,12] (considering a standard installed model). But one should remember that the mixing process is extremely turbulent. Notwithstanding this, at the design point,

Table 2 Results of the numerical simulation at entrance and exit sections

	Entrance		Exit
	Supersonic	Subsonic	
Stagnation pressure (kPa)	547.2	101.4	113.2
Specific entropy (J/(kg K))	150	676	633.0
Mass flow (kg/s)	2.76	20.00	22.90
Stagnation pressure ratio ^a	5.40	1	1.12
Mass flow ratio ^b	1	7.27	8.30

^aValues at the subsonic stream taken as reference.

^bValues at the supersonic stream taken as reference.

the gain resulted in $\lambda=1.085$, i.e., there is a real gain, and, therefore, a definite advantage in using the injection concept. The calculated injection efficiency resulted is $\eta=0.67$.

5 Conclusions

The flow in the injection chamber of a transonic wind tunnel, for conditions designated as the design point, was successfully simulated. A new finite-difference computer code, that incorporates an assortment of very powerful numerical tools, was developed, and proved to be extremely robust, reliable, and accurate. The physics of the three-dimensional mixing process, a very involved situation, was properly investigated. This is attested by the finding of the compression/expansion domes, the verification of the maps of the mixing layers, and the calculation of the parameters that characterize the injection process, among many other important results. In spite of the pressure losses, a consequence of the high turbulence activity at the mixing between high-speed streams, the operation presented a positive gain. An important aspect that should be stressed in our findings is the fact that the mixing process was not complete up to the end of the mixing chamber, which is confirmed especially by Figs. 16 and 20. This might have an impact in the functioning of the first diffuser.

Acknowledgment

The authors would like to express their gratitude to CNPq, the Brazilian National Council of Research and Development, for the partial funding of this research, under Grant No. 302863/2004-4.

Nomenclature

- a = sound speed (m/s)
- \bar{a} = average of freestream speeds of sound, $(a_1 + a_2)/2$ (m/s)
- A = cross sectional area (m²)
- b = mixing layer thickness between transverse locations where $u=(u_1-0.1\Delta u)$ and $u=(u_2+0.1\Delta u)$ (m)
- CFL = number of Courant, Friedrichs, and Levy
- c_p = specific heat at constant pressure (J/kg K)
- h = specific enthalpy (J/kg)
- H = height of tunnel section (m)
- i = computational field node counter
- K = pressure loss coefficient
- LES = large eddy simulation
- M = Mach number
- M_r = relative Mach number, $=\Delta u/\bar{a}$
- \dot{m} = mass flow (kg/s)
- nt = total number of cells in a cross section
- PTT = pilot transonic tunnel
- p = static pressure (Pa)

q = dynamic pressure (Pa)
 R = gas constant (J/kg K)
 Re = Reynolds number
 s = specific entropy (J/kg K)
 T = static temperature (K)
 u = local mean streamwise velocity (m/s)
 Δu = freestream velocity difference, $=u_1 - u_2$ (m/s)
 x = streamwise coordinate (m)
 y = vertical coordinate (m)
 z = lateral, or spanwise, coordinate (m)
 α = rotation flow angle (deg)
 γ = specific heat ratio
 δ = boundary layer thickness (m)
 η = injection efficiency
 θ = flow deflection angle due to shock wave (deg)
 λ = injection gain
 ϕ = mixing chamber wall angle (deg)

Subscripts

0 = stagnation condition
 $1,2$ = high and low speed, respectively
 i,e = inlet and exit cross section stations, respectively
 n = generic cell
 sh = shock impinging position at the flat plate
 w = wall conditions
 δ = boundary layer thickness
 ∞ = free stream value

References

- [1] Bedrzhitsky, E. I., and Roukavets, V. P., 1997, "Historical Review of the Creation and Improvement of Aerodynamic Test Facilities at TsAGI," Moscow, AGARD-CP-585 Paper No. 1.
- [2] Muhlstein, L., Jr., Petroff, D. N., and Jillie, D. W., 1974, "Experimental Evaluation of an Injector System for Powering a High Reynolds Number Transonic Wind Tunnel," AIAA Paper No. 74-632.
- [3] Cotter, R. W., 1973, "Transonic Operations With Ejectors at High Reynolds Number in the Calspan 8' Transonic Wind Tunnel," Proceedings of the 40th Semi-Annual Meeting of the Supersonic Tunnel Association (STA), Bedford, UK.
- [4] Rose, W. C., Hanly, R. D., Steinle, F. W., Jr., and Chudyk, D. W., 1982, "The Effect of Ejector Augmentation on Test-Section Flow Quality in the Calspan 8' Transonic Wind Tunnel," AIAA Paper No. 82-0571.
- [5] Arkadov, Y. K., and Roukavets, V. P., 1997, "Ejector-Driven Wind Tunnels," AGARD Conference Proceedings 585, Moscow, USSR, 1996, Article No. 22.
- [6] Carrière, P., 1973, "The Injector Driven Tunnel," Proceedings of the von Kármán Institute for Fluid Dynamics, Lecture Series on Large Transonic Wind Tunnels, von Kármán Institute for Fluid Dynamics, Brussels, Belgium.
- [7] Falcão, J. B. P. F., Ortega, M. A., and Góes, L. C. S., 2000, "Prediction of Transients and Control Reactions in a Transonic Wind Tunnel," J. Braz. Soc. Mech. Eng. Sci., **XXII**(2), pp. 317–339.

- [8] Falcão, J. B. P. F., 1996, "Modelling the Transients in the Aerodynamic Circuit of a Transonic Wind Tunnel," M.Sc. thesis, Division of Aeronautical Engineering, ITA, Technological Institute of Aeronautics, São José dos Campos, SP, Brazil (in Portuguese).
- [9] Pulliam, T. H., and Chaussee, D. S., 1981, "A Diagonal Form of an Implicit Approximate-Factorization Algorithm," J. Comput. Phys., **39**, pp. 347–363.
- [10] Spalart, P. R., and Allmaras, S. R., 1992, "A One-Equation Turbulence Model for Aerodynamic Flows," AIAA Paper No. 92-0439.
- [11] PTT Team, 1996, "Detailed Project of the CTA's Pilot Transonic Wind Tunnel," Classified Report, CTA-IAE, Aeronautics and Space Institute, São José dos Campos, SP, Brazil.
- [12] Sverdrup Technology Inc., 1989, "Brazilian Transonic Wind Tunnel Concept Definition Study," Contractor Report for TTS and TTP Projects, CTA-IAE, Aeronautics and Space Institute, São José dos Campos, SP, Brazil.
- [13] Nogueira, S. L., Ortega, M. A., Falcão, J. B. P. F., and Fico, N. G. R. C., Jr., 1988, "Injection Optimization and its Application to Wind Tunnels," Proceedings of the 2nd Brazilian Congress of Thermal Engineering and Sciences, ENCIT-1988, Águas de Lindóia, SP, Brazil, pp. 151–153.
- [14] Pulliam, T. H., 1986, "Artificial Dissipation Models for the Euler Equations," AIAA J., **24**(12), pp. 1931–1940.
- [15] Press, W. H., Teukolsky, S. A., Vetterling, W. T., and Flannery, B. P., 1992, *Numerical Recipes in Fortran 77—The Art of Scientific Computing*, Press Syndicate of the University of Cambridge, Cambridge, UK.
- [16] Falcão, J. B. P. F., and Ortega, M. A., 2006, "Numerical Study of the Injection Process in a Transonic Wind Tunnel: The Numerical Details," Int. J. Heat Fluid Flow, submitted.
- [17] Wilcox, D. C., 1974, "Numerical Study of Separated Turbulent Flows," AIAA Paper No. 74-584.
- [18] Reda, D. C., and Murphy, J. D., 1972, "Shock Wave—Turbulent Boundary Layer Interactions in Rectangular Channels," AIAA Paper No. 72-715.
- [19] Reda, D. C., and Murphy, J. D., 1973, "Shock Wave—Turbulent Boundary Layer Interactions in Rectangular Channels, Part II: The Influence of Sidewall Boundary Layers on Incipient Separation and Scale of the Interaction," AIAA Paper No. 73-234.
- [20] Ota, D. K., and Goldberg, U. C., 1991, "Computation of Supersonic Turbulent Shear Layer Mixing With Mild Compressibility Effects," AIAA J., **29**(7), pp. 1156–1160.
- [21] Freund, J. B., Lele, S. K., and Moin, P., 2000, "Numerical Simulation of a Mach 1.92 Turbulent Jet and its Sound Field," AIAA J., **38**(11), pp. 133–139.
- [22] Georgiadis, N. J., Alexander, J. I. D., and Reshotko, E., 2003, "Hybrid Reynolds-Averaged Navier-Stokes / Large-Eddy Simulations of Supersonic Turbulent Mixing," AIAA J., **41**(2), pp. 218–229.
- [23] Goebel, S. G., and Dutton, J. C., 1991, "Experimental Study of Compressible Turbulent Mixing Layers," AIAA J., **29**(4), pp. 538–546.
- [24] Chinzei, N., Masuya, G., Komuro, T., Murakami, A., and Kudou, K., 1986, "Spreading of Two-Stream Supersonic Turbulent Mixing Layers," Phys. Fluids, **5**, pp. 1345–1347.
- [25] Samimy, M., and Addy, A. L., 1986, "Interaction Between Two Compressible, Turbulent Free Shear Layers," AIAA J., **24**(12), pp. 1918–1923.
- [26] Clemens, N. T., and Mungal, M. G., 1992, "Two- and Three-Dimensional Effects in the Supersonic Mixing Layer," AIAA J., **30**(4), pp. 973–981.
- [27] Oberkampf, W. L., and Trucano, T. G., 2002, "Verification and Validation in Computational Fluid Dynamics," Prog. Aerosp. Sci., **38**, pp. 209–272.
- [28] Krosel, S. M., Cole, G. L., Bruton, W. M., and Szuch, J. R., 1986, "A Lumped Parameter Mathematical Model for Simulation of Subsonic Wind Tunnels," NASA Paper No. TM-87324.
- [29] Trentacoste, N., and Sforza, P., 1967, "Further Experimental Results for Three-Dimensional Free Jets," AIAA J., **5**(5), pp. 885–891.

Initial Stage of Natural Convection Over a Hot Aerosol Sphere

Elaad Mograbi

Department of Mechanical Engineering,
Ben-Gurion University of the Negev,
Beer-Sheva 84105, Israel

Ezra Bar-Ziv

Department of Mechanical Engineering and
Institute of Applied Research,
Ben-Gurion University of the Negev,
Beer-Sheva 84105, Israel

Background: Analytical study is presented on the transient problem of buoyancy-induced motion due to the presence of a hot aerosol sphere in unbounded quiescent fluid. *Method of Approach:* Because the initial flow field is identically zero, the initial stage of the process is governed by viscous and buoyancy forces alone where the convective inertial terms in the momentum and energy balances are negligible, i.e., the initial development of the field is a linear process. The previous statement is examined by analyzing the scales of the various terms in the Navier-Stokes and energy equations. This scale analysis gives qualitative limitations on the validity of the linear approximation. A formal integral solution is obtained for arbitrary Prandtl number and for transient temperature field. *Results:* We consider, in detail, the idealized case of vanishing Prandtl number for which the thermal field is developed much faster than momentum. In this case, analytical treatment is feasible and explicit expressions for the field variables and the drag acting on the particle are derived. Detailed quantitative analysis of the spatial and temporal validity of the solution is also presented. *Conclusions:* The linear solution is valid throughout space for $t < 10$ diffusion times. For $t > 10$, an island in space appears in which inertial effects become dominant. The transient process is characterized by two different time scales: for short times, the development of the field is linear, while for small distances from the sphere and finite times, it is proportional to the square root of time. The resultant drag force acting on the sphere is proportional to the square root of time throughout the process. [DOI: 10.1115/1.2734195]

Keywords: transient natural and mixed convection, buoyancy, small Reynolds and Grashoff numbers, drag force

1 Introduction

The problem of natural convection over finite bodies has a far reaching history (a comprehensive review can be found in the book by Gebhart et al. [1]). Many interesting phenomena regarding this process have arisen as a result of the various studies.

Earlier studies considered the steady flow induced by a point source of heat. Zel'dovich [2] introduced the notion of the self-similar axisymmetric thermal plume far from the hot body. Yih [3] derived a closed form solution to the reduced self-similar equations for the case of Prandtl (Pr) number $Pr = 1, 2$. Gutman [4] and later Fujii [5] considered the steady natural convection above point and line heat sources by numerical integration. More recently, Kurdyumov & Liñán [6] advanced this problem by performing numerical computations for different Pr numbers. Results for the heat transfer rate for a large range of Grashof numbers (Gr) are obtained for the flow around a point source.

Steady natural and combined convections for large Grashof numbers have been studied extensively (e.g., [7–9]). Potter and Riley [10] studied theoretically, using boundary layer approximation, the asymptotic behavior for $Gr \rightarrow \infty$ and found that the upper stagnation is a singular point, which suggests that, at that point, flow erupts from the boundary layer forming the edge of the thermal wake.

Geoola and Cornish [11] investigated the flow induced by natural convection around a sphere for Gr values 0.05–50 and extracted values of Nusselt (Nu) and drag coefficients. Jia and

Gogos [12] studied the free convection case for the parameter range $10 < Gr < 10^8$. They also obtained heat transfer and drag coefficients.

Studies more relevant to the present interest consider steady natural convection for small values of Gr (i.e., small particle dimensions). Fendell [13] showed that for the steady problem, linear approximation for $Re \rightarrow 0$ is physically inconsistent as it results in an unbounded velocity field. He also observed that the self-similar solution of the point source valid far from the source cannot be matched with the linear solution near the source because the regions of validity of the two solutions do not overlap. A remedy is offered by an inner regular asymptotic expansion and an outer expansion conforming to the Oseen approximation based on the velocity scale of the outer flow. Though, as was noted by Heiber and Gebhart [14], this approach lead to the erroneous result that the inner velocity is proportional to $Gr^{1/2}$ as opposed to Gr. Heiber and Gebhart [14], in turn, considered the effect of buoyancy on a dominant forced convection field for small Re and Gr, and for unit Pr number. A solution to the mixed convection flow is obtained by a unique inner-outer matched asymptotic scheme for small Re and Richardson number, $Ri = Gr/Re^2$. Expressions for the steady drag and heat transfer coefficients are extracted.

Regarding unsteady processes, most studies concern heat transfer in forced convection rather than in natural convection regimes; thus, effects of buoyancy are completely neglected. In such a case, the momentum equation is decoupled from the heat transfer problem and, thus, the flow field and drag on the particle is unaltered. For example, Abramzon and Elata [15] studied, numerically, the forced convection transient heat transfer from a sphere assuming Stokes velocity field, which is also steady during the cooling process. Feng and Michaelides [16] provide asymptotic analysis and numerical analysis [17] for the same problem for small Peclet numbers (Pe) [16] for spherical and nonspherical shapes, and for

Contributed by the Fluids Engineering Division of ASME for publication in the JOURNAL OF FLUIDS ENGINEERING. Manuscript received January 4, 2006; final manuscript received October 20, 2006. Review conducted by Malcolm J. Andrews.

large Re and Pr [17]; they extracted explicit results for the transient heat transfer rate from a sphere. Again, these results do not consider the effects of buoyancy on the flow field.

Geoola and Cornish [18] studied, numerically, the problem of transient natural convection by applying a finite difference scheme for the solution of the energy and vorticity-stream function equations. The calculations are performed for the initial state of zero fields and a step temperature function at the particle surface. Unfortunately, results are tabulated only for the final steady-state coefficients. The initial developed flow is only given graphically using plots of the instantaneous stream function, iso-vorticity lines, and isotherms. Time scales for the development of the flow and global parameters are not given.

Regarding experimental studies, Dudek et al. [19] used an electrodynamic chamber [20] to suspend a heated charged particle in space and reported a plot of the transient voltage (proportional to the drag force acting on the particle) required to suspend the particle in the chamber.

Thus many interesting and important questions are still open. In this study, we are interested in the initial time scales of evolution of the velocity field and, keeping application in mind, the resultant evolution of the drag force. It is of course obvious that without available solution of the steady, already developed field, it is impossible to obtain a solution to the transient problem for all times. However, dimensional inspection of the governing equations (Sec. 2) suggests that at the initial stage of the process, the problem of unsteady buoyancy-induced flow will not suffer from the singular behavior of the linearized (omission of the inertial terms) Navier-Stokes equation. The reason is that, for sufficiently short times, the disturbance developed near the particle will not reach distances where the processes are dominated mainly by inertial forces and also because the initial developed velocity field is very weak. The main interest of this study is thus to obtain a valid solution at the initial stages of natural convection when buoyancy and diffusion processes predominate and to provide conditions of validity of the approximation.

The paper is organized as follows. Section 2 discusses the linear approximation and the mathematical problem is formulated. In Sec. 3 the problem is solved and in Sec. 4 results for the simplest case of Prandtl number infinitely small are examined, i.e., the case is considered where the temperature field is already developed. The spatial and temporal range of validity of the linear approximation is examined with respect to the contribution of the nonlinear convective inertial terms. Section 5 discusses the applicability of the results to the mixed case where the particle is also subjected to motion; hence, the contribution of the buoyancy-induced flow may be superposed on the solution of the transient particle motion under isothermal conditions.

2 Linearization of Transport Equations

Consider the configuration presented in Fig. 1. The governing equations are continuity, momentum subject to Boussinesq conditions, and energy,

$$\nabla \cdot \mathbf{u} = 0$$

$$\frac{\partial \mathbf{u}}{\partial t} + (\mathbf{u} \cdot \nabla) \mathbf{u} = -\nabla \frac{p}{\rho} + \nu \Delta \mathbf{u} - \beta \tau \mathbf{g} \quad (1)$$

$$\frac{\partial \tau}{\partial t} + (\mathbf{u} \cdot \nabla) \tau = \kappa \Delta \tau$$

where (\mathbf{u}, p, τ) are the fluid velocity, pressure, and temperature, respectively; \mathbf{g} is the gravitational acceleration; ρ, ν, β, κ are the density, kinematic viscosity, thermal expansion, and thermal diffusivity, respectively. The spherical particle is fixed in an unbounded initially quiescent fluid. The homogeneous boundary condition for the hydrodynamic problem is the adherence of the fluid to the particle surface, i.e., the velocity vanishes on the par-

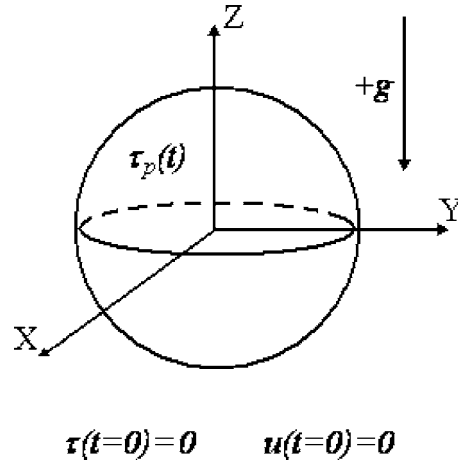


Fig. 1 Schematic view of the problem

ticle surface and also at infinity. Hence, the following conditions are to be satisfied:

$$\begin{aligned} \mathbf{u}(|r|=a, t) = \mathbf{u}(|r| \rightarrow \infty, t) = 0, \quad \mathbf{u}(\mathbf{r}, 0) = 0 \\ \tau(|r|=a, t) = \tau_p(t) \cdot H; \quad \tau(\mathbf{r}, 0) = 0 \end{aligned} \quad (2)$$

where a is the aerosol radius, H is the Heaviside step function, and τ_p is the particle surface temperature. It is assumed throughout that the particle is small enough such that its surface temperature may be considered uniform and that Gr is much smaller than unity at all times.

Equations (1) and (2) are normalized by introducing characteristic dimensions that will be defined as the argument progresses. The corresponding dimensionless equations (continuity remains unchanged) are

$$\begin{aligned} \text{StRe} \frac{\partial \mathbf{u}}{\partial t} + \text{Re}(\mathbf{u} \cdot \nabla) \mathbf{u} = -\nabla p + \Delta \mathbf{u} - \text{ReRi} \cdot \hat{\mathbf{g}} \\ \text{StPe} \frac{\partial \tau}{\partial t} + \text{Pe}(\mathbf{u} \cdot \nabla) \tau = \Delta \tau \end{aligned} \quad (3)$$

Equations (3) define the following general dimensionless numbers: Strouhal number $\text{St}=l/(U\tau^c)$, Reynolds number $\text{Re}=Ul/\nu$, Richardson number $\text{Ri}=\text{Gr}/\text{Re}^2$, Grashof number $\text{Gr}=\beta g \tau^c l^3/\nu^2$, Peclet number $\text{Pe}=\text{RePr}$, and Prandtl number $\text{Pr}=\nu/\kappa$. The characteristic dimensions are l for length, U for velocity, τ^c for time, and τ^c for temperature. The parameter multiplying p to yield the unit factor becomes μUl ; $\hat{\mathbf{g}}$ is the unit vector in the direction of gravity.

It is imperative to consider the relative importance of the different terms in the momentum and energy equations and to conclude whether, indeed, conditions exist in which the convective inertial terms may be neglected as a first approximation. The important parameter for this discussion is the characteristic speed U —yet to be defined—of the induced flow. At the initial stage, the velocity field is identically zero. In the approach to steady state, it is already known that in the thermal plume far from the sphere the velocity scales as $(\nu/a)\text{Gr}^{1/2}$ (see, e.g., [21]). With this scale, the singularity of the linearization of the momentum equation is evident. Indeed, taking $U=(\nu/a)\text{Gr}^{1/2}$ and $l=a$, one finds that $\text{Re}=\text{Gr}^{1/2}$ and also $\text{ReRi}=\text{Gr}^{1/2}$. Namely, both convective and buoyancy forces become comparable and inertia cannot be neglected. However, if the velocity scales linearly with Gr, which was noted by Hieber and Gebhart [14] as the proper velocity scale near the particle, the factor multiplying the convective term becomes $\text{Gr} \sim o(1)$ and the one for the buoyancy term becomes unity (standard notation for order of magnitudes are employed, namely, $o(*)$

stands for smaller than “*,” and $O(*)$ means of the same order of magnitude as “*.” If, furthermore, the time scale is $t^c = a^2/\nu$ (diffusion time scale), then it becomes apparent that $StRe = 1$, or

$$\frac{\partial \mathbf{u}}{\partial t} \sim \Delta \mathbf{u} \sim \tau \hat{\mathbf{g}} \quad (4)$$

In other words, an approximate condition of the validity of the linearization may be characterized by the condition that the scale of the velocity is such that the following condition holds everywhere

$$Re \ll O(Gr^{1/2}) \quad (5)$$

Thence, it is apparent that the linear solution would not converge to the steady thermal plume flow. However, for $Gr \sim o(1)$ we have $Gr \ll O(Gr^{1/2})$; hence, in the near vicinity of the sphere, the linear approximation is expected to yield valid results even for long times from initial conditions.

Using the same scale arguments and parameters for the energy equation, results in $StPe = Pr$ and $Pe = GrPr$. Thus, the energy equation is governed by three characteristic scales. For $Pr \sim O(1)$, the transient term scales as the thermal diffusion (conduction) term, where again convection falls behind with the scale of $Gr \sim o(1)$. In this case, it is apparent that thermal diffusion is comparable to vorticity diffusion (characteristic rate of vorticity diffusion is ν/a , while that of thermal conduction is κ/a , thus the ratio of the first to the second becomes Pr); thus, the unsteady temperature field must, in general, be incorporated into the solution of the velocity field. To avoid confusion, note that the convective term is neglected from the energy equation because of the small Pe (proportional to Gr) regardless the value of Pr .

It is concluded that under the above conditions, the inertial forces may be neglected and the problem reduces to

$$\nabla \cdot \mathbf{u} = 0$$

$$\frac{\partial \mathbf{u}}{\partial t} + \nabla p - \Delta \mathbf{u} = -\tau \hat{\mathbf{g}} \quad (6)$$

$$\frac{\partial \tau}{\partial t} = Pr^{-1} \Delta \tau$$

with the homogeneous normalized boundary conditions

$$\mathbf{u}(|r|=1, t) = \mathbf{u}(|r| \rightarrow \infty, t) = 0, \quad \mathbf{u}(r, 0) = 0 \quad (7)$$

All variables are normalized according to the above arguments where the coordinate r is considered relative to the center of the particle c .

The linearization decouples the heat equation from the hydrodynamic problem. This is why the temperature initial and boundary conditions are not specified in Eq. (7). The heat transfer is purely by conduction and hence is considered as solved for any given imposed temperature conditions. The temperature field thus obtained serves as a known source of momentum in the linearized momentum equation.

This model, in that sense, is a counterexample to the one used in the studies mentioned above. That is, here it is assumed that transport of fluid parcels is so slow relative to the transport by diffusion that the scalar temperature field is effectively unaffected by consequent changes in the flow field. This assumption is rational because of two main physical reasons: (i) the small dimension of the particle restricts small velocity scales and (ii) restriction to initial stages where the field is mainly developed near the particle. Thus the velocity decays sufficiently rapidly with distance from the sphere and thus no advection takes place at regions where diffusion gradients are absent.

3 Solution Procedure

Equations (6) with conditions (7) constitute a linear system. Because of the homogeneity of the boundary conditions, the ho-

mogeneous solution of Eq. (6) is the zero solution (τ is the only initiating mechanism of the flow). Thus, it remains to find a particular solution to the nonhomogeneous equation.

An axisymmetric solution to Eqs. (6) can be sought in the form

$$\mathbf{u} = \nabla \times \nabla \times [h(r, t) \hat{\mathbf{g}}] \quad (8)$$

This procedure is similar to the one employed by Landau and Lifshitz [22] for the solution of the Stokes problem; the difference is that now the underlying vector is the unit vector in the direction of gravity and the momentum equation is inhomogeneous. Taking the curl of Eq. (8) and using a well-known identity in conjunction with the fact that $\hat{\mathbf{g}}$ is a constant vector yields

$$\nabla \times \mathbf{u} = [\nabla(\nabla \cdot) - \Delta] \nabla \times (h(r, t) \hat{\mathbf{g}}) = -\Delta[\nabla h(r, t) \times \hat{\mathbf{g}}] \quad (9)$$

Taking the curl on the momentum equation and substituting Eq. (9) results in

$$\frac{\partial}{\partial t} \{\Delta[\nabla h(r, t) \times \hat{\mathbf{g}}]\} - \Delta^2[\nabla h(r, t) \times \hat{\mathbf{g}}] = \nabla \tau \times \hat{\mathbf{g}} \quad (10)$$

The cross product with respect to $\hat{\mathbf{g}}$ can be dropped, thus

$$\nabla \left\{ \frac{\partial}{\partial t} [\Delta h(r, t)] - \Delta[\Delta h(r, t)] \right\} = \nabla \tau \quad (11)$$

Defining $\chi = \Delta h(r, t)$ and integrating once, Eq. (11) yields

$$\frac{\partial \chi}{\partial t} - \Delta \chi = \tau + c(t) \quad (12)$$

In order to satisfy the convergence condition as $r \rightarrow \infty$, $c(t)$ must be zero. The conditions imposed on χ are

$$\chi(1, t) = \chi(r \rightarrow \infty, t) = 0, \quad \chi(r, 0) = 0 \quad (13)$$

The problem is thus reduced to a particular solution of the nonhomogeneous, one dimensional, heat equation for χ in spherical coordinates,

$$\frac{\partial \chi}{\partial t} = \frac{\partial^2 \chi}{\partial r^2} + \frac{2}{r} \frac{\partial \chi}{\partial r} + \tau(r, t; Pr) \quad (14)$$

Solution of Eq. (14) with conditions (13) is given by [23]

$$\chi(r, t) = \int_0^t \int_1^\infty \tau(\xi, \zeta; Pr) G(r, \xi, t - \zeta) d\xi d\zeta \quad (15)$$

where the kernel has the form

$$G(r, \xi, t) = \frac{\xi}{2r\sqrt{\pi t}} \left\{ \exp\left[-\frac{(r-\xi)^2}{4t}\right] - \exp\left[-\frac{(r+\xi-2)^2}{4t}\right] \right\} \quad (16)$$

In other words, the solution may be interpreted as follows: provide a temperature field, then “operate” Eq. (15) on it and obtain the solution to the induced flow field.

The field variables and global parameters, such as drag force, can be written in terms of the function $h(r, t)$ by manipulations on Eq. (8) (see the Appendix). The results are the velocity, stress, pressure, and drag in spherical coordinates (gravity is opposite to the z -axis)

$$\begin{aligned} \mathbf{u} &= \cos \theta (\Delta h - h'') \hat{\mathbf{r}} + \sin \theta \left(\frac{h'}{r} - \Delta h \right) \hat{\boldsymbol{\theta}} \\ p &= -\cos \theta \left(\Delta h - \frac{\partial h}{\partial t} \right)' \\ \sigma_{rr} &= 2 \cos \theta ((\Delta r h)' - h''') \end{aligned} \quad (17)$$

$$\sigma_{r\theta} = \sin \theta \left[2 \left(\frac{h''}{r} - \frac{h'}{r^2} \right) - (\Delta h)' \right]$$

$$F = \frac{4}{3}\pi \left[5 \left(\Delta h - \frac{\partial h}{\partial t} \right)' - 4 \left(\frac{1}{2} h''' + \frac{h''}{r} - \frac{h'}{r^2} \right) \right]_{r=1} \hat{z} \quad (18)$$

The dashes denote partial differentiation with respect to r . The stresses are normalized according to the pressure, and thus, the force scale is $\mu\nu$ Gr. On deriving the pressure distribution, the constant of integration vanishes. This is because the pressure here represents the disturbance relative to the pressure in equilibrium conditions, consistent with Boussinesq approximation.

4 Results

We consider in detail the following idealized case. Suppose the particle is heated by some means such that its temperature is maintained constant at all times (qualitatively similar conditions can be found, e.g., in coal particle combustion in power plants). It is further assumed that $Pr \sim o(1)$, which implies that the unsteady term must be much larger than the diffusion. Hence, in the limit of vanishingly small Pr , the transient process is characterized by fast development of the temperature field and a relatively much more slowly developed velocity field. Hence, during the momentum transport the temperature may be considered as if it has reached steady conditions. The temperature profile becomes $\tau = 1/r$. Integrating Eq. (15) with respect to the coordinate gives the following expression for χ :

$$\chi(r, t) = \frac{1}{r} \int_0^t \operatorname{erf} \left[\frac{r-1}{2\sqrt{\zeta}} \right] d\zeta \quad (19)$$

It is easy to see that Eq. (19) satisfies the conditions imposed on χ only for finite times, as expected. Performing the integration, the result is

$$\chi = \frac{1}{r} \left[-2\rho^2 + (t + 2\rho^2) \operatorname{erf} \left(\frac{\rho}{\sqrt{t}} \right) + \frac{2\rho}{\sqrt{\pi}} \sqrt{t} \exp \left(-\frac{\rho^2}{t} \right) \right] \quad (20)$$

The notation $\rho \equiv (r-1)/2$ is used for short. The last term in Eq. (20) suggests that the solution grows boundless as \sqrt{t} . This is not surprising because it was already emphasized that the linearization is valid either for short times or short distances from the particle (exact conditions are given in the following discussion). However, for finite times it is observed that as $r \rightarrow \infty$, $\chi \sim r^{-1}$, which will result in a vanishing velocity field far from the sphere. That is, in contrast to the linear steady solution (as elaborated in the Introduction), the linear transient solution is everywhere convergent in space while exhibiting uniform divergence in time.

Equation (20) shows that the growing field is characterized by two different time scales, t and \sqrt{t} , corresponding to the two opposite limits: $\rho^2/t \rightarrow \infty$ and $\rho^2/t \rightarrow 0$. Indeed, let

$$\frac{\rho}{\sqrt{t}} \gg 1 \quad (21)$$

This condition implies short times from initial conditions and large distances from the particle. For this condition, the error function may be approximated by the following asymptotic expansion [24]:

$$\operatorname{erf} \left(\frac{\rho}{\sqrt{t}} \right) = 1 - \frac{\sqrt{t}}{\rho\sqrt{\pi}} \exp \left(-\frac{\rho^2}{t} \right) \left[1 - \frac{t}{2\rho^2} + \frac{3t^2}{4\rho^4} - \frac{15t^3}{8\rho^6} + O \left(\frac{t^4}{\rho^8} \right) \right] \quad (22)$$

Substituting Eq. (22) into Eq. (20) gives the following result:

$$\chi \cong \frac{1}{r} \left\{ t + \frac{t^{3/2}}{\rho\sqrt{\pi}} \exp \left(-\frac{\rho^2}{t} \right) \left[-\frac{t}{\rho^2} + 3\frac{t^2}{\rho^4} + O \left(\frac{t^3}{\rho^6} \right) \right] \right\} \quad (23)$$

Equation (23) shows that the temporal behavior of the buoyancy-induced flow at the initial stage is a linear growth in time. By condition (21), this time scale is expected to hold at large distances from the source.

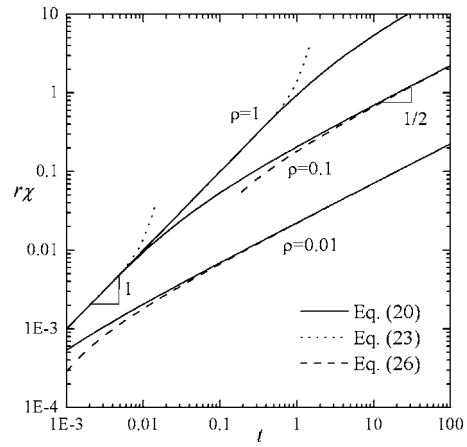


Fig. 2 Temporal behavior of the function χ for three distances from the sphere: $\rho=0.01, 0.1, 1$; based on Eqs. (20), (23), (26)

The asymptotic result obtained in Eq. (23) is not applicable for the opposite limit

$$\frac{\rho}{\sqrt{t}} \rightarrow 0 \quad (24)$$

i.e., in the vicinity of the particle. To obtain the temporal behavior in this case the error function and the exponential function in Eq. (20) may be approximated by

$$\operatorname{erf} \left(\frac{\rho}{\sqrt{t}} \right) = \frac{2}{\sqrt{\pi}} \left[\frac{\rho}{\sqrt{t}} - \frac{\rho^3}{t^{3/2}} + O \left(\frac{\rho^5}{t^{5/2}} \right) \right] \quad (25)$$

$$\exp \left(-\frac{\rho^2}{t} \right) = 1 - \frac{\rho^2}{t} + \frac{\rho^4}{t^2} + O \left(\frac{\rho^6}{t^3} \right)$$

Substituting these expansions into Eq. (20) yields

$$\chi \cong \frac{4}{\sqrt{\pi r}} \left[\sqrt{t} \rho - 2\rho^2 + \frac{\rho^3}{3\sqrt{t}} + O \left(\frac{\rho^4}{t^2} \right) \right] \quad (26)$$

which shows that near the particle the temporal behavior of the solution scales as \sqrt{t} . We note that this solution is invalid as $t \rightarrow 0$, but it satisfies the zero condition on the particle surface at all finite times. By condition (24), this time scale characterizes the evolution of the velocity field at regions near the particle at comparatively long times from initial conditions.

The above temporal behavior is illustrated in Fig. 2, which depicts χ as function of time for different distances from the particle based on Eqs. (20), (23), and (26). At the initial stage, the exact solution grows with a slope of near unity and gradually converges to behavior proportional to \sqrt{t} , characteristic for long times. The behavior of the solution with distance from the sphere for fixed times $t=0.1, 1$ is obtained in Fig. 3. The function satisfies the conditions at the boundaries, and it is characterized by fast growth near the sphere and a gradual decay at large distances. It may be extrapolated from this behavior that effects of inertia will become appreciable at long enough times, for distances near which the velocity assumes maximum value. That is, at a given time, either the solution is valid for the entire field or breaks up at a finite region in space; this region will grow monotonically with time.

A question arises: what are the quantitative conditions of validity of the linear solution? To answer that, one must compare the magnitude of the neglected inertia term based on the linear solution to the buoyancy driving term. By Eq. (4), the later scales as $1/r$. In order to approximate the inertial term, it is noted by Eq. (17) that $\mathbf{u} \sim \chi$, thus inertia scales as $Gr \chi \partial \chi / \partial r$. Employing the asymptotic result of χ obtained in Eqs. (23) and (26), the ratio of

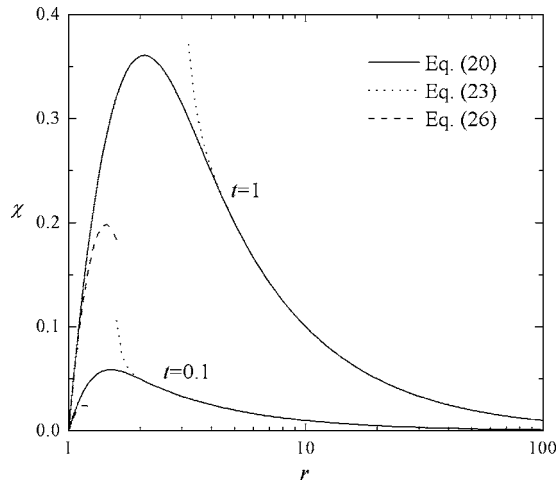


Fig. 3 Behavior of χ with distance based on Eqs. (20), (23), (26) for $t=0.1, 1$

the inertia to buoyancy scales as $(t/\rho)^2 Gr$ and $t\rho Gr$, respectively. To satisfy the condition that the ratio will remain small, e.g., comparable to Gr , one obtains the corresponding limit curves

$$\rho = t; \quad \text{consistent with Eq. (23)} \quad (27)$$

$$\rho = t^{-1}; \quad \text{consistent with Eq. (26)} \quad (28)$$

Above the limit of Eq. (27) and below that of Eq. (28), the ratio is smaller than $Gr \sim o(1)$.

A more accurate condition can be obtained by calculating the ratio exactly on the axis of symmetry above the sphere and obtaining the contour line at level Gr numerically, or alternatively the contour line at level one of

$$\left| ru_r \frac{\partial u_r}{\partial r} \right| = 1 \quad (29)$$

where u_r is the radial velocity component. By Eq. (17), u_r becomes $u_r = \cos \theta (\chi - h'')$, which, by integrating once the relation $\Delta h = \chi$, may also be written as

$$u_r = \frac{4 \cos \theta}{r^3} \int_0^{\rho} (1 + 2\xi)^2 \chi(\xi, t) d\xi \quad (30)$$

The tangential velocity component is $u_\theta = (h'/r - \chi) \sin \theta$, which can be written as

$$u_\theta = \left(\frac{1}{2 \cos \theta} u_r - \chi \right) \sin \theta \quad (31)$$

The contour given by Eq. (29) is illustrated in Fig. 4 (bold line). Figure 4 also depicts the validity of the asymptotic expressions given by Eqs. (27) and (28) (dots). Based on Eq. (27), convective inertia remains smaller than Gr throughout the field as long as the time elapsed is smaller than ten diffusion times. For $t > 10$, the influence of the convective inertial terms becomes appreciable at a finite region in space that grows monotonically with time. The apparent enclave obtained in Fig. 4 is the result of the velocity gradient diminishing near the maximum point of the velocity thus reducing the inertial forces.

In an attempt to clarify the evolution of the velocity field, Fig. 5 shows the development of streamline patterns in a rectangular domain (with cylindrical components (R, z)) above the sphere for various times. The pattern is symmetrical with respect to the inflow toward the sphere, and the updraft and qualitatively resembles the patterns obtained in the numerical study of Geoola and Cornish [18]. At short times, the streamlines are steep toward the sphere center, suggesting the domination of the (spherical)

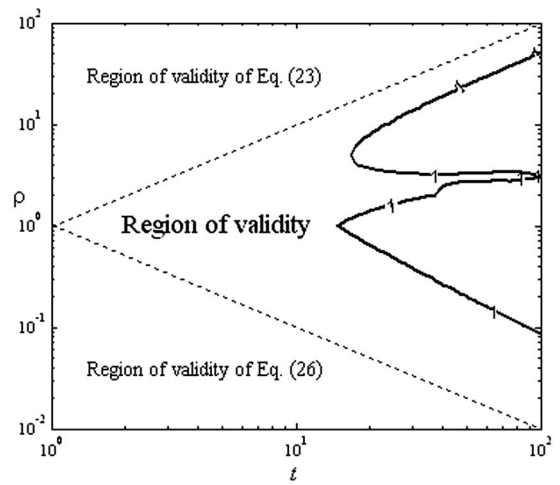


Fig. 4 Region of validity of the linear solution: based on Eq. (29) (bold line) and based on Eqs. (27) and (28) (dotted line)

radial velocity component and gradually become moderate; at longer times the flow is dominated by the velocity component in the z direction. Indeed, the initial stream patterns can be obtained by considering the first term in Eq. (23), t/r . The corresponding velocity components are $u_r = t/r(1 - 1/r^2) \cos \theta$ and $u_\theta = -t/(2r) \times (1 + 1/r^2) \sin \theta$, yielding the stream function

$$\psi = \frac{t}{2} \left(\frac{2 \sin^2 \theta}{r} + r \cos 2\theta - 1 \right) \quad (32)$$

Thus, initially the streamlines are self similar in time. For large distances, $r \gg 1$, the stream function is estimated by $\psi \approx r \cos 2\theta$ and the corresponding streamline patterns are obtained in Fig. 6.

5 Particle Dynamics

The initial motivation of this study was to gain further understanding of the dynamical behavior of a particle while initiating buoyancy-induced motion. The drag-force expression obtained in Eq. (18) reduces to

$$\mathbf{F} = 2\pi \left. \frac{\partial \chi}{\partial \rho} \right|_{\rho=0} \hat{z} \quad (33)$$

Performing the calculation, the result is

$$\mathbf{F} = 8\sqrt{\pi} t^{1/2} \hat{z} \quad (34)$$

Hence, at the initial stages, the buoyancy-induced flow results in a drag force that grows as \sqrt{t} . Again, Eq. (34) is expected to hold whenever the validity conditions are met. Thus, due to the fact that the drag on the sphere is caused by the entire field, it is concluded that Eq. (34) is valid for $t \leq 10$. Another condition for the validity of Eq. (34) may be evaluated by considering the scale of the drag force in developed free convection, which is known to be $\mu \nu Gr^{1/2}$ (it is also recalled that the scale factor for F is $\mu \nu Gr$). Ignoring any constant factor, Eq. (34) should not exceed this value; hence, one arrives at the condition $t \ll Gr^{-1}$.

At this point it is of interest to examine the validity of the current analysis to the mixed problem, i.e., to the case where the sphere is also subjected to motion with velocity U . The classical problem of particle motion under isothermal Stokes conditions was, and still is, the subject of intensive investigations (e.g., [25–27]). Under the above approximation, the resultant fields do not interact and the contribution of the buoyancy forces will be superposed on the isothermal solution. It remains to reexamine the limitations under this condition. To this end, the scale of the velocity field is now taken as U , where the time scale remains a^2/ν . Consistent with the Stokes approximation is the condition U

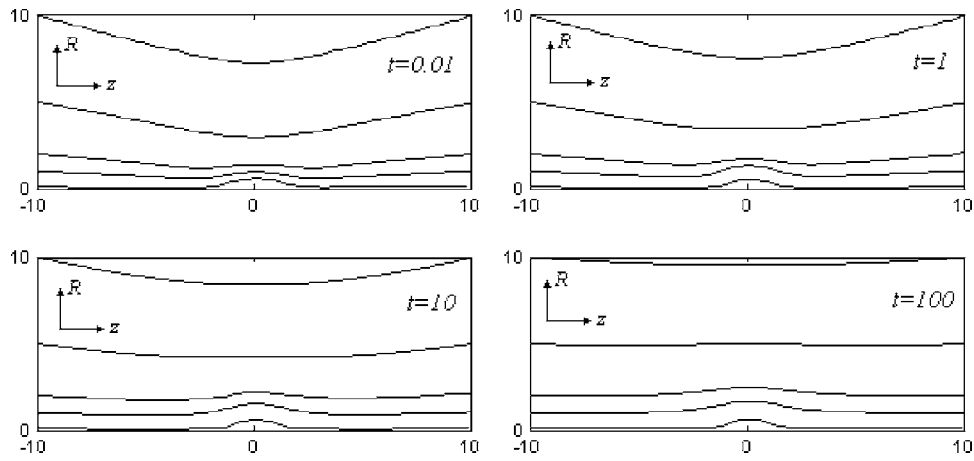


Fig. 5 Streamlines around the sphere for different times: $t=0.01, 1, 10, 100$

$\ll \nu/a$, or $Re \sim o(1)$. Thus the factor multiplying the convective inertial terms is Re , whereas the one for the buoyancy term is $\varepsilon = Gr/Re$. The condition of validity becomes $Re \ll \varepsilon$ or $Ri \gg 1$, i.e., strong buoyancy over particle advection. The conditions for the energy equation are similar to the fixed sphere case. The linear approximation formulation is now

$$\nabla \cdot \mathbf{u} = 0$$

$$\frac{\partial \mathbf{u}}{\partial t} + \nabla p - \Delta \mathbf{u} = -\varepsilon \cdot \tau \hat{\mathbf{g}} \quad (35)$$

$$\frac{\partial \tau}{\partial t} = Pr^{-1} \Delta \tau$$

With boundary and initial conditions for the velocity field

$$\mathbf{u}(\mathbf{r}, t) = \mathbf{V}(t), \quad \text{for } |\mathbf{r}| = 1$$

$$\mathbf{u}(\mathbf{r}, 0) = 0, \quad \text{for } |\mathbf{r}| > 1 \quad (36)$$

where $\mathbf{V}(t)$ is the sphere velocity, scaled by U , which, in general, may be time dependent. Thus we seek a solution as a superposition of the homogeneous problem, i.e., the problem without the buoyancy term satisfying Eq. (36), and a particular solution of the buoyancy-induced flow with homogeneous boundary and initial conditions. The homogeneous velocity field is denoted by \mathbf{u}_0 , whereby the particular solution corresponding to the buoyancy-induced flow is denoted by \mathbf{u}_t

$$\mathbf{u} = \mathbf{u}_0 + \mathbf{u}_t \quad (37)$$

The buoyancy-induced velocity thus satisfies

$$\nabla \cdot \mathbf{u}_t = 0$$

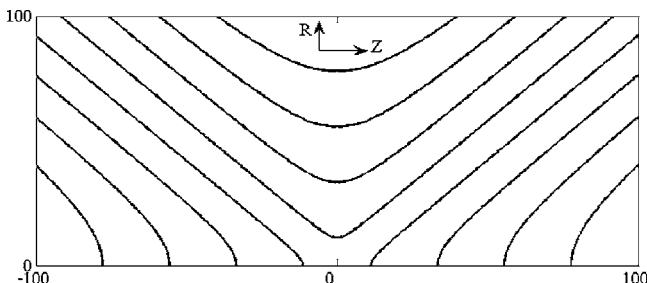


Fig. 6 Streamlines around the sphere for $t \rightarrow 0$

$$\frac{\partial \mathbf{u}_t}{\partial t} + \nabla p_t - \Delta \mathbf{u}_t = -\varepsilon \tau \hat{\mathbf{g}} \quad (38)$$

$$\mathbf{u}_t(|\mathbf{r}| = 1, t) = \mathbf{u}_t(|\mathbf{r}| \rightarrow \infty, t) = 0, \mathbf{u}_t(\mathbf{r}, 0) = 0$$

This formulation is identical to the one solved in Sec. 4, except that now the buoyancy term is multiplied times ε ; hence, the results are modified by the constant factor. The validity contour obtained in Fig. 4 now represents the condition where the ratio of inertia to buoyancy is smaller than $1/Ri = Re^2/Gr$, which is much more restrictive for small particles than the first condition. A realistic example that may comply with this case is the initial stages of a falling hot or cold sphere under gravity (in a host having $Pr \sim o(1)$); although the behavior of the isothermal sphere under this condition is still under debate (e.g., [27,28]).

6 Conclusions

The problem of the flow induced by buoyancy forces due to the presence of a hot sphere was considered for the initial stages where the flow is dominated by transient inertia, viscosity, and buoyancy, and convective processes may be neglected. A general integral solution is obtained for an arbitrary Pr number. The case $Pr=0$ was considered in detail. For this case, temporal and spatial conditions of validity of the linearization were given. The temporal behavior of the flow is characterized by two different time scales; both show an unbounded monotonic growth with time: initially the field is developed linearly with time and in later stages it becomes proportional to the square root of time. The resultant drag force induced on the sphere shows an unbounded growth proportional also to the square root of time at all stages. Under the above linear analysis, the results do not predict the behavior approaching the steady state, which by itself is, as yet, an unresolved problem. The results in this paper were confined to the case of vanishingly small Pr . However, the platform for the more general case of finite Pr is given and calls for further study—such as the more realistic case of a sphere whose temperature decreases with time for which the current analysis is expected to yield valid results at all times.

Acknowledgment

E.M. is grateful to the Kreitman Foundation for financial and moral support as a Kreitman Fellow during this study. This study was partially supported by US-Israel Binational Science Foundation (BSF) Grant No. 2002-408.

Appendix

In this section, a brief description is given for the derivation of Eqs. (17). Using well-known vector identities consecutively on Eq. (8), one has

$$\begin{aligned}\nabla \times \nabla \times (h\hat{\mathbf{g}}) &= \nabla(\nabla \cdot h\hat{\mathbf{g}}) - \Delta h\hat{\mathbf{g}} \\ &= (\hat{\mathbf{g}} \cdot \nabla) \nabla h + (\nabla h \cdot \nabla)\hat{\mathbf{g}} + \hat{\mathbf{g}} \times (\nabla \times \nabla h) \\ &\quad + \nabla h \times (\nabla \times \hat{\mathbf{g}}) - \Delta h\hat{\mathbf{g}} \\ &= h'(\hat{\mathbf{g}} \cdot \nabla)\mathbf{n} + \mathbf{n}(\hat{\mathbf{g}} \cdot \mathbf{n})h'' - \Delta h\hat{\mathbf{g}} \\ &= \frac{h'}{r}[\hat{\mathbf{g}} - (\hat{\mathbf{g}} \cdot \mathbf{n})\mathbf{n}] + \mathbf{n}(\hat{\mathbf{g}} \cdot \mathbf{n})h'' - \Delta h\hat{\mathbf{g}} \\ &= (\hat{\mathbf{g}} \cdot \mathbf{n})\mathbf{n} \left[h'' - \frac{h'}{r} \right] + \hat{\mathbf{g}} \left[\frac{h'}{r} - \Delta h \right]\end{aligned}$$

where \mathbf{n} is the unit normal in the direction of \mathbf{r} . In the third step, we used the fact that h depends only on the radial coordinate (except the time) and, thus, $\nabla = \mathbf{n} \partial / \partial r$. Introducing spherical coordinates, $\hat{\mathbf{g}}$ is in the direction of minus z and yields

$$\hat{\mathbf{g}} = -\cos \theta \mathbf{n} + \sin \theta \hat{\boldsymbol{\theta}} \rightarrow (\hat{\mathbf{g}} \cdot \mathbf{n})\mathbf{n} = -\cos \theta \mathbf{n}$$

Thus, one arrives at the expression for the velocity in Eqs. (17). The stresses are obtained by substituting the velocity components into the stress components

$$\sigma_{rr} = 2 \frac{\partial u_r}{\partial r}, \quad \sigma_{r\theta} = \frac{1}{r} \frac{\partial u_r}{\partial \theta} + \frac{\partial u_\theta}{\partial r} - \frac{u_\theta}{r}$$

The expression for the pressure is obtained by substituting Eq. (8) into the momentum equation in (6). This gives

$$\begin{aligned}\nabla p &= \Delta \mathbf{u} - \frac{\partial \mathbf{u}}{\partial t} - \boldsymbol{\tau} \hat{\mathbf{g}} = \Delta[\nabla \times \nabla \times (h\hat{\mathbf{g}})] - \frac{\partial}{\partial t}[\nabla \times \nabla \times (h\hat{\mathbf{g}})] - \boldsymbol{\tau} \hat{\mathbf{g}} \\ &= \Delta\{\nabla[\nabla \cdot (h\hat{\mathbf{g}})] - \Delta h\hat{\mathbf{g}}\} - \frac{\partial}{\partial t}\{\nabla[\nabla \cdot (h\hat{\mathbf{g}})] - \Delta h\hat{\mathbf{g}}\} - \boldsymbol{\tau} \hat{\mathbf{g}} \\ &= \nabla\{\Delta[\hat{\mathbf{g}} \cdot \nabla h] - \Delta^2 h\hat{\mathbf{g}}\} - \nabla \left[\frac{\partial}{\partial t}(\hat{\mathbf{g}} \cdot \nabla h) \right] + \hat{\mathbf{g}} \frac{\partial}{\partial t}(\Delta h) - \boldsymbol{\tau} \hat{\mathbf{g}} \\ &= \nabla \left[\hat{\mathbf{g}} \cdot \nabla \left(\Delta h - \frac{\partial h}{\partial t} \right) \right]\end{aligned}$$

In the last step, the second, fourth, and last terms cancel because of (11); thus, one arrives at the expression for the pressure.

References

- [1] Gebhart, B., Jaluria, Y., Mahajan, R., and Sammakia, B., 1988, *Buoyancy Induced Flows and Transport*, Hemisphere, Washington, DC.
- [2] Zel'dovich, Ya. B., 1937, "Limiting Laws of Freely Rising Convective Currents," *Zh. Eksp. Teor. Fiz.*, **7**, pp. 1463–1465 (in Russian).
- [3] Yih, C. S., 1953, "Free Convection Due to Boundary Sources: Fluid Models in Geophysics," *Proc. 1st Symposium on Use of Models in Geophysical Fluid Dynamics*, Government Printing Office, Washington, DC, pp. 117–133.
- [4] Gutman, L. N., 1949, "On Laminar Thermal Convection Above a Stationary Heat Source," *Prikl. Mat. Mekh.*, **13**, pp. 435–439 (in Russian).
- [5] Fujii, T., 1963, "Theory of Steady Laminar Convection Above a Horizontal Line Heat Source and a Point Heat Source," *Int. J. Heat Mass Transfer*, **6**, pp. 597–606.
- [6] Kurdyumov, V. N., and Liñán, A., 1998, "Free convection From a Point Source of Heat, and Heat Transfer From Spheres at Small Grashof Numbers," *Int. J. Heat Mass Transfer*, **42**, pp. 3849–3860.
- [7] Chen, T. S., and Mucoglu, A., 1977, "Analysis of Mixed Forced and Free Convection About a Sphere," *Int. J. Heat Mass Transfer*, **20**, pp. 867–875.
- [8] Wong, K. L., Lee, S. C., and Chen, C. K., 1986, "Finite Element Solution of Laminar Combined Convection From a Sphere," *ASME J. Heat Transfer*, **108**, pp. 860–865.
- [9] Cameron, M. R., Jeng, D. R., and De-Witt, K. J., 1991, "Mixed Forced and Natural Convection From Two-Dimensional or Axisymmetric Bodies of Arbitrary Contour," *Int. J. Heat Mass Transfer*, **34**, pp. 582–587.
- [10] Potter, J. M., and Riley, N., 1980, "Free Convection From a Heated Sphere at Large Grashof Numbers," *J. Fluid Mech.*, **100**(4), pp. 769–783.
- [11] Geoola, F., and Cornish, A. R. H., 1981, "Numerical Solution of Steady State Free Convection Heat Transfer From a Solid Sphere," *Int. J. Heat Mass Transfer*, **24**(8), pp. 1369–1379.
- [12] Jia, H., and Gogos, G., 1995, "Laminar Natural Convection Heat Transfer From Isothermal Sphere," *Int. J. Heat Mass Transfer*, **39**(8), pp. 1603–1615.
- [13] Fendell, F. E., 1968, "Laminar Natural Convection About an Isothermally Heated Sphere at Small Grashof Numbers," *J. Fluid Mech.*, **34**, pp. 163–176.
- [14] Hieber, C. A., and Gebhart, B., 1969, "Mixed Convection From a Sphere at Small Reynolds and Grashof Numbers," *J. Fluid Mech.*, **38**, pp. 137–159.
- [15] Abramzon, B., and Elata, C., 1983, "Unsteady Heat Transfer From a Single Sphere in Stokes Flow," *Int. J. Heat Mass Transfer*, **27**(5), pp. 687–695.
- [16] Feng, Z. G., and Michaelides, E. E., 1998, "Transient Heat Transfer From a Particle With Arbitrary Shape and Motion," *ASME J. Heat Transfer*, **120**, pp. 674–681.
- [17] Feng, Z. G., and Michaelides, E. E., 1999, "A Numerical Study on the Transient Heat Transfer From a Sphere at High Reynolds and Peclet Numbers," *Int. J. Heat Mass Transfer*, **43**, pp. 219–229.
- [18] Geoola, F., and Cornish, A. R. H., 1982, "Numerical Simulation of Free Convection Heat Transfer From a Solid Sphere," *Int. J. Heat Mass Transfer*, **25**, pp. 1677–1687.
- [19] Dudek, D. R., Fletcher, T. H., Longwell, J. P., and Sarofim, A. F., 1988, "Natural-Convection Induced Drag Forces on Spheres at Low Grashof Numbers—Comparison of Theory With Experiment," *Int. J. Heat Mass Transfer*, **31**, pp. 863–873.
- [20] Davis, E. J., and Schweiger, G., 2002, *The Airborne Microparticle, Its Physics, Chemistry, Optics, and Transport Phenomena*, Springer-Verlag, Berlin.
- [21] Mograbi, E., and Bar-Ziv, E., 2004, "Dynamics of a Spherical Particle in Mixed Convection Flow Field," *J. Aerosol Sci.*, **36**(3), pp. 387–409.
- [22] Landau, L. D., and Lifshitz, E. M., 1999, *Fluid Mechanics*, 2nd ed., Butterworth-Heinemann, Oxford.
- [23] Polyanin, A. D., 2002, *Handbook of Linear Partial Differential Equations for Engineers and Scientists*, Chapman & Hall/CRC, New York, p. 81.
- [24] Hinch, E. J., 1991, *Perturbation Methods*, Cambridge University Press, New York.
- [25] Basset, A. B., 1888, *A Treatise on Hydrodynamics*, Deighton Bell, London.
- [26] Maxey, M. R., and Riley, J. J., 1983, "Equation of Motion for a Small Rigid Sphere in a Nonuniform Flow," *Phys. Fluids*, **26**, pp. 883–889.
- [27] Lovalenti, P. M., and Brady, J. F., 1993, "The Hydrodynamic Force on a Rigid Particle Undergoing Arbitrary Time-Dependent Motion at Small Reynolds Number," *J. Fluid Mech.*, **256**, pp. 561–605.
- [28] Coimbra, C. F. M., and Rangel, R. H., 1998, "General Solution of the Particle Momentum Equation in Unsteady Stokes Flows," *J. Fluid Mech.*, **370**, pp. 53–72.

Gas–Solid Particle Flow in Horizontal Channels: Decomposition of the Particle-Phase Flow and Interparticle Collision Effects

Alexander Kartushinsky

Laboratory of Multiphase Media Physics,
Tallin University of Technology,
Tallinn 12618, Estonia
e-mail: aleksander.kartushinsky@ttu.ee

Efstathios E. Michaelides

Department of Mechanical and Energy
Engineering,
University of North Texas,
Denton, TX 76092
e-mail: emichael@unt.edu

This paper examines the turbulent flow of heavy particles in horizontal channels and pipes. Calculations for the fluid are performed within an Eulerian frame of reference, while the particulate phase is considered as several continuous polydisperse media, each constituting a separate phase. The interparticle collisions include two mechanisms: collisions with sliding friction and collisions without sliding friction. The collisions of particles are accounted for, by collisions due to the difference in the average and fluctuating velocities of the several particulate fractions. This work introduces an original model for the closure for the mass and momentum equations based on the collisions as well as an original description of the particle motion in a horizontal channel, by introducing the decomposition of the particle-phase motion into two types of particle phases: falling and rebounding particles. The decomposition allows the correct calculation of the influence of the wall on the motion of particles. [DOI: 10.1115/1.2734202]

Keywords: channel flow, rebounding particles, inter-particle collisions, high mass loading ratio

1 Introduction

Pneumatic conveying processes are influenced by several physical phenomena, such as particle sedimentation, interparticle collisions, rotation, and lift and drag forces. The combination of these phenomena and forces results in asymmetric flow in horizontal channels. The experiments by Tsuji and Morikawa [1] proved that a decrease of the magnitude of mean flow velocity leads to an increased asymmetry of the average velocity. These experiments also showed that a minimum mean flow velocity must be maintained for the particles to be transported. The magnitude of this minimum transport velocity was examined by Davies [2] and Cabrejos and Klinzing [3].

Sommerfeld [4] presented a number of diagrams for the average and rms velocity shapes obtained for a relatively large mean flow velocity. He did not observe any effect on the velocity profiles due to particle accumulation on the bottom wall. Sommerfeld and Zivkovic [5] estimated the effect of the particulate collisions using a stochastic approach in a Lagrangian frame of reference.

The effect of collisions is obviously important for dense particulate flows when the ratio of particle response time is larger than the time of interparticle collisions: $t_p/t_c > 1$. An order of magnitude estimate shows that the inequality $t_p/t_c > 1$ is satisfied at mass loadings higher than 10 [6].

It is well known that the presence of particles induces changes in the turbulence structure in the carrier fluid, which is described by a number of models such as Elghobashi and Abou-Arab [7], and Shraiber et al. [8]. Yuan and Michaelides [9] suggested several mechanisms for the modulation of turbulence in a gas–solids

mixture and Crowe and Gilland [10] incorporated them in a quantitative model to predict turbulence enhancement and attenuation in terms of the velocity slip. We use this model for the turbulence modulation because it agrees well with the experimental results of Tsuji and his co-workers ([1,11]). Also, together with the particle collisions and turbulence modulation phenomena, we take into account the effect of lift forces and particle rotation.

This paper presents the governing and closure equations for the turbulent flow of a gas–solids mixture. The model was implemented numerically and validated by comparisons with experimental data at intermediate and high mass loading ratios (up to 25) and for particles of various sizes in the range of diameters $0.1 < d < 1$ mm. The results show a modification of the flow structure and reveal the asymmetry of the average and rms velocity profiles, even at reasonably high mean transport velocities of the carrier fluid. The model also shows the importance of accounting for the particulate collisions for both intermediate and high mass ratios.

2 Description of the Model

2.1 Governing Equations of the Carrier Gas Phase. We use the boundary-layer approximation and the four-way coupling approach of Crowe et al. [12], where the gas-particle and interparticle forces are included in the k equation for turbulence. The conservation equations for the mass, momentum and turbulent energy are as follows:

$$\frac{\partial u}{\partial x} + \frac{\partial v}{\partial y} = 0 \quad (1)$$

$$u \frac{\partial u}{\partial x} + v \frac{\partial u}{\partial y} = -\frac{\partial p}{\rho \partial x} + \frac{\partial}{\partial y} (v + \nu_t) \frac{\partial u}{\partial y} - \sum_{i=1}^6 \alpha_i \frac{C'_{Di}}{\tau_i} (u - u_{si}) \quad (2)$$

Contributed by the Fluids Engineering Division of ASME for publication in the JOURNAL OF FLUIDS ENGINEERING. Manuscript received January 23, 2006; final manuscript received November 13, 2006. Review conducted by Malcolm J. Andrews.

$$u \frac{\partial k}{\partial x} + v \frac{\partial k}{\partial y} = \frac{\partial}{\partial y} (\nu_t + \nu) \frac{\partial k}{\partial y} + \nu_t \left(\frac{\partial u}{\partial y} \right)^2 - \nu \left(\frac{\partial \sqrt{k}}{\partial y} \right)^2 + \sum_{i=1}^6 \alpha_i \frac{C'_{Di}}{\tau_i} \left[(u - u_{si})^2 + (v - v_{si})^2 \right] - \sum \langle u'_{si} u' \rangle |_{\text{turb}} \left. \right\} - \frac{k \sqrt{k}}{L_h} \quad (3)$$

The closure equations for the of the turbulent viscosity of gas, ν_t , and length scale, L_h , are as follows

$$\nu_t = C_{\mu} \sqrt{k} L_T \quad (4)$$

$$L_h = 2L_T \lambda / (L_T + \lambda) \quad (5)$$

where

$$C_{\mu} = 0.07 (L_T \sqrt{k}) \exp[-2.5 / (1 + (L_T \sqrt{k} / 50 \nu))] \quad \text{and} \quad L_T = \frac{k_0^{3/2}}{\varepsilon_0} \quad (6)$$

The interparticle distance is: $\lambda = d_{\Sigma} [(\pi \rho_p / 6 \rho \alpha_{\Sigma})^{1/3} - 1]$. The parameters d_{Σ} and α_{Σ} are related to the diameters, d_i and mass fractions of the particles as follows

$$\alpha_{\Sigma} = \sum_{i=1,6} \alpha_i, \quad \text{and} \quad d_{\Sigma} = \frac{1}{\alpha_{\Sigma}} \sum_{i=1,6} d_i \quad (7)$$

2.2 Governing Equations for the Dispersed Flow. The model for the particles encompasses a finite number of particle types that are characterized by a diameter (size) and a mass fraction. Although this approach is general enough to include a large number of particle fractions, for simplicity and ease in the computations, we will consider only three particle fractions. The mass fractions of these particles are constant (that is, we assume no chemical reactions, condensation, or sublimation) and are known a priori. The model also distinguishes particles that approach a wall as “falling particles,” and particles that rebound from the wall as “rebounding particles,” and accounts for them as different types of particles. Therefore, the total number of particle fractions that must be considered is six: three fractions for the falling phases ($i=1,2,3$) and three for the corresponding rebounding phases ($i=4,5,6$). The governing equations of a given falling particle phase differ from the corresponding rebounding particle phase in the sign of the source terms.

One may use the Reynolds decomposition and time-averaging technique to derive the usual set of mass and momentum conservation equations for the particle phases. When the mass conservation equation is taken into account, one may write the momentum equations of the particle phases in terms of the fluctuation correlations. One may further simplify this set of equations by neglecting the triple correlations, the second-order correlations in the axial direction, and all the correlations pertaining to the fluctuations of the particle mass concentration, which are of a lesser order of magnitude according to the boundary layer theory. Thus, one may write the governing equations of the dispersed particulate phases as follows [13]

$$\frac{\partial}{\partial x} \rho \alpha_i u_{si} + \frac{\partial}{\partial y} \rho \alpha_i v_{si} = - \frac{\partial}{\partial y} \rho \langle \alpha_i' v_{si}' \rangle \quad (8)$$

$$\alpha_i \mu_{si} \frac{\partial u_{si}}{\partial x} + (\alpha_i \nu_{si} + \langle \alpha_i' v_{si}' \rangle) \frac{\partial u_{si}}{\partial y} = - \frac{\partial}{\partial y} \alpha_i \langle u_{si}' v_{si}' \rangle + \alpha_i \left[\frac{C'_{Di}}{\tau_i} (u - u_{si}) \mp C_{Mi} \Omega_i (v - v_{si}) \right] \quad (9)$$

$$\alpha_i \mu_{si} \frac{\partial v_{si}}{\partial x} + (\alpha_i \nu_{si} + \langle \alpha_i' v_{si}' \rangle) \frac{\partial v_{si}}{\partial y} = - \frac{\partial}{\partial y} \alpha_i \langle v_{si}'^2 \rangle + \alpha_i \left\{ \frac{C'_{Di}}{\tau_i} (v - v_{si}) \pm \left[C_{Mi} \Omega_i + F_{si} \frac{\text{sign} \left(\frac{\partial (u - u_{si})}{\partial y} \right)}{\left| \frac{\partial (u - u_{si})}{\partial y} \right|} \right] (u - u_{si}) \pm g \left(1 - \frac{\rho}{\rho_p} \right) \right\} \quad (10)$$

$$\alpha_i \mu_{si} \frac{\partial \omega_{si}}{\partial x} + (\alpha_i \nu_{si} + \langle \alpha_i' v_{si}' \rangle) \frac{\partial \omega_{si}}{\partial y} = - \frac{\partial}{\partial y} \alpha_i \langle v_{si}' \omega_{si}' \rangle - \alpha_i \frac{C'_{\omega i}}{\tau_i} \Omega_i \quad (11)$$

where ω is the angular velocity of the fluid,

$$\omega = \frac{1}{2} \text{rot } \vec{V}_k = \left(\frac{\partial v}{\partial x} - \frac{\partial u}{\partial y} \right)$$

and the angular velocity slip between the particles and fluid is: $\Omega_i = \omega_{si} - \omega$. The other closure equations for the source terms are as follows [14]:

1. For the drag multiplier, we use the expression: $C_{Di} = 1 + 0.15 \text{Re}_{si}^{0.687}$;
2. For the characteristic time of the particles: $\tau_i^{-1} = 18 \mu / \rho_p d_i^2$;
3. For the Reynolds number: $\text{Re}_{si} = d_i \sqrt{(u - u_{si})^2 + (v - v_{si})^2} / \nu$;
4. For the Magnus lift force and torque on the particles we used the correlations for the lift and torque coefficients proposed by Yamamoto et al. [15]

$$C_{Mi} = \frac{3 \rho \text{Re}_{si}}{\rho_p \text{Re}_{\omega i}} \min \left(0.5, \frac{\text{Re}_{\omega i}}{\text{Re}_{si}} \right), \quad (12)$$

$$C_{\omega i} = (C_1 \sqrt{\text{Re}_{\omega i}} + C_2 + C_3 \text{Re}_{\omega i}^2) / (16 \pi)$$

where $\text{Re}_{\Omega i} = d_i^2 |\Omega_i| / 4 \nu$ is the rotational Reynolds number and the numerical constants C_1, C_2, C_3 are tabulated by Yamamoto et al. [15] for a range of $\text{Re}_{\Omega i}$; and

5. For the Saffman lift force

$$F_{si} = \frac{6.44 \rho f_{si} (\text{Re}_{si}, \text{Re}_{\Omega i})}{\frac{1}{6} \pi \rho_p d_i} \sqrt{\nu \frac{\partial (u - u_{si})}{\partial r}}$$

where the coefficient f_{si} is obtained from Mei [16]

$$f_{si} = 1 - 0.3314\sqrt{\beta_i} \exp(-0.1\text{Re}_{si}) + 0.3314\sqrt{\beta_i}$$

for $\text{Re}_{si} \leq 40$

and $f_{si} = 0.054\sqrt{\beta_i \text{Re}_{si}}$ for $\text{Re}_{si} > 0$

2.3 Boundary Conditions. The boundary conditions of the gaseous phase at the upper and lower walls are simply the no-slip, no-penetration conditions

$$y=0 \quad \text{and} \quad y=h: \quad u=k=v=0 \quad (13)$$

The boundary conditions of all the particulate phases at the entrance of the channel may be written in terms of a lag coefficient, k_{lag} , which defines the velocity slip between the phases

$$\text{at } x=0: \quad u_{si} = k_{\text{lag}}u, \quad v_{si} = k_{\text{lag}}v, \quad \omega_{si} = k_{\text{lag}}(0.5 \text{ rot } \vec{v}) \quad (14a)$$

This lag coefficient k_{lag} is calculated from the terminal velocities of the particles. The particle mass concentration is calculated from the mass loading, which initially is assumed to be uniform across the cross-section of the channel

$$\text{at } x=0: \quad \alpha_i = \psi k_{\text{fri}} \bar{u} / \bar{u}_{si} \quad (14b)$$

where ψ is the ratio of the mass flux of the particles to the mass flux of the fluid; \bar{u} and \bar{u}_{si} are the average velocities of the gas-phase and particles over the cross section at $x=0$; and k_{fri} is the initial coefficient of the i th particle fraction: ($\sum_{i=1,6} k_{\text{fri}} = 1$).

The boundary conditions for the particles at the top and bottom walls differ because of the asymmetry of the flow. For the falling particles ($i=1-3$), which do not collide with the top channel wall, we have the following conditions at the top of the channel ($y=0$)

$$\text{at } y=0: \quad u_{si} = \lambda_i \frac{\partial u_{si}}{\partial y}, \quad \omega_{si} = -\lambda_i \frac{\partial \omega_{si}}{\partial y}, \quad v_{si} = 0 \quad (14c)$$

while at the bottom of the channel the boundary conditions are presented in a gradient form through an interparticle spacing parameter, λ_i [17]

$$\text{at } y=h: \quad u_{si} = -\lambda_i \frac{\partial u_{si}}{\partial y}, \quad \omega_{si} = \lambda_i \frac{\partial \omega_{si}}{\partial y}, \quad v_{si} = -\lambda_i \frac{\partial v_{si}}{\partial y} \quad (14d)$$

The boundary conditions for the particle mass concentration at both walls are the same. The particle mass concentration is determined by the normal velocity component of the particles using the no-penetration condition

$$y=0 \quad \text{and} \quad y=h: \quad \alpha_i v_{si} = (D_{\text{icol}} + D_{\text{iturb}}) \frac{\partial \alpha_i}{\partial y} \quad (14e)$$

The boundary conditions of the rebounding phases are linked to the boundary conditions for the particles of the falling particle phases. Then one may write the following expressions for the rebounding particle fractions at the bottom wall

$$\text{at } y=h: \quad u_{si} = -\lambda_i \frac{\partial u_{si}}{\partial y}, \quad v_{si} = -\lambda_i \frac{\partial v_{si}}{\partial y}, \quad \omega_{si} = \lambda_i \frac{\partial \omega_{si}}{\partial y}, \quad (14f)$$

$$u_{si}|_{i=4,6} \equiv u_{si}|_{i=1,3}, \quad v_{si}|_{i=4,6} \equiv v_{si}|_{i=1,3} \quad \text{and} \quad \omega_{si}|_{i=4,6} \equiv \omega_{si}|_{i=1,3}$$

If the falling particles have positive transverse velocity at the bottom wall, one may recalculate the linear and angular velocity components according to Matsumoto and Saito [18]. The velocities thus obtained are as follows

if $v_{si} > 0$ ($i=1-3$) at $y=h$

$$\text{and if } \left| u_{si} + \frac{d_i \omega_{si}}{2} \right| > \frac{7}{2} \mu_0 (1 + k_n) v_{si} \quad (i=1-3) \quad (14g)$$

$$\text{then } u_{si}''|_{i=4,6} = \left[u_{si} - \mu_d \text{sgn} \left(u_{si} + \frac{d_i \omega_{si}}{2} \right) (1 + k_n) v_{si} \right] \Big|_{i=1,3}$$

$$\omega_{si}''|_{i=4,6} = \left[\omega_{si} - 5\mu_d \text{sgn} \left(u_{si} + \frac{d_i \omega_{si}}{2} \right) (1 + k_n) \frac{v_{si}}{d_i} \right] \Big|_{i=1,3} \quad (14h)$$

$$\text{if } \left| u_{si} + \frac{d_i \omega_{si}}{2} \right| \leq \frac{7}{2} \mu_0 (1 + k_n) v_{si}, \quad (i=1,3)$$

$$u_{si}''|_{i=4,6} = \left[u_{si} - \frac{2}{7} \left(u_{si} - \frac{d_i \omega_{si}}{2} \right) \right] \Big|_{i=1,3} \quad (14i)$$

$$\omega_{si}''|_{i=4,6} = \left[\omega_{si} - \frac{10}{7d_i} \left(u_{si} - \frac{d_i \omega_{si}}{2} \right) \right] \Big|_{i=1,3} \quad (14j)$$

$$v_{si}''|_{i=4,6} = k_n v_{si}|_{i=1,3} \quad (14k)$$

It must be noted that, throughout this paper, the particle-phase fractions “4”, “5”, and “6” correspond to the particle-phase fractions “1”, “2”, and “3.”

For the top boundary, if the rebounding particles do not collide with the wall we have ($i=4-6$)

$$y=0: \quad u_{si} = -\lambda_i \frac{\partial u_{si}}{\partial y}, \quad \omega_{si} = \lambda_i \frac{\partial \omega_{si}}{\partial y}, \quad v_{si} = 0 \quad (14l)$$

If the particles collided with the top boundary, then we use the boundary gradient-type conditions of Matsumoto and Saito [18] as in Eqs. (14a)–(14e) by simply replacing the subscript that denotes the particle fraction, e.g., $i=4-6 \rightarrow i=1-3$ and $i=1-3 \rightarrow i=4-6$, respectively.

The boundary condition for the particle mass concentration at both walls at the top and bottom walls are also the no-penetration conditions and may be written as follows

$$y=0 \quad \text{and} \quad y=h: \quad \alpha_i v_{si} = (D_{\text{icol}} + D_{\text{iturb}}) \frac{\partial \alpha_i}{\partial y} \quad (14m)$$

3 Model of Interparticle Collisions

We consider the hard-sphere collision model for the particles [12] and use the translational and angular velocity change of single collisions to derive analytical formulae for the stresses in the particulate mixture. Thus, collision forces are considered in the same way as the other forces acting upon the particles, such as gravity, Magnus, and Saffman forces. The collisions are divided in two categories: (a) collisions due to the average velocity difference between the several particle fractions; and (b) collisions due to turbulent velocity fluctuations. In order to obtain closure equations for the particulate phases we also use a Boussinesq eddy-viscosity model and the concept of pseudoviscosity coefficients for the transport equations.

We distinguish two types of collisions: (a) collisions with sliding friction that obey Coulomb's friction law and where the tangential and normal components of the collision force are related by a friction coefficient f ; and (b) collisions without sliding friction. Sliding friction collisions take place when: $\vec{e} \cdot \vec{G}_{ji} / |\vec{G}_{ji}^c| < 2/7f(1+k_{pn})$. The translational angular velocity changes for the two types of collisions are as follows

$$\begin{aligned}
(a) \quad \vec{v}'_i - \vec{v}_i &= \beta_{ji}(1 + k_{pn})(\vec{e} - f\vec{\tau})(\vec{e} \cdot \vec{G}_{ij}), & \vec{v}'_j - \vec{v}_j &= -\beta_{ij}(1 + k_{pn})(\vec{e} - f\vec{\tau})(\vec{e} \cdot \vec{G}_{ij}) \\
\vec{\omega}'_i - \vec{\omega}_i &= \frac{5\beta_{ji}}{\delta_i}(1 + k_{pn})(\vec{e} \cdot \vec{G}_{ij})(\vec{e} \times \vec{\tau}), & \vec{\omega}'_j - \vec{\omega}_j &= \frac{5\beta_{ij}}{\delta_j}(1 + k_{pn})(\vec{e} \cdot \vec{G}_{ij})(\vec{e} \times \vec{\tau}) \\
(b) \quad \vec{v}'_i - \vec{v}_i &= \beta_{ji}(1 + k_{pn})(\vec{e} \cdot \vec{G}_{ij})\vec{e} + \frac{2}{7}|\vec{G}_{ij}^{ct}|\vec{\tau}, & \vec{v}'_j - \vec{v}_j &= -\beta_{ij}(1 + k_{pn})(\vec{e} \cdot \vec{G}_{ij})\vec{e} + \frac{2}{7}|\vec{G}_{ij}^{ct}|\vec{\tau} \\
\vec{\omega}'_i - \vec{\omega}_i &= \frac{10\beta_{ji}}{7\delta_i}|\vec{G}_{ij}^{ct}|(\vec{e} \times \vec{\tau}), & \vec{\omega}'_j - \vec{\omega}_j &= -\frac{10\beta_{ij}}{7\delta_j}|\vec{G}_{ij}^{ct}|(\vec{e} \times \vec{\tau})
\end{aligned}$$

where \vec{e} , $\vec{\tau}$ are the normal and tangential unit vectors and \vec{G}_{ij} , \vec{G}_{ij}^{ct} are the relative particle velocity and its tangential component before the collision, respectively. The parameters k_{pn} , f , and $\beta_{ji} = m_j/(m_i + m_j)$ are the restitution and friction coefficients and the ratio of the masses. For the derivation of the collision parameters we use the three collision coordinates, χ , θ , φ , and the procedure that was described in detail in Kartushinsky and Michaelides [6,13] and derive expressions for the velocity correlations of the particulate phases, which are given succinctly in the following subsections.

3.1 Velocity Correlations for Collisions With Sliding Friction. The six velocity correlations in the case of collision with sliding friction

$$\begin{aligned}
\langle (v'_{si} - v_{si})(u'_{si} - u_{si}) \rangle_{\varphi, \chi, \theta} &= \beta_{ji}^2 a^2 (V_i + V_j)^2 \{ (0.5 \langle A^2 \rangle - \langle B^2 \rangle) \sin 2\gamma_i \\
&+ \langle AB \rangle \cos 2\gamma_i \} A_{ij} \\
&- 0.5 [\langle A^2 \rangle - \langle B^2 \rangle] \sin 2\gamma_i \\
&+ 2 \langle AB \rangle \cos 2\gamma_i C_{ij} - (\langle A^2 \rangle \\
&- \langle B^2 \rangle) \cos 2\gamma_i - 2 \langle AB \rangle \sin 2\gamma_i B_{ij}] \} \\
(15a)
\end{aligned}$$

$$\begin{aligned}
\langle (v'_{si} - v_{si})^2 \rangle_{\varphi, \chi, \theta} &= \beta_{ji}^2 a^2 (V_i + V_j)^2 \{ \langle A^2 \rangle \sin^2 \gamma_i + \langle B^2 \rangle \cos^2 \gamma_i \\
&+ \langle AB \rangle \sin 2\gamma_i \} A_{ij} \\
&+ 0.5 [\langle A^2 \rangle - \langle B^2 \rangle] \cos 2\gamma_i - 2 \langle AB \rangle \sin 2\gamma_i C_{ij} \\
&- (\langle A^2 \rangle - \langle B^2 \rangle) \sin 2\gamma_i + 2 \langle AB \rangle \cos 2\gamma_i B_{ij}] \} \\
(15b)
\end{aligned}$$

$$\langle (u'_{si} - u_{si})^2 + (v'_{si} - v_{si})^2 \rangle_{\varphi, \chi, \theta} = \beta_{ji}^2 a^2 (V_i + V_j)^2 (\langle A^2 \rangle + \langle B^2 \rangle) A_{ij} \quad (15c)$$

$$\begin{aligned}
\langle (v'_{si} - v_{si})(\omega'_{si} - \omega_{si}) \rangle_{\varphi, \chi, \theta} &= \beta_{ji}^2 a^2 \frac{5(V_i + V_j)^2 \cos \gamma_i}{\delta_i} [\langle AC \rangle t g \gamma_i \\
&+ \langle BC \rangle L_{ij} - \langle AC \rangle - \langle BC \rangle t g \gamma_i M_{ij}] \\
(15d)
\end{aligned}$$

$$\begin{aligned}
\langle (u'_{si} - u_{si})(\omega'_{si} - \omega_{si}) \rangle_{\varphi, \chi, \theta} &= \beta_{ji}^2 a^2 \frac{5(V_i + V_j)^2 \cos \gamma_i}{\delta_i} [\langle AC \rangle \\
&- \langle BC \rangle t g \gamma_i L_{ij} + \langle AC \rangle t g \gamma_i \\
&+ \langle BC \rangle M_{ij}] \\
(15e)
\end{aligned}$$

$$\langle (\omega'_{si} - \omega_{si})^2 \rangle_{\varphi, \chi, \theta} = \beta_{ji}^2 a^2 \frac{5(V_i + V_j)^2 \langle C \rangle^2}{\delta_i^2} A_{ij} \quad (15f)$$

The coefficients, $\langle A \rangle$, $\langle B \rangle$, $\langle C \rangle$ in Eqs. (15a)–(15f) are obtained analytically and are given in Appendix A.

3.2 Velocity Correlations for Collisions Without Sliding Friction. If the collisions occur without sliding friction, one is able to obtain the following velocity correlations

$$\begin{aligned}
\langle (v'_{si} - v_{si})(u'_{si} - v_{si}) \rangle_{\varphi, \chi, \theta} &= \beta_{ji}^2 (V_i + V_j)^2 \{ g_1 A_{ij} \sin 2\gamma_i \\
&- g_1 (B_{ij} \cos 2\gamma_i + C_{ij} \sin 2\gamma_i) \\
&+ g_2 R_{ij} (D_{ij} \cos 2\gamma_i - F_{ij} \sin 2\gamma_i) \\
&+ g_3 R_{ij}^2 (G_{ij} \sin 2\gamma_i - 0.5 Q_{ij} \sin 2\gamma_i \\
&+ H_{ij} \cos 2\gamma_i) \} \\
(16a)
\end{aligned}$$

$$\begin{aligned}
\langle (v'_{si} - v_{si})^2 \rangle_{\varphi, \chi, \theta} &= \beta_{ji}^2 (V_i + V_j)^2 \{ (g_4 + 2g_1 \sin^2 \gamma_i) A_{ij} \\
&- g_1 (B_{ij} \sin 2\gamma_i - C_{ij} \sin 2\gamma_i) + g_2 R_{ij} (F_{ij} \cos 2\gamma_i \\
&+ D_{ij} \sin 2\gamma_i) \\
&+ g_3 R_{ij}^2 ((1 + \cos^2 \gamma_i) Q_{ij} - G_{ij} \cos 2\gamma_i \\
&+ H_{ij} \sin 2\gamma_i) \} \\
(16b)
\end{aligned}$$

$$\langle (u'_{si} - u_{si})^2 + (v'_{si} - v_{si})^2 \rangle_{\theta, \chi, \varphi} = \beta_{ij}^2 (V_i + V_j)^2 (g_8 A_{ij} + 3g_3 R_{ij}^2) \quad (16c)$$

$$\begin{aligned}
\langle (v'_{si} - v_{si})(\omega'_{si} - \omega_{si}) \rangle_{\varphi, \chi, \theta} &= \frac{\beta_{ji}^2 (V_i + V_j)^2}{0.4\delta_i} \cos \gamma_i \{ g_5 (L_{ij} + M_{ij} t g \gamma_i) \\
&+ g_6 R_{ij} (N_{ij} t g \gamma_i - O_{ij}) + g_7 R_{ij}^2 (P_{ij} \\
&- T_{ij} t g \gamma_i) \}, \\
(16d)
\end{aligned}$$

$$\begin{aligned}
\langle (u'_{si} - u_{si})(\omega'_{si} - \omega_{si}) \rangle_{\varphi, \chi, \theta} &= \frac{\beta_{ji}^2 (V_i + V_j)^2}{0.4\delta_i} \cos \gamma_i \{ g_5 (-L_{ij} t g \gamma_i \\
&+ M_{ij}) + g_6 R_{ij} (N_{ij} + O_{ij} t g \gamma_i) \\
&- g_7 R_{ij}^2 (P_{ij} t g \gamma_i + T_{ij}) \} \\
(16e)
\end{aligned}$$

$$\langle (\omega'_{si} - \omega_{si})^2 \rangle_{\varphi, \chi, \theta} = \beta_{ji}^2 \frac{(V_i + V_j)^2 (A_{ij} + 0.75 R_{ij}^2)}{1.4\delta_i^2} \quad (16f)$$

The parameters of the above are given by the following expressions

$$R_{ij} = \frac{\omega_i d_i + \omega_j d_j}{V_i + V_j}, \quad g_1 = (a + b)^2 / 8, \quad g_2 = 2b(2a + 3b) / 15,$$

$$g_3 = b^2 / 16, \quad g_4 = (a - b)^2 / 12, \quad g_5 = 4b(a - b) / 15,$$

$$g_6 = b(5a + 7b) / 12, \quad g_7 = 4b^2 / 15, \quad g_8 = [a^2 + 2g_1 + 16g_3] / 3$$

As in the previous case one is able to obtain an analytical form of the coefficients, A_{ij} to T_{ij} , which are given in Appendix B.

In the vertical axisymmetric channel flow there is no contribution of collisions caused by the velocity differences in the average motion of identical particle fractions. However, in the asymmetric horizontal channel flow there is such an effect, due to the difference in the velocities of the average motion of identical particle

fractions between falling and rebounding particle fractions. The difference in the motion of identical falling and rebounding particles is one of main differences in the mathematical description and modeling of particulate flows for vertical and horizontal channels and one of the major contributions of this study.

4 Application to an Eddy-Viscosity Model

The closure transport equations for a polydisperse solid mixture are obtained according to the Boussinesq eddy-viscosity concept. Their final form of these equations is

$$\langle (u'_{si} - u_{si})(v'_{si} - v_{si}) \rangle_{\varphi, x, \theta} = -\nu_{si}^x \frac{\partial u_{si}}{\partial y} \quad (17a)$$

$$\langle (v'_{si} - v_{si})^2 \rangle_{\varphi, x, \theta} = -2\nu_{si}^y \frac{\partial v_{si}}{\partial y} + \frac{2k_{si}}{3} \quad (17b)$$

$$k_{si} \equiv \langle (u'_{si} - u_{si})^2 + (v'_{si} - v_{si})^2 \rangle_{\varphi, x, \theta} \quad (17c)$$

$$\langle (\omega'_{si} - \omega_{si})(v'_{si} - v_{si}) \rangle_{\varphi, x, \theta} = -\nu_{si}^{\omega} \frac{\partial \omega_{si}}{\partial y} \quad (17d)$$

$$\langle \alpha'_i (v'_{si} - v_{si}) \rangle_{\varphi, x, \theta} = -D_{icol} \frac{\partial \alpha_i}{\partial y} \quad (17e)$$

The last correlation comes from Fick's law of diffusion and takes into account any mass transfer due to interparticle collisions. The coefficient D_{icol} may be called a pseudo-diffusivity coefficient.

The pseudo-viscosity coefficients, $\nu_{si}^{x, y, \omega}$, which are thus introduced in the corresponding linear and angular momentum equations of the dispersed phase, are obtained as the products of the velocity correlations for all the velocity components and are calculated by taking their averages over the collision coordinates during the time of the collisions, t_{ijcol}

$$\nu_{si}^x = \sum_{j=1}^6 \langle (u'_{si} - u_{si})(v'_{si} - v_{si}) \rangle_{\varphi, x, \theta} t_{ijcol} \quad (18a)$$

$$\nu_{si}^y = \sum_{j=1}^6 \langle (v'_{si} - v_{si})^2 \rangle_{\varphi, x, \theta} t_{ijcol} \quad (18b)$$

$$\nu_{si}^{\omega} = \sum_{j=1}^6 \langle (\omega'_{si} - \omega_{si})(v'_{si} - v_{si}) \rangle_{\varphi, x, \theta} t_{ijcol} \quad (18c)$$

$$D_{icol} = \sum_{j=1}^6 \langle (u'_{si} - u_{si})^2 + (v'_{si} - v_{si})^2 \rangle_{\varphi, x, \theta} t_{ijcol} \quad (18d)$$

The collision time was given by Marble [19] and confirmed by several other investigators

$$t_{ijcol} = \frac{2\rho_p d_j^3}{3\rho \alpha_j (d_i + d_j)^2 |V_j - V_i|} \quad (19)$$

where α_j is the volumetric concentration of the j th particle fraction and the velocity difference between the colliding particles in a polydisperse mixture is calculated from the integral

$$|\vec{V}_j - \vec{V}_i| \equiv \frac{\int_0^{\varphi_{ij}} d\varphi \int_0^1 x dx \int_0^{2\pi} \sqrt{V_i^2 + V_j^2 - 2V_i V_j \cos \varphi} d\theta}{\pi \varphi_{ij}} \quad (20)$$

For the calculation of the velocity differences, due to the fluctuating velocity components of the colliding particles we use the following conditions:

$$\varphi_{ij} \equiv 2\pi, \quad V_i \equiv \sqrt{u_{si}'^2 + v_{si}'^2}, \quad \text{and} \quad V_j \equiv \sqrt{u_{sj}'^2 + v_{sj}'^2} \quad (21a)$$

where u'_{si} , v'_{si} and u'_{sj} , v'_{sj} are the fluctuating velocity components of the i th and the j th particle fractions, respectively. For the calculation of the velocity differences due to the average velocity components of the colliding particles we use the following conditions:

$$\text{tg } \varphi_{ij} \equiv \left| \frac{\left(\frac{v_{sj}}{u_{sj}} - \frac{v_{si}}{u_{si}} \right)}{\left(1 + \frac{v_{si} v_{sj}}{u_{si} u_{sj}} \right)} \right|, \quad (21b)$$

$$V_i = \sqrt{u_{si}^2 + v_{si}^2}, \quad \text{and} \quad V_j = \sqrt{u_{sj}^2 + v_{sj}^2}$$

4.1 Other Parameters in the Numerical Computations.

The factors affected by the particulate motion and taken into account in the present model's computations are as follows:

4.1.1 Turbulence Intensity Parameters. A two-way coupling model is used for the turbulence intensity. This model contains one differential equation for the turbulence kinetic energy, k . We use the model of Crowe and Gilland [10]. Turbulence modulation is described by the generation of additional turbulent energy by the particles, which is proportional to the square of the average slip between the phases, and by the turbulence attenuation described by the sum of the correlations of the various particle-gas velocity components

$$\sum_{\substack{k=x,y \\ l=y,x}} \langle u'_{sik} u'_l \rangle_{\text{turb}} = \langle u'_{si} u'_i \rangle_{\text{turb}} + \langle v'_{si} u'_i \rangle_{\text{turb}} + \langle u'_{si} v'_i \rangle_{\text{turb}} + \langle v'_{si} v'_i \rangle_{\text{turb}} \quad (22a)$$

The dissipation rate is calculated in terms of the hybrid turbulence length scale

$$L_{hi} = 2L_T \lambda / (L_T + \lambda) \quad (22b)$$

The direct influence of the turbulence on the motion of the particles is manifested through the velocity fluctuations $\langle u'_{si} v'_{si} \rangle_{\text{turb}}$, $\langle v'_{si} v'_{si} \rangle_{\text{turb}}$, $\langle \omega'_{si} v'_{si} \rangle_{\text{turb}}$. Expressions for the fluid-particle and particle-particle turbulent fluctuating velocity correlations were obtained from Shraiber et al. [8]

$$\langle v_{si}'^2 \rangle = \frac{\gamma_{yy}^0}{\gamma_{yy}^0 + \varphi_{yy}^0} \langle v'^2 \rangle + \frac{(\gamma_{xx}^0)^2}{\gamma_{yy}^0 (\gamma_{yy}^0 + \varphi_{xx}^0)} \langle u'^2 \rangle + \frac{2\gamma_{xx}^0}{\gamma_{yy}^0 + \varphi_{xy}^0} \langle u' v' \rangle \quad (22c)$$

The parameters γ_{yy}^0 , γ_{yx}^0 are calculated from the response time of the particles; φ_{xx}^0 and φ_{xy}^0 come in the expressions for the velocities correlation of the gas phase along the trajectories of the particles [8]. One may extend Eq. (22c) to the so-called turbophoretic force, which is given as follows

$$F_{\text{turbph}} = -\rho \frac{\partial \alpha_i \langle v_{si}'^2 \rangle}{\partial y} \quad (22d)$$

The turbulent diffusion coefficient of the particles is given by the following expression

$$D_{\text{iturb}} = \frac{C_{i2} L_T}{\left(\sqrt{\frac{2k}{3}} + C_{i3} V_{ri} \right)^2} \left\{ \frac{2k}{3} \left(\sqrt{\frac{2k}{3}} + \frac{C_{i3} V_{ri}}{2} \right) \left(1 + \left(\frac{\gamma_{yx}^0}{\gamma_{yy}^0} \right)^2 \right) + \frac{C_{i3}}{2V_{ri}} \left(v_{ri}^2 + u_{ri}^2 \left(\frac{\gamma_{xx}^0}{\gamma_{yy}^0} \right)^2 \right) + 2 \langle u' v' \rangle \left(\frac{\gamma_{yx}^0}{\gamma_{yy}^0} \right) \left(\sqrt{\frac{2k}{3}} + \frac{V_{ri}}{2} + \frac{v_{ri}^2}{2V_{ri}} \right) \right\} \quad (22e)$$

where the numerical values of the constants are obtained from the turbulent kinetic energy equation

$$C_{t2} = 0.3, \quad C_{t1} = 0.925, \quad \text{and} \quad C_{t3} = 0.5$$

4.1.2 Particle-Particle Interactions. The effect of particle interactions in the governing equations is given by the pseudoviscosity coefficients $\nu_{si}^x, \nu_{si}^y, \nu_{si}^\omega$, and D_{icol} as well as by the stress tensor components $\langle u_{si}'^2 \rangle_{col}, \langle u_{si}'v_{si}' \rangle_{col}$, and $\langle \omega_{si}'u_{si}' \rangle_{col}$. Again, while considering the effect of collisions on the motion of the particle, two collision mechanisms are taken into account: (a) the collisions that are caused by the turbulent fluctuations of the carrier fluid; and (b) the collisions that are caused by the differences in the average velocity of the particle fractions. Therefore, these quantities may be thought of as consisting of two parts, the average and the fluctuating parts. Hence, their closure equations may be written as follows:

$$\begin{aligned} \nu_{si}^x &= \nu_{si}^{x,fluc} + \nu_{si}^{x,aver}, & \nu_{si}^y &= \nu_{si}^{y,fluc} + \nu_{si}^{y,aver}, & \nu_{si}^\omega &= \nu_{si}^{\omega,fluc} + \nu_{si}^{\omega,aver}, \\ D_{icol} &= D_{icol}^{fluc} + D_{icol}^{aver}, & k_{si} &= k_{si}^{fluc} + k_{si}^{aver}, \\ \langle u_{si}'^2 \rangle_{col} &= \langle u_{si}'^2 \rangle_{col}^{fluc} + \langle u_{si}'^2 \rangle_{col}^{aver}, & \langle u_{si}'v_{si}' \rangle_{col} &= \langle u_{si}'v_{si}' \rangle_{col}^{fluc} + \langle u_{si}'v_{si}' \rangle_{col}^{aver}, \\ \langle \omega_{si}'u_{si}' \rangle_{col} &= \langle \omega_{si}'u_{si}' \rangle_{col}^{fluc} + \langle \omega_{si}'u_{si}' \rangle_{col}^{aver} \end{aligned} \quad (23)$$

4.1.3 Effect of the Concentration of Particles (Rarefaction and Cluster Effects). Because the particle distribution across the horizontal channel is nonuniform, we use the concept of the particle mean free path, introduced by Louge et al. [20] to introduce corrections for the inhomogeneities in the volume fractions of the particles. Thus, the pseudoviscosity coefficients, $\nu_{si}^{x,y,\omega}$, D_{icol} , and the stress tensor components due to the collision, k_{si} , $\langle u_{si}'^2 \rangle_{col}$, $\langle u_{si}'v_{si}' \rangle_{col}$, $\langle \omega_{si}'u_{si}' \rangle_{col}$ are multiplied by the factor $f_\gamma = 1/(1 + \gamma/R)$, where γ is the mean free path of the particles and R is the radius of the pipe. The mean free path of the i th particle fraction is calculated according to Chapman and Cowling [21]: $\gamma_i = \rho_p d_i / 6\rho\alpha_i$. This factor is important when the concentration of the particles is significantly low in the vicinity of the top wall and, hence, a correction for the ‘‘rarefaction effect’’ might be needed. A similar correction for the ‘‘clustering effect’’ at the bottom wall is carried out automatically by using Eqs. (14e) and (14m) for the settling boundary conditions of the linear and angular velocity components of the particulate phases.

5 Numerical Method, Results, and Discussion

For the numerical simulation, a nonuniform grid has been applied according to a three-layer model that comprises the turbulent core the buffer zone and the laminar sublayer. A finite difference method has been used for the numerical solution of the governing equations of the gas phase and the dispersed phases with a standard tridiagonal algorithm that operates with a six-point formula and with an implicit upwind difference scheme [22]. The numerical scheme is a first-order scheme and a special procedure was used to overcome the problem of the nonlinear terms in the left-hand side of the momentum equations in the axial direction of all phases [23]. More details, a verification, and accuracy of the numerical scheme may be found in Frishman et al. [24]. A grid independence test was also performed for several values of the grid parameters that were used. The results of this test are depicted in Table 1. All values in this table have been made dimensionless by the quantity $1000H$, that is the units are in thousandths of the height H . It is observed that the values used for the grid yield results that are within 1% of values obtained by significantly smaller grid sizes, which is an indication of the validity of the grid used. The various entries of Table 1 are as follows: δy_c , δy_b , and δy_{s-l} are the dimensions in the transverse direction and represent the core region, the buffer zone, and viscous sublayer, respectively; δx is the dimension used in the longitudinal direction; $u(1)$

Table 1 Grid independence results

	δy_c	δy_b	δy_{s-l}	δx	$u(1)$	$u_s(1)$
Grid used	21.035	21.035	0.555	0.555	20.28	19.61
Test 1	14.725	4.07	0.594	0.594	20.59	19.41
Test 2	7.125	6.364	0.757	0.757	20.91	20.18
Test 3	40.159	12.021	0.925	0.925	19.99	19.29

is the gas velocity at the center of the channel; $h/H=1$; and $u_s(1)$ is the corresponding velocity of the solid particles at $y/H=1$.

Figure 1 shows the average longitudinal velocity profiles of the gas, u , and of the solid phase, u_s , across the flow channel for an air velocity of 6 m/s. The profiles are normalized by the mean flow velocity, \bar{u} , and the experimental data are from Tsuji and Morikawa [1]. It is observed that the numerical results show good qualitative and quantitative agreement with the experimental data. It is also evident that the inclusion of the collision mechanisms improves significantly the predictions of the model. We believe that the discrepancies between the experimental data and the predictions of the model are due to the three-dimensional effects (pipe versus channel) and the difference in the coefficients of the nonuniformity of the velocity profiles in flat channels and in pipes: in channel the coefficient of nonuniformity is 1.13, while in pipes it is 1.25.

Figure 2 shows the distributions of the gas-phase fluctuation velocity components for average gas velocities equal to 6 m/s and 15 m/s. It may be observed that the small particles ($d=210 \mu\text{m}$) result in an attenuation of the turbulence intensity in the experimental data as well as the results of the model. This reflects the well known phenomenon of turbulence modulation by small particles. As with Fig. 1, there is good agreement between the data and the results of the model.

The following set of figures show more detailed information of the various parameters that comprise the model. The figures pertain to the case of the two average flow velocities $\bar{u}=6$ m/s and $\bar{u}=15$ m/s and two mass loadings: the first is for a dilute flow, with $m=2.5$ and the second is for an intermediate flow $m=15$. Figure 3 depicts the profiles of particle mass concentration across the entire channel flow for different mean flow velocities and mass loadings. All six particle fractions that have been considered in the model have been summed up in this figure. The growth of particle mass concentration along the bottom wall reflects the importance of settling in horizontal flows. Obviously, settling is more pronounced for the low mean flow velocity.

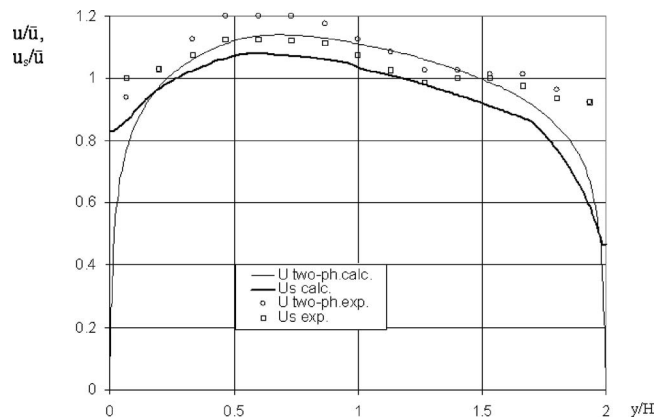


Fig. 1 Longitudinal dimensionless velocity profiles of the gas and solid phases across the horizontal pipe from the top ($y/H=0$) to the bottom ($h/H=2$): $d=210 \mu\text{m}$, $m=2.5 \text{ kg/kg}$, $\bar{u}=15 \text{ m/s}$

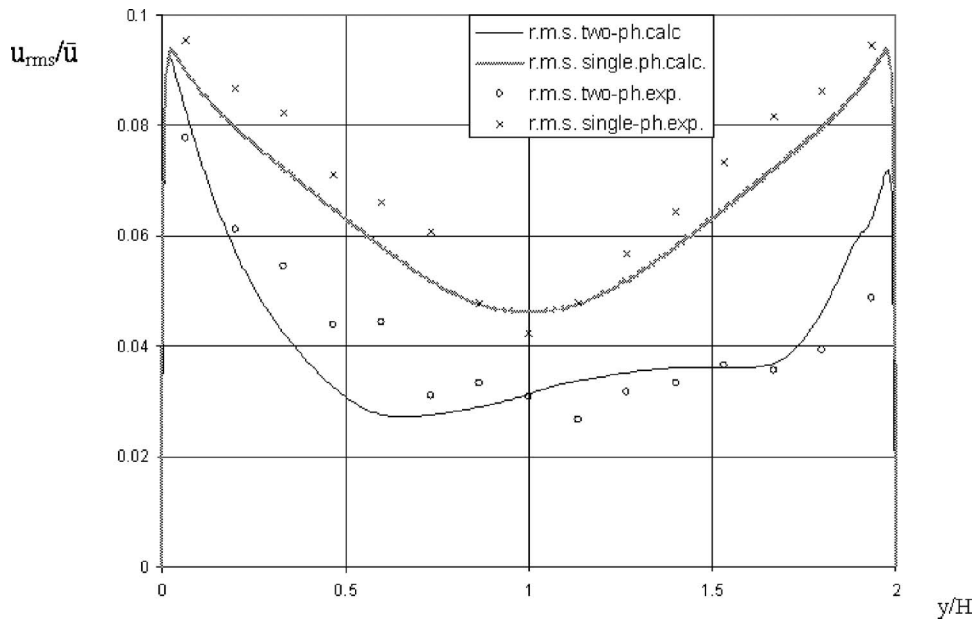


Fig. 2 Dimensionless fluctuation velocity, $d=210 \mu\text{m}$, $m=2.5$, $\bar{u}=15 \text{ m/s}$

Figure 4 depicts the normalized profiles of the kinetic energy, which is the result of the various collision processes modeled in this work. The figure shows the result of the collisions that originated from the particle fluctuating motion as well as from the average motion of the several particle fractions. It can be observed that the accumulation of particles at the bottom wall contributes significantly to the total kinetic energy. It is also observed that the profiles of the two contributions to the kinetic energy, $k_{s\Sigma}^{\text{fluc}}$ and $k_{s\Sigma}^{\text{aver}}$ are different both qualitatively and quantitatively. For example, the contribution of the fluctuation part is higher on the top wall than the bottom wall, while the contribution of the average part is higher at the bottom part of the channel. Obviously, this is due to the significant increase of particle concentration at the bottom wall, which results in the decrease of the turbulent energy of the carrier fluid. It is also apparent that the interactions and impacts of the particles with the bottom wall results in significant exchange of kinetic energy, which is manifested in the sharp rise of the profiles of the collision kinetic energy associated with the average motion of the particles, close to the bottom wall. The calculations have shown that, when the flow velocities are relatively low ($\bar{u} < 10 \text{ m/s}$) particle impacts and interactions with the

top wall are highly unlikely, because most particles travel close to the bottom wall. However, if the flow velocity is significantly high ($\bar{u} > 30 \text{ m/s}$) and the size of the particles relatively small ($d=10\text{--}60 \mu\text{m}$), then there is high probability that the particles will interact with both the lower and the upper wall. In such cases, the turbophoretic force is significant at both walls.

Figures 5 and 6 show profiles of the diffusion coefficients of the particles caused by the collision processes. The decrease of the diffusion coefficients of the particles towards the bottom wall in Fig. 5 is due to the fluctuation collisions, $D_{\Sigma\text{col}}^{\text{fluc}}$, as well as to their turbulent motion $D_{\Sigma\text{turb}}$. The latter is modulated by the general decrease of turbulent energy of the carrier fluid in the vicinity of a wall. The increase of the coefficient of the collision diffusion, $D_{\Sigma\text{col}}^{\text{aver}}$, in the vicinity of the bottom wall, shown in Fig. 6, results from the intensive particle–bottom wall interactions and impacts. This is more significant in the case of the higher flow velocity $\bar{u} = 15 \text{ m/s}$. Since there is significantly lower concentration of particles at the upper wall, the coefficient of collision diffusion there is much lower.

Figures 7 and 8 show the behavior of the gas–solid mixture at a very high transport velocity, $\bar{u}=50 \text{ m/s}$, where the Stokes number

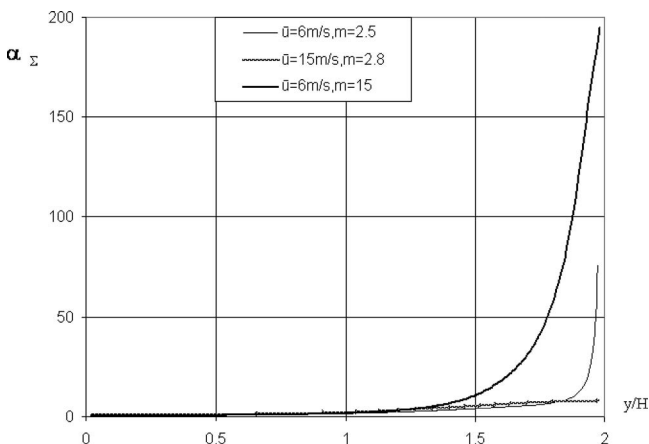


Fig. 3 Profiles of particle mass concentrations across the horizontal pipe, $d=210 \mu\text{m}$

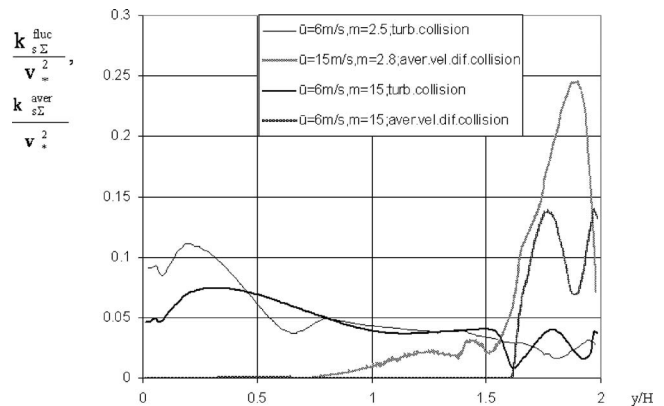


Fig. 4 Profiles of collision kinetic energy due to particle fluctuating motion (TNFLK) and average motion (TNAWK), $\bar{u} = 6 \text{ m/s}$ and 15 m/s , $m=2.5$ and 15

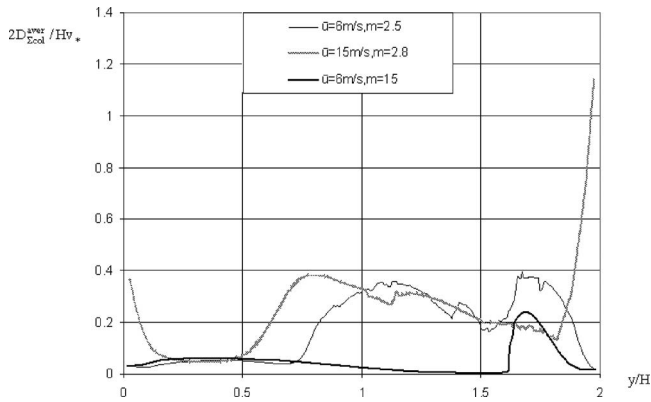


Fig. 5 Profiles of the coefficient of diffusion of collision kinetic energy due to the average motion of particles (DSPA)

of all the particle fractions is very small. It is apparent that, at this high transport velocity, the profiles of all quantities are almost symmetric with the particle sizes of $32 \mu\text{m}$ and $44 \mu\text{m}$ and very close to symmetric with the larger particles of $88 \mu\text{m}$. Figure 7 shows the distribution of the turbulent energy across the entire cross section of the pipe flow with practically symmetrical distribution of the kinetic energy profiles in the case of smaller particles. It is evident that the profiles of turbulent kinetic energy are very steep in the vicinity of both walls. This confirms the conjecture that the turbophoretic force would be high in both the upper

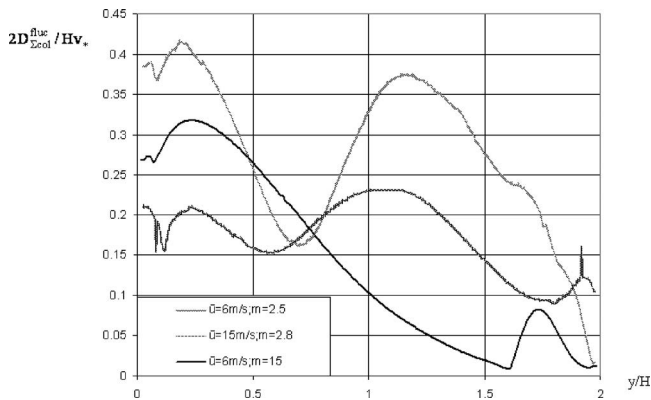


Fig. 6 Profiles of coefficient of diffusion of collision kinetic energy only due to the fluctuating motion of the particles (DSPFL)

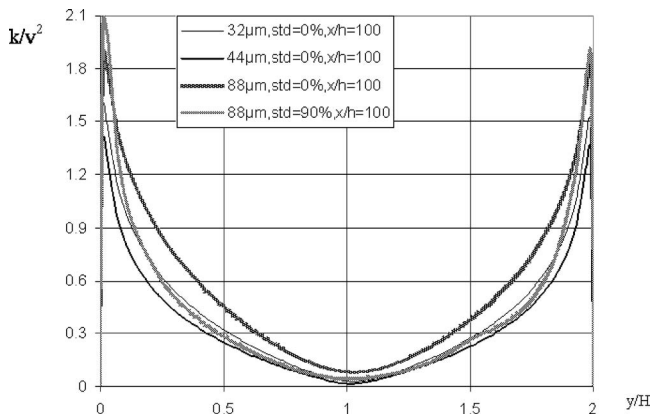


Fig. 7 Profiles of turbulent energy of along entire cross section: $d=32 \mu\text{m}$, $44 \mu\text{m}$, and $88 \mu\text{m}$

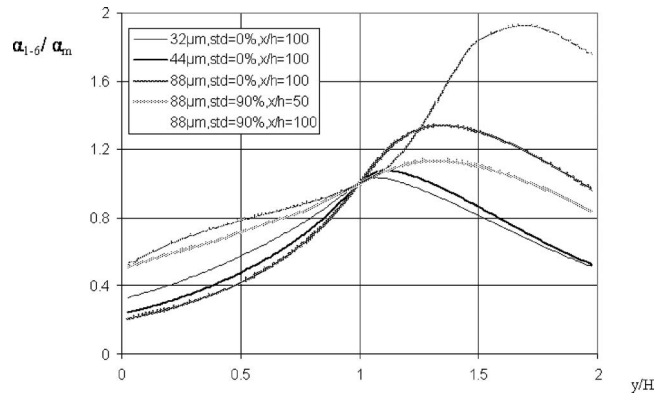


Fig. 8 Profiles of particle mass concentration across the flow channel for particles, $\bar{u}=50 \text{ m/s}$

and lower boundary, provided that the transport velocity is high enough to move the particles to the upper part of the flow channel. In this case, the flow profiles are almost symmetric. Figure 8 depicts the normalized profiles of the particle mass concentration. As in the previous figure, these profiles are symmetric for the small particles of $32 \mu\text{m}$ and $44 \mu\text{m}$ and almost symmetric for the larger particles of $d=88 \mu\text{m}$.

Figures 9–11 show the effects of certain parameters that come into the computations of particulate flows. The particles in all these figures are polystyrene with diameter $d=210 \mu\text{m}$ and density $\Delta_p=1000 \text{ kg/m}^3$. The mean flow velocity is equal to 5 m/s

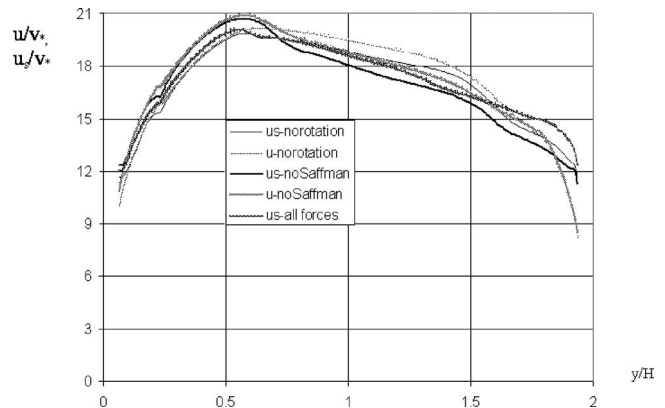


Fig. 9 The effect of the inclusion of the Magnus and Saffman lift forces on the normalized longitudinal velocities of the carrier phase and the particles

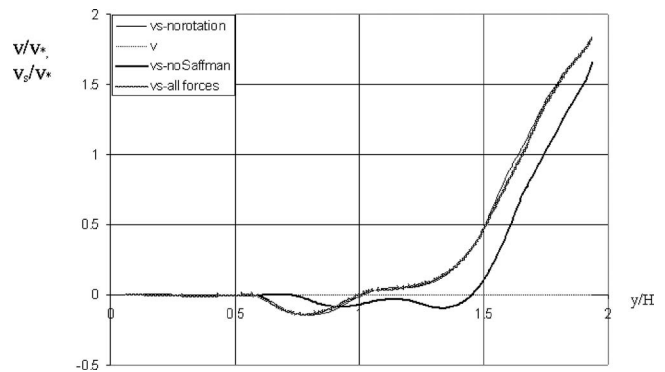


Fig. 10 Normalized transverse velocity profiles of the gas and particles with and without the lift forces

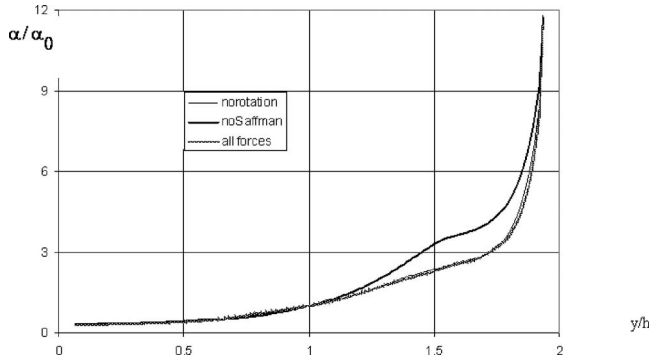


Fig. 11 Normalized profiles of particulate mass concentration calculated with and without the lift forces. α_0 is the particle mass concentration at the flow axis ($y/H=1$).

and the mass loading $m=2.5$. The results have been obtained at a distance $x/H=200$, which ensures that the flow has reached steady state. Figure 9 shows the effect of the inclusion of Magnus and Saffman forces in the computations of the longitudinal velocity, which is shown normalized by the friction velocity of the gas v^* . It is observed that the effect of the two lift forces is less than 10% in most of the flow domain, except in the vicinity of the walls, where it becomes significant. Figure 10 shows the effect of the lift forces on the normalized transverse velocity of the gas and the particles. It is observed that the Saffman lift force has a more significant (20%) influence on the transverse velocity profile. Figure 11 shows the effect of the inclusion of the lift forces on the concentration of the particles. Again, it is observed that the effect of the Saffman lift force is significant, especially in the lower part of the flow domain.

6 Conclusions

A model for the transport of particles by gases in horizontal channels and pipes has been developed from first principles, using the mechanisms of interparticle collisions and established methods for the derivation of closure equations, such as the Boussineq approximation. The closure of the transport equations for the polydisperse particulate phase is based on the interparticle collision theory, assuming that each type of particles may be separated into two phases: the particles that move toward the wall and those that are rebounding from the wall. The results of the model show all the expected trends that are met in a pneumatic conveying mixture as well as very good qualitative and quantitative agreement with available experimental data. Because the model is developed by taking into account the interparticle collisions, it may be used for predictions at very high loadings (concentrated flows) where other models may fail. The model is also capable of accounting for the turbulence modulation caused by the particles. Results on the effects of the lift forces on the parameters of the model show that the Magnus lift causes little difference in the results of the velocities and particle concentrations, while the effect of the Saffman lift is more significant [25].

Acknowledgment

This research was made possible by two visits of the first author to Tulane University, which were partly supported by a grant from the NOAA and USGS to the Tulane-Xavier Center for Bioenvironmental research, by the Ministry of Education of Estonia Project No. 0070055s98, and by HPC-Europa Transnational Program, No. 307. The authors are grateful for this support.

Appendix A: Coefficients for Collisions with Sliding Friction

We distinguish three cases for the translational velocities in this type of collisions:

1. The translational velocity of colliding particles is much smaller than the circumferential velocity, $\Delta_{ij} \ll \omega_{ij}$;
2. The translational and circumferential velocities are of the same order of magnitude, $\Delta_{ij} \approx \omega_{ij}$; and
3. The translational velocity is much larger than the particle circumferential velocity, $\Delta_{ij} \gg \omega_{ij}$.

In the **first case**, where $\Delta_{ij} \ll \omega_{ij}$ the following expressions are obtained for the average coefficients

$$\langle A^2 \rangle|_{\varphi,x,\theta} = \frac{1}{3} + \frac{f^2}{10}, \quad \langle B^2 \rangle|_{\varphi,x,\theta} = \frac{1}{12} + \frac{2f^2}{5},$$

$$\langle AB \rangle|_{\varphi,x,\theta} = \langle AC \rangle|_{\varphi,x,\theta} = 0, \quad \langle BC \rangle|_{\varphi,x,\theta} = -\frac{2f^2}{5},$$

$$\langle C^2 \rangle|_{\varphi,x,\theta} = \frac{5f^2}{12}$$

In the **second case**, where $\Delta_{ij} \approx \omega_{ij}$ the average coefficients are

$$\langle A^2 \rangle|_{\varphi,x,\theta} = \frac{1}{3} - \frac{2f}{5} + \frac{f^2}{10}, \quad \langle B^2 \rangle|_{\varphi,x,\theta} = \frac{1}{12} + \frac{f^2}{3},$$

$$\langle AB \rangle|_{\varphi,x,\theta} = \frac{f}{15}(f-4), \quad \langle AC \rangle|_{\varphi,x,\theta} = \frac{f}{3} - \frac{f^2}{15}$$

$$\langle BC \rangle|_{\varphi,x,\theta} = -f\left(\frac{1}{60} + \frac{f}{3}\right), \quad \langle C^2 \rangle|_{\varphi,x,\theta} = \frac{9f^2}{20}$$

Finally, in the **third case**, where $\Delta_{ij} \gg \omega_{ij}$ we have

$$\langle A^2 \rangle|_{\varphi,x,\theta} = \frac{1}{3} - \frac{\pi f}{8} + \frac{f^2}{6}, \quad \langle B^2 \rangle|_{\varphi,x,\theta} = \frac{1}{12} + \frac{\pi f}{16} + \frac{f^2}{6},$$

$$\langle AB \rangle|_{\varphi,x,\theta} = \langle AC \rangle|_{\varphi,x,\theta} = 0$$

$$\langle BC \rangle|_{\varphi,x,\theta} = -\frac{f}{5}\left(\frac{2}{3} + f\right), \quad \langle C^2 \rangle|_{\varphi,x,\theta} = \frac{f^2}{4}.$$

Appendix B: Coefficients for Collisions Without Sliding Friction

The analytical form of the coefficients of the velocity correlation equations A_{ij} through T_{ij} in the collisions without friction, are given analytically as follows

$$A_{ij} = 1 - \frac{k_{ij}^2}{2} \left(1 + \frac{\sin \varphi_{ij}}{\varphi_{ij}} \right),$$

$$B_{ij} = \frac{k_{ij}^2 \sin^2 0.5\varphi_{ij}}{\varphi_{ij}} \left(1 - \frac{V_j}{V_i} \cos^2 0.5\varphi_{ij} \right),$$

$$C_{ij} = \frac{V_j k_{ij}^2}{4V_i} \left(1 - \frac{\sin \varphi_{ij}}{\varphi_{ij}} \right)$$

$$D_{ij} = \left(1 - \frac{2(2-k_{ij}^2)V_j}{3k_{ij}^2} \right) \frac{E^{ij}}{\varphi_{ij}} + \frac{4(1-k_{ij}^2)V_j K^{ij}}{3k_{ij}^2 \varphi_{ij} V_i} - \frac{2 \sin \varphi_{ij} \bar{\Delta}_{\varphi_{ij}} V_j}{3\varphi_{ij} V_i}$$

$$F_{ij} = \left(1 + \frac{V_j}{V_i}\right) \frac{\sqrt{1-k_{ij}^2}}{\varphi_{ij}} \left(1 - \frac{\bar{\Delta}_{\varphi_{ij}}}{\sqrt{1-k_{ij}^2}}\right) \\ \times \left(1 - \frac{V_j}{V_i} + \left(1 + \frac{V_j}{V_i}\right) \frac{(1-k_{ij}^2)}{3} \left(1 + \frac{\bar{\Delta}_{\varphi_{ij}}}{\sqrt{1-k_{ij}^2}} + \frac{\bar{\Delta}_{\varphi_{ij}}}{1-k_{ij}^2}\right)\right) \\ G_{ij} = \frac{V_j}{V_i} \left(\frac{1-k_{ij}^2}{k_{ij}^2} + \frac{1}{2} \left(1 + \frac{\sin \varphi_{ij}}{\varphi_{ij}}\right) - \frac{2\sqrt{1-k_{ij}^2}}{\varphi_{ij}k_{ij}^2} \tan^{-1} \left(\frac{\tan 0.5\varphi_{ij}}{\sqrt{1-k_{ij}^2}}\right)\right),$$

$$H_{ij} = \frac{V_j \sin^2 0.5\varphi_{ij}}{V_i \varphi_{ij}} + \frac{1}{4} \left(1 - \frac{V_j^2}{V_i^2}\right) \ln \left(\frac{\bar{\Delta}_{\varphi_{ij}}}{1-k_{ij}^2}\right),$$

$$M_{ij} = \left(1 + \frac{V_j}{V_i}\right) \frac{(1-k_{ij}^2)^{3/2}}{3\varphi_{ij}} \left(1 - \frac{\bar{\Delta}_{\varphi_{ij}}^3}{(1-k_{ij}^2)^{3/2}}\right)$$

$$L_{ij} = \frac{k_{ij}}{3} \sqrt{\frac{V_j}{V_i}} \left(\frac{\sin \varphi_{ij}}{\varphi_{ij}} \bar{\Delta}_{\varphi_{ij}} + \frac{(1-k_{ij}^2)K^{ij}}{k_{ij}^2 \varphi_{ij}}\right) - \left(1 + \frac{(1-2k_{ij}^2)\sqrt{V_j}}{3k_{ij}\sqrt{V_i}}\right) \frac{E^{ij}}{\varphi_{ij}}$$

$$Q_{ij} = \frac{\varphi_{ij}}{E^{ij}}, \quad N_{ij} = \frac{\left(1 - \frac{V_j \sin \varphi_{ij}}{V_i \varphi_{ij}}\right)}{2\left(1 + \frac{V_j}{V_i}\right)}, \quad O_{ij} = \frac{V_j \sin^2 0.5\varphi_{ij}}{V_i \varphi_{ij} \left(1 + \frac{V_j}{V_i}\right)},$$

$$P_{ij} = \left(1 - \frac{V_j}{V_i}\right) \frac{K^{ij}}{\varphi_{ij}} + \left(1 + \frac{V_j}{V_i}\right) \frac{E^{ij}}{\varphi_{ij}}$$

$$T_{ij} = 2 \left(1 + \frac{V_j}{V_i}\right) \frac{\sqrt{1-k_{ij}^2}}{\varphi_{ij}} \left(1 - \frac{\bar{\Delta}_{\varphi_{ij}}}{\sqrt{1-k_{ij}^2}}\right),$$

$$\bar{\Delta}_{ij} = \sqrt{1-k_{ij}^2 \cos^2(0.5\varphi)}, \quad \bar{\Delta}_{\varphi_{ij}} = \sqrt{1-k_{ij}^2 \cos^2(0.5\varphi_{ij})}$$

and integrals

$$E^{ij} = \int_0^{\varphi_{ij}} \bar{\Delta}_{ij} d\varphi, \quad K^{ij} = \int_0^{\varphi_{ij}} d\varphi \bar{\Delta}_{ij}$$

When the angle φ_{ij} is very small, that is, $\varphi_{ij} \ll 1$, these coefficients may be simplified considerably to yield the following expressions

$$A_{ij} = 1 - k_{ij}^2 + \frac{k_{ij}^2 \varphi_{ij}^2}{4}, \quad B_{ij} = \frac{k_{ij}^2 \varphi_{ij}}{4} \left(1 - \frac{V_j}{V_i} + \frac{V_j \varphi_{ij}^2}{4V_i}\right),$$

$$C_{ij} = \frac{V_j k_{ij}^2 \varphi_{ij}^2}{2V_i}, \quad D_{ij} = \bar{\Delta}_{ij} \left(1 - \frac{V_j \varphi_{ij}^2}{3V_i \bar{\Delta}_{ij}^2}\right)$$

$$F_{ij} = - \left(1 + \frac{V_j}{V_i}\right) \frac{k_{ij}^2 \varphi_{ij}}{4\bar{\Delta}_{ij}} \left[1 - \frac{V_j}{V_i} + \frac{1}{3} \left(1 - \frac{V_j}{V_i}\right) \right. \\ \left. \times (1 - k_{ij}^2 + \sqrt{1-k_{ij}^2} \bar{\Delta}_{ij} + \bar{\Delta}_{ij}^2)\right]$$

$$G_{ij} = \frac{V_j k_{ij}^2 \varphi_{ij}^2}{4V_i \bar{\Delta}_{ij}^2}, \quad H_{ij} = \frac{\varphi_{ij}}{4} \left(\frac{V_j}{V_i} + \left(1 - \frac{V_j^2}{V_i^2}\right) \frac{k_{ij}^2}{2\bar{\Delta}_{ij}^2}\right),$$

$$M_{ij} = - \left(1 + \frac{V_j}{V_i}\right) \frac{k_{ij}^2 \varphi_{ij} \bar{\Delta}_{ij}}{4}$$

$$L_{ij} = \bar{\Delta}_{ij} \left[\frac{k_{ij}}{3} \sqrt{\frac{V_j}{V_i}} \left(1 + \frac{1-k_{ij}^2}{k_{ij}^2 \bar{\Delta}_{ij}^2}\right) - \left(1 + \frac{(1-2k_{ij}^2)\sqrt{V_j}}{3k_{ij}\sqrt{V_i}}\right)\right],$$

$$N_{ij} = \frac{\left(1 - \frac{V_j}{V_i} + \frac{V_j \varphi_{ij}^2}{4V_i}\right)}{2\left(1 + \frac{V_j}{V_i}\right)}$$

$$O_{ij} = \frac{V_j}{V_i} \frac{\varphi_{ij}}{4\left(1 + \frac{V_j}{V_i}\right)}, \quad P_{ij} = \bar{\Delta}_{ij} \left[\left(1 - \frac{V_j}{V_i}\right) \frac{1}{\bar{\Delta}_{ij}^2} + 1 + \frac{V_j}{V_i}\right],$$

$$Q_{ij} \equiv \frac{\varphi_{ij}}{E^{ij}} = \frac{1}{\bar{\Delta}_{ij}}, \quad T_{ij} = \left(1 + \frac{V_j}{V_i}\right) \frac{k_{ij}^2 \varphi_{ij}}{2\bar{\Delta}_{ij}},$$

$$\bar{\Delta}_{ij} \equiv \sqrt{1-k_{ij}^2 + \frac{k_{ij}^2 \varphi_{ij}^2}{4}}$$

In the particular case of $k_{ij}^2 \equiv 1$ and $\varphi_{ij} \ll 1$

$$A_{ij} = \frac{\varphi_{ij}^2}{4}, \quad B_{ij} = \frac{\varphi_{ij}^3}{16}, \quad C_{ij} = \frac{\varphi_{ij}^2}{2}, \quad D_{ij} = -\frac{\varphi_{ij}}{4}$$

$$F_{ij} = -\frac{\varphi_{ij}^2}{6}, \quad G_{ij} = 1, \quad H_{ij} = \frac{\varphi_{ij}}{4}, \quad L_{ij} = 0, \quad M_{ij} = -\frac{\varphi_{ij}^2}{12},$$

$$N_{ij} = \frac{\varphi_{ij}^2}{8}, \quad O_{ij} = \frac{\varphi_{ij}}{8}, \quad P_{ij} = \frac{\varphi_{ij}}{2}, \quad Q_{ij} = \frac{4}{\varphi_{ij}}, \quad T_{ij} = -2$$

References

- [1] Tsuji, Y., and Morikawa, Y., 1982, "LDV Measurements of an Air-Solid Two-Phase Flow in a Horizontal Pipe," *J. Fluid Mech.*, **120**, pp. 385–409.
- [2] Davies, J. T., 1987, "Calculation of Critical Velocities to Maintain Solids in Suspension in Horizontal Pipes," *Chem. Eng. Sci.*, **42**, pp. 1667–1670.
- [3] Cabrejos, F. J., and Klinzing, G. E., 1994, "Pickup and Saltation Mechanisms of Solid Particles in Horizontal Pneumatic Transport," *Powder Technol.*, **79**, pp. 173–186.
- [4] Sommerfeld, M., 2003, "Analysis of Collision Effects for Turbulent Gas-Particle Flow in a Horizontal Channel: Part I. Particle Transport," *Int. J. Multiphase Flow*, **29**, pp. 675–699.
- [5] Sommerfeld, M., and Zivkovic, G., 1992, "Recent Advances in the Numerical Simulation of Pneumatic Conveying Through Pipe Systems," *Comput. Methods Appl. Mech. Eng.*, **9**, pp. 201–212.
- [6] Kartushinsky, A., and Michealides, E. E., 2004, "An Analytical Approach for the Closure Equations of Gas-Solid Flows With Inter-Particle Collisions," *Int. J. Multiphase Flow*, **30**, pp. 159–180.
- [7] Elghobashi, S., and Abou-Arab, T. W., 1983, "A Two-Equation Turbulence Model for Two-Phase Flows," *Phys. Fluids*, **26**, pp. 931–938.
- [8] Shraiber, A. A., Yatsenko, V. P., Gavin, L. B., and Naumov, V. A., 1990, *Turbulent Flows in Gas Suspensions*, Hemisphere, New York.
- [9] Yuan, Z., and Michaelides, E. E., 1992, "Turbulence Modulation in Particulate Flows—A Theoretical Approach," *Int. J. Multiphase Flow*, **18**, pp. 779–791.
- [10] Crowe, C. T., and Gilliland, I., 1998, "Turbulence Modulation of Fluid-Particle Flows—A Basic Approach," *Proc. 3rd International Conference on Multiphase Flows*, Lyon, France, May.
- [11] Tsuji, Y., Morikawa, Y., and Shiomi, H., 1984, "LDV Measurements of an Air-Solid Two-Phase Flow in a Vertical Pipe," *J. Fluid Mech.*, **139**, pp. 417–434.
- [12] Crowe, C., Sommerfeld, M., and Tsuji, M., 1998, *Multiphase Flows with Droplets and Particle*, CRC, Boca Raton, FL.
- [13] Kartushinsky, A., and Michealides, E. E., 2006, "Particle-Laden Gas Flow in Horizontal Channels With Collision Effects," *Powder Technol.*, **1**, p. 89.
- [14] Michaelides, E. E., 2006, *Particles, Bubbles and Drops—their Motion, Heat and Mass Transfer*, Scientific Publishers, NJ.
- [15] Yamamoto, Y., Potthoff, M., Tanaka, T., Kajishima, T., and Tsuji, Y., 2001, "Large-Eddy Simulation of Turbulent Gas-Particle Flow in a Vertical Channel: Effect of Considering Inter-Particle Collisions," *J. Fluid Mech.*, **442**, pp. 303–334.
- [16] Mei, R., 1992, "An Approximate Expression for the Shear Lift Force on a Spherical Particle at Finite Reynolds Number," *Int. J. Multiphase Flow*, **18**, pp. 145–147.
- [17] Ding, J., Lyczkowski, R. W., Sha, W. T., Altobelli, S. A., and Fukushima, E., 1993, "Numerical Analysis of Liquid-Solids Suspension Velocities and Concentrations Obtained by NMR Imaging," *Powder Technol.*, **77**, pp. 301–312.
- [18] Matsumoto, S., and Saito, S. J., 1970, "Monte Carlo Simulation of Horizontal Pneumatic Conveying Based on the Rough Wall Model," *J. Chem. Eng. Jpn.*, **3**(2), pp. 223–230.

- [19] Marble, F. E., 1964, "Mechanism of Particle Collision in One-Dimensional Dynamics of Gas-Particle Admixture," *Phys. Fluids*, **7**, pp. 1270–1282.
- [20] Louge, M. Y., Mastorakos, E., and Jenkins, J. T., 1991, "The Role of Particle Collisions in Pneumatic Transport," *J. Fluid Mech.*, **231**, pp. 345–359.
- [21] Chapman, S., and Cowling, T. G., 1952, *The Mathematical Theory of Non-uniform Gases*, Cambridge University Press, Cambridge, UK.
- [22] Roache, P. J., 1972, *Computational Fluid Dynamics*, Hermosa Publication Corp., Albuquerque, NM.
- [23] Andersen, D. A., Tannehill, J. C., and Pletcher, R. H., 1984, *Computational Fluid Mechanics and Heat Transfer*, Vol. 2, Hemisphere, New York.
- [24] Frishman, F., Hussainov, M., Kartushinsky, A., and Rudi, U., 1999, "Distribution Characteristics of the Mass Concentration of Coarse Solid Particles in a Two-Phase Turbulent Jet," *J. Aerosol Sci.*, **30**(1), pp. 51–69.
- [25] Laats, M. K., and Mulgi, A. S., 1979, "An Experimental Investigation of Kinematic Behaviour of Fine-Dispersed Pipe Flow," *Proceedings of All-Union Conference, Part-II, Two-Phase Turbulent Flows*, Tallinn, April, pp. 32–46.

Numerical Investigation of Liquid-Liquid Coaxial Flows

Bhadraiah Vempati

Department of Mechanical Engineering &
Mechanics,
Lehigh University,
Bethlehem PA 18015

Mahesh V. Panchagnula

Department of Mechanical Engineering,
Tennessee Tech University,
Cookeville TN 38505

Alparslan Öztekin

Sudhakar Neti

Department of Mechanical Engineering &
Mechanics,
Lehigh University,
Bethlehem PA 18015

This paper presents numerical results of the interfacial dynamics of axisymmetric liquid-liquid flows when the denser liquid is injected with a parabolic inlet velocity profile into a coflowing lighter fluid. The flow dynamics are studied as a function of the individual phase Reynolds numbers, viscosity ratio, velocity ratio, Bond number, and capillary number. Unsteady, axisymmetric flows of two immiscible fluids have been studied using commercial software, FLUENT® with the combination of volume of fluid (VOF) and continuous surface force (CSF) methods. The flows have been categorized as “flow-accelerated regime (FAR) and “flow-decelerated regime” (FDR) based on acceleration/deceleration of the injected fluid. The injected jet diameter decreases when the average inlet velocity ratio is less than unity. The outer fluid velocity has a significant effect on the shape and evolution of the jet as it progresses downstream. As the outer liquid flow rate is increased, the intact jet length is stretched to longer lengths while the jet radius is reduced due to interfacial stresses. The jet radius appears to increase with increasing viscosity ratio and ratio of Bond and capillary numbers. The results of numerical simulations using FLUENT agree well with experimental measurements and the far-field self-similar solution. [DOI: 10.1115/1.2734223]

Keywords: VOF, CSF, interfacial flows, liquid-liquid flows, core-annular flows, self-similar solution

1 Introduction

Immiscible multifluid flows have been the subject of engineering study for over a century. These flows occur in a wide variety of industrial applications: dispersive flows [1], liquid extraction processes [2,3], core annular flows [4], and coextrusion flows [5]. Liquids can be dispersed into droplets by injecting a liquid through a nozzle or an orifice into another continuous liquid. The injected liquid may drip or may form a long jet at the nozzle, depending on the flow rate of the injected liquid relative to the continuous liquid. If the injected liquid flow rates are small, the liquid may drip continuously at the nozzle outlet. For higher injected liquid flow rates, it forms a continuous jet at the end of the nozzle. In other applications, liquid could be dispersed as tiny droplets into another liquid to form an emulsion. Liquid extraction is another widely used operation in which solutes dissolved in a liquid solution are separated by contact with another immiscible liquid. The polymer processing industry uses multilayer fluid flows for coextrusion applications, where the products are required to manifest a steady interface to obtain superior mechanical properties. Water-lubricated oil flows (core annular flows) are another major application in this area in which the less viscous water encapsulates the oil to reduce frictional losses.

The case of both fluids being in motion has been the subject of only a few studies [6–9]. Previous numerical studies have not investigated the interfacial dynamics of the liquid-liquid flows when velocity ratio of the injected fluid to that of the continuous phase is greater than unity. The case of heavier fluid being injected into a lighter fluid describes an even more interesting competition between buoyancy and viscous forces but has been the subject of even fewer studies. The present work is related to a numerical investigation of liquid-liquid systems when both the fluids are moving with arbitrarily different velocities both in countergravity and cogravity flow conditions.

Rayleigh [10] was among the early researchers to have studied drop formation by studying the breakup of viscous liquid jets in

air. Subsequently, Tyler [11] and Tomotika [12] assumed that disturbance waves on liquid jet are responsible for jet breakup and predicted that the resulting drops will be equal in volume to that of a cylinder of radius equal to that of the jet and length equal to the most unstable disturbance wave length.

Bogy [13], Mansour and Lundgren [14], Vassallo and Ashgriz [15], and Orme et al. [16] were among recent researchers to have studied jet breakup, but primarily in the presence of no or stationary outer fluid. Meister and Sheele [17] studied drop formation in liquid-liquid systems both below and above jetting conditions by employing both theoretical and experimental approaches. They performed experiments on 15 different liquid-liquid systems to validate the theoretical expressions derived. They described the jet behavior in the following manner: At low flow rates, the liquid droplets are observed to form, grow, and break off at the nozzle tip. When the injecting liquid velocity exceeds a certain critical value, a stable laminar jet will be formed at the end of the nozzle and eventually breaks up into droplets at a certain distance from the nozzle tip. At still greater injection velocities, the jet becomes turbulent and disintegrates into small droplets. If the injection velocity is below a certain critical velocity, the drop formation process was governed by the balance between the disruptive buoyant force and the stabilizing surface tension force for upwardly injected lighter fluids. Above the critical injection velocity, the drop size is governed by the jet stability.

Richards et al. [18], Richards [19], and Richards et al. [20] have developed an Eulerian numerical method with the combination of volume of fluid (VOF) [21] and continuous surface force (CSF) [22] methods to simulate the fully transient drop formation from startup to break off of the jet. In this simulation, they solved the time-dependent axisymmetric equations of motion and continuity with the appropriate boundary conditions. The interfacial surface forces are incorporated as body forces per unit volume in the Navier-Stokes equations rather than as boundary conditions. The CSF formulation approximates the discontinuities as continuous transitions, without increasing the overall error of approximation, within which the fluid properties vary smoothly from one fluid to the other over a distance of $O(h)$, where h is a computational grid spacing. Richards et al. [20] successfully simulated the dynamics

Contributed by the Fluids Engineering Division of ASME for publication in the JOURNAL OF FLUIDS ENGINEERING. Manuscript received May 9, 2006; final manuscript received December 8, 2006. Review conducted by Surya P. Vanka.

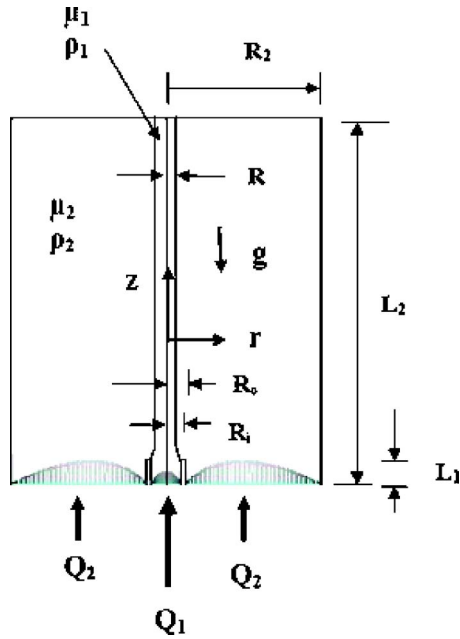


Fig. 1 Flow geometry

of drop formation of high Reynolds number (>400) liquid-liquid systems before and after jetting, including quantitative predictions of drop formation and velocity distribution with a relatively simple numerical method. Zhang and Stone [23] have developed a numerical method based on boundary layer integral method to simulate the drop formation from low Reynolds number flows in a capillary tube. They also considered ambient fluid effects on drop formation and breakup. This model identified the insensitivity of drop formation for low Reynolds number flows up to 0.1. Zhang [6] further extended Richard et al.'s [20] numerical simulations to include the complete process of drop formation, breakup, and ambient fluid motion. Cramer et al. [7] have studied the horizontal liquid jet stability in laminar flow experimentally when a liquid jet is injected into a cocurrent continuous liquid. Recently, Fischer et al. [8] studied the capillary-driven breakup mechanism of liquid jet when it is injected into a cocurrent flow by employing various injection geometry profiles and observed that the geometry may not affect the breakup mechanism for small changes to the nozzle geometry.

Much of the prior work has focused either on drop formation in single-fluid systems or on liquid-liquid systems with one of the fluids being stationary. The present work describes the interfacial dynamics of liquid-liquid vertical, coaxial low Reynolds number flows where injected phase liquid is introduced in the central portion of the annular continuous phase liquid with both fluids being in motion. Work prescribed here has direct applications to emulsions among other fields. In forming emulsions, controlling the drop size of injected fluid is important and it is directly proportional to the fully developed radius of the laminar jet. The focus of this work is to investigate the effect of velocity ratio, viscosity ratio, Bond number, and capillary number on the interface evolution of the liquid phases and injected liquid phase jet radius at low Reynolds numbers using FLUENT® [24]. The results from the numerical simulations are also compared to the experiments measurements of Kettering [9] and far-field self-similar solutions results.

2 Numerical Model and Governing Equations

The flow configuration investigated in the present work is shown in Fig. 1. An immiscible liquid is injected vertically upward through a circular nozzle into a moving continuous liquid in

a tube. The interfacial tension between the liquids is assumed to be constant. Gravity is acting in the downward direction. Both fluids enter the flow field with the fully developed velocity profiles, as shown in Fig. 1.

2.1 Numerical Model. The velocity field for immiscible liquid-liquid flows is solved with FLUENT [24] using VOF/CSF techniques to track the fluid interface. Other researchers including Killion and Garimella [25], Taha and Cui [26], and Valencia et al. [27] have also successfully employed this software for numerical simulation of similar problems. VOF method provides a simple and economical way to track free surfaces in complicated multi-fluid flows with the help of a scalar volume fraction step function (F). In this method, a single momentum equation is used to solve for the pressure and velocity distribution in a multifluid domain. The interfacial surface position is specified by the value of volume fraction function F . The volume fraction, F assumes values unity and zero in the two fluids respectively. F varies smoothly from zero to unity near the interface. The equation that governs the distribution of volume fraction function F is

$$\frac{\partial F}{\partial t} + (\mathbf{V} \cdot \nabla)F = 0 \quad (1)$$

A geometry reconstruction scheme [24] is used in these simulations to avoid diffusion at the interface. This scheme assumes that the interface between the two fluids has a linear slope within each cell, for the calculation of advection of fluid through the cell faces. The first step in this reconstruction scheme involves the calculation of the position of the linear interface relative to the center of each partially filled cell, based on F and its derivatives in the cell. The advected amount of fluid through each face is then calculated using the computed linear interface representation and information about the normal and tangential velocity distribution on the face. Calculations of the volume fractions in each cell are performed using the net fluxes.

2.2 Governing Equations. The flow is assumed to be axisymmetric, incompressible isothermal, and laminar. The viscosity of the two phases and their relative interfacial tension is assumed to be constant throughout the flow domain. The equations governing this flow are

$$\nabla \cdot \mathbf{V} = 0 \quad (2)$$

$$\rho \frac{\partial \mathbf{V}}{\partial t} + \rho \nabla \cdot (\mathbf{V}\mathbf{V}) = -\nabla p + \nabla \cdot \mu[(\nabla \mathbf{V}) + (\nabla \mathbf{V})^T] + \rho \mathbf{g} + \sigma \kappa \nabla F \quad (3)$$

The last term in Eq. (3) is the surface tension acting on the interface that is treated as a body force [22]. The liquid physical properties viz., density and viscosity of the two fluids at the interface are estimated by a weighted-averaged method

$$\rho = F\rho_2 + (1-F)\rho_1; \quad \mu = F\mu_2 + (1-F)\mu_1 \quad (4)$$

2.3 Boundary Conditions. The boundary conditions imposed on the velocity field in polar coordinate system (r, z) are as follows:

At the inlet ($z=0$), the injected phase and the continuous phase flows are considered as the fully developed Poiseuille flows

$$V_1(r, 0, t) = 2 \frac{Q_1}{\pi R_i^2} \left[1 - \left(\frac{r}{R_i} \right)^2 \right] \quad 0 < r < R_i \quad (5)$$

$$V_2(r,0,t) = 2 \frac{Q_2 \left[1 / \left(1 + (R_o/R_2)^2 - \frac{1 - (R_o/R_2)^2}{\ln(R_2/R_o)} \right) \right]}{\pi(R_2^2 - R_o^2)} \left[1 - \left(\frac{r}{R_2} \right)^2 + \frac{1 - (R_o/R_2)^2}{\ln(R_2/R_o)} \ln \left(\frac{r}{R_2} \right) \right] \quad R_0 < r < R_2 \quad (6)$$

where V_1 and V_2 are the axial velocities of injected and continuous phases, respectively.

No slip and no penetration conditions are imposed at the inner and outer walls of the nozzle and at the surface of the tube. At the outlet ($z=L$), the pressure is maintained constant.

2.4 Dimensionless Numbers. The lengths and velocities are measured in units of tube radius R_2 and average velocity of outer fluid, \bar{V}_2 . From a scaling analysis, it can be determined that the primary dimensionless numbers that govern the flow physics are the individual phase Reynolds numbers (Re); the capillary number (Ca), which measures the influence of viscous forces relative to the surface tension forces, the Bond number which evaluates the influence of gravitational forces to the surface tension forces, the velocity ratio γ , and the viscosity ratio η .

2.5 Numerical Scheme. The momentum equation is discretized with the "QUICK" scheme. The fluxes are calculated based on weighted average of second-order upwind and central interpolation of the variable. First-order implicit unsteady solver is employed to solve Eqs. (2)–(4) along with the appropriate boundary conditions, including (5) and (6) in a segregated solver. Since the flow in the present case is dominated by body forces rather than pressure gradients, a body-forced weighted scheme with "pressure implicit with splitting of operators" (PISO) algorithm is used for pressure correction.

Implicit first-order numerical scheme is employed for time stepping. Simulations were initiated with very small time steps ($\sim 10^{-5}$ s) but time steps (as per FLUENTS recommendation) were increased gradually for later times with no resultant spurious numerical oscillations in the solution. FLUENT calculates the volume of fluid (VOF) sub-time step internally based on the mesh resolution and fluxes in the interface cells. VOF sub-time step determines the minimum time to move the outer fluid out of an interface cell. FLUENT recommends using a time step no more than 10–20 times larger than the VOF sub-time step for stable simulations. The solution was assumed to have reached a steady state when the root-mean-square (rms) error between the interface profiles for successive time steps was found to be $< 10^{-8}$.

The computational domain consisted of an injection nozzle of dimensionless inner radius, $R_i/R_2=0.098$ and dimensionless outer radius, $R_o/R_2=0.126$, where R_i is the nozzle inner radius, R_o is the outer nozzle radius, and R_2 is the tube radius. The dimensional parameters of computational domain, R_i , R_o , and R_2 , are chosen to match the experimental setup and data to make direct comparisons of the results of the numerical simulations and experimental measurements. Numerical simulations were performed at different computational domain lengths L_2/R_2 of 5.90, 7.87, and 15.74. It has been shown that $L_2/R_2=7.87$ is sufficient to reach the fully developed conditions inside the flow domain even for the highest Reynolds numbers considered in the problem. Similarly, the dimensionless nozzle length, L_1/R_2 was sufficiently long (equal to 0.15) to yield fully developed velocity conditions at the end of the nozzle.

The computational grid used in the present simulations comprised of two regions. The injected liquid phase region including the interface has a dimensionless mesh size of 0.0039, where as a dimensionless mesh size of 0.0078 was used away from the interface in the continuous liquid region. Grid independence was tested at various dimensionless mesh sizes starting from 0.00197 to 0.0078. It was observed that the interface and fully developed injected phase jet radii were identical for dimensionless mesh

sizes 0.00197 and 0.0039. The mesh size 0.0039 was considered adequate for the current numerical simulations. The range of velocity ratios γ used in the numerical simulations for the flow-accelerated regime (explained in Sec. 4) is 0.42–0.78 and for the flow decelerated regime (also explained in Sec. 4) is 1.7–2.8. The results of numerical simulations obtained at these values of velocity ratio are compared to the experimental results. The other dimensionless parameters viscosity ratio η , Bond number (Bo), and capillary number (Ca) are also matched with the flow conditions in the experiments. The domains of these parameters are expanded over several orders of magnitude in these numerical simulations to better understand their effects on the flow characteristics.

3 Self-Similar Solution

For perfect core annular flow (PCAF), a self-similar analytical solution exists for the description of the pressure and velocity fields. A theoretical model based on this fully developed cocurrent two phase flow predicts the velocity profiles of the two fluids 1 and 2 for the flow system shown in Fig. 1 as

$$V_1(r,z) = \frac{f - \rho_1 g}{4\mu_1} (R^2 - r^2) + \frac{f - \rho_2 g}{4\mu_2} (R_2^2 - R^2) - \frac{R^2(\rho_1 - \rho_2)g}{2\mu_2} \ln \left(\frac{R_2}{R} \right), \quad 0 \leq r \leq R \quad (8)$$

$$V_2(r,z) = \frac{f - \rho_2 g}{4\mu_2} (R_2^2 - r^2) + \frac{R^2(\rho_1 - \rho_2)g}{2\mu_2} \ln \left(\frac{r}{R_2} \right), \quad R \leq r \leq R_2 \quad (9)$$

where f is the axial pressure gradient in each phase and is assumed to be equal in both phases. f is calculated from each phase of the fluid using volumetric flow rate expressions and set equal. The resulting equation for jet radius in terms of flow rate ratio λ , viscosity ratio, Bond number, and capillary number is presented below.

$$\frac{\pi \text{Bo}}{\text{Ca}} \left(\frac{b^3(1-b)}{4\eta} + b^2(1-b)^2 \left[\frac{1}{2} + \frac{\ln(b)}{4} - \frac{1}{8\eta} \right] \right) + \frac{b^2}{\eta} + 2b(1-b) - \lambda(1-b)^2 = 0 \quad (10)$$

The above nonlinear equation is numerically solved to obtain solutions of b (\sim fully developed jet radius) using a bisection algorithm for a given set of nondimensional parameters viz., Bo, Ca, λ , and η . This analysis is referred to as fully developed (FD) theory or self-similar solution. Equation (10) predicted one to three solutions may exist for injected jet radius for a range of Bond number (Bo), capillary number (Ca), flow ratio λ , and viscosity ratio η . The injected jet radius solutions are plotted in terms of liquid phases flow ratio and observed to follow a three-branched solution. The details of the three-branched solutions are not presented here because the parameters considered in this work resulted in a single solution.

4 Results and Discussion

Injected phase and continuous phase liquids are being introduced through the nozzle and annulus portion of the tube, respectively, at different average velocities. Since the velocities are not equal immediately downstream of the nozzle, a nonequilibrium condition between the liquid phases causes momentum exchange between them. If the injected phase velocity during this nonequilibrium stage is higher relative to the continuous phase velocity, then the injected liquid phase will lose a part of its momentum to the continuous liquid phase to reach an equilibrium stage. During this process, the injected liquid phase will decelerate and its diameter will increase. Otherwise, the injected phase will accelerate

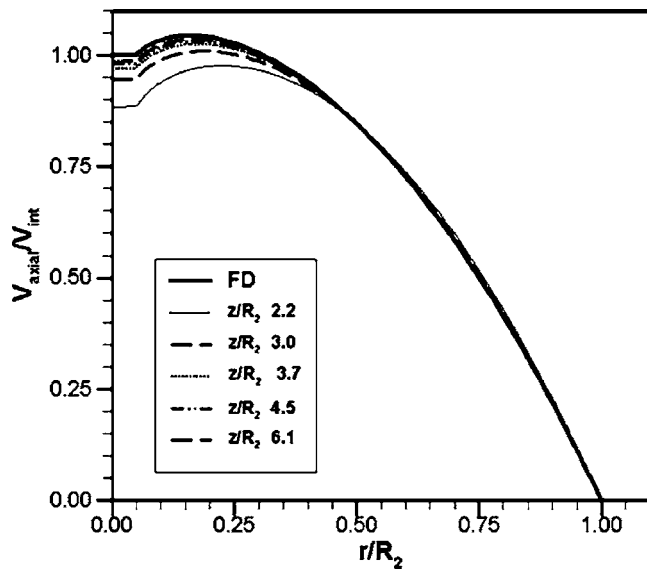


Fig. 2 Steady-state dimensionless axial velocity profile for different values of γ at $\eta=21$, $Re_1=0.3$, $Re_2=13$, and $Bo/Ca=91$

and its diameter will decrease. Once the fully developed flow is reached, the injected fluid jet reaches the asymptotic fully developed jet radius. It was observed that when the ratio of the inner and outer liquid average velocities in a cocurrent flow, called slip ratio, is less than unity, then the injected liquid jet radius decreases from the injected port radius and is referred to as “flow-accelerated regime” (FAR). If slip ratio is greater than unity, the injected liquid jet radius is found to increase from the nozzle radius, herein referred to as “flow-decelerated regime” (FDR). The above definition of slip ratio is valid for large viscosity ratios and Bond numbers ($\eta > 10$ and $Bo > 15$). Therefore, it was observed that the injected liquid radius may either increase or decrease based on the inlet conditions.

Fully developed state of the flow was identified by the axial invariance of the velocity profiles. The axial and radial velocity profiles of FAR case at different dimensionless axial distances are shown in Figs. 2 and 3. The axial location where the two fluids begin to exchange momentum is treated as zero axial position.

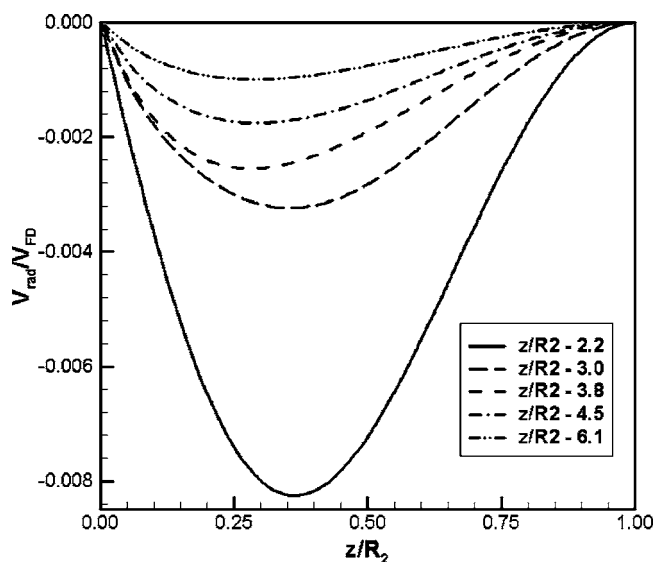


Fig. 3 Steady-state dimensionless radial velocity profile for different values of γ at $\eta=21$, $Re_1=0.3$, $Re_2=13$, and $Bo/Ca=91$

Table 1 Properties of fluids

Fluid Properties	PEG solution	Canola oil
ρ , Density (kg/m^3)	1070	900
μ , Viscosity (Pa s) @ 21 °C	1.086	0.0515
σ , Interfacial surface Tension of PEG and canola oil (N/m)	0.0177	

Downstream of the nozzle, the two fluids exchange momentum and radial velocity tends to zero while axial velocity reaches a maximum and constant value as the distance from the nozzle increases. Development length, the axial length where fully developed flow conditions (reaching constant and maximum axial velocity) are obtained, is measured from the zero axial position. In Fig. 2, axial velocity profiles are plotted in terms of dimensionless axial velocity (the ratio of the axial velocity and the theoretical fully developed centerline axial velocity) at various axial locations. Figure 3 presents radial velocity profiles in terms of dimensionless radial velocity (the ratio of the radial velocity and the theoretical fully developed centerline axial velocity) at various axial locations. With the mesh configuration (dimensionless mesh size=0.0039) used in the present work, discontinuities are observed in the radial velocity profiles at the liquid-liquid interface region when viscosity ratio is high, $\eta=21$. As the mesh is further refined to 0.00049 in the interfacial region, discontinuities in the radial velocity profiles across the interface region disappeared. Although, the accuracy of radial velocity is sensitive to the mesh size used in the simulations, the effect of very fine mesh on interface location and axial velocity profiles was found to be negligible. The interface position with the very fine mesh in the interfacial region change the values of competed velocities $< 1\%$ when compared to the result obtained using the coarse mesh results. Hence, the radial velocity profiles shown in Fig. 3 are obtained with the very fine mesh configuration (dimensionless mesh size equal to 0.00049) in the interfacial region. Since the computational time with very fine mesh is much larger, numerical simulations for other parameter cases were carried out with the coarse mesh configuration of 0.0039 in the interfacial region. It can be seen from Figs. 2 and 3 that approximately at an axial location z/R_2 of 3.8 the flow has reached fully developed conditions, i.e., the radial velocity is vanished and the axial velocity has become independent of z . Similarly, fully developed conditions were reached for all other cases approximately at an axial location z/R_2 of 3.8.

The fully developed jet radius predicted by numerical simulations was compared to the results of Kettering [9]’s experiments in which poly ethylene glycol (PEG) was injected through a nozzle into flowing Canola oil. The properties of fluids used in the experiments are shown in Table 1. The experiments were recorded with a video camera (Sony DCR-TRV250, Digital 8) at various flow rates. Image-analysis software is used to extract the information of the fully developed radius and the interfacial profiles from video frames. More detailed descriptions of the experimental setup and experimental methods are given in Kettering [9]. Numerical simulation results and fully developed theory results were compared to the experimental results, as shown in Table 2 for some representative values of γ and Ca at $\eta=21$ and $Bo=15$. It was observed that the deviation in the fully developed radius between Kettering [9] measurements and our predictions by numerical simulation is typically $< 8\%$. The results predicted by the similarity solution also agree well with the experimental results within $\sim 7\%$. A comparison of the PEG/canola oil interface measured by experiments and predicted by numerical simulation is shown in Fig. 4. The interface profile predicted by numerical simulations agrees well with the results obtained by the experimental measurements except near the nozzle outlet where the injected fluid jet

Table 2 Comparison of numerical simulation and similarity theory results to experiments at $\eta=21$, $Bo=15$

γ	Ca	Experimental R/R_2	FLUENT R/R_2	FD theory R/R_2
0.42	0.17	0.048	0.048	0.048
0.89	0.14	0.073	0.078	0.076
0.90	0.12	0.080	0.082	0.081
1.70	0.17	0.106	0.109	0.113
1.77	0.23	0.109	0.108	0.106
2.82	0.23	0.151	0.142	0.144

diameter increases rapidly. This increase could result from the fact that the contact angle between the inner fluid and the nozzle inner wall in numerical simulations was taken to be 90 deg (default value) even though its value is <90 deg as observed in the experiments. The actual value of the contact angle is not used in the numerical simulations since it is not easily determinable from the measurements. As a result, the inner fluid is not pinned properly at the three-phase-contact point (the point where nozzle inner wall, the inner fluid, outer fluid will meet) in the numerical simulations, resulting in spurious fluid swell immediately downstream of the nozzle. It can be seen from Fig. 4 that the numerical solution is also able to accurately capture the interface evolution in the developing region.

4.1 Effect of Velocity Ratio on Interface and Fully Developed Jet Radius. For a given viscosity ratio, Bond and capillary numbers, and continuous-phase fluid velocity, the effect of velocity ratio on the characteristics of the flow is the same as the effect of Re_1 . Steady-state interface profiles for the FAR case (for $\eta=21$, $Re_2=13$, $Bo/Ca=91$) and for the FDR case (for $\eta=21$, $Re_2=18$, $Bo/Ca=66$) for various values of γ , obtained using numerical simulations are shown in Fig. 5. The fully developed radii of injected fluid jet are compared with fully developed or self-similar solution results and experimentally measured values in Fig. 6. It is observed that the cases that have slip ratio less than unity are "FAR" flows where as slip ratio above unity yield FDR flows. Since the density of liquid is constant, an increase in velocity ratio, i.e., an increase in the injected fluid velocity must

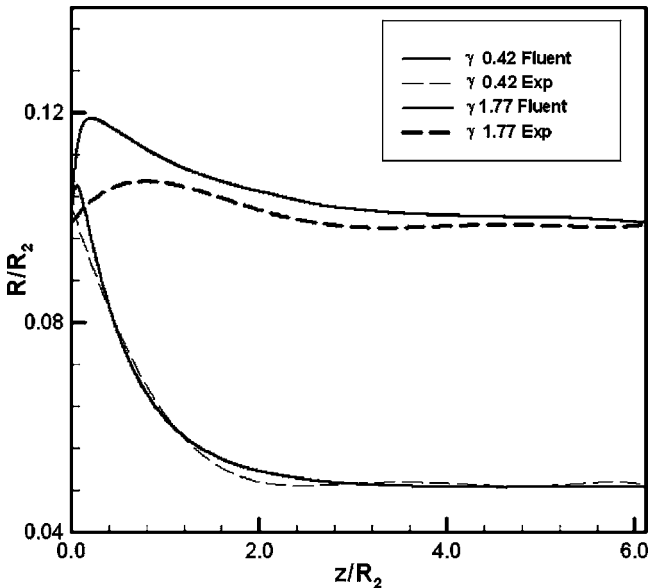


Fig. 4 Comparison of interfacial profiles predicted by numerical simulations to experimental measurements (for cases: $\gamma=0.42$, $Re_1=0.3$, $Re_2=13$, $\eta=21$, $Bo/Ca=91$; and $\gamma=1.77$, $Re_1=1.8$, $Re_2=18$, $Bo/Ca=66$)

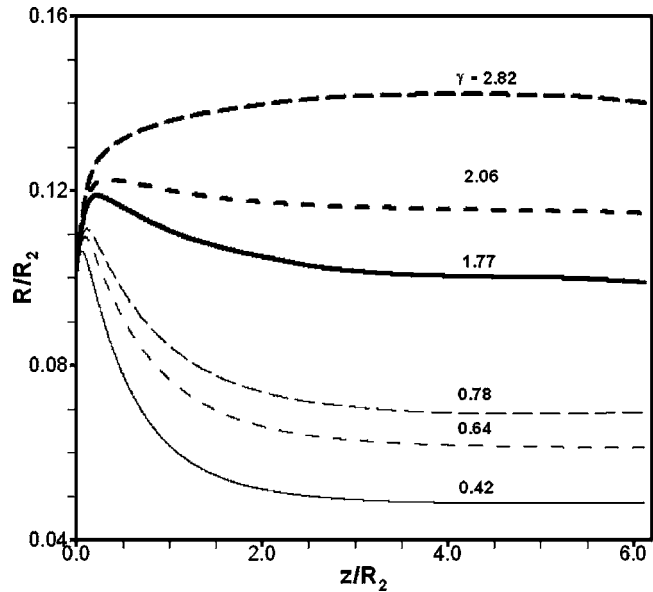


Fig. 5 Steady-state dimensionless interface profile for different values of γ for FAR case parameters ($\gamma < 1$): $\eta=21$, $Re_2=13$, $Bo/Ca=91$; and FDR case parameters ($\gamma > 1$): $\eta=21$, $Re_2=18$, $Bo/Ca=66$

increase the fully developed jet radius since the mass flow rate of each phase has to be constant. It is clearly seen from Figs. 5 and 6, that the fully developed jet radius increases as the velocity ratio is increased. It is also observed from simulations that the development length increases slightly with increase in velocity ratio (see Fig. 6). The reason for change in development length being very small is because both the magnitude and change of injected phase Reynolds number with velocity ratio are small compared to the fixed continuous phase fluid's Reynolds number.

4.2 Effect of Viscosity Ratio on Fully Developed Jet Radius. Numerical simulations were performed for the FAR case (for $\gamma=0.42$, $Re_2=13$, $Bo/Ca=91$) and for the FDR case (for $\gamma=1.77$, $Re_2=18$, $Bo/Ca=66$) at different viscosity ratios of 0.1, 1,

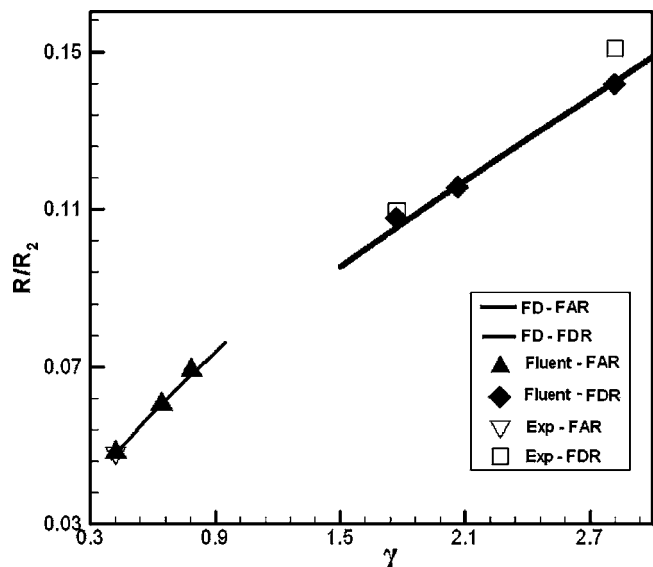


Fig. 6 Fully developed dimensionless radius as a function of γ for FAR case parameters: $\eta=21$, $Re_2=13$, $Bo/Ca=91$; and FDR case parameters: $\eta=21$, $Re_2=18$, $Bo/Ca=66$

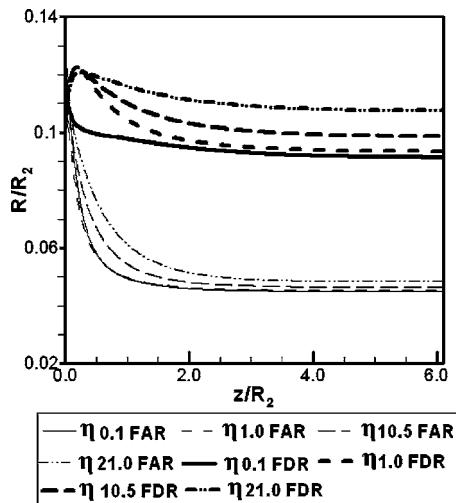


Fig. 7 Steady-state dimensionless interface profile for various values of η for FAR case parameters: $\gamma=0.42$, $Re_2=13$, $Bo/Ca=91$; and FDR case parameters: $\gamma=1.77$, $Re_2=18$, $Bo/Ca=66$

10, and 21. In these simulations, the viscosity ratio is decreased from 21 to 0.1 by decreasing the injected phase liquid viscosity. The results of these simulations are shown in Fig. 7 in terms of the steady-state interface profiles. Figure 8 presents the fully developed jet radii for similar conditions. As the viscosity ratio decreases, i.e., the decrease of injected phase liquid viscosity, the fully developed jet radius is decreased due to the decreased viscous shear resistance between the liquids. For the FDR flow regime, if viscosity ratio decreases below 10.5, the injected phase liquid jet will be accelerated causing the value of slip ratio tends to go below unity, resulting in the FAR flow regime. The same trend can also be observed from the results predicted by the self-similar solution. Fully developed jet radius results obtained with numerical simulations are in very good agreement with the results predicted by similarity solution. Moreover, the development length is hardly influenced by the variation of viscosity ratio. The development length is mostly determined by the highest Re in this

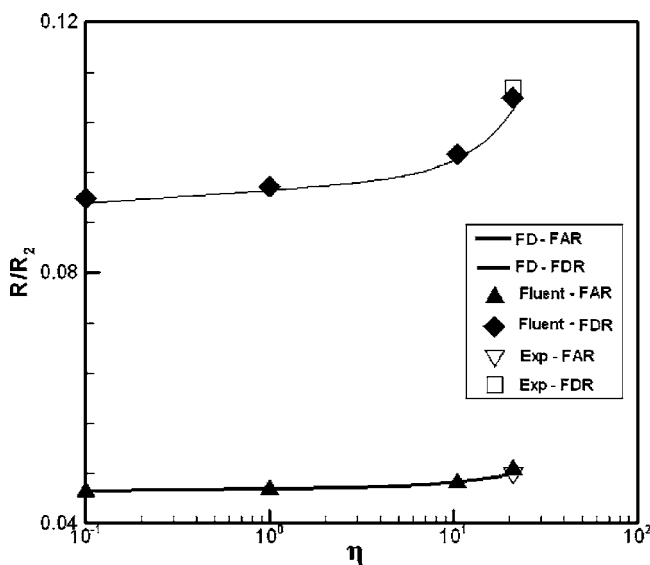


Fig. 8 Fully developed dimensionless radius as a function of η for FAR case parameters: $\gamma=0.42$, $Re_2=13$, $Bo/Ca=91$; and FDR case parameters: $\gamma=1.77$, $Re_2=18$, $Bo/Ca=66$

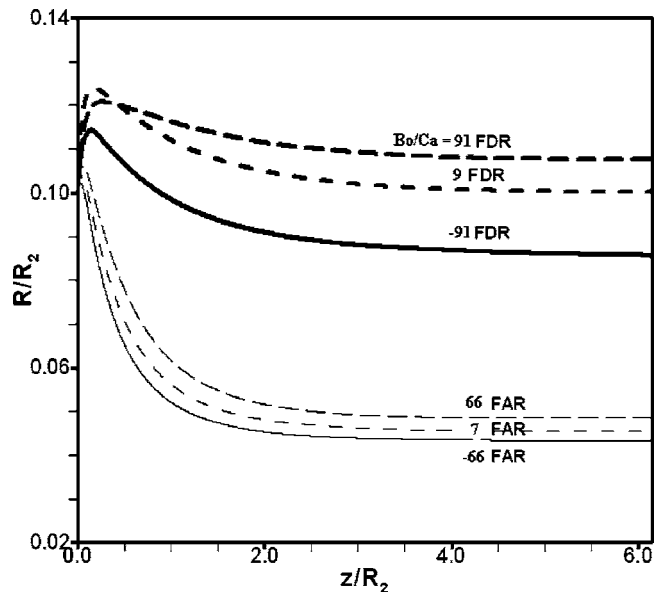


Fig. 9 Steady-state dimensionless interface as a function of Bo/Ca for FAR case parameters: $\gamma=0.42$, $Re_1=0.3$, $Re_2=13$, $\eta=21$; and FDR case parameters: $\gamma=1.77$, $Re_1=1.8$, $Re_2=18$, $\eta=21$

flow and as Re_2 is fixed while the viscosity ratio is varied, the development length changes only slightly as the viscosity ratio changes.

4.3 Effect of Ratio of Bond Number and Capillary Number on Fully Developed Interface. Numerical simulations were also performed for Bo/Ca ranging from -91 to 91 for FAR and from -66 to 66 for FDR cases. The flow parameters are fixed as $\gamma=0.42$, $\eta=21$, $Re_2=13$ for the FAR case and $\gamma=1.77$, $\eta=21$, $Re_2=18$ for the FDR case. Bo/Ca variation is performed by changing the gravity value from -9.8 to 9.8 . As Bo/Ca increases, the injected phase liquid jet will be decelerated due to additional gravitational buoyant deceleration and, correspondingly, the fully developed jet radius will increase. Simulation results of steady-state interface profile and fully developed radii of such cases are shown in Figs. 9 and 10. For the FDR flow regime, if $Bo/Ca < 66$, the injected liquid jet will be accelerated causing the value of slip ratio to be decreased below unity, resulting in the FAR flow regime. Both the numerical simulations and similarity theory predict that the fully developed jet radius will increase as Bo/Ca increases while the development length remains nearly unchanged, as shown in Fig. 10.

5 Conclusions

Interfacial dynamics of axisymmetric liquid-liquid flows are studied here using numerical simulation and self-similar theory. The results predicted by both numerical simulations and self-similar solution agree well with the experimental results obtained by Kettering [9]. The maximum deviations in the fully developed jet radius predicted by numerical simulation and self-similar solution compared to experimentally measured values are 8% and 7%, respectively. Our conclusions are as follows:

1. The fully developed jet radius of the injected fluid increases with increasing inlet average velocity ratio.
2. For large viscosity ratio, the injected jet radius is increased when the inlet average velocity ratio is greater than unity and decreases when the ratio is less than unity.
3. Increases in Bo/Ca and viscosity ratio increase the fully developed jet radius.
4. The increase in development length with velocity and vis-

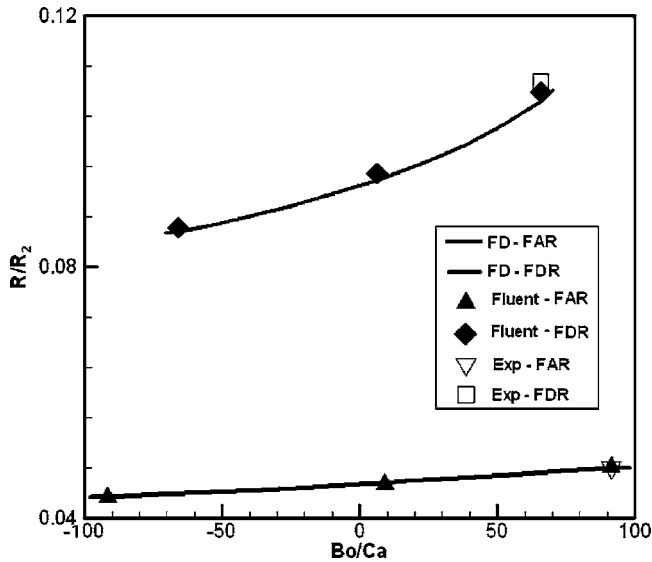


Fig. 10 Fully developed dimensionless radius as a function of Bo/Ca for FAR case parameters: $\gamma=0.42$, $Re_1=0.3$, $Re_2=13$, $\eta=21$; and FDR case parameters: $\gamma=1.77$, $Re_1=1.8$, $Re_2=18$, $\eta=21$

cosity ratios is very small because the Reynolds number of injected phase fluid is small compared to the continuous phase fluid's Reynolds number.

- The development length is primarily influenced by the largest of the individual phase Reynolds numbers. For a fixed set of Reynolds numbers, the development length remains nearly the same as Bo/Ca is varied.

Nomenclature

- b = ratio of squares of fully developed radius and tube radius, R^2/R_2^2
- Bo = Bond number, $[(\rho_2 - \rho_1)gR_2^2]/\sigma$
- Ca = capillary number, $\mu_2 \bar{V}_2 / \sigma$
- f = pressure gradient in axial direction, Pa/m
- F = volume fraction function
- g = acceleration due to gravity, ms^{-2}
- h = order of grid size, m
- L_1 = length of nozzle, m
- L_2 = length of tube, m
- p = pressure, Pa
- Q_i = flow rate of fluid phase i , m^3/s ; $i=1, 2$ for injected and continuous phases, respectively
- r = radial coordinate direction
- R = fully developed radius of the injected fluid, m
- R_2 = tube radius, m
- R_i = nozzle inner radius, m
- R_o = nozzle outer radius, m
- Re_i = Reynolds number, $\rho_i \bar{V}_i R_2 / \mu_i$, $i=1, 2$ for injected and continuous phases, respectively
- t = time, s
- V_{axial} = axial velocity, m/s
- \bar{V}_1 = average velocity of injected phase, m/s, $Q_1 / \pi R_i^2$
- \bar{V}_2 = average velocity of continuous phase, m/s, $Q_2 / \pi R_2^2$ (here, $R_o/R_2 \ll 1$)
- V_i = velocity of fluid phase i , m/s; $i=1, 2$ for injected and continuous phases, respectively
- V_{FD} = theoretical fully developed velocity, m/s

- V_{rad} = radial velocity, m/s
- V = velocity vector
- z = axial coordinate direction
- γ = ratio of injected and continuous phase inlet average velocities, \bar{V}_1 / \bar{V}_2
- η = ratio of injected phase to continuous phase fluid viscosities, μ_1 / μ_2
- λ = ratio of injected and continuous phase fluid flow rates, Q_1 / Q_2
- κ = curvature, m^{-1}
- μ = weighted average viscosity in the interface region, Pa s
- μ_i = viscosity of fluid phase i , Pa s, $i=1, 2$ for injected and continuous phases respectively
- ρ_i = density of fluid phase i , kg/m^3 ; $i=1, 2$ for injected and continuous phases respectively
- ρ = weighted average density in the interface region; kg/m^3
- σ = surface tension, N/m

References

- Meister, B. J., 1966, "The Formation and Stability of Jets in Immiscible Liquid Systems," Ph.D. dissertation, Cornell University, Ithaca.
- Treybal, R. E., 1963, *Liquid Extraction*, 2nd ed. McGraw-Hill, New York.
- Jeffreys, G., 1987, "Review of the Design of Liquid Extraction Equipment," *Chem. Ind.*, **6**, pp. 181–185.
- Joseph, D. D., and Renardy, Y., 1993, *Fundamentals of Two-Fluid Dynamics*, Springer-Verlag, Berlin.
- Mavridis, H., Hrymark, A. N., and Vlachopoulos, J., 1987, "Finite-Element Simulation of Stratified Multiphase Flows," *AIChE J.*, **33**, pp. 410–422.
- Zhang, X., 1999, "Dynamics of Drop Formation in Viscous Flows," *Chem. Eng. Sci.*, **54**, pp. 1759–1774.
- Cramer, C., Beruter, B., Fischer, P., and Windhab, E. J., 2002, "Liquid Jet Stability in a Laminar Flow Field," *Chem. Eng. Technol.*, **25**(5), pp. 499–506.
- Fischer, P., Maruyama, K., and Windhab, E. J., 2004, "The Influence of the External Imprinted Flow on Capillary Instability Driven Breakup Jet," *Chem. Eng. Technol.*, **27**(11), pp. 1161–1171.
- Kettering, C., 2005, "Fluid Dynamics of Two Immiscible Liquids in a Circular Geometry," Master's thesis, Lehigh University.
- Rayleigh, L., 1878, "On the Stability of Jets," *Proc. London Math. Soc.*, **10**, pp. 4–18.
- Tyler, E., 1933, "Instability of Liquid Jets," *Philos. Mag.*, **16**, pp. 504–518.
- Tomotika, S., 1935, "On the Instability of a Cylindrical Thread of a Viscous Liquid Surrounded by Another Viscous Fluid," *Proc. R. Soc. London, Ser. A*, **150**, pp. 322–337.
- Bogy, D. B., 1979, "Drop Formation in a Circular Liquid Jet," *Annu. Rev. Fluid Mech.*, **11**, pp. 207–228.
- Mansour, N. N., and Lundgren, T. S., 1990, "Satellite Formation in Capillary Jet Break Up," *Phys. Fluids A*, **2**, pp. 1141–1144.
- Vasallo, P., and Ashgriz, N., 1991, "Satellite Formation and Merging in Liquid Jet Break Up," *Proc. Math. Phys. Sci.*, **433**, pp. 269–286.
- Orme, M., Willis, K., and Nguyen, T. V., 1993, "Droplet Patterns From Capillary Stream Breakup," *Phys. Fluids A*, **5**, pp. 80–90.
- Meister, B. J., and Sheele, G. F., 1969, "Drop Formation From Cylindrical Jets in Immiscible Liquid Systems," *AIChE J.*, **15**, pp. 700–706.
- Richards, J. R., Beris, A. N., and Lenhoff, A. M., 1993, "Steady Laminar Flow of Liquid-Liquid Jets at High Reynolds Numbers," *Phys. Fluids A*, **5**, pp. 1703–1717.
- Richards, J. R., 1994, "Fluid Mechanics of Liquid-Liquid System," Ph.D. dissertation, University of Delaware.
- Richards, J. R., Beris, A. N., and Lenhoff, A. M., 1995, "Drop Formation in Liquid-Liquid Systems Before and After Jetting," *Phys. Fluids*, **7**, pp. 2617–2630.
- Hirt, C. W., and Nichols, B. D., 1981, "Volume of Fluid (VOF) Method for the Dynamics of Free Boundaries," *J. Comput. Phys.*, **39**, pp. 201–225.
- Brackbill, J. U., Kothe, D. B., and Zemach, C., 1992, "A Continuum Method for Modeling Surface Tension," *J. Comput. Phys.*, **100**, pp. 335–354.
- Zhang, D., and Stone, H. A., 1997, "Drop Formation in Viscous Flows at a Vertical Capillary Tube," *Phys. Fluids*, **9**, pp. 2234–2242.
- FLUENT® Inc., 2003, Lebanon, NH.
- Killion, J. D., and Garimella, S., 2004, "Simulation of Pendant Droplets and Falling Films in Horizontal Tube Absorbers," *ASME J. Heat Transfer*, **126**, pp. 1003–1013.
- Taha, T., and Cui, Z. F., 2004, "Hydrodynamics of Slug Flow Inside Capillaries," *Chem. Eng. Sci.*, **59**, pp. 1181–1190.
- Valencia, A., Paredes, R., Rosales, M., Godoy, E., and Ortega, J., 2004, "Fluid Dynamics of Submerged Gas Injection Into Liquid in a Model of Copper Converter," *Int. Commun. Heat Mass Transfer*, **31**(1), pp. 21–30.

A Numerical Tool for the Design/Analysis of Dual-Cavitating Propellers

Y. L. Young

Department of Civil and Environmental
Engineering,
Princeton University,
Princeton, NJ 08544
e-mail: yyoung@princeton.edu

Y. T. Shen

Carderock Division,
Naval Surface Warfare Center,
Bethesda, MD 20817
e-mail: young.shen@navy.mil

The motivation of this work is to develop a numerical tool to explore a new propeller design with dual-cavitating characteristics, i.e., one that is capable of operating efficiently at low speeds in subcavitating (fully wetted) mode and at high speeds in the supercavitating mode. To compute the hydrodynamic performance, a three-dimensional (3D) potential-based boundary element method (BEM) is presented. The BEM is able to predict complex cavitation patterns and blade forces on fully submerged and partially submerged propellers in subcavitating, partially cavitating, fully cavitating, and ventilated conditions. To study the hydroelastic characteristic of potential designs, the 3D BEM is coupled with a 3D finite element method (FEM) to compute the blade stresses, deflections, and dynamic characteristics. An overview of the formulation for both the BEM and FEM is presented. The numerical predictions are compared to experimental measurements for the well-known Newton Rader (NR) three-bladed propeller series with varying pitch and blade area ratios. Comparison of the performance of the Newton Rader blade section to conventional blade sections is presented. [DOI: 10.1115/1.2734224]

Keywords: dual-cavitating propeller, multispeed design, cavitation, Newton-Rader

1 Introduction

Conventional subcavitating propellers are designed for fully submerged operations in a regime absent of cavitation for good performance. With recent advances in computational capability and improvements in propeller design procedures, conventional propellers have been successfully designed to operate up to a speed of 36 knots on a small patrol craft with minor thrust breakdown due to blade cavitation [1]. In general, conventional propellers start to experience severe blade surface cavitation at speeds at or above 32–35 knots [2,3]. Excess cavitation causes noise, erosion, and performance decay due to thrust breakdown.

One method to overcome the blade surface cavitation erosion problem and serious performance decay for high-speed application is the use of fully submerged supercavitating/superventilated propellers (SCPs) [4,5] or partially submerged surface-piercing propellers (SPPs) [6–10], where the cavities terminate behind the blade trailing edge. Typically, the leading edge of this type of high-performance propeller is sharp and thin. Experiments show good efficiency at the high design speeds but with noticeable degraded performance at low speeds in off-design conditions due to large form drag [11]. A large prime mover is often needed for supercavitating or ventilated propellers to overcome the hump drag. Moreover, a high-speed navy ship is often required to operate substantial amount of its life-cycle time in speeds below 25 knots. Thus, the propeller for high-speed ship application is likely to require a multispeed design to achieve high-speed operation and adequate range of operation for mission requirement.

Supercavitating propellers have been extensively investigated for high-speed applications in the 1970s and 1980s [4,5,12]. Tulin's two-term camber sections were typically used in these propellers [12,13]. For a single-speed design, Tulin's two-term camber can be selected to match the design lift coefficient to achieve good lift to drag ratio and propeller efficiency. For multispeed

design, low cambers are required to match both lift coefficients at high speeds and low speeds if Tulin's two term sections are used. Limited calculations show that sections with S-shaped camber with unloaded leading edge and heavy loaded trailing edge produce much favorable hydrodynamic performance at both high and low speeds.

2 Dual-Cavitating Propellers

The motivation of this work is to explore a new propeller design with dual-cavitating characteristics that is capable of operating efficiently at low speeds and midspeeds with blade surfaces in subcavitating mode, and at highspeeds with blade surfaces in the supercavitating mode.

The proposed design, shown in Fig. 1, has a rounded leading edge and tapered trailing edge to streamline the blade section to produce efficient, low drag, and high lift in low-speed to midspeed ranges. The lower surface is shaped to produce the required lift and minimum viscous drag during high-speed operations. The design concept is based on a new hydrofoil section termed "dual-cavitating hydrofoil," developed by Shen [14], which was successfully evaluated experimentally with a dual-cavitating "TAP 2 strut/foil system" [15], shown in Fig. 2. The lift-to-drag ratio of the strut/foil system was 13 at 35 knots (takeoff, depth/chord = 3.0), 18 at 45 knots (cruise, depth/chord = 1.0), and 7.6 at 80 knots (depth/chord = 3.0).

The goal of this work is to extend the dual-cavitating hydrofoil concept for the design of dual-cavitating propellers. The immediate objective is to develop and validate a numerical tool to predict the hydrodynamic and hydroelastic response of propellers in subcavitating, partially cavitating, and supercavitating conditions. Later, the numerical tool will be used for the systematic design/optimization of dual-cavitating propellers.

3 Hydrodynamic Analysis

To model the hydrodynamics of dual cavitating propellers, a three-dimensional (3D) potential-based boundary element method (BEM), PROPCAV, is applied. The method was first developed for the analysis of fully wetted marine propellers in steady flow by [16,17] and unsteady flow by [18,19]. It was then extended for the

Contributed by the Fluids Engineering Division of ASME for publication in the JOURNAL OF FLUIDS ENGINEERING. Manuscript received June 7, 2006; final manuscript received November 30, 2006. Review conducted by Akira Goto. Paper presented at the 11th International Symposium on Transport Phenomena and Dynamics of Rotating Machinery, ISROMAC-11, 2006.

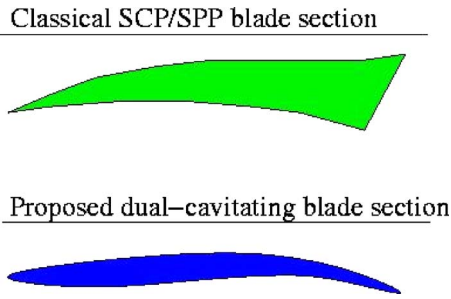


Fig. 1 Comparison of classical SCP/SPP blade section and the proposed dual-cavitating blade section

analysis of flow around two-dimensional (2D) partially cavitating and supercavitating hydrofoils [20], 3D partially cavitating hydrofoils [21], and 3D unsteady flow around cavitating propellers [22]. Later, the method was modified to search for midchord cavitation on either the back or the face of propeller blades [23]. Recently, the method has been further extended to predict simultaneous face and back cavitation on conventional fully submerged propellers [24], supercavitating propellers [25,26], surface-piercing propellers [25,27–29], and rudders [30] subjected to spatially varying inflow.

For a rigid propeller rotating at a constant angular velocity ω and subject to a general effective inflow wake \vec{q}_E , as shown in Fig. 3, the inflow velocity (\vec{q}_{in}) in rotating blade-fixed coordinates [$\vec{x} = (x, y, z)$] can be expressed as

$$\vec{q}_{in}(\vec{x}, t) = \vec{q}_E(x, r, \theta_B - \omega t) - \vec{\Omega} \cdot \vec{x} \quad (1)$$

where $r = \sqrt{y^2 + z^2}$, $\theta_B = \arctan(z/y)$, and $\vec{\Omega} = [-\omega, 0, 0]^T$. It should be noted that \vec{q}_E is defined in ship-fixed coordinates (x_s, y_s, z_s) and is assumed to be the *effective wake*, i.e., it includes the interaction between the vorticity in the inflow and the propeller [31,32]. The resulting flow is assumed to be incompressible and inviscid. The problem is solved with respect to the rotating blade-fixed coordinates system.

The total velocity \vec{q} can be expressed in terms of \vec{q}_{in} and the perturbation potential ϕ

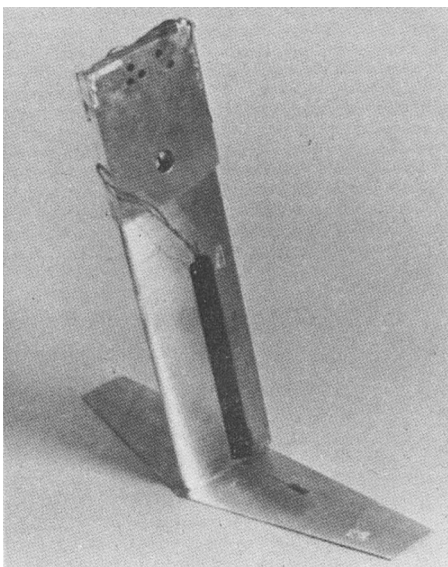


Fig. 2 TAP 2 strut/foil system shown in [15]

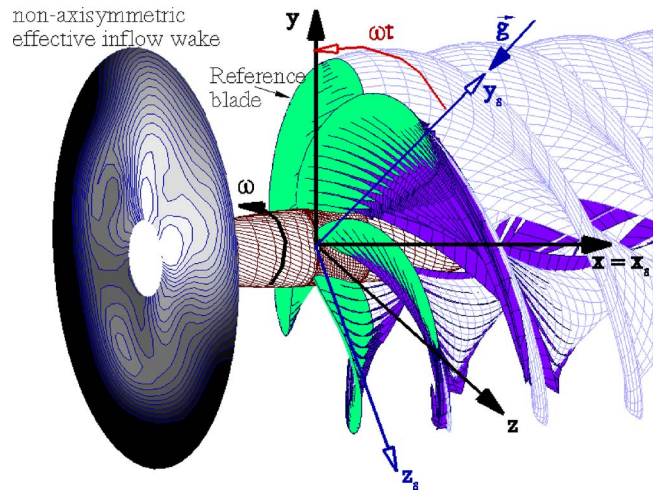


Fig. 3 Propeller-fixed (x, y, z) and ship-fixed (x_s, y_s, z_s) coordinate systems (from [26])

$$\vec{q}(\vec{x}, t) = \vec{q}_{in}(\vec{x}, t) + \vec{\nabla} \phi(\vec{x}, t) \quad (2)$$

The perturbation potential ϕ satisfies the Laplace's equation in the fluid domain (i.e., $\nabla^2 \phi = 0$) and, thus, can be determined via Green's third identity

$$2\pi\phi_p(t) = \int_{S_{BD}(t)} \left[\phi_q(t) \frac{\partial G(p; q)}{\partial n_q(t)} - G(p; q) \frac{\partial \phi_q(t)}{\partial n_q(t)} \right] dS + \int_{S_w(t)} \Delta \phi_w(r_q, \theta_q, t) \frac{\partial G(p; q)}{\partial n_q(t)} dS \quad (3)$$

where $S_{BD} = S_B(t) \cup S_C(t) \cup S_H(t)$. S_B , S_C , and S_H represent the wetted blade, cavitating, and hub surfaces. The subscript q corresponds to the variable point in the integration. $G(p; q) = 1/R(p; q)$ is the Green's function with $R(p; q)$ being the distance between points p and q . \vec{n}_q is the unit vector normal to the integration surface, pointing into the fluid domain. $\Delta \phi$ is the potential jump across the wake surface, $S_w(t)$.

3.1 Boundary Conditions. Kinematic Boundary Condition. The flow is tangent to the blade and cavity surfaces

$$\frac{\partial \phi}{\partial n} = -\vec{q}_{in}(\vec{x}, t) \cdot \vec{n} \quad (4)$$

Dynamic Boundary Condition. The pressure everywhere on the cavity surface is constant and equal to the prescribed pressure (p_c), i.e., $p_c = p_v$ (vapor pressure) for vapor-filled cavities, and $p_c = p_{atm}$ (atmospheric pressure) for ventilated cavities. It can be shown that this is equivalent to prescribing the known values of ϕ by integrating the following expression [22]:

$$\frac{\partial \phi}{\partial s} = -\vec{q}_{in} \cdot \vec{s} + V_v \cos \psi + \sin \psi \times \sqrt{n^2 D^2 \sigma_n + |\vec{q}_E|^2 + \omega^2 r^2 - 2gy_s - 2 \frac{\partial \phi}{\partial t} - V_v^2} \quad (5)$$

where $V_v \equiv \partial \phi / \partial v + \vec{q}_{in} \cdot \vec{v}$; \vec{s} and \vec{v} are the local unit vectors in the chordwise and spanwise directions, respectively, ψ is the angle between \vec{s} and \vec{v} . $\sigma_n \equiv (p_o - p_c) / (0.5 \rho n^2 D^2)$ is the cavitation number based on the propeller rotational frequency in revolutions per second (rps), n . ρ is the fluid density, and $r = \sqrt{y^2 + z^2}$ is the distance from the axis of rotation. p_o is the pressure far upstream on the shaft axis, g is the acceleration of gravity, and y_s is the vertical

ship fixed coordinate, shown in Fig. 3. $n=\omega/2\pi$ and D are the propeller rotational frequency and diameter, respectively.

Kutta Condition. The velocity at the blade trailing edge is finite.

Cavity Closure Condition. The cavity thickness at the end of partial or super cavities should equal zero.

3.2 Solution Algorithm. The unsteady cavity surface is determined in the framework of a moving mixed boundary value problem. For a given cavitation number, the extent and thickness of the cavity surface is determined in an iterative manner at each time step until all the boundary conditions are satisfied. The cavity detachment location is also determined iteratively by satisfying the Villat-Brillouin smooth detachment condition.

For cross sections with nonzero trailing-edge thickness, the method is able to predict the extent and thickness of the separated regions by assuming the base pressure (i.e., pressure behind the blade trailing edge) to be constant and equal to the prescribed cavity pressure.

For partially submerged surface-piercing propellers, the effect of the free surface is modeled using the “negative image” method, and the ventilated cavities are assumed to vent to the free surface. The detachments of the ventilated cavities are searched for iteratively using a modified smooth detachment condition.

Details of the formulation, implementation, and extensive numerical and experimental validation studies of the hydrodynamic model can be found in [22,24,26–30,33].

4 Hydroelastic Analysis

To study the hydroelastic characteristic of potential designs, the 3D BEM is coupled with a 3D finite element method (FEM) to compute the blade stresses, deflections, and dynamic characteristics. The hydroelastic coupling follows the linear-field decomposition scheme presented in [34]. The perturbation velocity potential is decomposed into two parts. One part corresponding to rigid blades rotating in non-axisymmetric wake and the other part corresponding to vibrating blades in uniform wake.

By applying linear decomposition of the perturbation potential, it can be shown that the total hydrodynamic pressure p can be decomposed into two parts: $p=p_r+p_v$, where p_r is the hydrodynamic pressure due to rigid blades rotating in non-axisymmetric wake, and p_v is the fluctuating pressure due to vibrating blades in a uniform wake.

At the fluid(BEM)-solid(FEM) interface, the velocity (\vec{q}) compatibility and the pressure (p) equilibrium conditions are applied: $\vec{q}_{BEM} \cdot \vec{n} = \vec{q}_{FEM} \cdot \vec{n}$ and $p_{BEM} = p_{FEM}$. The total hydrodynamic pressure from the BEM are expressed in terms of equivalent FEM nodal forces, which can be decomposed into two parts: $\{F_T(t)\} = \{F(t)\} + \{f(t)\}$. The first part, $\{F(t)\} = \int [N]^T \{p_r(t)\} dS$, represents the equivalent nodal force due to rigid blades rotating in nonuniform wake. $[N]$ is the displacement interpolation matrix. The second part, $\{f(t)\}$, represents the equivalent nodal force due to elastic blade deformations, which can be expressed in the form of added mass ($[M^h]$) and hydrodynamic damping ($[D^h]$) [35,36]:

$$\{f(t)\} = \int [N]^T \{p_v(t)\} dS = -[M^h]\{\ddot{u}(t)\} - [D^h]\{\dot{u}(t)\} \quad (6)$$

where $[N]$ is the displacement interpolation matrix and $\{\ddot{u}(t)\}$, $\{\dot{u}(t)\}$, and $\{u(t)\}$ are the nodal acceleration, velocity, and displacement vectors, respectively, of the solid surface.

The perturbation potential due to elastic blade deformations must satisfy the Laplace equation and, hence, can also be solved using a 3D potential-based BEM. It can be shown that the added mass and hydrodynamic damping matrices can be computed as follows [35,36]:

$$[M^h] = \rho \int [N]^T [C] [T] dS \quad \text{and} \quad [D^h] = \rho \int [N]^T [QD] [C] [T] dS \quad (7)$$

where $[C] = [A]^{-1}[B]$ and $[QD] = \vec{q} \cdot \vec{\nabla}$. $[A]$ and $[B]$ are the induced potential matrices due to unit strength dipoles and sources, respectively, and are taken directly from the rigid-blade BEM analysis. $[T]$ is the transformation matrix, which maps the vector of FEM nodal velocities, $\{\dot{u}\}$, to the vector of normal velocities at the centroid of the BEM panels.

The equilibrium equation of motion can be written as follows [35,36]:

$$([M] + [M^h(t)])\{\ddot{u}(t)\} + ([D] + [D^h(t)])\{\dot{u}(t)\} + [K]\{u(t)\} = \{F(t)\} + \{F_c\} \quad (8)$$

where $[M]$, $[D]$, and $[K]$ are the structural mass, damping, and stiffness matrices, respectively. $\{F_c\}$ denote the centrifugal and Coriolis force vector, which is necessary because the problem is solved with respect to the rotating blade-fixed coordinates.

The advantage of applying BEM to compute $[M^h]$ and $[D^h]$ is that it results in significant savings in computational time and effort since the influence coefficient matrix ($[C]$) can be taken directly from the rigid-blade BEM analysis.

It should be noted that $[C]$ is full and asymmetric. Thus, $[M^h]$ and $[D^h]$ will also be full and asymmetric. To reduce computational cost and storage requirement, an HRZ-like lumping technique is applied. Details of the lumping procedure are given in [35].

The commercial FEM package, ABAQUS Standard [37], is employed to solve the equilibrium equation of motion, Eq. (8). The Hilber-Hughes-Taylor implicit direct integration method in ABAQUS is applied to calculate the dynamic blade response. The rotational body force is applied as element-based loads in ABAQUS. Iterations are carried out between the BEM and FEM models to account for large blade deformations. In the FEM model, one-layer of quadratic 3D solid elements is used across the blade thickness. Quadratic elements are necessary to avoid hour-glass and shear-lock failures associated with first-order elements [35]. The nodes at the root of the blade are assumed to be fixed in the solid model. The lumped added mass and hydrodynamic

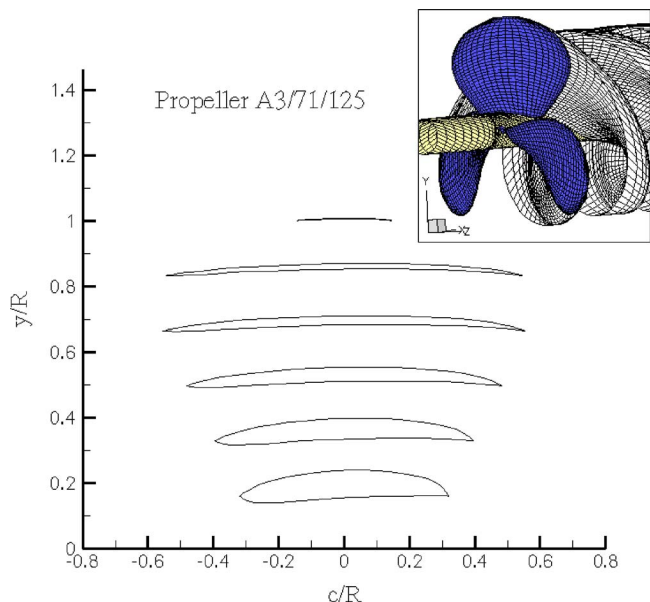


Fig. 4 Blade section and discretized geometry of NR propeller A3/71/125

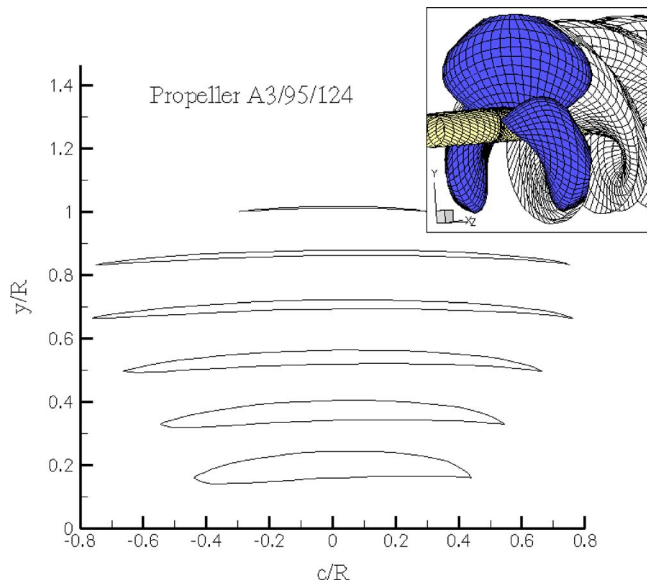


Fig. 5 Blade section and discretized geometry of NR propeller A3/95/124

damping matrices are superimposed on to the structural added mass and damping matrices via user-defined hydroelastic elements in ABAQUS. The hydroelastic elements have no stiffness, but contribute to the total mass and damping of the system.

The hydroelastic coupling algorithm has been validated for an elliptic cantilever beam, twisted cantilever plates, skewed cantilever plates, a series of highly skewed propellers, and a surface-piercing propeller. Details of the formulation, implementation, and validation studies of the unsteady hydroelastic model can be found in [28,35,36,38,39].

5 Results

The objective of the present study is to demonstrate the computational capability to simulate propeller performance in sub-cavitating, partially cavitating, and supercavitating conditions, which are critical for the design/analysis of dual-cavitating propellers. The well-known Newton-Rader (NR) three-bladed series [40] with varying pitch and blade area are selected for code validation. The NR series was developed specially for high-speed crafts. It consists of twelve 254 mm dia (10 in. dia), methodically varied, geometrically similar model propellers. The models were constructed of manganese bronze, and cavitation studies were conducted in the Vosper cavitation tunnel. Extensive thrust and torque data along with the photographs of cavitation patterns at various cavitation numbers and propeller advance coefficients have been documented [40].

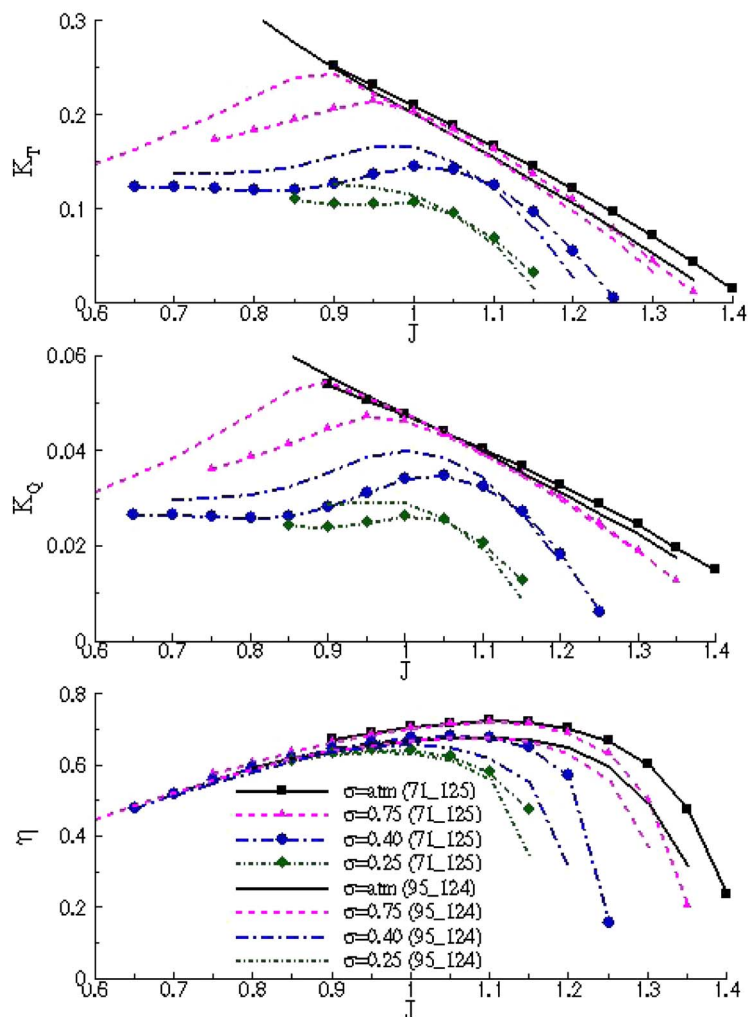


Fig. 6 Measured open water characteristics for propellers A3/71/125 and A3/95/124 by [40]

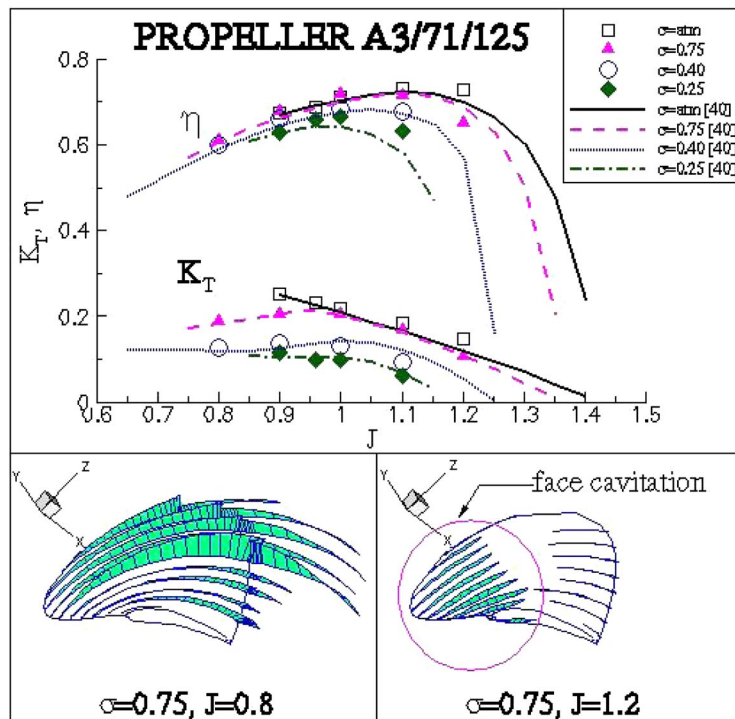


Fig. 7 Predicted and measured [40] thrust coefficients and efficiencies for propeller A3/71/125

Contrary to conventional SCP and SPP designs, which have a sharp leading edge and a blunt trailing edge, the NR propellers have a rounded leading edge and a relatively tapered trailing edge to achieve efficient operations in both subcavitating and cavitating regimes. During the manufacturing and testing phase of the parent propeller, the blade leading edge was modified twice to avoid face cavitation and to achieve high efficiency at the design condition [40]. The final blade sections and the discretized 3D geometry for two of the propeller in the NR series are shown in Figs. 4 and 5. Propeller A3/71/125 has a blade area ratio of 0.71 and a face pitch ratio of 1.25. Propeller A3/95/124 has a blade area ratio of 0.95 and a face pitch ratio of 1.24. According to [40], the point drilling method was used to manufacture the propellers, and the machine tolerance was $<0.5\%$.

The design operating conditions are [40]: $J=V/nD=0.993$ and $\sigma=(p_o-p_c)/0.5\rho V^2=\sigma_n/J^2=0.311$. V , n , and D denote the propeller advance speed, rotational frequency, and diameter, respectively, ρ is the fluid density. p_o and p_c denote the hydrostatic pressure far upstream on the shaft axis and the saturated vapor pressure of water, respectively. Comparisons of the measured thrust ($K_T=T/\rho n^2 D^4$), torque ($K_Q=Q/\rho n^2 D^5$), and efficiency ($\eta=JK_T/2\pi K_Q$) coefficients for propellers A3/71/125 and A3/95/124 at varying advance coefficients (J) and cavitation numbers (σ) are shown in Fig. 6, which is generated using data presented in [40]. Experimental uncertainties were not given in [40], but it was stated in the paper that the thrust and torque measurements were carried out two or three times to ensure accuracy and repeatability of the results.

In the subcavitating regime, propeller A3/71/125 produces higher thrust, torque, and efficiency than propeller A3/95/124 for nearly the full range of J shown. However, in the cavitating regime, the propeller performances differ for $J<1.0$ and $J>1.1$, with $1.0\leq J\leq 1.1$ being the transition region. Compared to propeller A3/95/124, the cavitating thrust and torque coefficients for propeller A3/71/125 are significantly lower for $J<1.0$, and slightly higher for $J>1.1$. Significant thrust and torque reduction due to cavitation can be observed for both propellers. However,

the cavitating efficiencies approach the subcavitating efficiencies for $J<1.0$, which is not common for conventional fully submerged propellers. This suggests that the NR propellers are good candidates for multispeed design. For $J>1.1$, the cavitating efficiencies decrease with decreasing cavitation number due to the transition from back cavitation to face cavitation, which suggest that the propeller efficiencies can be improved by modifying the blade sections to minimize face cavitation.

Comparisons of the predicted and measured thrust coefficients and efficiencies for the two propellers are shown in Figs. 7 and 8. The lines correspond to the measured data, and the symbols correspond to the numerical predictions. Glauert's formula [41] was used for the tunnel wall correction. Predicted and measured torque data are also available but are not shown in Figs. 7 and 8 to keep the graphs legible. Moreover, the torque coefficients K_Q can be deduced from J , K_T , and $\eta=JK_T/2\pi K_Q$. It should be noted that the numerical predictions are made using the above-mentioned coupled BEM/FEM method, i.e., the elasticity of the blades are considered. However, the rigid-blade and elastic-blade results are practically indistinguishable due to the high rigidity of the 254 mm dia (10 in. dia) manganese bronze blades. The predicted load coefficients and efficiencies compared well to experimental measurements. In particular, the magnitude of the predicted cavitation-induced thrust breakdown compared well to measured values.

Examples of the predicted cavitation patterns for $J<1.0$ (back cavitation regime) and $J>1.1$ (face cavitation regime) at $\sigma=0.75$ are shown in Figs. 7 and 8. The cavities are plotted normal to the propeller and wake surfaces. A circle is placed around the region with face cavitation to help distinguish the face cavities from the back cavities. As shown in Figs. 7 and 8, both propellers exhibit midchord back supercavitation at $J=0.8$ and primarily leading-edge face partial cavitation at $J=1.2$. Very thin midchord back cavities can also be observed for both propellers at $\sigma=0.75$ and $J=1.2$. In [40], photos of the observed cavitation patterns for propeller A3/71/125 at selected conditions were shown, but the

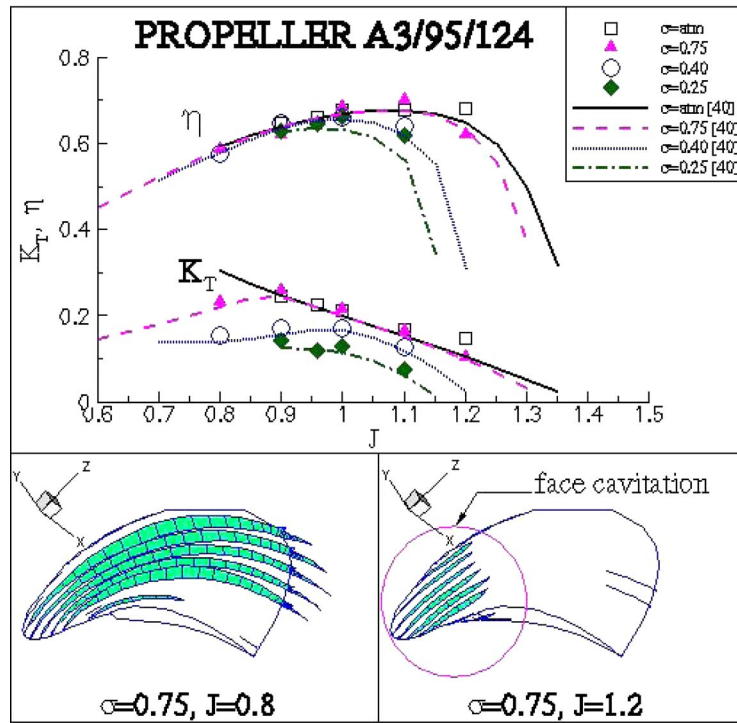


Fig. 8 Predicted and measured [40] thrust coefficients and efficiencies for propeller A3/95/124

qualities of the photos were poor. Nevertheless, qualitative comparisons show that the predicted cavitation patterns are in reasonable agreement with experimental observations.

In general, propeller A3/71/125 produces thicker and longer cavities than propeller A3/95/124 and, thus, exhibits more severe thrust and torque breakdown due to cavitation. For $J < 1.0$, the cavitating efficiencies approach the noncavitating efficiencies for all cavitation numbers for both propellers. The cavitating efficiencies decreased with decreasing cavitation number for $J > 1.1$ due to increase in face cavitation volume. For $J > 1.1$, the cavitating efficiencies of propeller A3/71/125 are higher than propeller A3/95/124 due to the development of a midchord back supercavity that counterbalances the leading edge face partial cavity.

To optimize the design of blade sections, different suction (back) side geometries are explored while keeping the pressure (face) side geometry unchanged for propeller A3/71/125. The blade sections tested include: MOD TE (modified trailing edge), MOD LE (modified leading edge), and 1/2 TK (half of the original thickness). Plots of the different blade sections are shown in Fig. 9. Comparisons of the thrust breakdown curves for the different blade sections for $J = 1.0$ and $J = 1.1$ are shown in Figs. 10

and 11, respectively. The corresponding cavitation patterns are shown in Figs. 12 and 13. The face cavitation regions are circled to facilitate viewing.

Compared to the original NR blade section, the MOD TE and MOD LE blade sections produced similar cavitation patterns and loading coefficients. The MOD TE blade section yielded slightly lower torque coefficient and higher efficiency in the subcavitating regime due to decreased loading near the blade trailing edge. In the supercavitating regime, the performance curves for the NR, MOD TE, and MOD LE blade sections are practically indistinguishable because the entire suction side is inside a supercavity and the pressure side geometry is identical for all three designs. Out of the four blade sections, the 1/2-TK blade section produced the highest overall efficiencies for both subcavitating and cavitating conditions due to the reduced loading. The cavities are also thinner and shorter for the 1/2-TK blade section due to the reduced blade thickness.

The results suggest that for most cases, when the entire suction side of the blade surface is inside a supercavity, the hydrodynamic performance depends only on the cavitation number, advance coefficient, and pressure-side geometry, but not the suction-side ge-

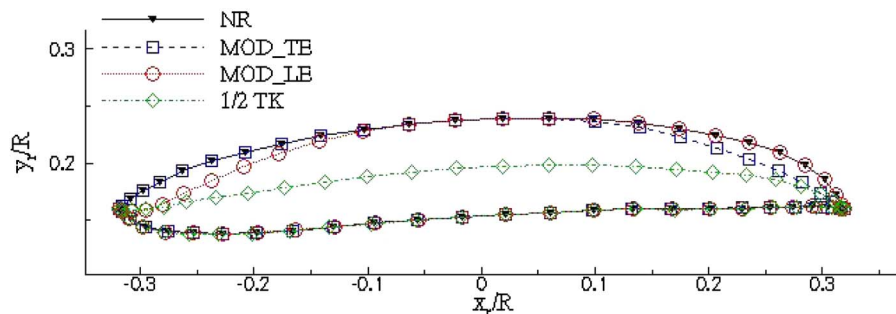


Fig. 9 Different blade section designs for propeller A3/71/125

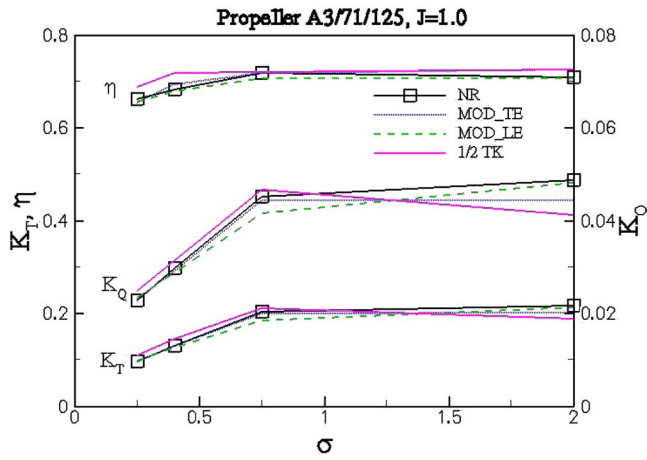


Fig. 10 Predicted thrust breakdown curves for the different blade section designs for propeller A3/71/125, $J=1.0$

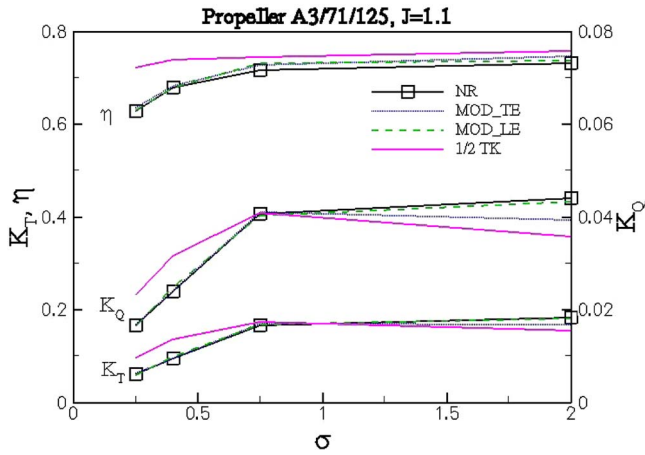


Fig. 11 Predicted thrust breakdown curves for the different blade section designs for propeller A3/71/125, $J=1.1$

ometry. However, when the blade thickness is significantly reduced, the hydrodynamic performance also becomes a function of the suction side geometry due to changes in the form drag as a result of the significantly thinner and shorter supercavity. The suction-side geometry also influences the hydrodynamic performance for partially cavitating or fully wetted conditions.

To investigate the hydroelastic performance of the difference blade sections, comparisons of the predicted pressure distributions, von Mises stress distributions, leading edge (LE) axial displacements, and modal responses for $J=1.1$ and $\sigma=2.0$ are shown in Figs. 14–17, respectively. The results are generated by assuming the propellers to be 0.81 m dia (32 in. dia), the shaft frequency to be 35 rps and by assigning the following material properties for manganese bronze: modulus of elasticity (E) equal to 104.8 GPa (15,200 ksi), Poisson's ratio (ν) equal to 0.3, material density (ρ_s) equal to 7900 kg/m³ (15.33 slug/ft³), yield strength (σ_y) equal to 345 MPa (50 ksi), and ultimate strength (σ_u) equal to 655 MPa (95 ksi).

The hydroelastic performance of the MOD TE blade section is very similar to the original NR blade section. However, slightly higher stress concentrations can be observed near the blade leading edge and near the root on both sides of the blade surface for the MOD LE blade section due to the reduced leading-edge thickness. Nevertheless, the maximum stresses and deflections for the NR, MOD TE, and MOD LE blade sections are within allowable limits. On the other hand, the 1/2-TK blade section design produced stresses that are higher than the material yield stress, which is not acceptable for design. Moreover, the maximum deflection for the 1/2-TK blade section is ~12% of the propeller radius, which is much too high for a rigid propeller. The mode shapes for all four blade section designs are very similar, but the natural frequencies for the 1/2-TK blade section are also approximately 50% lower than the other blade sections. It should be noted that the natural frequencies of propeller A3/71/125 are decreased by approximately one-third when submerged in water due to added mass effect.

The results imply that if the 1/2-TK blade section is used instead of the original NR blade section, material failure may occur due to tensile cracks, fatigue failure, and/or resonant blade vibration. In addition, out of the four different blade section designs, the MOD TE blade section appears to be the best design because

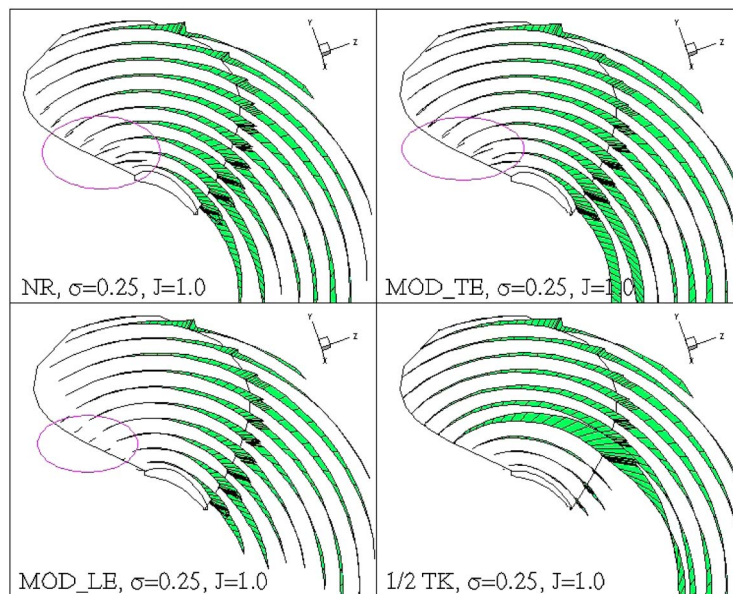


Fig. 12 Predicted cavitation patterns for the different blade section designs for propeller A3/71/125, $J=1.0$

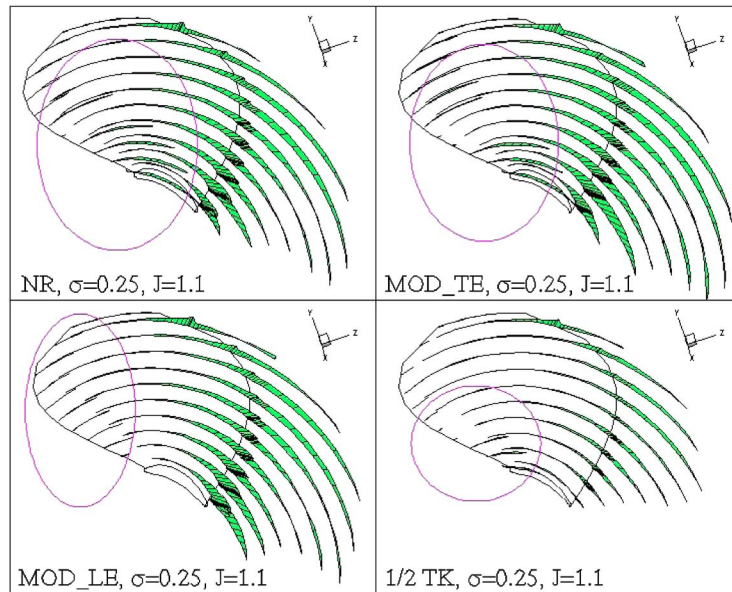


Fig. 13 Predicted cavitation patterns for the different blade section designs for propeller A3/71/125, $J=1.1$

it produced high efficiencies in the subcavitating and cavitating regimes, and acceptable blade stresses and deflections. The results also illustrated the importance of the hydroelastic analysis in order to avoid potential strength and/or vibration issues.

6 Conclusion

A numerical tool is presented for the time-domain analysis of the hydrodynamic and hydroelastic response of marine propellers.

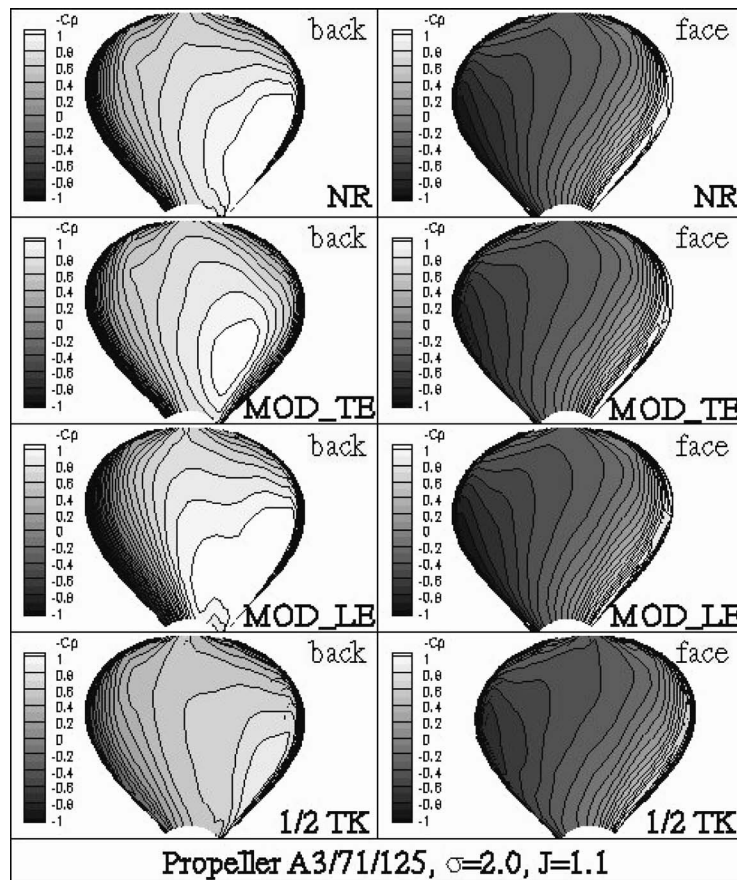


Fig. 14 Predicted pressure distributions for the different blade section designs for propeller A3/71/125 at $J=1.1$ and $\sigma=2.0$

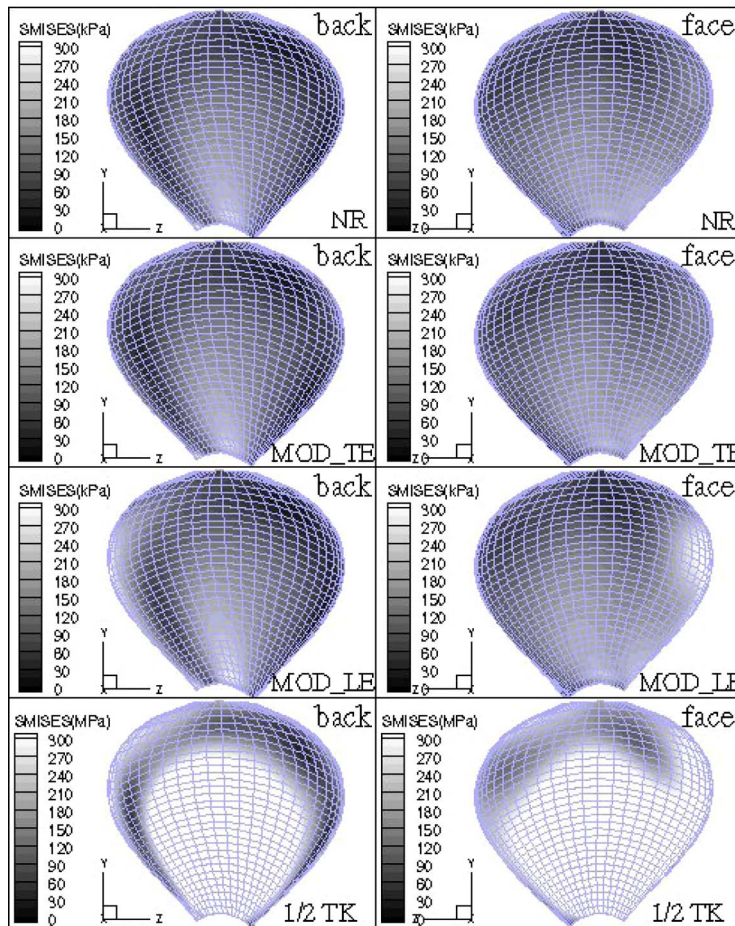


Fig. 15 Predicted von Mises stress distributions for the different blade section designs for propeller A3/71/125 at $J=1.1$ and $\sigma=2.0$

The method is able to predict complex cavitation patterns, blade forces, stress distributions, blade deflections, and dynamic characteristics of fully submerged and partially submerged propellers in

subcavitating, partially cavitating, fully cavitating, and ventilated conditions. Experimental validation studies are shown for the Newton-Rader propellers series [40], which have been designed successfully for a ship speed of 54 knots. The predicted blade loads compared well to experimental measurements in subcavitating, partially cavitating, and supercavitating conditions. The following conclusions can be drawn from the results of this study:

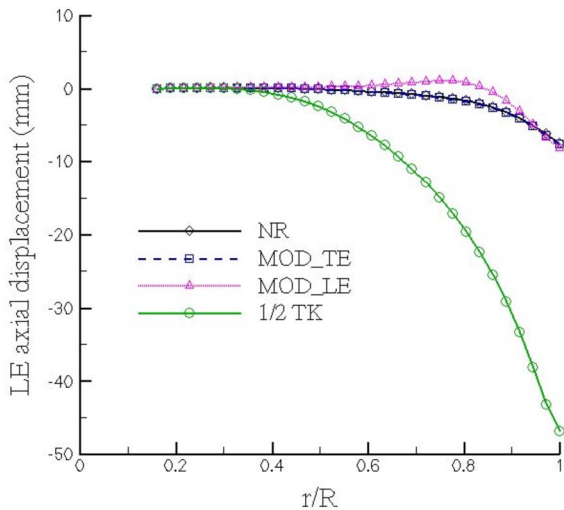


Fig. 16 Predicted leading-edge axial displacements for the different blade section designs for propeller A3/71/125 at $J=1.1$ and $\sigma=2.0$

1. The NR blade sections can be considered optimum in the sense that it produced cavitating efficiencies that approach the noncavitating efficiencies when the blades only exhibit back cavitation. However, the cavitating efficiencies decreased with decreasing cavitation number when the blades exhibit face cavitation. Thus, there is a potential to improve the hydrodynamic performance by modifying the blade sections to avoid or limit face cavitation.
2. The hydrodynamic efficiency of the NR blade sections can be further improved by streamlining the suction side of the blade trailing edge.
3. When the entire suction side of the blade surface is inside a supercavity, the hydrodynamic performance depends mostly on the cavitation number, advance coefficient, and pressure-side geometry, but not on the suction-side geometry. However, this is not true when the blade thickness is significantly reduced or when the blade is in partially cavitating or fully wetted conditions.
4. It is crucial to consider both face and back cavitation in the analysis and design of dual-cavitating marine propellers.
5. It is crucial to examine both the hydrodynamic and hydroelastic performance of marine propellers to avoid yield-

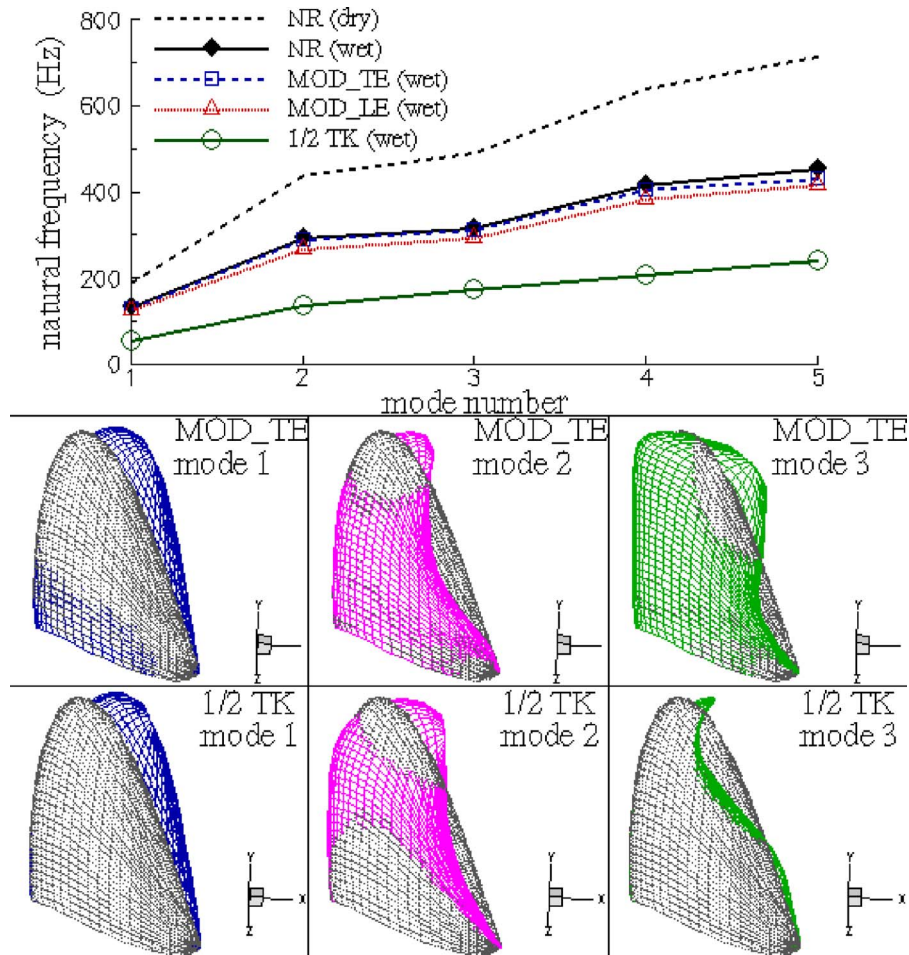


Fig. 17 Predicted natural frequencies and mode shapes for the different blade section designs for propeller A3/71/125

ing or fatigue failure, and to avoid resonant blade vibration issues.

6. It is possible to design a dual cavitating propeller that can operate efficiently in low-, middle-, and high-speed ranges.

Currently, the authors are working on implementing a generic algorithm to optimize the blade section geometry to minimize face cavitation and to improve the overall propeller performance in low-, middle-, and high-speed regimes. Additional studies are also underway to examine the unsteady behavior of the propellers in inclined and other non-axisymmetric flows.

Acknowledgment

Support for this research was provided by Naval Surface Warfare Center Carderock Division and Office of Naval Research (Contract No. N000167-05-M-0100 and No. N00014-05-1-0694). The authors would like to thank the support of Dr. K. H. Kim of ONR, and Dr. J. Corrado of the Naval Surface Warfare Center, Carderock Division.

Nomenclature

- [A] = induced potential matrix due to unit strength dipoles
- [B] = induced potential matrix due to unit strength sources
- [C] = combined induced potential matrix, $[C]=[A]^{-1}[B]$

- C_p = pressure coefficient, $C_p=(p-p_o)/(0.5\rho n^2 D^2)$
- D = propeller diameter
- [D] = structural damping matrix
- $[D^h]$ = hydrodynamic damping matrix
- g = gravitational acceleration
- G = Green's function
- {f} = Nodal hydrodynamic force vector due to vibrating blades rotating in uniform wake, $\{f\} = \int [N]^T \{p_v\} dS = -[M^h]\{\ddot{u}\} - [D^h]\{\dot{u}\}$
- {F} = nodal hydrodynamic force vector due to rigid blades rotating in nonuniform wake, $\{F\} = \int [N]^T \{p_r\} dS$
- $\{F_c\}$ = nodal centrifugal and the coriolis force vector
- $\{F_T\}$ = total nodal hydrodynamic force vector, $\{F_T\} = \{F\} + \{f\}$
- J = advance ratio based on V, $J=V/nD$
- [K] = structural stiffness matrix
- K_Q = torque coefficient in ship-fixed coordinates, $K_Q = Q/\rho n^2 D^5$
- K_T = thrust coefficient in ship-fixed coordinates, $K_T = T/\rho n^2 D^4$
- [M] = structural mass matrix
- $[M^h]$ = hydrodynamic added mass matrix
- n = propeller rotational frequency (rps), $n=\omega/2\pi$
- [N] = displacement interpolation matrix
- \vec{n} = local unit normal vector

p_o = hydrostatic pressure on the shaft axis far upstream
 p_c = cavity pressure
 p = total hydrodynamic pressure, $p = p_r + p_v$
 p_r = hydrodynamic pressure due to rigid blades rotating in nonuniform wake
 p_v = hydrodynamic pressure due to vibrating blades in uniform wake
 \vec{q} = total velocity (in blade-fixed coordinates)
 \vec{q}_E = effective wake velocity (in ship-fixed coordinates)
 \vec{q}_{in} = local inflow velocity (in blade-fixed coordinates)
 Q = propeller torque
 \vec{s} = local unit vector in the span-wise direction
 t = time
 T = propeller thrust
 $[T]$ = transformation matrix
 $\{u\}$ = nodal displacement vector
 $\{\dot{u}\}$ = nodal velocity vector
 $\{\ddot{u}\}$ = nodal acceleration vector
 \vec{v} = local unit vector in the chordwise direction
 V = advance speed of propeller
 x, y, z = blade-fixed coordinates
 x_s, y_s, z_s = ship-fixed coordinates
 η = propeller efficiency, $\eta = K_T J / 2\pi K_Q$
 ω = propeller angular velocity (rad/s)
 ϕ = perturbation velocity potential
 ρ = fluid density
 σ_n = cavitation number based on n , $\sigma_n = (p_o - p_c) / (0.5\rho n^2 D^2)$
 σ = cavitation number based on V , $\sigma = (p_o - p_c) / (0.5\rho V^2)$

References

- Jessup, S., and Wang, H.-C., 1997, "Propeller Design and Evaluation for a High-Speed Patrol Boat Incorporating Iterative Analysis with Panel Method," SNAME Propellers/Shafting Symposium, Virginia Beach, pp. 1101–1125.
- Bailar, J., Jessup, S., and Shen, Y., 1992, "Improvement of Surface Ship Propeller Cavitation Performance Using Advanced Blade Sections," 23rd ATTC Conference, New Orleans.
- Jessup, S., Berberich, W., and Remmers, K., 1994, "Cavitation Performance Analysis of Naval Surface Ship Propellers with Standard and New Blade Sections," 20th ONR Hydrodynamic Symposium, Santa Barbara, pp. 101–116.
- Tachmindji, A. J., and Morgan, W. B., 1958, "The Design and Estimated Performance of a Series of Supercavitating Propellers," *Proc. of 2nd Office of Naval Research Symposium on Naval Hydrodynamics*, pp. 489–532.
- Venning, E., and Haberman, W. L., 1962, "Supercavitating and Propeller Performance," *Soc. Nav. Archit. Mar. Eng., Trans.*, **70**, pp. 354–417.
- Hadler, J., and Hecker, R., 1968, "Performance of Partially Submerged Propellers," The 7th ONR Symposium on Naval Hydrodynamics, Rome.
- Kruppa, C. F. L., 1972, "Testing Partially Submerged Propellers," *13th ITTC Report of Cavitation Committee*, Hamburg, Berlin.
- Hecker, R., 1973, "Experimental Performance of a Partially Submerged Propeller in Inclined Flow," SNAME Spring Meeting, Lake Buena Vista, FL.
- Rains, D. A., 1981, "Semi-Submerged Propellers for Monohull Displacement Ships," *Propeller '81 Symposium*, Society of Naval Architects and Marine Engineers, Virginia Beach, pp. 15–40.
- Kruppa, C. F. L., 1992, *Hydrodynamics: Computations, Model Tests, and Reality*, Elsevier, New York, pp. 107–113.
- Allison, J., 1978, "Propellers for High-Performance Craft," *Mar. Technol. Soc. J.*, **15**, pp. 335–380.
- Tulin, M. B., 1962, "Supercavitating Propellers—History, Operating Characteristics, Mechanisms of Operation," *Fourth Symposium on Naval Hydrodynamics*, pp. 239–286.
- Tulin, M., and Burkart, M., 1955, "Linearized Theory for Flows about Lifting Foils at Zero Cavitation Number," Tech. Rep. Navy Report No. C-638, David Taylor Model Basin.
- Shen, Y., 1996, "Dual Cavitating Hydrofoil Structures," Tech. Rep., U.S. Patent No. 5,551,369.
- Shen, Y., and Wermter, R., 1979, "Recent Studies of Struts and Foils for High-speed Hydrofoils," *Mar. Technol. Soc. J.*, **16**.
- Lee, J.-T., 1987, "A Potential Based Panel Method for The Analysis of Marine Propellers in Steady Flow," Ph.D. thesis, Department of Ocean Engineering, Massachusetts Institute of Technology.
- Kerwin, J., Kinnas, S., Lee, J.-T., and Shih, W.-Z., 1987, "A Surface Panel Method for the Hydrodynamic Analysis of Ducted Propellers," *Soc. Nav. Archit. Mar. Eng., Trans.*, **95**, pp. 93–122.
- Hsin, C.-Y., 1990, "Development and Analysis of Panel Method for Propellers in Unsteady Flow," Ph.D. thesis, Department of Ocean Engineering, Massachusetts Institute of Technology.
- Kinnas, S., and Hsin, C.-Y., 1992, "A Boundary Element Method for the Analysis of the Unsteady Flow Around Extreme Propeller Geometries," *AIAA J.*, **30**, pp. 688–696.
- Kinnas, S., and Fine, N., 1991, "Non-Linear Analysis of the Flow Around Partially Super-Cavitating Hydrofoils by a Potential Based Panel Method," *Boundary Integral Methods—Theory and Applications, Proceedings of the IABEM-90 Symposium*, Rome, Oct. 15–19, 1990, Springer-Verlag, Heidelberg, pp. 289–300.
- Fine, N., and Kinnas, S., 1993, "A Boundary Element Method for the Analysis of the Flow Around 3-D Cavitating Hydrofoils," *J. Ship Res.*, **37**, pp. 213–224.
- Kinnas, S., and Fine, N., 1992, "A Nonlinear Boundary Element Method for the Analysis of Unsteady Propeller Sheet Cavitation," *Nineteenth Symposium on Naval Hydrodynamics*, Seoul, Korea, pp. 717–737.
- Mueller, A., and Kinnas, S., 1999, "Propeller Sheet Cavitation Predictions Using a Panel Method," *ASME J. Fluids Eng.*, **121**, pp. 282–288.
- Young, Y., and Kinnas, S., 2001, "A BEM for the Prediction of Unsteady Midchord Face and/or Back Propeller Cavitation," *ASME J. Fluids Eng.*, **123**, pp. 311–319.
- Young, Y., and Kinnas, S., 2001, "Numerical Modeling of Supercavitating and Surface-Piercing Propeller Flows," *CAV 2001: Fourth International Symposium of Cavitation*, California Institute of Technology, Pasadena.
- Young, Y., and Kinnas, S., 2003, "Numerical Modeling of Supercavitating Propeller Flows," *J. Ship Res.*, **47**, pp. 48–62.
- Young, Y., and Kinnas, S., 2004, "Performance Prediction of Surface-Piercing Propellers," *J. Ship Res.*, **48**, pp. 288–304.
- Young, Y., and Kinnas, S., 2003, "Numerical Analysis of Surface-Piercing Propellers," *2003 Propeller and Shaft Symposium*, Society of Naval Architects and Marine Engineers, Virginia Beach, pp. 4-1–4-20.
- Kinnas, S., and Young, Y., 2003, "Modeling of Cavitating or Ventilated Flows Using BEM," *Int. J. Numer. Methods Heat Fluid Flow*, **13**, pp. 672–697.
- Kinnas, S., Young, Y., Lee, H., Gu, H., and Natarajan, S., 2003, "Prediction of Cavitating Flow Around Single or Two-Component Propellers, Ducted Propellers, and Rudders," *RINA CFD 2003: CFD Technology in Ship Hydrodynamics Conference*, London.
- Kinnas, S., Choi, J., Lee, H., and Young, J., 2000, "Numerical Cavitation Tunnel," NCT50, International Conference on Propeller Cavitation, Newcastle-upon-Tyne, England.
- Choi, J., 2000, "Vortical Inflow—Propeller Interaction Using Unsteady Three-Dimensional Euler Solver," Ph.D. thesis, Department of Civil Engineering, The University of Texas at Austin.
- Young, Y., and Kinnas, S., 2003, "Analysis of Supercavitating and Surface-Piercing Propeller Flows via BEM," *Comput. Mech.*, **32**, pp. 269–280.
- Kuo, J., and Vorus, W., 1985, Tenth Ship Technology and Research (STAR) Symposium, Norfolk, pp. 39–69.
- Young, Y., 2006, "Time-Dependent Hydroelastic Analysis of Cavitating Propellers," *J. Fluids Struct.* (in press).
- Young, Y., 2005, "Time-Domain Analysis of the Hydroelastic Response of Cavitating Propellers," 3rd International Conference on Fluid Structure Interaction, La Coruna, Spain.
- ABAQUS, 2003, ABAQUS Version 6.5 Documentation, ABAQUS, Inc., Pawtucket, RI.
- Young, Y., and Kinnas, S., 2003, "Fluid and Structural Modeling of Cavitating Propeller Flows," Fifth International Symposium on Cavitation (CAV2003), Osaka.
- Young, Y., 2004, "Hydroelastic Modeling of Surface-Piercing Propeller Flows," Twenty-Fifth Symposium on Naval Hydrodynamics, St. John's, Newfoundland.
- Newton, R., and Rader, H., 1961, "Performance Data of Propellers for High-Speed Craft," *Trans. RINA*, **103**, pp. 93–129.
- Glauert, H., 1943, "Wind Tunnel Interference in Airplane Propellers," *Aerodynamic Theory*, Dover ed, Vol. 4, pp. 296–301.

Multifrequency Instability of Cavitating Inducers

Christopher E. Brennen

California Institute of Technology,
1201 East California Boulevard,
Pasadena, CA 91125

Recent testing of high-speed cavitating turbopump inducers has revealed the existence of more complex instabilities than the previously recognized cavitating surge and rotating cavitation. This paper explores one such instability that is uncovered by considering the effect of a downstream asymmetry, such as a volute on a rotating disturbance similar to (but not identical to) that which occurs in rotating cavitation. The analysis uncovers a new instability that may be of particular concern because it occurs at cavitation numbers well above those at which conventional surge and rotating cavitation occur. This means that it will not necessarily be avoided by the conventional strategy of maintaining a cavitation number well above the performance degradation level. The analysis considers a general surge component at an arbitrary frequency ω present in a pump rotating at frequency Ω and shows that the existence of a discharge asymmetry gives rise not only to beat components at frequencies, $\Omega - \omega$ and $\Omega + \omega$ (as well as higher harmonics), but also to rotating as well as surge components at all these frequencies. In addition, these interactions between the frequencies and the surge and rotating modes lead to "coupling impedances" that effect the dynamics of each of the basic frequencies. We evaluate these coupling impedances and show not only that they can be negative (and thus promote instability) but also are most negative for surge frequencies just a little below Ω . This implies potential for an instability involving the coupling of a surge mode with a frequency around 0.9Ω and a low-frequency rotating mode about 0.1Ω . We also examine how such an instability would be manifest in unsteady pressure measurements at the inlet to and discharge from a cavitating pump and establish a "footprint" for the recognition of such an instability. [DOI: 10.1115/1.2734238]

1 Introduction

Ever since the recognition of the POGO instability of liquid-propelled rockets more than 40 years ago [1,2], much attention has been directed at understanding the mechanisms for the promotion of instabilities associated with cavitating pumps. The simple forms of POGO, of cavitation surge and of rotating cavitation, have been successfully studied and related to dynamic features in the performance of pumps such as the cavitation compliance and mass flow gain factor [3].

However, recent experience in several space programs around the world has indicated that the preceding body of knowledge and understanding may not be adequate or sufficient. Specifically, there appear to be other, more complex instabilities associated with cavitating turbopumps that do not fit easily within the current understanding. This paper explores one particular complex instability which is uncovered by considering the effect of a downstream asymmetry, such as a volute on a rotating disturbance similar to (but not identical to) that which occurs in rotating cavitation. The analysis which follows uncovers a new instability which may be of particular concern because it occurs at cavitation numbers well above those at which conventional surge and rotating cavitation occur. This means that it will not necessarily be avoided by the conventional strategy of maintaining a cavitation number well above the performance degradation level.

2 Analysis

As is conventional [3], we consider unsteady linear perturbations in the total pressure p and mass flow rate m given by

$$p_i(t) = \bar{p}_i + \text{Re}\{\tilde{p}_{i,\omega} e^{j\omega t}\} \quad (1)$$

$$m_i(t) = \bar{m}_i + \text{Re}\{\tilde{m}_{i,\omega} e^{j\omega t}\} \quad (2)$$

where j is $(-1)^{1/2}$, the index i denotes a specific location in the fluid flow path, the overbar denotes a mean or time-averaged quantity, a tilde denotes a fluctuating quantity, and Re denotes the real part. Implicit in the above linearization is a summation of the fluctuating terms over all the frequencies ω of interest. Thus, the complex quantities $\tilde{p}_{i,\omega}$ and $\tilde{m}_{i,\omega}$ incorporate the amplitude and phase of the fluctuating total pressure and mass flow rate at the frequency ω and the location i .

It is both convenient and, nowadays, conventional (see [4]) to express the dynamic response of a cavitating pump at the frequency ω by the relations

$$\tilde{p}_{2,\omega} - \tilde{p}_{1,\omega} = G\tilde{p}_{1,\omega} - (R + j\omega L)\tilde{m}_{2,\omega} \quad (3)$$

$$\tilde{m}_{2,\omega} - \tilde{m}_{1,\omega} = -j\omega C\tilde{p}_{1,\omega} - j\omega M\tilde{m}_{1,\omega} \quad (4)$$

where the subscripts $i=1$ and $i=2$ refer to the pump inlet and discharge locations and $G+1$, R , L , C , and M are known respectively, as the pump gain, resistance, inertance, compliance, and mass flow gain factor. (Note the above differs slightly from the original form proposed by Brennen and Acosta [5] and used by Ng and Brennen [6] and Brennen et al. [7], Brennen [8], and Rubin [9], in measuring and analyzing the pump dynamic characteristics in that $\tilde{m}_{2,\omega}$ rather than $\tilde{m}_{1,\omega}$ is used at the end of Eq. (3). However, one form is readily transposed to the other.) Implicit in the above model (Eqs. (3) and (4)) is the assumption of linear relations; we note that although nonlinear effects undoubtedly occur, they are currently beyond our ability to analyze.

In this paper, we focus on the following issue originally suggested by Rubin [9]. The flow through the pump rotor consists of the sum of the flows through each of the blade passages. If all blade passages were identical at all moments in time, we could write the corresponding transfer function for each of the blade passages (say K in number) as

$$\tilde{p}_{2,\omega,k} - \tilde{p}_{1,\omega,k} = G\tilde{p}_{1,\omega,k} - (R + j\omega L)K\tilde{m}_{2,\omega,k} \quad (5)$$

Contributed by the Fluids Engineering Division of ASME for publication in the JOURNAL OF FLUIDS ENGINEERING. Manuscript received August 28, 2006; final manuscript received December 21, 2006. Review conducted by Akira Goto.

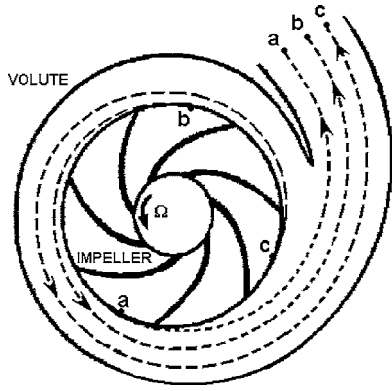


Fig. 1 Sketch of a pump volute showing typical streamlines *aa*, *bb*, and *cc* with different path lengths

$$\tilde{m}_{2,\omega,k} - \tilde{m}_{1,\omega,k} = -j\omega \frac{C}{K} \tilde{p}_{1,\omega,k} - j\omega M \tilde{m}_{1,\omega,k} \quad (6)$$

where the additional index $k=1,2,\dots,K$ denotes the total pressures and mass flow rates in each of the K blade passages. If this were all the dynamics to be concerned with, then, clearly, Eqs. (5) and (6) sum to yield the overall transfer function for the pump given by Eqs. (3) and (4), where

$$\tilde{p}_{2,\omega,k} = \tilde{p}_{2,\omega}; \quad \tilde{p}_{1,\omega,k} = \tilde{p}_{1,\omega} \quad (7)$$

$$\tilde{m}_{2,\omega} = \sum_{k=1}^K \tilde{m}_{2,\omega,k}; \quad \tilde{m}_{1,\omega} = \sum_{k=1}^K \tilde{m}_{1,\omega,k} \quad (8)$$

However, the effect that we wish to focus on here is the fact that the discharge from a pump is usually quite asymmetric. Often the discharging flow is collected in a single volute, such as that shown in Fig. 1, so that, at any instant in time, the flow exiting from one blade passage may have much farther to travel than the flow from another blade passage, as illustrated by the three typical streamlines *aa*, *bb*, and *cc* in Fig. 1. Of course, inlet flows may also be quite asymmetric. However, we should note the relative effects of inlet and discharge asymmetries on the flows through an inducer or impeller as investigated by Bhattacharyya [10]. Bhattacharyya found that inlet asymmetries have a remarkably small effect on the asymmetry of the flow through an inducer, even when that asymmetry consisted of an abrupt right-angle bend just upstream of the inducer inlet. On the other hand, asymmetries in the discharge flow had surprisingly strong effects on the asymmetry of the flow through the inducer. For this reason and for the added reason of simplicity, we confine ourselves here to asymmetries in the discharge.

The primary effect of simple discharge asymmetry, such as produced by a single volute or by a right-angle bend just downstream of the impeller, is that the effective length of each flow passage oscillates at the rotational frequency of the impeller Ω . This means that the instantaneous inductance of each blade passage flow is oscillating at a frequency Ω and with some amplitude, which

we will denote by L^* . Of course, the resistance will also oscillate but, for simplicity, we neglect this effect (it is also much easier to estimate the magnitude of L^*). This additional dynamic effect is then incorporated into our model of the pump, as shown in Fig. 2. Each blade passage now has the original dynamics as represented by Eqs. (5) and (6) but with $\tilde{p}_{2,\omega,k}$ now replaced by $\tilde{p}_{M,\omega,k}$, where the location M is the exit from the impeller blade passage, k ; thus,

$$\tilde{p}_{M,\omega,k} - \tilde{p}_{1,\omega,k} = G\tilde{p}_{1,\omega,k} - (R + j\omega L)K\tilde{m}_{2,\omega,k} \quad (9)$$

replaces Eq. (5), whereas Eq. (6) remains unchanged. As incorporated in Eq. (15), we then add the additional oscillating inductance L^{**} onto the original blade passage dynamics, where

$$L^{**} = \text{Re}\{L^* e^{j\Omega t + j2\pi k/K}\} \quad (10)$$

where L^* is a real constant and the term $j2\pi k/K$ incorporates the appropriate phase between the blade passages. Note that the direction of this phase or time delay is consistent with an index or passage label k that *increases* in the direction of rotation of the impeller. Note also that since

$$\sum_{k=1}^K e^{j2\pi k/K} = 0 \quad (11)$$

the arithmetic means of the blade passage pressures at discharge ($i=2$) and at the location $i=M$ are identical.

For later use, we also note that in a given blade passage k , the fluctuating mass flow rate at any general frequency, ξ (specifically ω , $\Omega - \omega$, $\Omega + \omega$, or higher-order combinations as anticipated below), namely, $\tilde{m}_{2,\xi,k}$, must necessarily consist of a "surge" component, $\tilde{m}_{2,\xi}/K$, which is identical and in phase for all blade passages plus a "rotating" component, $\tilde{m}_{\phi,\xi} e^{j2\pi k/K}$, which is caused by the downstream asymmetry. The phase of this second component must vary with k in the same manner as the oscillatory inductance while the "magnitude," $\tilde{m}_{\phi,\xi}$, is identical for all blade passages. Consequently,

$$\tilde{m}_{2,\xi,k} = \frac{\tilde{m}_{2,\xi}}{K} + \tilde{m}_{\phi,\xi} e^{j2\pi k/K} \quad (12)$$

for $\xi = \omega, \Omega, \Omega - \omega, \Omega + \omega, \dots$

In addition, we can anticipate that the existence of fluctuating components at the frequencies ω and Ω will, through the fluctuating inductance, spawn additional components at combination frequencies $\Omega - \omega$, $\Omega + \omega$, as well as higher harmonics and higher-order combinations. Thus, it becomes necessary to include flow fluctuations at frequencies Ω , $(\Omega - \omega)$, and $(\Omega + \omega)$ (and higher frequencies) as well as ω . Therefore, the flow rate in an individual blade passage, $m_{2,k}(t)$, will need to be expressed by

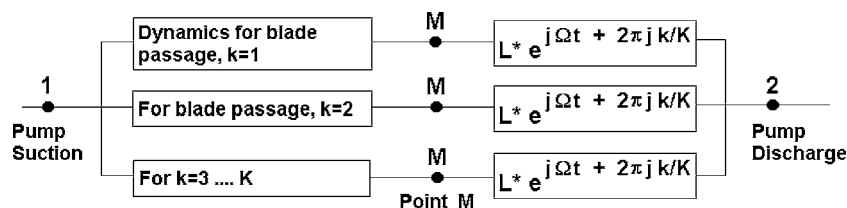


Fig. 2 Pump dynamic model with individual blade passage dynamics and an asymmetric discharge inductance

$$m_{2,k}(t) = \bar{m}_2/K + \text{Re} \left\{ \begin{array}{l} \tilde{m}_{2,\omega,k} e^{j\omega t} + \tilde{m}_{2,\Omega,k} e^{j\Omega t} \\ + \tilde{m}_{2,\Omega-\omega,k} e^{j(\Omega-\omega)t} + \tilde{m}_{2,\Omega+\omega,k} e^{j(\Omega+\omega)t} \\ + \tilde{m}_{2,2\Omega-\omega,k} e^{j(2\Omega-\omega)t} + \tilde{m}_{2,2\Omega+\omega,k} e^{j(2\Omega+\omega)t} \\ + \text{higher harmonics} \end{array} \right\} \quad (13)$$

Also, using the definition (1), the pressure difference, $p_{M,k} - p_2$, between the location $i=M$ and the discharge, $i=2$, should be similarly written as

$$p_{M,k} - p_2 = \bar{p}_M - \bar{p}_2 + \text{Re} \left\{ \begin{array}{l} (\tilde{p}_{M,\omega,k} - \tilde{p}_{2,\omega}) e^{j\omega t} \\ + (\tilde{p}_{M,\Omega,k} - \tilde{p}_{2,\Omega}) e^{j\Omega t} \\ + (\tilde{p}_{M,\Omega-\omega,k} - \tilde{p}_{2,\Omega-\omega}) e^{j(\Omega-\omega)t} \\ + (\tilde{p}_{M,\Omega+\omega,k} - \tilde{p}_{2,\Omega+\omega}) e^{j(\Omega+\omega)t} \\ + (\tilde{p}_{M,2\Omega-\omega,k} - \tilde{p}_{2,2\Omega-\omega}) e^{j(2\Omega-\omega)t} \\ + (\tilde{p}_{M,2\Omega+\omega,k} - \tilde{p}_{2,2\Omega+\omega}) e^{j(2\Omega+\omega)t} \\ + \text{higher harmonics} \end{array} \right\} \quad (14)$$

Neglecting the resistance of the volute or elbow, this pressure difference must be equal to the inductance, L^{**} , multiplied by the time derivative of the mass flow rate given by Eq. (13) so that

$$p_{M,k} - p_2 = L^{**} \text{Re} \left\{ \begin{array}{l} j\omega \tilde{m}_{2,\omega,k} e^{j\omega t} + j\Omega \tilde{m}_{2,\Omega,k} e^{j\Omega t} \\ + j(\Omega - \omega) \tilde{m}_{2,\Omega-\omega,k} e^{j(\Omega-\omega)t} \\ + j(\Omega + \omega) \tilde{m}_{2,\Omega+\omega,k} e^{j(\Omega+\omega)t} \\ + j(2\Omega - \omega) \tilde{m}_{2,2\Omega-\omega,k} e^{j(2\Omega-\omega)t} \\ + j(2\Omega + \omega) \tilde{m}_{2,2\Omega+\omega,k} e^{j(2\Omega+\omega)t} \end{array} \right\} \quad (15)$$

and substituting for L^{**} from Eq. (10), this becomes

$$= \frac{L^*}{2} \text{Re} \left\{ \begin{array}{l} j\Omega \tilde{m}_{2,\Omega,k} e^{-j2\pi k/K} \\ + j\Omega \tilde{m}_{2,\Omega,k} e^{2j\Omega t + j2\pi k/K} \\ + j(\Omega + \omega) \tilde{m}_{2,\Omega+\omega,k} e^{j\omega t - j2\pi k/K} \\ - j(\Omega - \omega) \tilde{m}_{2,\Omega-\omega,k} e^{j\omega t + j2\pi k/K} \\ + j\omega \tilde{m}_{2,\omega,k} e^{j(\Omega+\omega)t + j2\pi k/K} \\ - j\omega \tilde{m}_{2,\omega,k} e^{j(\Omega-\omega)t + j2\pi k/K} \\ + j(\Omega - \omega) \tilde{m}_{2,\Omega-\omega,k} e^{j(2\Omega-\omega)t + j2\pi k/K} \\ + j(\Omega + \omega) \tilde{m}_{2,\Omega+\omega,k} e^{j(2\Omega+\omega)t + j2\pi k/K} \\ + j(2\Omega - \omega) \tilde{m}_{2,2\Omega-\omega,k} e^{j(\Omega-\omega)t - j2\pi k/K} \\ + j(2\Omega + \omega) \tilde{m}_{2,2\Omega+\omega,k} e^{j(3\Omega-\omega)t + j2\pi k/K} \\ + \text{higher harmonics} \end{array} \right\} \quad (16)$$

Thus, the introduction of the additional oscillatory inductance causes the generation of other fluctuating flow frequencies in addition to the basic frequency ω under consideration. Clearly, then, higher harmonics, such as $(3\Omega - \omega)$, $(3\Omega + \omega)$, etc., may need to be included in the right-hand side of Eq. (14). However, since we will not pursue the solution for these higher frequencies, those terms will be dropped from further consideration here. For simplicity, we will retain only the terms that effect the frequencies ω , $(\Omega - \omega)$, and $(\Omega + \omega)$. It follows from Eqs. (14) and (16) that, to first order,

$$\tilde{p}_{M,\omega,k} - \tilde{p}_{2,\omega} = -0.5j(\Omega - \omega)L^* \tilde{m}_{2,\Omega-\omega,k} e^{j2\pi k/K} + 0.5j(\Omega + \omega)L^* \tilde{m}_{2,\Omega+\omega,k} e^{-j2\pi k/K} \quad (17)$$

$$\tilde{p}_{M,\Omega-\omega,k} - \tilde{p}_{2,(\Omega-\omega)} = -0.5j\omega L^* \tilde{m}_{2,\omega,k} e^{j2\pi k/K} + 0.5j(2\Omega - \omega)L^* \tilde{m}_{2,2\Omega-\omega,k} e^{-j2\pi k/K} \quad (18)$$

$$\tilde{p}_{M,\Omega+\omega,k} - \tilde{p}_{2,(\Omega+\omega)} = 0.5j\omega L^* \tilde{m}_{2,\omega,k} e^{j2\pi k/K} + 0.5j(2\Omega + \omega)L^* \tilde{m}_{2,2\Omega+\omega,k} e^{-j2\pi k/K} \quad (19)$$

where the additional overbar above the tilde denotes the complex conjugate.

Using the above relations, we can eliminate the intermediate pressures at the point M from the transfer function Eqs. (9) for the frequencies ω , $(\Omega - \omega)$, and $(\Omega + \omega)$. Then, we substitute the decomposition given in Eq. (12) and generate an array of relations for the various fluctuating pressures and mass flow rates by summing the resulting equations over the blade passages using the relations (7), (8), and (11). This yields

$$\tilde{p}_{2,\omega} - \tilde{p}_{1,\omega} = G\tilde{p}_{1,\omega} - (R + j\omega L)\tilde{m}_{2,\omega} + 0.5j(\Omega - \omega)L^* \tilde{m}_{\phi,\Omega-\omega} - 0.5j(\Omega + \omega)L^* \tilde{m}_{\phi,\Omega+\omega} \quad (20)$$

$$\tilde{p}_{2,\Omega-\omega} - \tilde{p}_{1,\Omega-\omega} = G\tilde{p}_{1,\Omega-\omega} - \{R + j(\Omega - \omega)L\}\tilde{m}_{2,\Omega-\omega} + 0.5j\omega L^* \tilde{m}_{\phi,\omega} - 0.5j(2\Omega - \omega)L^* \tilde{m}_{\phi,2\Omega-\omega} \quad (21)$$

$$\tilde{p}_{2,\Omega+\omega} - \tilde{p}_{1,\Omega+\omega} = G\tilde{p}_{1,\Omega+\omega} - \{R + j(\Omega + \omega)L\}\tilde{m}_{2,\Omega+\omega} - 0.5j(2\Omega + \omega)L^* \tilde{m}_{\phi,2\Omega+\omega} \quad (22)$$

Note the two new terms in the first and second transfer function equations and the one new term in the third and observe that these imply interactions between the frequencies. Specifically note how the fluctuating flow rate at the frequency ω feeds into the $(\Omega - \omega)$ frequency but not the $(\Omega + \omega)$ frequency.

Additional important relations are obtained by multiplying each of the array of relations by $e^{-j2\pi k/K}$ or $e^{-j2\pi k/K}$ before summing. These manipulations yield relations for the $\tilde{m}_{\phi,\omega}$ rotating components of the fluctuating mass flow rates as follows:

$$\tilde{m}_{\phi,\omega} = \frac{j(\Omega - \omega)L^*}{2K^2(R + j\omega L)} \tilde{m}_{2,\Omega-\omega} \quad (23)$$

$$\tilde{m}_{\phi,\Omega-\omega} = \frac{j\omega L^*}{2K^2\{R + j(\Omega - \omega)L\}} \tilde{m}_{2,\omega} \quad (24)$$

$$\tilde{m}_{\phi,\Omega+\omega} = -\frac{j\omega L^*}{2K^2\{R + j(\Omega + \omega)L\}} \tilde{m}_{2,\omega} \quad (25)$$

$$\tilde{m}_{\phi,2\Omega-\omega} = -\frac{j(\Omega - \omega)L^*}{2K^2\{R + j(2\Omega + \omega)L\}} \tilde{m}_{2,\Omega-\omega} \quad (26)$$

$$\tilde{m}_{\phi,2\Omega+\omega} = -\frac{j(\Omega + \omega)L^*}{2K^2\{R + j(2\Omega + \omega)L\}} \tilde{m}_{2,\Omega+\omega} \quad (27)$$

and the following for the higher-order surge components:

$$\tilde{m}_{2,\Omega+\omega} = \tilde{m}_{2,2\Omega-\omega} = \tilde{m}_{2,2\Omega+\omega} = \tilde{m}_{2,3\Omega-\omega} = \tilde{m}_{2,3\Omega+\omega} = 0 \quad (28)$$

Note the symmetry in the relations (23) and (24).

Using the above relations $\tilde{m}_{\phi,\omega}$, $\tilde{m}_{\phi,\Omega-\omega}$ and $\tilde{m}_{\phi,\Omega+\omega}$ can be eliminated from Eqs. (20)–(22) so to obtain the coupled transfer function equations for the frequencies ω and $\Omega - \omega$

$$\tilde{p}_{2,\omega} - \tilde{p}_{1,\omega} = G\tilde{p}_{1,\omega} - (R + j\omega L + X_\omega)\tilde{m}_{2,\omega} \quad (29)$$

$$\tilde{p}_{2,\Omega-\omega} - \tilde{p}_{1,\Omega-\omega} = G\tilde{p}_{1,\Omega-\omega} - \{R + j(\Omega - \omega)L + X_{\Omega-\omega}\}\tilde{m}_{2,\Omega-\omega} \quad (30)$$

$$\tilde{p}_{2,\Omega+\omega} - \tilde{p}_{1,\Omega+\omega} = G\tilde{p}_{1,\Omega+\omega} - \{R + j(\Omega + \omega)L + X_{\Omega+\omega}\}\tilde{m}_{2,\Omega+\omega} \quad (31)$$

where the “coupling impedances”

$$X_\omega = \frac{\omega L^{*2}}{2K^2} \frac{\{\omega R - j(\Omega^2 - \omega^2)L\}}{\{R - j(\Omega - \omega)L\}\{R + j(\Omega + \omega)L\}} = Z(\omega) \quad (32)$$

$$X_{\Omega-\omega} = \frac{(\Omega - \omega)L^{*2}}{2K^2} \frac{\{(\Omega - \omega)R - j\omega(2\Omega - \omega)L\}}{\{R - j\omega L\}\{R + j(2\Omega - \omega)L\}} = Z(\Omega - \omega) \quad (33)$$

$$X_{\Omega+\omega} = \frac{\omega L^{*2}}{4K^2} \frac{(\Omega + \omega)(2\Omega - \omega)}{\{R + j(2\Omega + \omega)L\}} \quad (34)$$

Note, again, the symmetry inherent in the impedances, X_ω and $X_{\Omega-\omega}$, such that they may be represented by the single function, $Z(\omega)$, as defined on the right in the Eqs. (32)–(34).

3 Pump Transfer Functions

In conclusion, we have determined the pump transfer function equations, that should be used for the stability analyses for the fluctuating pressures and mass flow rates:

- For the general frequency ω , Eqs. (29) (with Eq. (32) and (4))
- For the companion frequency, $\Omega - \omega$, Eqs. (30) (with Eq. (33) and (4) with $(\Omega - \omega)$ replacing ω)

The consequences of the interactive dynamics unveiled here, the actual stability analyses, will, of course, depend on the system within which the pump is operating. However, even without embarking on such a system-dependent analysis, we can investigate two consequences of the multifrequency transfer functions derived above; namely, we can examine:

- The pressures at various fixed circumferential locations upstream or downstream of the impeller since these are the commonly used diagnostic measurements that are made during testing
- The coupling impedances, $Z(\omega)$ and $Z(\Omega - \omega)$, since this function Z is a primary factor effecting the stability of the system in which the pump might be installed

4 Pressures at Fixed Locations

Commonly, pressure transducers are installed at a number of fixed circumferential locations in order to observe and analyze the instabilities that occur within a cavitating inducer or pump. To examine the form of the pressure fluctuations that the above flow would cause at a fixed circumferential location close to the impeller, we choose to examine the pressures at the blade passage outlet location $i=M$. The pressure fluctuations at other axial locations close to the impeller (upstream or downstream) will have the same basic form and frequency components so confining attention to $i=M$ does not limit the applicability of the results that follow.

First, we note that by using the expression (12) in Eqs. (17)–(19) (and using Eqs. (28)), the fluctuating pressures at the frequencies ω , $\Omega - \omega$, and $\Omega + \omega$ in the frame of reference *rotating with the impeller* can be written in the following form:

$$\text{Re} \left\{ \left(\tilde{p}'_{M,\omega} - \frac{j(\Omega - \omega)L^*}{2K} \tilde{m}_{2,\Omega-\omega} e^{j2\pi k/K} \right) e^{j\omega t} \right\} \quad (35)$$

$$\text{Re} \left\{ \left(\tilde{p}'_{M,\Omega-\omega} - \frac{j\omega L^*}{2K} \tilde{m}_{2,\omega} e^{j2\pi k/K} \right) e^{j(\Omega-\omega)t} \right\} \quad (36)$$

$$\text{Re} \left\{ \left(\tilde{p}'_{M,\Omega+\omega} + \frac{j\omega L^*}{2K} \tilde{m}_{2,\omega} e^{j2\pi k/K} \right) e^{j(\Omega+\omega)t} \right\} \quad (37)$$

where the primes denote modifications in amplitude that are inconsequential to the conclusions of this section; similar expressions for the frequencies $2\Omega - \omega$ and $2\Omega + \omega$ are also needed. These fluctuations in pressure must then be translated into a fixed

or nonrotating frame of reference. To do this, we define a set of nonrotating coordinates as follows: (i) an angular circumferential coordinate, $\theta^* = \Omega t + 2\pi k/K$ and (ii) time, $t^* = t$. One of the complications of this coordinate transformation is that the second terms in Eqs. (35)–(37) now need to be assigned to a different frequency. The resulting fluctuating pressures in the fixed coordinate frame at the frequencies ω , $\Omega - \omega$, and $\Omega + \omega$ then take the following form:

$$\text{Re} \left\{ \left(\tilde{p}'_{M,\omega} + \frac{j\omega L^*}{K} \cos \theta^* \tilde{m}_{2,\omega} \right) e^{j\omega t^*} \right\} \quad (38)$$

$$\text{Re} \left\{ \left(\tilde{p}'_{M,\Omega-\omega} + \frac{j(\Omega - \omega)L^*}{K} \cos \theta^* \tilde{m}_{2,\Omega-\omega} \right) e^{j(\Omega-\omega)t^*} \right\} \quad (39)$$

$$\text{Re} \left\{ \left(\tilde{p}'_{M,\Omega+\omega} \right) e^{j(\Omega+\omega)t^*} \right\} \quad (40)$$

Consequently, the pressure fluctuations that would be observed at fixed, nonrotating circumferential locations near the impeller as a result of the flow constructed in the preceding sections would have the following features:

1. The fluctuating pressures at the basic instability frequency ω would consist of a surge mode whose amplitude varies from one circumferential location to another. It would contain no rotating component. For convenience of discussion, we will refer to this as the “surge” mode and frequency.
2. The fluctuating pressures at the frequency $\Omega - \omega$ would be observed to have two components: a surge component and a component that has a single cell that rotates in the direction of impeller rotation. Though it does contain a surge component we will, for convenience refer to this as the “rotating” mode and frequency.
3. A fluctuating pressure at the frequency $\Omega + \omega$ that has only a surge component (no rotating component).
4. Higher harmonics, $2\Omega - \omega$, $2\Omega + \omega$, etc., and higher cell numbers (arising from terms with more than one circumferential cell).

This paper is focused on the interaction between the surge and rotating modes. We reserve comment on some measured pressure recordings until the end of Sec. 5.

5 Coupling Impedance

Now examine the stability issue in more detail by focusing on the coupling impedance, $Z(\omega)$, defined in Eqs. (32) and (33) and whose consequences are imbedded in Eqs. (29) and (30). Note that $Z(\omega)$ is proportional to the fluctuating inductance squared, L^{*2} . Indeed, the presence of the ratio L^*/K means that this coupling impedance, $Z(\omega)$, is proportional to the square of the inductance of the entire flow in the mixing section downstream of the impeller discharge and before the end of the asymmetry (since inductance is inversely proportional to the cross-sectional area of the flow). In the analysis that follows, this factor appears as the parameter L^*/KL or the ratio of the amplitude of the fluctuating inductance to the main pump inductance.

Next, we examine the variation of the coupling impedance over the range of instability frequencies, $0 < \omega < \Omega$, in order to evaluate its consequences. From Eqs. (29) and (30), we observe that if the real part of the coupling impedance were to become sufficiently negative so that it overcame the pump resistance R and led to a negative total resistance of the pump, $R + \text{Re}\{Z(\omega)\}$, then instability at that frequency ω would be a likely consequence. To investigate this further, we examine the real part of the coupling impedance, $\text{Re}\{Z(\omega)\}$, which, from Eq. (32), can be written as

$$\frac{\text{Re}\{Z(\omega)\}}{R} = \frac{1}{2} \left(\frac{L^*}{KL} \right)^2 Z^*(\xi) \quad (41)$$

where $\xi = \omega/\Omega$ and Z^* is defined as

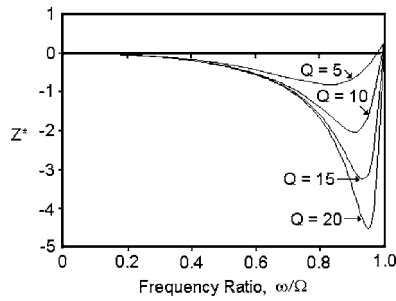


Fig. 3 Coupling resistance function Z^* plotted against the frequency ratio, ω/Ω , for four values of $Q = \Omega L/R$

$$Z^*(\xi) = \frac{\xi^2 \{\Omega L/R\}^2 [1 + (\xi^2 - 1) \{\Omega L/R\}^2]}{[1 + (1 - \xi)^2 \{\Omega L/R\}^2][1 + (1 + \xi)^2 \{\Omega L/R\}^2]} \quad (42)$$

Typical values of $Z^*(\omega/\Omega)$ are presented in Fig. 3 for various typical values of the parameter $\Omega L/R$. Note that Z^* is negative over most of the range $0 < \omega/\Omega < 1$. This negative value could cause $R + \text{Re}\{Z(\omega)\}$ to become negative. Consequently, the potential for instability exists though the outcome depends on the magnitude of L^*/KL , on the parameter $\Omega L/R$ and on the frequency ω .

In Fig. 3, we have chosen to present results for a range of values of $\Omega L/R$. Estimates of the magnitude of this parameter from measurements of the dynamics of a particular cavitating inducer by Ng and Brennen [6] and Brennen et al. [7] (see also [4]) yield values of $\Omega L/R$ that range between about 2 and 20. As another data point we note that a typical value for a centrifugal pump from the measurements of Anderson et al. [11] is ~ 6 . Within this range of $\Omega L/R$, it is clear from Fig. 3 that the most highly negative values of the coupling resistance occur for values of ω just a little less than Ω and in the neighborhood of 0.9Ω . Thus the instability that is most likely is one with a surge mode at a frequency a little less than Ω (say 0.9Ω) coupled with a rotating mode with a low frequency like 0.1Ω .

We might also ask whether the magnitude of $\text{Re}\{Z(\omega)\}$ could approach the magnitude of R so that $R + \text{Re}\{Z(\omega)\}$ could become negative. From Eq. (41), this depends on both Z^* and L^*/KL . From Fig. 3, the magnitude of Z^* can clearly be greater than unity. Moreover, Anderson et al. [11] measured separately the inertances of the impeller (L) and of the volute (L^*/K) for a typical centrifugal pump and found them to be of similar magnitude. Thus, at least in this single example, the magnitude of L^*/KL could be of order unity. Consequently, in the most unstable range of frequency around 0.9Ω , it is quite possible for $-\text{Re}\{Z(\omega)\}$ to exceed R and to cause instability.

In summary, the analysis predicts that if such a coupled instability were to occur for $\Omega L/R$ in the range of 2–20, it would consist of a surge component at a frequency of about 0.9Ω coupled with a rotating component at a frequency of about 0.1Ω . Unlike the conventional rotating cavitation or cavitation surge this instability is not a dynamic instability occurring where the quasistatic pump resistance is positive (and therefore requiring the dynamic cavitation characteristics, such as the mass flow gain factor for its onset) but rather a more basic quasistatic instability similar to compressor stall [3] in which the *effective* resistance becomes negative. It therefore does not depend directly on cavitation, though it is likely that cavitation compliance and mass flow gain factor will enter the analysis when the system response is included in the analysis and that cavitation is likely to encourage the onset of the instability by allowing flexibility for the growth of the surge component. But the bottom line is that this coupled instability, being relatively independent of the cavitation number, could occur at much higher values of that parameter.

The instability characteristics described in the preceding paragraphs precisely correspond with an unusual instability experienced during a recent liquid rocket engine test program. Pressure transducers in water facility tests of that inducer demonstrated the presence of a surge component at 0.9Ω coupled with a rotating component at 0.1Ω . Moreover, the instability developed at cavitation numbers of the order of 0.04–0.1, well above the values at which cavitation surge or rotating cavitation might be expected. It was also a function of the flow coefficient, showing a particular tendency to develop at flow coefficients below the design value.

6 Conclusions

Recent experience with rocket engine turbopumps has demonstrated that there exist instability modes in cavitating pumps/inducers that are more complex than the traditional rotating cavitation and cavitation surge instabilities. This paper investigates the possibility of such an instability that involves the coupling of a surge mode and a rotating mode. The instability is triggered, in part, by asymmetry in the pump discharge that excites surge within the individual blade passages. It is shown that this leads to a “coupling impedance” that has a negative resistance over a range of frequencies and can therefore lead to a negative pump resistance, which could cause instability. Moreover, it is shown that in a likely parameter range for cavitating inducers, the most unstable case involves the coupling of a surge mode at about 0.9Ω with a rotating component at 0.1Ω . Furthermore, since the instability does not depend essentially on the presence of cavitation (unlike the traditional cavitating surge) it could occur at significantly higher cavitation numbers than surge or rotating cavitation. All of the characteristics of this nontraditional instability described above were observed while conducting a recent series of liquid engine ground tests.

Acknowledgment

The author wishes to acknowledge the comments of Sheldon Rubin [9], who, many years ago, suggested that we should consider the dynamics inherent in the different parallel flow paths within a pump and volute system. I also wish to thank Tom Zoladz and the NASA George Marshall Space Flight Center for their support under Grant No. NAG8-1934.

Nomenclature

- C = pump cavitation compliance
- $G+1$ = pump gain
- j = $(-1)^{1/2}$
- k = 1, 2, ... K denotes a particular blade passage
- K = number of impeller blade passages
- L = pump inertance
- L^* = fluctuating discharge inertance amplitude
- L^{**} = fluctuating discharge inertance
- m_i = mass flow rate at the location, i
- $m_{i,k}$ = mass flow rate in the blade passage k at the location i
- \bar{m}_i = time-averaged mass flow rate at the location i
- $\tilde{m}_{i,\omega}$ = complex amplitude of the fluctuating mass flow rate at the location i and frequency ω
- $\tilde{m}_{i,\omega,k}$ = complex amplitude of the fluctuating mass flow rate at the location i in the impeller blade passage k and at frequency ω
- $\tilde{m}_{i,\xi}/K$ = surge component of the fluctuating mass flow rate at the location i and frequency ξ
- $\tilde{m}_{\phi,\xi}/K$ = rotating component of the fluctuating mass flow rate at the frequency ξ
- M = pump mass flow gain factor
- p_i = total pressure at the location i

$p_{M,k}$ = total pressure in the blade passage k at the location M
 \bar{p}_i = time-averaged total pressure at the location i
 $\tilde{p}_{i,\omega}$ = complex amplitude of the fluctuating total pressure at the location i and frequency ω
 $\tilde{p}_{i,\omega,k}$ = complex amplitude of the fluctuating total pressure at the location, i , in the impeller blade passage k and at frequency ω
 R = pump resistance
 $\text{Re}\{\}$ = denotes "the real part of"
 t = time
 X_ξ = coupling impedance for the frequency ξ
 $Z(\xi) = X_\xi$
 $Z^*(\omega/\Omega)$ = dimensionless coupling impedance function
 $\theta^* = \Omega t + 2\pi k/K$
 ξ = denotes a general radian frequency
 ω = radian frequency of fluctuation
 Ω = radian frequency of impeller rotation
 \sim = denotes complex conjugate when placed above

References

- [1] Rubin, S., 1966, "Longitudinal Instability of Liquid Rockets Due to Propulsion Feedback (Pogo)," *J. Spacecr. Rockets*, **3**(8), pp. 1188–1195.
- [2] NASA, 1970, "Prevention of Coupled Structure-Propulsion Instability," NASA SP-8055.
- [3] Brennen, C. E., 1994, *Hydrodynamics of Pumps*, Concepts ETI and Oxford University Press, London.
- [4] Rubin, S., 2004, "An Interpretation of Transfer Function Data for a Cavitating Pump," 40th AIAA/ASME/SAE/ASEE Joint Propulsion Conf., Paper No. AIAA-2004-4025.
- [5] Brennen, C. E., and Acosta, A. J., 1976, "The Dynamic Transfer Function for a Cavitating Inducer," *ASME J. Fluids Eng.*, **98**, pp. 182–191.
- [6] Ng, S. L., and Brennen, C. E., 1978, "Experiments on the Dynamic Behavior of Cavitating Pumps," *ASME J. Fluids Eng.*, **100**(2), pp. 166–176.
- [7] Brennen, C. E., Meissner, C., Lo, E. Y., and Hoffman, G. S., 1982, "Scale Effects in the Dynamic Transfer Functions for Cavitating Inducers," *ASME J. Fluids Eng.*, **104**, pp. 428–433.
- [8] Brennen, C. E., 1978, "Bubbly Flow Model for the Dynamic Characteristics of Cavitating Pumps," *J. Fluid Mech.*, **89**(2), 223–240.
- [9] Rubin, S., 1975, Personal communication.
- [10] Bhattacharyya, A., 1994, "Internal Flows and Force Matrices in Axial Flow Inducers," Ph.D. thesis, California Institute of Technology.
- [11] Anderson, D. A., Blade, R. J., and Stevens, W., 1971, "Response of a Radial-Bladed Centrifugal Pump to Sinusoidal Disturbances for Non-Cavitating Flow," NASA TN D-6556.

Experimental Investigation of the Fluid Motion in a Cylinder Driven by a Flat-Plate Impeller

Douglas Bohl

Department of Mechanical and Aeronautical
Engineering,
Clarkson University,
Potsdam, NY 13699-5725

The flow field in a cylindrical container driven by a flat-bladed impeller was investigated using particle image velocimetry (PIV). A range of Reynolds numbers (0.005–7200), based on the container radius r_w , were investigated using four Newtonian fluids: water ($Re=7200, 6800$), 85/15 glycerin/water mixture ($Re=108$), pure glycerin ($Re=8$), and corn syrup ($Re=0.02, 0.005$). Two impellers with a radius of $0.43r_w$ and $0.95r_w$ were used to drive the flow. The $0.43r_w$ impeller was shown to generate a vortex near the tip of the blades. The peak magnitude of the vortices and the size of the vortices in the radial direction decreased with increasing Reynolds number. Additionally, the vortex generated at the high Reynolds number was unsteady with a trailing shear layer that periodically shed vorticity into the flow field. The structure of the flow in the region between the blade and the cylinder wall showed a Reynolds number dependence, though the two lowest Reynolds number (0.02 and 8) flows investigated had quantitatively similar flow structures. These cases were found to have a closed region of reverse flow between the blade tip and the cylinder wall. No recirculating flow was indicated for the $Re=108$ and 7200 cases. These data indicate that there may be a critical condition below which there is little dependence in the flow structure on the Reynolds number.

[DOI: 10.1115/1.2734186]

1 Introduction

The Navy has an expressed interest in increasing the safety of its shipboard energetic materials (i.e., explosives, propellants, pyrotechnics). This desire has been driven by past accidents, such as the USS Forrester fire. The sensitivity of an energetic material (i.e., the response of an energetic material to external stimuli) depends on both the components in the formulation as well as in the production quality. Historically, work in decreasing the sensitivity of an energetic material has focused on the formulation components; however, the final mixture quality of the material can also affect the sensitivity. For example, many energetic materials are composed of energetic crystals (e.g., RDX or HMX) mixed in a polymeric binder that is then cured. Research has shown that coating individual energetic crystals reduces the sensitivity of the crystals [1]. By extension, it is accepted that a high fraction of an inert polymeric binder in an energetic formulation will reduce its sensitivity, but the benefits are negated if the mixture quality is poor and energetic crystals are clumped, touching each other, even if only at discrete locations dispersed throughout the composite. To increase the control over the manufacturing process and mixture quality, detailed understanding of the science of the mixing process must replace the art of the current methods.

Two methods are primarily used to manufacture energetic materials: batch (e.g., planetary mixers) and continuous systems (e.g., twin-screw extruders). Batch mixers, similar to food mixers, have been the primary method for the processing of energetic materials in the United States because they offer several advantages, including the possibility for long residence times, low damage potential to the energetic crystals, and the ability to add multiple ingredients relatively simply during processing. These advantages are balanced by the inherent drawbacks to a batch-mixing process: inconsistent mixture quality, residual voids and fissures, lower allowed material viscosity which limits the solids

that can be loaded into the mixture, limited pot life of the material being mixed, and the need for the use of environmentally hazardous solvents.

The use of batch mixers in industrial applications has a long history. The experimental study of these devices is, however, complicated by several factors, which include rheological properties of the fluids, complex geometries, and device scaling issues. Recent interest in developing more efficient, controllable mixing processes has focused attention on developing a better understanding on the physics of these devices. To facilitate improvements in designs and processes, both experimental and computational approaches have been utilized. The development of computational tools is attractive in that computational tools allow for relatively rapid and simple changes to both geometry and operating conditions to determine optimal mixing protocols. However, the development of computational tools has been hampered because of a lack of experimental data for model development and comparative validation.

Experimental work on planetary mixers is somewhat limited. Zhou et al. [2] investigated, experimentally, the power consumption in a double planetary mixer with Newtonian and non-Newtonian fluids. Time-dependant measurements of power indicated a dependence of the instantaneous power with the blade/wall distance. Instantaneous torque was found to vary by up to 170% between the minimum and maximum value, indicating care must be taken when scaling mixers up. The power curve for non-Newtonian fluids was found to collapse to the curve for Newtonian fluids when the Metzner-Otto Reynolds number was used for scaling. Tanguy et al. [3] numerically modeled the mixing process in a twin-blade planetary mixer for fluids with a Bingham number (Bi) ranging from 0 (Newtonian) to 40. It was concluded that the yield stress of the fluid affected the dispersive mixing characteristics and power consumption of the process. It was shown numerically that as Bi increased the fluctuations in the power consumption also increased. The cause of this behavior was inferred to be associated with a change in flow structure.

Youcefi et al. [4] experimentally and computationally investigated the effect of fluid elasticity on the flow induced by a rotating

Contributed by the Fluids Engineering Division of ASME for publication in the JOURNAL OF FLUIDS ENGINEERING. Manuscript received November 1, 2005; final manuscript received November 16, 2006. Review conducted by James A. Liburdy.

flat-plate impeller. In this work, pointwise measurements with a hot film anemometer, as well as flow computations, were made in the gap region between the blade and the cylinder walls. Torque measurements were also made and used to determine the power number as a function of the fluid type and Reynolds number. It was found that the power number data collapsed onto a single curve for all Newtonian and non-Newtonian pseudoplastic fluids when the effective Reynolds number was used for the pseudoplastic fluids. However, viscoelastic fluids did not follow the same linear decrease in power number with increasing Reynolds number. The deviation from the Newtonian curve occurred for apparent Reynolds numbers greater than $R_{crit}=20-28$. The viscoelastic fluids showed different velocity profiles in the gap region from those of the Newtonian fluids, and the difference in the power number relationship was inferred to be a result of the different flow fields.

Recently, researchers have started to apply optical measurement techniques to better understand the flow field in mixing devices. Examples include Jaffer et al. [5] who applied particle image velocimetry (PIV) to kneading elements in a twin-screw extruder; Balkis and Karwe [6] who used laser doppler velocimetry (LDV) to measure the velocity profiles in the nip and translation regions of a twin-screw extruder; Yoon et al. [7] who investigated the flow in a Rushton turbine using PIV. These studies have shown the utility in applying the nonintrusive diagnostic technique to better understand the flow fields in these devices.

Currently, there is a lack of fundamental understanding of the fluid motions and mixing process in batch mixers. Understanding the fluid motions and mixing characteristics in these devices is essential to taking full advantage of available ingredients when formulating insensitive energetic materials, as well as producing final product with consistent properties from run to run. The current work was undertaken in support of the development of computational tools for the modeling of low Reynolds number mixing devices. The goals of the work were to: (i) map out local flow properties (e.g., the velocity, vorticity) to identify the fluid structures and inferred mixing potential in a simplified batch mixer, (ii) determine the effects of Reynolds number on the flow structure, and (iii) support the development of computational tools for the processing of energetic materials being carried out in parallel with this study. In the first phase of the code development motion of Newtonian fluids in a two-dimensional (2D) flow field were to be calculated. This phase of the code work motivated the current work, which looks at a simple 2D flow field over a range (0.005–7200) of Reynolds numbers.

2 Low Reynolds Number, High-Viscosity Mixing

In moderate to high Reynolds number flows, mixing is accomplished via the large- and small-scale motions typically associated with turbulence. However, in the current flows under consideration (i.e., highly viscous, low-speed flows) small-scale motions are not available and mixing is a result of large-scale motion in the flow. Most energetic materials are a mixture of solid particles (energetic crystals, fuels, and oxidizers) with varying properties (i.e., size, density, chemical composition, etc.) in a polymeric binder. When mixing energetic compounds, the goal is to produce a homogenous distribution of solid particles isolated from each other by the polymeric binder. Mixing of multiple components under these conditions can be broken down into two categories [8]: dispersive and distributive mixing. In distributive mixing, multiple ingredients are homogenized into a single uniform mixture by applying high strain to the mixture. The strain increases the interfacial area between the materials causing the mixture to achieve uniformity. Dispersive mixing is the action of breaking material components down into smaller particles or regions. In this case, the reduction of particle sizes is a result of high stress (i.e., strain rate) in the flow field. The mixing of energetic materials requires dispersive mixing to break clumps of solids ingredi-

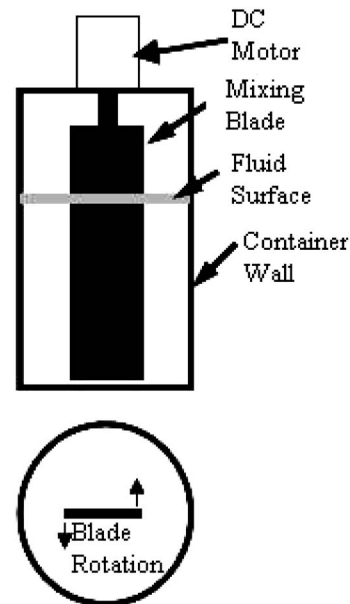


Fig. 1 Schematic representation of flat-plate mixer apparatus

ents into individual particles and distributive mixing to create a homogeneous distribution within the polymeric binder.

For many polymeric materials, the types of deformations that a material being processed experiences not only influences the dispersion of materials within a mixture but it can also influence the structure and final properties of the cured polymer [9]. In order to address this issue, three types of deformations can be defined [9]: extensional, shear, and rotational. Historically, a single parameter has been sought that would describe the local flow type based on vorticity and strain. There is no agreement on a universal definition for this parameter. In this work, the definition of a flow number, which describes the type of deformation experienced locally in the flow field, is taken from the works of Jongen [9] and Asatarita [10] and can be defined as a ratio of the strain and vorticity in a 2D flow as

$$D = \frac{1 - R^2}{1 + R^2} \quad (1)$$

$$R^2 = \frac{\omega^2}{s^2} \quad (2)$$

In Eq. (2), ω is the vorticity and s is the rate of strain. When $D = -1$, the flow is purely rotational, $D=0$ is a pure shear flow, and $D=1$ is a purely extensional flow. Dispersive and distributive mixing will be a primary result of extensional and shear flow. Rotational flow does not promote interaction between regions of the flow and is therefore ineffective in the mixing process [9]. It is important to realize that, in addition to flow type, the residence time and actual magnitudes (e.g., shear, shear rate) of the mixing process also play a significant role in the final material properties. Additionally, it should be noted that the definition of flow type is valid for planar flow and neglects motions in the third direction.

3 Experimental Methods

Figure 1 shows a schematic of the experimental apparatus. A clear acrylic cylindrical flat-bottomed container was constructed with an inside radius of $r_w=6.93$ cm. Fluid motion was generated by a flat stainless steel blade placed in the cylinder such that the long axis of the blade was parallel to the z -axis of the container. The blade was positioned in the center of the bowl and rotated about its long axis by a variable-speed DC motor. The geometry was chosen as a simplified first-order model of a batch mixer to

Table 1 Experimental parameters

Fluid	Impeller radius	Imp. freq.	ν (m ² /s ²)	Re
	r_b (cm)	f (hz)		
Water	6.58	0.240	1.0×10^{-6}	7200
Water	2.99	0.226	1.0×10^{-6}	6800
85/15	6.58	0.243	6.77×10^{-5}	108
Glycerin/water	2.99	0.246	6.77×10^{-5}	108
85/15				
Glycerin/water	6.58	0.243	9.13×10^{-4}	8
Glycerin				
Glycerin	2.99	0.236	9.13×10^{-4}	8
Corn syrup	6.58	0.0182	0.114	0.005
Corn syrup	2.99	0.0613	0.114	0.02

provide simple, well-defined boundary conditions that could be used to aid model development and provide validation data for the developed computational tools.

Four Newtonian fluids, water, and 85/15 (by mass) glycerin/water mixture, glycerin, and corn syrup were used as working fluids. The Reynolds number was defined as $Re = 2\pi f r_w^2 / \nu$, where f is the rotational frequency of the mixing blade and r_w is the radius of the mixing bowl. Experimental parameters can be found in Table 1. The Reynolds numbers ranged from 7200 to 0.005 while the rotational frequencies ranged from 0.24 to 0.06 Hz. Frequencies were chosen for the low Reynolds number cases to minimize the deformation of the free surface and prevent entrainment of air into the fluid. Youcefi et al. [4] showed a change in the flow structure at a Reynolds number of approximately 20 and the two mid-Reynolds number cases (8, 108) bracket this transition. Water was used as a reference case and provided a high Reynolds number data set. The fluid column was 17.75 cm ($2.6r_w$) high and open to the laboratory air on top. Two mixing plates with widths of $r_b = 2.99$ cm ($0.43r_w$; the “half” blade) and 6.58 cm ($0.95r_w$; the “full” blade) were used individually to drive the flow. The half blade provided a similar experimental setup to that studied by Youcefi et al. [4] and also allowed for off-center rotation in future studies while the full blade provided direct-driving motion over nearly the entire cylinder volume. The blades had a thickness of 0.14 cm ($0.02r_w$) with a gap of 0.6 cm ($0.09r_w$) between the blade and the bottom of the container.

The 2D velocity in the fluid was measured using particle image velocimetry (PIV) in the midplane of the fluid in the mixing bowl. Briefly, PIV relies on seed particles in a fluid that scatter light from a thin laser sheet created in the plane of interest. These particles may exist within the fluid naturally or be added to the fluid before measurements are made. The particles in the flow are imaged twice with a short, known delay between images. The displacement of the particles, or groups of particles, is determined via pattern matching techniques and a local velocity vector is calculated by dividing the displacement by the time between images. The velocity can be determined at discrete points over the entire image, and the 2D velocity field in the plane of the laser sheet can be assembled. Other kinematic quantities, such as vorticity, strain, and stress, can then be calculated using the planar velocity field. A detailed discussion of PIV can be found in Keane and Adrian [11].

In the current work, the working fluids were seeded with 10 μ m silver-coated glass spheres. The settling rate of these spheres in water was four orders of magnitude smaller than the flow speeds investigated and could therefore be considered neutrally buoyant in water during the short delay times used. They also showed no tendency to either settle or float in either glycerin or corn syrup. Light was provided by a 4W Spectra Physics Argon Ion laser. The mixing blades were painted with flat black paint to reduce the reflections due to the laser sheet in the measurement region. The laser light was pulsed using a NM Laser Products fast

mechanical shutter. This shutter had a minimum closed-open-closed cycle time of 1 ms. This was short enough that the imaged particles did not experience blurring during the exposure time. Images were captured using a Cooke Corporation Sencicam-QE CCD camera. The acquired images had a resolution of 1376 \times 1040 with eight bits of image depth.

The displacement of groups of particles was determined using the direct correlation technique described in Gendrich and Koochesfahani [12]. Each FOV was approximately 8.7 cm \times 12 cm in size (0.0087 cm/pixel). Delay times between the images ranged from 7 ms to 60 ms and were set to give maximum displacements of nominally ten pixels. The choice of delay time represents a compromise between maximizing dynamic range (i.e., high Δt decreases the effect of the correlation error on the velocity measurements) and making an instantaneous, local, measurement (i.e., if $\Delta t = 0$). The source windows used in the correlation technique were 45 \times 45 pixels with a 50% overlap.

The flow field under investigation was periodic in nature, with the periodicity linked to the motion of the mixing blade, which allowed the data to be phase averaged with respect to the motion of the blade. The blade phase, ϕ , was defined such that 1/2 rotation was given for $\phi = 0$ to 1 (i.e., ϕ ranged from 0 to 2 for a complete blade rotation). This allowed data from multiple experiments and multiple fields of view (FOV) to be combined to form a single data set. For all cases, except the highest Reynolds number cases, 788 images (4 sets of 197 images) were acquired. This resulted in ~ 12 measurements to be averaged at each phase bin over the measurement field. Investigation of the data showed that these results were repeatable to better than the experimental error at nine measurements per bin. At the highest Reynolds number, the flow field was significantly more unsteady. At this Reynolds number, 4925 images (25 sets of 197 images) were used. There were ~ 76 measurements averaged for each phase bin. These data also collapsed to within the measurement error.

The error in the velocity measurements is limited by the ability to measure the displacement of the particles between images. The correlation technique used to process the data in this work is well documented [11] and has a 95% uncertainty level of 0.1 pixel, meaning that 95% of the measurement will be correct to better than 0.1 pixel. Given the FOV for the images, and the delay time between images the uncertainty in the instantaneous velocity measurements was estimated to be 0.08 cm/s for the $f \sim 0.2$ Hz cases and 0.01 cm/s for the $f = 0.02$ and 0.006 cases. The data presented in this work are phase-averaged results. In addition to allowing multiple experimental results to be combined, phase averaging also reduces the measurement error in the final velocity. Phase averaging and the combining of multiple data sets allowed multiple individual measurements to be averaged for a single measurement location. This reduces the estimated error in the presented data by a factor of 2–0.04 cm/s and 0.003 cm/s, respectively. Local vorticity was calculated using a second-order finite difference method using the spatially nearest velocity measurements. The data point spacing is assumed to be precise, and therefore, only given the error levels in the phase-averaged velocity measurements affect the error level in the phase-averaged vorticity. Vorticity error values were estimated to be 0.38 s⁻¹ and 0.16 s⁻¹ for the high- and low-frequency cases, respectively.

All data presented in this work are from PIV measurements taken at the midheight of the fluid column. Data not shown here indicated that the flow field was independent of the z location over the middle half of the mixing blade.

4 Results and Discussion

4.1 Phase Averaged Velocity and Vorticity, “Half Blade.”

Figure 2 shows the vorticity and vector fields at $\phi = 0.008$ for the $Re = 0.02$, 109, and 6800 half-blade cases. Related velocity and vorticity profiles are shown in Fig. 3. In all cases, a vortex was observed at the tip of the mixing blade that rotated with the blade

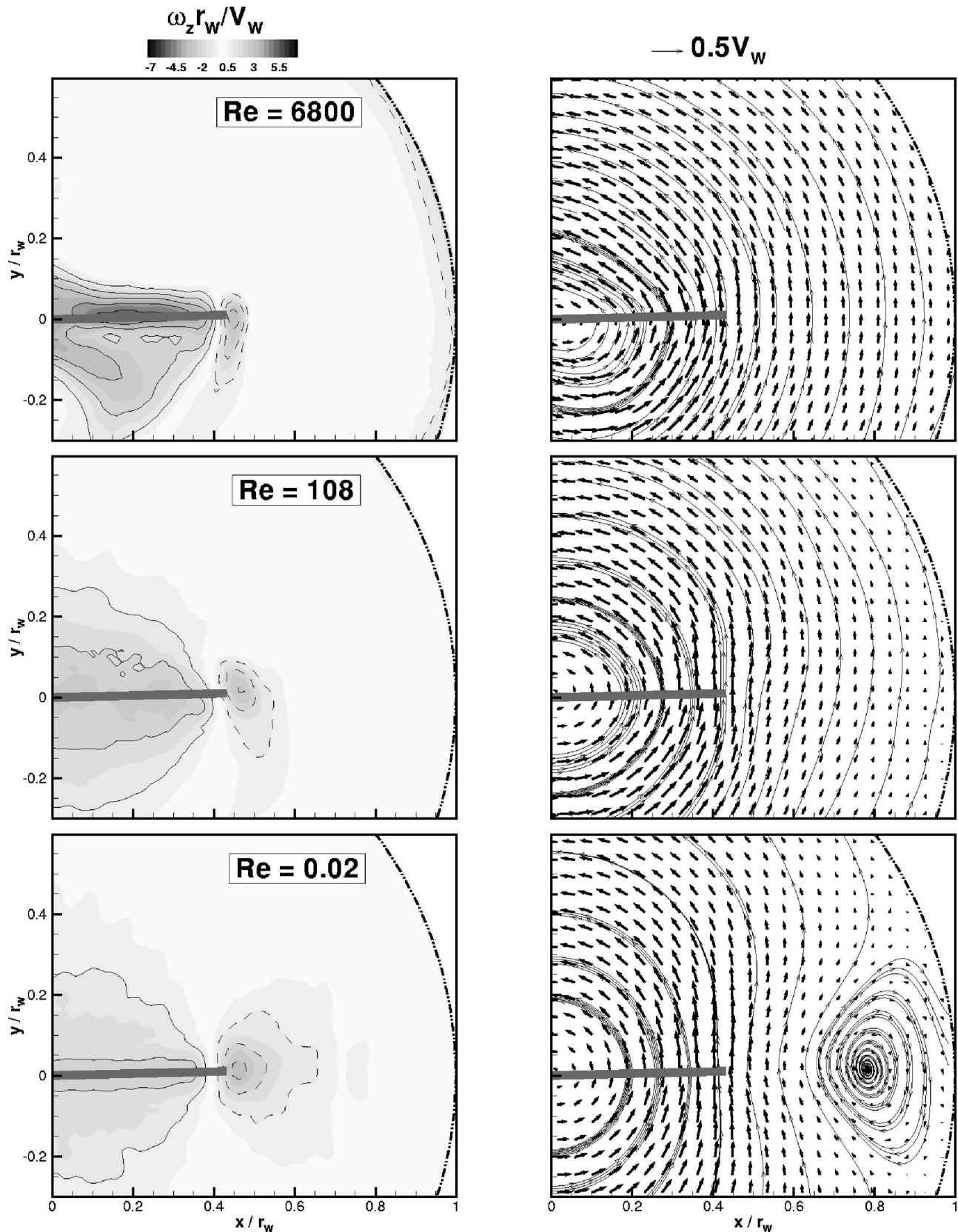


Fig. 2 Phase-averaged vorticity and velocity vectors for the low, mid, and high Reynolds number cases, half blade. Lined contours show $\langle \omega_z \rangle r_w / V_w = \pm 1, 2, 3, \dots$. Blade rotation is in the counterclockwise direction.

as it swept through the cylinder. The structure of these vortices was observed to be a function of the Reynolds number. At $Re = 6800$, a concentrated, locally maximum area of vorticity was

observed very near the tip of the blade with a region of vorticity trailing behind the vortex. Instantaneous data, not shown here, indicated that the vorticity in the trailing shear layer was unsteady

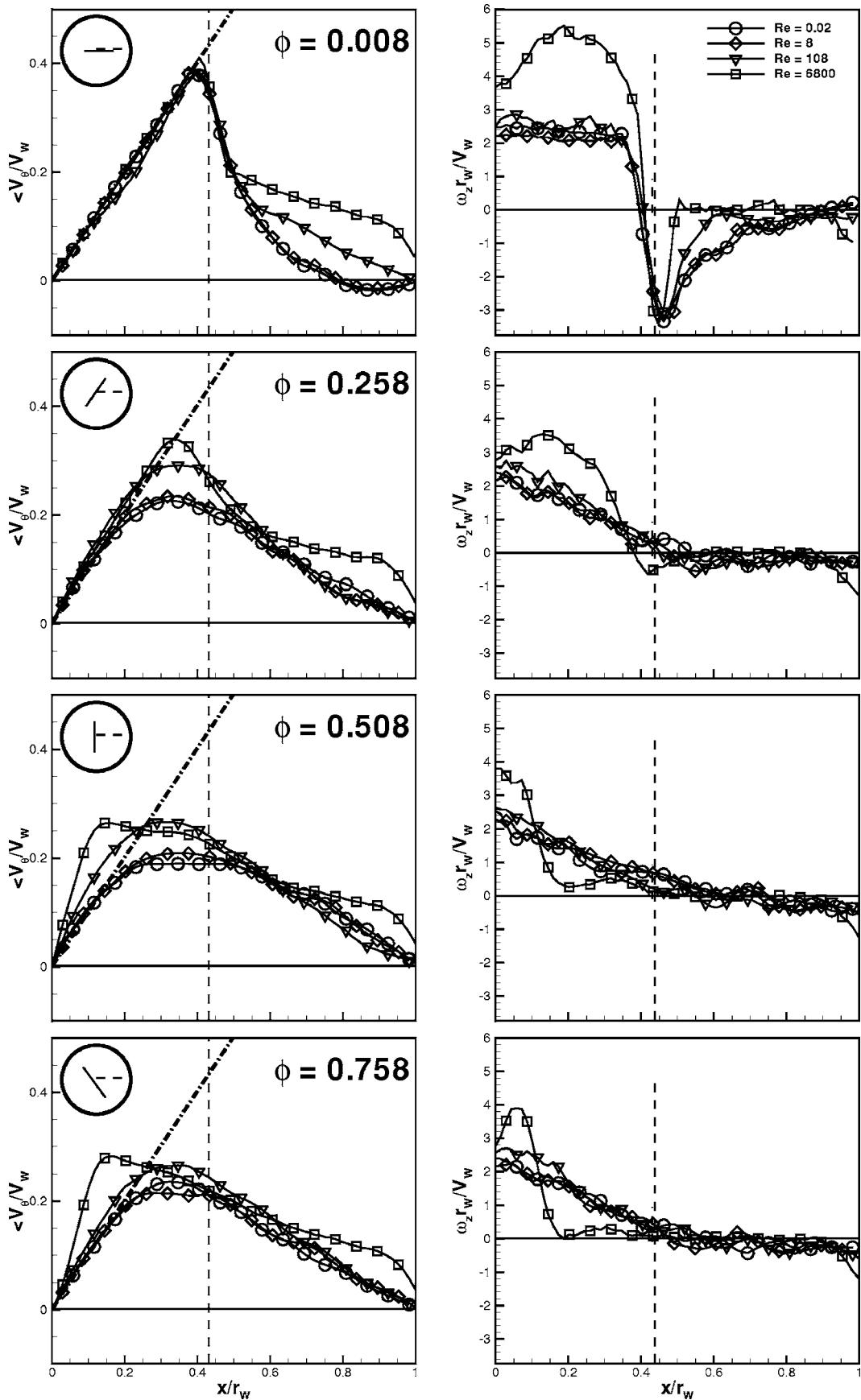


Fig. 3 Phase-averaged tangential velocity and vorticity profiles for the half-blade cases. Blade position (black line) shown schematically with respect to profile location (dashed). Blade tip location indicated by dashed-dotted line in plot. Dashed-dotted line in plot is linear velocity profile based on rotational frequency and radial location. Error levels indicated by symbol size.

and would periodically shed into the surrounding flow field. At $Re=109$, a compact region of vorticity was again observed at the tip of the blade though it extended further in the radial direction toward the cylinder wall. A trailing shear layer was also observed though it was thicker and had lower magnitudes than was observed at $Re=6800$. At $Re=0.02$, there was no trailing vorticity layer observed. The vortex appeared to be nearly symmetric about the blade tip and extended furthest, radially, of all cases.

Along the blade surfaces, the $Re=6800$ case shows asymmetry between the leading and trailing surfaces of the mixing blade. This asymmetry was not as pronounced for either the $Re=109$ or 0.02 cases. At $Re=6800$, a region of high vorticity (at $x \approx 0.1r_w$, $y \approx -0.1r_w$) lifted away from the blade surface on the trailing surface, indicating the flow may have separated from the blade surface. This separated region was observed to rotate with the blade. Instantaneous measurements not shown here also indicated that the vorticity in this region was also unsteady.

The velocity vector fields indicate that the flow structure changed as the Reynolds number changed. Streamlines for the $Re=0.02$ case show a closed recirculation region between the tip of the mixing blade and the cylinder wall. Note that the coordinate system was fixed in the laboratory frame of reference. The streamlines in the gap region were found to curve in towards the blade for this case. Within the region of the flow that the blade sweeps through ($x, y < 0.43r_w$), the streamlines appear to be nominally circular with some stretching in the direction perpendicular to the mixing blade. The $Re=109$ case shows the streamline curvature near the blade tip as was observed at $Re=0.02$; however, it was much less pronounced and no closed recirculation region was observed. Within the sweep of the blade, the streamlines appear flatter above and below the blade resulting in nominally oval, rather than round, patterns. The $Re=6800$ case showed no inward curvature of the streamlines near the blade tip. Within the blade sweep area, the streamline patterns were asymmetric.

Tangential velocity and vorticity profiles are shown in Fig. 3 for four different phases. The blade position relative to the profile location is shown schematically in Fig. 3 for each phase considered. It is instructive to note that the $Re=0.02$ and $Re=8$ cases showed very little difference in either the tangential velocity or vorticity profiles though small differences were observed in the tangential velocity profiles for $\phi=0.508$ and 0.758 near the location of the peak tangential velocity ($x \approx 0.35r_w$). This result indicates the flow structure may not be Reynolds number dependent below a certain threshold value.

For $\phi=0.008$, the flow on the upstream side of the mixing blade varied linearly with the x position matching the blade rotational speed as expected. The linear profile did not extend to the tip of the blade for any of the cases, though it did extend slightly further out for the $Re=6800$ and 109 cases with slightly higher maximum tangential flow speeds observed. All cases showed a similar initial decrease in the tangential velocity beyond the blade tip ($0.43r_w < x < 0.5r_w$). Beyond that point, the profiles show a Reynolds number dependency. At the $Re=8$ and 0.02 , the tangential velocity was negative for $x > 0.77r_w$, returning to zero at the wall consistent with the observed vector fields. Beyond $x \approx 0.5r_w$, the $Re=109$ case displayed a nominally linear decrease toward zero at the wall. A linear decrease in the tangential velocity was also observed for the $Re=6800$ case beyond $x \approx 0.5r_w$ though it was a slower decrease than was observed for the $Re=109$ case. At $x \approx 0.9r_w$, the decrease in the velocity profile became more rapid as the effects of the wall boundary layer were encountered. These data illustrate the decreasing importance of the fluid viscosity in the flow field as the Reynolds number increased.

The data in Fig. 3 for $\phi=0.008$ are in qualitative agreement with the calculated results of Youcefi et al. [4], which showed evidence of a recirculating region at a Reynolds number of 4 but not 40. Note that Youcefi et al. [4] defined the Reynolds number

using the plate radius ($0.5r_w$) rather than the cylinder radius. Numbers reported in this work are converted to the current definition for consistency. The profile at $Re=40$ is qualitatively similar to the profile shown here for the $Re=109$ case of the current work.

Constant vorticity was observed for the $Re=0.02$, 8 , and 109 cases along the blade ($\phi=0.008$), indicating that the flow experienced solid body rotation near to the blade surface for these cases. The $Re=6800$ case showed both significantly higher vorticity magnitudes and increasing vorticity magnitudes along the blade over the central half the blade length. After this point, the vorticity levels decreased as the tip of the blade was approached. This result was consistent with the lifting of the vorticity layer from the blade surface shown in Fig. 2. The magnitude of the peak vorticity value in the tip vortex decreased by 20% (from 3.05 to 2.39) as the Reynolds number increased. The radial extent of the tip vortex also decreased with increasing Reynolds number. The $Re=0.02$ and 8 cases showed slight positive vorticity at the wall due to the reverse flow.

The velocity profiles for the other phases shown deviate from the linear profile shown for $\phi=0.008$. The peak tangential speeds dropped for all cases, and the location of the peak moved toward the center of rotation for the $Re=6800$ case. The data at $\phi=0.508$ for the $Re=8$, 109 cases agree qualitatively with the Youcefi et al. [4] calculations at similar Reynolds numbers. The results do show some difference in the peak tangential velocity, which was lower in the current work. The shorter blade in the current work may explain this difference. It was interesting to note that the vorticity in the wall boundary layer showed only slight variation in magnitude after the blade tip passes (i.e., $\phi \neq 0.008$).

4.2 Phase-Averaged Velocity and Vorticity, "Full Blade".

Phase-averaged vorticity and velocity vectors for the full blade are shown in Fig. 4. Line profiles of the tangential velocity and vorticity at four phases in the cycle are shown in Fig. 5. The Reynolds number dependence of the flow is clear in these figures. The separation of the vorticity along the blade was again evident for the $Re=7200$ case, and the flow field was asymmetric about the mixing blade (Fig. 4). The $Re=108$ case showed a radial variation in the vorticity along the blade observable in both the contour maps of Fig. 4 and the vorticity profile in Fig. 5 at $\phi=0.008$. The highest vorticity was located further out ($x \approx 0.65r_w$) compared to the $Re=7200$ case ($x \approx 0.5r_w$). The vorticity along the blade at $Re=0.005$ was found to be nearly symmetric about the leading and following sides of the blade.

The vorticity near the cylinder walls showed a progressively decreasing peak level and an increasing penetration into the flow field with decreasing Reynolds number (Figs. 4 and 5). At $Re=7200$, the high vorticity (with nondimensional vorticity levels of < -10) was limited to a thin area ($0.09r_w$), approximately the size of the gap between the blade tip and the wall, and appeared to persist at nearly the same thickness along the entire circumference of the cylinder wall. While the peak wall vorticity value was observed at $\phi=0.008$ (~ 12), for this case the magnitude of the vorticity near the wall decreased only slightly at other phases from ~ 8 at $\phi=0.258$ to ~ 6 at $\phi=0.758$. The wall boundary layer has a different structure for the other Reynolds number cases. While the wall boundary layer also persisted around the circumference of the container, the vorticity levels were lower for the $Re=109$ and 0.005 cases, compared to the high Re case. In both the $Re=109$ and 0.005 cases, the wall boundary layer was thinnest at the tip of the blade and thickened on either side of the blade.

4.3 Time-Averaged Velocity and Vorticity. The mean velocity and vorticity fields are shown in Fig. 6. The high Reynolds number case showed distinct stages in the average tangential velocity profiles with clear transition points (Fig. 6(a)). In contrast, the low Reynolds number cases show smooth velocity profiles with no distinct transitions in the profile functionality. The half-

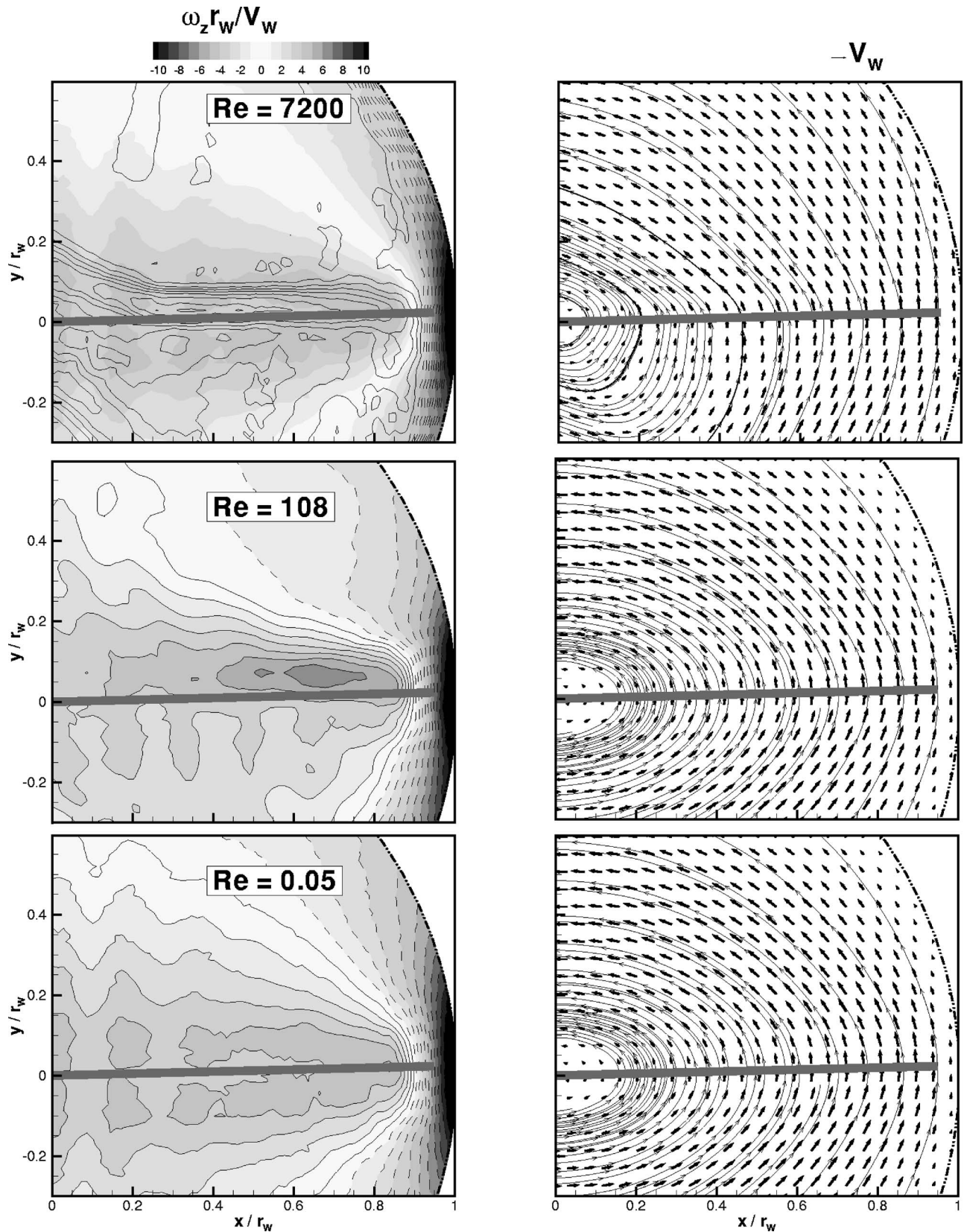


Fig. 4 Phase-averaged vorticity and velocity vectors for the low, mid, and high Reynolds number cases, full blade. Lined contours show $\langle \omega_z \rangle r_w / V_w = \pm 1, 2, 3, \dots$. Blade rotation is in the counterclockwise direction.

blade cases have a peak tangential velocity at nominally the same radial location, $x=0.37r_w$, though the peak magnitude for the $Re=0.02$ and 8 cases were 13% lower. The location of the peak

tangential velocity for the full-blade cases did not coincide spatially as was noted for the half-blade cases. The location of the peak tangential velocity was found at $x=0.58r_w$ for $Re=0.005$ and

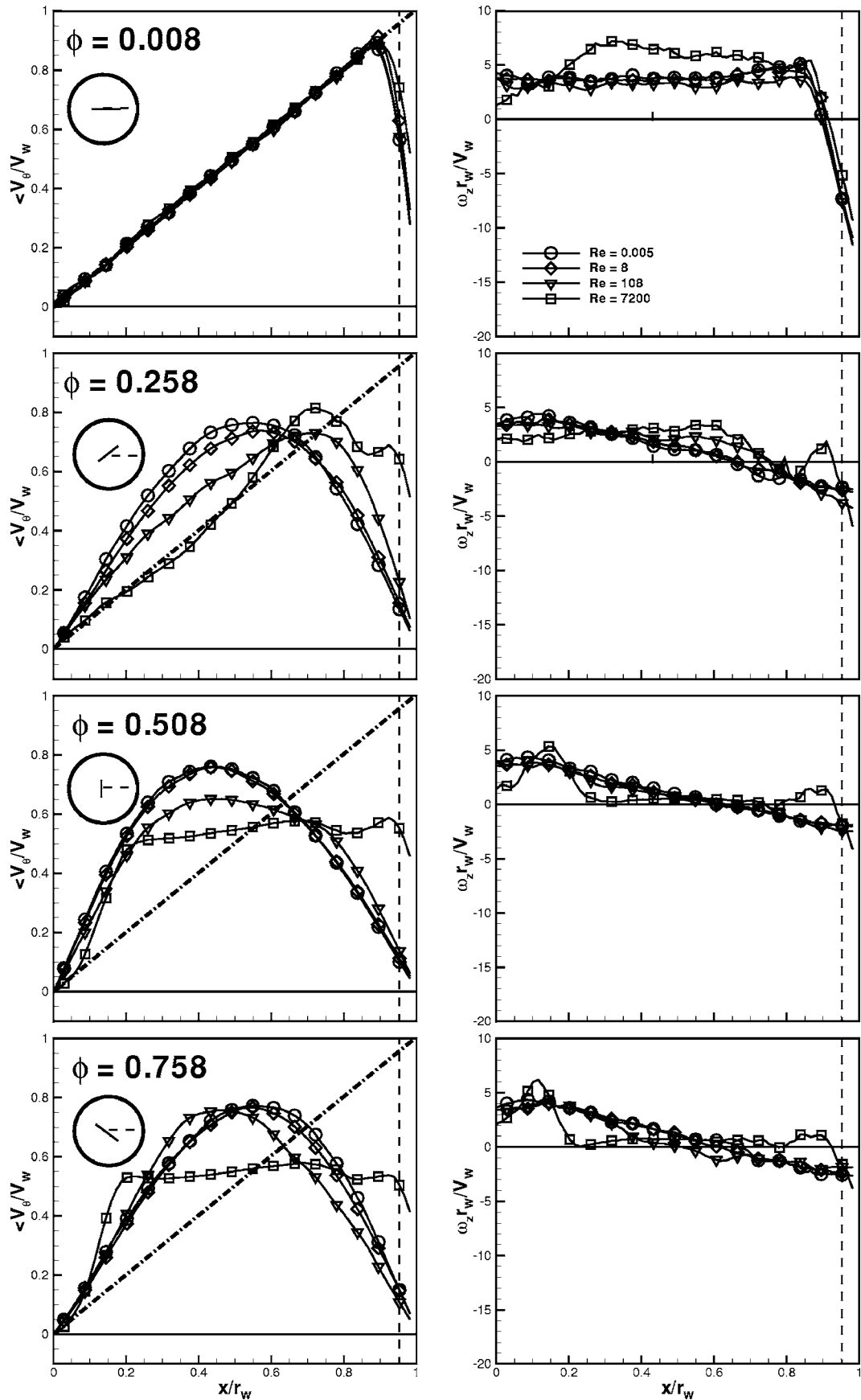


Fig. 5 Phase-averaged tangential velocity and vorticity profiles for the full-blade cases. Blade position (black line) shown schematically with respect to profile location (dashed). Blade tip location by dashed-dotted line in plot. Dashed-dotted line in plot is linear velocity profile based on rotational frequency and radial location. Error levels indicated by symbol size.

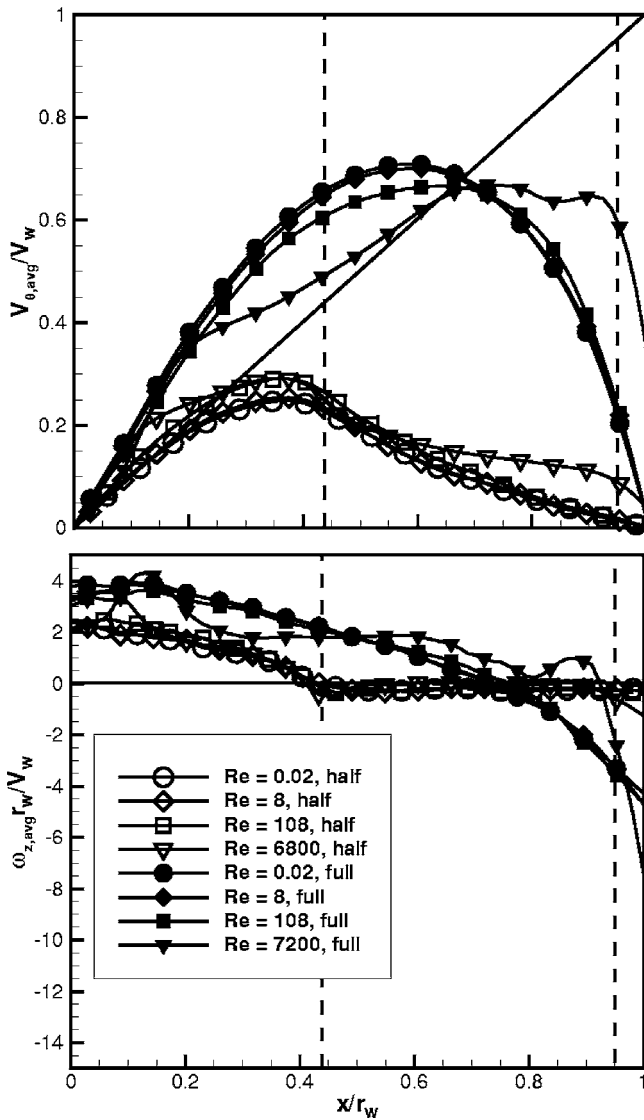


Fig. 6 Average tangential velocity and vorticity. Blade tip location indicated by dashed line. Linear velocity profile shown by solid black line in velocity profile plot.

8, at $0.65r_w$ for $Re=108$ and $x=0.79r_w$ for $Re=6800$. The high Reynolds number cases for both the full- and half-blades showed a rapid decrease in the tangential velocity near the wall, indicating the presence of a distinct wall boundary layer. The lower Reynolds number cases ($Re=0.005, 0.02, 8, 109$) showed a more gradual decrease in the tangential velocity to zero at the wall with no apparent rapid decrease, as was evident for the high Reynolds number case.

The phase-averaged vorticity field data indicated that the flow along the mixing blade had separated at high Reynolds number (Figs. 2 and 5). Evidence of the separation persists in the mean vorticity profiles and was indicated by the two local maximum in the vorticity profiles observed at high Reynolds number. The average vorticity magnitudes were higher in the wall region for the high Reynolds number cases when compared to the low Re cases. The half-blade cases showed mean vorticity very close to zero in the region between the blade tip and the wall. Only the $Re=6800$ case showed a significant mean vorticity near the wall.

4.4 Flow-Type Characterization. The flow number was calculated for both the half and full blades at the lowest Reynolds number using Eqs. (1) and (2). For $\phi=0.008$, the flow types indi-

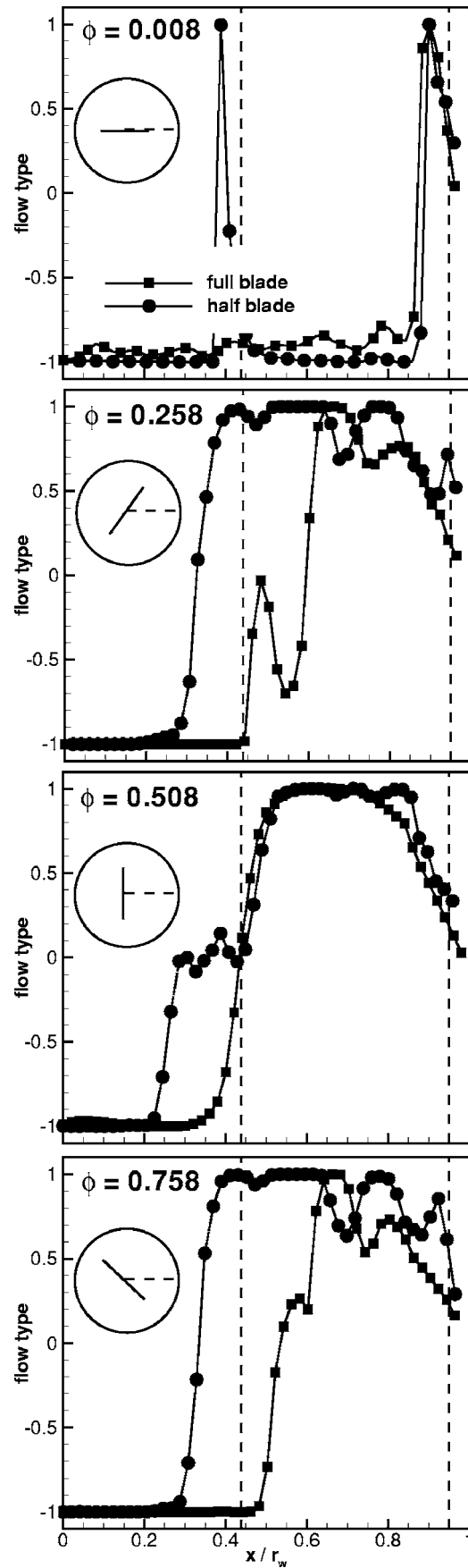


Fig. 7 Flow type for the lowest Re cases. Phase indicated. Dashed line indicates mixing blade tip location.

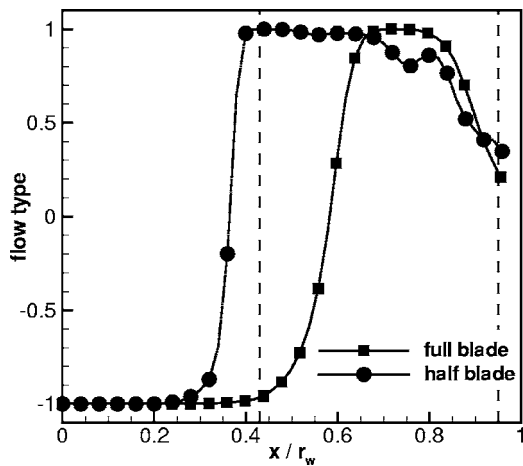


Fig. 8 Mean flow type. Blade tip location indicated by dashed lines.

cated solid body rotation along the profile except at the blade tip for the half-blade case and in the wall boundary layer region for both the half- and full-blade cases (Fig. 7). In these regions, the flow type was found to be extensional ($D=1$), though the flow number was tending toward $D=0$ (shear) in the boundary layer. At other phases, the transition point between the purely rotational flow and the shear and/or extensional flow moved towards the center of rotation. The half-blade case always transitioned from rotational flow closer to the center of rotation than the full-blade case did, indicating it was a better mixer.

The flow number was also calculated for mean field and is shown in Fig. 8. Both cases show solid body rotation initially; however, the region of rotation for the full blade cases extended further into the flow field. The half-blade case changed flow type to extensional flow at the tip of the blade and remained extensional over the range $0.4 < x/r_w < 0.68$. For $x/r_w > 0.68$, the flow transitioned to a shear flow at the wall. The full-blade case transitioned to an extensional flow at $x/r_w \approx 0.64$ and remained extensional for $x/r_w < 0.8$ after which it changed to a shear flow as the wall was approached.

5 Conclusions

In this work the flow in a cylindrical container, driven by the rotation of flat plates, was investigated using particle image velocimetry. Data for two different blade widths ($0.43r_w$ and $0.95r_w$) and four different Newtonian fluids (water, 85/15 water/glycerin mixture, glycerin, and corn syrup) were taken. The different fluids permitted an experimental Reynolds number range of 0.005–7200 to be investigated. The line profiles of the tangential velocity were in good agreement with the results of Youcefi et al. [4]. The whole field data in this work however permitted the flow structure to be investigated and clarified the differences observed as the Reynolds number changed. The results showed that the flow structure was similar between the two lowest Reynolds number cases but differed as a function of Reynolds number for the higher Reynolds

number cases. The results indicate that there may be a critical Reynolds number below which the flow structure dependence on the Reynolds number is minimal. All cases showed a vortex was developed at the tip of the rotating plate for the half-blade cases though the peak magnitude and size of these vortices decreased with increasing Reynolds number. Recirculating flow was observed for the two lowest Reynolds number half-blade cases. In these cases the sign of the vorticity in the region of the wall changed because of the closed recirculation region, indicating separation of the flow along the cylinder surface.

The data showed that the vorticity along the mixing blade lifted from the downstream surface at the highest Reynolds number case. The separated flow was unsteady and shed vorticity into the flow field. The wall boundary layer was more compact with higher magnitudes at high Reynolds number compared to the other cases.

The flow-type calculations showed that there was a large region of solid-body rotation for both the full- and half-blade cases. The region of solid-body rotation was larger for the full-blade case. The half-blade case showed extensional and shear flow types over 65% of the cylinder diameter while the full-blade case showed the extensional and shear flow over only 35% of the diameter. The results indicate that the half blade represents a potentially more effective mixer than the full blade.

Acknowledgment

The work present in this paper was conducted at the Naval Surface Warfare Center Indian Head Division in Indian Head, Maryland through the internal CORE research program.

References

- [1] Smetana, A. F., and Castorina, T. C., 1975, "Explosive and Physical Properties of Polymer Coated RDX," *Technical Report 4799*, Picatinny Arsenal, NJ, June.
- [2] Zhou, G., Tanguy, P., and Dubois, C., 2000, "Power Consumption in a Double Planetary Mixer With Non-Newtonian and Viscoelastic Materials," *Trans. Inst. Chem. Eng., Part A*, **78**, pp. 445–453.
- [3] Tanguy, P., Bertrand, F., Labrie, R., and Brito-De La Diente, E., 1996, "Numerical Modelling of the Mixing of Viscoplastic Slurries in a Twin-Blade Planetary Mixer," *Trans. Inst. Chem. Eng., Part A*, **74**, pp. 499–504.
- [4] Youcefi, A., Anne-Archard, D., Boisson, H., and Sengelin, M., 1997, "On the Influence of Liquid Elasticity on Mixing in a Vessel Agitated by a Two-Bladed Impeller," *ASME J. Fluids Eng.*, **119**, pp. 616–622.
- [5] Jaffer, S., Bravo, V., Wood, P., and Hrymak, A., 2000, "Experimental Validation of Numerical Simulations of the Kneading Section in a Twin-Screw Extruder," *Polym. Eng. Sci.*, **40**, pp. 892–901.
- [6] Balkis, S., and Karwe, M., 2002, "Velocity Distribution and Volume Flow Rates in the Nip and Translational Regions of a Co-Rotating, Self-Wiping, Twin-Screw Extruder," *J. Food. Eng.*, **51**, pp. 273–282.
- [7] Yoon, H., Hill, D., Balachandar, S., Adrian, R., and Ha, M., 2005, "Reynolds Number Scaling of Flow in a Rushton Turbine Stirred Tank. Part I—Mean Flow, Circular Jet and Tip Vortex Scaling," *Chem. Eng. Sci.*, **60**, pp. 3169–3183.
- [8] Rios, A., Gramann, P., Osswald, T., Noriega, M., and Estrada, O., 2000, "Experimental and Numerical Study of Rhomboidal Mixing Sections," *Int. Polym. Process.*, **15**, pp. 12–19.
- [9] Jongen, T., 2000, "Characterization of Batch Mixers Using Numerical Flow Simulations," *AIChE J.*, **46**(11), pp. 2140–2150.
- [10] Astarita, G., 1979, "Objective and Generally Applicable Criteria for Flow Classification," *J. Non-Newtonian Fluid Mech.*, **6**, pp. 69–76.
- [11] Keane, R., and Adrian, R., 1993, "Theory and Simulation of Particle Image Velocimetry," *Proc. SPIE*, **2052**, pp. 477–492.
- [12] Gendrich, C. P., and Koochesfahani, M. M., 1996, "A Spatial Correlation Technique for Estimating Velocity Fields Using Molecular Tagging Velocimetry (MTV)," *Exp. Fluids*, **22**, pp. 67–77.

Effect of Turbulence Intensity and Periodic Unsteady Wake Flow Condition on Boundary Layer Development, Separation, and Reattachment Along the Suction Surface of a Low-Pressure Turbine Blade

B. Öztürk
M. T. Schobeiri

Turbomachinery Performance and Flow Research
Laboratory,
Texas A&M University,
College Station, TX 77843-3123

This paper experimentally investigates the individual and combined effects of periodic unsteady wake flows and freestream turbulence intensity (FSTI) on flow separation along the suction surface of a low-pressure turbine blade. The experiments were carried out at a Reynolds number of 110,000 based on the suction surface length and the cascade exit velocity. The experimental matrix includes freestream turbulence intensities of 1.9%, 3.0%, 8.0%, and 13.0%, and three different unsteady wake frequencies with the steady inlet flow as the reference configuration. Detailed boundary layer measurements are performed along the suction surface of a highly loaded turbine blade with a separation zone. Particular attention is paid to the aerodynamic behavior of the separation zone at different FSTIs at steady and periodic unsteady flow conditions. The objective of the research is (i) to quantify the effect of FSTIs on the dynamics of the separation bubble at steady inlet flow conditions and (ii) to investigate the combined effects of Tu_{in} and the unsteady wake flow on the behavior of the separation bubble. [DOI: 10.1115/1.2734188]

Introduction

The continuous improvement of efficiency and performance of the low-pressure turbine component (LPT) has motivated industry and research communities to intensify the LPT aerodynamics research efforts. The efforts have been encompassing a wide variety of different research approaches, such as steady and unsteady cascade aerodynamics research and rotating turbine research. The research has contributed to better understanding the LPT flow physics, resulting in a state-of-the-art LPT design with a reduced number of blades without substantially sacrificing the efficiency of the LPT blading. This reduction contributes to an increase in thrust/weight ratio, thus, reducing the fuel consumption. Contrary to the high-pressure turbine (HPT) stage group that operates in a relatively high Reynolds number environment, dependent on operation conditions, the LPT experiences a variation in Reynolds numbers ranging from 50,000 to 250,000. Since the major portion of the boundary layer, particularly along the suction surface, is laminar, the low Reynolds number in conjunction with the local adverse pressure gradient makes it susceptible to flow separation, thus, increasing the complexity of the LPT boundary layer aerodynamics. The periodic unsteady nature of the incoming flow associated with wakes that originate from upstream blades substantially influences the boundary layer development, including the onset of the laminar separation, the extent of the separation bubble, and its turbulent reattachment. Although the phenomenon of the unsteady boundary layer development and transition in the absence of the separation bubbles has been the subject of intensive

research that has led to better understanding the transition phenomenon, comprehending the multiple effects of mutually interacting parameters on the LPT boundary layer separation and their physics still requires more research.

Lou and Hourmouziadis [1] investigated the mechanism of separation, transition, reattachment, and the effect of oscillating inlet flow conditions on laminar boundary layer separation along a flat plate under a strong negative pressure gradient, which was similar to the LPT pressure gradient. This was simulated by contouring the top wall. They studied the Reynolds number effect on the transition region. Their results showed that the higher Reynolds numbers cause an earlier transition and reduction of the transition length, while the separation point does not change its location. Kaszeta et al. [2] experimentally investigated the laminar-turbulent transition aspect within a channel with the side-walls resembling the suction and pressure surfaces of an LPT blade. Using the top wall contouring as in [1] Volino and Hultgren [3] performed an experimental study and measured the detailed velocity along a flat plate that was subjected to a similar pressure gradient as the suction side of a low-pressure turbine blade. They also stated that the location of the boundary layer separation does not strongly depend on the Reynolds number or freestream turbulence level as long as the boundary layer remains nonturbulent before separation occurs. Furthermore, they showed that the extent of the transition is strongly dependent on the Reynolds number and turbulence intensity.

Using the surface-mounted hot-film measurement technique, Brunner et al. [4], Cardamone et al., [5], Schröder [6], and Haueisen et al. [7] documented strong interactions between the wakes and the suction surface separation bubble on the LPT blades both in wind-tunnel cascade tests and in a turbine rig. Furthermore, they investigated the boundary layer transition under

Contributed by the Fluids Engineering Division of ASME for publication in the JOURNAL OF FLUIDS ENGINEERING. Manuscript received March 28, 2006; final manuscript received October 31, 2006. Review conducted by Phillip M. Ligrani.

the influence of the periodic wakes along the LPT surface and found that the interaction of the wake with the boundary layer greatly affects the loss generation. Shyne et al. [8] performed an experimental study on a simulated low-pressure turbine. The experiments were carried out at Reynolds numbers of 100,000 and 250,000 with three levels of freestream turbulences. They indicated that the transition onset and the length are strongly dependent on the freestream turbulence. As the freestream turbulence increases, the onset location and the length of the transition are decreased. Van Treuren et al. [9] performed an experimental study along an LPT surface at the very low Reynolds number of 25,000 and 50,000 with different freestream turbulence levels. They showed that a massive separation at the very low Reynolds number of 25,000 is persistent in spite of an elevated freestream turbulence intensity. However, at the higher Reynolds number of 50,000, there was a strong separation on the suction side for the low freestream turbulence level. The separation bubble was eliminated for the higher freestream turbulence level of 8–9%. The investigations by Halstead et al. [10] on a large-scale LP turbine uses surface-mounted hot films to acquire detailed information about the quasi-shear stress directly on the blade surface. Investigations by Cardamone et al. [5] and Schröder [7] indicate that the benefit of the wake–boundary layer interaction can be used for the design procedure of modern gas turbine engines with a reduced LPT blade number without altering the stage efficiency.

Recent comprehensive experimental studies by Schobeiri et al. [11] and Schobeiri and Öztürk [12] investigated the physics of the inception, onset, and extent of the separation bubble along a low-pressure turbine blade periodic under unsteady inlet flow condition. Surface pressure measurements were performed at $Re = 50,000, 75,000, 100,000,$ and $125,000$. Increasing the Reynolds number up to 125,000 has resulted in no major changes to the surface pressure distribution. The investigation reported in [11] showed that the unsteady wake flow with its highly turbulent vortical core traveling over the separation region caused a periodic contraction and expansion of the separation bubble. It was proposed that, in conjunction with the pressure gradient and periodic wakes, the temporal gradient of the turbulence fluctuation, or more precisely the fluctuation acceleration $\partial v_{rms}/\partial t$ provides a higher momentum and energy transfer into the boundary layer, energizing the separation bubble and causing it to partially or entirely disappear. Increasing the passing frequency associated with a higher turbulence intensity further reduced the separation bubble height [12]. Continuing the LPT research, Öztürk et al. [13] investigated the effect of Reynolds number and periodic unsteady wake flow condition on boundary layer development, separation, and reattachment along the suction surface of a low-pressure turbine blade. They also provided insight into the intermittent behavior of the separated boundary layer along the suction surface of a low-pressure turbine blade under periodic unsteady flow conditions [14].

Zhang and Hodson [15] investigated the combined effects of surface trips and unsteady wakes on the boundary layer development along the suction surface of a different type of LPT blade (T106C). They reported that the incoming wakes were not strong enough to periodically suppress the large separation bubble on the smooth suction surface of the T106C blade. Therefore, they argued that the profile loss is not reduced as much as one might expect. However, they found that the combined effects of the surface trip and unsteady wakes further reduce the profile losses. Zhang et al. [16] continued the above investigations with the emphasis on separation and transition control on an aft-loaded turbine blade at low Reynolds numbers.

A series of recent papers by Soranna et al. [17], Chow et al. [18], and Uzol et al. [19], dealing with the effect of wake impingement and its turbulence structure on the velocity field around leading and trailing edges of a rotor blade operating downstream of a

row of inlet guide vanes (IGV), emphasizes the need for better understanding the physics of interaction of wakes with blade surface and main turbine flow structure.

Parameters that substantially affect the stability of the suction surface laminar flow, laminar-turbulent transition, onset and extent of the separation zone, and turbulent reattachment can be summarized as unsteady wakes, Re number, turbulence intensity, and surface roughness. Studies in [11–15] showed that the impingement of unsteady wakes on the separation zone triggers a periodic process of contraction, suppression, and recovery of the separation zone. However, it does not completely prevent its generation. As extensively discussed in [11–15], the dynamic process of contraction and suppression of the separation zone is caused by an intensive exchange of momentum and energy from the main flow outside the boundary layer into the separation zone, thus, periodically energizing the boundary layer. Once the wake has passed over the separation zone, the bubble begins to recover and the process repeats periodically. This indicates that the combination of wake impingement and higher turbulence intensity may result in a complete suppression of the separation bubbles.

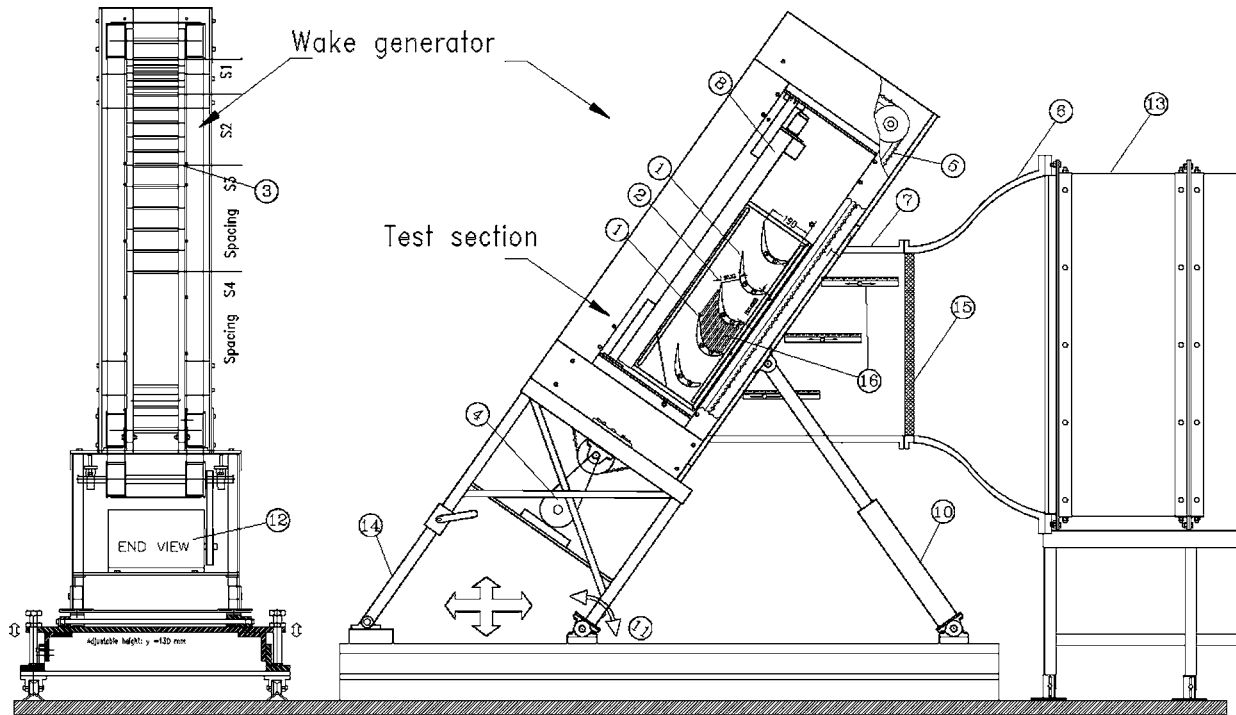
The objective of the present paper is to investigate the individual and combined effects of periodic unsteady flow and freestream turbulence intensity (FSTI) on the aerodynamics of a highly loaded turbine blade. Detailed boundary layer measurements are performed along the suction surface of a highly loaded turbine blade with a separation zone. Particular attention is paid to the aerodynamics of the separation zone at different FSTIs at steady and periodic unsteady flow conditions. Systematic, experimental investigations involve the following tasks: (i) variation of the unsteady wake frequency parameter in the absence of high turbulence intensity, (ii) variation of turbulence intensity parameter in the absence of unsteadiness, and (iii) combination of both parameters, namely, the unsteadiness and turbulence.

Experimental Research Facility

To investigate the effect of unsteady wake flow on turbine and compressor cascade aerodynamics, particularly on unsteady boundary layer transition, a multipurpose large-scale, subsonic research facility was designed and has been in operation since 1993. The research facility consists of a large centrifugal compressor, diffuser, settling chamber, nozzle, an unsteady wake generator, and a turbine cascade test section as shown in Fig. 1. The compressor, with a volumetric flow rate of $15 \text{ m}^3/\text{s}$, is capable of generating a maximum mean velocity of 100 m/s at the test section inlet. The settling chamber consists of five screens and one honeycomb flow straightener to control the uniformity of the flow.

Wake Generator. A two-dimensional periodic unsteady inlet flow is simulated by the translational motion of an unsteady wake generator (see Fig. 2) with a series of cylindrical rods attached to two parallel operating timing belts driven by an electric motor. To simulate the wake width and spacing that stems from the trailing edge of rotor blades, the diameter and number of rods can be varied. The rod diameter, its distance from the LPT blade leading edge, the wake width, and the corresponding drag coefficient, are chosen according to the criteria outlined by Schobeiri et al. [20]. The belt-pulley system is driven by an electric motor and a frequency controller. The wake-passing frequency is monitored by a fiber-optic sensor. The sensor also serves as the triggering mechanism for data transfer and its initialization, which is required for ensemble averaging. This type of wake generator produces clean, two-dimensional wakes whose turbulence structure, decay, and development is, to a great extent, predictable [20].

To account for a high flow deflection of the LPT cascade, the entire wake generator and test section unit, including the traversing system, was modified to allow a precise angle adjustment of the cascade relative to the incoming flow. This is done by a hydraulic platform that simultaneously lifts and rotates the wake generator and test section unit. The unit is then attached to the



- | | | | |
|-------------------------------|---------------------------------|--------------------------|---|
| ① Static pressure blade | ⑤ Timing belts, rod attachments | ⑨ Inlet nozzle | ⑬ Large silence chamber with honeycomb and five screens |
| ② Blade with hot film sensors | ⑥ Transition duct | ⑩ Hydraulic cylinders | ⑭ Telescope support |
| ③ Wake generating rods | ⑦ Straight duct | ⑪ Pivot point | ⑮ Honeycomb flow straightener |
| ④ Wake generator | ⑧ Traversing system | ⑫ Wake generator e-motor | ⑯ Traversing slots |

Fig. 1 Turbine cascade research facility with the components and the adjustable test section

tunnel exit nozzle with an angular accuracy of <0.05 deg, which is measured electronically. The special design of the facility and the length of the belts ($L_{\text{belt}}=4960$ mm) enables a considerable reduction of the measurement time. For the present investigation,

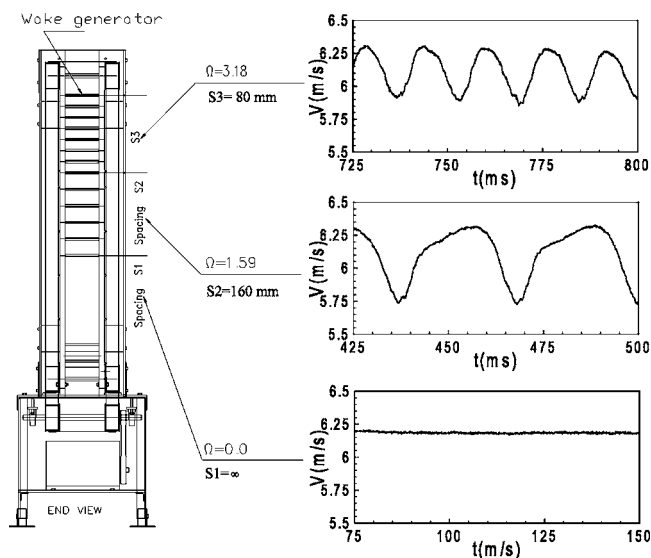


Fig. 2 Wake generator (left), generated velocity distributions (right)

two clusters of rods with a constant diameter of 2 mm are attached to the belts, as shown in Fig. 2. The two clusters, with spacings $S_R=160$ mm and $S_R=80$ mm, are separated by a distance that does not have any rods, thus, simulating steady-state case ($S_R=\infty$). Thus, it is possible to sequentially measure the effect of three different spacings at a single boundary layer point. To clearly define the influence domain of each individual cluster with the other one, the clusters are arranged with a certain distance between each other. Using the triggering system mentioned above and a continuous data acquisition, the buffer zones between the data clusters are clearly visible. The data analysis program cuts the buffer zones and evaluates the data pertaining to each cluster. Comprehensive preliminary measurements were carried out to make sure that the data were exactly identical to those when the entire belt length was attached with rods of constant spacing, which corresponded to each individual cluster spacing. The unsteady data were taken by calibrated, custom designed, miniature, single hot wire probes. At each boundary layer position, samples were taken at a rate of 20 kHz for each of 100 revolutions of the wake generator. The data were ensemble averaged with respect to the rotational period of the wake generator. Before final data were taken, the number of samples per revolution and the total number of revolutions were varied to determine the optimum settings for convergence of the ensemble-averaged results.

Grid-Generated Turbulence Characteristics. Three different turbulence grids were manufactured for producing inlet turbulence intensities of 3.0%, 8.0%, and 13.0%. The grids consist of square shaped aluminum rods with the thickness G_T and opening G_O

Table 1 Parameters of turbine cascade test section

Parameters	Values	Parameters	Values
Inlet velocity	$V_{in}=3.6, 4.9, 8.16$ m/s	Inlet turbulence intensity	FSTI=1.9%
Rod translational speed	$U=5.0$ m/s	Blade Re-number	$Re_{ss}=110,000$
Nozzle width	$W=200.0$ mm	Blade height	$h_B=200$ mm
Blade chord	$c=203.4$ mm	Cascade solidity	$\sigma=1.248$
Blade axial chord	$c_{ax}=182.85$ mm	Zweifel coefficient	$\Psi_A=1.254$
Blade suction surface length	$L_{ss}=270.32$ mm	Cascade angle	$\gamma=55^\circ$
Cascade flow coefficient	$\phi=0.80$	Cascade spacing	$S_B=163$ mm
Cascade inlet flow angle	$\alpha_1=0^\circ$	Cascade exit flow angle	$\alpha_2=90^\circ$
Rod diameter	$D_R=2.0$ mm	Rod distance to lead. edge	$L_R=122$ mm
Cluster 1 (no rod, steady)	$S_R=4$ mm	Ω -parameter steady case	$\Omega=0.0$
Cluster 2 rod spacing	$S_R=160.0$ mm	Ω -parameter for cluster 1	$\Omega=1.59$
Cluster 3 rod spacing	$S_R=80.0$ mm	Ω -parameter for cluster 2	$\Omega=3.18$
Turbulence grid TG1	$GT=6.35$ mm	Grid Opening GO=77%	FSTI=3.0%
Turbulence grid TG2	$GT=9.52$ mm	Grid Opening GO=55%	FSTI=8.0%
Turbulence grid TG3	$GT=12.7$ mm	Grid Opening GO=18%	FSTI=13.0%
Length scale for no grid	$\Lambda=41.3$ mm	Length scale for TG1	$\Lambda=32.5$ mm
Length scale for TG2	$\Lambda=30.1$ mm	Length scale for TG3	$\Lambda=23.4$ mm
Grid distance from leading edge	$G_{LE}=160$ mm		

given in Table 1. The grids were subsequently installed upstream of the wake generator, parallel to the plane of the cascade blade row with the distance from cascade leading edge G_{LE} defined in Table 1. The turbulence intensity values were measured at the cascade inlet with the location from the cascade leading edge listed in Table 1. An adequate description of the inlet flow condition requires, in addition to the time-dependent velocity distribution and freestream turbulence intensity, the information about the turbulence length scale. To document the turbulence length scales, one-dimensional power spectra of the velocity fluctuations were measured using a single-wire probe. The spectral measurements used 20,000 data points at 20 kHz (low-pass filtered at 10 kHz). From these data, the integral length scale Λ was calculated for each turbulence grid using the relations developed by Hinze [21] and the power density values were extrapolated to the frequency $f=0$. The results of these calculations presented in Table 1 indicate a decrease in length scale with increasing the freestream turbulence intensity.

Cascade Test Section. The cascade test section shown in Fig. 1, located downstream of the wake generator, includes five LPT blades with a height of 200.0 mm and the chord of 203.44 mm, as shown in Fig. 3. For boundary layer investigations, five identical “Pak B” airfoils, designed by Pratt & Whitney, were implemented whose cascade geometry is given in Table 1. The blade geometry resembles the essential feature, such as the laminar boundary layer separation that is inherent to typical LPT blades. The blade geometry was made available to NASA researchers and academia to study the specific problems of LPT flow separation, its passive and active control, and its prevention. As shown in [22], this blade number is necessary and sufficient to secure a spatial periodicity for the cascade flow. The periodicity is noted in the pressure distribution of the second and fourth blades for steady and unsteady flow conditions. These blades were specially manufactured for measurement of pressure and showed identical pressure distributions. A computer-controlled traversing system is used to measure the inlet velocities and turbulence intensities, as well as the boundary layers on suction and pressure surfaces. The traversing system (see Fig. 3) was modified to allow the probe to reach all streamwise positions along the suction and pressure surfaces. The three-axis traversing system is vertically mounted on the Plexiglas sidewall. Each axis is connected to a DC-stepper motor with an encoder and decoder. The optical encoder provides a continuous feedback to the stepper motor for accurate positioning of the probes. The system is capable of traversing along the suction and pressure surfaces in small steps up to 1 μ m, and the third axis is

capable of rotating with an angular accuracy of <0.05 deg, which is specifically required for boundary layer investigations where the measurement of the laminar sublayer is of particular interest.

A detailed description of instrumentation, data acquisition, and data reduction is found in previous papers [11–14].

**Fig. 3 Turbine cascade research facility with three-axis traversing system****Table 2 Uncertainty analysis for velocity measurement and Re number**

V (m/s)	Re	$\omega V/V$ (%)	$\omega Re/Re$ (%)
3.6	110,000	3.939	2.361
4.9	150,000	2.127	1.684
8.16	250,000	0.772	1.362

Table 3 Uncertainty analysis for pressure coefficient C_p , boundary layer momentum thickness δ_2 and form parameter H_{12} .

V (m/s)	Re	$\omega C_p / C_p$ (%)	$\omega \delta_2 / \delta_2$ (%)	$\omega H_{12} / H_{12}$ (%)
3.6	110,000	2.205	2.463	2.176
4.9	150,000	2.057	1.985	1.823
8.16	250,000	0.693	1.087	0.957

Table 4 This table shows uncertainty values for each corresponding Re number and freestream turbulence FSTI (%). As an example, for Re=110,000 and FSTI=1.9%, the uncertainty is $TFSTI/FSTI$ (%)=0.577.

Re/FSTI (%)	1.9	3	8	13
110,000	0.577	0.367	0.142	0.093
150,000	0.229	0.146	0.058	0.04
250,000	0.137	0.087	0.033	0.021

Uncertainty Analysis

The Kline and McClintock [23] uncertainty analysis method was used to determine the uncertainty of the flow quantities described in this paper. The uncertainties in velocity for the single-wire probe after data reduction and the Re numbers are given in Table 2. As shown, the uncertainty in the velocity increases as the flow velocity decreases. This is due to the uncertainty of the pneumatic pressure transducer at lower pressure during the calibration. The Re-number uncertainty exhibits similar behavior. It is worth nothing that the relatively minor Re changes caused by the uncertainty have only a minor influence on boundary layer development, separation, and reattachment as documented in [13].

Table 3 shows the uncertainties of the pressure coefficient C_p , the momentum thickness δ_2 , and the form parameter H_{12} for three different Re numbers. Table 4 exhibits the uncertainties of FSTIs

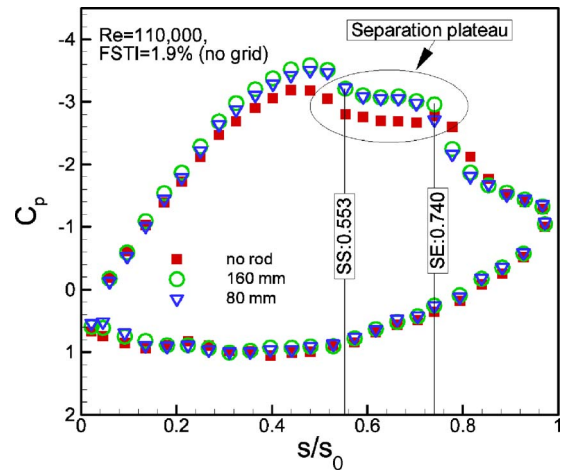


Fig. 4 Static pressure distributions at Re=110,000 and reduced frequencies $\Omega=0, 1.59, 3.18$ (no rod, 160 mm, 80 mm), SS=separation start, SE=separation end

at Re=110,000, 150,000, and 250,000. As described in the caption for Table 4, for each Re number, the corresponding FSTI uncertainty can be found.

Results and Discussion

Detailed surface pressure and boundary layer measurements were performed at a suction surface Reynolds number of $Re_{LSS} = 110,000$. This Reynolds number, which pertains to a typical cruise operation, is a representative value within the LPT operating range between 75,000 and 400,000 as discussed by Hourmouziadis [24]. Furthermore, it produces separation bubbles that can be accurately measured by miniature hot wire probes. For the Reynolds number of 110,000 with an FSTI of 1.9%, three different reduced frequencies were examined. For generation of the unsteady wakes, cylindrical rods with the diameter of $d_R = 2$ mm

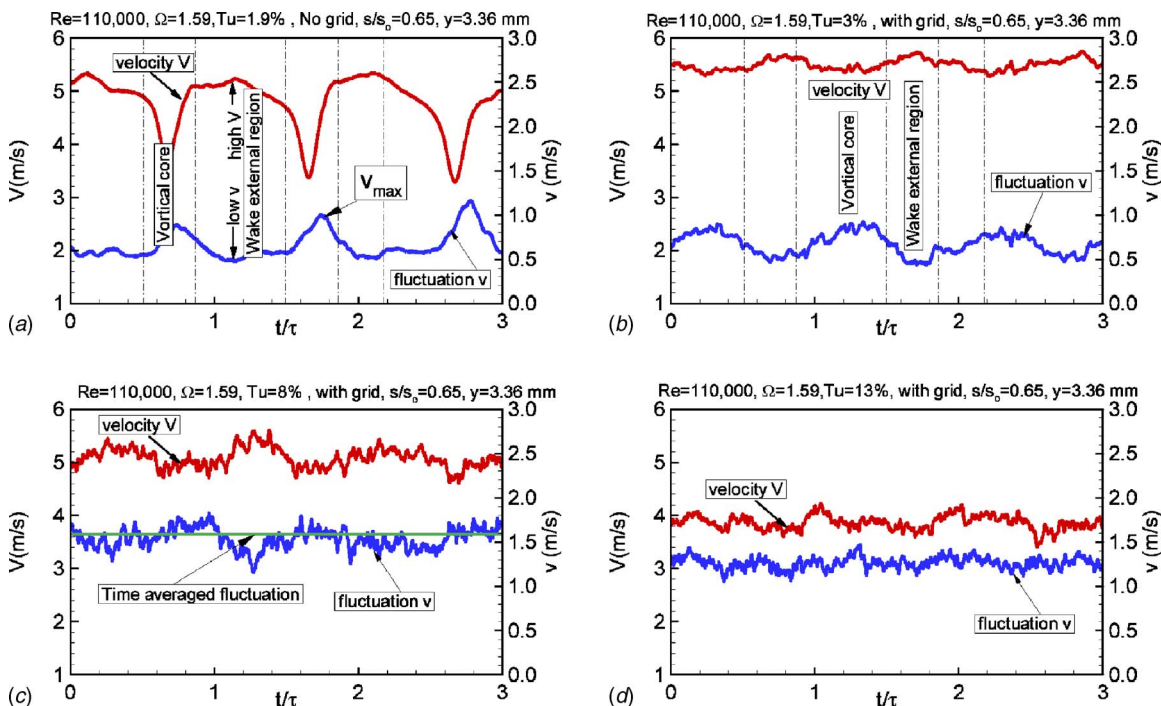


Fig. 5 (a–d). Time-dependent ensemble-averaged velocities and fluctuations for Re=110,000 at a constant location $s/s_0=3.36$ mm inside the bubble for different inlet turbulence intensities ranging from 1.9% to 13%

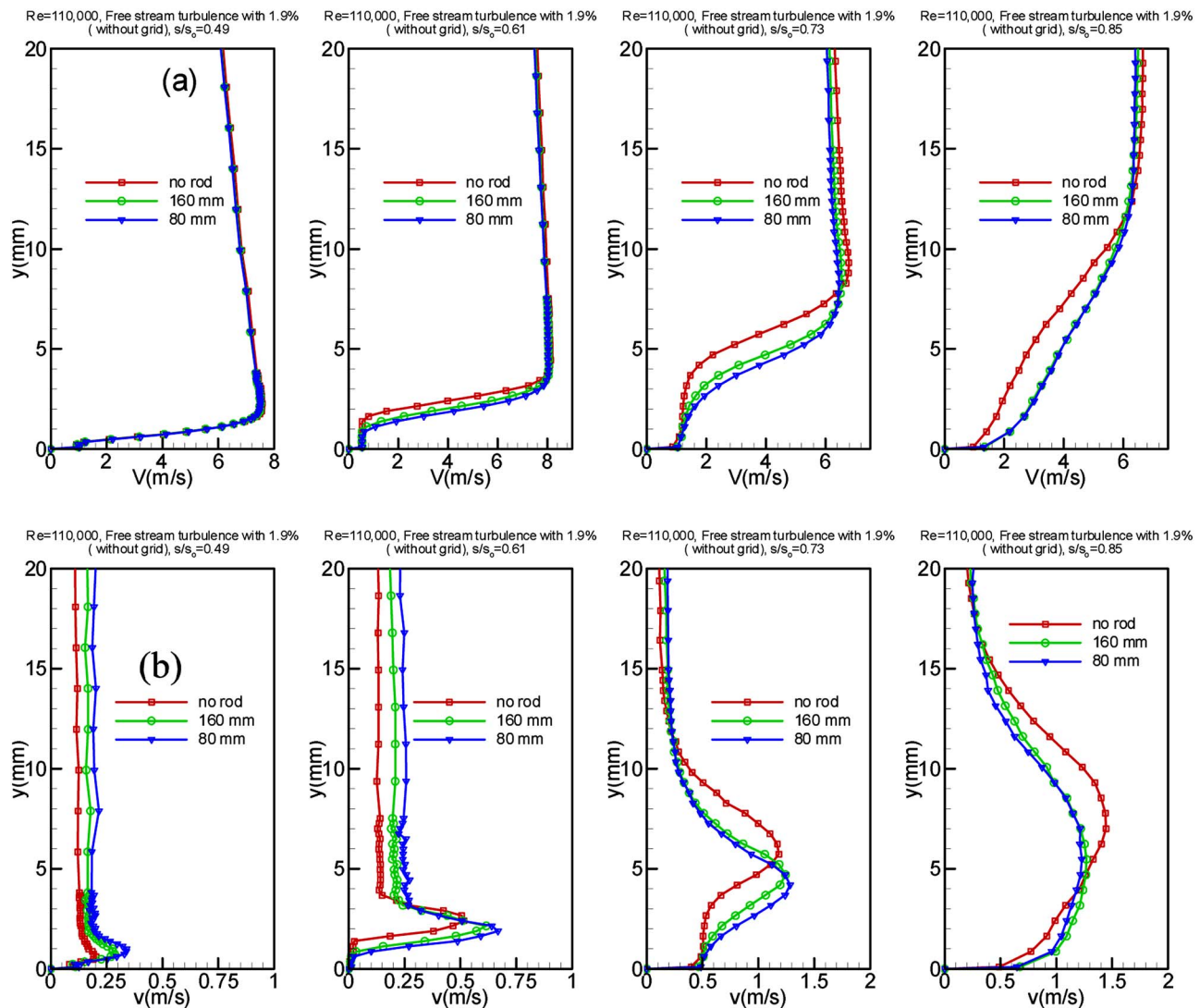


Fig. 6 Distribution of time-averaged velocity (a) and turbulence fluctuation root mean square (rms) (b) along the suction surface for steady case $\Omega=0$ ($S_R=\infty$) and unsteady cases $\Omega=1.59$ ($S_R=160$ mm) and $S=3.18$ ($S_R=80$ mm) at $Re=110,000$ and $FSTI=1.9\%$ (without grid)

were chosen to fulfill the criterion that requires the generation of a drag coefficient C_D that is approximately equal to the C_D of the turbine blade, with the chord and spacing given in Table 1 (for details, look for the studies in [20,25]).

To accurately account for the unsteadiness caused by the frequency of the individual wakes and their spacings, the flow velocity, and the cascade parameters, a reduced frequency Ω is defined that includes the cascade solidity σ , the flow coefficient ϕ , the blade spacing S_B , and the rod spacing S_R . Many researchers have used Strouhal numbers as the unsteady flow parameter, which only includes the speed of the wake generator and the inlet velocity. However, the currently defined reduced frequency Ω is an extension of Strouhal numbers in the sense that it incorporates the rod spacing S_R and the blade spacing S_B in addition to the inlet velocity and wake generator speed.

Surface Pressure Distributions. For the Reynolds number of 110,000 with an FSTI of 1.9%, three different reduced frequencies, namely, $\Omega=0.0$, 1.59, and 3.18, are applied that correspond to the rod spacings $S_R=80$ mm, 160 mm, and ∞ . The time-averaged pressure coefficients in Fig. 4 show the results of the steady case and two unsteady cases along the suction and pressure surfaces. The pressure signals inherently signify the time-

averaged pressure because of the internal pneumatic damping effect of the connecting pipes to the transducer. The noticeable deviation in pressure distribution between the steady and unsteady cases, especially on the suction surface, is due to the drag forces caused by the moving rods. The drag forces are imposed on the main stream and cause momentum deficiencies that lead to a reduction of the total and static pressure. The suction surface (upper portion) exhibits a strong negative pressure gradient. The flow accelerates at a relatively steep rate and reaches its maximum surface velocity, which corresponds to the minimum $C_p=-3.6$ at $s/s_o=0.48$. Passing through the minimum pressure, the fluid particles within the boundary layer encounter a positive pressure gradient that causes a sharp deceleration until $s/s_o=0.55$ has been reached. This point signifies the beginning of the laminar boundary layer separation and the onset of a separation bubble. As seen in the subsequent boundary layer discussion, the separation bubble characterized by a constant C_p plateau extends up to $s/s_o=0.74$, thus, occupying more than 19% of the suction surface and constituting a large separation. Passing the plateau, the flow first experiences a second sharp deceleration indicative of a process of reattachment followed by a further deceleration at a moderate rate. On the pressure surface, the flow decelerates at a very

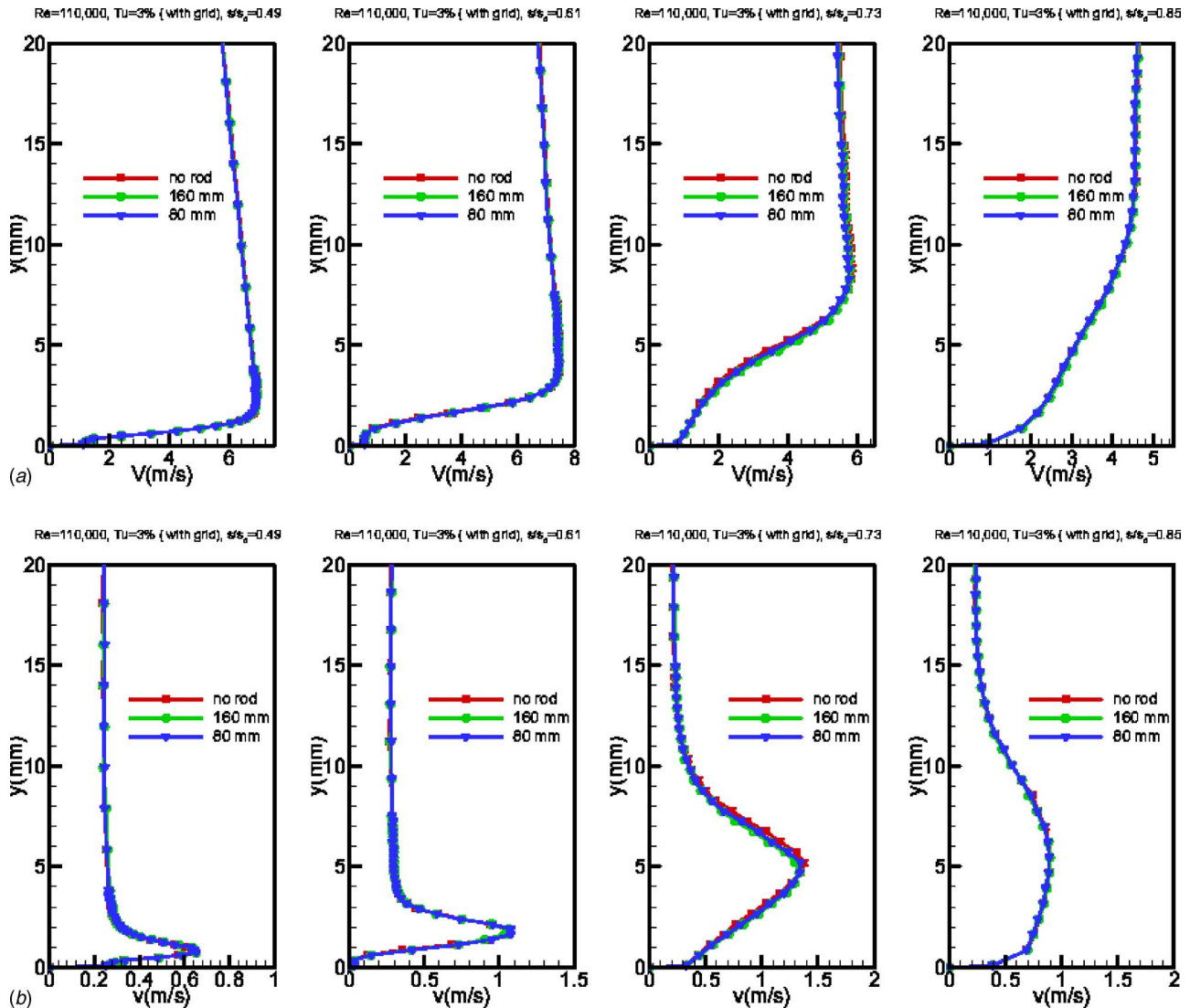


Fig. 7 Distribution of time-averaged velocity (a) and turbulence fluctuation rms (b) along the suction surface for steady case $\Omega=0$ ($S_R=\infty$) and unsteady cases $\Omega=1.59$ ($S_R=160$ mm) and $\Omega=3.18$ ($S_R=80$ mm) at $Re=110,000$ and $FSTI=3\%$ with grid TG1

slow rate, reaches a minimum pressure coefficient at $s/s_o=0.42$, and accelerates until the trailing edge has been reached. Unlike the suction surface, the pressure surface boundary layer does not encounter any adverse positive pressure gradient that triggers separation. However, close to the leading edge, a small plateau extending from $s/s_o=0.08$ – 0.16 indicates the existence of a small-size separation bubble that might be attributed to a minor inlet flow incident angle.

Considering the unsteady case with the reduced frequency $\Omega=1.59$ corresponding to a rod spacing of $S_R=160$ mm, Fig. 4 exhibits a slight difference in the pressure distribution between the steady and unsteady cases. As mentioned above, this deviation is attributed to the momentum deficiency that leads to a reduction of the total and static pressure. For $Re=110,000$, the wakes have a reducing impact on the streamwise extent of the separation plateau. As seen in Fig. 4, the trailing edge of the plateau has shifted from $s/s_o=0.74$ to $s/s_o=0.702$. This shift reduced the streamwise extent of the separation plateau from 19% to 15% of the suction surface length, which is, in this particular case, 21% of reduction in streamwise extent of the separation. Increasing the reduced frequency to $\Omega=3.18$ by reducing the rod spacing to $S_R=80$ mm causes a slight shift of the C_p distribution compared to the

$\Omega=1.59$ case. One should bear in mind that pneumatically measured surface pressure distribution only represents a time integral of the pressure events.

Unsteady Boundary Layer Measurement Results. Figures 5(a)–5(d) display representative temporal ensemble-averaged velocity distributions inside the separation bubble at $s/s_o=0.65$ for $Re=110,000$ for FSTI levels of 1.9%, 3%, 8%, and 13% at a reduced frequency of $\Omega=1.59$ and a normal distance of $y=3.36$ mm. Figure 5(a) exhibits two distinct regions: (i) a wake vortical core, occupied by vortices that originate from the moving cylindrical rods and generate high turbulence fluctuations and (ii) a wake external region between the adjacent vortical cores with relatively low turbulence activities. As seen in Figs. 5(a) and 5(b), an increase in turbulence intensity from 1.9% to 3% has reduced the amplitudes of the wake velocity as well as the turbulent fluctuations. Introducing higher FSTI levels of 8% and 13% leads to a complete degeneration of the deterministic periodic wake flow into a stochastic turbulent flow, as shown in Figs. 5(c) and 5(d). Comparing Figs. 5(a) and 5(c) leads to the following conclusion: The periodic unsteady wake flow definitely determines the separation dynamics, as extensively discussed in [11], as long as the

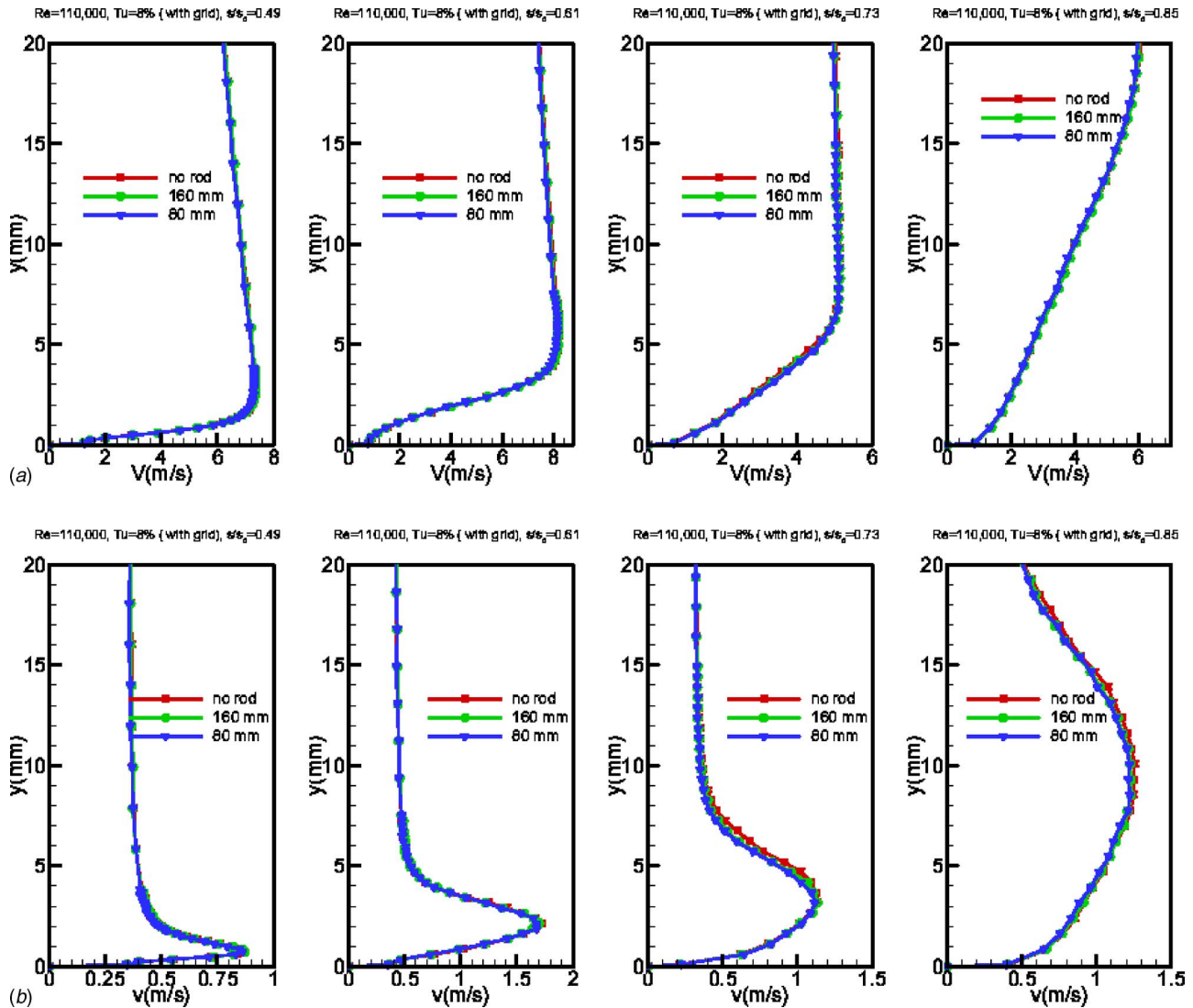


Fig. 8 Distribution of time-averaged velocity (a) and turbulence fluctuation rms (b) along the suction surface for steady case $\Omega=0$ ($S_R=\infty$) and unsteady cases $\Omega=1.59$ ($S_R=160$ mm) and $\Omega=3.18$ ($S_R=80$ mm) at $Re=110,000$ and $FSTI=8\%$ with grid TG2

level of the time-averaged turbulence fluctuations is below the maximum level of the wake fluctuation v_{max} , shown in Fig. 5(a). In our case, this apparently takes place at a turbulence level between 3% and 8%. Increasing the inlet turbulence level above v_{max} causes the wake periodicity to totally submerge in turbulence as shown in Figs. 5(c) and 5(d). In this case, the dynamics of the separation bubble is governed by the flow turbulence that is responsible for complete suppression of the separation bubble. One of the striking features this study reveals is that the separation bubble has not disappeared completely despite the high turbulence intensity and the significant reduction of its size, which is reduced to a tiny bubble. At this point the role of the stability of the laminar boundary layer becomes apparent, which is determined by the Reynolds number.

Time-Averaged Velocity and Fluctuation Distributions. The effect of wake frequency on time-averaged velocity and velocity fluctuation distributions is shown in Figs. 6–9 at three representative streamwise locations for $Re=110,000$ with a turbulence intensity level of 1.9%, 3.0%, 8.0%, and 13.0%. Figures 6–9 display the velocity and fluctuation distributions at one streamwise position upstream, one position within, and one position downstream of the separation bubble. The diagrams include the steady-state data for reference purposes, $\Omega=0.0$ ($S_R=\infty$), unsteady data for

$\Omega=1.59$ ($S_R=160$ mm) and $\Omega=3.18$ ($S_R=80$ mm). As Figs. 6–9 indicate in the upstream region of the separation bubble, the flow is fully attached. As seen in Fig. 6(a) upstream of the separation bubble at $s/s_o=0.49$, the velocity distributions inside and outside the boundary layer experience a slight decrease in magnitude with increasing reduced frequency. However, the time-averaged velocity distributions seen in Fig. 7(a), 8(a), and 9(a) display no changes with an increase in the reduced frequency. At the same position, the time-averaged velocity fluctuations shown in Fig. 6(b) exhibit substantial changes within the boundary layer as well as outside it. The introduction of the periodic unsteady wakes with highly turbulent vortical cores and the subsequent mixing has systematically increased the FSTI level from 1.9% for the steady case, to almost 3% for $\Omega=3.18$ ($S_R=80$ mm). Comparing the unsteady cases, $\Omega=1.59$ and 3.18, to the steady reference case, $\Omega=0.0$, indicates that with increasing Ω , the lateral position of the maximum fluctuation shifts away from the wall. This is due to the periodic disturbance of the stable laminar boundary layer upstream of the separation bubble. However, at the same position, the time-averaged velocity fluctuations shown in Fig. 7(b) hardly experience any changes with increasing the reduced frequency from $\Omega=1.59$ –3.18. Because of the combined effect of the FSTI

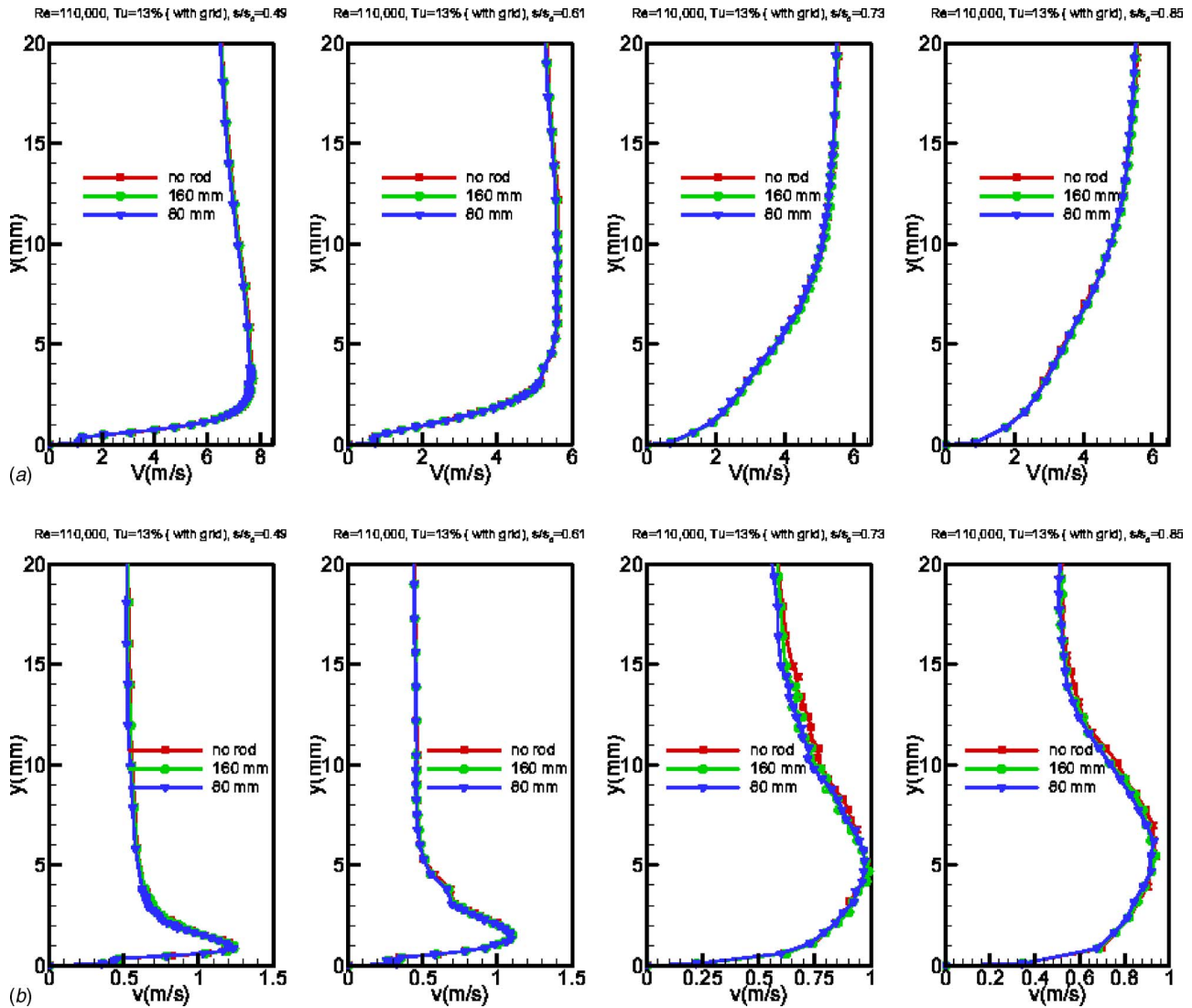


Fig. 9 Distribution of time-averaged velocity (a) and turbulence fluctuation rms (b) along the suction surface for steady case $\Omega=0$ ($S_R = \infty$) and unsteady cases $\Omega=1.59$ ($S_R=160$ mm) and $\Omega=3.18$ ($S_R=80$ mm) at $Re=110,000$ and $FSTI=13\%$ with grid TG3

level of 3% and unsteady wake flow, the lateral positions of the maximum velocity fluctuations remain the same with increasing the reduced frequency.

As seen in Fig. 6(a), a substantial influence of the wake frequency is observed inside the separation bubble at $s/s_0=0.73$. Although the impinging wakes are associated with velocity and momentum deficits, their high turbulence intensity vortical cores provide an intensive exchange and transfer of mass, momentum, and energy into the boundary layer, thus, energizing the low energetic boundary layer. This kinetic energy of the normal velocity fluctuation component plays a crucial role, which tries to reverse the separation tendency. As can be seen from the velocity profiles, wake impingement shortens the bubble height and reduces its streamwise extent. Compared to the steady case, however, the onset of the separation bubble has not changed substantially. This shows that although the impingement of the vortical wake core periodically reduces the separation bubble height, it does not have the sufficient momentum to completely suppress it. Figure 7(a) shows a substantial influence of the combined effect of the higher FSTI level of 3% and unsteady wake flow inside the separation bubble at the same position. The combination of higher turbulence intensity with unsteady wakes introduces higher fluctuation kinetic energy into the boundary layer than the case without the

turbulence grids (FSTI level of 1.9%), which tends to inhibit the separation tendency and shortens the streamwise extent of the separation bubble. It is observed that the starting point of the separation bubble moves further downstream and the reattachment point occurs earlier. Also, the size of the separation bubble is smaller. Although the combined effect of the turbulence intensity level of 3% and unsteady wake flow periodically reduces the separation bubble height, it does not have the sufficient momentum to completely suppress the bubble.

Introducing the higher FSTI level of 8% subdues the unsteady wake effect to such an extent that the velocity and fluctuation profiles do not reveal any changes with regard to the wake frequency, as shown in Figs. 8(a) and 8(b). Increasing the FSTI level to 13% further diminishes the effects of the periodic wakes. As seen in Fig. 9(a), the separation bubble is almost suppressed for $Re=110,000$ with the turbulence intensity level of 13%. Hence, the turbulence grid with 13% of turbulence intensity level has not sufficient momentum to completely suppress it. In both turbulence cases of 8% and 13%, the periodic unsteady wakes along with their high turbulence intensity vortical cores seem to be completely submerged in the stochastic high frequency freestream turbulence generated by grids.

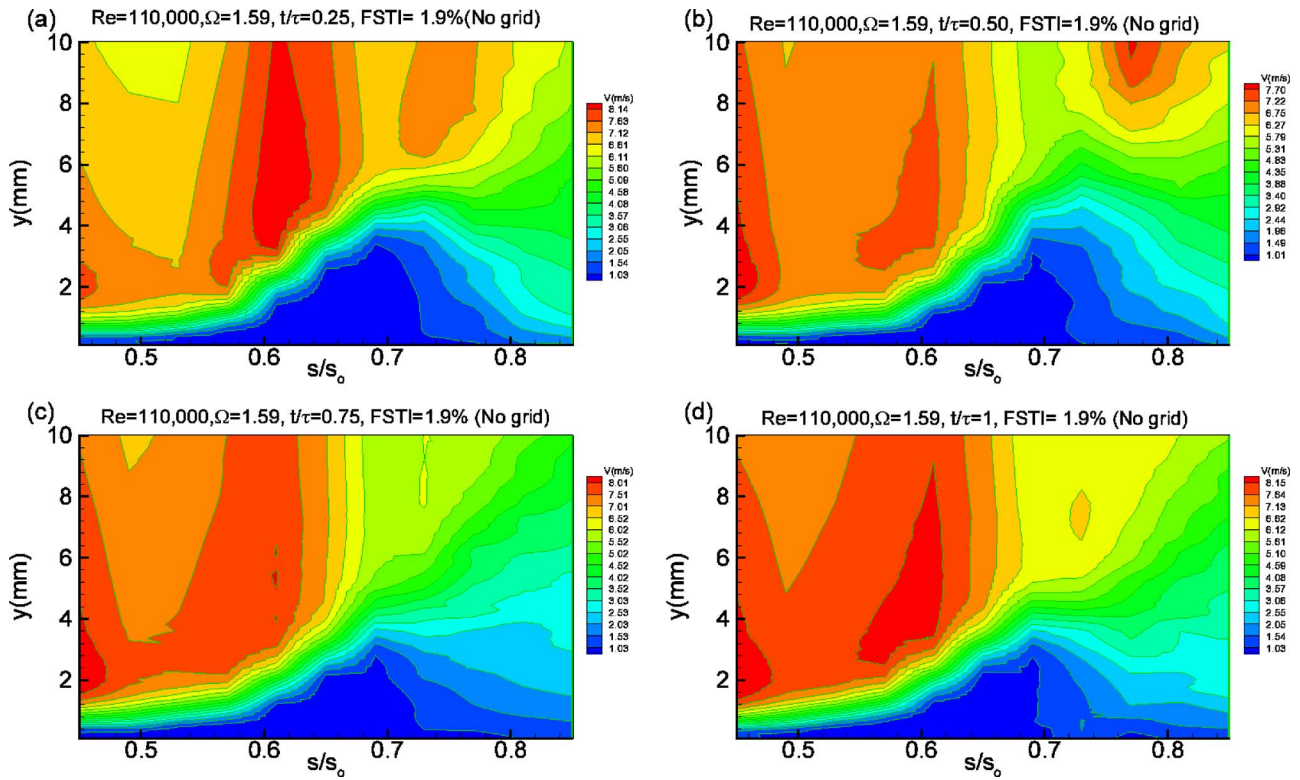


Fig. 10 Ensemble-averaged velocity contours along the suction surface for different s/s_0 with time t/τ as parameter for $\Omega = 1.59$ ($S_R=160$ mm) at $Re=110,000$ and $FSTI=1.9\%$ (without grid)

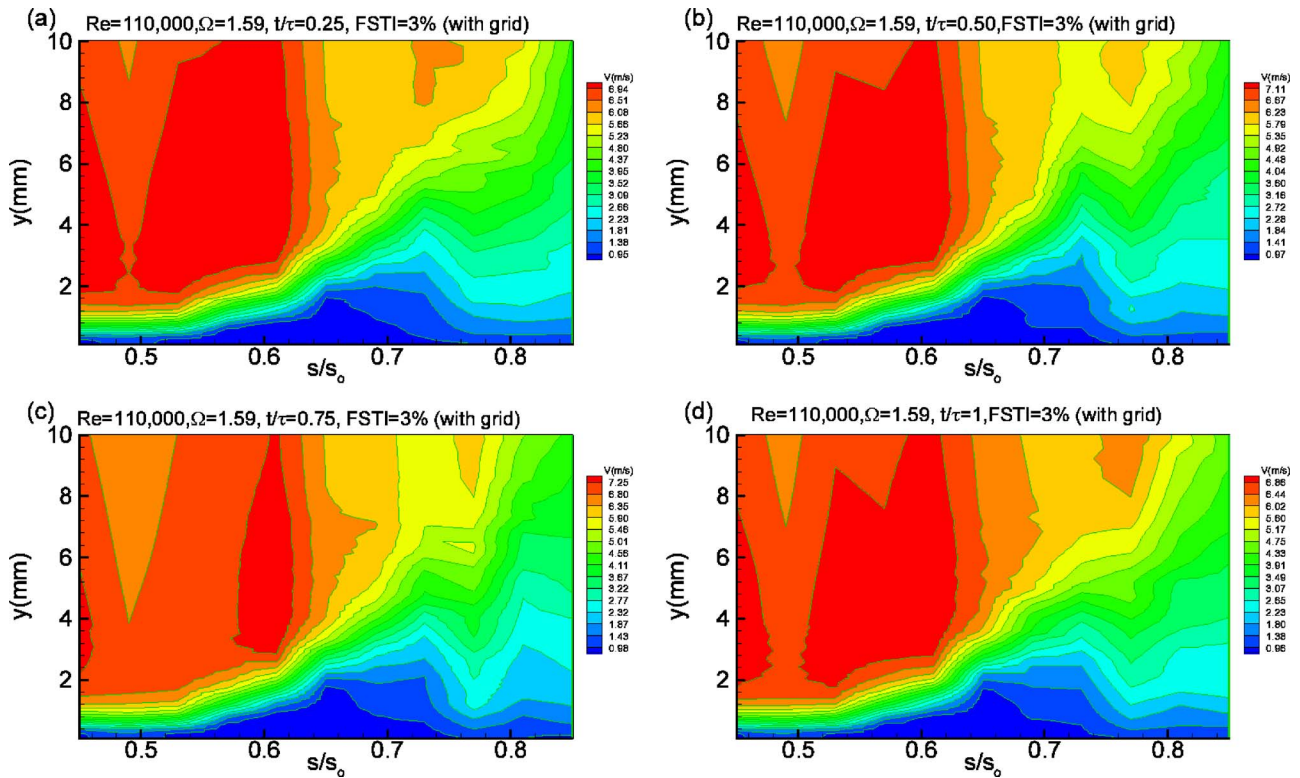


Fig. 11 Ensemble-averaged velocity contours along the suction surface for different s/s_0 with time t/τ as parameter for $\Omega = 1.59$ ($S_R=160$ mm) at $Re=110,000$ and $FSTI=3\%$ (with TG1)

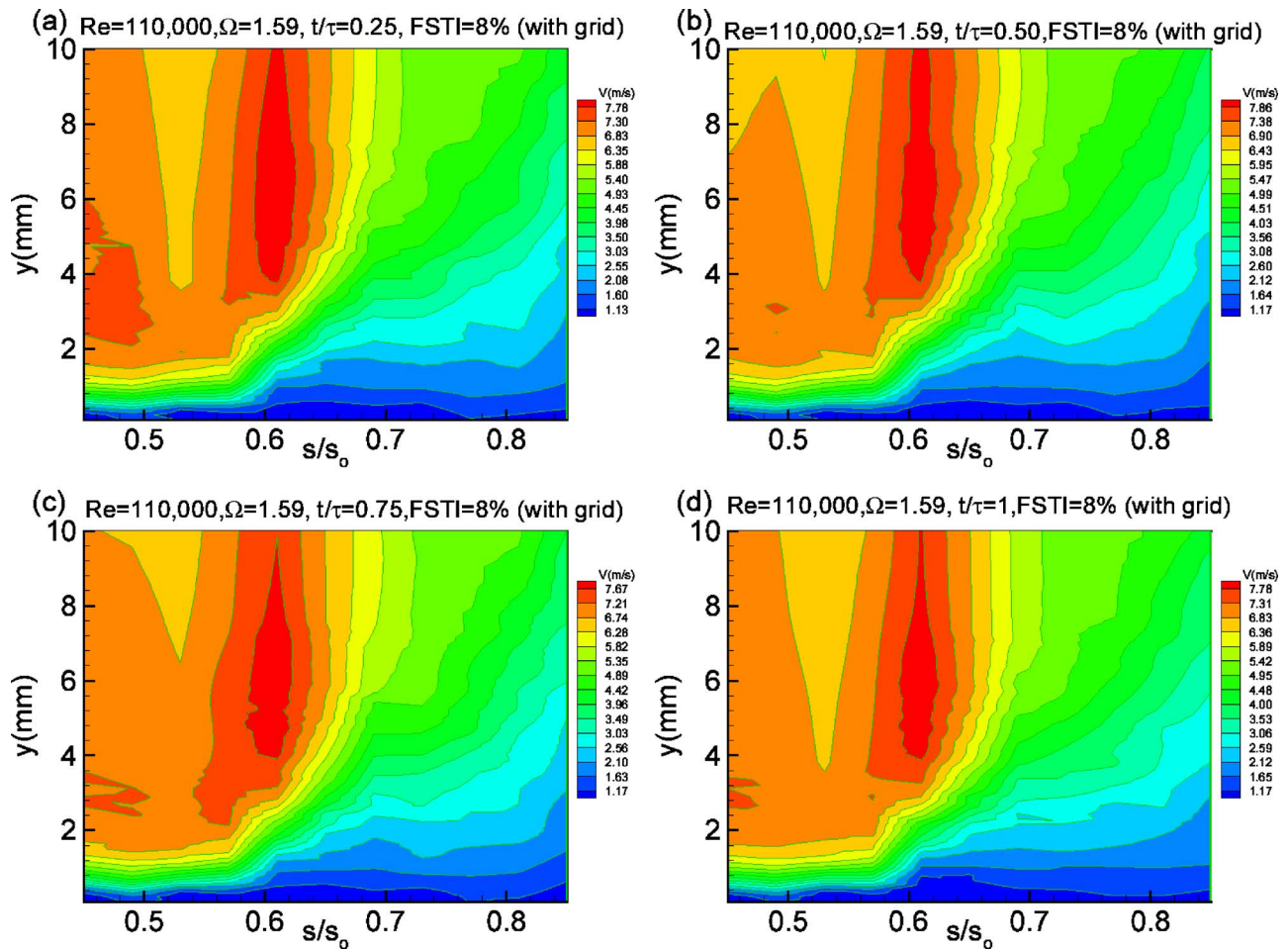


Fig. 12 Ensemble-averaged velocity contours along the suction surface for different s/s_0 with time t/τ as parameter for $\Omega = 1.59$ ($S_R = 160$ mm) at $Re = 110,000$ and $FSTI = 8\%$ (with TG2)

Behavior of Separation Bubble Under Periodic Wake Flow Condition. The combined effects of the periodic unsteady wakes and high turbulent intensity on the onset and extent of the separation bubble are shown in Figs. 10–17 for the Reynolds number of 110,000 with $FSTI$ s of 1.9%, 3.0%, 8.0%, and 13.0% for two different frequencies, namely, $\Omega = 1.59$ ($S_R = 160$ mm) and $\Omega = 3.18$ ($S_R = 80$ mm). These figures display the full extent of the separation bubble and its behavior under a periodic wake flow impingement at different t/τ . The value of t/τ corresponds to the point in the cycle at which the data acquisition system is triggered. During a rod-passing period, the wake flow and separation bubble undergo a sequence of flow states that are not noticeably different when the unsteady data are time averaged.

Variation of FSTI at $\Omega = 1.59$. Figure 10(a) exhibits the separation bubble in its full size at $t/\tau = 0.25$. At this instant of time, the incoming wakes have not reached the separation bubble. At $t/\tau = 0.5$, the wake, with its highly turbulent vortical core, passes over the blade and generates high turbulence kinetic energy. At this point, the wake turbulence penetrates into the bubble causing a strong mass, momentum, and energy exchange between the wake flow and the fluid contained within the bubble. This exchange causes a dynamic suppression and a subsequent contraction of the bubble. As the wake travels over the bubble, the size of the bubble continues to contract at $t/\tau = 0.75$ and reaches its minimum size at $t/\tau = 1.0$. At $t/\tau = 1$, the full effect of the wake on the boundary layer can be seen before another wake appears and the bubble moves back to the original position.

Increasing the turbulence level to 3% by attaching the turbu-

lence grid TG1 (detail specifications are listed in Table 1) and, keeping the same reduced frequency of $\Omega = 1.59$, has reduced the lateral extent of the bubble by $\sim 50\%$, as can be seen in Fig. 11. Furthermore, the instance of the wake traveling over the separation bubble, which is clearly visible in Fig. 10, has diminished almost entirely. Further increasing the turbulence intensity to 8% and 13%, respectively, has caused the bubble height to further reduce as shown in Figs. 12 and 13. Although the higher turbulence level has, to a great extent, suppressed the separation bubble, as Figs. 12 and 13 clearly show, it was not able to completely eliminate it. There is still a small core of separation bubble remaining. Its existence is attributed to the stability of the separation bubble at the present Re -number level of 110,000.

Variation of FSTI at $\Omega = 3.18$. Figures 14–17 reflect the dynamic behavior of the separation bubble at the same turbulence levels as above, but at a higher reduced frequency of $\Omega = 3.18$. Similar to the previous case, the case with the cascade $FSTI$ level of 1.9% exhibits the reference configuration for $\Omega = 3.18$ ($S_R = 80$ mm), where the bubble undergoes periodic contraction and expansion. The temporal sequence of events is identical with the previous case making a detailed discussion unnecessary. In contrast to the events described in Fig. 10, the increased wake frequency in the reference configuration (Fig. 14) is associated with higher mixing and, thus, higher turbulence intensity, which causes a more pronounced contraction and expansion of the bubble.

Increasing the turbulence level to 3% has slightly reduced the lateral extent of the bubble, as can be seen in Fig. 15. The instance of the wake traveling over the separation bubble proceeds in an

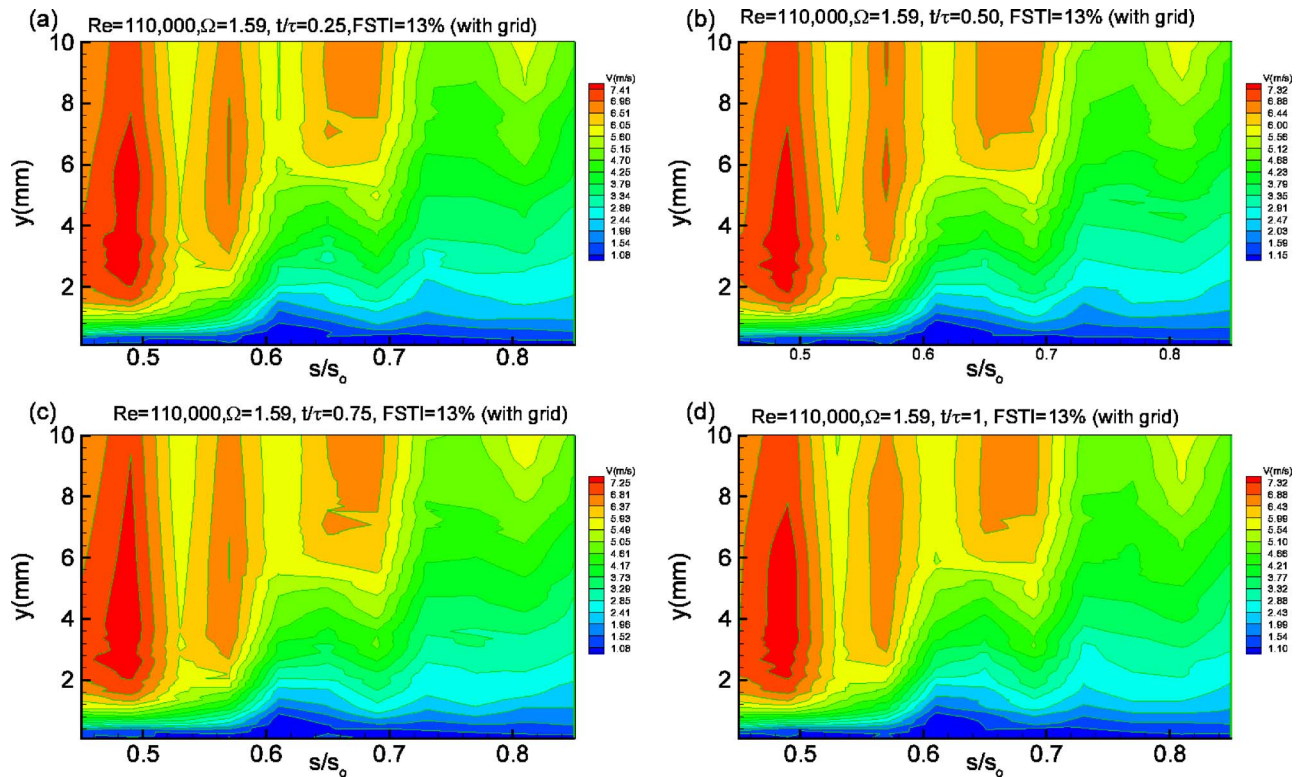


Fig. 13 Ensemble-averaged velocity contours along the suction surface for different s/s_0 with time t/τ as parameter for $\Omega = 1.59$ ($S_R=160$ mm) at $Re=110,000$ and $FSTI=13\%$ (with TG3)

analogous way (discussed in Fig. 10). Further increasing the turbulence intensity to 8% and 13%, respectively, has caused the bubble height to further reduce, as shown in Figs. 16 and 17. Although the higher turbulence level has to a great extent, suppressed the separation bubble, as Figs. 16 and 17 clearly show, it was not able to completely eliminate it. There is still a small core of separation bubble remaining. Its existence is attributed to the stability of the separation bubble at the present Re -number level of 110,000.

Time-Averaged, Ensemble-Averaged Boundary Layer Integral Quantities. The integral parameters, such as the momentum deficiency thickness δ_2 and shape factor H_{12} , are of particular interest to turbine designers, since they provide an accurate first estimation of the quality of the designed blade. Although the distribution of momentum deficiency thickness δ_2 provides insight into the loss behavior of the blade, the distribution of the shape factor H_{12} sufficiently furnishes accurate information about the flow separation behavior.

Time-Averaged δ_2 Distribution. For the reference case of $FSTI=1.9\%$, Fig. 18(a) upstream of the separation, start the δ_2 values for three different reduced frequencies experiences only minor changes. Passing the separation start, major systematic changes are observed with $\Omega=0$ (no rod) being the largest and $\Omega=3.18$ the smallest. Thus, increasing the reduced frequency causes a reduction of δ_2 , as seen in Fig. 18(a). A combination of higher $FSTI$ levels with unsteady wakes reveal that the noticeable deviation in δ_2 distribution between the steady and unsteady cases discussed above is diminishing with increasing the turbulence intensity level, as shown in Fig. 18(b)–18(d). The physical explanation of this phenomenon is directly derived from the influence of the wake impingement on the boundary layer. The vortical core of the passing wakes that are induced by the moving rods cause a periodic increase in turbulence resulting in higher losses and, thus, a periodic increase in δ_2 , as shown in Figs. 19(a)–19(c). After the

wakes have passed, the effects of the calmed region dominate and the momentum thickness reduces significantly. The time integral of the temporal distribution of δ_2 along the suction surface for three different frequencies, plotted in Figs. 18(a)–18(d), reflect the wake effects on boundary layer momentum thickness. The presence of the unsteady wakes decreases the boundary layer momentum thickness and, thus, the profile losses, as long as the level of the time-averaged turbulence fluctuations is below the maximum level of the wake fluctuation v_{max} (shown in Fig. 5(a)). However, the decreasing effect diminishes integrally whenever the $FSTI$ level approaches values that cause the wake fluctuation to partially or totally submerge into the freestream turbulence, as shown in Figs. 18(b)–18(d).

Time-Averaged H_{12} Distribution. For $FSTI=1.9\%$ upstream of the separation bubble, the shape factor for three different reduced frequencies experiences only minor changes, as shown in Fig. 20(a). However, approaching the separation bubble, the shape factor systematically increases at a relatively steep rate with $\Omega=0$ as the highest followed by $\Omega=1.59$ and $\Omega=3.18$. It reaches a maximum value of about $H_{12}=6.1$ at $s/s_0=0.65$. Passing the separation bubble, the shape factor sharply decreases approaching a level that is typical of an attached turbulent boundary layer flow. As in the δ_2 case, for $FSTI=1.9$, major systematic changes are observed with increasing the reduced frequency. However, the combination of higher turbulent intensity levels with unsteady wake flows result in a significant decrease of the shape factor.

Ensemble-Averaged δ_2 Distribution. Ensemble-averaged distributions of the momentum deficiency thickness δ_2 at $s/s_0 = 0.61, 0.65, \text{ and } 0.73$ within the separation bubble are shown in Figs. 19 and 21 for $\Omega=1.59$ and $\Omega=3.18$ values. The thickness values are nondimensionalized with the value of the steady case at $\Omega=0$. The period τ represents the wake-passing period that is specific to the individual wake-generating cluster, which is characterized by the Ω value under investigation. The periodic

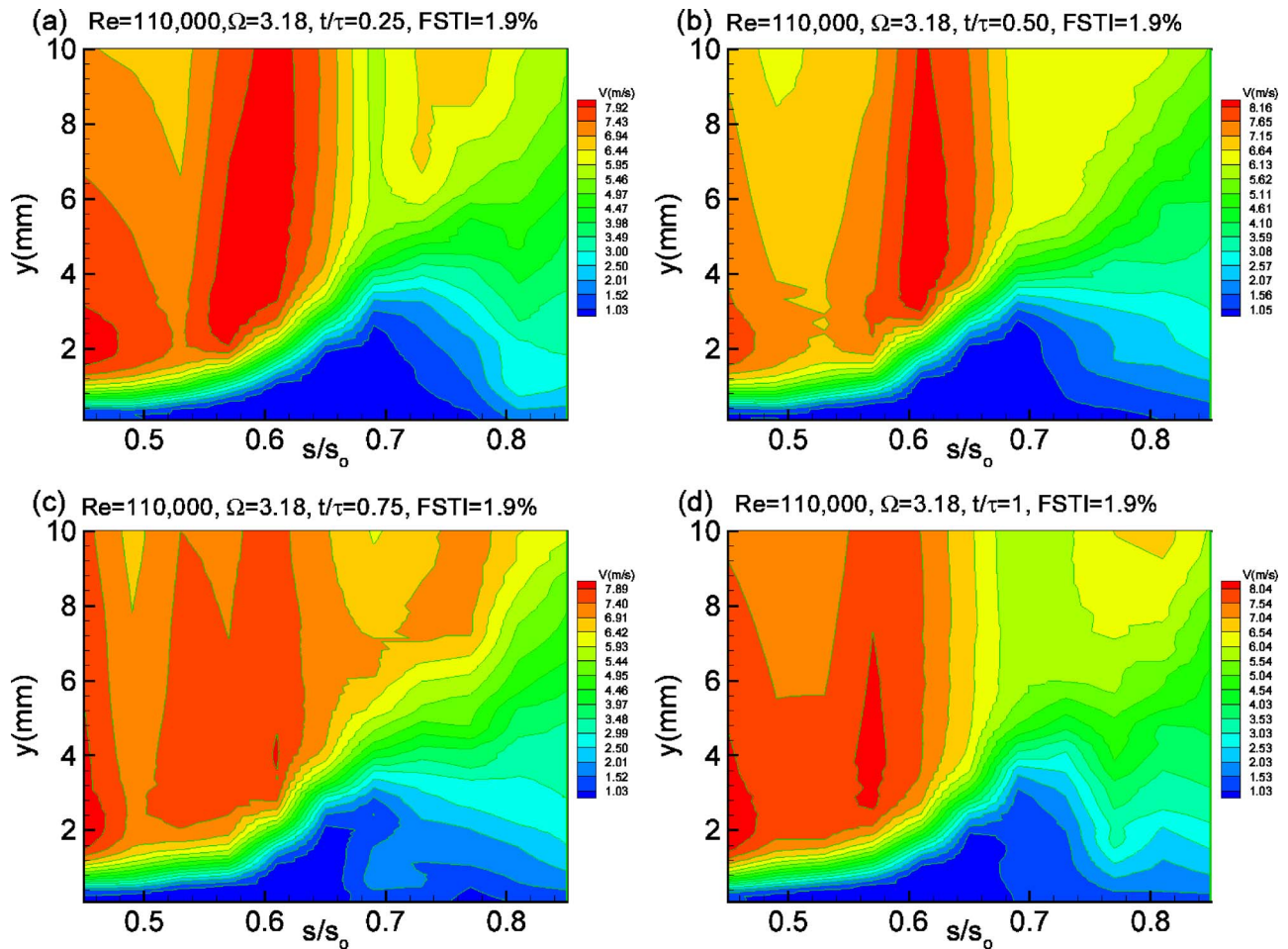


Fig. 14 Ensemble-averaged velocity contours along the suction surface for different s/s_0 with time t/τ as parameter for $\Omega=3.18$ ($S_H=80$ mm) at $Re=110,000$ and $FSTI=1.9\%$ (without grid)

behavior of the ensemble-averaged momentum thickness over the separation bubble as a result of the embedded periodic wake flow is clearly visible from Figs. 19(a) and 21(a). To avoid repetition, as a representative, the δ_2 distribution at $s/s_0=0.65$ location in Fig. 19(a) is generically discussed. For each wake-passing period, the periodic δ_2 distribution reveals one distinct maximum and one minimum with several peaks and valleys in between. The ensemble-averaged δ_2 has a maximum when the wake flow associated with a pronounced velocity deficit impinges on the separation bubble. This occurs at $t/\tau=0.6, 1.6,$ and 2.6 . These exactly correspond to the instants at which the ensemble-averaged velocity distributions have their minimum, as shown in Fig. 5(a). Likewise, the distinct minimum δ_2 values periodically encountered at $t/\tau=0.4, 1.4,$ and 2.4 correspond to the instance at which the wake external core flow impinges on the bubble. The δ_2 distribution for $\Omega=3.18$ is presented in Fig. 21(a), which are similar to the one presented above, and repeating the discussion is unnecessary.

Increasing the FSTI level does not affect the periodicity of δ_2 distributions, as shown in Fig. 19(b) and 19(d). However, the pronounced phase difference diminishes.

Similar results are observed when operating at a reduced frequency of $\Omega=3.18$, which is shown in Fig. 21(a)–21(d). However, the combination of higher turbulence intensity levels with unsteady wakes reveal that the noticeable deviation in momentum thickness distribution between the steady and unsteady cases discussed above is diminishing with increasing the turbulence intensity level, as shown in Fig. 21(a)–21(d).

The ensemble-averaged integral parameter discussed above is

essential to calculate the ensemble-averaged and time-averaged profile loss coefficients at each streamwise position. Furthermore, the integration of the time-averaged loss coefficient distribution over the entire blade surface provides the global profile loss coefficient. A simple procedure given in [26] describes how the loss coefficient can be calculated using the integral parameters.

Conclusions

A detailed experimental study on the behavior of the separation bubble on the suction surface of a highly loaded LPT blade, under combined effects of periodic unsteady wake flows and freestream turbulence intensity at $Re=110,000$, was presented. Varying the turbulence intensity levels, one steady and two different unsteady inlet wake flow conditions with the corresponding passing frequencies, the wake velocity, and the turbulence intensities were investigated by utilizing a large-scale, subsonic research facility. Periodic unsteady wake flow was established by translational motion of two parallel moving timing belts on which cylindrical rods are attached. The results of the unsteady boundary layer measurements were presented in the ensemble-averaged and contour plot forms. Detailed unsteady boundary layer measurements identified the onset and extension of the separation bubble as well as its behavior under the individual and combined effects of unsteady wake flow and high turbulence intensity. It was found that the periodic unsteady wake flow definitely determines the separation dynamics as long as the level of the time-averaged turbulence fluctuations is below the maximum level of the wake fluctuation

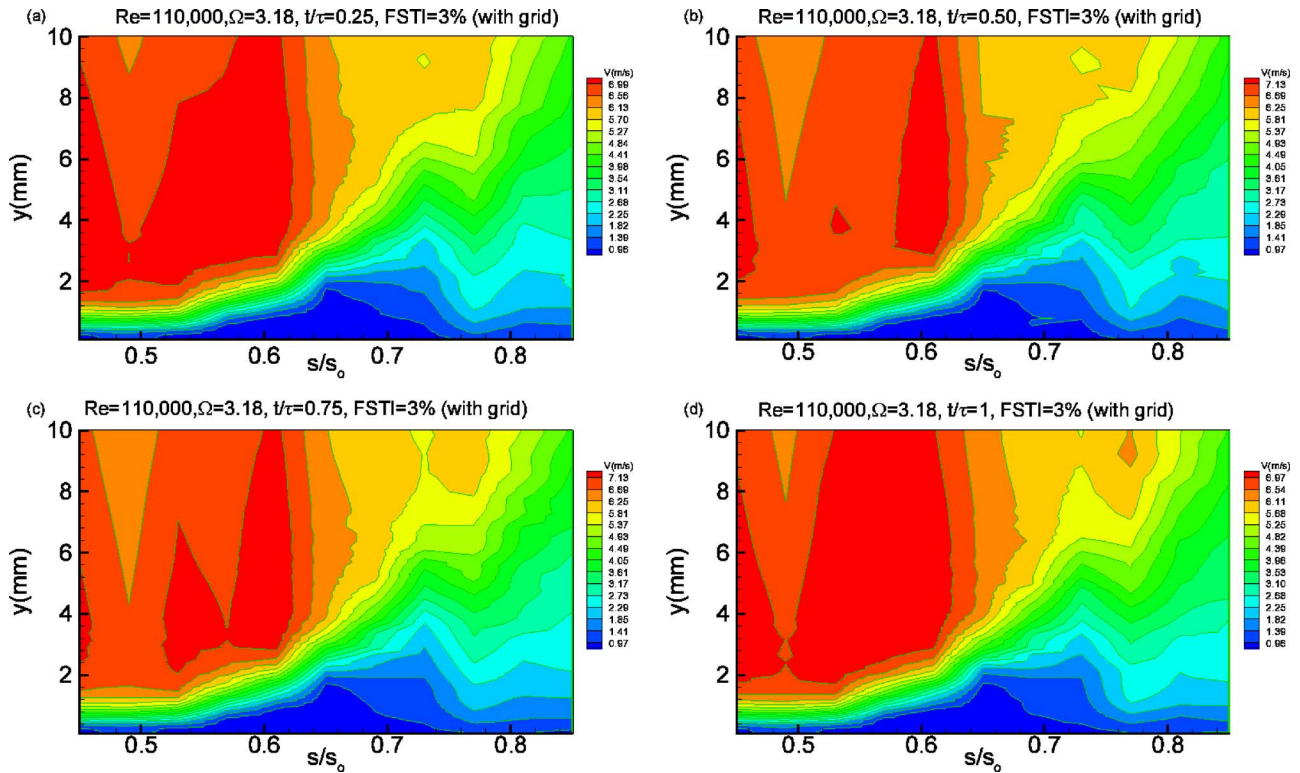


Fig. 15 Ensemble-averaged velocity contours along the suction surface for different s/s_0 with time t/τ as parameter for $\Omega = 3.18$ ($S_R = 80$ mm) at $Re = 110,000$ and $FSTI = 3\%$ (with TG1)

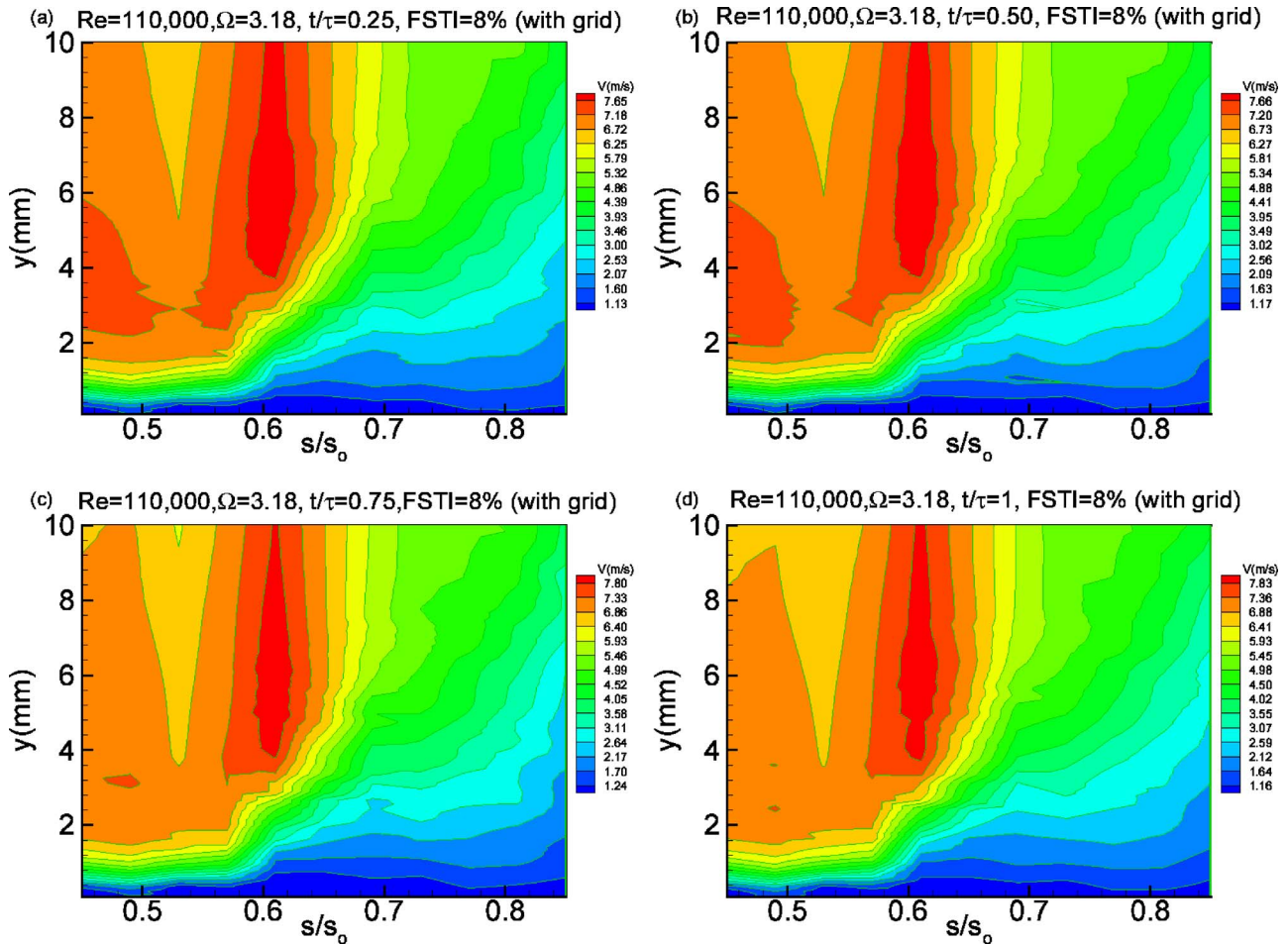


Fig. 16 Ensemble-averaged velocity contours along the suction surface for different s/s_0 with time t/τ as parameter for $\Omega = 3.18$ ($S_R = 160$ mm) at $Re = 110,000$ and $FSTI = 8\%$ (with TG2)

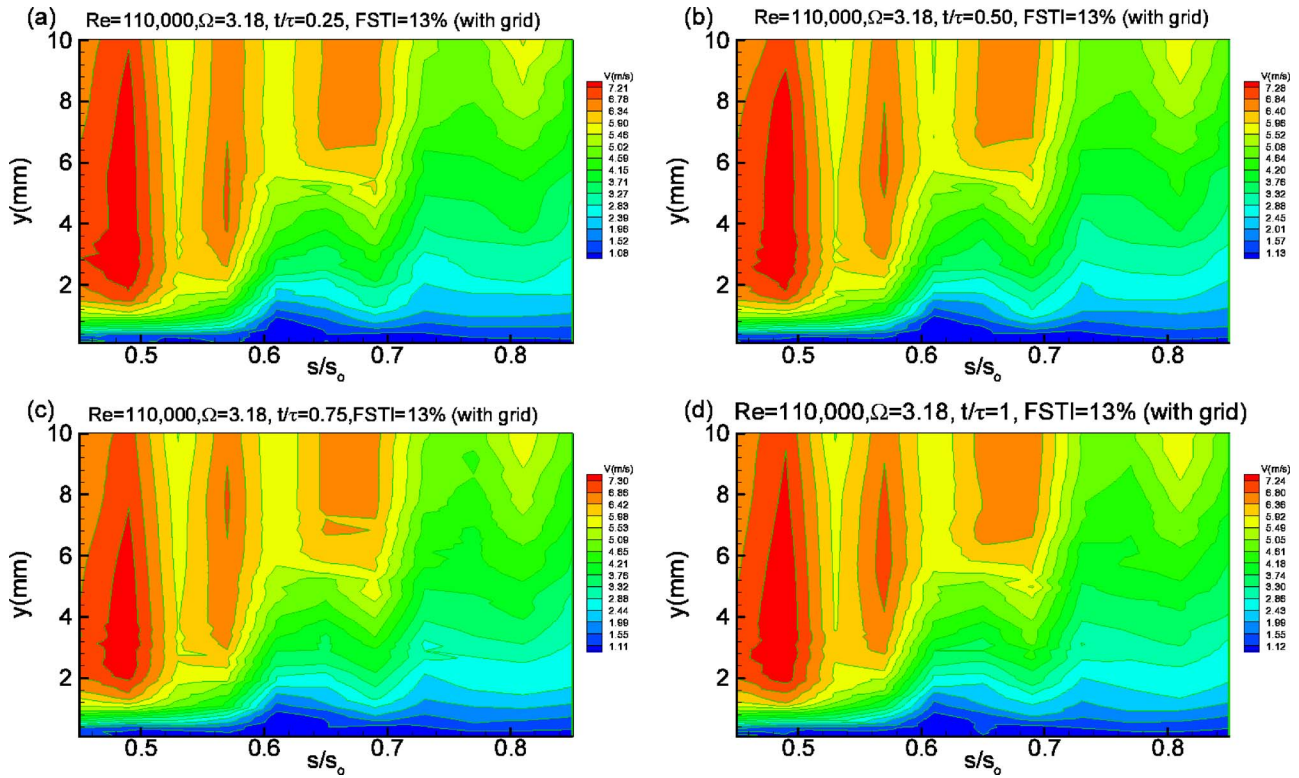


Fig. 17 Ensemble-averaged velocity contours along the suction surface for different s/s_0 with time t/τ as parameter for $\Omega = 3.18$ ($S_R = 160$ mm) at $Re = 110,000$ and $FSTI = 13\%$ (with TG3)

v_{max} . Increasing the inlet turbulence level above v_{max} caused the wake periodicity to totally submerge in turbulence. In this case, the separation dynamics of the separation bubble is governed by the flow turbulence that is responsible for complete suppression of the separation bubble. The time-averaged integral quantities showed the impact of the unsteady wake flow and the FSTI on the boundary layer parameters and, hence, on the profile loss coefficient and efficiency. Unsteady wake flow caused a reduction of the

losses due to suppressed or reduced separation boundary layers. One of the striking features this study reveals is that the separation bubble has not disappeared completely despite the high turbulence intensity and the significant reduction of its size which is reduced to a tiny bubble.

Acknowledgment

The presented study is a part of an ongoing LPT-aerodynamics project executed by the NASA Glenn Research Center. The au-

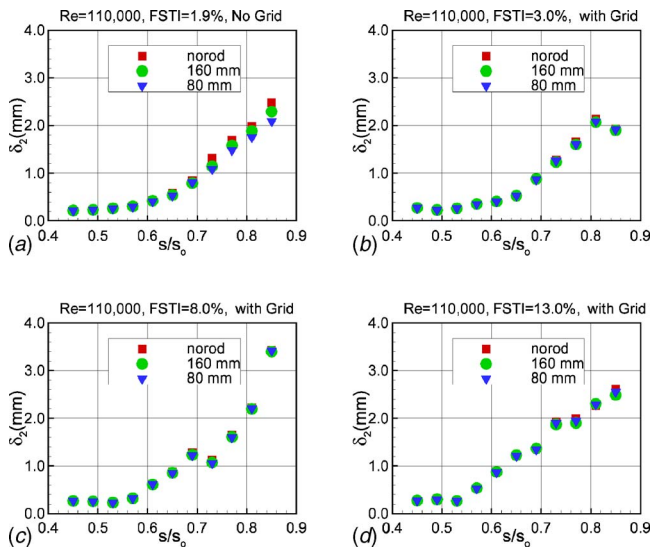


Fig. 18 Time-averaged momentum thickness for (a) $FSTI = 1.9\%$ (without grid), (b) $FSTI = 3\%$ (with grid TG1), (c) $FSTI = 8\%$ (with grid TG2), and (d) $FSTI = 13\%$ (with grid TG3) for three different reduced frequencies of $\Omega = 0, 1.59, 3.18$ (no rod, 160 mm, 80 mm) at $Re = 110,000$

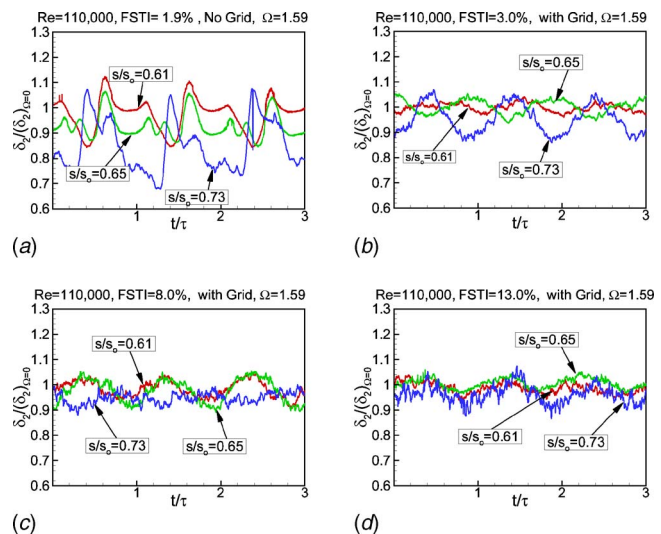


Fig. 19 Ensemble-averaged relative momentum thickness distribution along the suction surface for different streamwise positions for (a) $FSTI = 1.9\%$ (without grid), (b) $FSTI = 3\%$ (with grid TG1), (c) $FSTI = 8\%$ (with grid TG2), and (d) $FSTI = 13\%$ (with grid TG3) for $\Omega = 1.59$ (160 mm) at $Re = 110,000$

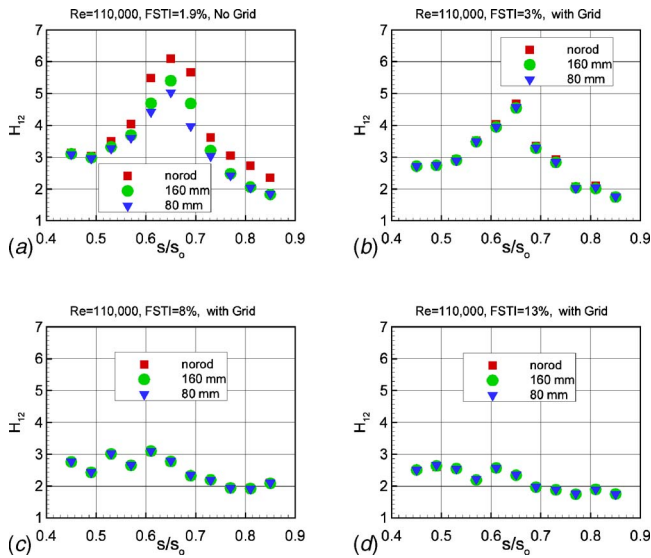


Fig. 20 Time-averaged shape factor for (a) FSTI=1.9% (without grid), (b) FSTI=3% (with grid TG1), (c) FSTI=8% (with grid TG2), (d) FSTI=13% (with grid TG3) for three different reduced frequency of $\Omega=0, 1.59, 3.18$ (no rod, 160 mm, 80 mm) at $Re=110,000$

thors were supported by NASA Cooperative Agreement NCC3-793 monitored by Dr. David Ashpis. The support and permission for publication is gratefully acknowledged. The authors also gratefully acknowledge Pratt & Whitney for providing the research community with the blade coordinates.

Nomenclature

- c = blade chord
- c_{ax} = axial chord
- C_p = pressure coefficient, $C_p = (p_i - p_s) / (p_i - p_s)_{inl}$
- D_R = rod diameter
- FSTI = freestream turbulence intensity
- H_{12} = shape factor, $H_{12} = \delta_1 / \delta_2$
- G_O = grid bar opening
- G_T = grid bar thickness
- G_{LE} = grid distance from blade leading edge
- L_{SS} = suction surface length
- p_i = static pressure taps $i=1, \dots, 48$
- p_s, p_t = static and total pressure at the inlet
- Re_{LSS} = Reynolds number based $Re_{LSS} = L_{SS} V_{exit} / \nu$
- S_B = blade spacing
- S_R = rod spacing
- s = streamwise distance from the leading edge of the blade
- s_o = streamwise distance from blade leading to trailing edge
- t = time
- TG = Turbulence generator grid
- U = belt translational velocity
- V = velocity
- \bar{V} = time-averaged velocity
- v = fluctuation velocity
- V_{ax} = axial velocity
- V_{exit} = exit velocity
- α = flow angle
- γ = blades stagger angle
- δ_1 = boundary layer displacement thickness
- δ_2 = boundary layer momentum thickness
- Λ = integral length scale $\Lambda = \bar{V} E_{(f=0)} / v_{rms}^2$

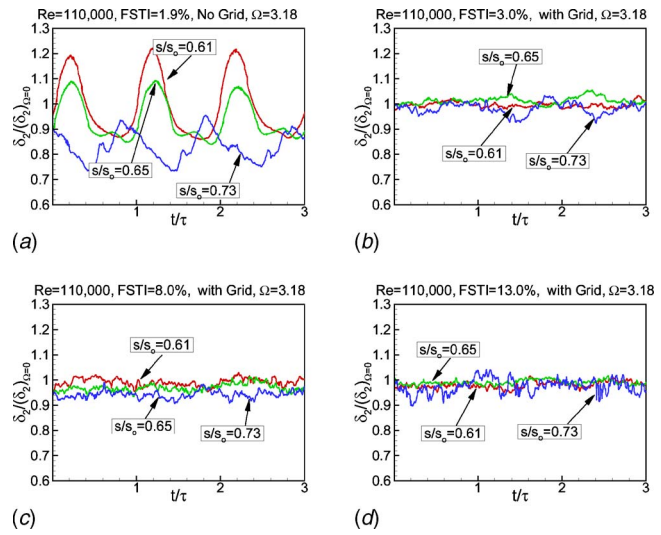


Fig. 21 Ensemble-averaged relative momentum thickness distribution along the suction surface for different streamwise positions for (a) FSTI=1.9% (without grid), (b) FSTI=3% (with grid TG1), (c) FSTI=8% (with grid TG2), and (d) FSTI=13% (with grid TG3) for $\Omega=3.18$ (80 mm) at $Re=110,000$

- ν = kinematic viscosity
- σ = cascade solidity, $\sigma = c / S_B$
- τ = one wake-passing period
- φ = flow coefficient, $\varphi = V_{ax} / U$
- Ψ_A = Zweifel coefficient
- $\Psi_A = 2 \sin^2 \alpha_2 (\cot \alpha_2 - \cot \alpha_1) S_B / c_{ax}$
- Ω = reduced frequency $\Omega = (c / S_R) (U / V_{ax}) = (\sigma / \varphi) \times (S_B / S_R)$

References

- [1] Lou, W., and Hourmouziadis, J., 2000, "Separation Bubbles Under Steady and Periodic Unsteady Main Flow Conditions," ASME Paper No. 2000-GT-270.
- [2] Kaszeta, R., Simon, T. W., and Ashpis, D. E., 2001, "Experimental Investigation of Transition to Turbulence as Affected by Passing Wakes," ASME Paper No. 2001-GT-0195.
- [3] Volino, R. J., and Hultgren, L. S., 2001, "Measurements in Separated and Transitional Boundary Layers Under Low-Pressure Turbine Airfoil Conditions," ASME J. Turbomach., **123**, pp. 189–197.
- [4] Brunner, S., Fottner, L., and Schiffer, H.-P., 2000, "Comparison of Two Highly Loaded Turbine Cascade Under the Influence of Wake-Induced Transition," International Gas Turbine and Aero-Engine Congress and Exposition, Munich, ASME Paper No. ASME 2000-GT-268, May 8–11.
- [5] Cardamone, P., Stadtmüller, P., Fottner, L., and Schiffer, H.-P., 2000, "Numerical Investigation of the Wake-Boundary Layer Interaction on a Highly Loaded LP Turbine Cascade Blade," International Gas Turbine and Aero-Engine Congress and Exposition, Amsterdam, ASME Paper No. ASME 2002-GT-30367, June 3–6.
- [6] Schröder, Th., 1989, "Measurements With Hot-Film Probes and Surface Mounted Hot Film Gages in a Multi-Stage Low Pressure Turbine," European Propulsion Forum, Bath, UK.
- [7] Haueisen, V., Hennecke, D. K., and Schröder, T., 1997, "Measurements With Surface Mounted Hot Film Sensors on Boundary Layer Transition in Wake Disturbed Flow," AGARD-CP-598.
- [8] Shyne, R. J., Sohn, K. H., and De Witt, K. J., 2000, "Experimental Investigation of Boundary Layer Behavior in a Simulated Low Pressure Turbine," ASME J. Fluids Eng., **122**, pp. 84–89.
- [9] Van Treuren, K. W., Simon, T., Koller, M. V., Byerley, A. R., Baughn, J. W., and Rivir, R., 2002, "Measurements in a Turbine Cascade Flow Under Ultra Low Reynolds Number Conditions," ASME J. Turbomach., **124**, pp. 100–106.
- [10] Halstead, D. E., Wisler, D. C., Okiishi, T. H., Walker, G. J., Hodson, H. P., and Shin, H.-W., 1997, "Boundary Layer Development in Axial Compressors and Turbines: Part 3 of 4," ASME J. Turbomach., **119**, pp. 225–237.
- [11] Schobeiri, M. T., Öztürk, B., and Ashpis, D., 2003, "On the Physics of the Flow Separation Along a Low Pressure Turbine Blade Under Unsteady Flow Conditions," ASME J. Fluids Eng., **127**, pp. 503–513.
- [12] Schobeiri, M. T., and Öztürk, B., 2004, "Experimental Study of the Effect of the Periodic Unsteady Wake Flow on Boundary Layer Development, Separation, and Re-attachment Along the Surface of a Low-Pressure Turbine Blade," ASME J. Turbomach., **126**(4), pp. 663–676.

- [13] Öztürk, B., Schobeiri, M. T., and Ashpis, D., 2005, "Effect of Reynolds Number and Periodic Unsteady Wake Flow Condition on Boundary Layer Development, Separation, and Re-attachment Along the Suction Surface of a Low Pressure Turbine Blade," ASME Paper No. GT2005-68600, ASME-IGTI-Conference, ASME Paper No. 6-9, Reno-Tahoe, Nevada, USA.
- [14] Öztürk, B., Schobeiri, M. T., and Ashpis, D., 2005, "Intermittent Behavior of the Separated Boundary Layer Along the Suction Surface of a Low Pressure Turbine Blade Under Periodic Unsteady Flow Conditions," ASME-IGTI-Conference, June 6-9, 2005, ASME Paper GT2005-68603, Reno-Tahoe.
- [15] Zhang, X. F., and Hodson, H., 2004, "The Combined Effects of Surface Trips and Unsteady Wakes on the Boundary Layer Development of an Ultra-High-Lift LP Turbine Blade," ASME, GT-2004-53081.
- [16] Zhang, X. F., Vera, M., Hodson, H., and Harvey, N., 2005, "Separation and Transition Control on an Aft-Loaded Ultra-High-Lift LP Turbine Blade at Low Reynolds Numbers Low-Speed Investigation," ASME, GT-2005-68892.
- [17] Soranna, F., Chow, Y., Uzol, O., and Katz, J., 2005, "The Effect Of IGV Wake Impingement on The Flow Structure And Turbulence around a Rotor Blade," ASME, GT2005-68801.
- [18] Chow, Y.-C., Uzol, O., and Katz, J., 2002, "Flow Non-Uniformities and Turbulent "Hot Spots" Due to Wake-Blade and Wake-Wake Interactions in a Multistage Turbomachine," ASME J. Turbomach., **124**(4), pp. 553-563.
- [19] Uzol, O., Chow, Y.-C., Katz, J., and Meneveau, C., 2002, "Experimental Investigation of Unsteady Flow Field Within A Two Stage Axial Turbomachine Using Particle Image Velocimetry," ASME J. Turbomach., **124**(4), pp. 542-552.
- [20] Schobeiri, M. T., John, J., and Pappu, K., 1996, "Development of Two-Dimensional Wakes Within Curved Channels, Theoretical Framework and Experimental Investigation," ASME J. Turbomach., July, 1996, Vol. **118**, pp. 506-518.
- [21] Hinze, J. O., 1975, "*Turbulence*," McGraw-Hill, New York, 2nd edition.
- [22] Chakka, P., and Schobeiri, M. T., 1999, "Modeling of Unsteady Boundary Layer Transition on a Curved Plate Under Periodic Unsteady Flow Condition: Aerodynamic and Heat Transfer Investigations," ASME J. Turbomach., **121**, pp. 88-97.
- [23] Kline, S. J., and McClintock, F. A., 1953, "Describing Uncertainties in Single-Sample Experiments," Mech. Eng. (Am. Soc. Mech. Eng.), **75**, pp. 3-8.
- [24] Hourmouziadis, J., 1989, "Blading Design for Axial Turbomachines," AGARD, Lecture Series LS-167.
- [25] Eifler, J., 1975, "Zur Frage der freien turbulenten Strömungen, insbesondere hinter ruhenden und bewegten Zylindern," Dissertation D-17, Technische Hochschule Darmstadt, Germany.
- [26] Schobeiri, M. T., 2001, "Experimental Determination of LPT-Profile Losses at Low Reynolds Numbers," Progress Report No. 12, Oct. 25, NASA GRC.

The Application of an Aerodynamic Shroud for Axial Ventilation Fans

D. R. Neal

e-mail: nealdoug@msu.edu

J. F. Foss

Department of Mechanical Engineering,
Michigan State University,
East Lansing, MI 48824

An experimental investigation of an aerodynamic shroud applied to an axial ventilation fan system is reported. The aerodynamic shroud consists of a pressurized plenum and Coanda attachment surface, which also serves as the shroud for the fan. This combination delivers a curved surface wall jet of high momentum air into the tip region of the fan and subsequently into the downstream diffuser region. Simultaneous improvements of performance and efficiency were found for a specific fan geometry with an aerodynamic shroud system when compared with a standard production fan (no shroud) system. Overall, the addition of the aerodynamic shroud was able to increase the system flowrate by 34% while simultaneously improving the efficiency by 13%. A higher efficiency condition (+17%) was also found that resulted in a somewhat lower improvement in flow rate (+23%). These results clearly show that the best blade design for the aerodynamic shroud system is different than the best blade design for a system that does not include the aerodynamic shroud. Particle image velocimetry measurements made at the exit plane of the system's diffuser provide insight into the mechanistic basis for the performance measurements. [DOI: 10.1115/1.2734206]

Introduction

Fresh air ventilation and air circulation within livestock production buildings affects the health and growth rate of confined animals. This is especially true during periods of high ambient temperatures when thermal stress resulting from the elevated temperatures within a livestock enclosure negatively alters the rates of production, growth, conception, and survival for almost all livestock species [1–4]. These effects are especially pronounced in the production of swine and poultry where the animals are confined at relatively high density. It has been quantitatively shown that a form of “tunnel ventilation,” in which an axial velocity of order 5.5 km/h (1.5 m/s) of evaporatively cooled air passing over the chickens in a poultry enclosure will significantly enhance their egg production (layers) and weight gain (broilers). This cooling airflow is induced by placing a bank of exhaust fans at the end of a (typically) 122 m long building (see Ref. [5]). The importance of ventilation in swine buildings has been documented by Mangold et al. [1] and Nienaber et al. [4]. However, implementing a tunnel ventilation system will substantially increase the producer's costs.

The exchange of fresh air and proper distribution of ventilating air within greenhouses also profoundly affects the health of the plants that are raised in these environments. Heat, dust, and other pollutants must be routinely removed from the air inside a greenhouse. Excess heat is generated through a process of trapped thermal energy that is commonly known as the greenhouse effect [6]. Solar energy can quickly elevate a closed greenhouse to temperatures that are well in excess of the optimum for plant health. Most commercial greenhouses rely on ventilation fans to discharge this warm air and replace it with cooler, outside air. Additionally, proper circulation of air in commercial greenhouses is critical to preventing mold and mildew, which can destroy crops. Most mechanically ventilated greenhouses use an exhaust, or negative pressure system [7]. Similar benefits exist for cattle barns and

other types of facilities. Details can be found in Ref. [8]. The ventilation fans are mounted on an exterior wall to exhaust air from the greenhouse, as shown in Fig. 1.

The opportunity to provide a higher flow rate for a given fan (that could lead to a reduced number of fans per building) and the opportunity to provide a more efficient installation with reduced power consumption, led to United States Department of Agriculture (USDA) support for the present study; see the Acknowledgements. The economic benefits to be derived from these improvements are presented in Ref. [8].

The documented evidence, cited above, clearly states the importance of adequate ventilation and air circulation in the operation of greenhouse and livestock buildings. Similar ventilation benefits are present in other industrial applications (warehouses, manufacturing facilities, etc.); however, the fractional costs are maximum in agricultural applications. This evidence also indicates the high costs associated with operating such ventilation systems. Developments in ventilation systems that would reduce the operating costs associated with greenhouse and livestock facilities would be of considerable benefit to United States producers. However, during the last decade, improvements to agricultural fans have been limited to passive devices such as better inlet shrouds and the addition of exit flow diffusers. Although current fans provide adequate airflow, they fail to achieve the maximum performance and efficiency that can be achieved by active control techniques. Given the narrow profit margins in agriculture and the significant cost of electricity to operate ventilation fans, it is appropriate to consider active techniques to improve efficiency and to obtain lower operating costs. Building ventilation requires fan systems that can produce high volume flow rates with high efficiencies at low pressure rise values (≈ 25 Pa). Specific quantities are cited below.

The aerodynamic shroud (see Fig. 2) was originally developed for engine driven automotive cooling fans where the relative motion of the engine with respect to the shroud requires a large gap between the fan tip and the outer shroud [9]. This tip clearance region is characterized by energy dissipation effects (i.e., losses) that are associated with the pressure-to-suction surface flows of the propeller blade. These “tip losses” can be a dramatic detriment

Contributed by the Fluids Engineering Division of ASME for publication in the JOURNAL OF FLUIDS ENGINEERING. Manuscript received June 27, 2006; final manuscript received January 2, 2007. Review conducted by Phillip M. Ligrani.



Fig. 1 Axial ventilation fans in greenhouse applications

to the performance and efficiency of an axial fan, and they are estimated to be 20–40% of the total losses, as reported by Lakshminarayana [10] and Bleier [11] among others.

Morris and Foss [9] conducted the initial study of the aerodynamic shroud application on the engine cooling fan for a light-duty truck. This fan had a diameter of 457 mm and the tip clearance was 25.0 mm. Because of the high system resistance for this configuration, which includes the grill, air conditioning condenser, radiator, and downstream blockage elements such as the engine, the pressure rise of this fan was relatively high (250–1000 Pa). The flow rates were moderate, ranging between 0.1 m³/s and 0.9 m³/s. Morris and Foss [9] found that the aerodynamic shroud was able to enhance the performance at higher flow rates, but that it degraded the performance at lower flow rates for the shroud design that terminates at its minimum radius. This trend in the experimental observations is compatible with the condition that an increasing pressure rise across an axial fan is associated with an increase in the radial component of the fan's discharge. The axially directed aerodynamic shroud flow therefore impedes the fan flow with an increasing pressure rise condition. With this understanding, it was realized that a contoured, and not a sudden expansion outlet passage, could take advantage of the aerodynamic shroud contribution. The performance benefits of these downstream geometry adjustments are documented in their study.

The fan system studied by Morris and Foss [9] represents a unique application within the wide spectrum of axial fan usages since it has an abnormally large tip clearance coupled with a high-pressure rise across the fan. It is apparent how the aerodynamic shroud can benefit fans with these operating parameters. The focus of this study was to determine if the aerodynamic shroud could benefit a fan system with a much smaller tip clearance and much lower-pressure rise values. These conditions are typical for ventilation fan systems.

Basic Considerations

The primary quantities of interest in turbomachinery exist in an integral form. These variables are the volumetric flow rate, Q (m³/s) and the pressure rise, ΔP_{sys} (Pa), across the fan blades or fan system. The flow rate and pressure rise values can also be made nondimensional using the radius of the fan (R_f) and the rotational speed (Ω) to define $U_{\text{tip}} = R_f \Omega$. By convention, these nondimensional forms are stated as

$$\phi = \frac{Q}{(R_f)^2 U_{\text{tip}}} = \frac{Q}{R_f^3 \Omega} \quad (1)$$

and

$$\psi = \Delta P_{\text{sys}} / \rho U_{\text{tip}}^2 \quad (2)$$

Conventional practice, within the community [12,13] that characterizes and utilizes ventilation fans, is to utilize dimensional representations. That practice will also be followed for ΔP_{sys} and Q_{sys} in this paper. A second community practice is to characterize the system efficiency by the ratio of “benefit/cost.” This leads to the dimensional ratio for efficiency (η)

$$\eta = \frac{Q}{\phi} \quad (3)$$

where ϕ is the input power to the fan's motor. Alternatively, and with the recognition that the principal objective of a ventilation fan is to provide a given flow rate, the nondimensional definition of efficiency as

$$\eta^* = \frac{Q \cdot (\frac{1}{2} \rho U_{\text{tip}}^2)}{\phi} \quad (4)$$

will be utilized herein. The definition was introduced by Neal [8]; it is used here as the appropriate nondimensional representation of efficiency that recognizes the volume flow rate as the principal benefit to be created by the fan systems.

When the efficiency was evaluated for a fan with an activated aerodynamic shroud (termed the “shroud on” condition), a more appropriate form of Eq. (4) was used

$$\eta^* = \frac{Q_{\text{total}} \cdot (\rho U_{\text{tip}}^2)}{\phi_f + \Delta P_{\text{shr}} \cdot Q_{\text{shr}} \cdot (1/\eta_{\text{shr}})} \quad (5)$$

This definition expands the denominator from Eq. (4) in order to separate the individual power consumption of the fan, denoted by ϕ_f , from the power consumed by the added apparatus of the aerodynamic shroud. The total volume flow rate: $Q_{\text{total}} = (Q_{\text{fan}} + Q_{\text{shroud}})$ is utilized in the numerator since the shroud flow is obtained from within the building. Hence, ΔP_{sys} represents the system pressure rise from within the building to the exterior. The

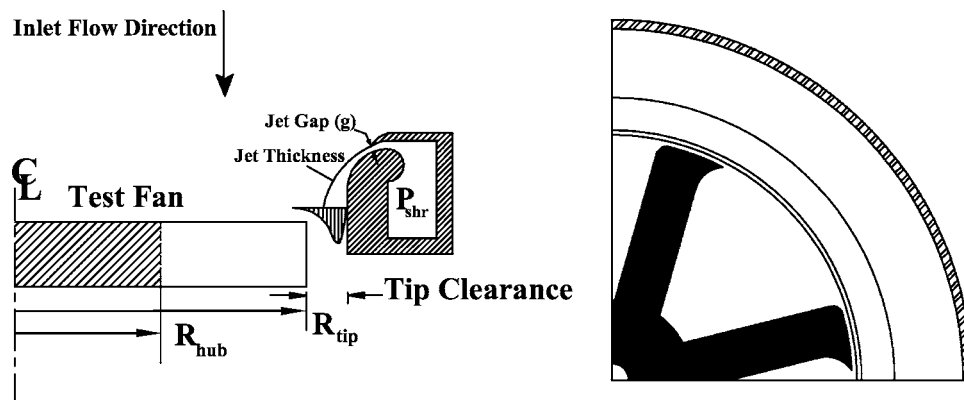


Fig. 2 The aerodynamic shroud concept

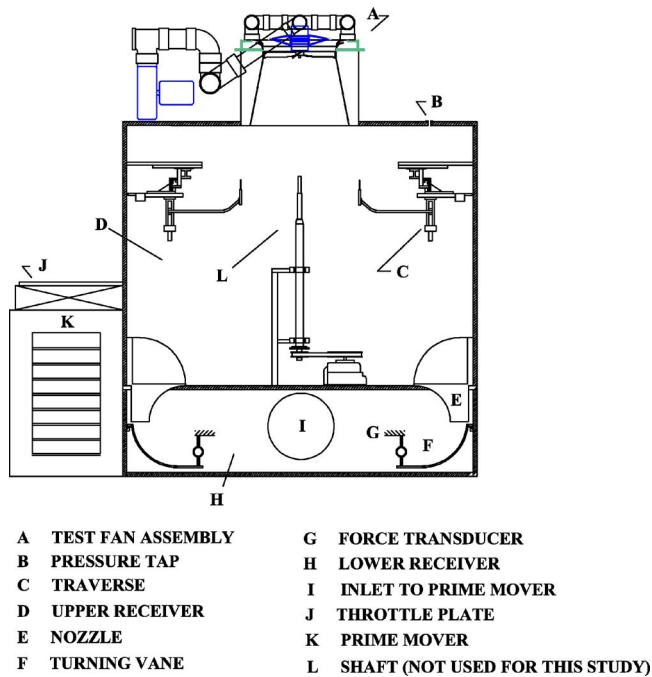


Fig. 3 AFRD facility with test fan assembly

term η_{shr} is the efficiency of the air delivery system for the aerodynamic shroud, which is estimated for this work. Since a non-optimized assembly was used in this investigation to pressurize the shroud, evaluating its efficiency directly would not be representative of a well-designed system. Therefore, a shroud efficiency value of $\eta_{shr}=0.70$ was used for all of the “shroud on” cases. This estimated η_{shr} value was also used by Morris and Foss [9].

Experimental Equipment and Procedures

The Axial Fan Research and Development (AFRD) facility [14], shown in Fig. 3, was used to acquire data for all of the fan tests. The fan assembly, including diffuser, was placed on the top surface of the facility (A). The shaft (L), which is used for driving automotive fans, was not used since these ventilation fan systems have electric motors that are integrated into their assembly. The pressure rise across the fan was monitored by a pressure transducer (0–134 Pa) that measured the differential pressure from the atmosphere to the upper receiver using a pressure tap located at (B). Air is moved from the lab into the upper receiver and then through a set of nozzles (E), where it enters the lower receiver (H) through the flow metering devices (F and G). The prime mover (K, Chicago Blower Co. SQ-36.5) draws air from the lower receiver and exhausts it back into the laboratory. The flow rate through the system can be controlled through a throttle plate (J) that is located at the exit of the prime mover.

The components E, F, and G represent a unique [15] mass flow rate measurement technique that utilizes a net moment of momentum flux to determine \dot{m} . Specifically, the ninety degree turning vane, which is supported on a knife edge, is held in place by a force transducer. The relationship between \dot{m} and the measured force is established by a calibration nozzle that replaces the fan assembly of Fig. 3. A nominal uncertainty of 0.06 kg/s (95% confidence level) is assigned to the mass flow rate measurement. This value derives from the results of Morris et al. [15].

The electrical power (ϕ_{fan}) was determined by measuring the instantaneous voltage across the motor (e_I) and the instantaneous current (i_I) delivered to the motor. Since the instantaneous voltage and current (and not the rms values) are measured, the phase relationship between them is not required for the evaluation of ϕ .

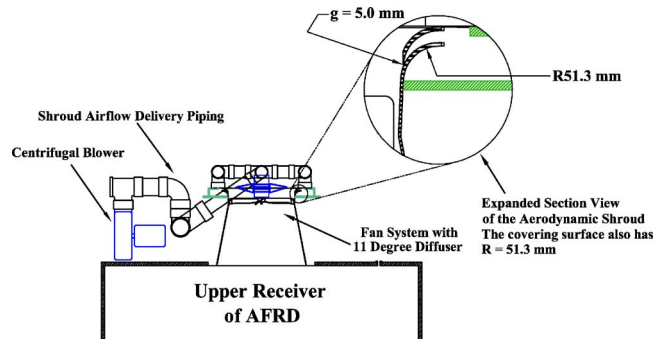


Fig. 4 Detailed view of the experimental configuration

The precision of the e_I and i_I measurements is established by the 16 bit analog to digital (A/D) converter. The uncertainty in ϕ_{fan} is conservatively estimated as $\pm 0.25\%$ given the independent measurements of voltage and current and their associated uncertainties.

The volume air flow delivered by the aerodynamic shroud jet was determined by an “elbow meter.” The calibration of the elbow meter was executed by recording the outside/inside pressure difference: ($P_{out}-P_{in}$) at the elbow for known flow rates. These known flow rates were derived from a Venturi meter that was calibrated on a sonic nozzle test stand. The latter has a NIST traceable accuracy of 0.5% of mass flow reading. The basic calibrations are understood to be a lesser factor than installation issues in establishing the appropriate uncertainty for the shroud flow rate. Care was taken to minimize these additional factors. The estimated 95% confidence level for Q_{shr} is $\pm 1.5\%$.

Data were collected in the AFRD facility with the fan and diffuser situated as shown in Fig. 3. Further details can be seen in Fig. 4, which shows the fan/diffuser combination with the dimensions of the aerodynamic shroud delivery system. The two fans and the two diffusers that were examined in this study are also part of the experimental equipment. Their detailed descriptions are presented in the section entitled “The Experimental Fan Systems.”

Neal [8] carried out a repeatability study to evaluate the complete measurement system capabilities for the “shroud off” condition. These results suggest 95% confidence levels of 1% uncertainty for the fan flow rate ($Q_{shr}=0$), and 4% for the efficiency.

A single-camera digital particle image velocimetry (PIV) system was used to acquire the velocity data in the wake of the test fan. A Rosco brand theatrical fog machine was used at the fan inlet to produce a relatively uniform seeding density at the measurement locations. Two ND-YAG pulsed 532 nm lasers and a Kodak Megaplug ES1.0 charge coupled device (CCD) camera were used. These ND-YAG lasers illuminated the region of interest (nominally 20 cm \times 20 cm) with a 1-mm-thick laser sheet. The two lasers were triggered sequentially with a typical separation time of 0.3 ms.

The CCD camera was used to acquire two grayscale digital images. The measurement region was divided into 32 \times 32 pixel interrogation regions to calculate the individual vector displacements. The calculation used a Gaussian window function and a two-dimensional (2D) Fourier transform of the image data to correlate the two images. The individual interrogation regions were overlapped by 25% (8 pixels) for increased resolution. This resulted in 1722 measured velocities for each set of images acquired.

The configuration described above provided accurate results given that the seeding was distributed in a nominally uniform manner in each image. However, at some locations high shear or poor seeding would cause poor signal to noise ratios that would lead to vector maps with many “bad” or “spurious” vectors. These vectors were post-processed using several validation techniques to

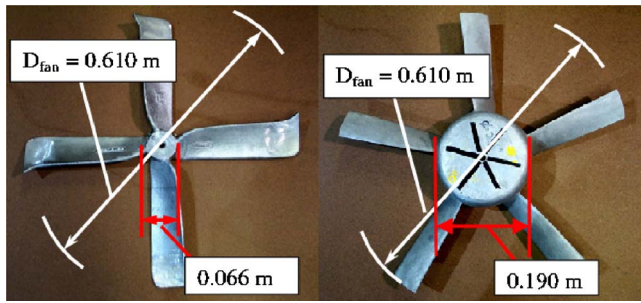


Fig. 5 Fan A (left) and Fan B (right)

ensure the integrity of the data. First, a “peak validation” was used to ensure that the maximum value of the cross correlation was a minimum of 1.2 times greater than the next highest value. This calculation removed typically 90% the suspect vectors. Second, a range validation was used such that the magnitude of the velocity in the plane of the laser light sheet could not exceed 25 m/s, which is 3.2 times the average axial velocity through the fan. Finally, a moving average validation was implemented as a final check. This moving average validation is used to accept or reject velocity magnitudes based on a comparison between neighboring values. Continuity of the flow field’s behavior is an implicit assumption in the moving-average validation method. Further details on the algorithms used for these validations can be found in Refs. [16,17].

A total of 1000 vector maps were recorded and processed for each of the measurement regions described in the following section. The time averaged velocity field was then computed from the validated vectors. Note that phase averaging the data to the rotating fan would have provided more information on the blade dynamics. However, it is the time averaged quantities that lead to the net flow rates of interest, and therefore the latter representations are used in this study.

The Experimental Fan Systems

Two separate fans were evaluated in this investigation. The first fan (Fan A), is a production design that is currently found in many agricultural buildings. This four-bladed fan is shown on the left-hand side of Fig. 5. The second fan (Fan B) is a prototype that is quite different from the fan designs that are currently found in production. The five-bladed Fan B is shown on the right-hand side of Fig. 5. The evaluation of these two fans was performed by installing each of them in the same system (i.e., shroud, housing, diffuser, and motor). Each of the two fan designs was then evaluated with the aerodynamic shroud disabled (termed the “shroud off” condition) and then with the aerodynamic shroud enabled (termed the “shroud on” condition). The aerodynamic shroud apparatus is included in the “shroud off” condition, but its flow path was blocked such that $Q_{shr}=0$. The details of the two fan designs are shown in Figs. 6 and 7, which present the details of the blade shapes, chord lengths, and inlet and outlet angles for the near-hub and the near-tip locations. Further details for the intermediate radial positions are also available at http://www.egr.msu.edu/tsfl/aeroshroud_paper. Additional information on the design of the aerodynamic shroud is provided below.

The aerodynamic shroud was designed to be integrated into a fan system which closely matches current production ventilation fans. The geometric details of the shroud design are shown in Fig. 4. A series of tests were run with Fan A in the same configuration as shown in Fig. 4, but with the “shroud off” condition to establish that the baseline measurements were comparable to those of a production fan. These data were compared with those measured and reported in Ford et al. [13], and good agreement, within the estimated uncertainties, was found.

The gap height for the aerodynamic shroud jet, g , as defined in Fig. 2, was set at $g \approx 5.0$ mm for all the tests. The effect of this parameter had previously been studied in the work of Neal [8], where it was shown that $g \approx 5.0$ mm was the optimal height for the delivery of the shroud jet. The relevant length scale to normalize this g value is the arc length from gap exit to the inlet of the

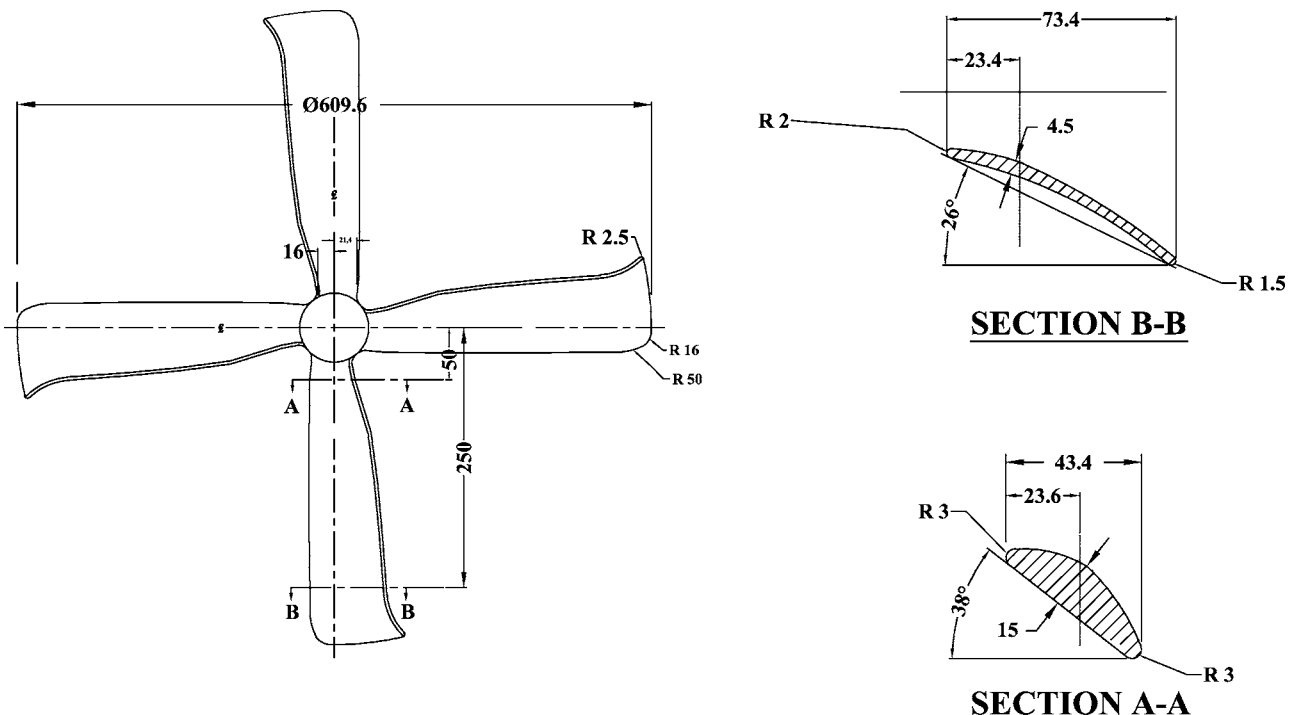


Fig. 6 Geometric details for Fan A

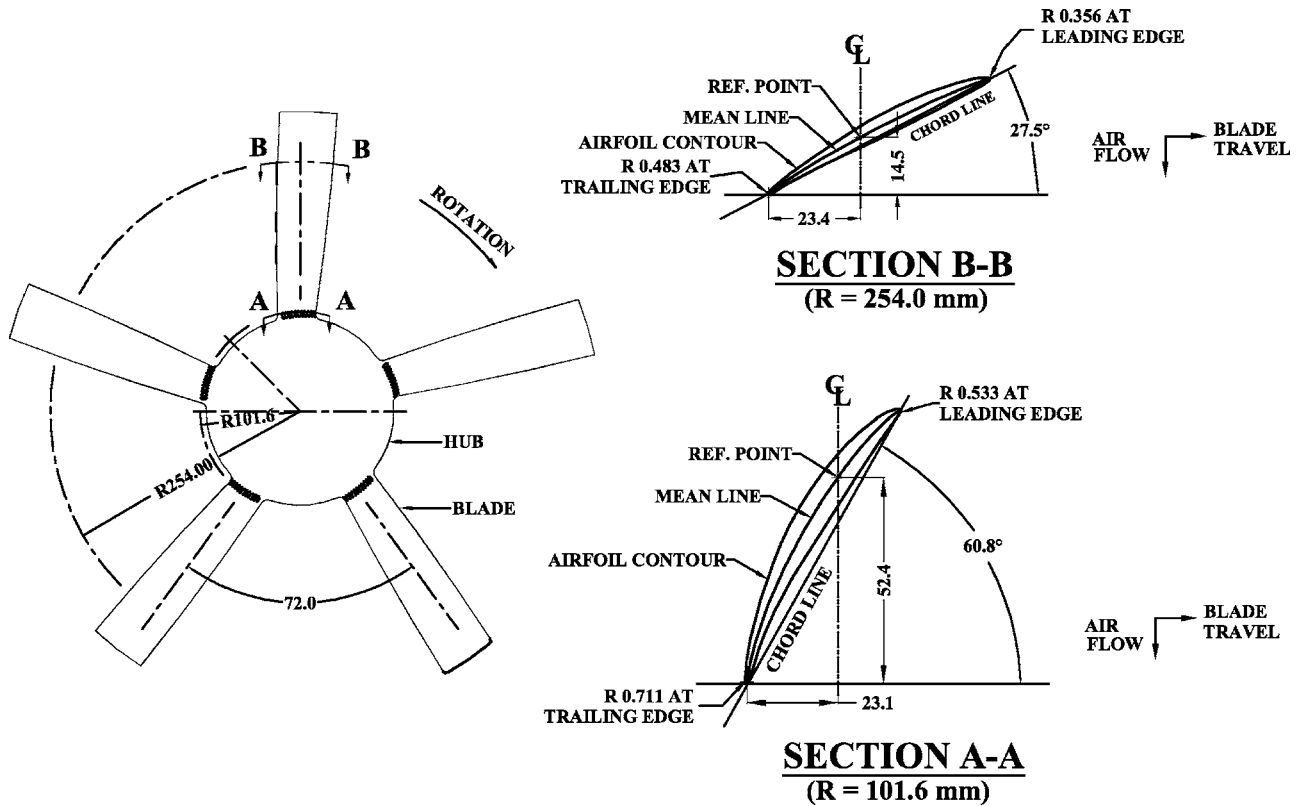


Fig. 7 Geometric details for Fan B

fan plane (L). The ratio (g/L) was 0.10 for this study. The jet momentum is altered by changing the pressure level in the shroud, ΔP_{shr} . Several ΔP_{shr} values were examined as described below. The geometry of the shroud surface is shown by the insert of Fig. 4.

The current production fan system of Fig. 8 includes a down-

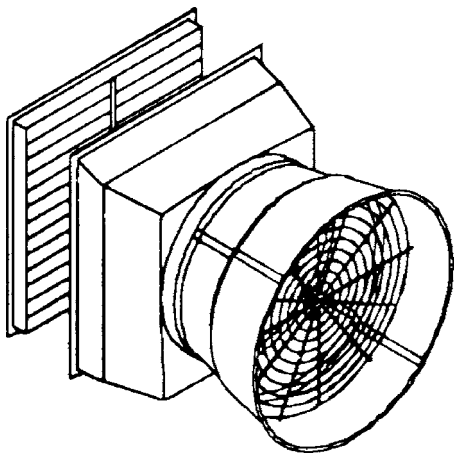


Fig. 8 Schematic of standard production assembly

Table 1 A comparison of the salient features of the tested diffusers (see Fig. 9 for a description of the variables: a , b , and L)

α (deg)	a (mm)	b (mm)	L (mm)	Inlet area (m ²)	Outlet area (m ²)	Area ratio
7	622.3	762.0	594.4	0.3042	0.4560	1.50
11	629.9	845.8	594.4	0.3116	0.5619	1.80

stream diffuser that has a 7 deg half angle (α) between the axial direction and the sidewall of the cone. This 7 deg diffuser has an exit area of 0.46 m², which is 1.5 times the area of the shroud at the exit plane of the fan. Agricultural ventilation fan manufacturers have tested diffusers with both larger and smaller angles, but the 7 deg diffuser has yielded the optimal increase in both performance and efficiency. In the present application, the diffuser length is restricted by practical considerations, such as snowloads, structural issues, etc.) to be nominally $L/D=1.0$. McDonald and Fox [18] provide a useful description of conical diffuser characteristics and performance features.

Numerous references, among them Wallis [19] and also Patterson [20] and Squire [21], have stated that, in general, axial fans equipped with diffusers that have half angles greater than 9 deg would exhibit a separated boundary layer (stall condition). This separated flow reduces the effective flow area at the diffuser exit and it offsets the static pressure recovery gains that would exist in the inviscid case. Even in the cases noted by Wallis [19], a diffuser of 9 deg represents the upper limit for an attached flow and is attainable only in a carefully controlled laboratory environment. Flow separation can be expected to appear in an actual installed condition for diffuser angles higher than nominally 7 deg.

Since the aerodynamic shroud introduces relatively high momentum fluid into the wall region at the inlet to the diffuser, a potential benefit of the aerodynamic shroud could derive from

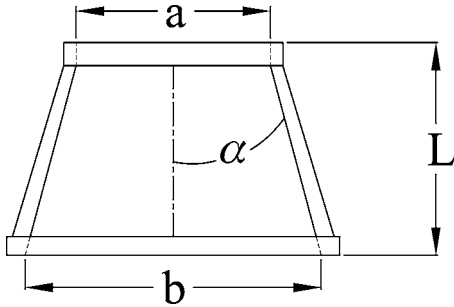


Fig. 9 Geometric variables for the diffuser (as described in Table 1)

gaining attached flow in a larger angle diffuser. A new diffuser, with an angle of 11 deg was fabricated to test this hypothesis. This nominally 11 deg diffuser (also with $L/D=1$) had a larger exit area: 0.56 m^2 or 1.9 times the shroud area at the exit plane of the fan.

The salient features of the two diffusers that were used in this study are shown in Table 1 and schematically explained in Fig. 9. The use of diffusers longer than the current production diffuser ($L=594.4 \text{ mm}$) is problematic because they will be vulnerable to structural failure from the weight of snow or heavy winds. Therefore, any new diffuser must remain within the currently accepted limits.

The experimental results for performance (ΔP_{sys} versus Q) and efficiency (η^*), provided in Ref. [8], show negligible gains for the 11 deg diffuser of the results for the 7 deg diffuser with Fan A. The comparative data for Fans A and B were obtained using the 11 deg diffuser.

Performance Results

Integral measurements of flow rate and efficiency were collected for Fan A (the four-blade fan that is identical to a production fan) and Fan B (the five-blade fan that is significantly different from the production fan). These two designs were each evaluated in the complete fan system (shroud, inlet, and downstream diffuser) in both the “shroud-on” and the “shroud-off” conditions. These results are shown as curves of pressure rise (ΔP_{sys}) versus volumetric flow rate (Q) and also pressure rise (ΔP_{sys}) versus efficiency (η^*). These measures of the fan performance are presented in dimensional form to be compatible with industry standards [22,13]. The information in the captions are to allow scaling of the present results to nondimensional form (Ψ versus ϕ and Ψ versus η^*). The nondimensional representations will permit extrapolation of these results to systems with nominally similar geometric configurations.

The data presented in the following section show the entire performance range (i.e., from “shut-off” condition to “free-delivery” condition). However, specific percentage gains or losses will be noted based on a typical operating condition. This operating condition, chosen to be nominally 25 Pa, is based on information obtained from Ford et al. [13] where they specifically state that a ventilation building fan will operate at nominally 25 Pa. They note that slight variations can occur if the housing and shutters of the fan system are excessively dirty (thereby increasing the ΔP_{sys}) or if there is a strong headwind facing the downstream exit plane of the diffuser (again increasing the ΔP_{sys}). Despite these variations, a typical fan system (fan + shroud + inlet shutters) will operate with a pressure rise of $\approx 25 \text{ Pa}$ for the majority of its operating life cycle.

Each of the tested conditions is compared with the reference case of Fan A with the 11 deg diffuser in the “shroud-off” condition. This reference case was selected since it closely matches the current production design. It was previously shown in Ref. [8] that

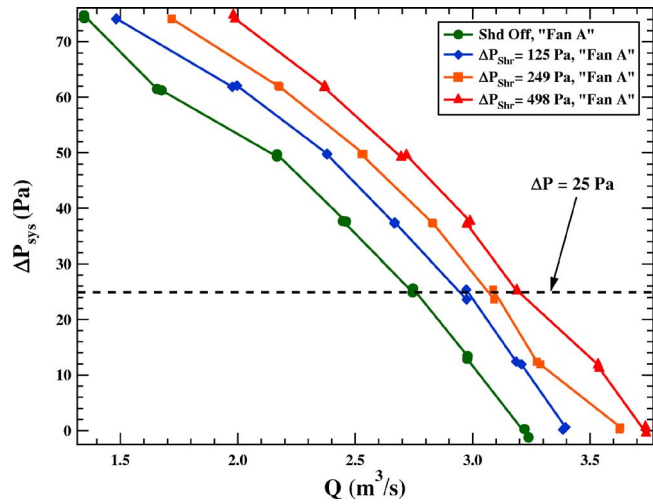


Fig. 10 Performance data for Fan A with various “shroud on” conditions. (Note: the uncertainty in the ordinate position 0.03 Pa is much smaller than the symbol for Figs. 10–13. The abscissa uncertainty is $0.02 \text{ m}^3/\text{s}$ for Figs. 10 and 12. This is also smaller than the symbol.) The scaling parameters for Ψ versus ϕ are found in Table 2.

there was a negligible difference between the 7 deg and 11 deg diffuser when used with Fan A in the “shroud-off” condition, hence only the 11 deg diffuser results are shown here.

The integral flow rate measurements for Fan A are shown in Fig. 10. These data show a systematic increase in flow rate as the “shroud-on” condition is increased from ΔP_{shr} values of 249 Pa and 498 Pa, respectively. Referring to the operating point of $\Delta P_{\text{sys}}=25 \text{ Pa}$, the flow rate increases for the “shroud-on” cases are +8.8%, +12.5%, and +16.1%. Figure 11 shows the results for the efficiency of Fan A. Unlike the results for the flow rate, there is only a slight efficiency gain for the “shroud-on” condition of $\Delta P_{\text{shr}}=125 \text{ Pa}$. The “shroud-on” condition of $\Delta P_{\text{shr}}=249 \text{ Pa}$ shows essentially no increase in efficiency (+0.3%) and the “shroud-on” condition of $\Delta P_{\text{shr}}=498 \text{ Pa}$ shows a substantial decrease in efficiency of -20.8% .

Similar pressure rise, flow rate, and efficiency data were acquired for Fan B, see Figs. 12 and 13. A striking result is the

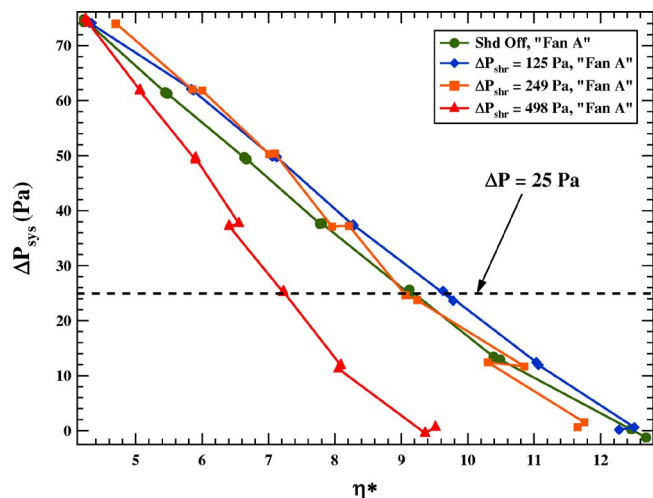


Fig. 11 Efficiency data for Fan A with various “shroud on” conditions. (Note: the uncertainty in η^* is of the order 1.5% for $\Delta P_{\text{sys}}=25 \text{ Pa}$.) The scaling parameters for Ψ versus η^* are found in Table 2.

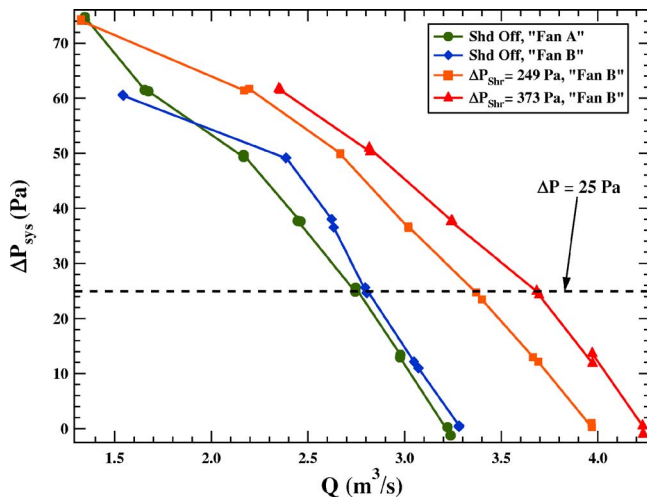


Fig. 12 Performance data for Fan B with “shroud on” conditions versus Fan A in the “shroud off” condition. The scaling parameters for Ψ versus ϕ are found in Table 2.

similarity of the flow rate results for the “shroud-off” condition of these two fans. However, the aerodynamic shroud adds considerably more performance benefit for Fan B than for Fan A as seen in the comparison of Figs. 10 and 12. For example, at $\Delta P_{\text{sys}} = 25$ Pa, the maximum increases in flow rate are 16.1% for Fan A and 32.8% for Fan B.

Efficiency gains are also realized with Fan B. Specifically 17% and 13% for $\Delta P_{\text{sys}} = 25$ Pa and ΔP_{shr} values of 249 Pa and 373 Pa, respectively. However, Fan A showed either negligible increases in efficiency (+0.3%) or substantial decreases in efficiency (−20.8%) for comparable operating conditions ($\Delta P_{\text{sys}} = 25$ Pa and ΔP_{shr} values of 259 Pa and 498 Pa, respectively). This result is further surprising given that the efficiency data of Fig. 13 shows that for these two fans in the “shroud-off” condition, Fan B has an equivalent efficiency over a substantial portion of the operating range.

The quantitative data of Figs. 10–13 can be characterized by uncertainty estimates for both ordinate (ΔP_{sys}) and abscissae (Q_{sys} and η^*) values. The ordinate uncertainty derives from the specification: “0.02% of full scale,” for the MKS Baratron transducer. This uncertainty is smaller than the height of the symbols on the

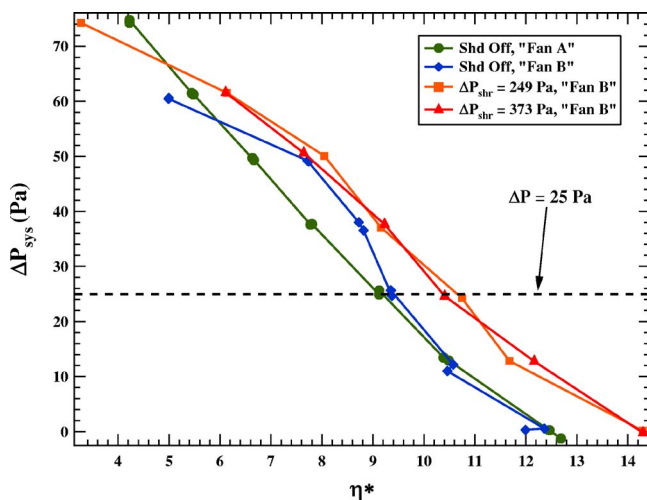


Fig. 13 Efficiency data for Fan B with “shroud on” conditions versus Fan A in the “shroud off” condition. The scaling parameters for Ψ versus η^* are found in Table 2.

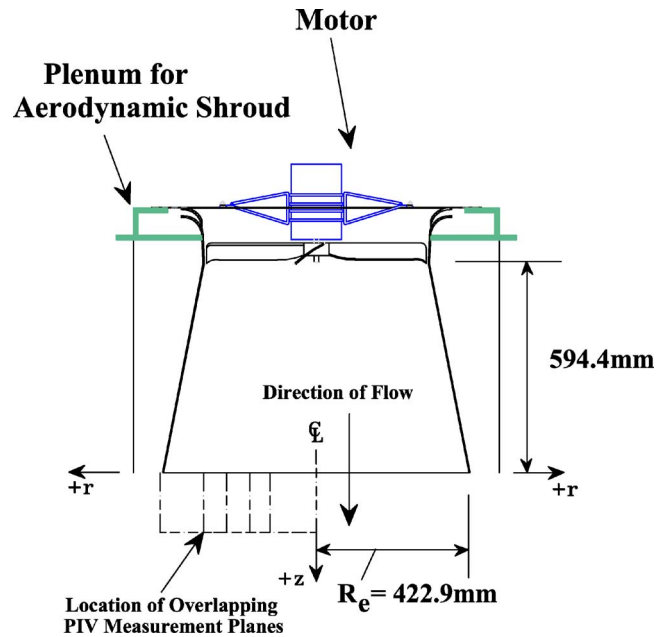


Fig. 14 Location PIV measurement regions

figures. The quoted uncertainty for Q_{sys} is from Morris et al. [15]. Namely, $\delta \dot{m} = 0.021 \text{ kg/s}/\rho$ or nominally $0.018 \text{ m}^3/\text{s}$. Converting this value to a 95% confidence interval, the $\pm 0.036 \text{ m}^3/\text{s}$ value is less than the width of the symbols.

The uncertainty in η^* is somewhat more complex to evaluate. An expression for η^* is developed in the next section (Eq. (9a)) that allows the evaluation of

$$\frac{\delta \eta^*}{\eta^*} = \left\{ \left(C_1 \frac{\delta \lambda}{\lambda} \right)^2 + \left(C_2 \frac{\delta \varepsilon_1}{\varepsilon_1} \right)^2 + \left(C_3 \frac{\delta \varepsilon_2}{\varepsilon_2} \right)^2 \right\}^{1/2} \quad (6)$$

for $\Delta P_{\text{sys}} = 25$ Pa. The second term on the right-hand side of Eq. (6) is dominant and its magnitude is estimated to be of the order of 1.5%. Again, this is of the order of the symbol width.

Interpretations of the Performance and Efficiency Results

The objective information provided above can be summarized as follows. Two quite different fans (hub-to-tip ratios (Fig. 5), blade shapes (Figs. 6 and 7) and number of blades (4 versus 5)) exhibit:

1. Similar performance (Figs. 10 and 12) and similar efficiencies (Figs. 11 and 13) for the typical operating range ($\Delta P_{\text{sys}} \approx 25$ Pa) when no aerodynamic shroud flow is present; and
2. Greater performance gains as well as dramatically improved efficiency values for Fan B cf. Fan A when the optimal aerodynamic shroud flow is present.

These observations are cited as the discovery that clarifies the potential contributions of the aerodynamic shroud to ventilation systems.

This section presents additional information that can guide further efforts to utilize the objective results cited above as the basis for enhanced ventilation fan systems. Specifically, velocity measurements at the exit plane of the conical diffuser have been acquired for the four conditions: Fans A/B, with and without the aerodynamic shroud flow, in order to clarify the mechanistic reasons for the performance and efficiency gains. These data have been acquired using planar PIV in the range $0 \leq r/R_e \leq 1$. Three separate overlapping PIV measurement planes, shown in Fig. 14,

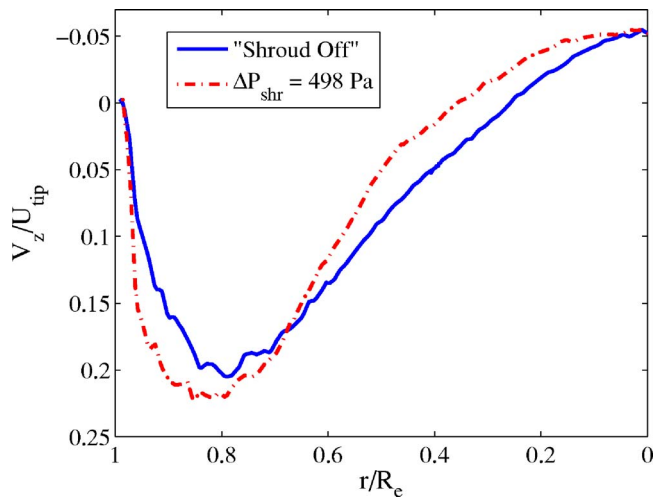


Fig. 15 Exit velocity profiles for Fan A in both the “shroud off” and best-case “shroud on” conditions

were interrogated and average velocity profiles were extracted. These velocity profiles are displayed as $V_z(r/R_e)/U_{tip}$ in Figs. 15 and 16.

The peak velocity magnitudes ($V_z/U_{tip} \approx 0.2$) for Fans A and B are similar with no shroud flow albeit their flow patterns are strongly different. The Fan A peak occurs at nominally $r/R_e = 0.8$ and the velocity distribution is rather “narrow.” In contrast, the Fan B peak is nominally at $r/R_e = 0.5$ and that velocity distribution is relatively wide. (Recall that, from Figs. 10 and 12, the flow rates at $\Delta P = 25$ Pa are the same for the two fans.) The slight “jump” that appears around $r/R_e \approx 0.55$ in Fig. 16 is the result of a small droplet of condensed fogging fluid on the lens of the PIV camera. This causes a small amount of distortion which results in a lower percentage of validated images at this location only.

The aerodynamic shroud flow provides a moderate change in the Fan A velocity distribution. As seen in Fig. 15 there are increased V_z/U_{tip} magnitudes for $r/R_e \geq 0.8$. In sharp contrast, the aerodynamic shroud flow has strongly modified the velocity distribution for the Fan B configuration. The peak value is reduced to 0.15, it is moved outward to $r/R_e \approx 0.65$ and the velocity at $r/R_e = 0.9$ is increased from 0.03 to 0.09 as an indication of why the flow rate is substantially increased.

The modified velocity profile for Fan B with the aerodynamic shroud flow provides quantitative support for the increased efficiency. Specifically, the kinetic energy flux (that is related to the input power) is determined by the cube of the velocity magnitude

$$\text{KE flux} = \int_A \rho \frac{V^2}{2} \vec{V} \cdot \hat{n} dA \quad (7)$$

whereas the mass flow rate is dependent upon the first power of the velocity

$$\text{mass flow rate} = \int \rho \vec{V} \cdot \hat{n} dA \quad (8)$$

Hence, a nonuniform velocity distribution implies excess kinetic energy and excess input power. The Fan B velocity distribution at the diffuser exit plane is “flatter” when the aerodynamic shroud flow is present in agreement with the increased efficiency and the reasoning associated with Eqs. (7) and (8).

These velocity field data clearly show why the fan blade design strongly impacts the contributions to the performance and efficiencies of an aerodynamic shroud equipped system. An optimal

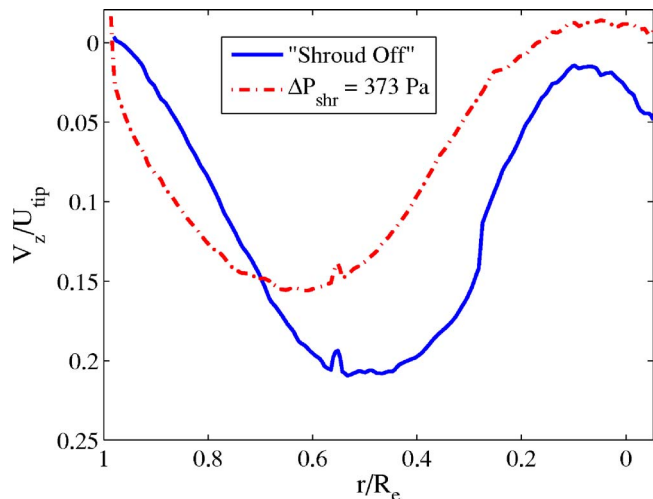


Fig. 16 Exit velocity profiles for Fan B in both the “shroud off” and best-case “shroud on” conditions

system will result if the aerodynamic shroud flow can interact with and complement a fan flow that favors the inner region of the fan plane.

A quantitative representation of the increased efficiency for Fan B can be obtained directly from the individual terms of Eq. (5). The efficiency, as defined by Eq. (5), can be rewritten in the following form

$$\eta^* = \frac{1 + \lambda}{\varepsilon_1 + \varepsilon_2 \lambda} \quad (9a)$$

Rewriting Eq. (5) as shown in Eq. (9a) allows the terms to be given quantitative expression as presented in Table 2, where the terms ε_1 , ε_2 , and λ are defined by

$$\lambda = \frac{Q_{shr}}{Q_{fan}} \quad (9b)$$

$$\varepsilon_1 = \frac{\phi}{Q_{fan}(\rho U_{tip}^2)} \quad (9c)$$

$$\varepsilon_2 = \frac{\Delta P_{shr}}{\eta_{shr}(\rho U_{tip}^2)} \quad (9d)$$

The quantitative values of Table 2 clarify that the shroud flow rate successfully decreases the nondimensional input power to the axial fan for all conditions. The successful conditions (increase in η^*) then follow if the shroud power term: ($\varepsilon_2 \lambda$), does not negate the increased flow rate term: $(1 + \lambda)$.

Summary

The aerodynamic shroud has been shown to successfully improve the flow rate and efficiency for a ventilation fan system. It is noteworthy that this application is entirely different from the original automotive application of this invention. The two fan systems evaluated here were characterized by their high flow rates, low-pressure rise values, and small tip clearances. By carefully selecting the best operating conditions for Fan B, specifically the shroud flow rate and shroud pressure, the volume flow rate for the prototype fan system was improved by 34% while simultaneously improving the efficiency by 13%.

Additionally, it was shown that the effectiveness of the aerodynamic shroud is highly dependent on the design of the fan. Specifically, in contrast with the successful results for Fan B, the

Table 2 Factors that define η^* at $\Delta P_{\text{sys}}=25$ Pa

Test condition	ρU_{tip}^2 (Pa)	Q_{fan} (m ³ /s)	ϕ (W)	λ	ε_1	ε_2	η^*	$\Delta\eta^*$ (%)
Fan A - shd off ($\Delta P_{\text{shr}}=0$ Pa)	1292.1	2.75	396.5	0.0	0.1118	0.0	8.94	—
Fan A - shd on ($\Delta P_{\text{shr}}=249$ Pa)	1322.8	2.85	369.9	0.084	0.0981	0.269	8.99	+5.6
Fan A - shd on ($\Delta P_{\text{shr}}=498$ Pa)	1330.2	3.03	364.3	0.114	0.0958	0.537	7.09	-20.7
Fan B - shd off ($\Delta P_{\text{shr}}=0$ Pa)	1319.6	2.75	402.7	0.0	0.1108	0.0	9.02	—
Fan B - shd on ($\Delta P_{\text{shr}}=249$ Pa)	1385.7	3.15	352.7	0.078	0.0819	0.258	10.56	+17.1
Fan B - shd on ($\Delta P_{\text{shr}}=373$ Pa)	1370.5	3.42	352.1	0.08	0.0752	0.381	10.23	+13.3

aerodynamic shroud provided only a modest increase in flow rate and minimally positive to distinctly negative effects on the efficiency for Fan A.

Acknowledgment

This work was partially supported under the NSF major research instrumentation Grant No. CTS 9601833 and also USDA Grant No. 98-33610-5970. Additional support was also provided by Aerotech, Inc. of Mason, MI. Their support, and the technical counsel of their engineering staff, is gratefully acknowledged. D. R. Neal was employed by Digital Flow Technologies Inc., as a research engineer for the period of the reported research.

Nomenclature

Latin

- e = motor voltage (V)
- g = shroud gap height (mm) (see Fig. 2)
- i = motor current (A)
- \dot{m} = mass flow rate (kg/s)
- ϕ = input shaft power (watts)
- r = radial position (m)
- D = diameter (m)
- P = pressure (Pa)
- R = radius (m)
- Q = volume flow rate (m³/s)
- U_{tip} = tip velocity magnitude = $\Omega R_{\text{fan}}(2\pi/60)$
- V_z = axial velocity (m/s)

Greek

- α = diffuser half angle
- η = efficiency (nondimensional) (see Eq. (3))
- η^* = efficiency (nondimensional) (see Eq. (5))
- ρ = density (kg/m³)
- ϕ = flow coefficient (nondimensional) (see Eq. (1))
- ΔP = pressure rise (Pa)
- Ψ = pressure rise coefficient (nondimensional) (see Eq. (2))
- Ω = fan rotational speed (rad/s)

Subscripts

- I = instantaneous quantity
- e = exit plane quantity
- fan = fan quantity
- shr = aerodynamic shroud quantity

sys = system quantity
total = total quantity

References

- [1] Mangold, D. W., Hazen, T. E., and Hays, V. W., 1967, "Effect of Air Temperature on Performance of Growing-Finishing Swine," *Trans. ASAE*, **10**(3), 370-375, 377.
- [2] Fuquay, J. W., 1981, "Heat Stress as it Affects Animal Production," *J. Anim. Sci. (Savoy, Ill.)*, **52**(10), pp. 164-174.
- [3] Nienaber, J. A., Shanklin, M. D., Hahn, G. L., and Manak, R. C., 1985, "Performance of Neonatal and Newly-Weaned Pigs as Affected by Temperature and Diet," *Trans. ASAE*, **28**(5), pp. 1626-1634.
- [4] Nienaber, J. A., Hahn, G. L., and Yen, J. T., 1987, "Thermal Environmental Effect on Growing-Finishing Swine: Part I—Growth, Feed Intake and Heat Production," *Trans. ASAE*, **30**(6), pp. 1772-1775.
- [5] Overhults, D. G., and Gates, R. S., 1993, "Energy Use in Tunnel Ventilated Broiler Houses," *Proceedings Livestock Environment IV*, 4th Int Symposium, Coventry, England, July 6-9, pp. 339-346.
- [6] Hanan, J. J., 1998, *Greenhouses, Advanced Technology Protected Horticulture*, CRC Press, Boca Raton, FL.
- [7] Wheeler, E. F., and Both, A. J., 2002, "Evaluating Greenhouse Mechanical Ventilation System Performance," *Agriculture and Biological Engineering Fact Sheet I-42*, The Pennsylvania State University, University Park, PA.
- [8] Neal, D. R., 2002, M.S. thesis, Michigan State University, East Lansing, MI.
- [9] Morris, S. C., and Foss, J. F., 2001, "An Aerodynamic Shroud for Automotive Cooling Fans," *J. Fluids Eng.*, **123**(2), pp. 287-292.
- [10] Lakshminarayana, B., 1996, *Fluid Dynamics and Heat Transfer of Turbomachinery*, Wiley, New York.
- [11] Bleier, F. P., 1998, *Fan Handbook: Selection, Application and Design*, McGraw-Hill, New York.
- [12] AMCA, 2000, *Directory of Agricultural Products With Certified Ratings*, Air Movement and Control Association, Inc., Publication No. 262-00.
- [13] Ford, S. E., Christianson, L. L., Riskowski, G. L., and Funk, T. L., 1999, "Agriculture Ventilation Fans, Performances and Efficiencies," Paper No. UILLU ENG 99-7001.
- [14] Morris, S. C., Foss, J. F., and Pakkala, J. E., 1997, "The Automotive Cooling Fan Research and Development Facility," *Proceedings of the 3rd SAE Vehicle Thermal Management Systems Conference*, Indianapolis, IN.
- [15] Morris, S. C., Neal, D. R., Foss, J. F., and Cloud, G. L., 2001, "A Moment-of-Momentum Flux Mass Air Flow Measurement Device," *Meas. Sci. Technol.*, **12**(2), pp. N9-N13.
- [16] Høst-Madsen, A., and McCluskey, D. R., 1994, "On the Accuracy and Reliability of PIV Measurements," *Proceedings of the 7th International Symposium on Application of Laser Techniques to Flow Measurements*, Lisbon, Portugal, July 11-14.
- [17] Keane, R. D., and Adrian, R. J., 1992, "Theory of Cross-Correlation Analysis of PIV Images," *Appl. Sci. Res.*, **49**, pp. 191-215.
- [18] McDonald, A. T., and Fox, R. W., 1966, "An experimental Investigation of Incompressible Flow in Conical Diffusers," *Int. J. Mech. Sci.*, **8**(2), pp. 125-139.
- [19] Wallis, R. A., 1983, *Axial Flow Fans and Ducts*, Wiley, New York.
- [20] Patterson, G. N., 1938, "Modern Diffuser Design," *Aircr. Eng.*, **10**, p. 267.
- [21] Squire, H. B., 1950, "Experiments on Conical Diffusers," *Aeronautical Research Council Technical Report*, R & M 2751.
- [22] AMCA, 1985, *Laboratory Methods of Testing Fans for Rating*, Air Movement and Control Association, Inc., Publication No. 210-85.

Observation of Centrifugal Compressor Stall and Surge in Phase Portraits of Pressure Time Traces at Impeller and Diffuser Wall

Chunwei Gu

Key Laboratory for Thermal Science and Power Engineering of Ministry of Education, Tsinghua University, Beijing, 100084, China
e-mail: gcw@mail.tsinghua.edu.cn

Kazuo Yamaguchi

Toshio Nagashima

Department of Aeronautics and Astronauts, University of Tokyo, Tokyo, 113-8656, Japan

Hiroataka Higashimori

Nagasaki Res. Lab., Mitsubishi Heavy Industry Co. Ltd., Nagasaki, 8510392, Japan

Unsteady static pressure signals due to flow instability in two types of centrifugal compressors were analyzed by employing the phase portrait reconstruction method. The sampled data corresponded to several streamwise locations along the shroud wall over a wide range of operation from design to near surge. Singular value decomposition analysis yielded successfully the discernable features of flow instability, i.e., stall and surge, which were observed with a decrease of mass flow rate. The effects of the signal-to-noise ratio was found to be the most troublesome in predicting the onset of flow instability upon pursuing the attractor behavior of the portraits. Under the latter difficult circumstance, the correlation integrals were also conveniently calculated to help to check the onset. It was clearly indicated that the behavior near rotating stall was not always recognized by the phase portrait in three-dimensional space, while the corresponding correlation integral obviously decreased close to stall. Monitoring of unsteady signals based on the phase portraits and the correlation integrals, therefore, led to a good judgement of a nonlinear fluid dynamic system response and to prevent compressors from a disastrous damage due to flow instability. [DOI: 10.1115/1.2734249]

1 Introduction

As the mass flow is reduced at constant speed, fluid dynamic instability, i.e., rotating stall or surge, occurs in compressors, which yields a limit to their operating range. These unstable phenomena have been studied for many years, but many questions still remain unanswered. For example, it is well known that surge is preceded by stall in axial compressors. In centrifugal compressors, however, it remains an open question whether rotating stall has any role on surge. Rotating stall was found in impeller and diffuser before surge at a low-speed compressor by Kammer and Rautenberg [1], and Abdel-Hamid et al. [2]. However, the flow measurements in a high-speed centrifugal compressor by Toyama et al. [3] and Fink and Greitzer [4] did not show rotating stall prior to surge. Instead, they found that surge was preceded by stall either at the inlet region of a vaned diffuser or in the inducer with a vaneless diffuser. Rotating stall inception in a centrifugal blower was researched by Ishida et al. [5,6].

In axial compressors, recently, a chaos theory has been applied to analyze the time series data of experiments, exhibiting the dynamics of rotating stall and to anticipate the latter from the phase portraits reconstructed at a critical operating state. Palomba and Breugelmans [7] and Palomba et al. [8] successfully gave the phase portrait of small and large rotating stall measured by different kinds of sensors in multistage compressors. In centrifugal compressors, Hagino et al. [9] researched prediction of surge inception with phase portrait reconstruction method. A difficulty arises from the noise present in data to often cause a fatal ambiguity in identifying the attractor of the relevant dynamic system. The correlation integral becomes useful in such cases, but the correlation dimension itself is again very difficult to exactly calculate because of noise that affects the distance between two

points of M-embedding dimension on the trajectory and the respective correlation integral. As discussed by Lener [10], the presence of noise influences absolute values of the distance, thus, the correlation integral. However, at a given distance, very little influence is observed on the relative magnitude among the correlation integral distributions. The correlation integral method was applied for an analysis of instability in axial compressors [11], showing that the correlation integral decreases just before rotating stall.

The present paper, therefore, focuses on an investigation of the instability onset in two types of centrifugal compressors, i.e., a high-speed centrifugal compressor with a vaned diffuser operated at part speeds (30,000 rpm and 50,000 rpm), and a low-speed centrifugal compressor with vaneless diffuser operated at design speed (11,000 rpm). Both methods, the phase portrait reconstruction and the correlation integral, are employed to observe the changes in the system dynamics over various mass flows, especially, near the stall condition.

2 Phase Portrait and Correlation Integral

Reconstruction of a phase portrait from experimental data is not as easy and exact as from the data calculated based upon mathematical equations. In general, the number of degrees of freedom of a system is not known a priori, so that only a finite number of noise contaminated data can be extracted from a given system. All reconstruction techniques are based upon Takens' theorem [12] called the method of delay. However, Takens' theorem supposes no direct connection with the measuring process nor how to reduce the noise effect in experimental data. Neither is there any indication regarding a choice of the time scales. Broomhead and King [13] proposed a statistical approach to deal with these problems. A mathematical approach of SVD (singular value decomposition) is used to extract a new matrix \bar{X} from the trajectory matrix X built by experimental data, accordingly to the following formula:

Contributed by the Fluids Engineering Division of ASME for publication in the JOURNAL OF FLUIDS ENGINEERING. Manuscript received September 7, 2005; final manuscript received November 22, 2006. Review conducted by Joseph Katz.

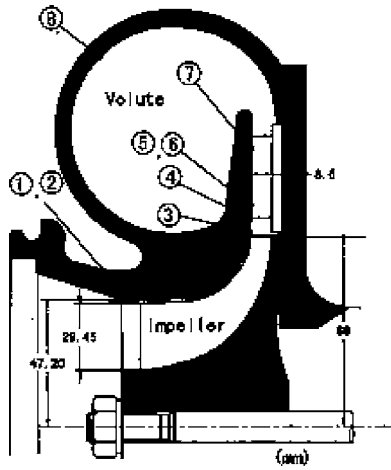


Fig. 1 Test compressor

$$\bar{X} = \sum_{\delta_i > \text{noise}} (X a_i) a_i^T$$

where the eigenvalues and associated basic vectors are denoted by δ_i and a_i , respectively. The superscript T indicates a transposed matrix. Phase portrait is visually configured according to a new three-dimensional coordinate system, (a_1, a_2, a_3) .

Correlation integral is computed from the fraction of number of pairs of M-embedding dimension points that are within a given distance r of each other on the trajectory

$$C(r) = \lim_{N \rightarrow \infty} \frac{1}{N^2} (\text{number of pairs } (i, j) \text{ with distance } S_{ij} < r)$$

In centrifugal compressors, just like axial compressors, the correlation integral is expected to change prior to the onset of instability. In the following sections, two types of centrifugal compressors, a high speed one with vaned diffusers and a low speed one with vaneless diffuser, are investigated for this purpose.

3 High-Speed Rig With Vaned Diffuser

3.1 Experimental Facility and Instrument. Experiments of instability in a high-speed centrifugal compressor with flat-plate (FP) and double circular arc (DCA) vaned diffusers were carried out, by employing a test turbocharger driven by a hot air turbine. A cross section of the instrumented impeller and vaned diffuser is shown in Fig. 1. The impeller full and splitter blades are back swept at the exit by 30 deg. The diffuser installs vanes of flat plate or double circular arc profiles. There is no inlet guide vane. Design parameters and the geometry are summarized in Table 1.

In addition to conventional probes for pressure and temperature measurements to yield overall performance, eight static pressure taps were provided on the compressor casing wall. There are two taps (① and ②) at 45 deg. apart circumferentially at the impeller inlet, one (③) at the impeller outlet, one (④) at the diffuser inlet,

Table 1 Compressor design data

Outlet radius	136 mm
Inlet radius (hub)	35.5 mm
Inlet radius (shroud)	94.4 mm
Number of full blade	10
Number of splitter	10
Number of FP or DCA vane	21
Total temperature	288 K
Total pressure	101,300 Pa
Max. revolution	76,000 rpm
Max. pressure ratio	3.6

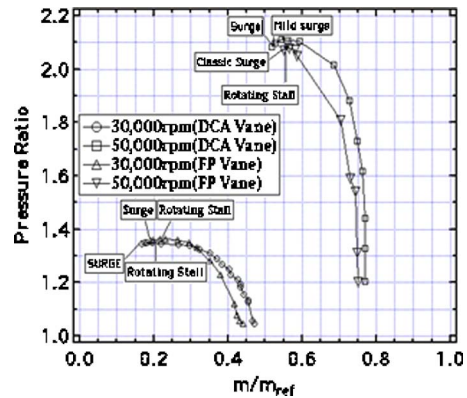


Fig. 2 Performance map

two deg. circumferential position (⑤ and ⑥) at 120 at the diffuser throat, one (⑦) in front of the diffuser outlet, and one (⑧) at the scroll. Four high-response pressure transducers (d-c coupled Kulite model) were installed at a time, and four-channel LeCroy recorder was employed for unsteady pressure data.

3.2 Performance Maps. Measured performance curves of pressure ratio versus mass flow at 30,000 rpm and 50,000 rpm are shown in Fig. 2. The compressor characteristic at 50,000 rpm speed line is steeper than at 30,000 rpm because of compressibility. Two types of diffuser vanes, FP and DCA, were tested, and the operating range exhibited a little larger with DCA than FP. At 30,000 rpm, rotating stall always appeared prior to surge in the diffuser inlet region, showing a different mass flow between FP and DCA. The rotating stall grew gradually as the mass flow rate was reduced. At 50,000 rpm, however, the unstable phenomena were very different. The centrifugal compressor with DCA directly entered both mild and deep surge, while, with FP, the rotating stall was encountered in sequence at the diffuser inlet region.

3.3 Phase Portraits. Figure 3 gives the phase portraits of rotating stall, with FP vaned diffuser at 30,000 rpm, which were reconstructed from the pressure traces measured at the impeller outlet, the diffuser throat, and the diffuser outlet, respectively [14]. The phase portraits at the impeller outlet and diffuser throat show a clear feature of rotating stall, but the one looks random at the diffuser outlet, owing to low signal to noise ratio.

The phase portraits of surge shown in Fig. 4 were reconstructed from the pressure time traces at a reduced mass flow rate of 0.55 with FP along 50,000 rpm speed line [14]. The phase portrait at the impeller inlet indicates the feature of surge, "knee" and quasi-periodic oscillation. The others at different three positions, however, show the feature of classic surge (surge and rotating stall), especially, with a clear indication at the diffuser throat.

From the phase portraits of the rotating stall and surge (Figs. 3 and 4), it is clear that successful reconstruction of the phase portrait for rotating stall is very dependent on the streamwise location, since rotating stall is locally unstable phenomenon that leads to different signal to noise ratio along the streamwise direction. On the other hand, the phase portrait of surge does not depend on the location. Therefore, if the phase portrait reconstruction is employed to detect the onset of rotating stall, the selection of measurement locations becomes very important.

3.4 Fundamental Phase Portrait and Its Correlation Integral. Concerning the inception of rotating stall, a well-known observation in axial compressors is the appearance of a disturbance of long or short length scale close to the stall line [15] exhibiting the propagation speed equal to or less than the rotor revolution, respectively. In order to catch such small disturbances, there are two ways of phase portrait reconstruction. One is that the window length in SVD method be determined based on BPF

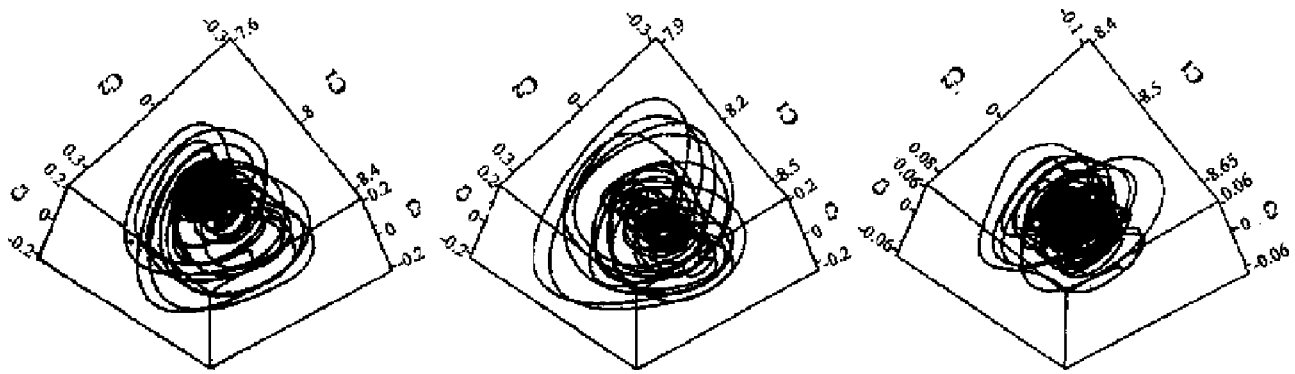


Fig. 3 Phase portraits of rotating stall at 30,000 rpm ($m/m_{ref}=0.198$)

(blade passing frequency), while the other is that the window length is chosen based on the rotor rotating frequency to eliminate BPF.

The former has to be of more practical importance, since it can be easily imagined that the latter treatment does not reflect, in the phase portrait, the correct unsteadiness away from near-stall operation, neither involving the nonlinear growth of disturbance, which is the primary concern, presently. The phase portrait reconstructed according to the former way will hereafter be called the fundamental phase portrait. The phase portrait thus differs from

the fundamental, if the window length is taken based on the rotating stall frequency. If any disturbance appears suddenly in the flow field, it must enforce some points to deviate from the trajectory on the phase portrait so that the fundamental phase portrait must be changed in phase space.

Based on this consideration, Fig. 5 compares the fundamental phase portraits at different mass flow rates; that is, Fig. 5(a)–5(c) show those far from rotating stall, near rotating stall, during small rotating stall, respectively. They were reconstructed from the pres-

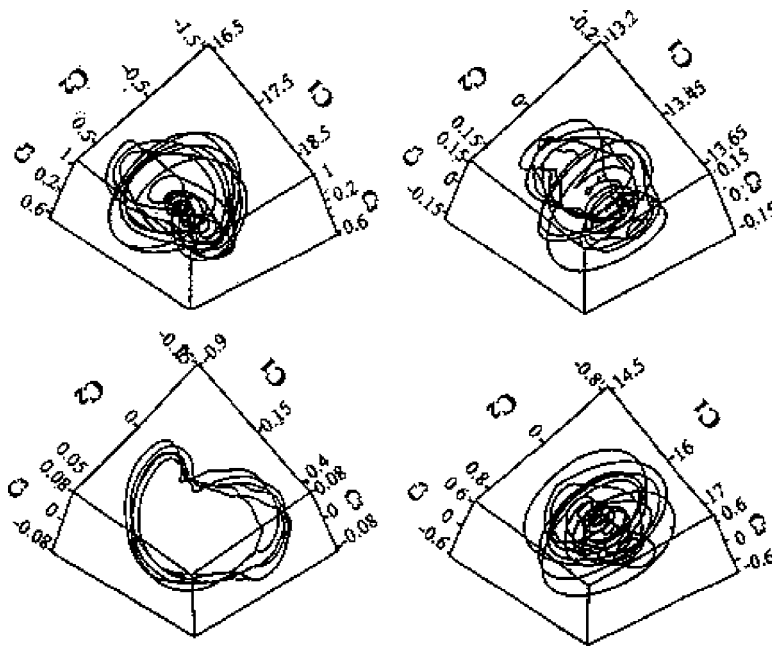


Fig. 4 Phase portraits of classic surge at 50,000 rpm ($m/m_{ref}=0.55$)

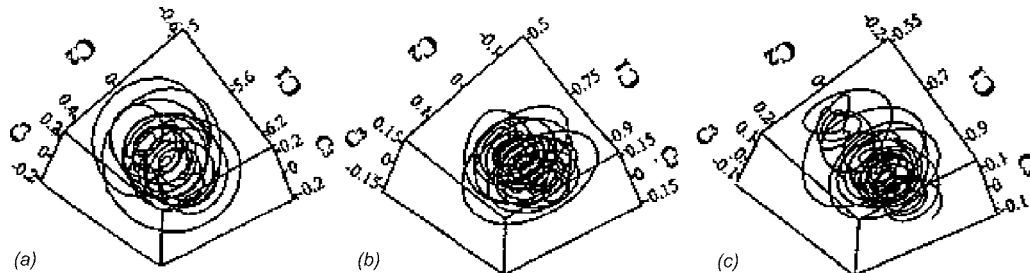
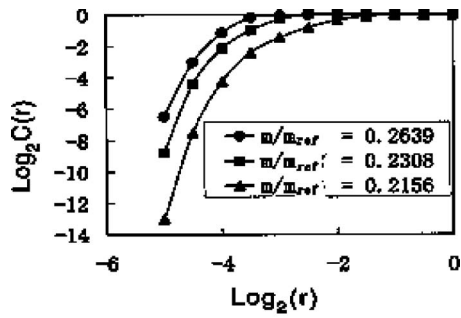
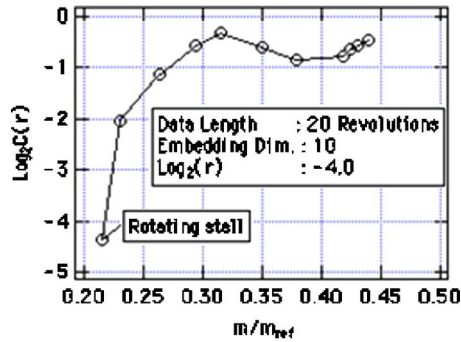


Fig. 5 Fundamental phase portraits at 30,000 rpm: (a) $m/m_{ref}=0.2639$, (b) $m/m_{ref}=0.2308$, and (c) $m/m_{ref}=0.2156$



(a)



(b)

Fig. 6 (a) Correlation integral plots with three mass flow at 30,000 rpm and (b) Distribution of the correlation integral versus mass flow at 30,000 rpm

sure time traces at the diffuser inlet of FP vanes at 30,000 rpm operation. It is immediately apparent from the very tangled appearance of the fundamental phase portraits that the behavior of the pressure time traces may be too complex to be represented in three dimensions.

The correlation integral becomes useful for analyses of this three operation states. In order to obtain absolute correlation integral, calculation of correlation dimension should be convergent with suitable selection of the parameter, delay time, embedding dimension. However, the correlation dimension itself can not calculated correctly with any selection of parameters (sampling time, delay time, embedding dimension) if there is noise in experimental data [16]. Because noise affects the distance between two-points of M-embedding dimension on the trajectory, Fig. 6(a) gives distribution of correlation integral versus correlation distance of two-point corresponding to phase portraits in Fig. 5. The parameters are selected as 20 revolution for data length, 10 for embedding dimension, $2 \mu s$ for sampling time, $2 \mu s$ for delay time. If the correlation distance selected largely, for example $\text{Log}_2(r) = -4$, as Fig. 6(b) shown, the corresponding correlation integrals give a clear tendency of sharp drop on their evaluated curve when the mass flow is reduced close to stall. This drop must be the indication of a drastical change in the compressor dynamics before stall and during stall. It is indicated that very little influence is resulted on the relation among the correlation integral distributions at a given correlation distance [10,11]. Theoretically, the data length must be long enough to contain all the information relevant to the system dynamics. Empirically, to meet the computational time, the data length may be sufficient to take more than ten rotor revolutions.

3.5 Near-Stall Correlation Integral. Figure 7 shows a detailed distribution of the correlation integrals near rotating stall, calculated from the pressure traces at 30,000 rpm operation at FP diffuser inlet. In these calculations, the data length and embedding dimension were chosen to be the same as those of Fig. 6. Unfor-

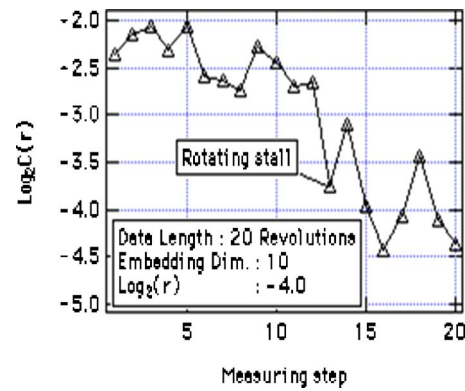


Fig. 7 Detailed distribution of the correlation integral near rotating stall at 30,000 rpm

tunately, the mass flow was not measured due to male operation of the measurement instrument, but the abscissa corresponds to a regular throttling covering about 1.3% of the valve area closing near the onset of rotating stall. The plottings oscillate due to the unstable flow, but the descending trend is vividly shown with a steep slope past the onset point. In the present configuration of the FP vane diffuser, therefore, the threshold level of the correlation integral for secure operation is between -2.5 and -3 ; thus, the judgement is that the compressor plunges in rotating stall, when the correlation integral becomes < -3 .

3.6 Effect of Locations. Figure 8 shows similar plottings calculated from the pressure traces at the impeller outlet, diffuser

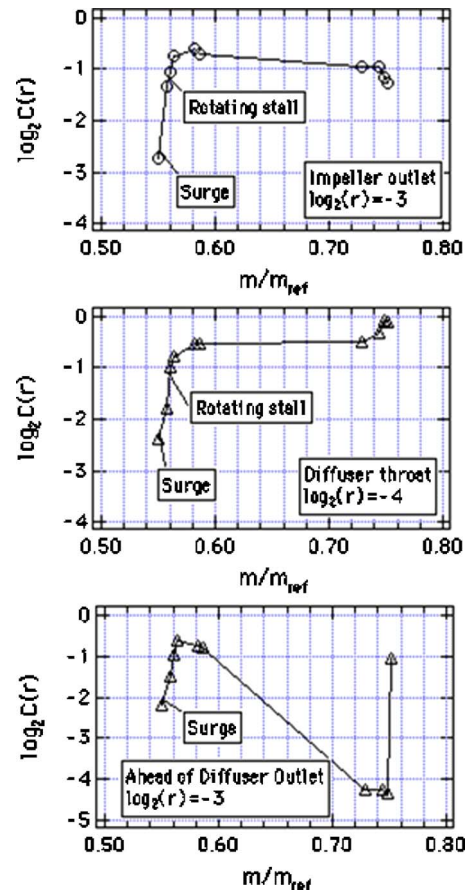


Fig. 8 The correlation integral versus the mass flow at various mass at 50,000 rpm



Fig. 9 The correlation integrals around surge at four positions (FP vanes, 50,00 rpm)

throat and in front of the diffuser outlet, respectively. FP vane diffuser was installed as previously, but the rotational speed was increased to 50,000 rpm. It can be observed that all curves reveal a sharp drop in the ordinates close to surge. At the position in front of the diffuser outlet, another interesting drop at the mass flow rate about 0.72 is obviously seen, which was because of flow choking; consequently, a shock wave appeared in front of the diffuser outlet. The correlation integral is sensitive to any flow disturbance in the flow field.

Detailed changes of dynamics near rotating stall with FP vane diffuser at 50,000 rpm were also investigated in Fig. 9. The plottings correspond to four positions, namely, impeller inlet, two diffuser throat positions, and scroll casing wall, covering a range of mass flow rate from 0.57 to surge by means of 1–2% reduction of throttle area. Rotating stall appeared at the abscissa 5 at the diffuser inlet region before surge. The ordinates are almost constant along the abscissa before surge at the impeller inlet and scroll. At the diffuser throat, they decrease just before and during the developing process of rotating stall until surge. Between the circumferential two positions of the diffuser throat, the trend of plottings is almost the same.

3.7 Effect of Diffuser Vane Profile. Figure 10 shows the correlation integrals versus mass flow rate, with DCA vane diffuser at 50,000 rpm, at the impeller inlet, impeller outlet, diffuser throat, and in front of the diffuser outlet, respectively. All correlation integral curves have a drop just before surge, among those a gradually descending trend at the diffuser throat and impeller inlet can be recognized. Since, in this case, rotating stall was never observed at four positions before the surge, the latter descend may be due to locally stationary stall phenomena. Compared to the FP

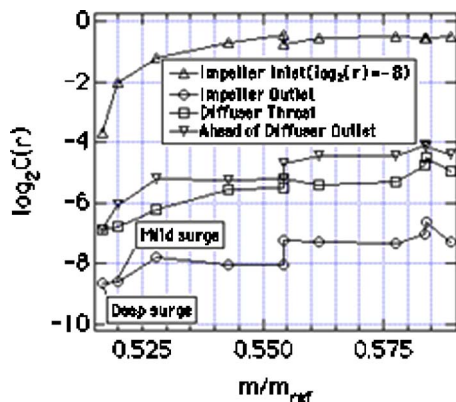


Fig. 10 The correlation Integrals vs. mass flow at four positions (DCA vanes, 50,000 rpm)

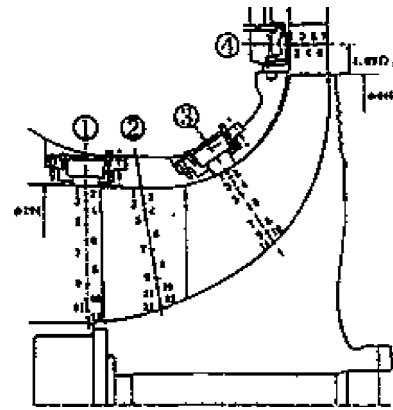


Fig. 11 Test compressor and measurement positions

correlation integral curve in Fig. 9, DCA therefore gave less decent in the correlation integral at the diffuser throat.

4 Low-Speed Rig With Vaneless Diffuser

The experiments for investigating the flow field in a centrifugal compressor with a larger impeller and vaneless diffuser, operated at design speed 11,000 rpm, were reported by Lener [10]. A primary objective is detailed velocity measurements by using LDV, but as shown in Fig. 11, unsteady pressure was also measured at

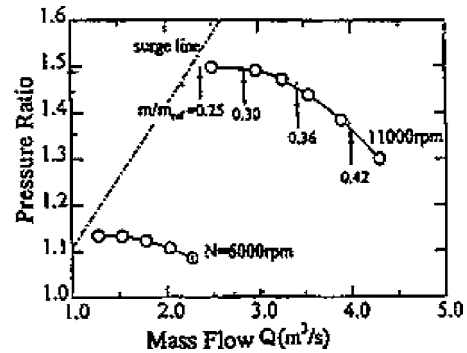


Fig. 12 Performance map

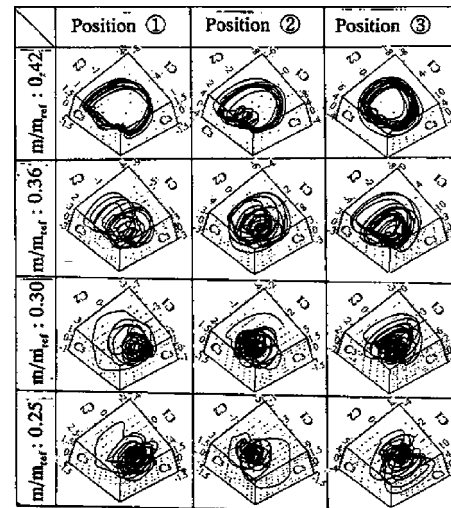


Fig. 13 Fundamental phase portraits reconstructed from experimental data

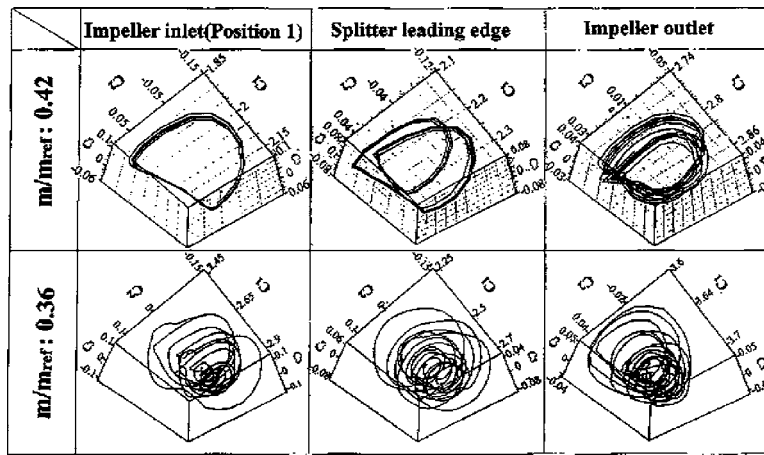


Fig. 14 Fundamental phase portraits reconstructed from CFD data

three streamwise positions on the casing wall, namely, full blade inlet ①, between full blade and splitter leading edges ②, and behind splitter leading edge ③. The compressor performance map is given in Fig. 12, which shows the surge line near the mass flow rate of 0.25.

The fundamental phase portraits corresponding to various mass flow rates are shown in Fig. 13, which were reconstructed from the experimental pressure time traces at positions ①–③. Due to the absence of impeller and diffuser interaction, the structure of fundamental phase portraits at large mass flow rate of 0.42 expresses clearly the quasi-periodic pattern. The results yield a good agreement with those of CFD simulation at mass flow rate of 0.42 and 0.36 (Fig. 14) based on the unsteady Euler equation imposing pressure distortion at the impeller outlet [17], which indicates that the viscous effect near wall at a large mass flow rate is very small.

As seen in Fig. 13, however, the structure became gradually tangled, when the mass flow was reduced. That is because the viscous effect can be no longer neglected due to the occurrence of significant boundary layer separation, as well as other noises due to throttling that leads to flow instability. These effects make the system dimension increase, consequently, the flow behavior in the compressor cannot be properly expressed by the phase portrait in only three dimensions.

The correlation integrals were, therefore, calculated again, in Fig. 15. At the measuring positions ① and ②, the descent of the correlation integrals is small at the four mass flow rates chosen. However, at the measuring position ③, the plotting shows a sudden drop at the mass flow rate of 0.25, which reflects the appearance of a small rotating stall at the impeller outlet region. It is clearly demonstrated that, to discern the danger of this low-speed compressor rig operation, signal monitoring at the rear part of the impeller passage is crucial.

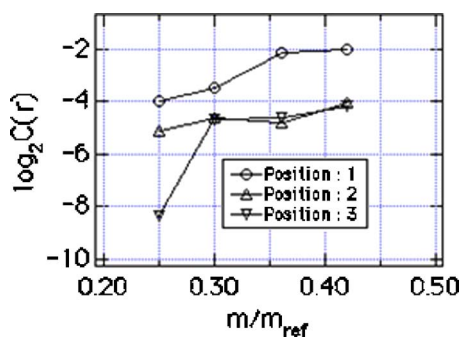


Fig. 15 The correlation integrals versus mass flow (low-speed rig with vaneless diffuser)

5 Conclusion

Phase portrait analysis of time series of pressures, acquired in two types of centrifugal compressors over various mass flow rates, gives a good visual and qualitative representation of the system dynamics response to the occurrence of flow instability. Inspection of the trajectories resulted discernable differences in phase portrait, when the compressor operation moves toward stall along a stable characteristic line. The behavior reflecting complex phenomena near rotating stall becomes difficult to be properly expressed by the phase portrait in three dimensions. The sensitive correlation integral method is then appropriate to check the dynamics of unsteady and unstable flow. The following are the summary of findings:

1. Rotating stall and surge in centrifugal compressors may be represented, such as in axial compressors, by the phase portraits in low dimensions. In the case of rather local rotating stall phenomenon, the selection of streamwise measurement positions is very important for successful reconstruction of the phase portrait. Whereas, in case of surge phenomenon, the measurement position is of relatively little influence on its reconstruction.
2. For highly nonlinear unstable phenomena near stall, the correlation integral method becomes very useful and effective. In the two types of compressors investigated, the correlation integral yielded always a large constant value far from the rotating stall, and decreased to a threshold value gradually according to throttling procedure toward rotating stall. It is manifested that the correlation integral method is applicable to identify the onset of rotating stall.
3. Relatively, the correlation integrals are insensitive to the onset of surge. When the centrifugal compressor directly entered surge, there was no preference of measuring locations, nor indication of discernable changes, but a sudden drop was observed during surge in the correlation integral curves.

References

- [1] Kammer, N., and Rautenberg, M., 1982, "An Experimental Investigation of Rotating Stall Flow in a Centrifugal Compressor," ASME Paper 82-GT-82.
- [2] Abdel-Hamid, A. N., Cowill, W. H., and Barrows, J. F., 1978, "Experimental Investigation of Unsteady Phenomena in Vaneless Radial Diffuser," ASME Paper No.78-GT-23.
- [3] Toyama, K., Runstadler, P. W., and Dean, R. C., 1977, "An Experimental Study of Surge in Centrifugal Compressor," ASME J. Fluids Eng., **99**, pp. 115–131.
- [4] Fink, D. A., and Greitzer, E. M., 1992, "Surge Dynamics in a Free-Spool Centrifugal Compressor System," ASME J. Turbomach., **114**, pp. 125–131.
- [5] Ishida, M., Sakaguchi, D., and Ueki, H., 1995, "Detection of Rotating Stall Precursor in Vaneless Diffuser of a Centrifugal Blower," Proc. of 2nd Joint ASME/JSME Fluids Engineering Conference, Hilton Head Island, ASME, New York, FED-Vol. 222, pp. 155–160.

- [6] Ishida, M., Sakaguchi, D., and Ueki, H., 1995, "Pressure Fluctuation on Casing Wall of Centrifugal Blowers at Low Flow Rates," *Proc. of 2nd International Conference on Pumps and Fans*, Beijing, Vol. 1, Paper No. E4, pp. 375–386.
- [7] Palomba, C., and Breugelmans, F. A. E., 1995, "Phase Portraits From Rotating Stall Time Series," XII ISABE Conference, Melbourne, pp. 312–318.
- [8] Palomba, C., Horst, L., and Breugelmans, F. A. E., 1997, "Strange Attractor Characterization of Rotating Stall in an Axial Flow Compressor," JSME ICFE-97-718, Tokyo, pp. 201–207.
- [9] Hagino, N., Uda, K., and Kashiwabara, Y., 2003, "Prediction of Surge Inception of a Centrifugal Compressor With Attractor Behaviors in Phase Portraits," JSME Int. J., Ser. B, **69**(679), pp. 65–71.
- [10] Lener, D. E., 1996, "Monitoring Changing Dynamics With Correlation Integral: Case Study of an Epileptic Seizure," *Physica D*, **97**, pp. 563–576.
- [11] Bright, M. M., Qammar, H. K., Weigl, H. J., and Paduano, J. D., 1997, "Stall Precursor Identification in High-Speed Compressor Stages Using Chaotic Time Series Analysis Methods," *ASME J. Turbomach.*, **119**, pp. 491–500.
- [12] Takens, F., 1981, "Detecting Strange Attractors in Turbulence," *Lecture Notes in Mathematics*, D. A. Rand and L.-S. Young, eds., Springer-Verlag, Berlin, pp. 366–382.
- [13] Broomhead, D. S., and King, G. P., 1986, "Singular System Analysis With Application to Dynamical Systems," *Physica D*, pp. 101–110.
- [14] Gu, C. W., Yamaguti, K., and Nagashima, T., 1999, "Phase Portraits of Centrifugal Compressor Operation From Design to Near Stall," ICET'99, Beijing, pp. 314–320.
- [15] Day, I. J., 1993, "Stall Inception in Axial Flow Compressors," *ASME J. Turbomach.*, **115**, pp. 1–9.
- [16] Wu, Z., 1995, "Remark on Metric Analysis of Reconstructed Dynamics From Chaotic Time Series," *Physica D*, **85**, pp. 485–495.
- [17] Gu, C. W., Nagashima, T., and Yamane, T., 1999, "Design to Near-Stall Flows in a Centrifugal Compressor According to Euler-Based Numerical Analysis," ICET'99, Beijing, pp. 25–221.

Modeling of Effect of Inflow Turbulence Data on Large Eddy Simulation of Circular Cylinder Flows

M. Tutar¹

Department of Mechanical Engineering,
Mersin University,
Çiftlikköy, 33343, Mersin, Turkey
e-mail: m_tutar@mersin.edu.tr

I. Celik

I. Yavuz

Department of Mechanical and Aerospace
Engineering,
West Virginia University,
Morgantown, WV 26506-6106

A random flow generation (RFG) algorithm for a previously established large eddy simulation (LES) code is successfully incorporated into a finite element fluid flow solver to generate the required inflow/initial turbulence boundary conditions for the three-dimensional (3D) LES computations of viscous incompressible turbulent flow over a nominally two-dimensional (2D) circular cylinder at Reynolds number of 140,000. The effect of generated turbulent inflow boundary conditions on the near wake flow and the shear layer and on the prediction of integral flow parameters is studied based on long time average results. Because the near-wall region cannot be resolved for high Reynolds number flows, no-slip velocity boundary function is used, but wall effects are taken into consideration with a near-wall modeling methodology that comprises the no-slip function with a modified form of van Driest damping approach to reduce the subgrid length scale in the vicinity of the cylinder wall. Simulations are performed for a 2D and a 3D configuration, and the simulation results are compared to each other and to the experimental data for different turbulent inflow boundary conditions with varying degree of inflow turbulence to assess the functionality of the RFG algorithm for the present LES code and, hence, its influence on the vortex shedding mechanism and the resulting flow field predictions. [DOI: 10.1115/1.2734225]

Keywords: LES method, turbulent inflow data, random flow generation (RFG) algorithm, circular cylinder, turbulent wake, subcritical flow regime, turbulence

1 Introduction

The turbulent flow field around a circular cylinder is of great practical importance for many engineering applications, such as hydrodynamic loading on ocean marine piles and risers, which are utilized for modern offshore structures used for the production of hydrocarbons. Since many of the new developments for production are located at water depths of 1000 m and possibly more, the length of risers are considerable, and it is necessary to accurately predict the time-dependent hydrodynamic forces induced by currents and waves to optimize riser, riser system, and riser bundle design with a high confidence level for such water depths. Because of a geometric similarity between a circular cylinder and a riser the fluid flow investigation can be initially conducted for a cylinder with a circular cross section and then can be extended to the real fluid flow solution for risers and riser systems. The early experimental studies [1,2] show that the transition from laminar to turbulent flow regime in the boundary layer can take place even at very low Reynolds numbers and the boundaries of the flow regimes can vary significantly depending upon the actual values of surface roughness, freestream turbulence, length-to-diameter ratio, wind-tunnel blockage as well as the Reynolds number [3]. Because of the occurrence of turbulence in the boundary layer the computational studies of the vortex shedding from the cylinder may require turbulence modeling.

In the literature, there is a wide variety of numerical studies based on different types of turbulence modeling ranging from Reynolds averaged Navier-Stokes equations (RANS) based turbulence models [4,5] to LES [6–9] to predict the turbulent vortex

shedding from a bluff body. Tutar and Holdo [9] conducted various transient simulations of the turbulent flow around a nominally two-dimensional circular cylinder and conclude that LES calculations yield much more realistic flow field prediction than the RANS-based turbulence model calculations even for two-dimensional mesh systems including moderate spatial resolutions. Despite its superiority to RANS-based turbulence models there are still some unresolved issues in LES applications to the turbulent flow simulations. Turbulent inflow boundary conditions and the near-wall treatment are two of most important ones. When there is high Reynolds number flow, the inflow turbulence cannot be ignored and some methods of generation of turbulence with prescribed turbulence intensity (i.e., wind tunnel turbulence level) at the inflow boundary are required in order to account for the turbulence effects. In order to generate inflow turbulence, two groups of approaches in the numerical studies may be used. One is to conduct the auxiliary simulations of turbulent flow fields using LES approach [10,11] and to store the time series of fluctuating velocity components for inflow boundary conditions of the main simulations. In this approach, the velocity field extracted from a plane near the domain exit is basically rescaled and then is reintroduced as a boundary condition at the inlet. This method requires a large computational load, and its success mainly depends on the accurate calculation of turbulence statistics that account for prescribed target characteristics. This approach will not be applicable to cases where scale laws are nontrivial. Another approach is to artificially generate time series of random velocity fluctuations by performing an inverse Fourier transform for prescribed spectral densities. There are several numerical studies with varying degrees of success in this approach [12–14]. This method may require a fairly lengthy development section as a transient region due to the fact that the synthetic velocity field generated by the random fluctuation approach may lack both turbulent structure

¹Corresponding author.

Contributed by the Fluids Engineering Division of ASME for publication in the JOURNAL OF FLUIDS ENGINEERING. Manuscript received June 16, 2006; final manuscript received November 3, 2006. Review conducted by Ugo Piomelli.

and nonlinear energy transfer. Therefore, a more robust boundary data generation method is required. To eliminate the disadvantage of other methods, Celik et al. [14] suggested a relatively simple random flow generation (RFG) algorithm, which can be used to prescribe inlet condition as well as initial conditions for spatially developing inhomogeneous anisotropic turbulent flows. The algorithm is based on the study of Kraichnan [15] and is successfully applied to particle dispersion modeling, flat plate wake and shear layer flows by Smirnov et al. [16]. This is the approach used in the present study.

Near-wall treatment is another issue to be addressed in LES. "Law of the wall" boundary conditions can reduce the cost of the simulations. However, they do not seem to be reliable enough to be used with confidence in bluff body flows where the unsteady separation occurs [17]. The best treatment, therefore, may be to avoid any kind of wall functions and to resolve the boundary layer with a high mesh resolution while using no-slip boundary conditions at the wall. The LES study conducted by Breuer [6] shows that an increase in mesh resolution does not automatically lead to an improvement of the flow predictions, and special attention is needed for LES to accurately simulate the wall affected region in the subcritical flow regime. Tutar and Holdo [9] suggested a near-wall modeling methodology, which comprises the no-slip wall function with a damping term to reduce the length scale up to some point from the cylinder wall. They argued that the use of the standard van Driest wall function for bluff body flows is questionable and a modified form of the van Driest damping function should be employed to reduce the subgrid scale length within the variable distance in the vicinity of the wall. The recent LES study of de With et al. [18] employs a dynamic grid adaptation (DGA) algorithm that concentrates mesh refinement in near-wall region to overcome the unsteadiness of the transitional flow field, which makes a conventional mesh insufficient.

The present numerical study attempts to improve the LES predictions for bluff body flows with the use of a random flow generation algorithm for generating turbulent inflow boundary conditions for a LES code previously established by Tutar [19]. The turbulent inflow data for LES are produced with a varying degree of isotropic turbulence. The wall effects are taken into account for different mesh resolutions with a near-wall modeling methodology, which combines the no-slip function with a damping variable, which is responsible for the subgrid scale reduction in the near-wall region. The investigated flow has a Reynolds number of 140,000, which indicates subcritical flow regime, and it is necessary to simulate the effects of turbulence in the near wake of the cylinder after separation.

2 Governing Equations

The Navier-Stokes equations and continuity equations are filtered in order to give a foundation for the LES method in which the larger eddies can be resolved explicitly by the fine mesh, while the small scales referred to as subgrid (SGS) scales are modeled. For the turbulent flow computations the filtered Navier-Stokes equations and the continuity equation can be written as follows:

$$\frac{\partial}{\partial t}(\rho \bar{u}_i) + \frac{\partial}{\partial x_j}(\rho \bar{u}_i \bar{u}_j) = \frac{\partial}{\partial x_j} \left(\mu \frac{\partial \bar{u}_i}{\partial x_j} \right) - \frac{\partial \bar{p}}{\partial x_i} - \frac{\partial \tau_{ij}}{\partial x_j} \quad (1)$$

$$\frac{\partial \rho}{\partial t} + \frac{\partial \rho \bar{u}_i}{\partial x_i} = 0 \quad (2)$$

where ρ is the fluid density, μ is the dynamic viscosity of the fluid, \bar{u}_i is the filtered value of the velocity, \bar{p} is the filtered value of the pressure, and τ_{ij} is the subgrid scale stress defined by

$$\tau_{ij} = \overline{\rho u_i u_j} - \overline{\rho} \bar{u}_i \bar{u}_j \quad (3)$$

To close the filtered equations, the subgrid scale stress is modeled using a viscous analogy. The subgrid scale stress can thus be expressed as

$$\tau_{ij} = -2\mu_s \bar{S}_{ij} + \frac{2}{3} k_{SGS} \delta_{ij} \quad (4)$$

where k_{SGS} is the subgrid scale kinetic energy, \bar{S}_{ij} is the strain rate tensor of the resolved flow field and μ_s is the sub-grid scale viscosity term calculated by the Smagorinsky model [20] given as

$$\mu_s = \rho l^2 (2\bar{S}_{ij} \bar{S}_{ij})^{1/2} \quad (5)$$

with l is the characteristic subgrid length scale, which is related to the width of the filter, Δ used as

$$l = C_s \Delta \quad (6)$$

The first term on the right-hand side of Eq. (6), the Smagorinsky constant C_s , is chosen in a range from 0.10 to 0.30. The second term, the filter width Δ , as an indication of the characteristic length scale separates large and small-scale eddies from each other and can be considered to be an average cell size. It is calculated for 2D and 3D elements in the present finite element method (FEM) based code [21] due to Tutar and Holdo [9] as

$$\Delta = (\Delta_x \Delta_y)^{1/2} \quad (2D)$$

$$\Delta = (\Delta_x \Delta_y \Delta_z)^{1/3} \quad (3D) \quad (7)$$

Therefore, the subgrid length is calculated directly from the local grid size and the grid size distribution is thus very important for the present subgrid scale (SGS) model. The calculation of the subgrid viscosity is performed using a subroutine that returns an array of values at each integration point of the finite element in the computational domain at each time step.

3 Random Flow Generation (RFG) Algorithm

The present RFG algorithm is a modified form of the previously developed algorithm [14] which is based on a method of synthesizing the divergence free vector fields from a sample of Fourier harmonics and is incorporated into a general purpose finite element code [21] with which the LES code is applied to generate a realistic inflow field. The RFG algorithm can be used to prescribe inlet conditions as well as initial conditions for spatially developing inhomogeneous, anisotropic turbulent flows [16]. When the RFG algorithm is used for LES, the fluid particles should follow a time-dependent flow-field and fluctuating component should still be added to it at smaller turbulent scales [16]. The fluctuating component is derived from the turbulence intensity and length scales, provided by the turbulence model or via empirical relations. In this procedure adopted here, a homogeneous isotropic transient flow field is realized as a superposition of harmonic functions as previously suggested by Kraichnan [15]

$$\vec{v}(\vec{x}, t) = \sqrt{\frac{2}{N}} \sum_{n=1}^N [\vec{v}_1(\vec{k}_n) \cos(\vec{k}_n \cdot \vec{x} + \omega_n t) + \vec{v}_2(\vec{k}_n) \sin(\vec{k}_n \cdot \vec{x} + \omega_n t)], \quad (8)$$

In Eq. (8),

$$\vec{v}_1(\vec{k}_n) = \vec{\zeta}_n x \vec{k}_n, \quad \vec{v}_2(\vec{k}_n) = \vec{\zeta}_n x \vec{k}_n \quad (9)$$

with

$$\vec{k}_n \cdot \vec{v}_1(\vec{k}_n) = \vec{k}_n \cdot \vec{v}_2(\vec{k}_n) = 0 \quad (10)$$

where the components of vectors $\vec{\zeta}_n$ and $\vec{\zeta}_n$ and the frequency ω_n are chosen independently from a Gaussian distribution with a standard deviation of unity, $N(0, 1)$. Each component of \vec{k}_n is a Gaussian random number with a standard deviation of 1/2. Here, N is the number of terms in series. The generated flow field is then homogeneous, isotropic, and divergence free [16].

The RFG algorithm utilized here is realized in 3D manner using a subroutine written in a hybrid code language. For this purpose, the subroutine, which is located in the present LES code for the

imposition of velocity boundary conditions performs a calculation of velocity fluctuations in accordance with a proper selection of length and time scales for the turbulence conditions and then returns the calculated values of fluctuating velocity components at each grid point of the inflow boundary at each time step.

4 Near-Wall Treatment

Near-wall treatment of the LES method needs consideration in order to account for the fact that, on a solid wall, the large eddies dissipate energy directly rather than by the usual energy cascade involving smaller eddies. Therefore, the LES method should account for the fact that, at the wall, the strain rate term in the subgrid viscosity equation does not vanish, whereas the subgrid stresses does, implying that the subgrid turbulent viscosity has to become zero at the walls. Because of this fact, in the present study, a near-wall modeling methodology that combines the no-slip wall boundary conditions approach with a damping function approach based on the van Driest mixing length formulation [22] is used. In this approach, wall effects are taken into consideration by reducing the subgrid length scale in the boundary layer up to some point from the cylinder wall, where the effects on the turbulence become negligible. In order for the near-wall methodology to perform well, the boundary layer is resolved by high mesh density. A damping function D_f is introduced to reduce the subgrid length up to a location in the boundary layer, where $y=0.10D$, where D is the cylinder diameter, and is calculated by an alternative form [9] of van Driest's function as follows:

$$D_f = \left[1 - \exp\left(\frac{-y^+}{A^+}\right)^3 \right]^{1/2} \quad (11)$$

where A^+ is a constant for which a value of 25 is used. Equation (11) has the property of yielding not only $l=0$, but also $\partial l / \partial y = 0$ on the wall. This may be preferable for numerical reasons (e.g., to avoid sharp gradients of l). Thus, to take wall effects into account, in the wall region the length scale is damped and the new length scale is determined according to

$$l = C_s \Delta D_f \quad (12)$$

All calculations in the present study are carried out with a Smagorinsky constant of $C_s = 0.10$, which is a typical value for practical applications of the LES computations of nonhomogeneous and anisotropic flows leading to improved results [6].

5 Mesh Configuration and Numerical Details

The flow is described in a Cartesian coordinate system (x, y, z) , in which the x -axis is aligned with the streamwise direction, z -axis is parallel with the spanwise direction or the cylinder axis, and y -axis is perpendicular to both directions, as shown in Fig. 1. The geometric size of the flow domain and the corresponding velocity boundary conditions for all 3D numerical simulations are also shown in Fig. 1. A stationary 3D circular cylinder with a nondimensional unit diameter D is situated in the center of the vertical plane and exposed to a time- and spanwise-averaged freestream velocity U . The Reynolds number based on the freestream velocity and the cylinder diameter is 140,000. Inlet (upstream), upper, and lower boundaries are extended laterally to minimize the effects of the boundaries on the cylinder. The blockage ratio of the cylinder within the flow domain is 0.071, less than the value of 0.08 needed to eliminate blockage effects on the flow due to the study of Ramamurthy and Ng [23]. The blockage ratio of the experimental study of Cantwell and Coles [24], on the other hand, is noted as a value of 0.04. In the present study, there are also no boundary layers on the sidewalls of the flow domain (boundary layers are, of course, present on the wind-tunnel walls) due to the symmetry boundary conditions; thus, the effect of blockage is less than for a typical experimental case. The flow domain is also extended long enough downstream to eliminate the far field effects on the near wake and to produce full development of the

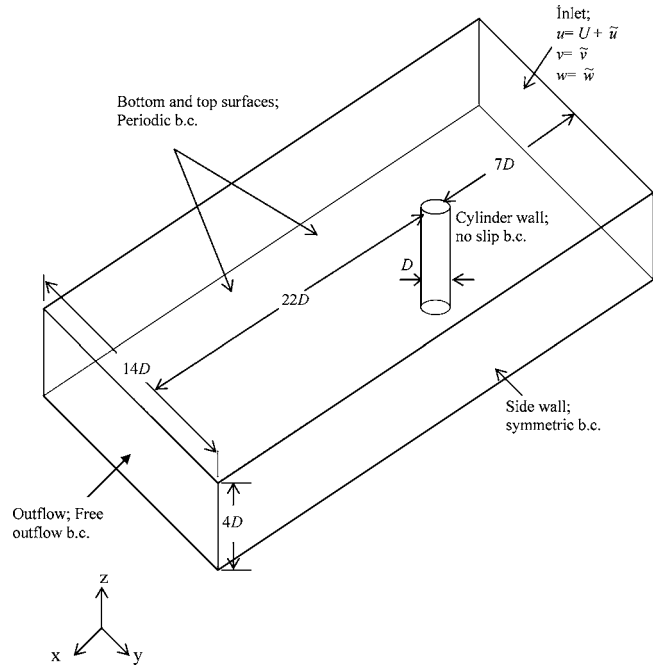


Fig. 1 The geometric configuration of the flow domain and the corresponding velocity boundary conditions. The fluctuating velocity components $(\tilde{u}, \tilde{v}, \tilde{w})$ at the inflow boundary are computed by the RFG algorithm and are superimposed on the time-averaged velocity values.

vortex street. The chosen spanwise domain size of $4D$ is larger than that of πD , which is found to be adequate for the flow at subcritical Reynolds numbers [25]. Then simulations are carried out for the mesh resolution of 325×300 and 435×300 grid points in the (x, y) direction and $435 \times 300 \times 32$ and $435 \times 300 \times 44$ grid points in the (x, y, z) direction to study the effect of mesh resolution and 3D effects on the flow results.

The structured meshes for the present study are illustrated in Fig. 2. The computational domain contains grid points, which are nonuniformly spaced in the x and y directions and uniformly spaced in the z direction. Very fine mesh resolution is used surrounding the cylinder vicinity. The mesh size is increased with the distance from the cylinder surface, and the location of the first grid point from the cylinder wall is chosen to be $0.0015D$ to adequately resolve the boundary layer. Mesh space is stretched using a geometric progression function with expansion factors in the streamwise and lateral directions. On the other hand, equally distributed grid points are used in the spanwise direction in which the length of the computational domain is not so large so that our attention is restricted to eddies that are small compared to the diameter of the cylinder. The whole computational domain is subdivided into a finite number of small two-dimensional four-noded finite elements for 2D simulations and eight-noded brick elements for 3D simulations. All simulations are carried out using a finite element solver [21]. The nonlinear equation systems resulting from the finite element discretization of the flow equations are solved using a segregated solution algorithm with a second-order trapezoid time integration scheme in order that the advection terms may have a higher order of accuracy and the solution may be stable. All fluid properties, including density and the dynamic viscosity, are assumed constant. Nondimensional time step, t^* ($=Ut/D$), where U is the time-averaged streamwise velocity at the inflow boundary, D is the cylinder diameter, and t is the time, is chosen at a value of 0.005. The iterative convergence criteria is set to 10^{-3} for all solution variables in simulations. All integral variables are made nondimensional by using U and D . In the present

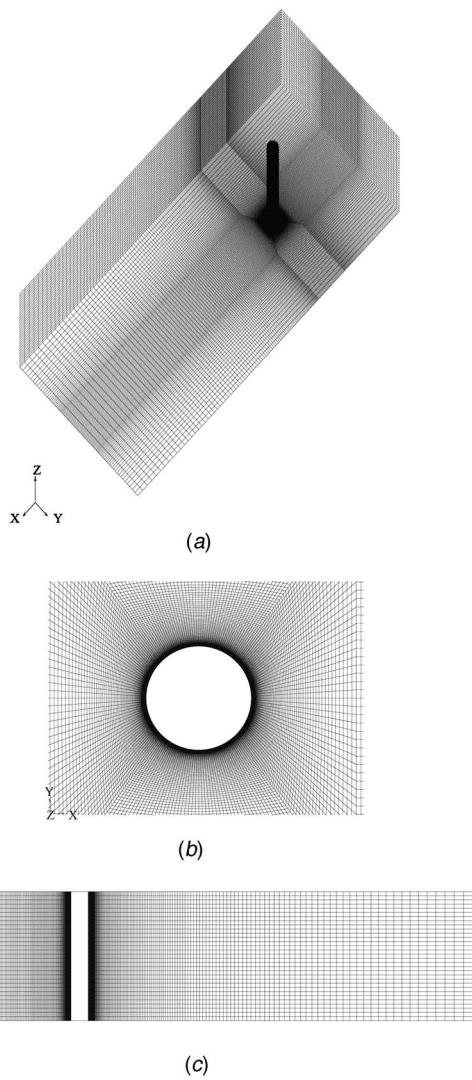


Fig. 2 A computational mesh used for the present LES calculations. The mesh contains $435 \times 300 \times 32$ grid points: (a) Global 3D mesh view, (b) 2D local mesh view around the cylinder in the x - y plane, and (c) 2D mesh view in the x - z plane.

study, simulations are carried out considering the following boundaries and the following corresponding velocity boundary conditions:

1. Inflow boundary: Random velocity fluctuations ($\tilde{u}, \tilde{v}, \tilde{w}$) generated by the RFG algorithm are superimposed on the corresponding velocity components. The time- and spanwise-averaged streamwise velocity component is assumed to be uniform, ($\langle u \rangle_{tz} = U$) while other velocity components are assumed to be zero ($\langle v \rangle_{tz} = \langle w \rangle_{tz} = 0$).
2. Outflow boundary: Free out flow boundary conditions are imposed. Diffusion fluxes for all flow variables in the direction normal to the exit plane are assumed to be zero.
3. Top-bottom boundaries: Periodic boundary conditions at the top and bottom boundaries are used to simulate a small portion of the infinitely long cylinder.
4. Lateral boundaries: Symmetry boundary conditions at the transverse boundaries are applied in order to take into account a small portion of an infinite domain is modeled. The normal velocity components and the normal gradients of all velocity components are assumed to be zero.
5. Cylinder surface: A no-slip velocity boundary condition is

prescribed at the cylinder surface. A near-wall methodology, which comprises the no-slip velocity boundary condition and a damped mixing length model, is used to simulate the flow in the vicinity of the cylinder surface.

6 Results and Discussions

The influence of turbulent inflow data on the turbulent vortex-shedding mechanism and, hence, on the flow predictions is studied to assess the functionality of the RFG algorithm for the present LES code and to constitute a better mechanism for the treatment of velocity fluctuations at the inflow boundary in future LES calculations of bluff body flows. For this reason, numerical simulations are performed in conjunction with the RFG algorithm for different turbulent inflow boundary conditions (i.e., varying degree of turbulence), which are completely ignored in the previous numerical studies [6,7,18] conducted, at a Reynolds number of 140,000. At this Reynolds number, the flow is in the subcritical flow regime and the reported wind-tunnel inflow turbulence of which isotropic turbulence level I_u is 0.6% due to the experiment of Cantwell and Coles [24] and a selected nondimensional length scale of turbulence l_t/D of 0.02. The simulations are performed in 3D manner as the turbulent vortex shedding from the cylinder is considered to be 3D and vortex shedding mechanism plays a major role in the near wake turbulent flow characteristics [24]. 2D simulations are also performed to show the necessity for 3D calculations in the present LES code. All 2D and 3D simulations are performed trying to maintain similar characteristics of mesh configuration, solver-setup and turbulence modeling parameters in order to make the results comparable. The simulations and integral flow parameter values, namely, the nondimensional vortex-shedding frequency St_v , time-averaged drag coefficient \bar{C}_D , fluctuating lift coefficient \bar{C}_L , time-averaged base pressure coefficient \bar{C}_{pb} , and separation angle $\bar{\theta}_s$ calculated for each simulation, are summarized in Table 1.

6.1 Primary Flow Features. In the subcritical flow regime, the boundary layer developing along the cylinder surface remains laminar up to and after the separation point and becomes turbulent somewhere in the free shear layer region as suggested by Achenbach [1]. For this reason, the vortex-shedding prediction requires turbulence models. Franke and Rodi [26] show that the occurrence and quality of the vortex-shedding prediction depend strongly on the turbulence models used and the integral flow parameter calculations are significantly affected by the vortex-shedding predictions. Bearing this in mind, the formation and shedding of vortices in the near wake of the cylinder are studied by considering different turbulent inflow boundary conditions. Basic flow features, such as primary and secondary separations, vortices developing from the cylinder surface, and the well-known von Karman vortex street with periodic vortex shedding, are observed for each simulation. For brevity, only those obtained from a simulation conducted at turbulence intensity of 0.6% for a mesh resolution of 435×300 grid points in 2D (case 2) and $435 \times 300 \times 44$ grid points in 3D simulations (case 4) are presented in this section. Figures 3(a)–3(c) show the instantaneous velocity vectors for cases 2 and 4 at two different spanwise locations at nondimensional time of $t^* = 105.2$ in the near wake flow field of the cylinder. As can be easily seen in Figs. 3(a)–3(c), there is a clear demarcation between the flow patterns obtained from 2D and 3D computations. The different flow patterns are also observed in the different spanwise locations for the 3D computations and can be attributed to the lack of two-dimensionality in the present calculations. The main difference between the 2D and 3D calculations occurs in the simulated counterrotating secondary eddies attached to the backward side of the cylinder and the small-scale eddies in the base region. It can be observed in Fig. 3(a) that large secondary eddies in the separated shear layer are obtained from the 2D simulation. In contrast, the secondary eddies formed in the 3D

Table 1 Overview of calculated integral parameters at Re=140,000

Simulation	Turbulent inflow data		Mesh resolution	\bar{C}_D	\bar{C}_L	\bar{C}_{pb}	St_v	$\bar{\theta}_s$
	I_u	isotropic turbulence intensity (%)						
Case 1	$I_u=0.6$		335 × 300	1.370	0.710	-1.56	0.201	91.2
Case 2	$I_u=0.6$		435 × 300	1.351	0.701	-1.506	0.203	91.8
Case 3	$I_u=0.6$		435 × 300 × 32	1.287	0.663	-1.286	0.195	88.7
Case 4	$I_u=0.6$		435 × 300 × 44	1.275	0.643	-1.267	0.195	90.3
Case 5	$I_u=6$		435 × 300 × 44	0.902	0.298	-0.976	0.264	107.1
Case 6	Smooth inflow		435 × 300 × 44	1.305	0.674	-1.33	0.19	89.4
	Experiment (Cantwell and Coles [24])			1.237	-	-1.21	0.179	77
	$I_u=0.6\%$ isotropic turbulence)							

simulations are much smaller and fewer in number as seen in Figs. 3(b) and 3(c). The secondary vortices may occur due to a separation of the back flow from the cylinder surface, i.e., a second separation of the flow and play important role in determining some important flow features, such as the transient behavior of the separation position and small scale of turbulent fluctuations, which give rise to the turbulent momentum exchange towards free shear layers [9]. However, the presence of these vortices, previously observed experimentally by Bouard and Coutanceau [27] for lower Reynolds numbers, does not have any significant effect on the surface pressure distribution for either the 2D or 3D case, and hence, the predictions of the drag forces computed from present 2D and 3D calculations. The discrepancy between the 2D and 3D force coefficient calculations is probably due to the small-scale vortices originating near the backward stagnation point due to the interaction of the two separated shear layers. The 3D calculations clearly indicate the existence of small-scale eddies with three-dimensional structures in the base region, which is presumably associated with the transition to turbulence in the near wake for subcritical flows as indicated previously by Kato and Ikegawa [28]. In addition to the simulation differences in the existence of those small-scale eddies in the base region, the discrepancy in the simulated strength of the large vortices appearing in the near wake region can also lead to the variations in the force coefficient determinations for 2D and 3D computations as summarized in Table 1. The simulated strength of the large vortices is found to be weaker for the 3D case than for the 2D case due to more elongated large-scale vortices in the formation region in the near wake for the 3D case. As the wake further develops, the large vortices slowly shift away from the cylinder due to their self-induced velocity fields and the instabilities originating from the rounding errors and numerical dispersion in addition to the upstream effects lead the flow to eventually become asymmetric. While the asymmetry dominates the near wake flow behind the cylinder, for the present set of calculations, the large vortex on the lower side of the cylinder grows more rapidly than the one on the upper side of the cylinder, and is shed at $t^*=18.4$ for the 2D simulation. On the other hand, the first large vortex is shed from the upper side of the cylinder at $t^*=12.3$ for the 3D simulation. The smaller time taken for the first vortex to be shed from the cylinder surface in the 3D case can be attributed to rapid interaction between the two separated shear layers with opposite vorticity, resulting in earlier roll-up and cutoff of vortex sheet to vortices and strong 3D flow behaviors in association with the existence of small-scale eddies interacting with the large ones in the base region. Two elongated large vortices shed at about the same time are discernable for the 3D case as shown in Fig. 3(c) while alternating vortex shedding is seen in Fig. 3(a) for the 2D case. The different vortex shedding mechanisms obtained in the different spanwise locations can be closely related to the vortex stretching mechanism in the near wake for the present 3D computations as seen in Figs. 3(b) and 3(c).

The instantaneous vorticity contours obtained from 2D and 3D cases in different 2D planes in the wake of the cylinder are seen in Figs. 4(a)–4(c) at a nondimensional time of $t^*=47.6$. The vorticity

patterns obtained from the 3D case indicate that some random small-scale structures appear in the near wake of the cylinder in the large-scale structures, as illustrated in the x - y plane at a spanwise location of $z/D=2$ in Fig. 4(b). In contrast to the 3D simulation, the 2D simulation cannot reproduce these small-scale eddies, which interact with the large-scale Karman vortices as seen in Fig. 4(a). This is probably due to highly turbulent and 3D flow structures in the wake region and the inability of 2D simulation in capturing these small-scale structures. However, the well-known von Karman vortex street with periodic vortex shedding is discernable in the 2D case and the more pronounced asymmetric vortex shedding mechanism obtained from the 2D case. Figure 4(b) shows that the separated shear layers are found to be more elongated in the streamwise direction in the 3D case because of vortex stretching mechanism. At the far field, there is also clear evidence of large-scale irregularities as presented at the midtransverse plane in Fig. 4(c). The primary separation point shows oscillatory behavior during the simulations and the predicted time-averaged separation angle θ_s is about 91.3 deg for the 2D case and 90.8 deg for the 3D case. The vortex-shedding period is also determined using the power spectral density of the vorticity generation at a point $(x,y)=(8D,7D)$ in the near wake of the cylinder and is presented in Table 1. The predicted nondimensional vortex-shedding frequencies are 0.195 and 0.203 for 3D and 2D computations, respectively, while the experimental study produces 0.179 for the nondimensional vortex-shedding frequency. The computed value of 0.179 from the study of Cantwell and Coles [24] is extremely low and not in good agreement with most of the other experimentally determined values of ~ 0.20 [1,29,30]. The large deviations between the 2D and 3D results indicate that highly turbulent 3D structures strongly influence the near wake flow characteristics and, hence, the predictions of the integrated force coefficient calculations. The application of the present RFG algorithm seems to slightly improve the 2D results as illustrated in Table 1. However, much better agreement between the experimental data and the 3D results are observed.

6.2 Influence of Mesh Resolution. The effect of mesh resolution on the present calculations is tested for four different mesh systems (cases 1–4) containing 335 × 300 and 435 × 300 grid points in the (x, y) direction, 435 × 300 × 32 and 435 × 300 × 44 grid points in the (x, y, z) direction with isotropic inflow turbulence level of 0.6%. This value corresponds to the isotropic turbulence intensity value measured in the wind-tunnel experiment by Cantwell and Coles [24]. Figure 5 illustrates the time-averaged streamwise velocity distributions in the near wake along a constant $x/D=1$ position for all four mesh systems and that of experimental data of Cantwell and Coles [24]. The time averaging is applied to the LES calculations for a period of 16 shedding cycles at the end of the each simulation. It is found that time averaging over 16 shedding cycles is sufficient to achieve statistical steady state of the near wake turbulence for 3D calculations. In general, it is seen in Fig. 5 that the agreement with the experimental data is satisfactory in consideration of 2D simulations except for small differences in the regions of peak velocity and in the very near

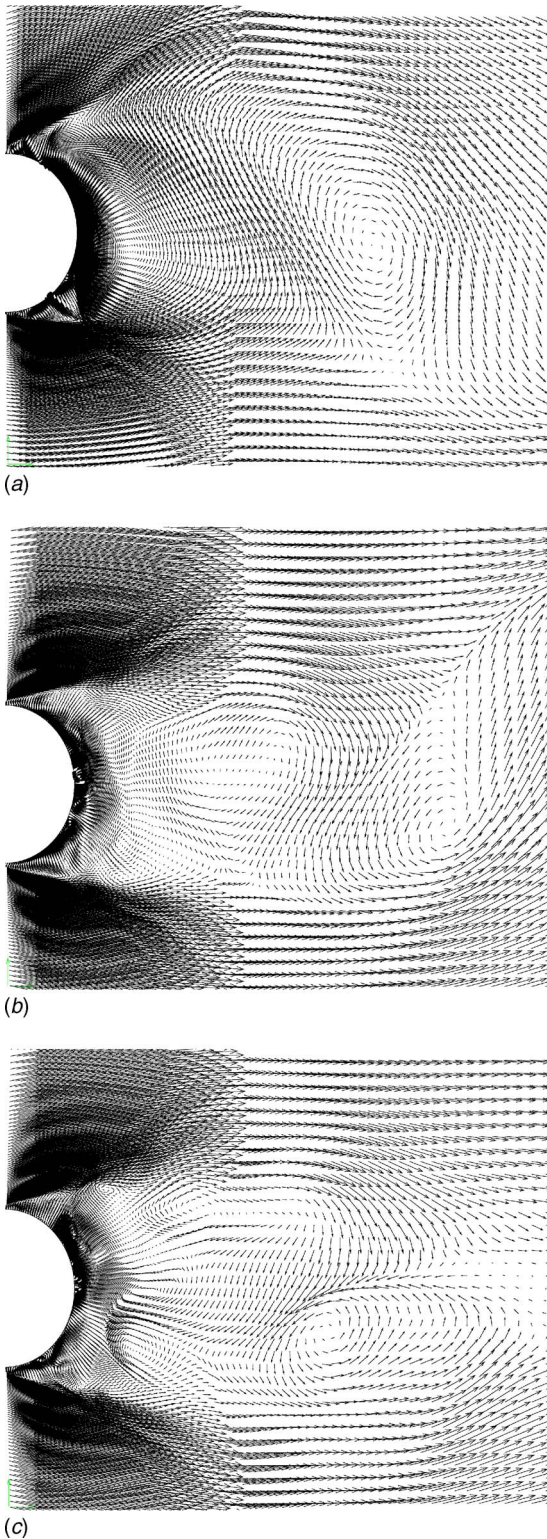


Fig. 3 The instantaneous velocity vectors obtained from 2D and 3D LES computations at two different spanwise locations at a nondimensional time of $t^+ = 105.2$ at inflow turbulence level of 0.6%: (a) Case 2, (b) case 4, 2D view in the x - y plane at $z/D = 0.8D$, (c) case 4, 2D view in the x - y plane at $z/D = 3.5D$

wake region near the centerline. All LES calculations with each mesh system underestimate the velocity profile in the free shear layer region while overestimating it in the recirculation zone. The increase in the mesh resolution slightly improves the predictions

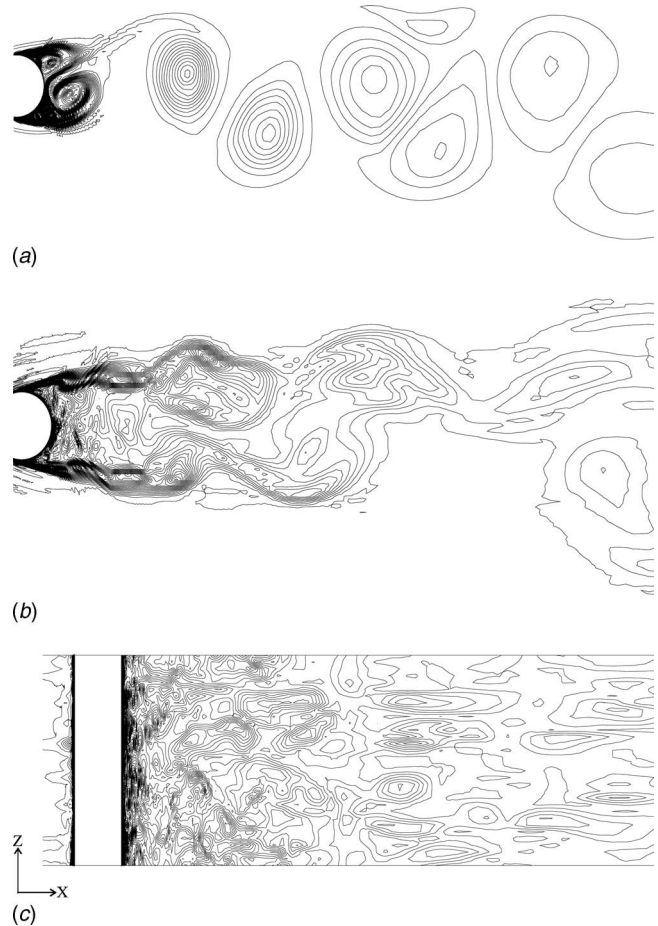


Fig. 4 The instantaneous vorticity contours obtained from 2D and 3D LES at a nondimensional time of $t^+ = 47.6$ at inflow turbulence level of 0.6%: (a) Case 2, (b) case 4, 2D view in the x - y plane at $z/D = 0.8D$, (c) case 4, 2D view in the x - z plane at $y/D = 0$

of the streamwise velocity distribution in 2D calculations. However, the much higher streamwise velocity values obtained on the centerline of the cylinder may be an indication of the much smaller recirculation length predictions than that of experimental value of Cantwell and Coles [24] and this can be attributed to the nature of 2D simulations, which ignores the vortex-stretching mechanism, resulting in a shorter vortex formation length behind the cylinder as indicated by Mittal and Balachandar [31]. In contrast to 2D calculations, 3D calculations clearly improve the prediction of streamwise velocity distribution especially in the regions of peak velocity, i.e., free shear layer and the near wake to reproduce much better recirculation length behind the cylinder. The predicted recirculation lengths still seem to be underestimated by the 3D calculations but are found to be in better agreement with the experimental values. The improved recirculation length in the 3D calculation can be attributed to the more elongated separated shear layers as observed in Fig. 4(b) and the existence of small-scale eddies with 3D structure in the base region. The deviations from the experimental data decrease with the increase in mesh resolution.

The influence of mesh resolution on the present flow is also investigated through the further calculations of time-averaged pressure distributions over the cylinder surface as illustrated in Fig. 6. The experimental data of Cantwell and Coles [24] are also included in Fig. 6 for a comparison. Here, the pressure coefficient \bar{C}_p results from the finest mesh system (case 4) come closer to the measurements. Also, the mesh refinement study shows that the \bar{C}_p

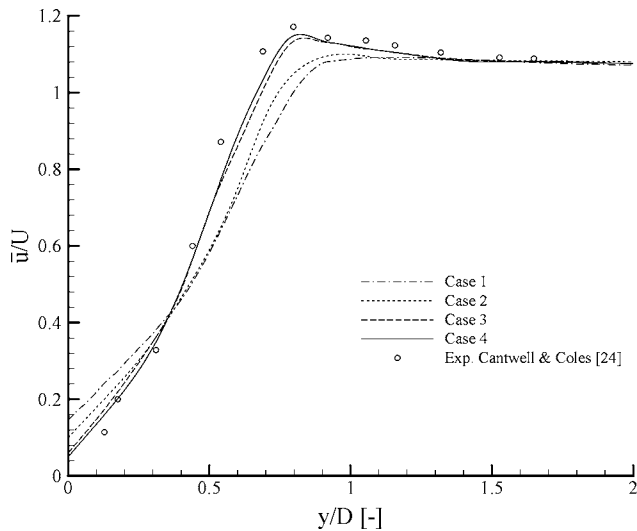


Fig. 5 The time-averaged streamwise velocity distributions in the near wake along a constant $x/D=1$ position for different mesh systems (cases 1–4) and that of experimental data of Cantwell and Coles [24]

values seem to be less mesh dependent than the time-averaged streamwise velocity for both the 2D and 3D cases. As seen in Fig. 6, on the upstream cylinder half, the time-averaged pressure values for each mesh system agree well with each other and with the experimental data. However, on the downstream cylinder half, the calculated pressure distributions of all mesh systems deviate from each other and from the experimental data. The deviations in the pressure distributions become more significant, depending on the dimensionality of the simulation models. The time-averaged pressure coefficients calculated by the 3D simulations become much flatter after the separation point, which is an important behavior of the wake flow in the subcritical regime and qualitatively in better agreement with the experimental data than the 2D results. This is mainly due to the fact that on the downstream cylinder half, where the boundary layer separation takes place, the resolutions of some important flow features, such as the transition of the flow regime to the turbulent flow and the small-scale fluctuations associated

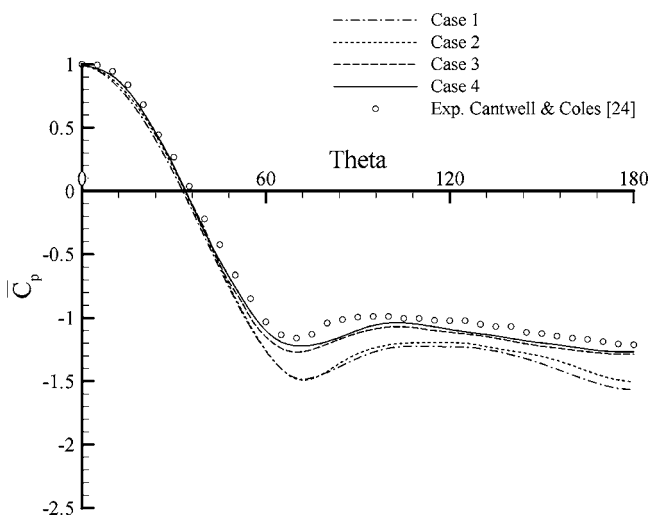


Fig. 6 Pressure distributions in terms of time-averaged pressure coefficient \bar{C}_p over the cylinder surface for different mesh systems (cases 1–4) and that of experimental data of Cantwell and Coles [24]

with the three-dimensional nature of the near wake flow are not predicted well with the 2D simulations and both the minimum pressure coefficient $-\bar{C}_{P_{\min}}$ and the base pressure coefficient $-\bar{C}_{P_b}$ are overpredicted. Consequently, the time-averaged drag coefficients \bar{C}_D obtained from 2D simulations are found to be larger than those obtained from 3D simulations, as illustrated in Table 1. These parameters strongly correlate with the vortex formation length, vortex shedding frequency, and strength of the primary vortices and need to be accurately calculated from the hydrodynamic point of view.

As the mesh resolution is increased, the vortex structures near the separation point becomes larger and the time-averaged location of the separation point moves further downstream as noted in Table 1, which illustrates the improvement of pressure profiles and, hence, the time-averaged base pressure and drag coefficient values with the higher mesh resolution for each case. Therefore, the mesh resolution of $435 \times 300 \times 44$ grid points (case 4) shows the better agreement with the experimental data compared to the other mesh systems tested and is adopted for all subsequent computations of the present study.

6.3 Influence of Inflow Turbulence. The influence of turbulent inflow boundary conditions on the present flow is extensively studied with varying degree of isotropic turbulence for mesh system of $435 \times 300 \times 44$ grid points. With this regard, numerical simulations are performed in conjunction with the RFG algorithm to generate the isotropic inflow turbulence of which the turbulence level is varied from 0.6% to 6%. Figures 7(a) and 7(b) show the time history of x and y velocity components at the inflow boundary at two different inflow locations of $P(0, 7D, 2D)$ and $P(0, 7.5D, 2.25D)$ points for varying degree of inflow turbulence (cases 4 and 5). All velocity components are nondimensionalized with respect to the time-averaged streamwise velocity component at the inflow boundary. Figures 7(a) and 7(b) clearly demonstrate the effect of turbulence on flow at the inflow boundary. The frequency and amplitude of the velocity fluctuations increase as the inflow turbulence level is increased from 0.6% to 6%. The spatial variations (i.e., phase lag) observed in the history of each velocity component for each simulation case can be attributed to spatial inhomogeneity that is satisfied at the inflow boundary for realistic flow simulations. The present RFG algorithm therefore ensures the spatially evolving isotropic turbulence along the inflow boundary.

The corresponding one-dimensional energy spectrums of y velocity component for different inflow turbulence conditions at the inflow boundary and at two more selected locations along the centerline of the cylinder are computed. The energy spectrums are nondimensionalized with respect to the total energy in each case and are plotted with respect to the nondimensional vortex shedding frequency fD/U , where f is the frequency, U is the time-averaged streamwise velocity at the inflow boundary, and D is the cylinder diameter. The energy spectrum of the y velocity perturbation is calculated using a method based on a Fourier transformation approach as follows:

$$S_1(\omega_n) = E \left[\frac{h_T}{M_d} \left| \sum_{m=1}^{M_d} U_1'(t_m) \exp(-i\omega_n t_m) \right| \right]_{N_d}^2 \quad (n = 1, \dots, M_d) \quad (13)$$

where $\omega_n = 2\pi n / (h_T M_d)$ is the nondimensional circular frequency, M_d is the number of time series data, and $E[\cdot]_{N_d}$ denotes the averaging over N_d samples. In the present study, about 10,000 samples at each location of streamwise velocity component are collected over a time interval Ut/D of 100. The energy spectrum can then be converted into wave number domain as

$$E_1(\alpha_n) = U_c S_1(\omega_n) \quad (14)$$

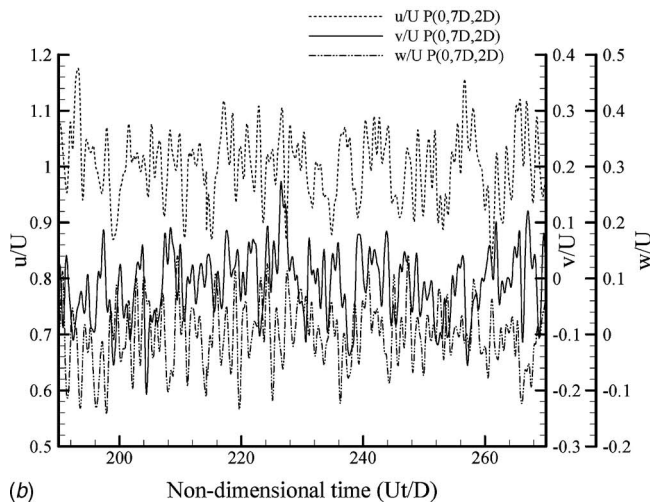
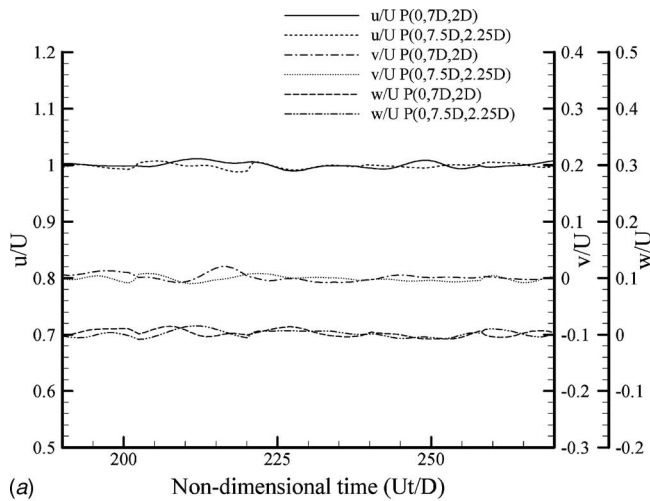


Fig. 7 Time history of nondimensional x and y velocity components for the 3D LES computations at two different points $P(0, 7D, 2D)$ and $(0, 7.5D, 2.25D)$ at the inflow boundary for different turbulence inflow boundary conditions generated by the RFG algorithm: (a) Case 4 at $I_u=0.6\%$ and (b) case 5 at $I_u=6\%$

where $\alpha = \omega_n / U_c$ is the wave number.

Figures 8(a)–8(c) show the energy spectrums at three different locations along the centerline of the cylinder for three cases (cases 4–6). The energy spectrums are consistent with the instantaneous flow visualizations, where the presence of small scales is clearly observed even at this very low isotropic turbulence intensity value of 0.6%. Figure 8(a) shows the energy spectrum at a point $P(0, 7D, 2D)$ at the inflow boundary for isotropic inflow turbulence of 0.6% and 6%. The energy spectrum is confined to a narrowband for case 4 and a broader-banded energy spectrum is obtained for case 5. Both cases can capture the inertial subrange as observed in Fig. 8(a). Figure 8(b) shows the energy spectrums for three different cases, including the smooth inflow case very near to the front stagnation point of the cylinder. The small velocity fluctuations generated by the RFG algorithm at low inflow turbulence intensity of 0.6% at the inflow boundary are able to reach the cylinder, and a good portion of the inertial subrange is captured here. The energy spectra for the y velocity component appear to exhibit an inertial subrange about a half decade of inertial subrange from about the nondimensional frequency of 2–10, where energy spectra exhibit a slope close to $-5/3$ predicted by Kolmogorov theory. The energy spectrum determined at point $P(8.5D,$

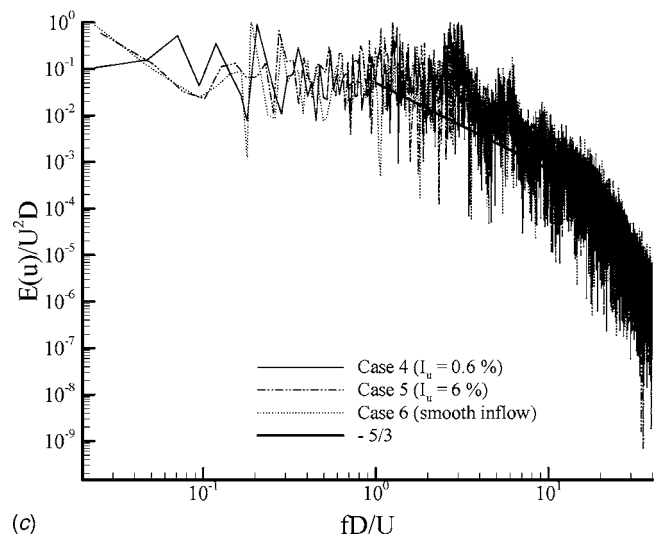
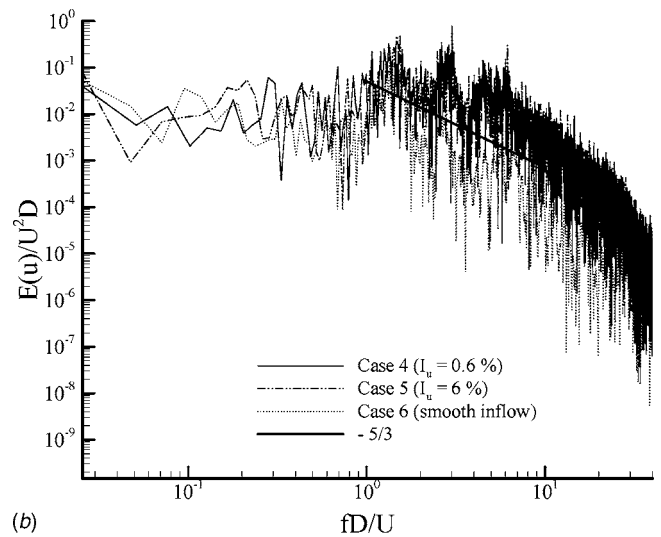
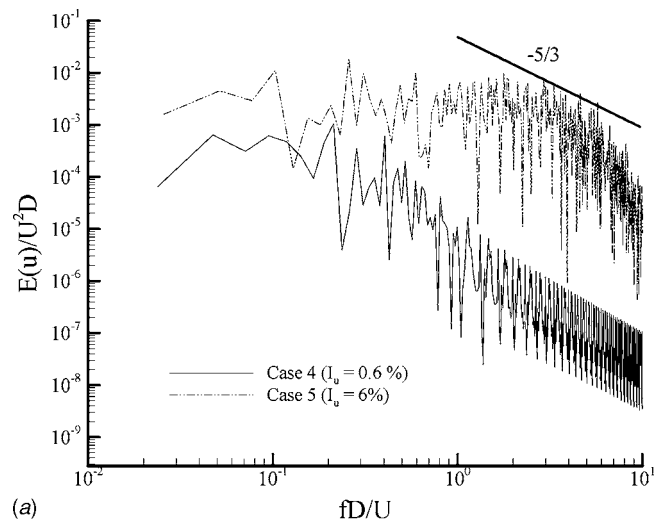


Fig. 8 One-dimensional energy spectrums for the y velocity component obtained from the 3D LES computations at the inflow boundary and at two more selected locations along the centerline of the cylinder for different turbulent inflow data: (a) $P(0, 7D, 2D)$, (b) very near to the front stagnation point of the cylinder $P(0, 6.985D, 2D)$, and (c) $P(8.5D, 7D, 2D)$, $-5/3$ slope

7D, 2D) behind the cylinder can be also seen in Fig. 8(c). The more energy is contained at the larger frequencies compared to the near front stagnation point spectrum. The broader-banded distribution of the energy at this in-wake location compared to that at the selected front stagnation point for each case can be attributed to the occurrence of the near wake turbulence and the associated large irregular wake velocity fluctuations.

Figure 8(c) clearly shows dominant frequencies at nondimensional vortex shedding frequencies. The increase in the turbulence intensity from 0.6% to 6% increases the nondimensional vortex-shedding frequencies. This can be explained by the closer interactions between the two separated shear layers. It is evident in Table 1 that the time-averaged separation locations become closer with increasing turbulence intensity, and the closer interaction of the two separated shear layers results in early roll up and shedding of vortices from the cylinder. Though there still exists a dominant frequency representing the nondimensional vortex-shedding frequency at 6% of inflow turbulence, the magnitude of the dominant frequency seems to become less pronounced at this turbulence level. This is probably due to the fact that the resolved turbulent kinetic energy in the near wake is a sum of periodic vortex shedding oscillations and the resolved turbulent fluctuations. As the turbulence intensity increases, the vortex-shedding motion is superimposed by strong turbulent fluctuations, resulting in a smaller spectral density of vortex shedding and larger spectral density of turbulent fluctuations at higher frequencies (Fig. 8(c)). It is also illustrated in Fig. 8(c) that when the isotropic turbulence intensity is increased from 0.6% to 6% (case 5), the energy spectrum shows more energy at the larger frequencies in the inertial subrange and the distribution of the energy is much broader banded. Simulations with the RFG algorithm show a slightly slower decay of the energy spectra and more energy at the high frequencies with increasing turbulence intensity.

The effect of inflow turbulence on the time-averaged pressure distributions over the cylinder surface is illustrated in Fig. 9. As clearly seen in Fig. 9, the positive pressure distribution on the upstream cylinder half is barely affected by the inflow turbulence. However, on the downstream cylinder half, where the boundary layer separation and the transition to turbulence occur, the pressure distributions are significantly affected by the inflow turbulence. The position of the minimum time-averaged pressure coefficient $\bar{C}_{p \min}$ moves slightly rearward on the cylinder as the inflow turbulence intensity increases for all turbulence inflow data generated by the RFG algorithm. The minimum pressure decreases, and the base pressure increases with the increasing turbulence intensity. This is mainly due to the direct effect of the inflow turbulence on the boundary layer, which leads to changes in the position of the separation lines, and also, there is an effect on the flow in the separated shear layer after the boundary layer separation in the near wake of the cylinder. The calculated time-averaged base pressure coefficient \bar{C}_{pb} values for the smooth inflow case (case 6) and isotropic inflow turbulence of which turbulence level is 0.6% (case 4) are -1.330 and -1.267 , respectively. The calculated time-averaged base pressure values are found to be slightly lower than the experimental value of -1.21 for the isotropic turbulence intensity of 0.6%. This is probably due to the fact that 3D simulations produce slightly shorter separation zone than the experimental study as illustrated in Fig. 5. When the turbulence intensity is further increased to 6% the calculated time-averaged base pressure coefficients become lower with the values of -0.976 (case 5). The time-averaged drag coefficients \bar{C}_D obtained by integrating the circumferential time-averaged pressure distribution are to decrease with the increasing turbulence intensity as indicated in Table 1. In case of 0.6% isotropic inflow turbulence (case 4), the calculated time-averaged drag coefficient is 1.275 and this value is in better agreement with the experimental value of 1.237 than that of smooth inflow (case 6) of 1.305, indicating that there is an improvement in the prediction of time-

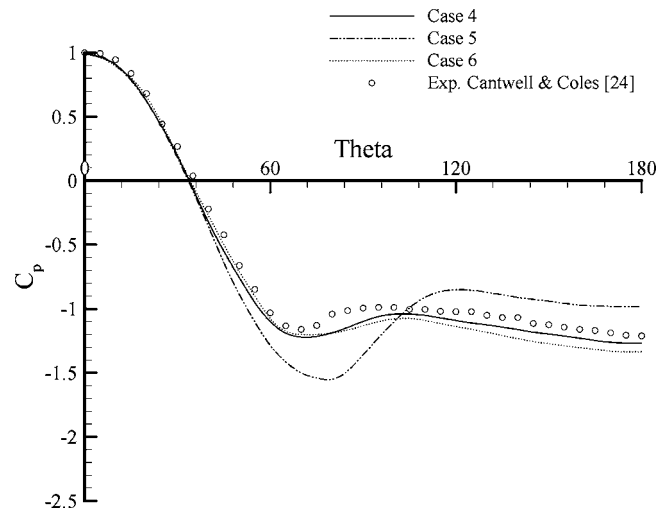


Fig. 9 Pressure distributions in terms of time-averaged pressure coefficient \bar{C}_p over the cylinder surface for different turbulent inflow boundary conditions for the 3D LES computations

averaged drag coefficient values with the use of RFG algorithm. The further increase in the level of the inflow turbulence leads to much lower predicted time-averaged drag coefficient of 0.902 for case 5 as seen in Table 1. The amplitude of the time varying lift coefficients $|\tilde{C}_l|$ for each inflow turbulence case is also illustrated in Table 1. The pressure distributions shown in Fig. 9 indicate that when the turbulence intensity is high, e.g., 6%, at the inflow boundary, the boundary layer separation moves rearward (see Table 1), which, in turn, reduces the lateral spacing of vortices being shed as well as reducing the coherence and the strength of these shed vortices due to vortex stretching mechanism. As a result, the absolute value of the base pressure decreases. The point at which transition to turbulence occur in the wake should also approach the cylinder surface. That is the flow regime shifted to the critical regime under the influence of inflow turbulence as expected from the experimental evidence [24]. This regime change is also evident in Figs. 10 and 11, which show contours of instantaneous vorticity magnitude and velocity vectors, respectively, in different 2D planes with varying inflow turbulence in the wake of the cylinder.

Figures 10(a)–10(c) present the instantaneous vorticity contours at the midspanwise plane of $z/D=2$ for different inflow turbulence levels. It is observed in Figs. 10(a)–10(c) that the length of the two separated shear layers and the size of the vortex formation region seem to be sensitive to the degree of inflow turbulence. The separated shear layers are found to become more elongated as the turbulence intensity increases, and stronger interactions of these two shear layers reduce the coherence and strength of the simulated small-scale vortices in the base region. The wake destabilization time for each case becomes different and as a result of this the phase lag occurs in the formation of the large vortices behind the cylinder for each case as seen in Figs. 10(a)–10(c). The phase lag can be attributed to the onset of the wake instability leading to vortex shedding (the wake fluctuates more at low inflow turbulence levels). The wake instability is expected to have an earlier onset for case 5 due to a higher level of turbulence intensity. Some random small-scale eddies in the base region are found to be slightly closer to the cylinder surface with an increase in turbulence intensity, and this may presumably promote early transition to turbulence at higher turbulence intensity.

The instantaneous velocity vectors obtained from 3D simulations at the midtransverse plane of $y/D=0$ are illustrated in Fig. 11(a)–11(c). At the far wake, there is evidence of 3D large-scale

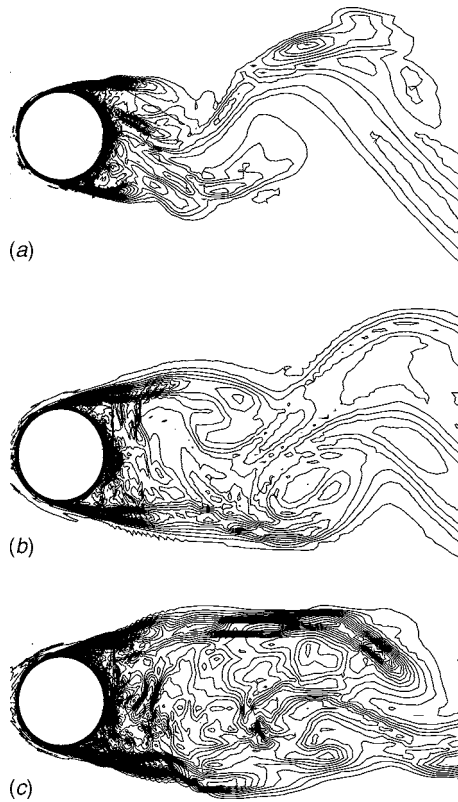


Fig. 10 Instantaneous vorticity contours at the midspanwise plane of $z/D=2$ in the near wake of the cylinder for the 3D LES computations at a nondimensional time of $t=43.6$: (a) Case 6, smooth inflow; (b) case 4; $I_u=0.6\%$, and (c) case 5, $I_u=6\%$

irregularities for each case. As the turbulence intensity increases there are less compact and weaker vortices being shed and shifted away in the wake.

The results presented above indicate that the inflow turbulence has significant effect on the flow around a circular cylinder in the subcritical flow regime. The RFG algorithm adopted here to generate the turbulent inflow data for the present LES calculations tends to promote the turbulent wake characteristics, pressure distribution, separation angle, and force coefficients associated with the higher level of inflow turbulence. These effects are thought to be largely due to the complex interaction between freestream turbulence in the approaching flow and the separated shear layers in the wake of the cylinder and in particular the distortion of turbulence around the stagnation zone of the cylinder. The prediction of the critical integral parameters seems to be strongly dependent on the accurate resolution of the flow in the near wake, where the boundary layer separation, secondary eddies, and transition to turbulence occur. The transitional behavior of the flow is affected with the increasing inflow turbulence generated by the RFG algorithm and the integral parameters vary rapidly with changes in turbulent inflow data. The better predictions of the time-averaged integral parameters using the RFG algorithm for the LES calculations suggest that the proposed method yields more accurate physical picture of the flow in the wake region. Though the present LES predictions for the integral parameters becomes more realistic with the use of the proposed RFG algorithm, the resolution of the local turbulent characteristics still poses a challenge for LES since it does not function very well in simulating turbulent characteristics in the separated shear layer and the wake region. In addition, the 2D LES calculations introduce much stronger fluctuations compared to the 3D calculations and occur closer to the cylinder surface. This is probably due to the fact that the vortex-stretching mechanism in the near wake is ignored with the present

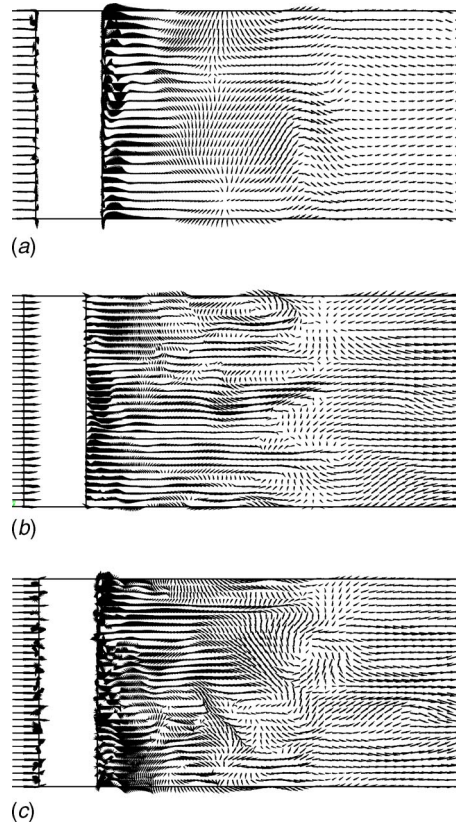


Fig. 11 Instantaneous velocity vectors at the mid-transverse plane of $y/D=0$ in the wake of the cylinder for the 3D LES computations at different inflow turbulence levels $t=43.6$: (a) Case 6, smooth inflow; (b) case 4, $I_u=0.6\%$, and (c) case 5; $I_u=6\%$

2D LES calculations, and this leads to a shorter recirculation length behind the cylinder resulting in prediction of higher values for the integral parameters, minimum and base pressure coefficients, drag coefficient, etc., as illustrated in Table 1.

7 Conclusions

The following conclusions can be withdrawn from the present study:

1. The RFG algorithm promotes the boundary layer characteristics, pressure distribution, and other integral parameters with increasing level of inflow turbulence for the LES computations. The flow resolution and the Reynolds stress in the near wake strongly correlate with the integral parameters. The integral parameters vary rapidly with changes in inflow turbulence.
2. The position of the separation points shift rearward as the turbulence intensity increases at the investigated Reynolds number. The base pressure increases and the minimum pressure, time-averaged, and fluctuating drag and fluctuating lift coefficients decrease with increasing inflow turbulence level. The present model (i.e., LES + RFG algorithm) predicts this trend in accordance with experimental observations.
3. As the turbulence intensity increases the deviation in the predictions of integral parameters becomes larger.
4. The differences in the energy spectra between simulations with and without RFG applications of different level of isotropic inflow turbulence are found to become smaller in the near wake of the cylinder compared to that of inflow boundary. This is probably due to the fact that the vortex-shedding motion dominates the turbulent fluctuations there. However,

as the turbulence intensity increases the vortex-shedding motion seems to be slightly superimposed by stronger turbulent fluctuations in the near wake.

5. The numerical results show that the present model (i.e., LES + RFG algorithm) improve the flow resolution in the near wake and, hence, the predictions for the integral parameters even for 2D calculations. However, much better agreement between the experimental and the 3D simulations indicate that the 3D LES application in association with the RFG algorithm gives more realistic flow field prediction compared to the 2D applications and can further remove over-conservatism in the prediction of the force coefficients.

Acknowledgment

The present study was conducted at West Virginia University in Morgantown, Virginia with a research grant awarded in scope of the NATO Science Fellowship Programme (NATO-B2) from The Scientific and Technical Research Council of Turkey (TUBITAK). Thanks are expressed to all concerned for this Partnership Programme.

References

- [1] Achenbach, E., 1968, "Distribution of Local Pressure Skin Friction Around a Circular Cylinder Flow up to $Re=5 \times 10^6$," *J. Fluid Mech.*, **109**, pp. 239–251.
- [2] Bearman, P. W., 1969, "On Vortex Shedding From a Circular Cylinder in the Critical Reynolds Number Regime," *J. Fluid Mech.*, **37**, pp. 577–585.
- [3] Farell, C., and Blesmann, J., 1983, "On Critical Flow Around Circular Cylinders," *J. Fluid Mech.*, **136**, pp. 375–391.
- [4] Majumdar, S., and Rodi, W., 1985, "Numerical Calculations of Flow Past Circular Cylinder," *Proc. of 3rd Symposium on Numerical and Physical Aspects of Aerodynamic Flows*, Long Beach, CA, San Francisco, pp. 13–25.
- [5] Bosch, G., and Rodi, W., 1998, "Simulation of Vortex Shedding Past a Square Cylinder With Different Turbulence Models," *Int. J. Numer. Methods Fluids*, **28**, pp. 601–616.
- [6] Breuer, M. A., 2000, "Challenging Test Case for Large Eddy Simulation: High Reynolds Number Circular Cylinder Flow," *Int. J. Heat Fluid Flow*, **21**, pp. 648–654.
- [7] Jordan, S. A., and Ragab, S. A., 1998, "A Large-Eddy Simulation of the Near Wake of a Circular Cylinder," *ASME J. Fluids Eng.*, **120**, pp. 243–252.
- [8] Tutar, M., and Holdo, A. E., 2000, "Large Eddy Simulation of a Smooth Circular Cylinder Oscillating Normal to a Uniform Flow," *ASME J. Fluids Eng.*, **122**, pp. 694–702.
- [9] Tutar, M., and Holdo, A. E., 2001, "Computational Modelling of Flow Around a Circular Cylinder in Sub-Critical Flow Regime With Various Turbulence Models," *Int. J. Numer. Methods Fluids*, **35**, pp. 763–784.
- [10] Spalart, P. R., 1988, "Direct Simulation of a Turbulent Boundary Layer up to $Re_\rho=1410$," *J. Fluid Mech.*, **187**, pp. 61–81.
- [11] Lund, T. S., Wu, X., and Squires, K. D., 1998, "Generation of Turbulent Inflow Data for Spatially Developing Boundary Layer Simulations," *J. Comput. Phys.*, **140**, pp. 233–258.
- [12] Lee, S., Lele, S. K., and Moin, P., 1992, "Simulation of Spatially Evolving Turbulence and the Applicability of Taylor's Hypothesis in Compressible Flow," *Phys. Fluids A*, **4**, pp. 1521–1530.
- [13] Kondo, K., Murakami, S., and Mochida, A., 1997, "Generation of Velocity Fluctuations for Inflow Boundary Conditions of LES," *J. Wind. Eng. Ind. Aerodyn.*, **67–68**, pp. 51–64.
- [14] Celik, I., Smirnov, A., and Smith, J., 1999, "Appropriate Initial and Boundary Conditions for LES of a Ship Wake," *Proc. of 3rd ASME/JFE Joint Fluids Engineering Conference*, San Francisco, ASME, New York, ASME Paper No. FEDSM99-7851, pp. 1–9.
- [15] Kraichnan, R. H., 1970, "Diffusion by a Random Velocity Field," *Phys. Fluids*, **13**, pp. 22–31.
- [16] Smirnov, A., Shi, S., and Celik, I., 2000, "Random Flow Simulations With a Bubble Dynamic Model," *Proc. of FEDSM00 ASME Fluids Eng. Division Summer Meeting*, June 11–15, Boston, ASME, New York, pp. 1–8.
- [17] Rodi, W., Ferziger, J. H., Breuer, M., and Pourquie, M., 1997, "Status of Large Eddy Simulation: Results of Workshop," *ASME J. Fluids Eng.*, **119**, pp. 248–262.
- [18] de With, G., Holdo, A. E., and Huld, T. A., 2003, "The Use of Dynamic Grid Adaptation Algorithms for the Modelling of Flow Around a Circular Cylinder in Sub-Critical Flow Regime," *Int. J. Numer. Methods Fluids*, **41**, pp. 789–808.
- [19] Tutar, M., 1998, "Computational Modelling of Vortex Shedding From Off-shore Risers," Ph.D. dissertation, University of Hertfordshire, UK.
- [20] Smagorinsky, J., 1963, "General Circulation Experiments With the Primitive Equations," *Mon. Weather Rev.*, **91**, pp. 99–152.
- [21] Fluent, 1998, *Fidap Users Manual Version 8.6*, Fluent Inc., Lebanon, New Hampshire.
- [22] van Driest, E. R., 1956, "On The Turbulent Flow Near a Wall," *J. Aeronaut. Sci.*, **23**, pp. 1007–1011.
- [23] Ramamurthy, A. S., and Ng, C. P., 1973, "Effect of Blockage a Steady Force Coefficients," *Proc. ASCE, ASCE*, New York, NY, EM4, pp. 755–772.
- [24] Cantwell, B., and Coles, D., 1983, "An Experimental Study of Entrainment and Transport in the Turbulent Near Wake of a Circular Cylinder," *J. Fluid Mech.*, **139**, pp. 321–374.
- [25] Beudan, P., and Moin, P., 1994, "Numerical Experiments on the Flow Past a Circular Cylinders at Sub-Critical Reynolds Numbers," Report No. TF-62, Thermosciences Division, Dept. of Mech. Eng., Stanford Univ.
- [26] Franke, R., and Rodi, W., 1993, "Calculation of Vortex Shedding Past a Square Cylinder With Various Turbulence Models," *Turbulent Shear Flows*, F. Durst et al., eds., Vol. 8, Springer, New York, pp. 189–204.
- [27] Bouard, R., and Coutanceau, M., 1980, "The Early Stage of Development of The Wake Behind an Impulsively Started Cylinder for $40 < Re < 10^4$," *J. Fluid Mech.*, **101**(3), pp. 583–607.
- [28] Kato, C., and Ikegawa, M., 1991, "Large Eddy Simulation of Unsteady Turbulent Wake Flow of a Circular Cylinder Using the Finite Element Method," *Advances in Numerical Simulation of Turbulent Flows*, ASME 1991, FED-Vol. 117, pp. 49–56.
- [29] Fey, U., Köning, M., and Eckelmann, H., 1998, "A New Strouhal-Reynolds Number Relationship for the Circular Cylinder in the Range $47 < Re < 2 \times 10^5$," *Phys. Fluids*, **10**(7), pp. 1547–1549.
- [30] Zdravkovich, M. M., 1997, *Flow Around Circular Cylinders, Fundamentals 1*, Oxford University Press, London.
- [31] Mittal, R., and Balachandar, S., 1995, "Effect of Three-Dimensionality on the Lift and Drag of Nominally Two-Dimensional Cylinders," *Phys. Fluids*, **7**(8), pp. 1841–1865.

Development of a New Simulation Technique Based on the Modal Approximation for Fluid Transients in Complex Pipeline Systems With Time-Variant Nonlinear Boundary Conditions

E. Kojima

Professor
e-mail: kojime01@kanagawa-u.ac.jp

T. Yamazaki

Associate Professor
e-mail: toru@kanagawa-u.ac.jp

M. Shinada

Senior Lecturer
e-mail: shinam01@kanagawa-u.ac.jp

Department of Mechanical Engineering,
Kanagawa University,
3-27-1, Rokkakubashi, Kanagawa-ku,
Yokohama, 221-8686, Japan

A new simulation technique called the system modal approximation method (SMA) for fluid transients in complex pipeline systems has been proposed. The superiority of this technique compared to other existing methods has been verified. Thus far, however, detailed considerations have been limited to pipelines having elementary boundary conditions. In the present paper, for the generalization of the SMA method, calculation methods are newly proposed for the case in which the boundary conditions are given by the time-variant nonlinear relationship between pressure and flow rate, such as the conditions in a safety valve, and its usefulness is verified by comparison to experimental measurements. [DOI: 10.1115/1.2734237]

1 Introduction

Reducing the shock and vibration due to fluid transients in pipeline systems and improving the dynamic characteristics of total systems by controlling the fluid transients have been important technical subjects in numerous fields of fluid transportation engineering. In order to achieve these goals in an efficient manner, the development of a simulation technique capable of quickly and accurately predicting the fluid transients and application of this technique as a design tool would be most effective.

Thus far, the method of characteristics has been used widely for the numerical simulation of fluid transients [1–3]. However, when the pipeline becomes a complex system with several line elements involving different lengths and speeds of sound, the solution procedures become very tedious. In order to solve the difficulties of numerical analysis in the method of characteristics, the modal approximation technique for fluid line modeling was first introduced by Hullender and Healey [4], and this method was subsequently enhanced by several researchers [5–12]. At present, the modal approximation approach has been considered to be a more effective method of modeling complex pipeline systems. Improved approaches are also basically based on a technique for approximating the flow model in the individual line element by the product series of a finite number of rational polynomials in the Laplace domain and expressing variables in the form of a state-space representation (simultaneous first-order differential equation) in the time domain. In this sense, the existing modal approximation method is herein called the element modal approximation method (EMA) so as to distinguish this method from the newly proposed modal approximation method. However, the approximation accuracy of the EMA method when applied to a complex

pipeline system consisting of several line elements was found to become considerably worse.

To solve this problem with respect to the EMA method, a new simulation technique, called the system modal approximation method (SMA), for fluid transients in complex pipeline systems has been devised by the authors [13,14]. The SMA is able to quickly and accurately predict the behavior of such systems. The distinctive feature of the proposed method is that it makes use of a modal approximation of the frequency transfer function itself of the output (required variable) to input (source variable) considering the entire system dynamics, including every boundary condition. This is different from other existing approaches, which are based on the modal approximations of the input-output causality of an individual line element. The new method also has the feature whereby the only numerical data needed relate to the frequency response of the transfer matrix parameters of an individual line element, which may be given by either a theoretical model or experimental measurements. In addition, the required output response in the time domain can be calculated by a simple algebraic expression in the form of a quasi-recurrence formula. In the above literature, the advantages of this technique over other existing methods with respect to accuracy, applicability, flexibility, and computation time, for example, have been verified by comparing the simulation results to the results of the EMA method, solutions from the method of characteristics, and experimental results. In these previous studies, however, emphasis was placed on the establishment of fundamental computing procedures. Therefore, detailed considerations have been limited to cases in which either the pressure or the flow rate can be given as a known variable of time at every boundary.

In several applications of fluid transportation fields, however, complex pipeline systems provided with safety valves, pressure-relief valves, pressure-regulating valves, and air-inlet valves, for

Contributed by the Fluids Engineering Division of ASME for publication in the JOURNAL OF FLUIDS ENGINEERING. Manuscript received September 11, 2006; final manuscript received November 24, 2006. Review conducted by Dimitris Drikakis.

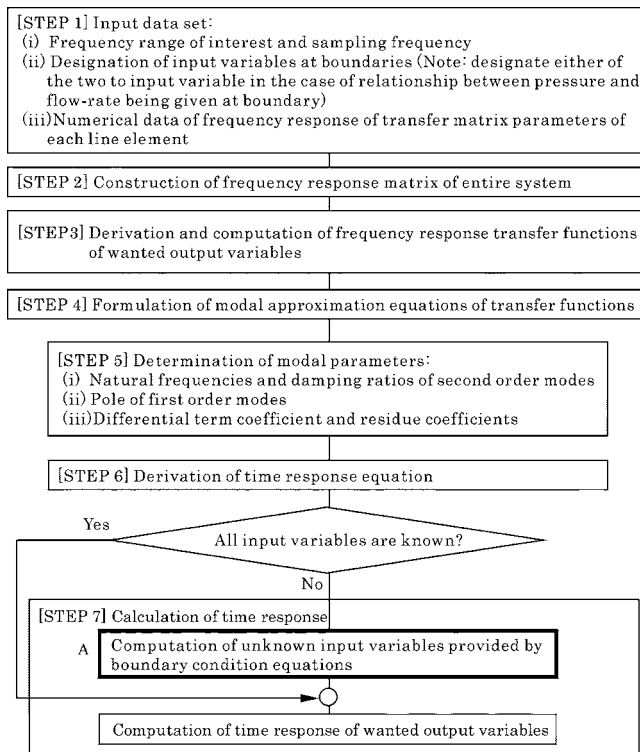


Fig. 1 Flowchart showing the computation procedure for the general-purpose SMA method

example, for controlling the fluid transients, are used regularly. In such a pipeline system, neither the pressure nor the flow rate is known, individually, at these boundaries.

On the basis of the above considerations and the background information, the objective of the present paper is to enhance the analytical functions of the SMA method so as to be widely applicable to the complex pipeline systems with various kinds of system components and boundary conditions. Specifically, we herein propose calculation methods of fluid transients in complex pipeline systems having boundary conditions that are given by the time-variant nonlinear relationship between the pressure and the flow rate and verify the usefulness of the newly proposed general-purpose SMA method by comparing the simulation results to experimental results of fluid transients produced in three types of complex pipeline systems with a safety valve by the instantaneous closure of the directional control valve.

2 Outline of Calculation Procedure of the Proposed System Modal Approximation Method

Variables in the SMA method are pressure and flow rate both upstream and downstream of each line element, which denote the fluctuation component from the initial steady-state value. In addition, variables written in upper- and lowercase letters indicate the values in the Laplace domain (in the frequency domain) and in the time domain, respectively. The total number of variables J of the complex pipeline system composed of I line elements is $4I$.

Figure 1 shows a flowchart of the calculation procedure of the proposed SMA method. Before calculation, the known variables (pressure or flow rate) at boundaries should be designated as the input variables and the unknown variables should be designated as the output variables. For the case in which neither the pressure nor the flow rate are individually known but the relation between them

is given, either of the two should be designated as the input variable and the other as output variable. In the present paper, the calculation method used for the case of the boundary conditions being given by the time-variant nonlinear relationship between pressure and flow rate, such as the conditions in a safety valve, is newly proposed.

Each step of the computing procedure of the proposed SMA method is explained in steps 1-7 (for further details regarding steps 1-6, the reader may refer to abovementioned literature).

Step 1. Provision of the numerical data of the frequency response of the transfer matrix parameters $A_i \sim D_i$ of line elements expressed in the following equation at a specified interval $\Delta\omega$ of angular frequency over the frequency range of interest

$$\begin{Bmatrix} P_{i,1}(j\omega) \\ Q_{i,1}(j\omega) \end{Bmatrix} = \begin{bmatrix} A_i(j\omega) & B_i(j\omega) \\ C_i(j\omega) & D_i(j\omega) \end{bmatrix} \begin{Bmatrix} P_{i,2}(j\omega) \\ Q_{i,2}(j\omega) \end{Bmatrix} \quad (1)$$

where subscript i is a number indicating the i th line element, and the second subscripts 1 and 2 of variables denote the values upstream and downstream of i th line element, respectively.

Note that in the SMA method, none of the line elements are required to be lines, such as tubes, pipes, or hoses, and the numerical data of these matrix elements can be obtained through experimental measurements, for instance, by the "four pressures/two systems" method devised by Kojima and Edge [15], rather than by the theoretical model.

Step 2. Construction of the frequency response matrix of the entire system, considering the input variables, boundary conditions, and the manner of junctions of each line element. This is expressed by a $J \times J$ matrix ($4I \times 4I$ matrix) as follows, for the case in which the total number of line elements is I , which is constituted by the matrix parameters of individual line element in Eq. (1)

$$[E_{j,j'}(j\omega)]\{Y_{j'}(j\omega)\} = [F_{j,k}(j\omega)]\{X_k(j\omega)\} \quad (2)$$

A concrete expression of the frequency response matrix of the entire system for the complex pipeline system in the case of seven line elements is shown by Eq. (A1) in the Appendix.

Step 3. Derivation of the frequency transfer function $G_{j,k}(j\omega)$ of output variables to input variables indicated in the following equation from Eq. (2) using the Gauss-Jordan method, and computation of $G_{j,k}(j\omega)$ at an interval of $\Delta\omega$ ($=0.4\pi$ rad/s, herein) of angular frequency over the frequency range of interest:

$$Y_j(j\omega) = \sum_{k=1}^K \{G_{j,k}(j\omega)X_k(j\omega)\} \quad (3)$$

A concrete expression of $G_{j,k}(j\omega)$ is shown by Eq. (A2) for the preceding complex pipeline system.

Step 4. Representation of the modal approximation of $G_{j,k}(j\omega)$, $G^*(s)$, using the sum of one constant term, one differential term, and a finite number of first- and second-order terms, as shown in Eq. (4). For the purpose of simplifying the description, here, only the equation for the case of single input and single output is shown. In addition, X_k , Y_j , and $G_{j,k}$ are written simply as X , Y , and $G(s)$, respectively

$$G(s) = \frac{Y(s)}{X(s)} \cong G^*(s) = a_0s + b_0 + \sum_{n=1}^N \frac{a_n s + b_n}{s^2 + 2\zeta_n s + \omega_n^2} + \sum_{m=1}^M \frac{c_m}{s + \eta_m} \quad (4)$$

where b_0 is the correction term introduced in order to eliminate the inevitable steady-state error caused by a modal approximation by a finite number of modes.

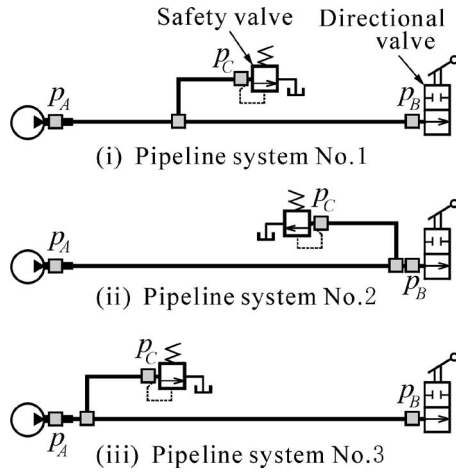


Fig. 2 Three types of compound pipeline systems herein

Step 5. Numerical determination of modal parameters in Eq. (4) from the numerical data of the original equation of transfer function, $G_{j,k}(j\omega)$. For further details of the numerical estimation method, the reader may refer to the abovementioned literature.

Step 6. Derivation of the time response equation for the output variable $y(t)$, from a known input variable $x(t)$, an impulse response of $G^*(s)$, $g(t)$, and a time interval for calculation Δt . This equation can be expressed by the quasi-recurrence formula using a numerical convolution integral as shown in Eq. (5)

$$y(t + \Delta t) = h(t) + h_0 x(t + \Delta t) \quad (5)$$

The details of the expressions of $h(t)$ and h_0 in Eq. (5) are described in the above-mentioned literature.

Step 7. Calculation of the time response of the required output variable. The calculation procedure for the time response of output variable is divided into the following two main cases:

Case (i). The input variables at all boundaries (total number: K) are known in the time domain: The time response of the output variable to the multiple inputs expressed by Eq. (3) can be calculated easily by the following quasi-recursion formula from the linear sum given in Eq. (5),

$$y_j(t + \Delta t) = \sum_{k=1}^K \{h_{j,k}(t) + h_{0j,k} x_k(t + \Delta t)\} \quad (6)$$

where $h_{j,k}(t)$ and $h_{0j,k}$ are parameters corresponding to $h(t)$ and h_0 in Eq. (5) for the case of the input being $x_k(t)$ and the output being $y_j(t)$.

Case (ii). Neither the pressure nor the flow rate are known variables at some of the boundaries: For the case in which the relationship between the pressure and flow rate is given by a

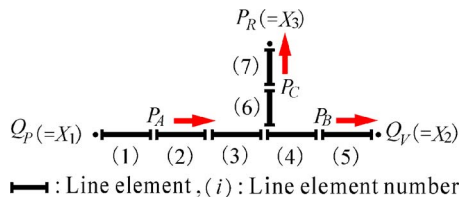


Fig. 3 Complex pipeline system consisting of seven elements used as an example for the explanation of the computing procedure

Table 1 Lengths of pipe elements for three types of pipeline systems (pipe inner diameter: 1, 2=19.4 mm, 3–7=7.8 mm)

Element	Pipeline		
	No. 1 (mm)	No. 2 (mm)	No. 3 (mm)
1	200	200	200
2	100	100	100
3	640	3520	50
4	2840	60	3400
5	20	20	20
6	960	310	310
7	20	20	20

boundary condition equation at K' boundaries among the total K boundaries, the time response of the required output variable at any point is calculated in the following manner. First, either the pressure or the flow rate is designated as the input variable. The relationship between input x and output y at the k' th boundary ($k'=1 \sim K' \in K$) is regarded to be provided by the following boundary condition equation:

$$\Phi_{k'}\{x_{k'}(t + \Delta t), y_{k'}(t + \Delta t)\} = 0 \quad (7)$$

which can be nonlinear. Since the input x_k at the k ($=K'+1 \sim K$) remaining boundaries are known variables, the output at k' th boundaries can be expressed from Eq. (6), as follows:

$$y_{k'}(t + \Delta t) = \sum_{k=1}^K \{h_{k',k}(t) + h_{0k',k} x_k(t + \Delta t)\} \quad (8)$$

Solving the K' set of alliance equations given by Eqs. (7) and (8), K' input variables $x_{k'}$ (and output variables $y_{k'}$) are determined, and the required output variable y_j at any point can then be calculated from Eq. (6). Note that the boundary condition equation may be given by a time-variant nonlinear relationship in the form of a differential equation, as for a pressure control valve, for example. In the present paper, special emphasis is placed on the verification of the effectiveness of the newly proposed calculation method (specifically, for the special case of part A enclosed by thick lines in Fig. 1) for a complex pipeline system with such a complicated boundary condition.

3 Test Complex Pipeline Systems Provided With a Safety Valve and Its Mathematical Model

In the present study, three types of oil hydraulic pipelines, as shown in Fig. 2, were examined as complex pipeline systems provided with a safety valve (for controlling the hydraulic transients). These complex pipeline systems (Nos. 1–3) are all composed of seven rigid tube elements with different dimensions, including the series, branch, and stepped junctions, as shown by Fig. 3. Here, element (1) is a single tube corresponding to the discharge passageway in a pump casing, and its equivalent length (~ 200 mm) was experimentally determined from the frequency

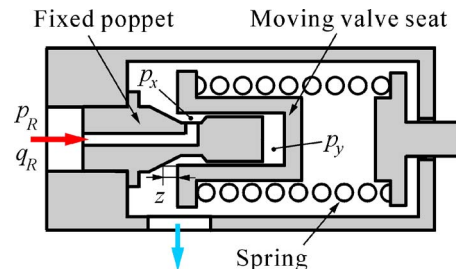


Fig. 4 Schematic diagram of the safety valve used in the test pipeline systems

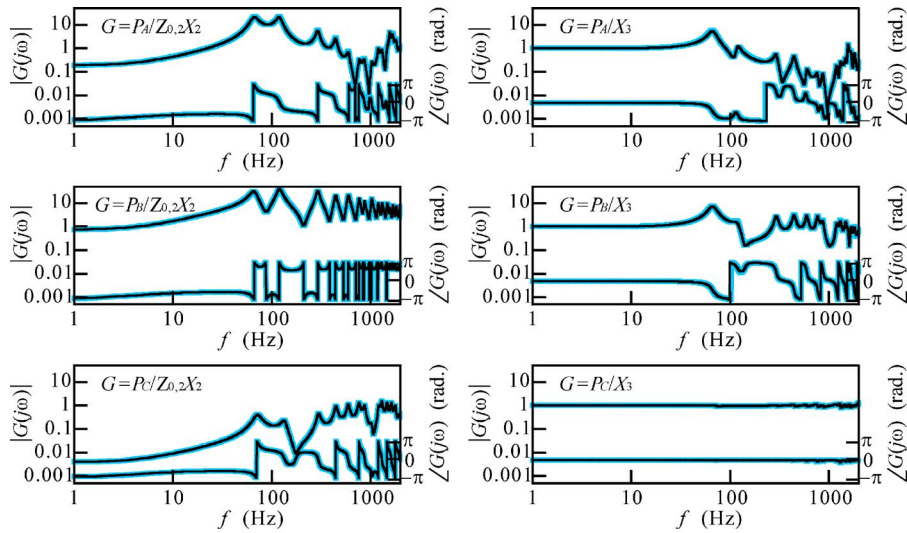


Fig. 5 Comparisons of SMA simulations with exact solutions for frequency response functions (pipeline system No. 1, thin line: Exact; thick line: SMA)

characteristics of the pump source impedance obtained by the “two-pressures/two-systems” method devised by Kojima [16]. The lengths of other pipe elements for the three types of pipeline systems tested are indicated in Table 1. The inner diameter of pipe elements is 19.4 mm for elements (1) and (2) and 7.8 mm for elements (3)–(7).

A directly operated relief valve of the construction shown in Fig. 4 was used as the test safety valve. The equation of motion of the moving valve seat, the equation of laminar flow in the annular clearance between the stationary poppet and the moving valve seat, the continuity equation of the flow rate at the inlet of the valve orifice, and the equation of laminar flow in the capillary within the poppet are expressed, respectively, as follows:

$$\begin{aligned}
 M_r \frac{d^2 z}{dt^2} + C_r \frac{dz}{dt} + K_r(z + z_0) &= A_r(p_y + p_{y0}) + K_f z(p_x + p_{x0}) \\
 p_x - p_y &= K_s \frac{dz}{dt} \\
 q_R &= K_q z \sqrt{(p_x + p_{x0})} + A_r \frac{dz}{dt} \\
 p_R - p_x &= K_p q_R
 \end{aligned} \quad (9)$$

The coefficients in the above equations are given by the following equations. Here, the subscript 0 of the variables (valve displacement z , pressure fluctuation at the orifice upstream p_x , and pressure fluctuation in the valve chamber p_y) denotes their initial steady-state values.

$$\begin{aligned}
 A_r &= \frac{\pi d_s^2}{4}, \quad C_r = \frac{\mu \pi d_s l_s}{h_s}, \quad K_p = \frac{128 \mu l_p}{\pi d_p^4}, \\
 K_s &= \frac{12 \mu l_s}{\pi d_s h_s^3} \left(A_r - \frac{\pi d_s h_s}{2} \right), \\
 K_f &= C_d C_u \pi d_s \sin(2\phi_s) \\
 K_q &= C_d \pi d_s \sin \phi_s \sqrt{2/\rho}
 \end{aligned} \quad (10)$$

where C_d is the discharge coefficient of the valve orifice (0.6), C_u is the velocity coefficient of the valve orifice (1.0), d_s is the inner diameter of the moving valve seat (8 mm), d_p is the diameter of the capillary in the stationary poppet (4.3 mm), h_s is the radial clearance between the poppet and the valve seat (50 μm), K_r is

the spring constant (71.6 kN/m), l_s is the length of the annular clearance between the poppet and the valve seat (10 mm), l_p is the length of the capillary in the stationary poppet (25 mm), M_r is the mass of the moving valve seat (30 g), z_0 is the initial displacement of the spring (which is dependent on the set pressure of the safety valve), ϕ_s is the half vertical angle of the poppet (20 deg), μ is the coefficient of viscosity of the fluid (70 cSt), and ρ is the density of the fluid (867 kg/m³).

Eliminating p_x and p_y analytically and z numerically in Eq. (9), the time-variant nonlinear boundary condition equation expressing the relationship between pressure and flow rate at the inlet of the safety valve, p_R and q_R , which is, the equation corresponding to $\Phi(x, y)$ of Eq. (7), can be obtained. The three boundaries of the test complex pipeline system ($K=3$) are the pump end, the directional valve end, and the safety valve end. Expressing the flow rate q in values relative to the time-averaged discharge flow of the pump, q_{in} , the input variable at the pump end and the directional valve end after valve closure, x_1 and x_2 , are given as known functions of time, as follows:

$$x_1(=q_p) = 0 \quad (11)$$

$$x_2(=q_v) = -q_{in} \quad (12)$$

The input variable at the safety valve end, $x_3(=p_R)$, is unknown and must be found numerically from the simultaneous equation of

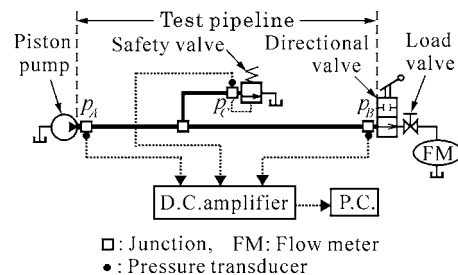


Fig. 6 Schematic diagram of the instrumentation systems used in the experiment

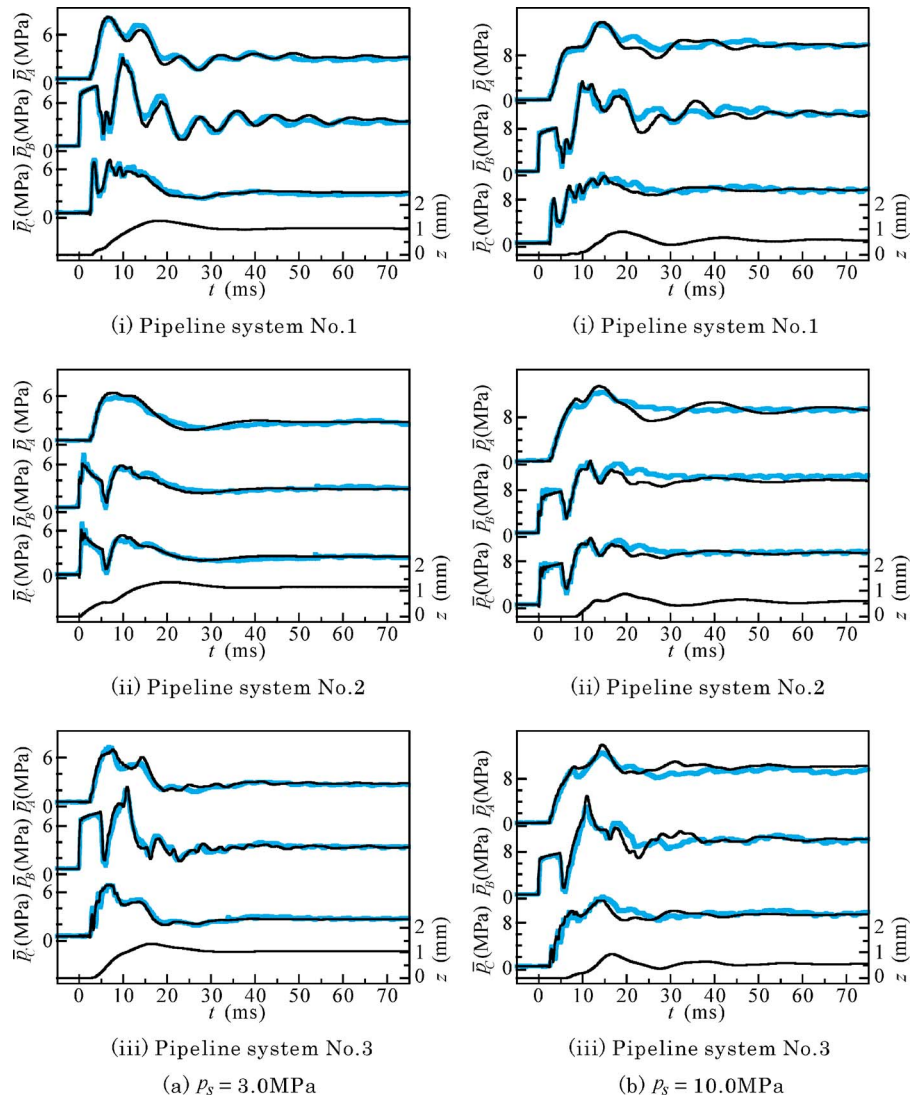


Fig. 7 Comparisons of SMA simulations with experimental results for pressure transients at instantaneous valve closure at $p_{A0}=0.6$ MPa and $q_{in}=0.227$ l/s (thin line: Experiment; thick line: Simulation)

Eq. (7) (obtained by Eq. (9)) and the following equation, corresponding to $K'=1$ of Eq. (8):

$$y_K(t + \Delta t) = \sum_{k=1}^{K-1} \{h_{K,k}(t) + h_{0K,k}x_k(t + \Delta t)\} + h_{K,K}(t) + h_{0K,K}x_K(t + \Delta t) \quad (13)$$

In the present study, the Runge-Kutta method was used to solve Eq. (7). Once the input variable at the safety valve end is determined, the desired output variables y_j can be obtained from Eq. (6) in the same manner as in the case of all of the input variables being known.

4 Comparison of SMA Simulation Results With Experimental Measurements and Considerations

Before the time-response analyses of the output variables, in order to examine the accuracy of the modal approximation in calculation procedures (steps 4 and 5), the frequency characteristics of the transfer functions of the output variable to the input variables X_2 and X_3 , obtained from the exact model, $G(s)$, and the

SMA model, $G^*(s)$, were compared. The example output variables, being the pressure near the pump outlet P_A , the pressure near the directional pressure inlet P_B , and the pressure near the safety valve P_C , and the pipeline system being No.1, are shown in Fig. 5. Here, $Z_{0,2}$ is the characteristic impedance of the pipe element (2), where the input $X_2 (=q_v=-q_{in})$ is acted on. As shown in Fig. 5, the approximation of the SMA method agrees very well with the exact solutions in almost the entire frequency range of interest (up to 2 kHz). These facts suggest that the proposed treatment of the poles of the first lag terms, which have a significant influence on the characteristics in the low-frequency range, as well as the natural frequencies and damping ratios of the second-order lag terms and residue coefficients of modes, is appropriate, and that the numerical searching method is also very accurate. Although no detailed physical reason can be found, the total number of poles of the first-order lag terms in each of the three pipeline systems investigated herein was 1.

A schematic diagram of the instrumentation of the experiment for fluid transients is shown in Fig. 6. The complex pipeline systems tested herein were all composed of steel tubes having the dimensions indicated in Table 1 and were equipped with a hydra-

lic fluid power pump (an axial piston pump) at the beginning end of the test pipeline, a manually operated spool-type directional valve at the closing end, and a safety valve (directly operated relief valve) between the above two ends through a side branch tube. Downstream from the directional valve, a throttle valve and a displacement-type flowmeter were equipped for the adjustment of the initial line pressure and for the measurement of the initial pump discharge flow, respectively.

The experimental procedures were as follows. First, with the directional valve closed and the axial pump operated a constant speed (1500 rpm), the set pressure of the safety valve was adjusted to the specified value. Next, with the directional valve opened, the initial line pressure was adjusted to the specified value by a load valve. Lastly, the directional valve was closed swiftly by striking the valve spool with a hammer and, hence, the fluid transients were generated in the test pipeline system. The pressure fluctuations, P_A , P_B , and P_C (pressures at the respective points indicated in Fig. 6), were measured simultaneously by the semiconductor pressure transducers.

Figures 7(a) and 7(b) show the comparisons of the experimental measurements to the SMA simulation results for the cases in which the safety valve set pressure was 3 MPa and 10 MPa, respectively, and (i)–(iii) in Fig. 7 show the results of the pipeline system of Nos. 1–3, respectively. The initial pump discharge flow rate and initial line pressure at the pump outlet port were 0.225 l/s and 0.6 MPa, respectively. In addition, we chose 2 kHz as the frequency range of interest, 0.4π rad/s as the interval of angular frequency $\Delta\omega$, and 0.1 ms as the time interval Δt in this numerical simulation. As these results show (and from the results for the other test conditions abbreviated herein due to space limitations), the simulations of the proposed SMA method agree relatively well with the experimental measurements, considering the complexity of the pipeline, as far as the values of the pressure peaks of engineering interest are concerned. In addition, although very close agreement between measured and SMA-simulated values was also obtained for the fluid transients caused by the swift opening of the directional valve, the details of the results are omitted herein due to space limitations.

Finally, note that the computation time required for execution of the procedures from Steps 1–7, indicated in Sec. 2, was only 3–5 s for Fig. 7, (i)–(iii), respectively.

5 Conclusions

The present paper investigated the enhancement of the analytical functions of the SMA method, which was developed by Kojima et al. [13,14] for fluid transients in complex pipeline systems, so as to be widely applicable to pipelines with various types of system setups and boundary conditions. Specifically, the calculation methods for the time responses of the required output variables for the case in which the boundary conditions are given by the time-variant nonlinear relationship between the pressure and the flow rate, as in the pipeline equipped with a safety valve, were proposed. The fluid transients produced in three types of relatively complicated pipeline systems under various specified set pressures of the safety valve and the initial values of line pressures were examined. Good agreement between the measured and simulated values was observed.

In conclusion, the proposed generalized SMA method has been found to have a very high engineering usefulness with respect to accuracy, applicability, flexibility, and computation time, for example, as well as in the application to fluid transients in complex pipeline systems with time-variant nonlinear boundary conditions.

Thus far, the fluid transients produced in complex liquid pipelines have only been investigated in developing the SMA method. At present, we are studying the application of the SMA method in

fields of the fluid transients produced in various types of gas transportation complex pipeline systems, including the intake and exhaust systems of engines.

Nomenclature

Only the symbols immediately related to the SMA method are described.

- $A_i(j\omega) \sim D_i(j\omega)$ = transfer matrix parameter of the i th element defined by Eq. (1)
- a_n, b_n = numerator coefficient in the n th second-order mode of $G^*(j\omega)$ defined by Eq. (4)
- b_0 = steady-state correction factor
- c_m = numerator coefficient in the m th first-order mode of $G^*(j\omega)$ defined by Eq. (4)
- $[E_{j,j'}(j\omega)]$ = $J \times J$ matrix defined by Eq. (2)
- $[F_{j,k}(j\omega)]$ = $J \times K$ matrix defined by Eq. (2)
- f = frequency
- $G_{j,k}(s) = G(s)$ = exact (theoretical) transfer function of output $Y_j(s)$ to input $X_k(s)$
- $G^*(s)$ = modal approximation of $G(s)$
- I = total number of line elements
- i = number indicating the i th line element
- J = total number of variables (=4I)
- K = total number of input variables (total number of pipeline boundaries)
- l_i = length of i th line element
- M = total number of first-order modes to be included in the approximation
- m = number indicating the m th first-order mode
- N = total number of second-order modes to be included in the approximation
- n = number indicating the n th second-order mode
- $P_{i,1}, P_{i,2}$ = upstream and downstream pressures of the i th line element
- $Q_{i,1}, Q_{i,2}$ = upstream and downstream volume flow rates of the i th line element
- s = laplace operator
- t = Time
- $\{X_k(j\omega)\}$ = input vector ($k=1 \sim K$) of K rows in the frequency domain
- $x(t)$ = input variable in the time domain
- $\{Y_j(j\omega)\}$ = output vector ($j=1 \sim J$) of J rows in the frequency domain
- Δt = step width of time in numerical calculation
- $y(t)$ = output variable in the time domain
- ζ_n = damping ratio of the n th second-order mode of $G^*(s)$
- η_m = pole of the m th first-order mode of $G^*(s)$
- ω = angular frequency
- ω_n = natural frequency of the n th second-order mode of $G^*(s)$

Appendix

The derivation method of concrete expressions of Eqs. (2) and (3) in the text is explained, taking the case of the complex pipeline system indicated in Fig. 3 as an example. This pipeline system is composed of seven line elements ($I=7$). The relationship between state variables in the frequency domain can be expressed in matrix form as Eq. (A1), where rows 1–14 represent the transfer characteristics of the respective pipe elements (Eq. (1)). In addition, rows 15–18, 22–25, and 19–21 represent a continuity equation of flow rate, and equivalence relationships of the pressures at the

Experimental Leak-Rate Measurement Through a Static Metal Seal

Christophe Marie

Département Génie Chimique,
IUT de l'Aisne, 48, rue d'Ostende,
02100 Saint-Quentin, France

Didier Lasseux¹

Esplanade des Arts et Métiers,
Trefle (UMR CNRS 8508),
Site ENSAM,
33405 Talence Cedex, France
e-mail: didier.lasseux@bordeaux.ensam.fr

This paper presents an experimental study to characterize fluid leakage through a rough metal contact. The focus is on an original experimental setup and procedure designed to measure the fluid micro (or nano) leak rate with great precision over several orders of magnitude. Liquid leak-rate measurements were carried out under two distinct operating conditions, i.e., in the case of a pressure gradient applied between contact edges and in the case of a pure diffusive effect resulting from a species concentration gradient. Experimental leak-rate results are discussed in terms of effective contact permeability—or transmissivity—and in terms of effective contact diffusivity versus contact tightening. [DOI: 10.1115/1.2734250]

Keywords: seal, experiments, micro flow-rate measurement, gas phase chromatography, transmissivity, effective diffusivity

1 Introduction

Metal gaskets are commonly used for spatial and nuclear applications and, more generally, whenever severe thermodynamic conditions are met excluding the use of a rubber-sealant component. In such cases, the seal is performed by a direct-metal/metal-tight contact of rough surfaces for which many parameters controlling the leakage might be involved. Among others, one can cite the material of each surface, the topology at different scales of observation as a result of machining processes, the distribution and level of applied tightening, and the nature and thermodynamic state of the fluid to be sealed. Prediction and further optimization of the sealing efficiency of the contact are made difficult by (i) the identification of the relevant parameters and the way they can be controlled in contact design, (ii) the derivation of complete enough models able to correctly capture the physics of flow that can occur near the percolation threshold and of deformation which can be in the elastic and/or plastic regime [1], and (iii) last but not least, precise measurements of leak rate under well-controlled conditions for sometimes extremely small flow rates. The present paper is focused on this last issue since such measurements can be of interest with many respects.

In most reported experimental studies, seal performance of metal gaskets is investigated in very particular situations and generalization of leak rate results to other configurations or operating conditions has not been yet achieved. Most of the existing leak-rate measurements were performed with a gas and, to our knowledge, no direct comparison to liquid leakage was proposed in the literature in spite of some empirical relationship that justification still leaves much to be desired [2]. In fact, very few papers are reporting metal seal behavior with a detailed dependence of the leakage with the relevant parameters. An early contribution to this problem was proposed from a theoretical and experimental point of view in [3–5]. However, the reported work in these papers dealt with gas leakage in the free molecular regime through the contact between a rough surface and a perfectly flat and nondeformable plane while roughness distribution was assumed to be Gaussian. More recently, Yanagisawa et al. [6] studied the influence of tightening on gas leakage (air or helium), for a C seal from an experi-

mental point of view only. The leak rate was measured using a “water bubble” method, but their investigation was limited to moderate loads because their maximum apparent contact pressure was roughly 200 MPa. Resulting deformations of the gasket under load and microscopic contact areas were also investigated, but no leak-rate predictions were proposed. In a subsequent work by the same authors [7] in 1991, the important role of a lead-coating layer was demonstrated from experiments at ambient and cryogenic temperatures (70 K) performed on C seals. During the same period, an experimental investigation on the influence of the type of machining on leakage was proposed by Matsuzaki and Kazamaki [8]. In their work, gas leak rates observed through contacts of turned, polished, and lapped surfaces made of different materials, such as copper, stainless steel, or other alloy steels were related to surface roughness and contact pressure. A nitrogen leak was detected using gas chromatography. Later, the same analysis was applied to the behavior of knife-edge seals [9], but no model was proposed to predict the leak.

From a theoretical and numerical point of view, some contact models of rough surfaces were reported recently in the literature. One can quote, for example, the numerical work of Kogut and Etsion [1] to describe the contact between a smooth rigid surface and a single asperity in the elastic-plastic domain. Such models, where no interaction between asperities is assumed along with no deformation of the substrate, had been also used before by Polycarpou and Etsion to predict an equivalent dimensionless aperture and gas leakage through the contact ([10,11]). This represents an interesting approach of leakage estimation although the simplified description of surface topology made by a Gaussian distribution of heights of asperities is quite far away from real surface finish frequently used and obtained by a turning process. Moreover, existing models are based on the hypothesis that leakage is mainly controlled by asperities, i.e., by microscopic defects on the surface. Complete studies in terms of scales of investigation (from the microscale to the entire contact scale) are necessary to improve the understanding of all the mechanisms controlling the leak and to capture the role of microscopic and macroscopic parameters. To this end, a complementary approach, consisting in accurate leakage measurements obtained under quasi-real but well-controlled conditions and, in particular, on real machined rough surfaces seems to be needed as pointed out in [12]. The experimental work reported in this paper is a first step to contribute to this task and is a starting point for subsequent comparison to models.

¹Author to whom correspondence should be addressed.

Contributed by the Fluids Engineering Division of ASME for publication in the JOURNAL OF FLUIDS ENGINEERING. Manuscript received September 7, 2004; final manuscript received November 23, 2006. Review conducted by Joseph Katz.

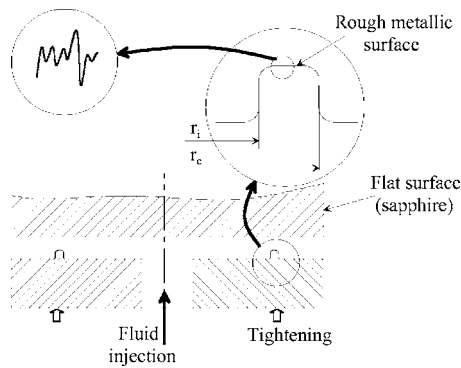


Fig. 1 Configuration of the contact under study

A precise and original method to measure leakage under well-defined conditions was designed and is presented below. It can be applied to flow-rate measurements ranging over six orders of magnitude in any configuration involving an annular contact between two rough surfaces and for both liquid and gas. The leak detection threshold is equivalent to that of mass spectrometry (i.e., typically 1 ppm), which represents a significant breakthrough for detection of a liquid flow rate. It is especially well adapted to measurements of very small flow rates expected for leak tests on systems requiring high sealing levels as well as in many other applications in the domain of microfluidics. In fact, many drawbacks of existing microliquid flow-rate devices are circumvented, such as sensitivity to temperature and/or pressure fluctuations, leakage, evaporation, etc. [13]. An experimental setup using this method was developed, and leak-rate measurements were performed under well-defined conditions on a model configuration close to a real design. Flow rates measured on the entire contact are analyzed in terms of the macroscopic properties of the assembly versus contact pressure. These macroscopic properties are the *effective transmissivity* and *effective diffusivity* and are direct signatures of the connected aperture field, i.e., of interconnected zones of no local effective contact between the two surfaces. These experimental results will serve as a basis for further comparison to predictive estimates of leakage obtained from topological analysis of the surfaces along with numerical simulation of deformation and flow through the contact. A detailed presentation of such a comparison, which is beyond the scope of this paper, will be reported later on. Here, we lay the emphasis upon the methodology which reveals to be very effective.

Section 2 of this paper is dedicated to the description of the experimental apparatus used to perform leak-rate measurements. Results obtained for liquid leakage are presented in Sec. 3. For both pressure-driven and diffusive flows, results were obtained while varying tightening applied to the assembly as well as liquid pressure in the case of viscous flows.

2 Experimental Setup

2.1 Contact Configuration. The configuration for seal tests investigated in the experiments presented below is that of a plane annular and circular contact between a machined metallic surface obtained by turning and made of 316L stainless steel pressed against the plane cross section of a cylinder made of sapphire as schematically represented in Fig. 1. The turning process generates defects ranging from the microscale (metallic grain scale) to the macroscale (error of forms at the scale of the entire contact) [14].

The ring-shaped contact has an inner radius r_i of 19.85 mm and an outer radius r_e of 20.15 mm, yielding an apparent contact area of 38 mm². Two surfaces, referred to as A and B and obtained in very different machining conditions, were used in our experiments. Parameters used for the machining of surface B are re-

Table 1 Turning parameters used for metallic surfaces B

Speed	1200 rpm
Advance by turn	0.05 mm
Depth of cut	0.02 mm
Turning tool	45 deg
Tool radius	0.2 mm

ported in Table 1.

Our objective here is not to mimic metal/metal contact as employed in real configurations but rather to acquire data under simple but well-controlled conditions in the perspective of direct comparison to models. Within this context, a sapphire was chosen for the antagonist and this was motivated by several reasons. First, this allows great simplifications in the description of the contact topology tractable for future use in predictive tools. Indeed, polished surfaces as well as excellent flatness properties can be obtained on the sapphire. Moreover, hardness and Young's moduli ratios between the sapphire and 316 L stainless steel are roughly 10 and 2, respectively, as indicated in Table 2. Under these circumstances, the sapphire can be considered as a flat nondeformable surface; thus, the topological and mechanical properties of the contact are those of the metallic surface only. In other words, this configuration is an excellent experimental support for a straightforward description of the contact with the surface-sum concept without ambiguity. This concept, first introduced in [15], was later confirmed as a relevant one in several works [16–18]. Second, transparency will allow direct visualization of the contact for future study. Of course, the experimental device can be used with any pair of materials and other dimensions of the contact.

2.2 Experimental Device. The experimental setup used in this work is schematically represented in Fig. 2 [19]. It consists of a very rigid leakage cell designed to contain and support the different parts of the contact. Within the leakage cell, the metallic rough surface is pressed against the sapphire disk using a jack

Table 2 Mechanical properties of stainless steel and sapphire used in the experiments

	316L stainless steel	Sapphire
Vickers Hardness	155–190	1570–1750
Young's modulus	1.9×10^5 – 2.1×10^5 MPa	4.4×10^5 MPa
Tensile strength	460–860 MPa	190 MPa
Poisson's ratio	0.3	0.3
Compressive strength	-	2100 MPa

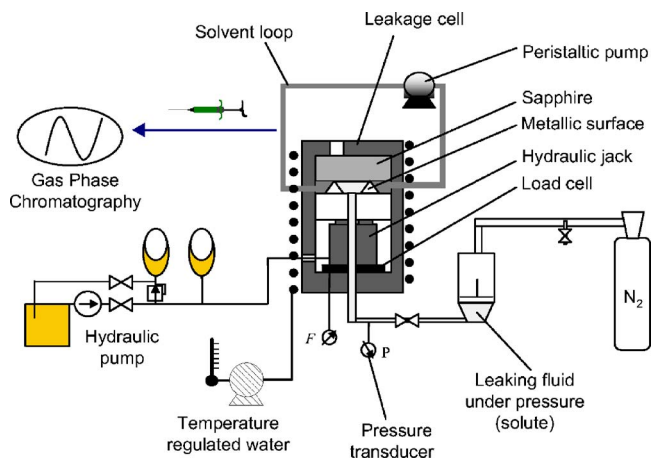


Fig. 2 Schematic representation of the experimental apparatus (viscous flow conditions)

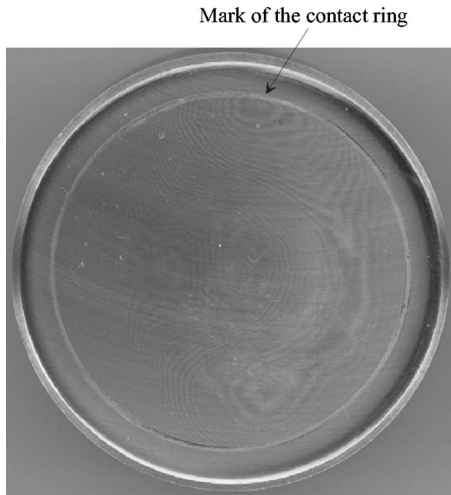


Fig. 3 Indentation of a polished copper surface by the rough metallic ring, $P_{ca}=50$ MPa

connected to a hydraulic pump. Tightening is controlled by a load cell made of a gage bridge sensor, ensuring a continuous measurement during experiments. From this measurement, the apparent contact pressure, referred to as P_{ca} in the rest of this work is defined as the nominal force F , divided by the apparent contact area

$$P_{ca} = \frac{F}{\pi(r_i^2 - r_e^2)} \quad (1)$$

The leakage cell is kept at 20°C during experiments using a coil in which temperature regulated water flows.

Excessive care was taken to avoid out of parallelism errors between the metallic surface and the sapphire by introducing a ring of soft material (rubber or polytetrafluoroethylene) above the sapphire cylinder and below the metallic surface. Because these materials are far less rigid than both the metal and sapphire and since their Poisson's ratio are close to 0.5, they behave like a fluid ball-and-socket joint and ensure an excellent correction of this error. This was verified with a test experiment where the sapphire disk was replaced by a copper cylinder while a 50 MPa contact pressure was applied. As sketched on Fig. 3, the mark corresponding to the ring indentation of the 316L surface on the polished copper face is extremely regular excluding any significant deflection between the metallic surface and the sapphire.

The liquid for which leakage is measured is stored in a tank axially connected to the inner part of the contact and may be put under pressure using nitrogen. The pressurized liquid—or solute—leaks through the contact and is collected in a closed loop of solvent. Circulation of the solvent loop is necessary to improve homogeneity of the mixture and is carried out with a peristaltic pump. It is kept slow enough to avoid a significant pressure gradient in the outer part of the contact, which is supposed to remain at the atmospheric pressure. Leak-rate measurements are performed by measuring the mass of solute passing through the contact in the solvent, during a given period of time. This is achieved by sampling the solvent loop, regularly, taking 1 μ l from the mixture with a microsyringe. The sample is analyzed by gas phase chromatography (GPC) providing the solute concentration.

For experiments under diffusive conditions, the setup is modified by simply replacing the nitrogen and liquid storage tanks by a U tube containing the liquid for which leakage is measured. One end of the tube is connected to the inner region of the contact while the other end is left opened, the liquid level being adjusted at the height of the metal/sapphire contact so that no pressure difference exists between contact edges.

In our experiments, the fluid for which the leak rate was mea-

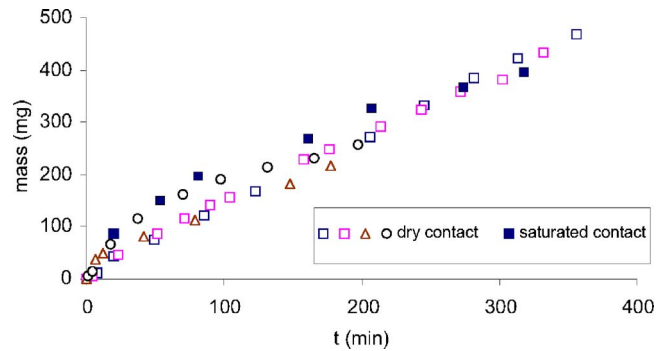


Fig. 4 Mass of leaking fluid through the contact versus time - $P_{ca}=240$ MPa - $\Delta P=9$ bar. Open and dark symbols correspond to an initial dry and wet contact respectively

sured is 1-butanol while the collector solvent is ethanol. These alcohols were strongly wetting both metal and sapphire surfaces in the presence of air. Accuracy of leak-rate measurement was improved significantly by adding an internal standard (1-propanol) to the solvent, and using calibration performed prior to experiments [20]. Chromatograms were recorded by making use of a flame ionization detector. This technique ensures a rapid, accurate, and high sensitive measurement and has an excellent compatibility with the alcohols used in our experiments.

Experimental results reported below were obtained with a tightening ranging from 3.8 kN to 30.4 kN. This corresponds to an apparent contact pressure (P_{ca}) between 100 and 800 MPa. During pressure-driven experiments, the pressure difference, ΔP , between the solute in the inner region of the contact and the solvent in the loop (remaining roughly at atmospheric pressure) ranged from 1 to 30 bar and was measured using a pressure transducer with a precision of 60 mbar.

2.3 Experimental Protocol. Leak-rate measurements were carried out every P_{ca} increment of 100 MPa from low to high tightening. This procedure avoids possible roughness plastic deformation at high loads that might otherwise remain during measurements at lower loads. Because expected leak rates are extremely small (sometimes $<1 \mu\text{g}/\text{min}$), special attention must be addressed to the experimental protocol. For instance, excessive care must be taken of surfaces cleanliness since trapped or adsorbed solute might be slowly solubilized in the solvent loop and might be a source of significant error while estimating the leak rate.

For the initial state, two different configurations of the contact may be considered. In fact, the contact can be first wetted and saturated with the leaking fluid before load is applied or the experiment can be started with a dry contact. The former case would ensure leakage under the one-phase flow condition, whereas in the later, a leak initiates under the two-phase flow condition at least during a short period during which the contact is partially saturated by air and is being invaded by imbibition. Tests were performed to explore both cases. As shown in Fig. 4, no significant effects were noted between the two situations and, for simplicity reasons regarding cleanliness, experiments were started with a dry contact.

After pressure was applied in the solute during pressure-driven experiments, the resulting force exerted on the sapphire and the metallic surface, which tends to unload the contact, was corrected by increasing the tightening of the corresponding value. Once both pressure in the fluid phase and tightening reached stabilized values, the solvent loop was analyzed by GPC at regular intervals of time. This provides the time evolution of the mass of butanol leaking through the contact.

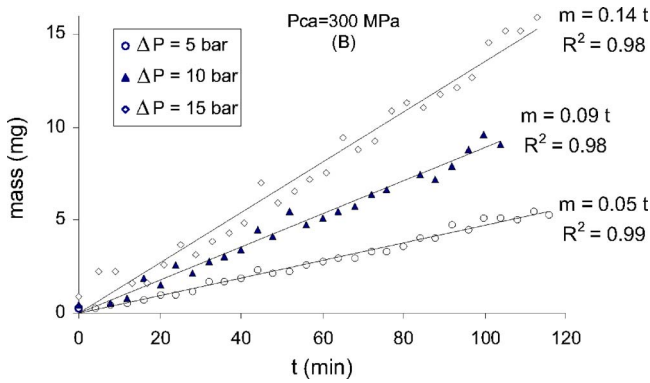


Fig. 5 Time evolution of the mass of butanol in the solvent loop - Surface B1

3 Experimental Results

In this section, we report some results of leak-rate measurements performed during experiments under viscous and diffusive conditions. In both cases, the leak rate was recorded while varying the apparent contact pressure P_{ca} and the pressure difference between contact edges during viscous flow experiments. As mentioned above, two different types of surfaces—A and B—were used in these experiments. Moreover, two surfaces of type B (i.e., B1 and B2) obtained under the same machining conditions were employed for comparison purposes.

3.1 Leak-Rate Measurements Under Pressure-Driven Conditions. In Fig. 5, we have represented the time evolution of the mass of butanol leaking through the contact between the sapphire and the metallic surface B1, for three different values (5 bar, 10 bar, and 15 bar) of the pressure difference ΔP . Experimental results reported in Fig. 5 were obtained with an apparent contact pressure equal to 300 MPa. Measurements were performed over roughly 100 min.

As can be seen in Fig. 5, the mass of butanol present in the solvent loop evolves linearly versus time and we shall insist on the excellent values of the associated determination coefficient [21]. This linear evolution is confirmed on similar results obtained on surface A and reported in Fig. 6, indicating moreover an excellent reproducibility between two measurements performed under identical conditions without dismantling between two successive experiments [22].

As expected, the leak can be characterized by a unique value of the mass flow rate for each value of both the apparent contact pressure and pressure drop between contact edges. The experimental value of this flow rate can be clearly extracted from the

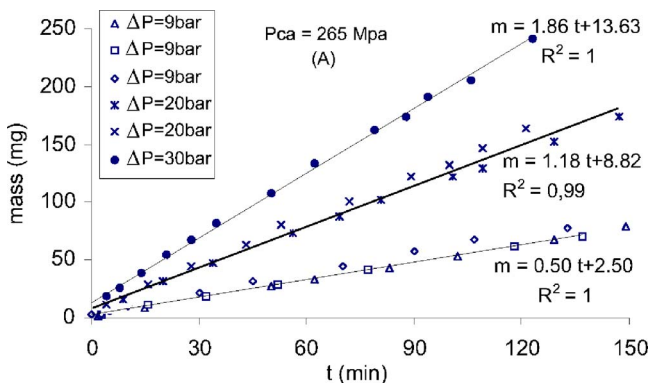


Fig. 6 Time evolution of the mass of butanol in the solvent loop - Surface A

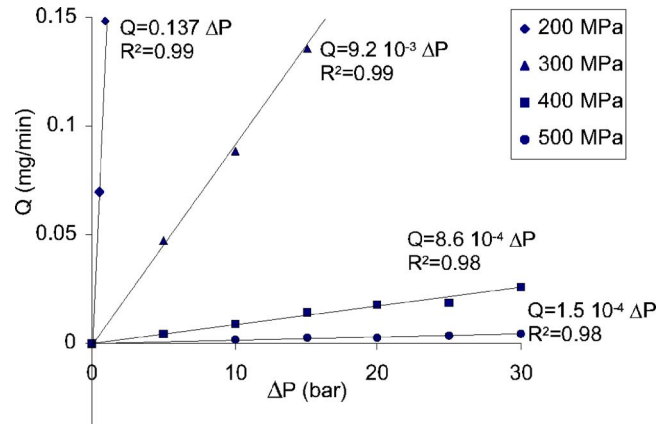


Fig. 7 Mass leak-rate versus pressure drop through the contact for four values of tightening - Surface B1

slope of trend lines issued from $m(t)$ data illustrated above using a least-squares linear fit approach. By doing so, we assume that the error on the measurement of $m(t)$ remains the same at any time so that the optimal estimation of the flow rate is, in fact, that resulting from a linear least-squares approach. Results of this procedure applied to data obtained on surface B1 are depicted in Fig. 7, where we have represented the mass leak rate Q versus pressure drop for four values of the apparent contact pressure.

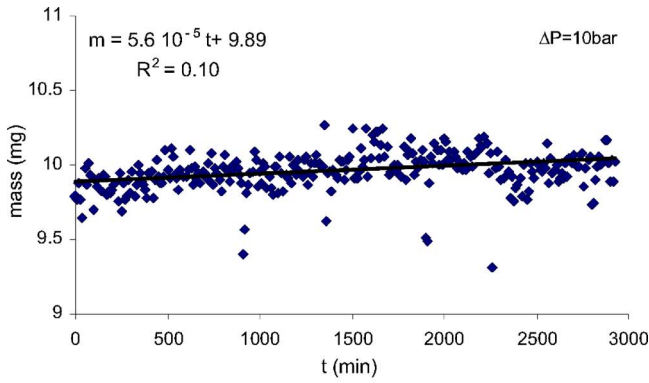
Again, as expected, one can observe that the mass leak rate depends linearly on the pressure drop with excellent determination coefficients. In addition, the method used in the present work turns out to be extremely sensitive to detect liquid leakage and is actually as sensitive as mass spectrometry classically used for gas leak detection [2,23,24]. In fact, leak rates as weak as 10^{-4} mg/min can be measured with the system used in the present work and this can be achieved by increasing the period of observation and, eventually, by reducing the volume of the solvent loop. Examples of results in this range of leak rate obtained on surface B2 for P_{ca} equal to 700 MPa and fluid pressure drops equal to 10 bar, 20 bar, and 30 bar respectively are reported in Fig. 8.

One can note, in Fig. 8, that butanol was initially introduced in the solvent loop so that this species is initially above the chromatograph detection threshold. Here, the noise is very significant compared to the amount of solute collected in the loop and this leads to small values of the determination coefficients. Nevertheless, in the particular case of a linear regression, one can approximate the variance, $\text{Var}(Q)$, on the estimator of the mass leak rate (i.e., on the slope of the trend line issued from $m(t)$ data). This variance is given by

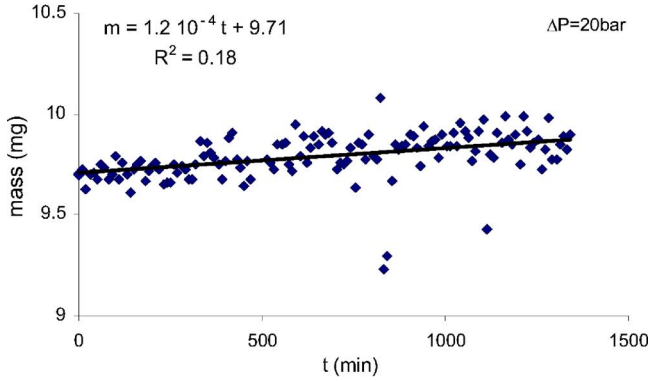
$$\text{Var}(Q) = \frac{1}{(n-1)} \frac{\sum (Y^{\text{model}} - Y)^2}{\sum X^2} \quad (2)$$

where n is the number of $Y(X)$ measurements, Y being the mass of butanol measured at time X and Y^{model} , representing the mass of butanol estimated at time X from the trend line equation [25]. For measurements reported in Fig. 8, this leads to standard deviations $<14\%$ for $\Delta P=10$ bar, 10% for $\Delta P=20$ bar, and 5% for $\Delta P=30$ bar. These very low flow rates obtained for $P_{ca}=700$ MPa on surface B2 are represented versus ΔP in Fig. 9, where, again, an excellent linear relationship can be observed along with a zero flow rate for a zero pressure drop.

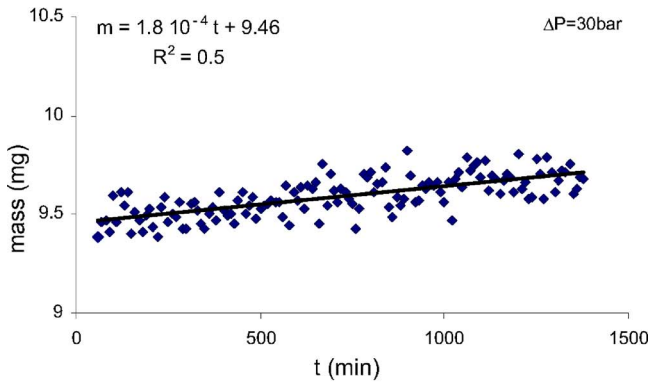
The linearity between mass leak rate and pressure drop allows a description of the flow through the contact by a macroscopic Reynolds law classically used for flow in fractures [26,27], which, for the ring-shaped contact under study, can be written under the form



(a)



(b)



(c)

Fig. 8 Time evolution of the mass of butanol in the solvent loop - Surface B2 - $P_{ca}=700$ MPa - a) $\Delta P=10$ bars - b) $\Delta P=20$ bars - c) $\Delta P=30$ bars

$$\frac{Q}{2\pi} = \rho \frac{K \Delta P}{\mu \ln(r_e/r_i)} \quad (3)$$

In this relationship, r_e and r_i are the external and internal radii of the contact, μ is the dynamic viscosity of the leaking fluid (for butanol at 20°C , $\mu=2.95 \times 10^{-3}$ Pa s) and ρ is the density of butanol ($\rho=810$ kg/m³ at 20°C) considered as an incompressible phase in the pressure range investigated in these experiments, and K is the contact transmissivity having the unit of cubic meters. It must be emphasized that, from an engineering point of view, K is a key parameter since it is an intrinsic characteristic of the contact at a given P_{ca} and should be used to qualify sealing efficiency. By making use of Eq. (3), one can easily estimate the transmissivity of the contact from slopes of trend lines of $Q(\Delta P)$ data for each value of P_{ca} using again a least-squares linear fit approach if one

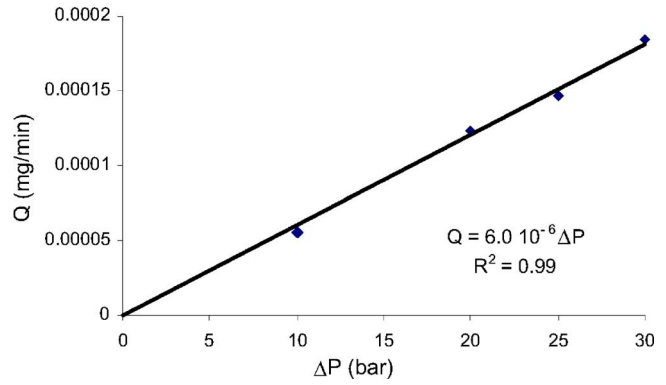


Fig. 9 Mass leak-rate versus pressure drop - $P_{ca}=700$ MPa - Surface B2

assumes a constant error on $Q(\Delta P)$. In Fig. 10, we have represented the evolution of transmissivity obtained on surfaces B1 and B2 versus the apparent contact pressure. Estimations of the corresponding errors are provided in Sec. 3.

These results clearly highlight the strong dependence of sealing efficiency on tightening. In fact, transmissivity varies over approximately seven orders of magnitude while the apparent contact pressure varies between 100 MPa and 700 MPa. As shown in Fig. 11, the evolution seems to roughly obey a power law and fits performed on our experimental data indicate that K can be scaled as

$$K \propto P_{ca}^{-6.4} \quad (4)$$

for surface B1 and

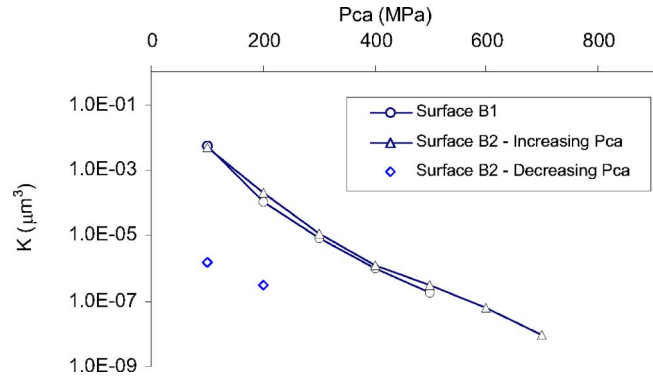


Fig. 10 Contact transmissivity versus tightening for two similar rough surfaces B1 and B2

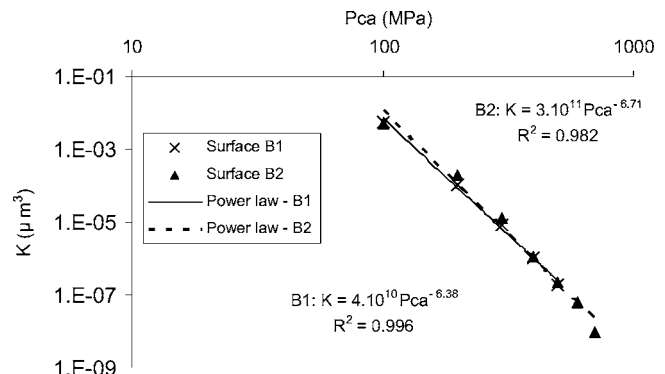


Fig. 11 Power law fits on $K(P_{ca})$ - Surfaces B1 and B2

$$K \propto P_{ca}^{-6.7} \quad (5)$$

for surface B2.

No leak was detected for $P_{ca} > 800$ MPa on surface B2, and after this value of P_{ca} has been reached and tightening is decreased, a completely different behavior of transmissivity is observed since at 200 MPa and 100 MPa leak rates are respectively divided by a factor 700 and 2400. This hysteresis must be the proof of permanent deformations of surface defects in the plastic domain remaining during the contact pressure release.

As shown in Fig. 10, transmissivities for both surfaces are very similar over the range of apparent contact pressure investigated here. However, as will be seen below with results obtained on effective diffusivities, it is not sufficient to conclude that aperture fields are completely similar. This can be explained by the fact that viscous flow explores a complex average operating on the cube of the aperture field whereas diffusive flux is related to another average formed on the aperture field only [28]. As said before, a direct comparison of these experimental data to a theoretical and numerical analysis of both surface deformation and flow within the aperture field will be reported later on.

3.2 Leak-Rate Measurements Under Diffusive Operating Conditions. Experiments described in this section aim at the determination of solute mass flux through the contact resulting from a diffusion process due to the concentration gradient of chemical species between contact edges without any pressure gradient. This type of experiment is motivated by the fact that a diffusive leak provides a signature of the aperture field, which differs from that revealed by viscous leak. In these experiments, we only consider the flux of butanol contained inside the contact into ethanol (and propanol) contained in the solvent loop. Diffusive leak-rate measurements were carried out on surfaces B1 and B2 while, as for viscous leak rate measurements, contact pressure was varied between 100 MPa and 800 MPa. Because fluxes are extremely small and close to the chromatography detection threshold, measurements were performed over large periods of time (typically several hundreds of hours).

If the aperture field is slowly varying all over the contact, i.e., if the local slope on the rough surface everywhere is small compared to unity, it can be easily shown by integration of a classical Fick's law that the diffusive mass flux Q_d (here, butanol in ethanol) is given by a relation similar to Eq. (3)

$$\frac{Q_d}{2\pi} = D_{\text{eff}} \frac{(c_i - c_e)}{\ln(r_e/r_i)} \quad (6)$$

In Eq. (6), r_e and r_i are the external and internal radii of the contact, c_e and c_i are the external and internal mass concentrations of the leaking fluid (butanol), and D_{eff} the effective "diffusivity" of the contact (in cubic meters per second). If one assumes that c_e remains extremely small ($c_e \approx 0$) in the solvent loop and that the inverse flux of ethanol (and propanol) is negligible, an alternate form of Eq. (6) is

$$\frac{Q_d}{2\pi} = D_{\text{eff}} \frac{\rho}{\ln(r_e/r_i)} \quad (7)$$

where ρ is the density of butanol.

Our experimental results of diffusive mass leak rate measurement were used in Eq. (7) to identify D_{eff} following the same procedure as the one used to determine K . In Fig. 12, we have represented the ratio D_{eff}/D versus P_{ca} , D being the molecular diffusion coefficient of butanol in ethanol. Here, we took $D = 10^{-9}$ m²/s. It should be emphasized that, as for K , D_{eff}/D is an intrinsic property of the contact which only depends on the aperture field topology for a given P_{ca} .

No leak rate was detected at 300 MPa on surface B1, and at 500 MPa on surface B2. As can be observed on results on surface B2, effective diffusivity strongly decreases over roughly four orders of magnitude when tightening increases from 100 MPa to

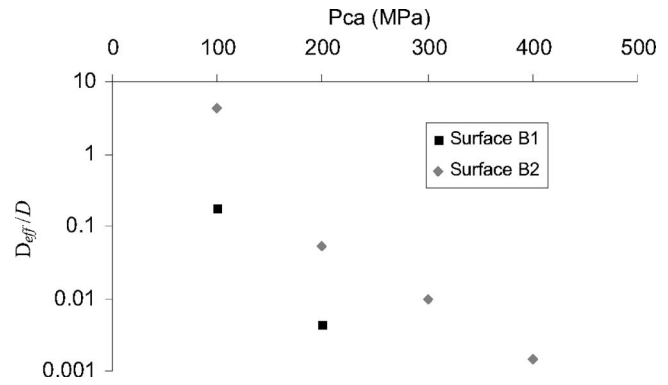


Fig. 12 Ratio of effective diffusivity to molecular diffusion coefficient determined from experimental leak rate measurements - Surfaces B1 and B2

400 MPa. Moreover, the values of D_{eff} significantly differ between the two surfaces although transmissivities were very similar.

3.3 Measurements Uncertainty. Global uncertainty on transmissivity and effective diffusivity can be expressed in a simplified manner as

$$\frac{\Delta K}{K} = \frac{\Delta Q}{Q} + \frac{\Delta \mu}{\mu} + \frac{\Delta(\Delta P)}{\Delta P} + \frac{\Delta r}{\ln(r_e/r_i)} \left(\frac{1}{r_e} + \frac{1}{r_i} \right) \quad (8)$$

$$\frac{\Delta D_{\text{eff}}}{D_{\text{eff}}} = \frac{\Delta Q_d}{Q_d} + \frac{\Delta r}{\ln(r_e/r_i)} \left(\frac{1}{r_e} + \frac{1}{r_i} \right) \quad (9)$$

where no error was assumed on ρ . The corresponding value of tightening must also be considered with its own uncertainty

$$\frac{\Delta P_{ca}}{P_{ca}} = \frac{\Delta F}{F} + \frac{2\Delta r}{r_e - r_i} \quad (10)$$

keeping in mind that these three last expressions are actually *overestimations* of the relative errors.

In Eqs. (8) and (9), ΔQ and ΔQ_d were simply approximated by the mean values of the standard deviations given by Eq. (2) on all the values of Q and Q_d used to estimate K and D_{eff} , respectively. The term $\Delta \mu/\mu$ in Eq. (8) results from temperature fluctuations, and we estimated this relative error to 0.25%. This corresponds to the viscosity variation of butanol at 20°C due to a temperature fluctuation of 0.1°C. The error on ΔP results from measurement accuracy performed with the pressure transducer and is equal to 60 mbar. To account for fluctuations over time due to microleakage in the nitrogen circuit, we also took a relative error of 1% on ΔP . The contribution of the pressure drop error on $\Delta K/K$ in Eq. (8) was taken as the average value of all the values of $\Delta(\Delta P)/\Delta P$ used to determine K . As for ΔP , the error on F results from the measurement with the load cell which accuracy is 75 N as well as fluctuations over time due to microleakage in the hydraulic circuit of the jack and we took $\Delta F/F$ equal to 1% to account for this. It must be noted that ΔP and F are coupled parameters since solute pressure variations induce tightening fluctuations. However, coupling was not considered in the present estimation. Finally, for the error on the external and internal radii of the contact ring, we took

$$\Delta r_e = \Delta r_i = \Delta r = 0.01 \text{ mm} \quad (11)$$

As an illustration, estimations of the relative errors on P_{ca} and on experimental results obtained for K and D_{eff} on surface B2 are reported in Table 3.

One can see on these results that the relative error on P_{ca} is <10% and slightly decreases while increasing the load. This is due to the fact that $\Delta F/F$ decreases, whereas the major contribu-

Table 3 Uncertainties on P_{ca} transmissivities, and effective diffusivities obtained on surface B2

P_{ca} (MPa)	$\frac{\Delta P_{ca}}{P_{ca}}$ (%)	$\frac{\Delta K}{K}$ (%)	$\frac{\Delta D_{eff}}{D_{eff}}$ (%)
100	9.7	15	7
200	8.7	15	7
300	8.3	10	8
400	8.2	11	16
500	8.1	10	
600	8.0	11	
700	8.0	19	

tion, which comes from the term involving Δr , remains constant. For K , the relative error is large for small values of P_{ca} , decreases for moderate loads and increases again for larger values of P_{ca} . In fact, for small values of P_{ca} , leak rate measurements require small values of ΔP for which relative errors are very significant. For large values of P_{ca} , flow rates are very small and the relative error on Q is the major contribution to $\Delta K/K$. In the same manner, the relative error on D_{eff} increases with P_{ca} due to the increase of $\Delta Q_d/Q_d$.

4 Conclusion

In this work, an original experimental method and device were designed and used to measure leak rate through a metal contact seal. The experimental technique allows measurements of liquid mass flow rates as small as 10^{-4} mg/min with great precision under well-controlled conditions of temperature, pressure in the fluid to be sealed, and tightening (i.e., apparent pressure) applied to the contact. Here, a uniform apparent contact pressure P_{ca} was considered. The technique reveals to be as sensitive as mass spectrometry classically employed for gas leak-rate measurements, and this represents a significant breakthrough in comparison to existing methods. Although any other configuration could be used, experiments were performed on a model contact between a plane metallic ring obtained by turning and a sapphire surface. This choice was motivated by the fact that the topology of the contact can be described in this case by that of the metallic surface only, which will significantly simplify future comparison to predictive models. Because of the sensitivity of the method, the leak was investigated in the rather classical viscous flow regime but also in the pure diffusive regime resulting from a species gradient.

As expected, experimental results reproduce linear dependence of the flow rate on the driving force (i.e., the pressure or concentration gradient) and excellent correlation coefficients are obtained. The linear dependence provides the *transmissivity*, K in the viscous case and the *effective diffusivity* D_{eff} , in the diffusive case. These coefficients are the macroscopic characteristics of the whole contact essential for engineering purposes. Because they explore two different averages of the aperture field, K and D_{eff}/D provide interesting complementary data on the contact behavior regarding seal efficiency. Experimental results indicate that, in the configuration under study, these coefficients vary very strongly with the apparent contact pressure following stiff power laws (K decreases over roughly six orders of magnitude in the range of 100–800 MPa for P_{ca}). The methodology developed in the present study, coupled to deformation and flow descriptions with appropriate models along with topological analysis at different scales of observation, should contribute to understand (and further improve) seal behavior under very different operating conditions.

Use of this experimental technique can also be interesting in many other domains of the microfluidic whenever very small liquid flow rates are to be accurately measured or controlled.

Acknowledgment

This work was performed within the framework of a group of research including CNRS, CNES, EDF, and SNECMA from which financial support is gratefully acknowledged. We also thank G. Carillon for his help.

References

- [1] Kogut, L., and Etsion, I., 2003, "A Finite Element Based Elastic-Plastic Model for the Contact of Rough Surfaces," *Tribol. Trans.*, **46**(3) pp. 383–390.
- [2] Amesz, J., 1966, "Conversion of Leak Flow-Rates for Various Fluids and Different Pressure Conditions," Report of the ORGEL program, European Atomic Energy Community—EURATOM, EUR2982.e.
- [3] Armand, G., Lapujoulade, J., and Paigne, J., 1964, "A Theoretical and Experimental Relationship Between the Leakage of Gases Through the Interface of Two Metals in Contact and Their Superficial Micro-Geometry," *Vacuum*, **14**(2), pp. 53–57.
- [4] Armand, G., and Lejay, Y., 1967, "Déformation des microgéométries de surfaces planes en contact: Application à l'écoulement gazeux interfacial (cas des déformations plastiques)," *Rev. Fr. Méc.*, **21**, pp. 15–29.
- [5] Lejay, Y., 1967, "Déformation des microgéométries de surfaces planes en contact: Application à l'écoulement gazeux interfacial (cas du recouvrement élastique)," *Rev. Fr. Méc.*, **21**, pp. 31–40.
- [6] Yanagisawa, T., Sanada, M., Koga, T., and Hirabayashi, H., 1990, "Fundamental Study of the Sealing Performance of a C-Shaped Metal Seal," *2nd International Symposium on Fluid Sealing*, La Baule, Sep. 18–20, pp. 389–398.
- [7] Yanagisawa, T., Sanada, M., Koga, T., and Hirabayashi, H., 1991, "The Influence of Designing Factors on the Sealing Performance of C-Seal," *SAE Trans.*, **100**(6), pp. 651–657.
- [8] Matsuzaki, Y., and Kazamaki, T., 1988, "Effect of Surface Roughness on Compressive Stress of Static Seals," *JSME Int. J., Ser. III*, **31**, pp. 99–106.
- [9] Matsuzaki, Y., Hosokawa, K., and Funabashi, K., 1992, "Effect of Surface Roughness on Contact Pressure of Static Seals," *JSME Int. J., Ser. III*, **35**, pp. 470–476.
- [10] Polycarpou, A. A., and Etsion, I., 1998, "Static Sealing Performance of Gas Mechanical Seals Including Surface Roughness and Rarefaction Effects," *Tribol. Trans.*, **41**(4) pp. 531–536.
- [11] Polycarpou, A. A., and Etsion, I., 2000, "A Model for the Static Sealing Performance of Compliant Metallic Gas Seals Including Surface Roughness and Rarefaction Effects," *Tribol. Trans.*, **43**(2) pp. 237–244.
- [12] Etsion, I., and Front, I., 1994, "A Model for Static Sealing Performance of End Face Seals," *Tribol. Trans.*, **37**(1) pp. 111–119.
- [13] Colin, S., 2004, *Microfluidique*, Lavoisier, Paris.
- [14] Rakhit, A. K., Sankar, T. S., and Osman, M. O. M., 1976, "The Influence of Metal Cutting Forces on the Formation of Surface Texture in Turning," *Int. J. Mach. Tool Des. Res.*, **16**(4), pp. 281–292.
- [15] Greenwood, J. A., and Tripp, J. H., 1970, "The Contact of Two Nominally Flat Rough Surfaces," *Proc. Inst. Mech. Eng.*, **71**(185), pp. 48–71.
- [16] O'Callaghan, P. W., and Probert, S. D., 1987, "Prediction and Measurement of True Areas of Contact Between Solids," *Wear*, **120**, pp. 29–46.
- [17] Francis, H. A., 1977, "Application of Spherical Indentation Mechanics to Reversible and Irreversible Contact Between Rough Surfaces," *Wear*, **45**, pp. 221–269.
- [18] McCool, J. L., 1985, "Comparison of Models for the Contact of Rough Surfaces," *Wear*, **107**, pp. 37–60.
- [19] Marie, C., 2002, "Fuite monophasique au travers d'un contact rugueux: Contribution à l'étude de l'étanchéité statique," Ph.D. thesis, Université Bordeaux 1.
- [20] Tranchant, J., 1995, *Manuel pratique de chromatographie en phase gazeuse*, 4th ed., Masson, Paris.
- [21] Marie, C., and Lasseux, D., 2001, "Analyse expérimentale d'une fuite liquide au travers d'un contact statique métal/métal," 15ème Congrès Français de Mécanique, Nancy, Sep. 3–7.
- [22] Marie, C., and Lasseux, D., (2002), "Fuite monophasique dans un contact rugueux," Journées CNES Jeunes Chercheurs, Centre Spatial de Toulouse, Apr. 24–26, pp. 138–139.
- [23] Pregelj, A., Drab, M., and Mozetic, M., 1997, "Leak Detection Methods and Defining the Size of Leaks", The 4th International Conference of Slovenian Society for Non Destructive Testing, Ljubljana, Slovenia.
- [24] Brunet, J. C. Poncet, A., and Trilhe, P., (1994), "Leak-Tightness Assessment of Demountable Joints for the Super Fluid Helium System of the CERN Large Hadron Collider (LHC)," *Adv. Cryog. Eng.*, **39**, pp. 657–662.
- [25] Beck, J. V., and Arnold, K. J., 1976, *Parameter Estimation in Engineering and Science*, Wiley, New York.
- [26] Zimmerman, R. W., Kuzar, S., and Bodvarsson, G. S., 1991, "Lubrication Theory Analysis of the Permeability of Rough-Walled Fractures," *Int. J. Rock Mech. Min. Sci. Geomech. Abstr.*, **28**(4), pp. 325–331.
- [27] Prat, M., Plouraboué, F., and Letalleur, N., 2002, "Averaged Reynolds Equation for Flow Between Rough Surfaces in Sliding Motion," *Transp. Porous Media*, **48**, pp. 291–313.
- [28] Geoffroy, S., and Prat, M., 2004, "On the Leak Through a Spiral-Groove Metallic Static Ring Gasket," *ASME J. Fluids Eng.*, **126**(1), pp. 48–54.

Cosserat Modeling of Turbulent Plane-Couette and Pressure-Driven Channel Flows

Amin Moosaie

e-mail: aminmoosaie@mail.iust.ac.ir

Gholamali Atefi

Department of Mechanical Engineering,
Iran University of Science and Technology,
Narmak, Tehran 16844, Iran

The theory of micropolar fluids based on a Cosserat continuum model is utilized for analysis of two benchmarks, namely, plane-Couette and pressure-driven channel flows. In the obtained theoretical velocity distributions, some new terms have appeared in addition to linear and parabolic distributions of classical fluid mechanics based on the Navier-Stokes equations. Utilizing the principles of irreversible thermodynamics, a new dissipative boundary condition is developed for angular velocity at flat plates by taking the couple-stress vector into account. The obtained results for the velocity profiles have been compared to results of recent and classical experiments. This paper demonstrates that continuum mechanical theories of higher orders, for instance Cosserat model, are able to describe a complex phenomenon, such as hydrodynamic turbulence, more precisely.

[DOI: 10.1115/1.2734251]

Keywords: Cosserat continua, micropolar fluids, turbulence, Couette flow, channel flow, dissipative boundary condition

1 Introduction

Classical continuum mechanics considers the interaction of microstructural units of the material through stresses and displacements of material points. To describe the material behavior of fluids and solids by means of a continuum mechanical theory, a set of field equations containing mass, linear, and angular momentum balance and some particular constitutive equations is needed. However, in reality, interaction of grains may include rotations and the corresponding couple stresses. Therefore, the averaging scheme of classical continuum mechanics should consider rotation and couple stresses as well. If the microstructure of the material is mechanically significant and Noll's theory of simple materials cannot solve the problem, a more sensitive continuum theory,

such as nonlocal, micropolar, multipolar, microstretch, and gradient theories [1–6] with higher kinematic status will be applied more successfully. A comprehensive review of existing theories of microcontinuum fluid mechanics with various applications has been presented in [7].

The basic idea of a Cosserat continuum was first proposed by two French brothers, Eugene and Francois Cosserat in their landmark publication in 1909 [8]. Their proposed theory was later reworked by Gunther [9] and Mindlin [10,11], who laid out the kinematics and statics of Cosserat continuum in a useful form for applied mechanics applications. Eringen coined the name micropolar continuum for the Cosserat medium in 1968 [12,13]. The essential equations of Cosserat fluid mechanics as pertains to the current work are summarized in the following sections based on an axiomatic conception of a polar and nonlocal continuum theory for materials of order m and grade n by Trostel [1,5]. In such a continuum, we consider the effect of couples on a material element in addition to and independent of the effect of forces.

Plane-Couette flow is the shear-induced motion of a fluid contained between two infinite flat plates, which are in parallel, straight-line motion in opposite directions relative to each other at a distance of $2h$. It represents the simplest type of shear flow known. The outstanding feature of this motion, schematically depicted in Fig. 1, is that this flow configuration appears to provide a unique environment for furthering insight into the basic mechanisms of turbulence and hydrodynamic stability. Moreover, of course, plane-Couette flow is also of considerable practical importance in the contexts of, for instance, fluid-film tribology and vehicular transportation. There is no pressure gradient in plane-Couette flow. The flow in a similar configuration as depicted in Fig. 1 but in presence of the pressure gradient and with $U=0$ is a called pressure-driven channel flow. This flow configuration also makes an excellent benchmark to study properties of turbulent flows. Reichardt studied turbulent plane-Couette flow problem, experimentally [14,15]. He also carried out experiments to study turbulent pressure-driven channel flow [16]. Hagiwara et al. [17], Bech et al. [18] and Aydin et al. [19] performed experiments to study properties of turbulent plane-Couette flow. The results of present work have been validated by the use of experimental data reported in [16–18].

The Cosserat model and the gradient theory are good candidates for modeling turbulence phenomenon in fluids. The turbulent plane-Couette and pressure-driven channel flows have been investigated analytically by some authors, using a continuum mechanical gradient theory of higher grades fluids [2,20–23] and the theory of Cosserat fluids of grades 1 and 2 [24]. The turbulent flow through smooth pipes has been investigated by the use of a Cosserat model of grade 1 in [25]. In a recent paper, Eringen proposes a so-called micromorphic model of turbulence [26]. The micropolar fluid mechanics is a special case of the micromorphic model. In present work, the micropolar model is employed because of its mathematical simplicity in contrast with the more general theory of micromorphic fluids. However, the micropolar model yields precise results as demonstrated by the results of present work. In order to obtain results of more physical meaning,

Contributed by the Fluids Engineering Division of ASME for publication in the JOURNAL OF FLUIDS ENGINEERING. Manuscript received December 26, 2004; final manuscript received January 26, 2007. Review conducted by Dennis Siginer.

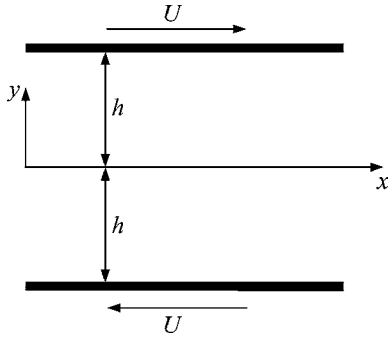


Fig. 1 Schematic diagram of channel configuration

a new dissipative boundary condition has been developed. The results of the experiments and also the results of present analysis are reported for the mean velocities defined by

$$\bar{\mathbf{v}}(\mathbf{x}) = \frac{1}{\Delta t} \int_{t_0}^{t_0+\Delta t} \mathbf{v}(\mathbf{x}, t) dt \quad (1)$$

2 Governing Equations

The basic equations of Cosserat continuum mechanics can be found in [1,3,4]. Here, just a brief list of constitutive and governing field equations is given. We choose linear constitutive equations that describe the material behavior. They can be considered as a generalization of Newtonian fluids in the classical Navier-Stokes theory

$$t_{kl} = (-\pi + \lambda_v u_{r,r}) \delta_{kl} + \mu_v (v_{k,l} + v_{l,k}) + k_v (v_{l,k} - \varepsilon_{klr} \omega_r) \quad (2)$$

$$m_{kl} = \alpha_v \omega_{r,r} \delta_{kl} + \beta_v \omega_{k,l} + \gamma_v \omega_{l,k} \quad (3)$$

where comma denotes the partial differentiation and ε_{ijk} is the permutation tensor. Moreover, π is the thermodynamic pressure.

Introducing the above constitutive equations to the equations of linear and angular momentum balance along with the mass balance gives the desired governing field equations

$$\frac{\partial \rho}{\partial t} + \nabla \cdot (\rho \mathbf{v}) = 0 \quad (4)$$

$$(\lambda_v + 2\mu_v + k_v) \nabla \nabla \cdot \mathbf{v} - (\mu_v + k_v) \nabla \times \nabla \times \mathbf{v} + k_v \nabla \times \boldsymbol{\omega} - \nabla \pi + \rho \left(\mathbf{f} - \frac{D\mathbf{v}}{Dt} \right) = \mathbf{0} \quad (5)$$

$$(\alpha_v + \beta_v + \gamma_v) \nabla \nabla \cdot \boldsymbol{\omega} - \gamma_v \nabla \times \nabla \times \mathbf{v} + k_v \nabla \times \mathbf{v} - 2k_v \boldsymbol{\omega} + \rho \left(\mathbf{l} - j \frac{D\boldsymbol{\omega}}{Dt} \right) = \mathbf{0} \quad (6)$$

where ρ , j , f_i and l_i are the mass density, microinertia, body force per unit mass, and body couple per unit mass, respectively, and D/Dt denotes the substantial time derivative.

By the incompressibility assumption, the thermodynamic pressure π becomes an undetermined pressure p , which must be determined by the given boundary conditions. For incompressible flow condition, Eq. (4) is also replaced by

$$\nabla \cdot \mathbf{v} = \partial_i v_i = 0 \quad (7)$$

3 A Notion on Dissipative Boundary Conditions

Boundary conditions enforced to the problems occurred in continuum mechanics can be classified with respect to the second law of thermodynamics. According to this point of view, two classes of boundary conditions can be used in general. The first kind is the isoenergetic boundary condition in which the power of surface

vanishes ($P_{\Sigma_o} = 0$), and it describes the ideal reversible condition. For the second kind, namely, the case of a nonzero power of surface ($P_{\Sigma_o} \neq 0$), which describes the real irreversible condition, Trostel [1,5] developed a concept of slip velocity at the solid wall. This concept is generalized by Alizadeh [23] for the case of fluids of grades 2 and 3 with one kinematic vector field, i.e., the velocity field.

In present work, this concept combined with the principles of irreversible thermodynamics is used to derive a dissipative boundary condition relating the angular velocity and the couple-stress vector at the solid wall. The couple-stress vector and the value of angular velocity at the boundary may be assumed as generalized thermodynamic flux and force, respectively. The couple-stress vector is given by

$$\mathbf{n} \cdot \mathbf{m} = n_y \mathbf{e}_y \cdot m_{yz} \mathbf{e}_y \circ \mathbf{e}_z = m_z \mathbf{e}_z \quad (8)$$

The only component of angular velocity vector which exists in a channel configuration is ω_z . Recalling the Onsager-Eckart principle, which postulates that the thermodynamic flux must be a function of all thermodynamic forces, and since a single irreversible process is considered here, we have the following functional relation for the channel configuration describing our dissipative boundary condition:

$$m_z \mathbf{e}_z = \mathbf{f}(\omega_z \mathbf{e}_z) = f(\omega_z \mathbf{e}_z) \mathbf{e}_z \quad (9)$$

Considering the scalar form of Eq. (9), we have

$$m_z = f(\omega_z) \quad (10)$$

A Taylor's series expansion of functional (10) about $\omega_z = 0$ yields

$$m_z = m_0 + \frac{df}{d\omega_z} \omega_z + \frac{d^2 f}{d\omega_z^2} \omega_z^2 + \dots = m_0 + \Lambda_1 \omega_z + \Lambda_2 \omega_z^2 + \dots \quad (11)$$

According to the generalized version of zeroth law of thermodynamics, which states that the thermodynamic fluxes vanish in the absence of thermodynamic forces, we have $m_0 = 0$. Thus, assuming the linear approximation, Eq. (11) reduces to the following one:

$$m_z = \frac{df}{d\omega_z} \omega_z = \Lambda_1 \omega_z \quad (12)$$

Because of the Onsager's linear phenomenological theory of irreversible processes, the physical meaning of linear approximation is that the deviation from thermodynamic equilibrium is small. A new parameter Λ_1 occurs in the obtained boundary condition (12), which is a material constant and should be calculated as a part of solution.

We can also assume that the boundary exerts a moment to the adjacent fluid element. Because of our knowledge about the influence of surface roughness on turbulent flow properties and since we can model the effect of roughness with a moment exerted by the surface to the fluid element, the following boundary condition would be of more physical meaning:

$$m_z = \gamma_v \frac{d\omega_z}{dy} = M \quad (13)$$

where M is the moment exerted by the unit area of the surface. It is also an unknown parameter and should be a part of solution. This is another kind of dissipative boundary condition and the power of surface in this case becomes

$$P_{\Sigma_o} = \int_{\Omega} M \omega_z d\omega \quad (14)$$

in which the surface integral (14) is defined on the boundary surface Ω . In Eq. (13), M is a function of thermophysical properties of fluid, roughness of the wall, and the flow parameters, for instance, the Reynolds number.

4 Problem Definition

The flow between two stationary parallel plates at the distance of $2h$ (i.e., in a channel) is depicted in Fig. 1. The Ox axis overlaps the main line; the Oy axis is perpendicular to the flow direction, whereas the Oz axis is perpendicular to the plane of flow. In this case, the velocity components and the microrotation velocities are

$$v_y = v_z = 0, \quad v_x = u(y) \quad (15)$$

$$\omega_x = \omega_y = 0, \quad \omega_z = \omega(y) \quad (16)$$

The mass conservation law (7) is identically satisfied with $\rho = \text{const}$. Neglecting the body forces and body couples, the equations of motion (5) and (6) are reduced to the following form:

$$(\mu_v + k_v) \frac{d^2 u}{dy^2} + k_v \frac{d\omega}{dy} - \frac{dp}{dx} = 0 \quad (17)$$

$$\gamma_v \frac{d^2 \omega}{dy^2} - k_v \frac{du}{dy} - 2k_v \omega = 0 \quad (18)$$

The above two coupled ordinary differential equations ((17) and (18)) should be subjected to boundary conditions at $y=0$ and $y=h$. The boundary conditions at $y=0$ imply the kinematic status at centerline of channel, which states that the velocity distribution must be an odd function, i.e., $u(-y)=-u(y)$ in the case of plane-Couette flow and it must be an even function, i.e., $u(-y)=u(y)$ in the case of pressure-driven channel flow. The boundary conditions at upper plate for plane-Couette flow are

$$\text{At } y=h: u = U, \quad \gamma_v \frac{d\omega}{dy} = M \quad (19)$$

which hold for pressure-driven channel flow by setting $U=0$.

5 Problem Solution

The general solution for plane-Couette flow is obtained by setting $dp/dx=0$ in Eq. (17). Hence, the general solutions of homogeneous Eqs. (17) and (18) for the linear and angular velocities in this case are given by

$$u(y) = C_1 + C_2 y + \zeta(C_3 \sinh \xi y - C_4 \cosh \xi y) \quad (20)$$

$$\omega(y) = C_2 + C_3 \sinh \xi y + C_4 \cosh \xi y \quad (21)$$

where

$$\xi = \sqrt{\frac{k_v(2\mu_v + k_v)}{\gamma_v(\mu_v + k_v)}} \quad (22)$$

$$\zeta = \sqrt{\frac{k_v \gamma_v}{(\mu_v + k_v)(2\mu_v + k_v)}} \quad (23)$$

The kinematic condition of being an odd function requires that $C_1=C_4=0$. The remaining integration constants are determined by using boundary conditions (19)

$$C_2 = \frac{U}{h} - \frac{M\zeta \tanh \xi h}{\gamma_v \xi h} \quad (24)$$

$$C_3 = \frac{M}{\gamma_v \xi \cosh \xi h} \quad (25)$$

The general solution for inhomogeneous set of two ordinary differential equations governing the pressure-driven channel flow is

$$u(y) = C_1 + C_2 y + \frac{dp/dx}{2\mu_v + k_v} y^2 + \zeta(C_3 \sinh \xi y - C_4 \cosh \xi y) \quad (26)$$

$$\omega(y) = C_2 - \frac{dp/dx}{2\mu_v + k_v} y + C_3 \sinh \xi y + C_4 \cosh \xi y \quad (27)$$

where ξ and ζ are defined in (22) and (23). The kinematic condition of being an even function implies that $C_2=C_3=0$. The remaining constants are determined by enforcement of boundary conditions at the upper wall

$$C_1 = \frac{\zeta \coth \xi h}{\xi} \left[\frac{M}{\gamma_v} + \frac{dp/dx}{2\mu_v + k_v} \right] - \frac{dp/dx}{2\mu_v + k_v} h^2 \quad (28)$$

$$C_4 = \frac{1}{\xi \sinh \xi h} \left[\frac{M}{\gamma_v} + \frac{dp/dx}{2\mu_v + k_v} \right] \quad (29)$$

The values of material coefficients and also the surface moment M and the pressure gradient in the case of pressure-driven channel flow should be known in order to obtain the velocity profiles. Since the material coefficients of Cosserat fluids are unknown, we have to determine them from the experimental data by the use of a numerical recipe for nonlinear optimization.

6 Material Identification and Numerical Results

In order to determine the material coefficients ξ , ζ , and γ_v , surface moment M , and pressure gradient dp/dx occurred in Eqs. (20), (21), and (24)–(29) on the basis of experimental data, the well-known Levenberg-Marquardt numerical algorithm for nonlinear optimization has been employed. For the case of plane-Couette flow, the experimental data reported by Hagiwara et al. [17] are used for optimization routine. The experiment has been done in a channel with $2h=30$ mm, and the working fluid was water. The velocity of upper and lower plates was $U=86.996$ mm/s, and thus, the Reynolds number based on U , h and the kinematic viscosity of water ν was 1.3×10^3 . The optimization of theoretical velocity profile (20) with calculated integration constants (24) and (25) on the basis of the measurements leads to the following material parameters and surface moment:

$$\xi = 640.67, \quad \zeta = 1.83, \quad \gamma_v = 0.079, \quad M = 1.84 \quad (30)$$

The obtained theoretical dimensionless velocity profile u/U and the experimental data of Hagiwara et al. [17] have been shown in Fig. 2. The abscissa is also the dimensionless coordinate y/h . In order to have more insight and better comparison, the experimental data of Bech et al. [18] have been depicted in Fig. 2, which reported for a Reynolds number of 1260, very close to the considered Reynolds number of 1300. Note that the critical Reynolds number, for which turbulence can be sustained, was 360 in the similar experiment [27].

The experimental data reported by Reichardt [16] are applied to obtain the theoretical velocity profile of pressure-driven channel flow. The experiments were carried out for turbulent water flow in a channel with $2h=246$ mm and in presence of pressure gradient. The material parameters ξ , ζ , and γ_v depend on the material and, for instance, temperature. Thus, they are the same for both plane-Couette and pressure-driven channel flows as water was the working fluid of both experiments. Now, we have to determine M and dp/dx , because they also depend to flow parameters as well as to material properties. In order to carry out the optimization recipe, we have a problem with the term $2\mu_v + k_v$ appears in integration constants C_1 and C_4 . Thus far, we obtained ξ and ζ from the optimization process for plane-Couette flow. However, one can divide ξ by ζ to obtain

$$2\mu_v + k_v = \frac{\gamma_v \xi}{\zeta} \quad (31)$$

Now, we can proceed to the optimization routine. The optimization of theoretical velocity profile (26) on the basis of the measurements [16] leads to the following surface moment and pressure gradient:

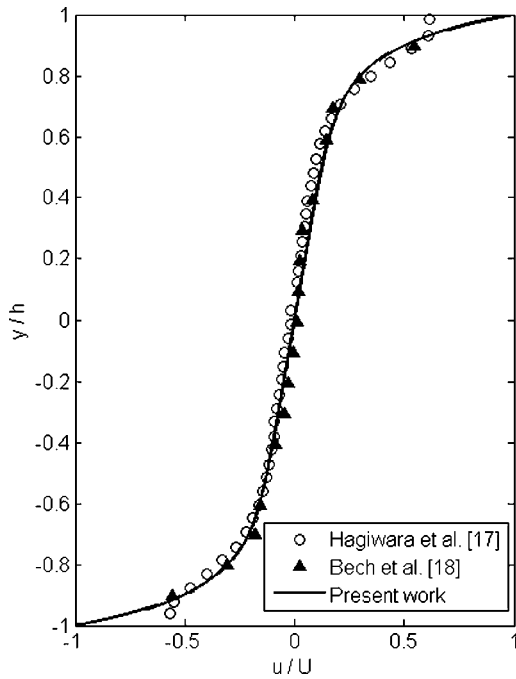


Fig. 2 Axial mean velocity profile for plane-Couette flow

$$M = 26.09, \quad \frac{dp}{dx} = -725.74 \quad (32)$$

The negative value of obtained pressure gradient has the physical meaning that the fluid flows in the direction of decreasing pressure, and it is an extra check for our optimization process. The obtained theoretical dimensionless velocity profile $u(y)/u(0)$ and the experimental data of Reichardt [16] have been shown in Fig. 3. The abscissa is the dimensionless coordinate y/h .

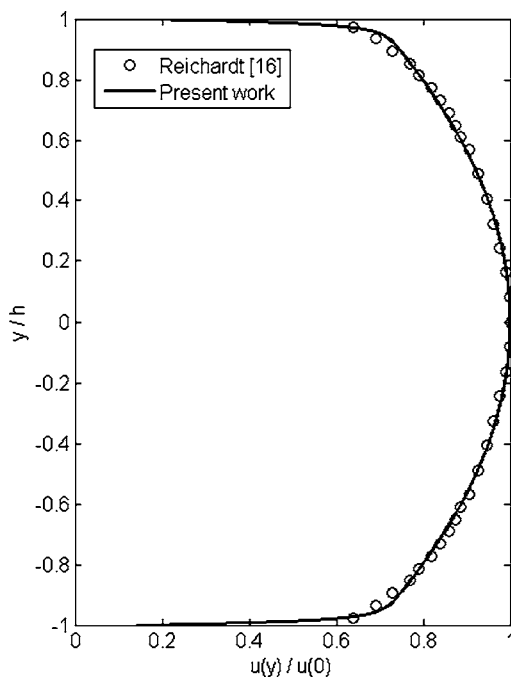


Fig. 3 Axial mean velocity profile for pressure-driven channel flow

7 Concluding Remarks

The present work extends the limited available knowledge on continuum mechanical description of turbulence in Newtonian incompressible fluids. The views in the literature for characterizing turbulent flows by means of continuum mechanical models have been presented. The governing equations of micropolar fluid mechanics have been adjusted for two benchmarks: plane-Couette and pressure-driven channel flows. This adjustment was carried out by the solution of the equations of motion and enforcing classical kinematic and a new dissipative boundary condition, which relate the couple-stress vector and the angular velocity gradient at a solid wall. After the material identification by the use of the Levenberg-Marquardt algorithm for nonlinear optimization, the obtained turbulent velocity profiles were compared to available similar experimental results in the recent and elder literature. Figures 2 and 3 show a good agreement and satisfying consistency in quality and quantity with published experimental data. The paper demonstrates that a complex phenomenon such as turbulence can be modeled by the use of nonclassical continuum mechanical theories such as a Cosserat model.

References

- [1] Trostel, R., 1988, *Gedanken zur konstruktion mechanischer Theorien II*, Technische Universität Berlin, Forschungsberichte Nr. 7, Berlin.
- [2] Silber, G., Trostel, R., Alizadeh, M., and Benderoth, G., 1998, "A Continuum Mechanical Gradient Theory With Applications to Fluid Mechanics," *J. Phys. IV*, **8**, pp. 365–373.
- [3] Eringen, A. C., 1976, *Continuum Physics: Polar and Nonlocal Field Theories*, Academic Press, New York, Vol. 4.
- [4] Stokes, V. K., 1984, *Theories of Fluids With Microstructure*, Springer-Verlag, Berlin.
- [5] Trostel, R., 1985, *Gedanken zur konstruktion mechanischer Theorien*, Beiträge zu den Ingenieurwissenschaften, Universitäts-Bibliothek der TU-Berlin.
- [6] Eringen, C. A., 2001, *Microcontinuum Field Theories II: Fluent Media*, Springer-Verlag, Berlin.
- [7] Ariman, T., Turk, A., and Sylvester, N. D., 1974, "Applications of Microcontinuum Fluid Mechanics," *Int. J. Eng. Sci.*, **12**, pp. 273–293.
- [8] Cosserat, E., and Cosserat, F., 1909, *Théorie des Corps Déformables*, Hermann, Fils, Paris.
- [9] Gunther, W., 1958, "Zur Statik und Kinematik des Cosseratschen Kontinuums," *Abh. Braunschweig Wiss. Ges.*, **10**, pp. 195–213.
- [10] Mindlin, R. D., 1963, "Effect of Couple Stresses on Stress Concentrations," *Experimental Mechanics*, **3**, pp. 1–7.
- [11] Mindlin, R. D., 1963, "Microstructure in Linear Elasticity," *Arch. Ration. Mech. Anal.*, **16**, pp. 51–78.
- [12] Eringen, C. A., 1968, "Theory of Micropolar Elasticity," *Fracture*, Academic Press, New York, H. Liebowitz, ed., Vol. 2, pp. 662–729.
- [13] Forest, S., 2001, "Cosserat Media," *Encyclopedia of Materials, Science and Technology*, Elsevier, New York, pp. 1715–1718.
- [14] Reichardt, H., 1956, "Über die Geschwindigkeitsverteilung in einer geradlinigen turbulenten Couetteströmung," *Z. Angew. Math. Mech.*, Sonderheft, pp. 26–29.
- [15] Reichardt, H., 1959, "Gesetzmäßigkeiten der geradlinigen turbulenten Couetteströmung," *Mitteilungen aus dem Max-Planck Institut für Strömungsforschung und der Aerodynamischen Versuchsanstalt Göttingen*, Nr. 22.
- [16] Reichardt, H., 1951, "Vollständige Darstellung der turbulenten Geschwindigkeitsverteilung in glatten Leitungen," *Z. Angew. Math. Mech.*, **31**, pp. 208–219.
- [17] Hagiwara, Y., Sakamoto, S., Tanaka, M., and Yoshimura, K., 2002, "PTV Measurement on Interaction Between Two Immiscible Droplets and Turbulent Uniform Shear Flow of Carrier Fluid," *Exp. Therm. Fluid Sci.*, **26**, pp. 245–252.
- [18] Bech, K. H., Tillmark, N., Alfredsson, P. H., and Andersson, H. I., 1995, "An Investigation of Turbulent Plane Couette Flow at Low Reynolds Numbers," *J. Fluid Mech.*, **286**, pp. 291–325.
- [19] Aydin, E. M., and Leutheusser, H. J., 1991, "Plane-Couette Flow Between Smooth and Rough Walls," *Exp. Fluids*, **11**, pp. 301–312.
- [20] Silber, G., 1986, "Eine Systematik nichtlokaler kelvinhafter Fluide vom Grade drei auf der Basis eines klassischen Kontinuumsmodelles," *VDI-Fortschrittsberichte, Reihe 18, Nr. 26*.
- [21] Silber, G., 1988, "Nichtlokal nichtpolar oder lokalpolar mit kinematischem Zwang?," *Mechanik-Beiträge zur Theorie und Anwendungen*, Universitäts-Bibliothek der TU-Berlin.
- [22] Silber, G., 1988, "Nonlocal Theories and Modelling of Fully Developed

Turbulence," *Mech. Res. Commun.*, **15**, pp. 199–203.

- [23] Alizadeh, M., 2001, Eine Randwertsystematik für Gradientenfluide vom Grade drei auf der Basis von Porositätensoren, Universitäts-Bibliothek der TU-Berlin, Ph.D. dissertation.
- [24] Alexandru, C., 1989, "Systematik nichtlokaler kelvinhafter Fluide vom Grade zwei auf der Basis eines Cosserat Kontinuummodelles," VDI-Fortschrittsberichte, Reihe 18/Nr. 61, VDI Verlag Düsseldorf.
- [25] Moosaie, A., and Atefi, Gh., 2005, "An Analytical Approach to Turbulent Flow Through Smooth Pipes," 3rd WSEAS/IASME Int. Conf. on Fluid Mechanics and Aerodynamics, Corfu, Greece, Aug. 20–22, pp. 273–277.
- [26] Eringen, C. A., 2005, "On a Rational Theory of Turbulence," *Int. J. Eng. Sci.*, **43**, pp. 209–221.
- [27] Tillmark, N., and Alfredsson, P. H., 1992, "Experiments on Transition in Plane Couette Flow," *J. Fluid Mech.*, **235**, pp. 89–102.

Interested in Cavitation Erosion?

ASTM's Subcommittee G02.10 on Erosion would like to hear from you if you have any interest in cavitation erosion testing. Do you (or your organization):

- Use (or have used) ASTM Method G 32 for cavitation erosion testing?
- Use (or have used) any other cavitation erosion, or liquid impingement erosion, test method? (For example, ASTM G 73 or G 134.)
- Have any concern with cavitation erosion as a field problem or research topic?

If any of above apply, please contact the following with a brief explanation:

Frank J. Heymann, task group chairman
25 Thornton Way # 205, Brunswick, ME 04011, USA
Email: marseah@gwi.net
Phone: 207-725-7073

The objective of this effort is to help us determine the degree of interest in, and importance of, cavitation erosion test methods at the present time. If you respond, we will send you a questionnaire and hope you will be willing to reply to that also!

Paul A. Swanson
Subcommittee G02.10 chairman